Which mechanisms rule the current flow across a nanostructure? We address in this thesis two aspects concerning this question. At first, we deal with a theory of electron transfer through a quantum system weakly coupled to metallic leads. The charge carriers can only be exchanged by tunnelling processes. Although the tunnelling probability decreases with the number of simultaneously tunnelling electrons, still such higher order processes are responsible for various remarkable effects. We reveal a new structuring within the transport theory, which eases numerical as well as analytical studies of these higher order events. In the second part of this work, we apply the theory to four different quantum-dot systems. A single-level quantum-dot and a double-quantum-dot system serve as simple models for the investigation of transport up to fourth order (simultaneous tunnelling of two electrons). Narrow graphene nanoribbons and thin carbon nanotubes require first a sophisticated theoretical description to determine their complex electronic spectra and eigenstates. In particular, the peculiar spin configurations of the eigenstates manifest themselves for both systems in specific phenomena in unpolarised as well as in spin-polarised transport with or without magnetic field.

Universitätsverlag Regensburg

ISBN 978-3-86845-045-3

gefördert von:

Alumni der physikalischen Fakultät der Universität Regensburg e.V.

Universität Regensburg

Dissertationsreihe Physik - Band 10

Sonja Koller

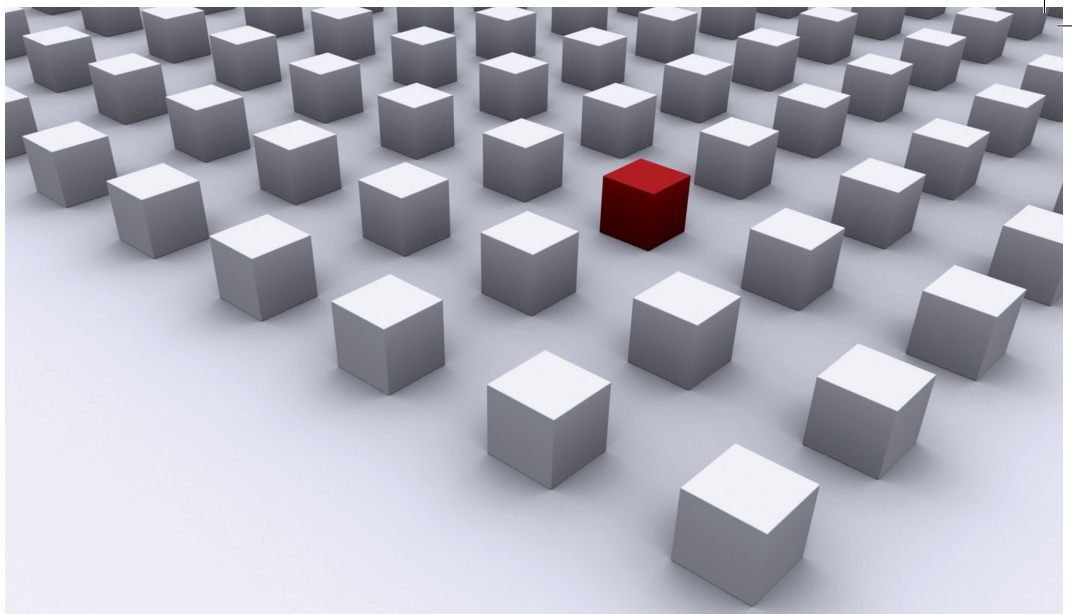

Sonja Koller

Spin phenomena and higher order effects in transport across interacting quantum-dots

Universitätsverlag Regensburg

10

Dissertationsreihe Physik

Sonja Koller

Spin phenomena and higher order effects in transport across interacting quantum-dots

Spin phenomena and higher order effects in transport across interacting quantum-dots

Dissertation zur Erlangung des Doktorgrades der Naturwissenschaften (Dr. rer. nat.)
der naturwissenschaftlichen Fakultät II - Physik der Universität Regensburg
vorgelegt von

Sonja Koller

aus Regensburg
September 2009

Die Arbeit wurde von Prof. Dr. Milena Grifoni angeleitet.
Das Promotionsgesuch wurde am 30.06.2009 eingereicht.
Das Kolloquium fand am 30.09.2009 statt.

Prüfungsausschuss:	Vorsitzender:	Prof. Dr. Franz Gießibl
	1. Gutachter:	Prof. Dr. Milena Grifoni
	2. Gutachter:	Prof. Dr. Christoph Strunk
	weiterer Prüfer:	Prof. Dr. Andreas Schäfer

Dissertationsreihe der Fakultät für Physik der Universität Regensburg, Band 10

Herausgegeben vom Präsidium des Alumnivereins der Physikalischen Fakultät:
Klaus Richter, Andreas Schäfer, Werner Wegscheider, Dieter Weiss

Sonja Koller

Spin phenomena and higher order effects in transport across interacting quantum-dots

Universitätsverlag Regensburg

Bibliografische Informationen der Deutschen Bibliothek.
Die Deutsche Bibliothek verzeichnet diese Publikation
in der Deutschen Nationalbibliografie. Detaillierte bibliografische Daten
sind im Internet über http://dnb.ddb.de abrufbar.

1. Auflage 2010

Leibnitzstraße 13, 93055 Regensburg

Konzeption: Thomas Geiger
Umschlagentwurf: Franz Stadler, Designcooperative Nittenau eG
Layout: Sonja Koller
Druck: Docupoint, Magdeburg
ISBN: 978-3-86845-045-3

Weitere Informationen zum Verlagsprogramm erhalten Sie unter:
www.univerlag-regensburg.de

Spin phenomena and higher order effects in transport across interacting quantum-dots

DISSERTATION ZUR ERLANGUNG DES DOKTORGRADES DER NATURWISSENSCHAFTEN (DR. RER. NAT.)
DER FAKULTÄT II - PHYSIK

DER UNIVERSITÄT REGENSBURG

vorgelegt von

Sonja Koller

aus

Regensburg

im Jahr 2009

Promotionsgesuch eingereicht am: 30.06.2009
Die Arbeit wurde angeleitet von: Prof. Dr. Milena Grifoni

Prüfungsausschuss:	Vorsitzender:	Prof. Dr. Franz Gießibl
	1. Gutachter:	Prof. Dr. Milena Grifoni
	2. Gutachter:	Prof. Dr. Christoph Strunk
	weiterer Prüfer:	Prof. Dr. Andreas Schäfer

Contents

INTRODUCTION

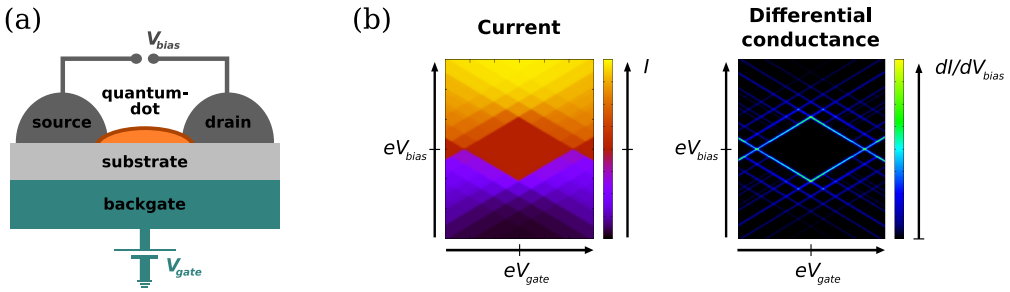

Figure 1: (a) Typical measurement circuit for transport across a quantum-dot. (b) Left: Exemplary dependence of the current on the bias and gate voltage. Right: In a stability diagram, the differential conductance $\mathrm{d}I/\mathrm{d}V_{\mathrm{bias}}$ is plotted versus bias and gate voltage.

In December 1947, the world saw the first version of the device the digital age is founded on: the transistor [1]. Nine years later, John Bardeen, Walter Brattain and William Shockley were awarded the Nobel prize for the famous invention, allowing to control high power current flows in an output circuit by a low power signal current in an input circuit. Since then, these all-electrical switches have revolutionised communication industry [2], thanks to ongoing minimisation and optimisation of transistor devices. In April 2008, the University of Manchester announced [3] the fabrication of "the world's smallest transistor" by the group of Kostya Novoselov and Andre Geim, with one atom in thickness and ten atoms in width, several thousand times smaller than the exemplar presented sixty-one years earlier.

Crucially, however, once the system size compares or falls below the phase coherence length of the intrinsic charge carriers, those start to feel that they live in a confined object, a so-called *quantum-dot* [4, 5, 6]. The experimental progress in fabrication of such ultra-small electrical devices has made them one of the standard components in fundamental as well as application oriented research. Apart from coherence phenomena, upon shrinking in dimension different types of scattering processes can gain an important role: While impurity scattering is excluded in *ballistic* (defect-free) quantum-dots, there remains the scattering at the boundaries and between quasi-particles, in particular Coulomb induced repulsion among the charge carriers. A necessary condition for the relevance of the latter is a *weak coupling* between quantum-dot and 'the outer world', such that particles cannot freely enter or escape from the system. In this thesis, we focus, as sketched in Fig. 1(a), on gate controlled transport across weakly coupled ballistic quantum-dots. 'The outer world' is formed by two electronic reservoirs, the

source and drain lead, which can exchange electrons with the quantum-dot via a sufficiently large tunnelling barrier. A source-drain voltage V_{bias} is applied in order to drive a current across the device, while via the gate voltage V_{gate} the number of electrons on the device is moderated capacitively.
Experimentally, the actual preparation of the setup strongly depends on the type of quantum-dot studied. Semiconducting heterostructures can directly be grown on a waver by epitaxy. Carbon allotropes as nanotubes (formed by settling out of sublimated carbon) or graphene (obtained by cleaving of natural graphite flakes) have to be deposited on the oxidised surface of a waver, which might previously be prepared to serve as a back-gate. Metallic contacts and, in case, side gate structures can be realized by electron-beam lithography. The wavers have to be broken down into slices with some millimetres edge length in order to fit on a chip carrier. Thus, different samples can easily be mounted on measurement instruments and tested at temperatures ranging typically from 4.2 K in a standard liquid helium bath, down to 20 mK in dilution cryostates.

Nowadays, high-resolution transport measurements in the low temperature regime have reached a high degree of sophistication and reveal data dominated by complex many-body phenomena [7, 8, 9]. Thereby, the observed effects strongly depend on the transparency of the tunnelling barrier.

In the limit of extremely weak coupling, only single electrons can be transferred sequentially onto or out of the dot [4, 10] [single electron/sequential tunnelling, Fig. 2, leftmost]. Fig. 1(b) shows an example for a typical current characteristic (left) and the resulting *stability diagram* (right) for this case. The stability diagram encodes in colour the differential conductance $\mathrm{d}I/\mathrm{d}V_{\mathsf{bias}}$, measured versus gate and bias voltage. The lines mark thus changes in the current I. Central to the plots is a *Coulomb blockade diamond*, where the quantum-dot is populated with a fixed electron number, and the current flow is widely blocked [red region in the middle of Fig. 1(b), left]. The diamond shape can be explained in simple terms upon assuming that quantum-dot and gate form a capacitor with charging energy E_c: Let the gate voltage be adjusted such that the dot is charged with N electrons, and source (s) and drain (d) contact be biased with voltages $V_{s/d} = \pm V_{\mathsf{bias}}/2$. An N+1st electron can now only enter the dot when the energy gain for leaving the positively biased lead is higher than an energy cost E_c demanded for putting an additional charge onto the dot. In turn, due to the gate potential, the Nth electron also cannot leave the quantum-dot unless putting it into the negatively biased electrode brings more energy than must be paid for removing the charge from the dot. This translates into respective energy conditions for transport ($-e$ is the electron charge)

$$\frac{1}{2}E_c\left((N\pm1)^2-N^2\right)-eV_{\mathsf{gate}}\left((N\pm1)-N\right)=E_c\left(\pm N+\frac{1}{2}\right)\mp eV_{\mathsf{gate}}\overset{!}{<}e\frac{|V_{\mathsf{bias}}|}{2},$$

or equivalently

$$\frac{E_c}{2}\overset{!}{<}e\frac{|V_{\mathsf{bias}}|}{2}+\left|eV_{\mathsf{gate}}-E_cN\right|.$$

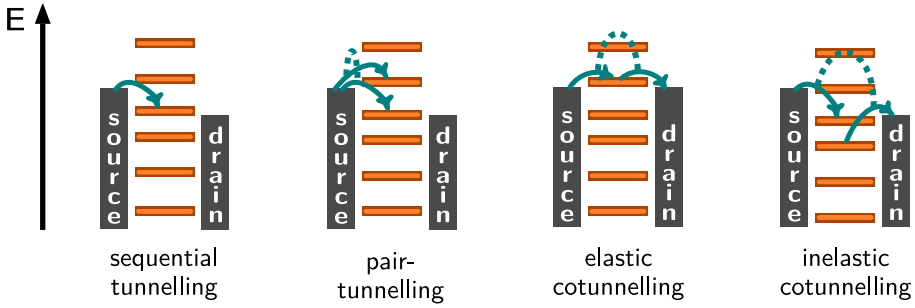

Figure 2: Exemplary sketch of a one-electron and of correlated two-electron processes. The height difference between the gray blocks symbolising the source and drain electrodes reflects the applied bias voltage eV_{bias}. The orange lines mark the energy cost for populating a certain level of the quantum-dot. The green arrows denote tunnelling of a single electron onto or out of the quantum-dot, whereas dashed connections indicate a correlation between two such events.

At $eV_{\text{gate}} = E_c N$, we reside in the middle of the Coulomb diamond, where a maximum value $|eV_{\text{bias}}| = E_c$ of the bias voltage of is required to let current flow. Raising/lowering the gate voltage, the value of $|eV_{\text{bias}}|$ necessary for adding/removing an electron shrinks linearly. Thus the typical shape arises.
While this Coulomb blockade is a *universal* feature, i.e. observable for any interacting quantum-dot device, the positions of the additional lines in the stability diagram Fig. 1(b) are specific to the spectrum of the studied nanostructure. Their intensity is ruled by the tunnelling properties of the involved eigenstates, and these properties are not purely determined intrinsically, but also dependent on parameters concerning the coupling to the contacts. In particular, the spin of electrons, in connection with a contact magnetisation, can be source of rich phenomena. Since the discovery of the giant magneto-resistance[1] in 1988, the field of spintronics has been exploring possibilities to make use not only of the charge, but also of the electrons' spin degree of freedom, and hence both universal, but also strongly system specific spin effects in quantum-dots are always of particular interest.

In the contrary limit of extremely high coupling, Coulomb interactions loose their importance as the quantum-dot can now freely exchange particles with the electronic reservoirs. In this regime, Green's function based methods allow a description of electron transport non-perturbative in the tunnelling coupling. The conductance as a function of the gate voltage exhibits irregular, but reproducible mesoscopic fluctuations determined by interference of coherent electron wave packets, which scatter at impurities or at the system boundaries [5].

As already anticipated, the focus of thesis is set far from that latter limit. We are going to fully account for electron interactions on the quantum-dot, while assuming

[1] The 2007 Nobel laureates Albert Fert [11] and Peter Grünberg [12] demonstrated – in independent experiments – control of conductivity in certain structured materials via an external magnetic field, relying on a blocked transmission of electrons across anti-parallel magnetised layers.

values of the tunnelling coupling small enough to justify a perturbative treatment in the related parameter. However, we will not restrict to sequential tunnelling, which corresponds to the lowest order of the perturbation theory, but also allow for coherent processes involving up to two electrons.
Among those events, the probably most prominent one is *cotunnelling* (Fig. 2, rightmost and second to right), theoretically studied and experimentally observed in numerous works: While one electron enters the dot from the source, another electron leaves to the drain, resulting in a net transfer of a single charge. If the energy gained thereby ($= eV_{\mathsf{bias}}$) is high enough, the quantum-dot can be left in an excited state, a process called inelastic cotunnelling.
Another possibility is *electron pair-tunnelling* (Fig. 2, second to left) [13]: two electrons enter (or leave) the dot simultaneously from (or to) the same electrode.
Also comprised are all kinds of *charge fluctuations* during a single electron tunnelling process, yielding a correction to that sequential tunnelling event. However, to reproduce related, experimentally observed level renormalisation effects [14, 15, 16] , inclusion of such terms in *all* orders of the tunnelling coupling is required (we give an outlook to this towards the end of the thesis).
Due to its famousness, a last phenomenon which should be mentioned at this place is the Kondo effect [17, 18]. Though we lay in the following the cornerstones for approaching the Kondo regime, the effect itself cannot be reproduced in the framework of this thesis, as the underlying process involves *three* correlated electrons.

The work at hand splits into two parts, presenting both an approach to the transport problem and its application to specific quantum-dot systems, where a focus is on spin effects.

The first part forms the theoretical transport core of the thesis.
In Sect. 1 we explain how to set up an equation of motion which is exact up to fourth order in the tunnelling coupling to the leads and thus covers a description of single electron and correlated two electron tunnelling processes, referred as *second* and *fourth order* transport, respectively. In Sect. 2 the arising terms are visualised in form of diagrams and a closer examination of those results in a classification which has not been described so far and brings advantage from the numerical, analytical and interpretational point of view. Importantly, the presented theory is valid on a very general level. It imposes normal conducting metals for the electronic reservoirs, but does not specify the type of quantum-dot studied. The eigenstates and spectrum of this system enter the transport equations as input parameters.

In the second part we investigate, applying our theoretical concepts, spin phenomena and higher order effects in transport across two classes of systems:
In Sect. 3 we study minimal models for an interacting quantum single- and double-dot. The former is minimally described by an isolated level with Coulomb interaction, while for the latter two such levels are assumed to be coupled, permitting a hopping of electrons and leading to the distinction of on-site and inter-site Coulomb interactions.

In the focus of Sect. 4 and Sect. 5 are two kinds of metallic quasi one-dimensional carbon based structures, armchair nanoribbons (Sect. 4) and single wall armchair nanotubes (Sect. 5), respectively. For both these systems, short-ranged electron-electron interactions gain crucial importance on scaling down in dimension, i.e. with shrinking width of a ribbon, respectively with shrinking diameter of a tube. The impact on carbon armchair nanoribbons has not been discussed before and is investigated within this thesis.

Various evaluations too lengthy to appear in the main part of the thesis have been moved to the appendices App. A and App. B. While the former belongs to the transport theoretical part, Sects. 1-2, the latter holds calculations related to the low energy description of carbon armchair nanoribbons, Sect. 4.

THEORY:

TRANSPORT ACROSS QUANTUM-DOTS

This first part of the thesis is dedicated to an analysis of the generalised *fourth order* quantum master equation, which accounts for electron transfer across quantum-dots up to fourth order in the tunnelling coupling, i.e., includes all tunnelling processes involving one or two electrons.
A compact introduction to this theory is provided in Sect. 1, where we briefly review notations, present our model and derive the basic equations. Founding on these preparations, Sect. 2 shows the explicit connection to the diagrammatic representation [19] and exploits it for a thorough investigation of the fourth order contributions to the generalised master equation. Major insights are given by a so far unrecognised grouping of diagrams as discussed in Sect. 2.3. It allows to draw a relation to underlying physical processes as well as to T-matrix based rate approaches. Further, it leads to improvements in the KinEq [20] project, which offers a numerical implementation of the theory addressed here.

The contents of Sects. 1-2 were worked out in collaboration with Martin Leijnse, Maarten Wegewijs and Milena Grifoni.

For the understanding of the transport properties of the miscellaneous quantum-dot systems discussed in the second part of this thesis, the theoretical background conveyed by Sect. 1 is sufficient.

1 Generalised fourth order quantum master equation

The standard approach to transport across a quantum-dot which is separated from the electronic reservoirs by large tunnelling barriers is provided by the Pauli-master equation [21, 22]. To calculate the occupations of the dot states, the resulting current and other transport quantities, it invokes rates calculated by Fermi's Golden rule to second order in the tunnelling coupling [21]. The validity of this technique is limited, as it does not take into account *coherences*: all non-diagonal element of a density matrix describing the dot are assumed to be zero. For more complex quantum-dots with degenerate states [23, 24, 25, 26, 27] and/or non-collinearly polarised magnetic electrodes [28, 29, 30, 31, 32], this is fatal as the non-diagonal density matrix elements give crucial contributions to the state occupations and can thus not be neglected. Instead, the solution of a *generalised master equation* for the full density matrix is required. Such an equation can be obtained by various different methods [33], whereas the relations among those are not always obvious.

In the following we provide a short formal introduction to the basics of a generalised master equation approach. We start in Sect. 1.1 with the model, defining the Hamiltonian, the *reduced density matrix* (RDM) describing the quantum-dot as part of the whole system as well as the time-evolution and transport *kernels*. Subsequently, in Sect. 1.2, the generalised fourth order quantum master equation for the time-evolution of the RDM is derived in iterative steps from the Liouville equation. Amendments to this can be found in App. A.1. Finally, Sect. 1.3 addresses the *secular approximation*. This concept is often applied in order to reduce the number of non-vanishing entries in a density matrix, as it sets to zero all coherences between non-degenerate states. Importantly, however, it turns out that in fourth order an inclusion of non-secular contributions is required.

1.1 Model and generalised master equation

The standard Hamilton operator of a quantum-dot system coupled to contacts reads

$$\hat{H}_{\mathsf{tot}} = \hat{H}_{\odot} + \hat{H}_T + \hat{H}_R \,. \tag{1}$$

The Hamiltonian

$$\hat{H}_R = \sum_{l=s,d} \sum_{\sigma} \sum_{q} \left(\epsilon_q - \mu_l\right) \hat{c}^{\dagger}_{l\sigma q} \hat{c}_{l\sigma q}$$

models the reservoirs, i.e., the source and the drain contact; the operator $\hat{c}_{l\sigma q}$ annihilates a quasi-particle in a state q with kinetic energy ϵ_q in the source ($l = s$) or drain lead ($l = d$), where σ denotes the spin degree of freedom. The source respectively drain voltage $V_{s/d} = \pm V_{\mathsf{bias}}/2$ is included in μ_l, which is the chemical potential for electrons in lead l with spin σ. The tunnelling Hamiltonian,

$$\hat{H}_T = \sum_{l} \hat{H}_{Tl} \equiv \sum_{l} \sum_{m\sigma q} \left(T_{lmq}\, \hat{d}^{\dagger}_{m\sigma} \hat{c}_{l\sigma q} + T^{*}_{lmq}\, \hat{c}^{\dagger}_{l\sigma q} \hat{d}_{m\sigma} \right) , \tag{2}$$

characterises the coupling between the quantum-dot and the leads. The first term describes tunnelling into, the second term tunnelling out of the quantum-dot. The condition for weak coupling is that the linewidth $\hbar\Gamma$, which scales with the squares $|T_{lmq}|^2$ of the tunnelling coefficients, is small compared to the thermal energy k_BT.
Finally, the Hamiltonian $\hat{H}_\odot$ stands for the central part of the system, the quantum-dot. It already includes the effect of the gate voltage:

$$\hat{H}_\odot = \hat{H}_\odot^{(0)} - e\alpha V_{\mathsf{gate}}\hat{\mathcal{N}}_c, \tag{3}$$

with $\hat{\mathcal{N}}_c := \sum_\sigma \hat{d}^\dagger_{m\sigma}\hat{d}_{m\sigma}$ denoting the particle counting operator on the dot, $\hat{H}_\odot^{(0)}$ the Hamiltonian of the isolated quantum-dot, and a dimensionless conversion factor α incorporating the complexity (influence of source and drain electrodes, dielectricity of the substrate, etc.) of the whole setup.
Under the assumption that the coupling to the leads is weak, it is convenient to split $\hat{H}_{\mathsf{tot}}$ in a main part $\hat{H}_0 = \hat{H}_\odot + \hat{H}_R$ plus the perturbation $\hat{H}_I = \hat{H}_T$.

The object we are finally interested in is the reduced density matrix [34] (RDM),

$$\hat{\rho}_\odot(t) = \mathsf{Tr}_R\left\{\hat{\rho}_{\mathsf{tot}}(t)\right\}, \tag{4}$$

which describes the state of the quantum-dot in the presence of the leads, which are traced out of the total density matrix $\hat{\rho}_{\mathsf{tot}}$, as prescribed by Tr_R. All relevant information required to calculate observables of the total system – as e.g. the current across the device – is thus contained in the RDM. Before the interaction $\hat{H}_T$ is switched on at time $t = t_0$, the system is unperturbed and the total density matrix $\hat{\rho}_{\mathsf{tot}}$ is the direct product of the (arbitrary) initial state $\hat{\rho}_\odot(t_0)$ of the quantum-dot and the equilibrium state $\hat{\rho}_R$ of the leads. Afterwards, i.e. for times $t > t_0$, correlations, which are of the order of the tunnelling coupling [34], build up between leads and quantum-dot, causing $\hat{\rho}_{\mathsf{tot}}(t)$ to deviate from the factorised form:

$$\begin{aligned}\hat{\rho}_{\mathsf{tot}}(t) &= e^{-\frac{\mathrm{i}}{\hbar}\hat{H}_{\mathsf{tot}}(t-t_0)}\hat{\rho}_{\mathsf{tot}}(t_0)e^{\frac{\mathrm{i}}{\hbar}\hat{H}_{\mathsf{tot}}(t-t_0)} \\ &= e^{-\hat{Z}}e^{-\frac{\mathrm{i}}{\hbar}\hat{H}_I(t-t_0)}\; e^{-\frac{\mathrm{i}}{\hbar}\hat{H}_0(t-t_0)}\;\hat{\rho}_\odot(t_0)\hat{\rho}_R\; e^{\frac{\mathrm{i}}{\hbar}\hat{H}_0(t-t_0)}\, e^{\frac{\mathrm{i}}{\hbar}\hat{H}_I(t-t_0)}e^{\hat{Z}} \\ &= \hat{\rho}_\odot(t)\hat{\rho}_R(t) + \theta(t-t_0)\,\mathcal{O}(\hat{H}_I).\end{aligned} \tag{5}$$

Here, $\hat{Z}$ emerges from the Baker-Campbell-Hausdorff/Zassenhaus relation and contains commutators involving both $\hat{H}_0$ and $\hat{H}_I$. Therefore the last equality is certainly justified. In the following we will always set $\hat{\rho}_R(t) \equiv \hat{\rho}_R$, because each lead is assumed to be in contact with a larger bath of constant temperature and chemical potential and thus stays in thermal equilibrium all the time.

A crucial point is a consistent calculation of the correlations between leads and quantum-dot. There are several ways to obtain an equation of motion (also called kinetic equation) for the time evolution of the RDM, and both the derivation we present in Sect. 1.2 as well as the well-known Nakajima-Zwanzig projection operator technique [35, 36, 37, 38] which is shortly revised in Sect. A.1.3 account for these correlations by explicitly solving for the deviation from the factorised state. In contrast,

a real-time approach, famous for its diagrammatic representation [39, 40, 19], incorporates them automatically by directly integrating out the leads for times $t > t_0$, as sketched in Sect. A.1.4. All these methods, when consistently applied, are perfectly equivalent [41], leading to the same *time-nonlocal*[2] *generalised quantum master equation* for the RDM, in the form:

$$\dot{\hat{\rho}}_\odot(t) = -\frac{\mathrm{i}}{\hbar}\left[\hat{H}_0, \hat{\rho}_\odot(t)\right] + \int_{t_0}^{t} \mathrm{d}t'\ \hat{\mathcal{K}}(t-t')\hat{\rho}_\odot(t'). \tag{6}$$

Here, the first term accounts for the time evolution due to the local dynamics of the quantum-dot. In the second term, the *time evolution kernel* $\hat{\mathcal{K}}(t-t')$ is a superoperator acting on the density matrix operator. Convoluted in time with $\hat{\rho}_\odot(t')$, it gives that part of the time evolution which is generated by the tunnelling.
We are interested in the steady state limit $t_0 \to -\infty$ and $\dot{\hat{\rho}}_\odot(t) = 0\ \forall t$, where the density matrix has become time independent: $\lim_{t\to\infty} \hat{\rho}_\odot(t) = \hat{\rho}_\odot^\infty = \lim_{\lambda\to 0} \lambda\hat{\rho}_\odot(\lambda)$. In this limit, Eq. (6) yields

$$\lim_{t\to\infty} \dot{\hat{\rho}}_\odot(t) = 0 = -\frac{\mathrm{i}}{\hbar}\left[\hat{H}_0, \hat{\rho}_\odot^\infty\right] + \lim_{\lambda\to 0} \lambda\hat{K}(\lambda)\hat{\rho}_\odot(\lambda) = -\frac{\mathrm{i}}{\hbar}\left[\hat{H}_0, \hat{\rho}_\odot^\infty\right] + \hat{K}(\lambda=0)\hat{\rho}_\odot^\infty, \tag{7}$$

where $\hat{K}(\lambda) = \int_0^\infty \mathrm{d}\tau\ e^{-\lambda\tau}\,\hat{\mathcal{K}}(\tau)$ is the Laplace transform of the time evolution kernel $\hat{\mathcal{K}}(\tau)$. Taking matrix elements with respect to $\hat{H}_\odot$, we obtain from Eq. (6) a set of linear coupled equations for all states a, a' of the RDM:

$$\lim_{t\to\infty} \left(\dot{\hat{\rho}}_\odot(t)\right)_{bb'} = 0_{bb'} = -\frac{\mathrm{i}}{\hbar}\sum_{aa'} \delta_{ab}\,\delta_{a'b'}\,(E_a - E_{a'})\,\rho_{aa'} + \sum_{aa'} K_{bb'}^{aa'}\,\rho_{aa'}, \tag{8}$$

with $K_{bb'}^{aa'} := \langle b|\,\hat{K}[\,|a\rangle\langle a'|\,]\,|b'\rangle$, where we use square brackets to make clear that the kernel superoperator must first act on the density operator $\hat{\rho}_\odot^\infty =: \sum_{aa'} \rho_{aa'}|a\rangle\langle a'|$, and then the elements of the resulting matrix are taken. Throughout this work we use the convention that whenever such square brackets are omitted, it implies that a superoperator is just to be applied to all objects to its right.
Each diagonal element of the RDM reflects the probability of finding the system in a certain state. Thus, the normalisation condition

$$\sum_a \rho_{aa} = 1. \tag{9}$$

must be fulfilled and is indeed preserved by the kinetic equation. The restriction Eq. (9) is actually required to solve the system of linear equations obtained from Eq. (8), because they are under-determined due to the existence of the sum-rule

$$\sum_b K_{bb}^{aa'} = 0 \quad \forall\, a, a'. \tag{10}$$

[2] App. A.1.1 provides some information on a *time-local* quantum master equation.

The demand of Eq. (10) holds for arbitrary a, a' and hence in particular for $a = a'$, where it guarantees that gain and loss of probability are balanced in the stationary state. In Sect. 2.3, gain and loss relations for the fourth order will be a key ingredient for physical classification and grouping of terms.

The expectation value of any non-local observable can be expressed in a form similar to Eq. (6). In particular, we can write the current through lead l as

$$I_l(t) = \mathsf{Tr}_{\mathsf{tot}}\left\{\hat{I}_l\hat{\rho}_{\mathsf{tot}}(t)\right\} = \mathsf{Tr}_{\odot}\int_{t_0}^{t}\mathrm{d}t'\;\hat{\mathcal{K}}_{I_l}(t-t')\hat{\rho}_{\odot}(t'), \tag{11}$$

with $\hat{\mathcal{K}}_{I_l}$ the kernel associated to the current operator

$$\hat{I}_l = -\mathrm{i}\,\frac{e}{\hbar}\left[\hat{H}_{Tl}, \hat{\mathcal{N}}_l\right] = -\mathrm{i}\,\frac{e}{\hbar}\sum_{m\sigma q}\left(T_{lmq}\hat{d}^{\dagger}_{m\sigma}\hat{c}_{l\sigma q} - T^{*}_{lmq}\hat{c}^{\dagger}_{l\sigma q}\hat{d}_{m\sigma}\right)\,. \tag{12}$$

Here, $\hat{\mathcal{N}}_l = \sum_{\sigma q}\hat{c}^{\dagger}_{l\sigma q}\hat{c}_{l\sigma q}$ is the number operator in lead l and $I_l(t)$ describes the net particle current flowing out of lead l (i.e. the number of electrons leaving lead l per unit time). Taking the steady state limit of Eq. (11), the DC current is given by the zero-frequency component $\hat{K}_{I_l} := \hat{K}_{I_l}(\lambda = 0)$ of the Laplace transform of the current kernel and the stationary density matrix $\hat{\rho}^{\infty}_{\odot}$:

$$\lim_{t\to\infty} I_l(t) = \mathsf{Tr}_{\odot}\left\{\hat{K}_{I_l}(\lambda = 0)\hat{\rho}^{\infty}_{\odot}\right\} = \sum_{aa'}\sum_{b}(\hat{K}_{I_l})^{aa'}_{bb}\,\rho_{aa'}. \tag{13}$$

We will now shortly address how to explicitly derive Eq. (6) and Eq. (11) with the related time evolution and current kernels up to fourth order in the tunnelling coupling. We thereby employ an iterative procedure in the time domain [42, 43, 44]. Two previously mentioned alternative methods, namely the Nakajima-Zwanzig projection operator technique and the real-time approach, can be found in appendices Sect. A.1.3 and Sect. A.1.4, respectively.

1.2 Derivation of the fourth order quantum master equation

For the derivation of the generalised master equation, no other ingredient is needed than the Liouville equation for the total density matrix $\hat{\rho}_{\mathsf{tot}}$ in the interaction picture [34]:

$$\dot{\hat{\rho}}^{I}_{\mathsf{tot}}(t) = -\mathrm{i}\,\hat{\mathcal{L}}^{I}_{T}(t)\hat{\rho}^{I}_{\mathsf{tot}}(t), \tag{14}$$

where we have introduced a *Liouville superoperator* by the abbreviation

$$\hat{\mathcal{L}}^{I}_{T}(t)\hat{\mathrm{X}}^{I} := \frac{1}{\hbar}\left[\hat{H}^{I}_{T}(t), \hat{\mathrm{X}}^{I}\right]\,, \tag{15}$$

with $\hat{\mathrm{X}}^{I}$ in general an arbitrary product of time-dependent operators and $\hat{H}^{I}_{T}(t)$ the tunnelling Hamiltonian Eq. (2) in the interaction picture. Here,

$$\hat{B}^{I}(t) = e^{+\frac{\mathrm{i}}{\hbar}\hat{H}_0 t}\,\hat{B}\,e^{-\frac{\mathrm{i}}{\hbar}\hat{H}_0 t}\,, \quad |n(t)\rangle_I = e^{+\frac{\mathrm{i}}{\hbar}\hat{H}_0 t}\,|n(t)\rangle = e^{-\frac{\mathrm{i}}{\hbar}\hat{H}_I t}\,|n(0)\rangle\,,$$

if $\hat{B}$ is an operator and $|n(t)\rangle$ a state in the Schrödinger picture.
The method to be applied now [45] is the same as normally invoked to derive the second order quantum master equation [34]: Eq. (14) has to be integrated and reinserted into itself to obtain the expression

$$\dot{\hat{\rho}}^I_{\mathsf{tot}}(t) = -\mathrm{i}\,\hat{\mathcal{L}}^I_T(t)\hat{\rho}^I_{\mathsf{tot}}(t_0) - \int_{t_0}^{t} \mathrm{d}\tau\ \hat{\mathcal{L}}^I_T(t)\hat{\mathcal{L}}^I_T(\tau)\hat{\rho}^I_{\mathsf{tot}}(\tau). \tag{16}$$

As we are interested in an equation to fourth order in the tunnelling coupling, we do not stop at this stage but repeat the iteration steps: we transform Eq. (16) to an integral equation,

$$\hat{\rho}^I_{\mathsf{tot}}(t) = \hat{\rho}^I_{\mathsf{tot}}(t_0) - \mathrm{i}\int_{t_0}^{t} \mathrm{d}\tau\ \hat{\mathcal{L}}^I_T(\tau)\hat{\rho}^I_{\mathsf{tot}}(t_0) - \int_{t_0}^{t}\mathrm{d}\tau_1 \int_{t_0}^{\tau_1} \mathrm{d}\tau\ \hat{\mathcal{L}}^I_T(\tau_1)\hat{\mathcal{L}}^I_T(\tau)\hat{\rho}^I_{\mathsf{tot}}(\tau), \tag{17}$$

which is once more reinserted into Eq. (14). After integration of the such obtained equation for $\hat{\rho}^I_{\mathsf{tot}}$, one arrives at

$$\begin{aligned}\hat{\rho}^I_{\mathsf{tot}}(t) = \hat{\rho}^I_{\mathsf{tot}}(t_0) - \mathrm{i}\int_{t_0}^{t} \mathrm{d}\tau\ \hat{\mathcal{L}}^I_T(\tau)\hat{\rho}^I_{\mathsf{tot}}(t_0) - \int_{t_0}^{t}\mathrm{d}\tau_1 \int_{t_0}^{\tau_1} \mathrm{d}\tau\ \hat{\mathcal{L}}^I_T(\tau_1)\hat{\mathcal{L}}^I_T(\tau)\hat{\rho}^I_{\mathsf{tot}}(t_0) \\ + \mathrm{i}\int_{t_0}^{t}\mathrm{d}\tau_2 \int_{t_0}^{\tau_2}\mathrm{d}\tau_1 \int_{t_0}^{\tau_1} \mathrm{d}\tau\ \hat{\mathcal{L}}^I_T(\tau_2)\hat{\mathcal{L}}^I_T(\tau_1)\hat{\mathcal{L}}^I_T(\tau)\hat{\rho}^I_{\mathsf{tot}}(\tau).\end{aligned} \tag{18}$$

After a final back-insertion of Eq. (18) into the Liouville equation Eq. (14) we perform the trace over the leads in order to obtain the RDM. Thereby, terms involving in total an odd number of lead operators – which are contained linearly in $\hat{\mathcal{L}}^I_T$ – vanish. Due to the relations $\hat{\rho}^I_{\mathsf{tot}}(t_0) = \hat{\rho}^I_{\odot}(t_0)\hat{\rho}_R$ and with Eq. (5) we are thus allowed to write in fourth order perturbation:

$$\begin{aligned}\dot{\hat{\rho}}^I_{\odot}(t) = &-\int_{t_0}^{t}\mathrm{d}\tau_2\ \mathsf{Tr}_R\left\{\hat{\mathcal{L}}^I_T(t)\hat{\mathcal{L}}^I_T(\tau_2)\hat{\rho}^I_{\odot}(t_0)\hat{\rho}_R\right\} \\ &+\int_{t_0}^{t}\mathrm{d}\tau_2\int_{t_0}^{\tau_2}\mathrm{d}\tau_1\int_{t_0}^{\tau_1}\mathrm{d}\tau\ \mathsf{Tr}_R\left\{\hat{\mathcal{L}}^I_T(t)\hat{\mathcal{L}}^I_T(\tau_2)\hat{\mathcal{L}}^I_T(\tau_1)\hat{\mathcal{L}}^I_T(\tau)\hat{\rho}^I_{\odot}(\tau)\hat{\rho}_R\right\} + \mathcal{O}\left((\hat{\mathcal{L}}^I_T)^6\right).\end{aligned} \tag{19}$$

The second order contribution in Eq. (19) contains $\hat{\rho}^I_{\odot}(t_0)$ instead of $\hat{\rho}^I_{\odot}(\tau)$. This is not desirable, but can be healed easily. Setting the upper integration limit to τ_2 instead of t and taking the trace over the leads, from Eq. (17) follows:

$$\hat{\rho}^I_{\odot}(\tau_2) = \hat{\rho}^I_{\odot}(t_0) - \int_{t_0}^{\tau_2}\mathrm{d}\tau_1\int_{t_0}^{\tau_1}\mathrm{d}\tau\ \mathsf{Tr}_R\left\{\hat{\mathcal{L}}^I_T(\tau_1)\hat{\mathcal{L}}^I_T(\tau)\hat{\rho}^I_{\odot}(\tau)\hat{\rho}_R\right\} + \mathcal{O}\left((\hat{\mathcal{L}}^I_T)^4\right). \tag{20}$$

The time dependence on τ_2 is crucial to obtain a convolution form. In contrast, the dependence on t would lead to a *time-local* quantum master equation, as it is shortly discussed in App. A.1.1. Upon setting Eq. (20) into Eq. (19) in order to eliminate the

initial condition we arrive at the so-called *time-nonlocal* fourth order quantum master equation,

$$\begin{aligned}\dot{\hat{\rho}}^I_\odot(t) = &- \int_{t_0}^{t} \mathrm{d}\tau \; \mathsf{Tr}_R \left\{ \hat{\mathcal{L}}^I_T(t) \hat{\mathcal{L}}^I_T(\tau) \hat{\rho}^I_\odot(\tau) \hat{\rho}_R \right\} \\ &\text{(i)} + \int_{t_0}^{t} \mathrm{d}\tau_2 \int_{t_0}^{\tau_2} \mathrm{d}\tau_1 \int_{t_0}^{\tau_1} \mathrm{d}\tau \; \mathsf{Tr}_R \left\{ \hat{\mathcal{L}}^I_T(t) \hat{\mathcal{L}}^I_T(\tau_2) \hat{\mathcal{L}}^I_T(\tau_1) \hat{\mathcal{L}}^I_T(\tau) \hat{\rho}^I_\odot(\tau) \hat{\rho}_R \right\} \\ &\text{(ii)} - \int_{t_0}^{t} \mathrm{d}\tau_2 \int_{t_0}^{\tau_2} \mathrm{d}\tau_1 \int_{t_0}^{\tau_1} \mathrm{d}\tau \; \mathsf{Tr}_R \left\{ \hat{\mathcal{L}}^I_T(t) \hat{\mathcal{L}}^I_T(\tau_2) \, \mathsf{Tr}_R \left\{ \hat{\mathcal{L}}^I_T(\tau_1) \hat{\mathcal{L}}^I_T(\tau) \hat{\rho}^I_\odot(\tau) \hat{\rho}_R \right\} \hat{\rho}_R \right\} . \end{aligned} \tag{21}$$

The fourth order parts of this equation, (21(i)) and (21(ii)), have the following significance: from (21(i)) all possible fourth order contributions emerge, among them also *reducible* ones, which basically describe two sequential, but uncorrelated second order events. Those are already accounted for in the second order contribution and thus need to be excluded, which is indeed achieved by the subtraction (21(ii)). Notice that the Markov-approximation was neither needed for the derivation of Eq. (21), nor for the following reformulation.

If the nested integrations in Eq. (21) are rewritten according to

$$\int_{t_0}^{t} \mathrm{d}\tau_2 \int_{t_0}^{\tau_2} \mathrm{d}\tau_1 \int_{t_0}^{\tau_1} \mathrm{d}\tau \;\; \rightarrow \;\; \int_{t_0}^{t} \mathrm{d}\tau \int_{\tau}^{t} \mathrm{d}\tau_1 \int_{\tau_1}^{t} \mathrm{d}\tau_2 \, ,$$

we can introduce the kernel superoperator

$$\hat{\mathcal{K}}^I(t,\tau) := \hat{\mathcal{K}}^{I(2)}(t,\tau) + \int_{\tau}^{t} \mathrm{d}\tau_1 \int_{\tau_1}^{t} \mathrm{d}\tau_2 \; \hat{\mathcal{K}}^{I(4)}(t,\tau_2,\tau_1,\tau) \, , \tag{22a}$$

which absorbs all the Liouville operators via the definitions

$$\begin{aligned} \hat{\mathcal{K}}^{I(2)}(t,\tau)\hat{\mathrm{X}}^I &:= - \, \mathsf{Tr}_R \left\{ \hat{\mathcal{L}}^I_T(t) \hat{\mathcal{L}}^I_T(\tau) \hat{\mathrm{X}}^I \hat{\rho}_R \right\} , \\ \hat{\mathcal{K}}^{I(4)}(t,\tau_2,\tau_1,\tau)\hat{\mathrm{X}}^I &:= + \, \mathsf{Tr}_R \left\{ \hat{\mathcal{L}}^I_T(t) \hat{\mathcal{L}}^I_T(\tau_2) \hat{\mathcal{L}}^I_T(\tau_1) \hat{\mathcal{L}}^I_T(\tau) \hat{\mathrm{X}}^I \hat{\rho}_R \right\} \\ &\quad - \mathsf{Tr}_R \left\{ \hat{\mathcal{L}}^I_T(t) \hat{\mathcal{L}}^I_T(\tau_2) \mathsf{Tr}_R \left\{ \hat{\mathcal{L}}^I_T(\tau_1) \hat{\mathcal{L}}^I_T(\tau) \hat{\mathrm{X}}^I \hat{\rho}_R \right\} \hat{\rho}_R \right\} , \end{aligned} \tag{22b}$$

and allows to cast Eq. (21) in a compact form:

$$\dot{\hat{\rho}}^I_\odot(t) = \int_{t_0}^{t} \mathrm{d}\tau \; \hat{\mathcal{K}}^I(t,\tau) \hat{\rho}^I_\odot(\tau) \, . \tag{23}$$

While the equivalence with the Nakajima-Zwanzig technique, Sect. A.1.3, is obvious upon comparison of Eqs. (22a), (22b) to Eq. (111), the relation to the real-time approach, i.e. between Eqs. (22a), (22b) and Eq. (118), is perhaps not so perfectly

evident. The key difference between the two is related to Wick's theorem for the trace over the lead operators: in the real-time approach it has already been applied, allowing the reservoirs to be integrated out explicitly, at the earliest possible stage of the derivation of the fourth order master equation. In Eq. (21), however, as well as in the projection operator result Eq. (111), Wick's theorem has not yet been exploited: Line (i) of Eq. (21) will build all possible contractions, and then line (ii) cancels the ones which are reducible.

As the correct condition for the steady state of the quantum-dot is $\dot{\hat{\rho}}_\odot(t) = 0$, we still have to transform Eq. (23) to the Schrödinger picture, which is achieved with the relation

$$\dot{\hat{\rho}}^I_\odot(t) = e^{+\frac{\mathrm{i}}{\hbar}\hat{H}_0 t}\,\dot{\hat{\rho}}_\odot(t)\,e^{-\frac{\mathrm{i}}{\hbar}\hat{H}_0 t} + e^{+\frac{\mathrm{i}}{\hbar}\hat{H}_0 t}\frac{\mathrm{i}}{\hbar}\left[\hat{H}_0, \hat{\rho}_\odot(t)\right] e^{-\frac{\mathrm{i}}{\hbar}\hat{H}_0 t}.$$

We arrive then at the generalised master equation, as it was anticipated in Eq. (6), with the kernel superoperator

$$\begin{aligned}\hat{\mathcal{K}}(t-\tau)[\hat{\rho}_\odot(\tau)] = {} & e^{-\frac{\mathrm{i}}{\hbar}\hat{H}_0 t}\left(\hat{\mathcal{K}}^{I(2)}(t,\tau)[e^{+\frac{\mathrm{i}}{\hbar}\hat{H}_0\tau}\hat{\rho}_\odot(\tau)\,e^{-\frac{\mathrm{i}}{\hbar}\hat{H}_0\tau}]\right) e^{+\frac{\mathrm{i}}{\hbar}\hat{H}_0 t} \\ & + e^{-\frac{\mathrm{i}}{\hbar}\hat{H}_0 t}\left(\int_\tau^t \mathrm{d}\tau_1 \int_{\tau_1}^t \mathrm{d}\tau_2\;\; \hat{\mathcal{K}}^{I(4)}(t,\tau_2,\tau_1,\tau)[e^{+\frac{\mathrm{i}}{\hbar}\hat{H}_0\tau}\hat{\rho}_\odot(\tau)\,e^{-\frac{\mathrm{i}}{\hbar}\hat{H}_0\tau}]\right) e^{+\frac{\mathrm{i}}{\hbar}\hat{H}_0 t}. \quad (24)\end{aligned}$$

Square brackets were introduced here to point out on which quantities the kernel superoperators act. In fact the kernel in the Schrödinger picture depends merely on the time difference $t-\tau =: \tau'$, as it will further be clarified in Sect. 2.1 and App. A.2.2.

Current kernel With the knowledge gathered during the derivation of the time evolution kernel, we can come back now to the current formula Eq. (11), which can be equivalently formulated in the interaction picture as

$$I_l(t) = \mathsf{Tr}_{\mathsf{tot}}\left(\hat{I}^I_l(t)\hat{\rho}^I_{\mathsf{tot}}(t)\right) = \mathsf{Tr}_\odot \int_{t_0}^t \mathrm{d}\tau\;\hat{\mathcal{K}}^I_{I_l}(t,\tau)\hat{\rho}^I_\odot(\tau), \quad (25)$$

where it is clear that $\hat{I}^I_l(t)$ is the operator for electron loss from lead l:

$$\hat{I}^I_l(t) = -\frac{\mathrm{i}}{\hbar}\left[\hat{H}^I_{Tl}(t), \hat{\mathcal{N}}^I_l(t)\right] = -\mathrm{i}\,\hat{\mathcal{L}}^I_T(t)\hat{\mathcal{N}}^I_l(t) \overset{(\blacklozenge)}{=} -\dot{\hat{\mathcal{N}}}^I_l(t).$$

We know from Eq. (12) that the current operator $\hat{I}_l(t)$ differs, besides a prefactor, from $\hat{H}_{Tl}$ only in the fact that the part related to out-tunnelling from the quantum-dot has to be counted negative. In particular, it is also of first order in the tunnelling coupling. Thus, to evaluate a DC current which is correct up to fourth order, we have to use in the first equality of Eq. (25) the total density matrix $\hat{\rho}^I_{\mathsf{tot}}(t)$ in its (exact) representation Eq. (18). When it is inserted into Eq. (25), the contributions involving

$(\blacklozenge)$ Here we deal with the time evolution of an *operator* in the interaction picture, while the density matrix evolves according to a state, Eq. (14).

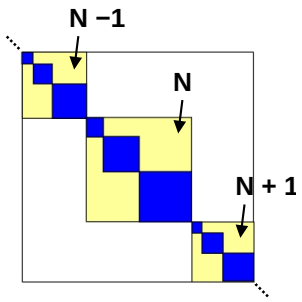

Figure 3: Under the assumption that the dot is always in a state with defined electron number, the reduced density matrix splits into blocks belonging to fixed charge N.

zero and two Liouville operators drop immediately, as they yield in the product with $\hat{I}_l^I(t)$ an odd number of lead operators under the trace. The highest order term in Eq. (18) can remain as it is, while in the one containing the single Liouville operator, $\hat{\rho}(t_0)$ has to be replaced with help of Eq. (20). This results in

$$\begin{aligned} I_l(t) = &- \mathrm{i}\,\mathsf{Tr}_\odot \int_{t_0}^{t} \mathrm{d}\tau\ \mathsf{Tr}_R \left\{ \hat{I}_l^I(t) \hat{\mathcal{L}}_T^I(\tau) \hat{\rho}_\odot^I(\tau) \hat{\rho}_R \right\} \\ &+ \mathrm{i}\,\mathsf{Tr}_\odot \int_{t_0}^{t} \mathrm{d}\tau_2 \int_{t_0}^{\tau_2} \mathrm{d}\tau_1 \int_{t_0}^{\tau_1} \mathrm{d}\tau\ \mathsf{Tr}_R \left\{ \hat{I}_l^I(t) \hat{\mathcal{L}}_T^I(\tau_2) \hat{\mathcal{L}}_T^I(\tau_1) \hat{\mathcal{L}}_T^I(\tau) \hat{\rho}_\odot^I(\tau) \hat{\rho}_R \right\} \\ &- \mathrm{i}\,\mathsf{Tr}_\odot \int_{t_0}^{t} \mathrm{d}\tau_2 \int_{t_0}^{\tau_2} \mathrm{d}\tau_1 \int_{t_0}^{\tau_1} \mathrm{d}\tau\ \mathsf{Tr}_R \left\{ \hat{I}_l^I(t) \hat{\mathcal{L}}_T^I(\tau_2)\, \mathsf{Tr}_R \left\{ \hat{\mathcal{L}}_T^I(\tau_1) \hat{\mathcal{L}}_T^I(\tau) \hat{\rho}_\odot^I(\tau) \hat{\rho}_R \right\} \hat{\rho}_R \right\} . \end{aligned} \tag{26}$$

Upon comparison with Eq. (21) it is obvious that current kernel $\hat{\mathcal{K}}_{I_l}^I(t,\tau)$ employed in Eq. (25) differs, besides the i as prefactor, from the time evolution kernel $\hat{\mathcal{K}}^I(t,\tau)$, Eq. (22a), just in the fact the Liouvillian $\hat{\mathcal{L}}_T^I(t)$ is to be substituted by $\hat{I}_l^I(t)$. This will be of importance for the diagrammatic analysis in Sect. 2.1.

1.3 The role of coherences

Including the full set of emerging second and fourth order contributions, Eq. (26) provides together with Eq. (21) for any gate and bias voltage the correct non divergent second and fourth order solution for the current across a quantum-dot. But due to the fact that a system which lives in an l-dimensional Hilbert space is in general described by a $l \times l$ density matrix, this comes at the price of calculating a time evolution kernel of dimension l^4, which means a rather drastic numerical effort even for systems with a moderate number of states.

Fortunately, for most actual problems there exist *selection rules* which allow to set to zero certain elements of the density matrix from the beginning: Whenever two states

a and a' of the system differ by some quantum number which is conserved in the *total* system (including the reservoirs), a coherence can be excluded, i.e. for the related element of the RDM it holds $\langle a|\hat{\rho}_{\odot}^{\infty}|a'\rangle = \rho_{aa'} = 0$. Throughout this work, only one of such selection rules is postulated a priori: the conservation of total charge[3]. As a consequence, the RDM acquires a block matrix form, as depicted in Fig. 3.
Additionally, very commonly coherences between non-degenerate states are neglected with the statement that they correspond to rapidly oscillating terms [34]. However, as was shown in [47], it is only valid to apply this so-called *secular approximation* to the terms containing the *highest* considered order in the perturbation expansion. The reason is that in fact non-secular contributions produce corrections of the order of the linewidth $\hbar\Gamma$ (as introduced in Sect. 1.1, this quantity scales with the squares $|T_{lmq}|^2$ of the tunnelling coefficients and the condition for weak coupling is $\hbar\Gamma \ll k_B T$).
Expanding and generalising the discussion in [47], we show now that nevertheless there exists a way to effectively eliminate density matrix elements between non-degenerate states.

We start by splitting the density matrix into two parts,

$$\hat{\rho}_{\odot}^{\infty} =: \begin{pmatrix} \hat{\rho}_s \\ \hat{\rho}_n \end{pmatrix},$$

where $\hat{\rho}_s$ is the *secular* (energy diagonal) part and $\hat{\rho}_n$ is the non-secular (energy non-diagonal) part, containing all matrix elements $\rho_{aa'}$ between states with an energy difference exceeding what is provided by temperature, $|E_a - E_{a'}| > k_B T$. All other elements can be found in $\hat{\rho}_s$ (including the diagonal components, $a = a'$, corresponding to the populations).
Our aim is to include the effect of non-secular elements $\hat{\rho}_n$ as corrections to the rates determining the secular part. For this purpose we write Eq. (8) in block matrix form,

$$\begin{pmatrix} 0 \\ 0 \end{pmatrix} = \begin{pmatrix} (\hat{K}_0)_{ss} + \hat{K}_{ss}^{(2)} + \hat{K}_{ss}^{(4)} & \hat{K}_{sn}^{(2)} + \hat{K}_{sn}^{(4)} \\ \hat{K}_{ns}^{(2)} + \hat{K}_{ns}^{(4)} & (\hat{K}_0)_{nn} + \hat{K}_{nn}^{(2)} + \hat{K}_{nn}^{(4)} \end{pmatrix} \begin{pmatrix} \hat{\rho}_s \\ \hat{\rho}_n \end{pmatrix},$$

where the free evolution of the system, cf. Eq. (6), is taken into account via $(\hat{K}_0)_{bb'}^{aa'} \equiv \mathrm{i}\,\delta_{ab}\delta_{a'b'}\,\hbar^{-1}(E_{a'} - E_a)$, which is thus zero in the ns and sn blocks. Solving for $\hat{\rho}_n$ one obtains

$$\hat{\rho}_n = -\left((\hat{K}_0)_{nn} + \hat{K}_{nn}^{(2)} + \hat{K}_{nn}^{(4)}\right)^{-1}\left(\hat{K}_{ns}^{(2)} + \hat{K}_{ns}^{(4)}\right)\hat{\rho}_s, \tag{27}$$

which obviously contains all orders in Γ due to the inverse,

$$\left((\hat{K}_0)_{nn} + \hat{K}_{nn}^{(2)} + \hat{K}_{nn}^{(4)}\right)^{-1} = \left((\hat{K}_0)_{nn}\right)^{-1}\left[1 + \left((\hat{K}_0)_{nn}\right)^{-1}\left(\hat{K}_{nn}^{(2)} + \hat{K}_{nn}^{(4)}\right)\right]^{-1}. \tag{28}$$

[3] Conservation of total charge is violated only in the case of superconducting electrodes, where the present theory has to be modified, see e.g. Ref. [46]. Besides charge, another example for a good quantum number can be the total spin-projection in case of un- or collinearly polarised electrodes.

Since we assumed $k_B T \gg \hbar\Gamma$ and hence by construction $|\Gamma/(\hat{K}_0)_{nn}| \ll 1$, we can expand

$$\left[1 + \left((\hat{K}_0)_{nn}\right)^{-1}\left(\hat{K}^{(2)}_{nn} + \hat{K}^{(4)}_{nn}\right)\right]^{-1} \approx 1 - \left((\hat{K}_0)_{nn}\right)^{-1}\left(\hat{K}^{(2)}_{nn} + \hat{K}^{(4)}_{nn}\right) \approx 1,$$

and use it together with Eq. (28) in Eq. (27). Neglecting all contributions beyond order Γ^2 we can then set up the following equation for the energy diagonal part of the RDM:

$$0 = \left((\hat{K}_0)_{ss} + \hat{K}^{(2)}_{ss} + \hat{K}^{(4)}_{ss}\right)\hat{\rho}_s + \left(\hat{K}^{(2)}_{sn} + \hat{K}^{(4)}_{sn}\right)\hat{\rho}_n = \left((\hat{K}_0)_{ss} + \hat{K}^{(2)}_{ss} + \hat{K}^{(4)}_{\mathsf{eff}}\right)\hat{\rho}_s, \tag{29a}$$

where we have defined the *effectively secular fourth order part of the time evolution kernel*

$$\hat{K}^{(4)}_{\mathsf{eff}} := \hat{K}^{(4)}_{ss} + \hat{K}_C \tag{29b}$$

containing the correction

$$\hat{K}_C = -\hat{K}^{(2)}_{sn}\left((\hat{K}_0)_{nn}\right)^{-1}\hat{K}^{(2)}_{ns} \tag{29c}$$

to the secular density matrix due to coherences between non-secular states.

This effective treatment allows to restrict the master equation to the purely secular part $\hat{\rho}_s$ of the density matrix, which significantly reduces the numerical effort needed to evaluate the kernels and solve the generalised master equation.

2 Diagrammatic analysis

A powerful tool for perturbative quantum transport calculations has been introduced in the mid-1990s [39, 48, 49, 50] by Gerd Schön together with Herbert Schoeller and Jürgen König. The *diagrammatic technique* allows a formulation of the quantum master equation in a completely graphical language. Each term in the perturbation expansion can be visualised as a diagram. Cleverly, there exist simple rules ([19], App. A.2.3), which permit to directly extract from the diagram the corresponding analytical expression.

While the basic ingredients for our studies of transport across different types of interacting quantum-dots, Sects. 3-5, were given in Sect. 1, the present section is dedicated to a closer look on the transport theory itself.
In the following we exploit the convenience of the diagrammatic representation for a more detailed analysis of the contributions to the effectively secular generalised fourth order steady state master equation, Eq. (29a),

$$\left((\hat{K}_0)_{ss} + \hat{K}^{(2)}_{ss} + \hat{K}^{(4)}_{ss} + \hat{K}_C\right)\hat{\rho}_s = 0.$$

As a preparation, Sect. 2.1 demonstrates on an explicit level a one-to-one mapping between the single contributions to the kernels $\hat{K}^{(2)}$ and $\hat{K}^{(4)}$ as they arise from Eq. (22b) and **irreducible** diagrams. A compact overview is given in Tab. 1, and supplements to the main text can be found in A.2, in particular a full list of second and fourth order contributions to the master equation in analytical form, along with the corresponding diagrams. Importantly, also the correction $\hat{K}_C$, Eq. (29c), can be depicted, in form of **reducible** diagrams.
The further goal is to analyse the resulting effectively secular fourth order part of the kernel, $\hat{K}^{(4)}_{\mathsf{eff}} = \hat{K}^{(4)}_{ss} + \hat{K}_C$, Eq. (29b). For an assignment of its components to underlying physical processes, gain and loss relations, as exemplified in Sect. 2.2, play an important role. We demonstrate in Sect. 2.3 how the contributions to $\hat{K}^{(4)}_{\mathsf{eff}}$ can be classified. Sorting them into 3×3 groups, according to Fig. 6, allows a significant simplification for the actual analytical as well as numerical evaluation of the transport rates, as partial cancellations occur among the members of each group. App. A.3 holds some additional details on this. On the basis of Sect. 2.2, we further explore the physical background of the grouped expressions.
Finally, with help of the grouping we can trace in Sect. 2.4 the relation to T-matrix based rate approaches and the origin of divergences encountered within those.

2.1 Kernel components and diagrammatic representation

Our starting point is Eq. (22b), and for an evaluation we have to substitute the definition of the Liouville operator, Eq. (15). Splitting the tunnelling Hamiltonian Eq. (2) contained in there into an in-tunnelling (+) and out-tunnelling part (-), we can

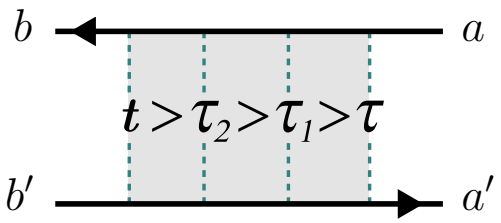

Figure 4: Time ordering in a diagram associated to a fourth order process. Every term arising from Eq. (21) can uniquely be translated into a specific diagram. While the time-order is crucial for this mapping, the resulting diagram itself is time independent and represents the Laplace transformed expression.

represent $\hbar^{-1}\hat{H}_T^I(t_i)$ as

$$\frac{1}{\hbar}\hat{H}_T^I(t_i) = \hat{A}_i^+ + \hat{A}_i^-, \quad \text{with} \quad \begin{aligned} \hat{A}_i^+ &=: \hat{D}_i^+\hat{C}_i^- := \sum_{lm\sigma q}\Big(\hbar^{-1}\hat{d}^\dagger_{m\sigma}(\tau_i)\Big)\Big(T_{lmq}\,\hat{c}_{l\sigma q}(\tau_i)\Big), \\ \hat{A}_i^- &=: \hat{C}_i^+\hat{D}_i^- := \sum_{lm\sigma q}\Big(T^*_{lmq}\,\hat{c}^\dagger_{l\sigma q}(\tau_i)\Big)\Big(\hbar^{-1}\hat{d}_{m\sigma}(\tau_i)\Big), \end{aligned} \tag{30}$$

and $\tau_0 = \tau$, $\tau_3 = t$ (see also Fig. 4). It holds $\hat{C}_i^\pm\hat{D}_i^\mp = -\hat{D}_i^\mp\hat{C}_i^\pm$, as the fermionic operators of the leads anti-commute with the quantum-dot operators. The inverse $\hbar^{-1}$ of the Planck constant appearing in Eq. (15) was also included here. The kernel components as defined in Eq. (22b) then read

$$\hat{\mathcal{K}}^{I(2)}(t,\tau)\hat{\rho}^I_\odot(\tau) = -\sum_{\substack{p_0,p_3\\ \in\{+,-\}}} \mathsf{Tr}_R\Big[\,\hat{A}_3^{p_3},\big[\,\hat{A}_0^{p_0},\hat{\rho}^I_\odot(\tau)\hat{\rho}_R\,\big]\,\Big], \tag{31a}$$

$$\begin{aligned} \hat{\mathcal{K}}^{I(4)}(t,\tau_2,\tau_1,\tau)\hat{\rho}^I_\odot(\tau) = \sum_{p_0,p_1,p_2,p_3\in\{+,-\}} \Big(&\mathsf{Tr}_R\Big[\,\hat{A}_3^{p_3},\Big[\,\hat{A}_2^{p_2},\big[\,\hat{A}_1^{p_1},\big[\,\hat{A}_0^{p_0},\hat{\rho}^I_\odot(\tau)\hat{\rho}_R\,\big]\,\big]\,\Big]\,\Big] \\ -\mathsf{Tr}_R\Big[\,\hat{A}_3^{p_3},\Big[\,\hat{A}_2^{p_2},&\mathsf{Tr}_R\Big\{\big[\,\hat{A}_1^{p_1},\big[\,\hat{A}_0^{p_0},\hat{\rho}^I_\odot(\tau)\hat{\rho}_R\,\big]\,\big]\Big\}\hat{\rho}_R\Big]\,\Big]\,\Big). \end{aligned} \tag{31b}$$

Evaluating the multiple commutators is a lengthy but standard task, which is carried out in App. A.2.1. The cyclic property of the trace, as well as Wick's theorem must be invoked to split off and contract two fermionic operators each. Relying on the outcomes of this procedure, Eqs. (120a), (120b), we list in Tab. 1, under exclusion of hermitian conjugate terms, all resulting second and fourth order contributions, alongside with a related *diagram* each. The assignment to it works as follows:

In general we take as basis a $2n$-th order contribution in the interaction picture,

$$\prod_\alpha \Big\langle \hat{C}^I_\alpha \Big\rangle \langle b|\,\hat{D}^I\,|a\rangle\,\langle a|\,\hat{\rho}^I_\odot(\tau)\,|a'\rangle\,\langle a'|\,\hat{D}'^I\,|b'\rangle\,,$$

where each $\hat{C}^I_\alpha$ is formed by a product of two (time dependent) lead operators, $\prod_\alpha \langle \hat{C}^I_\alpha \rangle$ denotes the product of n Wick contractions of those two lead operators and $\hat{D}^I, \hat{D}'^I$ contain together the associated $2n$ dot operators (also time dependent). As depicted in Fig. 4 for the fourth order case, the diagram consists of an upper and a lower *contour*, taking the state b' to a' and a to b, as indicated by the arrows. Throughout the diagram, time grows from right to left[4], such that states a, a' (associated with $\hat{\rho}^I_\odot(\tau)$) are called the *initial*, and b, b' are called the *final* states. In the shaded area an irreducible processes of fourth (in general $2n$th) order in the tunnelling takes place, starting at time τ and ending at time t. Every quantum-dot operator standing to the left ($\hat{D}^I$) of the RDM creates a vertex at its given time (see Tab. 1) on the upper, every quantum-dot operator on the right ($\hat{D}'^I$) of the RDM creates a vertex on the lower contour. At each vertex, the charge of the evolving state changes by ± 1. The vertices of two quantum-dot operators which are contracted via their lead operators have to be connected by a fermion line, which points to the creation operator vertex, because here the charge grows by 1, while the action of the annihilation operator is to reduce the charge by 1. It is important to mention that upon writing out the sum over the leads and spin-projections in Eq. (30), each fermion line acquires a lead index l_i as well spin index σ_i.
In Tab. 1, the sums are still hidden in the placeholders $C^{\bar{p}}_i D^p_i / C^{\bar{p}'}_i D^{p'}_i$ and correspondingly these indices are omitted in the diagrammatic representation. Further, no directions were assigned to the fermion lines, because we also did not specify p and p', i.e. which are the creation and which the annihilation operators. The hermitian conjugated terms, which are not shown, would in terms of diagrams just correspond to a horizontal mirroring, i.e. all vertices on the upper contour have to be flipped to the lower one and vice versa. So each second order diagram shown in Tab. 1 stands for a sum of four, each fourth order diagram for a sum of eight distinct diagrams. A complete list of the hence emerging 8+128 single diagrams is found in App. A.2.4. Notice that from the diagrams it can be verified at a glance that all our contributions are irreducible: Between the first and the last vertex at times t, respectively τ, there is no time point at which the diagram could be separated into two parts without cutting a fermion line: the two tunnelling processes represented by the fermion lines are correlated.

A big advantage of the diagrams is that there exist simple rules [39, 40, 19], explained at length in App. A.2.3, which directly allow to read off the contribution to $\hat{K}(\lambda = 0)$, i.e. the zero frequency component of the Laplace transformed time evolution kernel. This is in fact the object we are finally looking for in order to calculate the stationary state RDM $\hat{\rho}^\infty_\odot$, see Eq. (7).

The formulation in terms of single kernel elements, which is given by Eq. (8), can now symbolically be rewritten as

[4] Time is unrelated to the direction of the contours.

$\hat{\mathcal{K}}^{I(2)}(t,\tau)\hat{\rho}^I_\odot(\tau)$	$\hat{K}^{(2)}$	$\hat{\mathcal{K}}^{I(4)}(t,\tau_2,\tau_1,\tau)\hat{\rho}^I_\odot(\tau)$	$\hat{K}^{(4)}$
$+\left\langle \hat{C}_0^p \hat{C}_3^{\bar{p}} \right\rangle \left(\hat{D}_3^p \, \hat{\rho}^I_\odot(\tau) \, \hat{D}_0^{\bar{p}} \right)$		$+\left\langle \hat{C}_2^{\bar{p}'} \hat{C}_1^{p'} \right\rangle \left\langle \hat{C}_3^{\bar{p}} \hat{C}_0^{p} \right\rangle \hat{D}_3^p \hat{D}_2^{p'} \hat{D}_1^{\bar{p}'} \hat{D}_0^{\bar{p}} \, \hat{\rho}^I_\odot(\tau)$	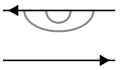
$-\left\langle \hat{C}_3^{\bar{p}} \hat{C}_0^{p} \right\rangle \left(\hat{D}_3^p \hat{D}_0^{\bar{p}} \, \hat{\rho}^I_\odot(\tau) \right)$	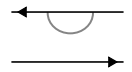	$-\left\langle \hat{C}_3^{\bar{p}} \hat{C}_1^{p} \right\rangle \left\langle \hat{C}_2^{\bar{p}'} \hat{C}_0^{p'} \right\rangle \hat{D}_3^p \hat{D}_2^{p'} \hat{D}_1^{\bar{p}} \hat{D}_0^{\bar{p}'} \, \hat{\rho}^I_\odot(\tau)$	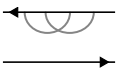
		$+\left\langle \hat{C}_1^{p} \hat{C}_3^{\bar{p}} \right\rangle \left\langle \hat{C}_0^{p'} \hat{C}_2^{\bar{p}'} \right\rangle \hat{D}_3^p \hat{D}_2^{p'} \, \hat{\rho}^I_\odot(\tau) \, \hat{D}_0^{\bar{p}'} \hat{D}_1^{\bar{p}}$	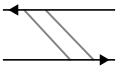
		$-\left\langle \hat{C}_0^{p} \hat{C}_3^{\bar{p}} \right\rangle \left\langle \hat{C}_1^{p'} \hat{C}_2^{\bar{p}'} \right\rangle \hat{D}_3^p \hat{D}_2^{p'} \, \hat{\rho}^I_\odot(\tau) \, \hat{D}_0^{\bar{p}} \hat{D}_1^{\bar{p}'}$	
		$+\left\langle \hat{C}_0^{p'} \hat{C}_2^{\bar{p}'} \right\rangle \left\langle \hat{C}_3^{\bar{p}} \hat{C}_1^{p} \right\rangle \hat{D}_3^p \hat{D}_1^{\bar{p}} \, \hat{\rho}^I_\odot(\tau) \, \hat{D}_0^{\bar{p}'} \hat{D}_2^{p'}$	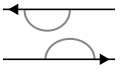
		$-\left\langle \hat{C}_0^{p} \hat{C}_3^{\bar{p}} \right\rangle \left\langle \hat{C}_2^{\bar{p}'} \hat{C}_1^{p'} \right\rangle \hat{D}_3^p \hat{D}_1^{\bar{p}'} \, \hat{\rho}^I_\odot(\tau) \, \hat{D}_0^{\bar{p}} \hat{D}_2^{p'}$	
		$+\left\langle \hat{C}_1^{p'} \hat{C}_2^{\bar{p}'} \right\rangle \left\langle \hat{C}_3^{\bar{p}} \hat{C}_0^{p} \right\rangle \hat{D}_3^p \hat{D}_0^{\bar{p}} \, \hat{\rho}^I_\odot(\tau) \, \hat{D}_1^{\bar{p}'} \hat{D}_2^{p'}$	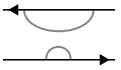
		$-\left\langle \hat{C}_1^{p} \hat{C}_3^{\bar{p}} \right\rangle \left\langle \hat{C}_2^{\bar{p}'} \hat{C}_0^{p'} \right\rangle \hat{D}_3^p \hat{D}_0^{\bar{p}'} \, \hat{\rho}^I_\odot(\tau) \, \hat{D}_1^{\bar{p}} \hat{D}_2^{p'}$	
		$+\left\langle \hat{C}_2^{\bar{p}'} \hat{C}_1^{p'} \right\rangle \left\langle \hat{C}_3^{\bar{p}} \hat{C}_0^{p} \right\rangle \hat{D}_3^p \hat{D}_1^{\bar{p}'} \hat{D}_0^{\bar{p}} \, \hat{\rho}^I_\odot(\tau) \, \hat{D}_2^{p'}$	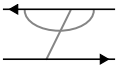
		$-\left\langle \hat{C}_3^{\bar{p}} \hat{C}_1^{p} \right\rangle \left\langle \hat{C}_2^{\bar{p}'} \hat{C}_0^{p'} \right\rangle \hat{D}_3^p \hat{D}_1^{\bar{p}} \hat{D}_0^{\bar{p}'} \, \hat{\rho}^I_\odot(\tau) \, \hat{D}_2^{p'}$	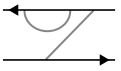
		$+\left\langle \hat{C}_1^{p} \hat{C}_3^{\bar{p}} \right\rangle \left\langle \hat{C}_0^{p'} \hat{C}_2^{\bar{p}'} \right\rangle \hat{D}_3^p \, \hat{\rho}^I_\odot(\tau) \, \hat{D}_0^{\bar{p}'} \hat{D}_1^{\bar{p}} \hat{D}_2^{p'}$	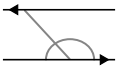
		$-\left\langle \hat{C}_0^{p} \hat{C}_3^{\bar{p}} \right\rangle \left\langle \hat{C}_1^{p'} \hat{C}_2^{\bar{p}'} \right\rangle \hat{D}_3^p \, \hat{\rho}^I_\odot(\tau) \, \hat{D}_0^{\bar{p}} \hat{D}_1^{\bar{p}'} \hat{D}_2^{p'}$	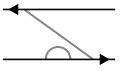
		$+\left\langle \hat{C}_0^{p'} \hat{C}_2^{\bar{p}'} \right\rangle \left\langle \hat{C}_3^{\bar{p}} \hat{C}_1^{p} \right\rangle \hat{D}_3^p \hat{D}_2^{p'} \hat{D}_1^{\bar{p}} \, \hat{\rho}^I_\odot(\tau) \, \hat{D}_0^{\bar{p}'}$	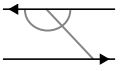
		$-\left\langle \hat{C}_0^{p} \hat{C}_3^{\bar{p}} \right\rangle \left\langle \hat{C}_2^{\bar{p}'} \hat{C}_1^{p'} \right\rangle \hat{D}_3^p \hat{D}_2^{p'} \hat{D}_1^{\bar{p}'} \, \hat{\rho}^I_\odot(\tau) \, \hat{D}_0^{\bar{p}}$	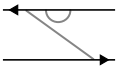
		$+\left\langle \hat{C}_1^{p'} \hat{C}_2^{\bar{p}'} \right\rangle \left\langle \hat{C}_3^{\bar{p}} \hat{C}_0^{p} \right\rangle \hat{D}_3^p \hat{D}_2^{p'} \hat{D}_0^{\bar{p}} \, \hat{\rho}^I_\odot(\tau) \, \hat{D}_1^{\bar{p}'}$	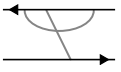
		$-\left\langle \hat{C}_1^{p} \hat{C}_3^{\bar{p}} \right\rangle \left\langle \hat{C}_2^{\bar{p}'} \hat{C}_0^{p'} \right\rangle \hat{D}_3^p \hat{D}_2^{p'} \hat{D}_0^{\bar{p}'} \, \hat{\rho}^I_\odot(\tau) \, \hat{D}_1^{\bar{p}}$	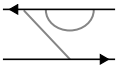

Table 1: On the top we give the second, on the right the fourth order contributions to the time evolution kernel, both as they arise in the time domain from the fourth order quantum master equation in the interaction picture, Eqs. (31a), (31b), as well as the corresponding diagrammatic representations, which absorbs any negative signs. We use placeholders $p, p' = \pm$ and $\bar{p} = -p$, $\bar{p}' = -p'$, which means for the diagrams that we do not specify the directions of the fermion lines. Moreover we omit hermitian conjugates. Importantly, the diagrammatic rules, App. A.2.3, allow to read off automatically the *Laplace transform* of the time evolution kernel contributions, which are needed for the calculation of the steady state RDM, see Eqs. (7), (8). In App. A.2.4 we explicitly list all 8 second and 128 fourth order contributions emerging upon specifying p and p' and including hermitian conjugates.

$$\dot{\rho}^{\infty}_{bb'} = 0 = \sum_{aa'} K^{aa'}_{bb'} \rho^{\infty}_{aa'} = \sum_{aa'} \Bigg(\quad \rho^{\infty}_{aa'} \Bigg).$$

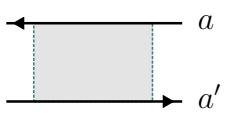

To make the relation between $\hat{K}(\lambda = 0)$ and our expression for the time evolution kernel, Eq. (24), which is still in time space, more explicit, we write the element $K^{aa'}_{bb'}$ as a sum determined by the order in the tunnelling coupling,

$$(\hat{K})^{aa'}_{bb'} = (\hat{K}^{(2)})^{aa'}_{bb'} + (\hat{K}^{(4)})^{aa'}_{bb'} + \cdots ,$$

and find

$$\begin{aligned}
\left(\hat{K}^{(2)}\right)^{aa'}_{bb'} &= \lim_{\lambda\to 0} \int_0^\infty \mathrm{d}\tau'\, e^{-\lambda\tau'} e^{\frac{\mathrm{i}}{\hbar}(E_a - E_{a'})(t-\tau')} e^{-\frac{\mathrm{i}}{\hbar}(E_b - E_{b'})t} \left\langle b \left| \hat{\mathcal{K}}^{I(2)}(t, t-\tau')[|a\rangle \langle a'|] \right| b' \right\rangle , \\
\left(\hat{K}^{(4)}\right)^{aa'}_{bb'} &= \lim_{\lambda\to 0} \int_0^\infty \mathrm{d}\tau'\, e^{-\lambda\tau'} \int_0^{\tau'} \mathrm{d}\tau_1' \int_0^{\tau_1'} \mathrm{d}\tau_2'\ e^{\frac{\mathrm{i}}{\hbar}(E_a - E_{a'})(t-\tau')} e^{-\frac{\mathrm{i}}{\hbar}(E_b - E_{b'})t} \\
&\qquad \times \left\langle b \left| \hat{\mathcal{K}}^{I(4)}(t, t-\tau_2', t-\tau_1', t-\tau')[|a\rangle \langle a'|] \right| b' \right\rangle .
\end{aligned} \tag{32}$$

Here we shifted integration variables according to $\tau' = t - \tau, \tau_1' = t - \tau_1, \tau_2' = t - \tau_2$. The kernel components are, see Tab. 1, time dependent only via the involved lead and dot operators, which decompose as

$$\begin{aligned}
\left\langle \hat{C}_i^{p_i} \hat{C}_j^{p_j} \right\rangle D^{\bar{p}_{i/j}}_{i/j} \cdots D^{\bar{p}_{j/i}}_{j/i} &= \delta_{p_j, -p_i} \hbar^{-2} \int \mathrm{d}\omega\, f_l^{p_i}(\omega)\, \tilde{\rho}_{l\sigma} \sum_{q|\omega} e^{p_i \frac{\mathrm{i}}{\hbar}\omega(\tau_i - \tau_j)} \\
\times \sum_\sigma \sum_{mm'} T_{lmq} T^*_{lm'q} &\begin{cases} e^{\frac{\mathrm{i}}{\hbar}\hat{H}_\odot \tau_{i/j}} \hat{d}_{m'\sigma} e^{-\frac{\mathrm{i}}{\hbar}\hat{H}_\odot \tau_{i/j}} \cdots e^{\frac{\mathrm{i}}{\hbar}\hat{H}_\odot \tau_{j/i}} \hat{d}^\dagger_{m\sigma} e^{-\frac{\mathrm{i}}{\hbar}\hat{H}_\odot \tau_{j/i}} & p_i = +, \\ e^{\frac{\mathrm{i}}{\hbar}\hat{H}_\odot \tau_{i/j}} \hat{d}^\dagger_{m\sigma} e^{-\frac{\mathrm{i}}{\hbar}\hat{H}_\odot \tau_{i/j}} \cdots e^{\frac{\mathrm{i}}{\hbar}\hat{H}_\odot \tau_{j/i}} \hat{d}_{m'\sigma} e^{-\frac{\mathrm{i}}{\hbar}\hat{H}_\odot \tau_{j/i}} & p_i = -, \end{cases}
\end{aligned} \tag{33}$$

with $f_l^+(\omega) \equiv f(\beta\omega + \beta e V_l) = (e^{\beta\omega + \beta e V_l} + 1)^{-1}$ the Fermi function for the lead l, $f_l^-(\omega) \equiv 1 - f_l(\omega)$, $\beta = (k_B T)^{-1}$ the inverse of the thermal energy and $\tilde{\rho}_{l\sigma}$ in general being the spin-dependent density of states in lead l. The sum over q is restricted to states of the electron with energy ω. For simplicity, we assume here energy-independent tunnelling couplings, such that we can define *tunnelling matrix elements* (TMEs)

$$T^+_{l\sigma}(a,b) := \sqrt{\tilde{\rho}_{l\sigma}} \sum_m \sum_{q|\omega} T_{lmq} \langle a | \hat{d}^\dagger_{m\sigma} | b \rangle \quad \text{respectively} \quad T^-_{l\sigma}(a,b) := [T^+_{l\sigma}(b,a)]^\dagger \tag{34}$$

which are not dependent on ω. Using Eq. (33) for all operators contained in Eq. (32) it turns out in general that the dependence on t cancels among all the exponentials in the integrands. This is clearly seen in App. A.2.2, where we give examples for the calculation of a kernel element in second and fourth order starting from Eq. (32). Further, it is found that the expression for $(\hat{K}^{(2)})^{aa'}_{bb'}$ respectively $(\hat{K}^{(4)})^{aa'}_{bb'}$ splits into a product of TMEs multiplied by an energy dependent function. As explained in Sect. A.2.3, that result is also obtained directly from the diagrams by applying the aforementioned diagrammatic rules.

Current kernel Having learned of the convenience of the diagrammatic representation, it would be advantageous to also formulate the current kernel in terms of diagrams. We have demonstrated in Sect. 1.2 that there is a close similarity between the equation of motion for the RDM, Eq. (26), and the expression for the current, Eq. (21). The fact that the current kernel $\hat{\mathcal{K}}^I_{I_l}(t,\tau)$ differs from the time evolution kernel $\hat{\mathcal{K}}^I(t,\tau)$ only by replacement of the Liouville superoperator $\hat{\mathcal{L}}^I_T(t)$ with the current operator $\hat{I}_l(t)$ has actually the implication that $\hat{K}_{I_l}(\lambda=0)$ is constructed from the same diagrams as $\hat{K}(\lambda=0)$, except for the following restrictions:

1. As $\hat{I}_l$ contains only operators from lead l, there is no sum over the lead index of the fermion line connected to the latest vertex (at time t), because it must exclusively belong to lead l.

2. As $\hat{I}_l$, being a normal operator instead of a superoperator, involves no commutator, the vertex at time t must lie on the upper contour.

3. As $\hat{I}_l$ differs from $\hat{H}_{Tl}$ by the sign of the out-tunnelling contribution, the sign of diagrams with the fermion line pointing away from the latest vertex must be inverted.

The cyclic property of the full trace in Eq. (25) allows actually to rephrase the second and third condition: alternative to these two rules, one can also employ all diagrams with the latest vertex on the upper contour and the fermion line pointing towards this vertex, as well as all the diagrams with the latest vertex on the lower contour and the fermion line pointing away from it, whereas the sign of these must be inverted.

Non-secular corrections We stated, and now demonstrate, that the correction term $\hat{K}_C$, Eq. (29c),

$$\hat{K}_C = -\hat{K}^{(2)}_{sn}\left((\hat{K}_0)_{nn}\right)^{-1}\hat{K}^{(2)}_{ns},$$

in the effectively secular fourth order part $\hat{K}^{(4)}_{\mathsf{eff}}$ of the time evolution kernel can be seen as a sum of *reducible* fourth order diagrams:

The inverse of the kernel $(\hat{K}_0)^{aa'}_{aa'}$, which corresponds to free evolution of the state a on the upper contour and a' on the lower contour, agrees with what is obtained from the diagrammatic rules for a diagram without tunnelling lines, see App. A.2.3,

$$\hbar\left[\left(\hat{K}_0\right)^{-1}\right]^{aa'}_{aa'} = \frac{-\mathrm{i}}{E_{a'}-E_a} \equiv$$

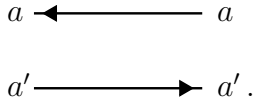

Note that this "free evolution" term is always finite since the expansion is only carried out in the non-secular subspace.
Representing a general second order contribution diagrammatically as

$$\left[\hat{K}^{(2)}\right]^{aa'}_{bb'} \equiv$$

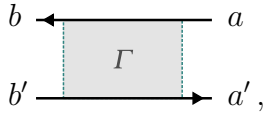

the correction term due to coherences between non-secular states is given by

$$\left(\hat{K}^{(4)}_C\right)^{aa'}_{bb'} = \sum_{cd}$$

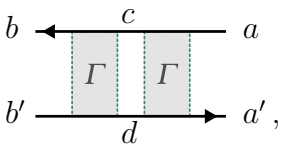

where the sum is performed over all pairs of states c and d with $|E_d - E_c| > k_B T \gg \hbar\Gamma$. Hence $\hat{K}^{(4)}_C$ as represented in Eq. (29c) can be evaluated by using the diagrammatic rules, App. A.2.3, as for an *irreducible* fourth order diagram[5].

We have thus shown that the non-secular corrections can be included through an additional sum of reducible diagrams, to which the same diagrammatic rules as for irreducible terms apply. Since the intermediate free evolution only involves non-degenerate states c, d there is no problem with divergences.

2.2 Intermezzo: Gain and loss relations

Before we continue, we have to get a basic understanding of what we call gain and loss relations. To anticipate, the idea is to identify *gain-loss partners*, i.e., diagram pairs which cancel in the sum-rule Eq. (10). The gain-loss partnerships are crucial for the upcoming core section, Sect. 2.3, with respect to both the group formation and the subsequent assignment of underlying physical processes.

To realize what is the connection between the rates of physical events and the elements of the kernel ruling the time evolution, it is sufficient to consider a very simple example system: a single-level quantum-dot, also known as Anderson impurity model with Coulomb interaction and spin. The system, addressed in more detail later in Sect. 3.1, is characterised by the four states $|0\rangle$, $|\uparrow\rangle$, $|\downarrow\rangle$, $|2\rangle$, corresponding respectively to zero, one spin-up, one spin-down or two spin-paired electrons on the dot. Assuming unpolarised or collinearly polarised contacts, spin is a conserved quantity such that there exist no coherences between $|\uparrow\rangle$ and $|\downarrow\rangle$ sectors. The density matrix has only the diagonal entries $\langle 0|\hat{\rho}|0\rangle =: P_0$, $\langle\uparrow|\hat{\rho}|\uparrow\rangle =: P_\uparrow$, $\langle\downarrow|\hat{\rho}|\downarrow\rangle =: P_\downarrow$, $\langle 2|\hat{\rho}|2\rangle =: P_2$. With $\Gamma^{\alpha\to\beta}$ denoting the rate for a transition from state $|\alpha\rangle$ to state $|\beta\rangle$, the equations determining the time evolution of the single-level populations can be written down formally as ($\sigma \in \{\uparrow,\downarrow\}$, $\sigma =\uparrow \Rightarrow \bar{\sigma} =\downarrow$, $\sigma =\downarrow \Rightarrow \bar{\sigma} =\uparrow$):

[5] Thereby, the minus sign in Eq. (29c) is indeed correct, as by putting the three parts together and applying the diagrammatic rules to the reducible fourth order diagram, one misses an additional i^2 which would arise from the two isolated second order contributions.

Figure 5: Constructing gain and loss partners in second order.

$$
\begin{aligned}
\dot{P}_0 &= \underbrace{-\Big(\sum\nolimits_\sigma \Gamma^{0\to\sigma} + \Gamma^{0\to 2}\Big)}_{=K_{00}^{00}} P_0 + \sum\nolimits_\sigma \underbrace{\Gamma^{\sigma\to 0}}_{=K_{00}^{\sigma\sigma}} P_\sigma + \underbrace{\Gamma^{2\to 0}}_{=K_{00}^{22}} P_2, \\
\dot{P}_\sigma &= \underbrace{-\Big(\Gamma^{\sigma\to 0} + \Gamma^{\sigma\to\bar{\sigma}} + \Gamma^{\sigma\to 2}\Big)}_{=K_{\sigma\sigma}^{\sigma\sigma}} P_\sigma + \underbrace{\Gamma^{0\to\sigma}}_{=K_{\sigma\sigma}^{00}} P_0 + \underbrace{\Gamma^{\bar{\sigma}\to\sigma}}_{=K_{\sigma\sigma}^{\bar{\sigma}\bar{\sigma}}} P_{\bar{\sigma}} + \underbrace{\Gamma^{2\to\sigma}}_{=K_{\sigma\sigma}^{22}} P_2, \\
\dot{P}_2 &= \underbrace{-\Big(\sum\nolimits_\sigma \Gamma^{2\to\sigma} + \Gamma^{2\to 0}\Big)}_{=K_{22}^{22}} P_2 + \sum\nolimits_\sigma \underbrace{\Gamma^{\sigma\to 2}}_{=K_{22}^{\sigma\sigma}} P_\sigma + \underbrace{\Gamma^{0\to 2}}_{=K_{22}^{00}} P_0.
\end{aligned}
\tag{35}
$$

We identified here all the nonzero components of the time evolution kernel, such that it is easy to verify the sum-rule Eq. (10). For instance for the processes starting from the state $|2\rangle$ it holds:

$$
\underbrace{K_{22}^{22}}_{\text{'loss'}} = -\Big(\underbrace{K_{00}^{22}}_{\text{'gain'}} + \sum\nolimits_\sigma \underbrace{K_{\sigma\sigma}^{22}}_{\text{'gain'}}\Big).
$$

We denoted K_{22}^{22} as a *loss* contribution. The reason is that it appears in the equation for $\dot{P}_2$, and it comprises all rates of processes depopulating the initial state $|2\rangle$. On the other hand, each rate $\Gamma^{2\to\alpha}$ contained in K_{22}^{22} must appear in a second place, namely in the equation for $\dot{P}_\alpha$, inside $K_{\alpha\alpha}^{22}$. Here, it is a *gain* contribution, as the process feeds the population of state $|\alpha\rangle$. This is the physical background of the sum-rule Eq. (10). Importantly, we can further conclude that not every kernel component, and therewith not every diagram, has a physical meaning of its own.

Let us visualise this for the second order. Here, $\Gamma^{2\to 0} = 0 = K_{00}^{22}$, so the gain contributions are $K_{\sigma\sigma}^{22} = \Gamma^{2\to\sigma}$, $\sigma \in \{\uparrow, \downarrow\}$, and the loss term is $K_{22}^{22} = -\sum_\sigma \Gamma^{2\to\sigma}$. Diagrammatically,

$$
K_{22}^{22} = -\sum\nolimits_\sigma \Gamma^{2\to\sigma};
$$

$$
-\Gamma^{2\to\sigma} =
$$

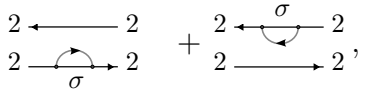

,

$$
K_{\sigma\sigma}^{22} = +\Gamma^{2\to\sigma} =
$$

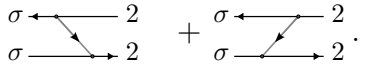

.

First, notice that every rate is constructed from more than one diagram. In our simple second order example, it is only the hermitian conjugate partners, but for fourth order diagrams there can be several contributions. The physical interpretation of $K^{22}_{\sigma\sigma}$ is obvious: both diagrams it is constructed of describe electron tunnelling out of the quantum-dot, changing its state from $|2\rangle$ to $|\sigma\rangle$ (remember that time evolves from right to left throughout the diagram). For K^{22}_{22}, the first look at the two upper 'bubble' diagrams might suggest that they describe a temporary tunnelling event from state $|2\rangle$ to $|\sigma\rangle$. That is *not* true, as it can be seen from the construction Fig. 5: upon moving the vertex at the latest time t to the opposite contour, one diagram emerges from the other. According to the diagrammatic rules, this manipulation changes merely the sign of the analytical contribution associated with a diagram, such that it is really these gain-loss partners which originate from one and the same tunnelling process and cancel in the sum-rule Eq. (10). A necessary condition is that the final states – named b in Eq. (10) – are diagonal, otherwise shifting the vertex as depicted in Fig. 5 is not possible.
Temporary (so-called *virtual*) transitions are in fact incorporated in any second order diagram via the imaginary part of the related energy dependent function Eq. (124a), where energy is integrated over (i.e. due to its temporary nature the virtual tunnelling process may be energy non-conserving). That imaginary part, however, cancels out upon summation of hermitian conjugates, except for bubble diagrams off-diagonal in the initial or final states. So the association of bubble diagrams with quantum fluctuations can also be justified.

At this point, let us underline that it is not a choice, but a physical demand that we move the vertex at the latest (and not the one at the earliest) time[6]: A physical process leading from state $|\alpha\rangle$ to a state $|\beta\rangle$ must always start initially from state $|\alpha\rangle$, but influences the population of both $|\alpha\rangle$ and $|\beta\rangle$, which requires diagrams differing in their final states.

In the following, the identification of gain-loss partners will help us for the grouping as well as for a physical interpretation of the fourth order diagrams.

2.3 Grouping of diagrams

We have arrived now at the core section of the first, transport theoretical, part of this thesis. In the following we consider the *full set* of diagrams required for an effectively secular fourth order calculation, i.e., all the – irreducible – entries of Tab. 1 constructing $\hat{K}^{(4)}_{ss}$ plus all possible reducible diagrams needed for $\hat{K}_C$.

In Sect. 2.3.1 we wish to demonstrate that within this full set, there exists a structure, namely the grouping, which allows analytical simplifications and as a consequence numerical speed-ups for the evaluation of Eq. (29a) for the effectively secular density matrix $\hat{\rho}_s$.

[6] Translating for the sum-rule Eq. (10) into the summation over diagonal *final* states b.

In Sect. 2.3.2 we treat the physical aspect behind the new structure. While, unsatisfyingly, single diagrams cannot straightforwardly be assigned to underlying physical processes, the grouping opens a possibility for such interpretations. An important ingredient for the progress in this direction are the previously addressed gain and loss relations.

2.3.1 The grouping

The basic figure we will refer to throughout this section is Fig. 6. It contains 16+8 representatives for the 128 irreducible plus 64 reducible fourth order diagrams constructing the effectively secular fourth order part of the time evolution kernel,

$$\hat{K}^{(4)}_{\mathsf{eff}} \equiv \hat{K}^{(4)}_{ss} + \hat{K}^{(4)}_{C},$$

according to Eq. (29b). Allowing both reducible and irreducible diagrams, there are 2^4 distinct ways to place four vertices time ordered on the contours, and – without specifying directions of the fermion lines – three different ways to connect them. Picking one representative for each hermitian conjugate pair, we arrive thus at the 24 diagrams shown in Fig. 6. Notice that unlike in Fig. 1 we have not always chosen the representative with the latest vertex on the upper contour, which is for reasons of clarity in the upcoming gain-loss discussion.
The first step is now to acquire a basic understanding of the structure of Fig. 6. Afterwards we analyse the advantage of the grouping from the analytical side and finally we turn to a physical interpretation.

Grouping structure In Fig. 6 we have identified three supergroups, labelled A, B and C, corresponding to three different ways of connecting the vertices.
Within each supergroups G$\in$ {A,B,C}, the diagrams are subdivided into groups G.(0), G.(1) and G.(2) according to the number of vertices on their upper contour. Further, as indicated in the figure, we distinguish between stand-alone diagrams (s) and groups of three diagrams (t). Group G.(0) consists of only one 'basic' diagram G.(0)(s), with all the vertices on the lower contour, exactly reflecting the three possible types of connecting.
Supergroup A obviously collects the diagrams where the fermion lines are crossed. These are all irreducible. Supergroups B and C contain both irreducible and reducible diagrams. Except for the diagram C.(0)(s), supergroup C comprises all diagrams with the earliest (rightmost) vertex on the upper contour connected to the earliest vertex on the lower contour. The connection to C.(0)(s) is its gain-loss partnership with C.(1)(s): as described in Sect. 2.2, moving the latest vertex to the opposite contour, the diagrams transform into each other.

As just explained for supergroup C, we can verify in general that the diagrams G.(0)(s)

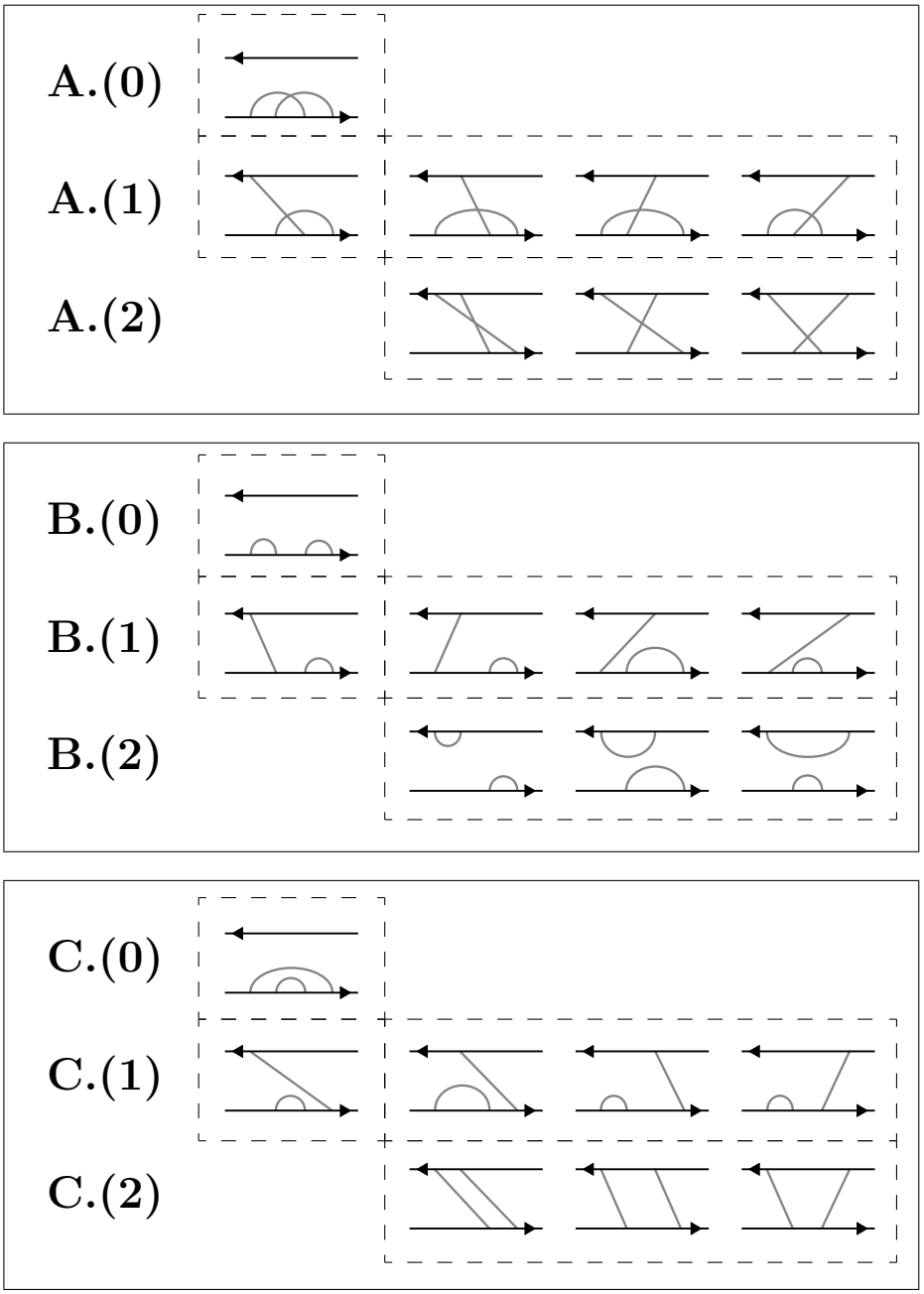

Figure 6: The sixteen irreducible 4th order diagrams, together with the eight reducible correction diagrams, can be sorted by topology into three supergroups A, B and C. Within each supergroup, there exist the subgroups (0),(1) and (2), labelled by the number of vertices on the upper contour. Further we distinguish between stand-alone diagrams (s) and triple groups (t).

and G.(1)(s) are gain-loss partners[7]. There remain the triple groups, consisting either of diagrams with two vertices on each contour, groups G.(2)≡G.(2)(t), or three vertices, among those the latest one, on the lower contour, giving the three diagrams in groups G.(1)(t). Diagrams with three vertices on the upper contour are hermitian conjugates of diagrams contained in G.(1) and thus omitted, and for the same reason, group G.(2)(t) contains just $\frac{1}{2}\times\binom{4}{2}=3$ diagrams. Again we can observe a gain-loss relation: each diagram from a G.(1)(t) group has its gain-loss partner in the G.(2)(t) group.

Diagram summations We have stated in Sect. 2.1 and confirmed in App. A.2.2 that the analytical expression related to a diagram splits into two parts, namely on the one hand into a product of tunnelling matrix elements, as defined in Eq. (34), and on the other hand an energy dependent function. This is also clear from the diagrammatic rules, App. A.2.3.

Within any group G.(x), x $\in \{0,1,2\}$, all diagrams have the same topology. As a consequence, for a fixed sequence of states, the members of the group *always* come with the same tunnelling matrix elements[8], such that the energy dependent parts of their analytical expressions can be added up to a new energy dependent function $\tilde{G}_{(\mathrm{x})}$. This allows *in general* to condense the group's contribution to the time evolution kernel into one compact analytical expression, as shown in Tab. 2, with the functions $\tilde{G}_{(\mathrm{x})}$ given in App. A.3.1, Eq. (129). Specifically, an arbitrary element of the effectively secular kernel can then – in full generality – be written as[9]

$$\left(\hat{K}^{(4)}_{\mathsf{eff}}\right)^{aa'}_{bb'} = \sum_{\mathrm{x}\in\{0,1,2\}} \left(\left(A_{(\mathrm{x})}\right)^{aa'}_{bb'} + \left(B_{(\mathrm{x})}\right)^{aa'}_{bb'} + \left(C_{(\mathrm{x})}\right)^{aa'}_{bb'} + \mathrm{c.c.} \right). \tag{36}$$

Moreover, given now the condition that the chosen initial states a, a' have the same energy (i.e. diagonal or secular non-diagonal states), the three diagrams in the subgroups G.(1)(t) or G.(2)(t) have an *additional* property which allows to perform the summation of their energy dependent parts at the earliest possible stage. From Tab. 1 we can read off their specific contributions to the kernel component $\hat{\mathcal{K}}^{(4)}(t,\tau_2,\tau_1,\tau)[\hat{\rho}^I_\odot(\tau)]$, Eq. (22b). It is easy to verify that for all groups G.(x)(t) (x$\in\{1,2\}$), those can formally be written as

$$\hat{\mathcal{G}}^I_{(\mathrm{x})}(t,\tau_2,\tau_1,\tau)[\hat{\rho}^I_\odot(\tau)] + \hat{\mathcal{G}}^I_{(\mathrm{x})}(t,\tau_1,\tau_2,\tau)[\hat{\rho}^I_\odot(\tau)] + \hat{\mathcal{G}}^I_{(\mathrm{x})}(t,\tau,\tau_2,\tau_1)[\hat{\rho}^I_\odot(\tau)], \tag{37}$$

because the ordering of the operators is for the three diagrams of the group identical up to the permutation of time arguments (for an explicit assignment see App. A.3.1,

[7] They are stand-alone diagrams, as there exists, concerning diagrams G.(0)(s), only one way to distribute the four vertices on the lower contour, respectively for the resulting gain-loss partners G.(1)(s) only one choice in putting the latest vertex on the upper and all others on the lower contour.

[8] Of course, for *special* values of the state indices this may coincidentally also hold for diagrams from different groups, such that the reverse is not true in general.

[9] The complex conjugate must be added because $G_{(\mathrm{x})}$, as defined in Tab. 2, refers only to one out of a hermitian conjugate pair of diagrams.

$$\left(A_{(0)}\right)_{bb'}^{aa'} = -\sum_{m_1',m_2',m_3'}\sum_{pp'}\sum_{ll'}\Big(\sum_{\sigma\sigma'} T_{l\sigma}^{\bar{p}}(a',m_3')\,T_{l'\sigma'}^{\bar{p}'}(m_3',m_2')\,T_{l\sigma}^{p}(m_2',m_1')\,T_{l'\sigma'}^{p'}(m_1',b')\Big)$$
$$\times\,\tilde{A}_{(0)}(E_{am_1'}-p'eV_{l'},E_{am_3'}-peV_l,E_{am_2'}-peV_l-p'eV_{l'})$$

$$\left(A_{(1)}\right)_{bb'}^{aa'} = +\sum_{m_1',m_2'}\sum_{pp'}\sum_{ll'}\Big(\sum_{\sigma,\sigma'} T_{l\sigma}^{p}(b,a)\,T_{l'\sigma'}^{\bar{p}'}(a',m_2')\,T_{l\sigma}^{\bar{p}}(m_2',m_1')\,T_{l'\sigma'}^{p'}(m_1',b')\Big)$$
$$\times\,\tilde{A}_{(1)}(E_{am_2'}-p'eV_{l'},E_{ba}+peV_l,E_{am_1'}-peV_l-p'eV_{l'};E_{aa'},E_{bb'})$$

$$\left(A_{(2)}\right)_{bb'}^{aa'} = -\sum_{m,m'}\sum_{pp'}\sum_{ll'}\Big(\sum_{\sigma,\sigma'} T_{l\sigma}^{p}(b,m)\,T_{l'\sigma'}^{p'}(m,a)T_{l\sigma}^{\bar{p}}(a',m')\,T_{l'\sigma'}^{\bar{p}'}(m',b')\Big)$$
$$\times\,\tilde{A}_{(2)}(E_{am'}-peV_l,E_{ma}+p'eV_{l'},E_{ab'}-peV_l-p'eV_{l'};E_{aa'})$$

$$\left(B_{(0)}\right)_{bb'}^{aa'} = +\sum_{m_1',m_2',m_3'}\sum_{pp'}\sum_{ll'}\Big(\sum_{\sigma\sigma'} T_{l'\sigma'}^{\bar{p}'}(a',m_3')\,T_{l'\sigma'}^{p'}(m_3',m_2')\,T_{l\sigma}^{\bar{p}}(m_2',m_1')\,T_{l\sigma}^{p}(m_1',b')\Big)$$
$$\times\,\tilde{B}_{(0)}(E_{am_1'}-peV_l,E_{am_3'}-p'eV_{l'},E_{am_2'})$$

$$\left(B_{(1)}\right)_{bb'}^{aa'} = -\sum_{m_1',m_2'}\sum_{pp'}\sum_{ll'}\Big(\sum_{\sigma\sigma'} T_{l\sigma}^{p}(b,a)\,T_{l'\sigma'}^{\bar{p}'}(a',m_2')\,T_{l'\sigma'}^{p'}(m_2',m_1')\,T_{l\sigma}^{\bar{p}}(m_1',b')\Big)$$
$$\times\,\tilde{B}_{(1)}(E_{am_2'}-p'eV_{l'},E_{ba}+peV_l,E_{am_1'};E_{aa'},E_{bb'})$$

$$\left(B_{(2)}\right)_{bb'}^{aa'} = +\sum_{m,m'}\sum_{pp'}\sum_{ll'}\Big(\sum_{\sigma\sigma'} T_{l\sigma}^{\bar{p}}(b,m)\,T_{l\sigma}^{p}(m,a')\,T_{l'\sigma'}^{\bar{p}'}(a',m')\,T_{l'\sigma'}^{p'}(m',b')\Big)$$
$$\times\,\tilde{B}_{(2)}(E_{am'}-p'eV_{l'},E_{ma}+peV_l,E_{ab'};E_{aa'})$$

$$\left(C_{(0)}\right)_{bb'}^{aa'} = +\sum_{m_1',m_2',m_3'}\sum_{pp'}\sum_{ll'}\Big(\sum_{\sigma\sigma'} T_{l'\sigma'}^{\bar{p}'}(a',m_3')\,T_{l\sigma}^{\bar{p}}(m_3',m_2')\,T_{l\sigma}^{p}(m_2',m_1')\,T_{l'\sigma'}^{p'}(m_1',b')\Big)$$
$$\times\,\tilde{C}_{(0)}(E_{am_1'}-p'eV_{l'},E_{am_3'}-p'eV_{l'},E_{am_2'}-peV_l-p'eV_{l'})$$

$$\left(C_{(1)}\right)_{bb'}^{aa'} = -\sum_{m_1',m_2'}\sum_{pp'}\sum_{ll'}\Big(\sum_{\sigma\sigma'} T_{l'\sigma'}^{p'}(b,a)\,T_{l'\sigma'}^{\bar{p}'}(a',m_2')\,T_{l\sigma}^{\bar{p}}(m_2',m_1')\,T_{l\sigma}^{p}(m_1',b')\Big)$$
$$\times\,\tilde{C}_{(1)}(E_{am_2'}-p'eV_{l'},E_{ba}+p'eV_{l'},E_{am_1'}-peV_l-p'eV_{l'};E_{aa'},E_{bb'})$$

$$\left(C_{(2)}\right)_{bb'}^{aa'} = +\sum_{m,m'}\sum_{pp'}\sum_{ll'}\Big(\sum_{\sigma\sigma'} T_{l\sigma}^{p}(b,m)\,T_{l'\sigma'}^{p'}(m,a)\,T_{l'\sigma'}^{\bar{p}'}(a',m')\,T_{l\sigma}^{\bar{p}}(m',b')\Big)$$
$$\times\,\tilde{C}_{(2)}(E_{am'}-p'eV_{l'},E_{ma}+p'eV_{l'},E_{ab'}-peV_l-p'eV_{l'};E_{aa'})$$

Table 2: In the three boxes for G∈ {A,B,C}, the analytical expressions related to the groups G.(0), G.(1) and G.(2) from Fig. 6 are listed. For the omitted hermitian conjugate diagrams, the corresponding expressions are just the complex conjugate of the listed contributions. The involved intermediate states are summed over; for clarity, we have numbered them according to their order of appearance on the contour. Additionally, the states on the lower contour are primed. The definition of the energy dependent functions is given in App. A.3 in Eq. (129) for the general, and in Eq. (130) for the special case of secular initial states, i.e. $E_{aa'} = 0$.

177 ff.). For the contribution to $(\hat{K}^{(4)})^{aa'}_{bb'}$ this means we deal, according to Eq. (32), with

$$\begin{aligned}
&\lim_{\lambda\to 0}\int\limits_{\infty\geq\tau'\geq\tau_1'\geq\tau_2'\geq 0} \mathrm{d}\tau'\,\mathrm{d}\tau_1'\,\mathrm{d}\tau_2'\; e^{-\lambda\tau'}\, e^{\frac{\mathrm{i}}{\hbar}(E_a-E_{a'})(t-\tau')} e^{-\frac{\mathrm{i}}{\hbar}(E_b-E_{b'})t} \\
&\times\Big\langle b\Big|\hat{\mathcal{G}}^I_{(\mathrm{x})}(t,t-\tau_2',t-\tau_1',t-\tau')[|a\rangle\langle a'|] \\
&\qquad\qquad + \hat{\mathcal{G}}^I_{(\mathrm{x})}(t,t-\tau_1',t-\tau_2',t-\tau')[|a\rangle\langle a'|] \\
&\qquad\qquad\qquad + \hat{\mathcal{G}}^I_{(\mathrm{x})}(t,t-\tau',t-\tau_2',t-\tau_1')[|a\rangle\langle a'|]\Big| b'\Big\rangle
\end{aligned}$$

$$\begin{aligned}
\overset{E_a=E_{a'}}{=}\lim_{\lambda\to 0}&\left(\int\limits_{\infty\geq\tau'\geq\tau_1'\geq\tau_2'\geq 0}\mathrm{d}\tau'\,\mathrm{d}\tau_1'\,\mathrm{d}\tau_2'\; e^{-\lambda\tau'} + \int\limits_{\infty\geq\tau'\geq\tau_2'\geq\tau_1'\geq 0}\mathrm{d}\tau'\,\mathrm{d}\tau_1'\,\mathrm{d}\tau_2'\; e^{-\lambda\tau'} + \int\limits_{\infty\geq\tau_1'\geq\tau_2'\geq\tau'\geq 0}\mathrm{d}\tau'\,\mathrm{d}\tau_1'\,\mathrm{d}\tau_2'\; e^{-\lambda\tau_2'}\right) \\
&\times\Big\langle b\Big|\hat{\mathcal{G}}^I_{(\mathrm{x})}(t,t-\tau_2',t-\tau_1',t-\tau')[|a\rangle\langle a'|]\Big| b'\Big\rangle\, e^{-\frac{\mathrm{i}}{\hbar}(E_b-E_{b'})t} =
\end{aligned}$$

$$\begin{aligned}
=\lim_{\lambda\to 0}&\int\limits_{\infty\geq\tau'\geq\tau_1'\geq 0}\mathrm{d}\tau'\,\mathrm{d}\tau_1'\; e^{-\lambda\tau'}\int\limits_{\infty\geq\tau_2'\geq 0}\mathrm{d}\tau_2\; e^{-\lambda\tau_2'} e^{-\frac{\mathrm{i}}{\hbar}(E_b-E_{b'})t} \\
&\times\Big\langle b\Big|\hat{\mathcal{G}}^I_{(\mathrm{x})}(t,t-\tau_2',t-\tau_1',t-\tau')[|a\rangle\langle a'|]\Big| b'\Big\rangle\,. \qquad (38)
\end{aligned}$$

In order to combine the integrations we had to introduce a factor $\exp(-\lambda\tau_2')$ into the first and second, and $\exp(-\lambda\tau')$ into the third integrand (importantly, doing so is perfectly valid from the mathematical point of view, as explained in App. A.3.1). Consequently, the summation over the three contributions separates off the integration over τ_2': it is taken out of the time order, running now from 0 to ∞ independent of τ_1' and τ'. In the language of the diagrams, this means that time ordering of the vertices on the single contour is preserved ($t > \tau_1 = t-\tau_1' > \tau = t-\tau'$, $t > \tau_2 = t-\tau_2'$), but there is no further restriction on τ_2 (or, equivalently, τ_2'). Visually, this implies that the three earliest vertices can be shifted around freely without overtaking each other as long as the vertex at time t remains the latest. And actually, this is obvious by inspecting the diagrams within any of the G.(1)(t) or G.(2)(t) groups.

The resulting simplified versions of the generally valid analytical expressions Eq. (129) are listed in App. A.3.1, Eq. (130). They hold for secular initial states. We remark that if the initial states are not degenerate, still two out of the three analytical expressions, namely the first two, which differ from each other by an interchange of τ_1 and τ_2, can be combined in the way shown in Eq. (38). As a consequence, also in the generally valid case, Eq. (129), partial cancellations are expected in the sums over the different energy dependent functions.

To demonstrate the practical relevance of this finding, we pick as specific example the contribution $(C_{(2)})^{aa}_{bb}$ of group C.(2)(t) to a diagonal component $(\hat{K}^{(4)}_{\mathsf{eff}})^{aa}_{bb} = (\hat{K}^{(4)}_{ss})^{aa}_{bb} + (\hat{K}^{(4)}_{C})^{aa}_{bb}$ of the effective time evolution kernel for a secular density matrix. Later, in Sect. 2.4, $(C_{(2)})^{aa}_{bb}$ will turn out to be tightly related with the typical regularisation demanding T-matrix cotunnelling expressions.

To $(\hat{K}^{(4)})^{aa}_{bb}$, the only two contributions from group C.(2)(t) are the single irreducible diagram,

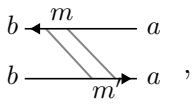

,

and its hermitian conjugate, which is omitted here as it just yields the complex conjugate to the contribution of our example. The associated term in time domain can be read off Tab. 1:

$$\left\langle b \left| \hat{\mathcal{C}}^I_{(2)}(t,\tau_2,\tau_1,\tau)[|a\rangle\langle\langle a|] \right| b \right\rangle = \sum_{pp'} \left\langle \hat{C}^p_1 \hat{C}^{\bar{p}}_3 \right\rangle \left\langle \hat{C}^{p'}_0 \hat{C}^{\bar{p}'}_2 \right\rangle \left\langle b \left| \hat{D}^p_3 \hat{D}^{p'}_2 \right| a \right\rangle \left\langle a \left| \hat{D}^{\bar{p}'}_0 \hat{D}^{\bar{p}}_1 \right| b \right\rangle .$$

For space reasons, the intermediate states have not yet been labelled to m, m' as in the above sketch of our example. We have to consider all possibilities for the intermediate states, hence m and m' must be summed over, and for a non-secular constellation, $E_m \neq E_{m'}$, also the two reducible members of the group,

$$\left\langle b \left| \hat{\mathcal{C}}^I_{(2)}(t,\tau_1,\tau_2,\tau)[|a\rangle\langle\langle a|] \right| b \right\rangle + \left\langle b \left| \hat{\mathcal{C}}^I_{(2)}(t,\tau,\tau_2,\tau_1)[|a\rangle\langle\langle a|] \right| b \right\rangle ,$$

need to be taken into account via $(\hat{K}^{(4)}_{C})^{aa}_{bb}$. For this case, we can apply Eq. (38):

$$\begin{aligned}
&\lim_{\lambda\to 0} \sum_{p,p'\in\{+,-\}} \int_{\infty\geq\tau'\geq\tau'_1\geq\tau'_2\geq 0} \mathrm{d}\tau' \,\mathrm{d}\tau'_1 \,\mathrm{d}\tau'_2 \; e^{-\lambda\tau'} \, e^{\frac{\mathrm{i}}{\hbar}(E_a - E_{a'})(t-\tau')} e^{-\frac{\mathrm{i}}{\hbar}(E_b - E_{b'})t} \\
&\qquad \times \Bigg(\left\langle \hat{C}^p_1 \hat{C}^{\bar{p}}_3 \right\rangle \left\langle \hat{C}^{p'}_0 \hat{C}^{\bar{p}'}_2 \right\rangle \left\langle b \left| \hat{D}^p_3 \hat{D}^{p'}_2 \right| a \right\rangle \left\langle a \left| \hat{D}^{\bar{p}'}_0 \hat{D}^{\bar{p}}_1 \right| b \right\rangle \\
&\qquad\quad + \left\langle \hat{C}^p_2 \hat{C}^{\bar{p}}_3 \right\rangle \left\langle \hat{C}^{p'}_0 \hat{C}^{\bar{p}'}_1 \right\rangle \left\langle b \left| \hat{D}^p_3 \hat{D}^{p'}_1 \right| a \right\rangle \left\langle a \left| \hat{D}^{\bar{p}'}_0 \hat{D}^{\bar{p}}_2 \right| b \right\rangle \\
&\qquad\quad + \left\langle \hat{C}^p_2 \hat{C}^{\bar{p}}_3 \right\rangle \left\langle \hat{C}^{p'}_1 \hat{C}^{\bar{p}'}_0 \right\rangle \left\langle b \left| \hat{D}^p_3 \hat{D}^{p'}_0 \right| a \right\rangle \left\langle a \left| \hat{D}^{\bar{p}'}_1 \hat{D}^{\bar{p}}_2 \right| b \right\rangle \Bigg) \\
&= \lim_{\lambda\to 0} \int_{\infty\geq\tau'_1\geq\tau'\geq 0} \mathrm{d}\tau' \,\mathrm{d}\tau'_1 \; e^{-\lambda\tau'} \int_{\infty\geq\tau'_2\geq 0} \mathrm{d}\tau_2 \; e^{-\lambda\tau'_2} e^{-\frac{\mathrm{i}}{\hbar}(E_b - E_{b'})t} \\
&\qquad\qquad \times \left\langle \hat{C}^p_1 \hat{C}^{\bar{p}}_3 \right\rangle \left\langle \hat{C}^{p'}_0 \hat{C}^{\bar{p}'}_2 \right\rangle \left\langle b \left| \hat{D}^p_3 \hat{D}^{p'}_2 \right| a \right\rangle \left\langle a \left| \hat{D}^{\bar{p}'}_0 \hat{D}^{\bar{p}}_1 \right| b \right\rangle .
\end{aligned}$$

The combination of all three terms is allowed for our example, as the initial states (a) are diagonal. Labelling the intermediated states as in the above sketch with m, m', the

contribution can in general be written as:

$$\left(C_{(2)}\right)^{aa}_{bb} = \sum_{m,m'}\sum_{pp'}\Big(\sum_{\sigma\sigma'} T^{p}_{\sigma}(b,m)\,T^{p'}_{\sigma'}(m,a)T^{\bar{p}'}_{\sigma'}(a,m')\,T^{\bar{p}}_{\sigma}(m',b)\Big) \times\Big(\sum_{ll'}\tilde{C}_{(2)}(E_{mb}+peV_l, E_{am'}+p'eV_{l'}, E_{ab'}+peV_l+p'eV_{l'})\Big).$$

Here, $p, p' \in \{+,-\}$. As we stated before, the contribution is split into a part containing merely the tunnelling matrix elements and an energy dependent function $\tilde{C}_{(2)}$ specific for the diagram group. This function distinguishes the two cases of secular ($E_m = E_{m'}$) and non-secular ($E_m \neq E_{m'}$) intermediate states,

$$\tilde{C}_{(2)}(\mu,\mu',\Delta) = \frac{\beta}{\mathrm{i}\hbar}\int \mathrm{d}\omega \int \mathrm{d}\omega'\, f^{-}(\omega)\, f^{-}(\omega') \times\begin{cases} \lim_{\eta\to 0}\ \frac{1}{\omega-\beta\mu+\mathrm{i}\eta}\ \frac{1}{\omega'-\beta\mu'+\mathrm{i}\eta}\ \frac{1}{\omega+\omega'-\beta\Delta+\mathrm{i}\eta} & \mu+\mu'=\Delta\,, \\ -\lim_{\eta\to 0}\ \frac{1}{\omega-\beta\mu'+\mathrm{i}\eta}\ \frac{1}{\omega+\beta(\Delta-\mu)-\mathrm{i}\eta}\ \frac{1}{\omega+\omega'-\beta\Delta+\mathrm{i}\eta} & \mu+\mu'\neq\Delta\,. \end{cases} \tag{39}$$

Here, as usual, $\beta = (k_B T)^{-1}$. We remark that the second expression is one commonly encountered in T-matrix based rate approach calculations and diverges in the limit $\mu+\mu' \to \Delta$ (which is equivalent to $E_m \to E_{m'}$). We investigate it in more detail in Sect. 2.4, where we show in particular that the typical regularisation *cannot* recover the solution for $E_m = E_{m'}$ exactly.

2.3.2 Physical background

So far we have succeeded to identify three supergroups G$\in$ {A, B, C} of topologically related diagrams, which can be subdivided into groups G.(0), G.(1), G.(2). Within each of these groups, diagrams have the same number of vertices – namely zero, one or two, respectively – on the upper contour and add up, as they always come with the same matrix elements. We further could classify stand-alone diagrams (s) and triple groups (t). The grouping allowed us to condense into Tab. 2 the full set of analytical contributions relevant for a secular calculation including effectively non-secular corrections (cf. Sect. 1.3). Hence, the structuring clearly brings advantage from both the numerical and the analytical point of view. However, it is also of use for the physical understanding of the diagrams. In particular, one can trace three prominent higher order effects: pair-tunnelling, cotunnelling and level renormalisation.

For reasons of clarity, it is best to refer to the single-level model introduced in Sect. 2.2. We start with explicitly setting up Eq. (36) for the kernel elements appearing in Eq. (35). Thereby notice that G.(0) / G.(1) can contribute just if the charge between the initial and final state differs by $0/\pm 1$, while G(2) can connect initial and final states of same charge as well as of a charge difference ± 2. We can identify in fourth

order the following nonzero contributions:

$$
\begin{aligned}
(\hat{K}^{(4)})^{00}_{00} &= -\left(\sum\nolimits_{\sigma} \Gamma^{0\to\sigma}_{(4)} + \Gamma^{0\to 2}_{(4)}\right) = (A_{(0)})^{00}_{00} + (C_{(0)})^{00}_{00} + (B_{(2)})^{00}_{00} + (C_{(2)})^{00}_{00},\\
(\hat{K}^{(4)})^{\sigma\sigma}_{00} &= +\Gamma^{\sigma\to 0}_{(4)} = (A_{(1)})^{\sigma\sigma}_{00} + (B_{(1)})^{\sigma\sigma}_{00} + (C_{(1)})^{\sigma\sigma}_{00},\\
(\hat{K}^{(4)})^{22}_{00} &= +\Gamma^{2\to 0}_{(4)} = (A_{(2)})^{22}_{00} + (C_{(2)})^{22}_{00},
\end{aligned}
$$

$$
\begin{aligned}
(\hat{K}^{(4)})^{\sigma\sigma}_{\sigma\sigma} &= -\left(\Gamma^{\sigma\to 0}_{(4)} + \Gamma^{\sigma\to\bar{\sigma}}_{(4)} + \Gamma^{\sigma\to 2}_{(4)}\right)\\
&= (A_{(0)})^{\sigma\sigma}_{\sigma\sigma} + (C_{(0)})^{\sigma\sigma}_{\sigma\sigma} + (A_{(2)})^{\sigma\sigma}_{\sigma\sigma} + (B_{(2)})^{\sigma\sigma}_{\sigma\sigma} + (C_{(2)})^{\sigma\sigma}_{\sigma\sigma},\\
(\hat{K}^{(4)})^{\bar{\sigma}\bar{\sigma}}_{\sigma\sigma} &= +\Gamma^{\bar{\sigma}\to\sigma}_{(4)} = (A_{(2)})^{\bar{\sigma}\bar{\sigma}}_{\sigma\sigma} + (C_{(2)})^{\bar{\sigma}\bar{\sigma}}_{\sigma\sigma},\\
(\hat{K}^{(4)})^{00}_{\sigma\sigma} &= +\Gamma^{0\to\sigma}_{(4)} = (A_{(1)})^{00}_{\sigma\sigma} + (B_{(1)})^{00}_{\sigma\sigma} + (C_{(1)})^{00}_{\sigma\sigma},\\
(\hat{K}^{(4)})^{22}_{\sigma\sigma} &= +\Gamma^{\sigma\to 2}_{(4)} = (A_{(1)})^{22}_{\sigma\sigma} + (B_{(1)})^{22}_{\sigma\sigma} + (C_{(1)})^{22}_{\sigma\sigma},
\end{aligned}
$$

$$
\begin{aligned}
(\hat{K}^{(4)})^{22}_{22} &= -\left(\sum\nolimits_{\sigma} \Gamma^{2\to\sigma}_{(4)} + \Gamma^{2\to 0}_{(4)}\right) = (A_{(0)})^{22}_{22} + (C_{(0)})^{22}_{22} + (B_{(2)})^{22}_{22} + (C_{(2)})^{22}_{22},\\
(\hat{K}^{(4)})^{\sigma\sigma}_{22} &= +\Gamma^{\sigma\to 2}_{(4)} = (A_{(1)})^{\sigma\sigma}_{22} + (B_{(1)})^{\sigma\sigma}_{22} + (C_{(1)})^{\sigma\sigma}_{22},\\
(\hat{K}^{(4)})^{00}_{22} &= +\Gamma^{0\to 2}_{(4)} = (A_{(2)})^{22}_{00} + (C_{(2)})^{00}_{22}.
\end{aligned}
\tag{40}
$$

Thereby, $\Gamma^{\alpha\to\beta}_{(4)}$ denotes the fourth order part of a rate $\Gamma^{\alpha\to\beta} = \sum_{n\in\mathbb{N}}^{\infty} \Gamma^{\alpha\to\beta}_{(2n)}$. Notice that in this sum a nonzero contribution for $n = 1$ only exists if $|N_\alpha - N_\beta| \neq 1$. The reducible stand-alone diagram B.(0) can never be involved due to the secularity of all states for each charge, and contributions from supergroup A can partially be ruled out from the equation for $\dot{P}_0/\dot{P}_2$, because they demand transitions to a higher as well as to a lower charge state.

Setting in the analytical expressions given in Tab. 2 and App. A.3.1, we can make now Eq. (35) more explicit. The intention is to first extract the physical meaning of the contributions to the single rates and afterwards draw a relation to the diagram groups. We want to anticipate that inconveniently, there exist almost *no* one-to-one relations between a certain physical process and a single diagram class. Nevertheless, the upcoming analysis brings some light into the relation between diagrammatic representation and physical reality. Due to the number and complexity of the involved expressions, it is sensible, and for our purpose sufficient, to analyse Eq. (35) at zero bias voltage, which keeps the involved formulas rather compact. Moreover we assume the symmetric unpolarised case, where all tunnelling matrix elements simplify to $\sum_\sigma T^{+}_{l\sigma}(n,m) = \pm\sqrt{\hbar\Gamma/2}\delta_{N_n,N_m+1}$. For the energy dependent functions the analytical expressions found in App. A.3.1, Eq. (130) are in the case of the single-level quantum-dot appropriate. We use $E_1 := E_\uparrow (= E_\downarrow)$ and $E_{ab} = E_a - E_b - e\alpha V_{\mathsf{gate}}\{N_a - N_b\}$.

Then, Eq. (35) can be reformulated as:

$$\begin{aligned}\frac{\dot{P}_0}{\frac{1}{2}\Gamma} =& -P_0\left(2f^+(E_{10})+\frac{\hbar\Gamma}{k_BT}\{\gamma_{\rm II}^-(E_{10})-2\gamma_{\rm II}^+(E_{10})+\gamma_{pt}^+(E_{10},E_{21})-\gamma_{\rm III}^+(E_{10},E_{21},0)\}\right)\\ &+\frac{1}{2}\left(P_\uparrow+P_\downarrow\right)\left(2f^-(E_{10})+\frac{\hbar\Gamma}{k_BT}\{2\gamma_{\rm II}^+(E_{10})-\gamma_{\rm II}^-(E_{10})+\gamma_{\rm III}^-(E_{10},E_{21},1)\}\right)\\ &+P_2\frac{\hbar\Gamma}{k_BT}\gamma_{pt}^-(E_{21},E_{10}),\end{aligned} \tag{41a}$$

$$\begin{aligned}\frac{\dot{P}_\sigma}{\frac{1}{2}\Gamma} =& -\frac{1}{2}P_\sigma\left(2f^+(E_{21})+2f^-(E_{10})+\frac{\hbar\Gamma}{k_BT}\{\gamma_{\rm III}^-(E_{10},E_{21},1)+\gamma_{\rm III}^+(E_{21},E_{10},1)\right.\\ &\left.-\gamma_{\rm II}^-(E_{10})-\gamma_{\rm II}^+(E_{21})+\gamma_{cot}^-(E_{10},E_{21})+\gamma_{cot}^+(E_{21},E_{10})+2\gamma_{\rm II}^+(E_{10})+2\gamma_{\rm II}^-(E_{21})\}\right)\\ &+\frac{1}{2}P_0\left(2f^+(E_{10})+\frac{\hbar\Gamma}{k_BT}\{\gamma_{\rm II}^-(E_{10})-2\gamma_{\rm II}^+(E_{10})-\gamma_{\rm III}^+(E_{10},E_{21},0)\}\right)\\ &+\frac{1}{2}P_{\bar\sigma}\frac{\hbar\Gamma}{k_BT}\left(\gamma_{cot}^-(E_{10},E_{21})+\gamma_{cot}^+(E_{21},E_{10})\right)\\ &+\frac{1}{2}P_2\left(2f^-(E_{21})+\frac{\hbar\Gamma}{k_BT}\{\gamma_{\rm II}^+(E_{21})-2\gamma_{\rm II}^-(E_{21})-\gamma_{\rm III}^-(E_{21},E_{10},0)\}\right),\end{aligned} \tag{41b}$$

$$\begin{aligned}\frac{\dot{P}_2}{\frac{1}{2}\Gamma} =& -P_2\left(2f^-(E_{21})+\frac{\hbar\Gamma}{k_BT}\{\gamma_{\rm II}^+(E_{21})-2\gamma_{\rm II}^-(E_{21})+\gamma_{pt}^-(E_{21},E_{10})-\gamma_{\rm III}^-(E_{21},E_{10},0)\}\right)\\ &+\frac{1}{2}\left(P_\uparrow+P_\downarrow\right)\left(2f^+(E_{21})+\frac{\hbar\Gamma}{k_BT}\{2\gamma_{\rm II}^-(E_{21})-\gamma_{\rm II}^+(E_{21})+\gamma_{\rm III}^+(E_{21},E_{10},1)\}\right)\\ &+P_0\frac{\hbar\Gamma}{k_BT}\gamma_{pt}^+(E_{10},E_{21}).\end{aligned} \tag{41c}$$

Noticeably, we have achieved to express the fourth order contributions to the rate completely in terms of four physically meaningful functions,

$$\begin{aligned}\gamma_{\rm II}^\pm(\mu) =& \pm\left(\tilde\Psi_1(\mu)\,f^\pm(\mu)\mp 2\pi f^+(\mu)f^-(\mu)\tilde\Psi(\mu)\right),\\ \gamma_{\rm III}^\pm(\mu,\mu',\delta) =& \pm\left(\left[f^\pm(\mu')-\delta\right]\tilde\Psi_1(\mu)\pm 2\pi f^+(\mu)f^-(\mu)\,\tilde\Psi(\mu')+4\pi\frac{\tilde\Psi(\mu)-\tilde\Psi(\mu')}{\mu-\mu'}f^\pm(\mu)\right),\\ \gamma_{cot}^\pm(\mu,\mu') =& \pm\left(\pm\frac{1}{2\pi}\tilde\Psi_2(\mu)-\tilde\Psi_1(\mu)\,f^\pm(\mu)-\tilde\Psi_1(\mu')\,f^\pm(\mu')\pm\frac{\tilde\Psi_1(\mu)-\tilde\Psi_1(\mu')}{\mu-\mu'}\right),\\ \gamma_{pt}^\pm(\mu,\mu') =& \pm\left(\left\{b^\pm(\mu+\mu')+f^\pm(\mu)\right\}\tilde\Psi_1(\mu')+\left\{b^\pm(\mu+\mu')+f^\pm(\mu')\right\}\tilde\Psi_1(\mu)\right.\\ &\left.-4\pi\frac{\tilde\Psi(\mu)-\tilde\Psi(\mu')}{\mu-\mu'}\,b^\pm(\mu+\mu')\right).\end{aligned} \tag{42}$$

Thereby, we abbreviated the polygamma functions $\Psi^{(n)}$ corresponding to the nth derivative of the digamma function $\Psi^{(0)}$ [51] according to $\tilde{\Psi}_0(\mu) = \mathsf{Re}\Psi^{(0)}\left(\frac{1}{2} + \frac{\mathrm{i}\beta\mu}{2\pi}\right) - \Psi^{(0)}\left(\frac{1}{2} + \frac{W}{2\pi}\right)$, $\tilde{\Psi}_1(\mu) = \mathsf{Im}\Psi^{(1)}\left(\frac{1}{2} + \frac{\mathrm{i}\beta\mu}{2\pi}\right)$, $\tilde{\Psi}_2(\mu) = \mathsf{Re}\Psi^{(2)}\left(\frac{1}{2} + \frac{\mathrm{i}\beta\mu}{2\pi}\right)$, where W denotes the bandwidth.
The interpretation of the functions γ_{cot} and $\gamma_{pt}^{\pm}$ is straightforward: they belong to processes which transfer **two** electrons between quantum-dot and leads, namely *co-tunnelling*, $N \to N$, and *pair-tunnelling*, $N \to N \pm 2$, respectively. In addition, there are also fourth order processes which merely transfer **one** electron, $N \to N \pm 1$ while a second electron undergoes a virtual transition. We want to speak of *fourth order amendments to the sequential tunnelling*, to which the functions $\gamma_{\mathrm{III}}^{\pm}$ and $\gamma_{\mathrm{II}}^{\pm}$ belong. Thereby, the former function relates to processes involving all three, the latter processes involving only two charge states.

As promised, we establish now a connection between these three classes of physical events and the diagram groups.

Pair-tunnelling Let us pick for our explanations the process $|2\rangle \to |0\rangle$, where two electrons leave the fully populated dot coherently. We have already exploited in Eq. (40) for $K_{00}^{22} \equiv +\Gamma_{(4)}^{2\to 0}$, which represents the related 'gain' rate for the state $|0\rangle$, that the only diagrams which can transfer two electrons are the ones in groups A.(2) and C.(2). In Fig. 7(a), one representative for each of the two groups is shown [leftmost] along with its loss partner [middle left], which is found among the diagrams in group A.(1)(t) respectively C.(1)(t). Those merely carry the 'loss' rate $-\Gamma_{(4)}^{2\to 0}$ by which the state $|2\rangle$ is depopulated and hence describe no physical process of their own. What is flustering, however, is that A.(1)(t) and C.(1)(t), see their indices in Fig. 7(a) and/or Eq. (40), obviously add to the kernel element $K_{\sigma\sigma}^{22}$ instead of K_{22}^{22}. The latter is the one corresponding to the loss term for the state $|2\rangle$, i.e., where $-\Gamma_{(4)}^{2\to 0}$ should appear, cf. Eq. (40). Hereby, the connection to A.(1)(s) and C.(1)(s) [Fig. 7(a), middle right] is crucial: Those add up with A.(1)(t) and C.(1)(t) in $K_{\sigma\sigma}^{22}$, and must include a contribution $+\Gamma_{(4)}^{2\to 0}$ in order to cancel out this misplaced rate from $K_{\sigma\sigma}^{22}$. And indeed, it makes perfectly sense: namely in turn, their loss partners A.(0)(s) and C.(0)(s) [Fig. 7(a), rightmost], which contribute to K_{22}^{22}, must then contain $-\Gamma_{(4)}^{2\to 0}$. So via the gain-loss chain depicted in Fig. 7(a), the loss rate $-\Gamma_{(4)}^{2\to 0}$ has actually been transferred into the correct kernel element K_{22}^{22} describing the depopulation of the state $|2\rangle$.
These claims are also nicely backed by Eqs. (41a)-(41c). The function $\gamma_{pt}^{-}(E_{21}, E_{10})$ holds the Bose function $b^{-}(E_{20})$ and relates to the pair-tunnelling process $|2\rangle \to |0\rangle$. It appears on the 'gain side' for $\dot{P}_0$, namely in the last line of Eq. (41a), which emerges from the sum $(A_{(2)})_{00}^{22} + (C_{(2)})_{00}^{22}$. Its second occurrence is in the loss term for $\dot{P}_2$, in the first line of Eq. (41c). In the equation for $\dot{P}_\sigma$, Eq. (41b), the remnant of the gain-loss chain Fig. 7(a) is a fourth order correction to the sequential tunnelling in form of the function $\gamma_I^{-}(E_{10}, E_{21}, 0)$: Indeed the diagrams in groups A.(1)(t) and C.(1)(t), as loss partners of the 'physical' pair-tunnelling diagrams A.(2)(t) and C.(2)(t), carry only the rate $-\Gamma_{(4)}^{2\to 0}$ and have no physical background of their own. But the stand-

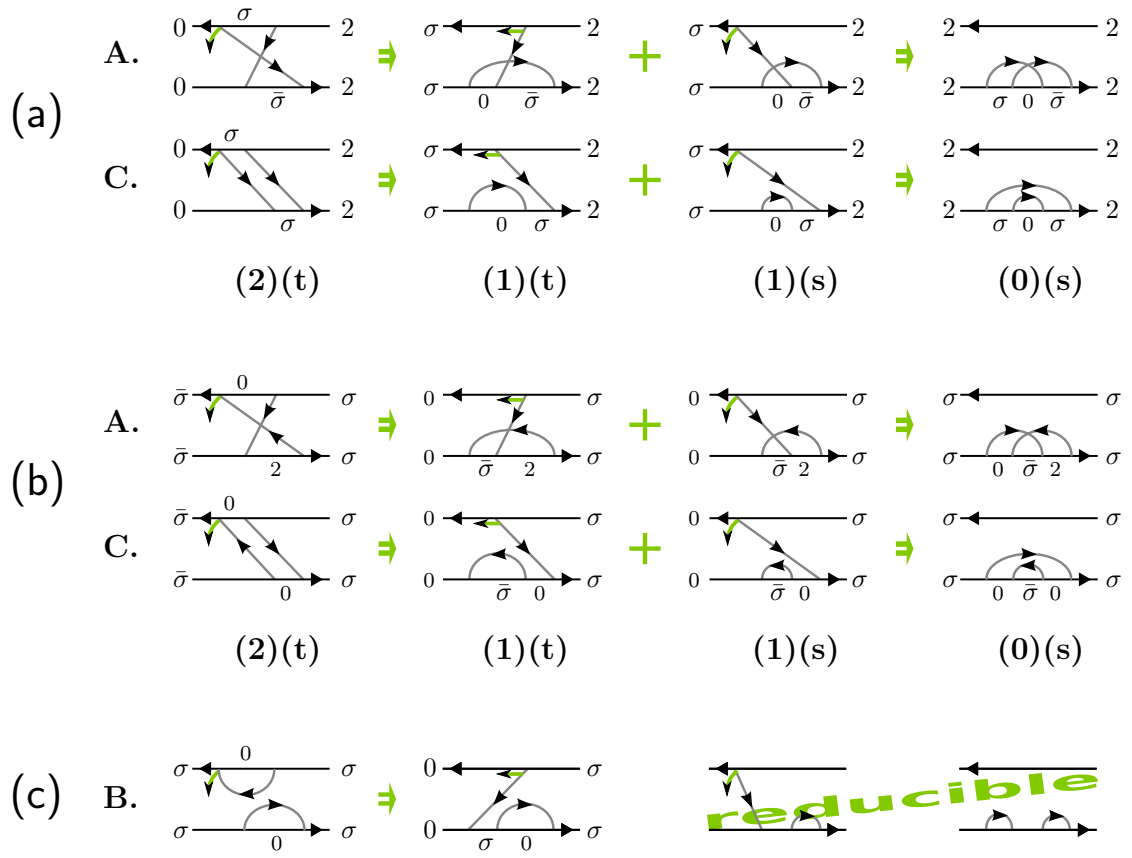

Figure 7: Examples for gain-loss chains in the single level quantum-dot model. For the triple groups (t), only one of the three diagrams is representatively drawn. (a) The full set of diagrams describing the pair-tunnelling process $|2\rangle \to |0\rangle$. (b) For the single-level quantum-dot, supergroup A can only contribute to cotunnelling events $|\sigma\rangle \to |\bar{\sigma}\rangle$ due to spin selection rules and because its crossed structure demands inclusion of a higher as well as a lower charge state. Supergroup C supports all kinds of cotunnelling events in the single-level quantum-dot, but here we focus on the process $|\sigma\rangle \to |\bar{\sigma}\rangle$.
(c) For supergroup B, the stand-alone diagrams are reducible and cannot contribute in our example.

alone diagram A.(1)(s) and C.(1)(s) can, in addition to the physical necessary, but meaningless annihilation term $+\Gamma^{2\to 0}_{(4)}$, contain a contribution to $\Gamma^{2\to\sigma}_{(4)}$. It reflects the possibility that in course of an out-tunnelling process $|2\rangle \to |\sigma\rangle$, also a second electron might have temporarily left the dot, taking the dot intermediately to charge state zero [verify from Fig. 7(a), (1)(s)].

Cotunnelling In order to contribute to pair-tunnelling, $N \to N \pm 2$, the fermion lines in the diagrams of groups A.(2) and C.(2) had, as seen from Fig. 7(a), to point towards the same contour. If one fermion line inverts its direction, initial and final states of the diagram are of the same charge and it describes a cotunnelling process $N \to N$. As an example, we choose the process $|\sigma\rangle \to |\bar{\sigma}\rangle$ as depicted in Fig. 7(b). We thereby restrict to the diagrams influencing the charge state $N = 0$. Upon exchanging

the charges $N = 0$ and $N = 2$, the full set of contributions to this process would be obtained. Upon comparison with Eq. (40) it is confirmed that only groups A.(2) and C.(2) contribute to the corresponding ('gain'-)rate $+\Gamma^{\sigma\to\bar{\sigma}}_{(4)} \equiv K^{\sigma\sigma}_{\bar{\sigma}\bar{\sigma}}$, and the gain-loss chains are constructed in analogy to the one for the pair-tunnelling, as it can be seen upon comparison of Fig. 7(b) and (a). Let us trace now the signatures of the cotunnelling event $|\sigma\rangle \to |\bar{\sigma}\rangle$ in the equations for the populations, Eqs. (41a)-(41c). The functions $\gamma^{-}_{cot}(E_{10}, E_{21})$ and $\gamma^{+}_{cot}(E_{21}, E_{10})$ occur merely in the time evolution of P_σ, Eq. (41b). In the first line, they come as a loss contributions, relating in fact to the 'reverse' event $|\sigma\rangle \to |\bar{\sigma}\rangle$, while the fourth line is the gain term stemming from the process $|\sigma\rangle \to |\bar{\sigma}\rangle$. Notice that for our assumptions on the TMEs and due to the degeneracy of the two singly occupied states it holds in our case $P_\sigma = P_{\bar{\sigma}}$ and $\Gamma^{\sigma\to\bar{\sigma}} = \Gamma^{\bar{\sigma}\to\sigma}$. Additionally, as for the pair-tunnelling, the gain-loss chain shown in Fig. 7(b) leaves another fingerprint, in form of a fourth order amendment to the out-tunnelling process $|\sigma\rangle \to 0$, caused by a temporary in-tunnelling of another electron. Thereby, notice that the A.(1)(s) diagram involves all three charge states, while C.(1)(s) employs only the empty and the singly occupied states. Analytically, the effect is contained in the second line of Eq. (41a), in the functions $\gamma^{-}_{\mathrm{III}}(E_{21}, E_{10}, 1)$ and $\gamma^{-}_{\mathrm{II}}(E_{10})$, respectively. The latter function comes with a prefactor of 2 as the diagram group C.(2) supports another cotunnelling process involving the lower charge state, namely $|\sigma\rangle \to |\sigma\rangle$, with identical involved energies. Notice that by spin selection rules, this process is forbidden for diagram group A.(2). $(C_{(0)})^{\sigma\sigma}_{\sigma\sigma}$ and $(C_{(2)})^{\sigma\sigma}_{\sigma\sigma}$ add up directly in $K^{\sigma\sigma}_{\sigma\sigma}$, see Eq. (40), cancelling out any rate $\Gamma^{\sigma\to\sigma}_{(4)}$, which should indeed not appear in an equation for the populations.

So far we have not spent any words on diagrams from supergroup B. Intuitively, it seems that those cannot describe a transfer of two electrons, as we have related 'bubbles' in Sect. 2.2 either to the loss contribution of a single electron transfer or to charge fluctuations. In more detail, by inspection of Fig. 6 or Fig. 7(c), it becomes obvious that starting in general from some state with charge N, B diagrams will just contain other N or $N \pm 1$ electron states: not even virtually they can connect to states with $N \pm 2$ electrons. Thus it is clear that they can never contribute to pair-tunnelling events. Further, unlike as for the A and C supergroups, Fig. 7(a)/(b), a gain-loss chain between the B.(2)(t) group and the B.(0)(s) stand-alone diagram does *not* always exist [as shown e.g. in Fig. 7(c) on the single-level quantum-dot example]: Only if the energies of the initial and the final state in the diagram B.(2)(t) differ, the reducible stand-alone diagrams B.(0)(s) and B.(1)(s) must be included for reasons of non-secular corrections. Consequently, supergroup B will never contribute to elastic cotunnelling. Last but not least, also a a connection to the inelastic cotunnelling can be ruled out in general: First, as it can be verified with help of Eq. (130), there appears never a Bose function in the energy dependent function $\tilde{B}_{(2)}$, Tab. 2. However, some occurrence of a Bose function, as it is the case for both $\tilde{A}_{(2)}$ and $\tilde{C}_{(2)}$ would be expected for a cotunnelling contribution. Second, the fact that within the gain-loss chain Fig. 7(c) – given it exists – it is for all diagrams the *same* fermion line which connects to the latest vertex at time t has the implication that any $N \to N$ rate stemming from these supergroup would drop from the current. This can be proven by recalling from which

diagrams the current kernel is constructed of, Sect. 2.1. It is only a little exercise to verify that for supergroups A and C, the cotunnelling rate drops due to compensation of the contributions among groups A.(0) and A.(2) respectively C.(0) and C.(2) exactly when both involved fermion lines belong to the same lead. In contrast, for supergroup B the elimination always takes place. Thus, all what is physically left from supergroup B are corrections to single electron tunnelling processes, contained in Eqs. (41a)-(41c) via the functions $\gamma^{\pm}_{\mathrm{III}}$ or $\gamma^{\pm}_{\mathrm{II}}$, depending on whether two or three different charge states are involved.

Amendments to sequential tunnelling So far we have not given a proper distinction between the fourth order amendments the single supergroups yield to sequential tunnelling $N \to N \pm 1$. In fact we can go beyond the classification by the number of involved charge states. We have pointed out before that for supergroups A and C, the diagram carrying the effects is A.(1)(s) respectively C.(1)(s), because the groups A.(1)(t) respectively C.(1)(t) provide merely the loss terms for the two electron transfer processes. For supergroup B, the case is different. If initial and final states of the group B.(2) diagrams are identical in energy, no stand-alone diagrams must be included. This is in particular the case if initial and final states of the group B.(2)(t) diagrams are identical, as in our example Fig. 7(c) where $a{=}a'{=}b{=}b'$. Then group B.(2) holds just the loss partners for the group B.(1)(t) diagrams describing an $N \to N \pm 1$ process. Subtlety, for non-identical, but energy degenerate initial and final states (e.g. $a{=}a' \neq b{=}b'$, $E_a = E_b$) neither the group B.(2) nor the group B.(1)(t) contributes to a 'loss' rate $-\Gamma^{a\to b}$ in K^{aa}_{aa}. This, however, does not contradict our considerations: in fact, such case can only occur if selection rules do not exclude a coherence between states a and b. Then, the corresponding off-diagonal element must be kept in the density matrix. Hence an argumentation which restricts to populations and rates as we can apply for the single-level quantum-dot model, Eq. (35), is not sufficient any longer.

In any case, we can verify from Fig. 7 at one glance that all diagrams A.(1)(s), B.(1) and C.(1)(s) which can describe a fourth order process $N \to N \pm 1$ have a common property: the fermion line connecting upper and lower contour starts or ends in the latest vertex, which means that it is strictly the electron transfer event which ends at the time t.
What concerns the starting time, for supergroup A the virtual transition is always initiated before the transfer event. Due to their structure, the group A.(1)(s) diagrams always involve three different charge states, such that their contributions are exclusively contained in $\gamma^{\pm}_{\mathrm{III}}$, where they are the origin of the term scaling with the difference $\mu - \mu'$ in Eq. (42).
For supergroups B and C, the diagrams in group B.(1) respectively C.(1)(s) have a concrete interpretation: they describe a charge fluctuation in the initial respectively final state. In both cases, either two or three different charge states can be involved, compare e.g. C.(1)(s) in Fig. 7(a) and (b). In correspondence, from the charge fluctuations – no matter if taking place in the initial or final state – the function $\gamma^{\pm}_{\mathrm{II}}$ and the first two contributions $\gamma^{\pm}_{\mathrm{III}}$ emerge. The similarity is obvious in Eq. (42), in fact the

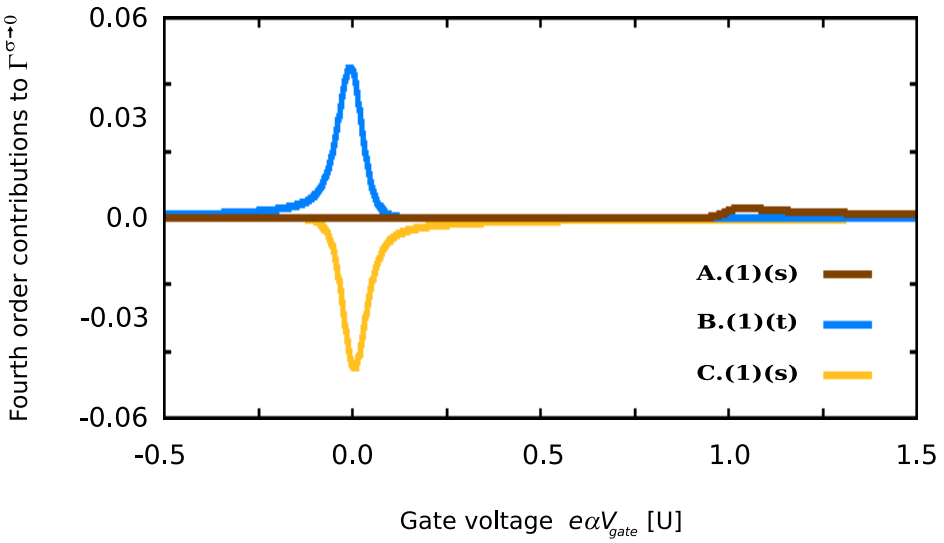

Figure 8: Fourth order corrections in the rate $\Gamma^{\sigma\to 0}$ by the processes depicted in Fig. 7(b) and (c). The effect is carried by the diagrams A.(1)(s), B.(1)(t) and C.(1)(s). The latter two describe a charge fluctuation in the initial respectively final state and involve merely charges 0 and 1. Therefore their contribution is large around the resonance $N = 0 \leftrightarrow N = 1$ at $V_{\text{gate}} = 0$. In contrast, A.(1)(s) is of minor relevance, because for any gate voltage at least one of the three charge states it involves is strongly disfavoured.

main difference is the inclusion of a third energy for the contributions in $\gamma^{\pm}_{\text{III}}$, as they relate to an additional charge states. Particularly related to the charge fluctuation, as not appearing in any other function in Eq. (42), is the term involving the derivative of the Fermi function. In fact, it forms the linear contribution to a Taylor expansion in a renormalisation of the energy argument of the Fermi function. In fact, summing diagrams in all orders, the complete series can be obtained and yields what is known as tunnelling-induced level renormalisation effects [15, 16], as sketched in an outlook in Sect. 5.3.3.

Finally, we compare in Fig. 8 for the three supergroups their contributions to the out-tunnelling event $|\sigma\rangle \to |0\rangle$ as emerging from the processes shown in Fig. 7(b), A.(1)(s) and C.(1)(s) and Fig. 7(c), B.(1)(t), respectively.
The first thing one notices is the minor relevance of the A.(1)(s) contribution, which on the scale of the curves in Fig. 8 is practically zero everywhere except around the resonance $N = 1 \leftrightarrow N = 2$ (at $e\alpha V_{\text{gate}} = 1.0$). The behaviour can be explained by the fact that the process it describes involves besides states of charges $N = 0$ and $N = 1$ also the doubly occupied state $|2\rangle$. For any gate voltage, at least one of the three charge states is energetically strongly disfavoured. In particular, the temporary transition $|\sigma\rangle \to |2\rangle$, which must be initiated before the out-tunnelling event can take place, is only favourable for gate voltages $e\alpha V_{\text{gate}} > 1.0$, where we find a small positive contribution, i.e. a slight enhancement of the rate $\Gamma^{\sigma\to 0}$.
For B.(1)(t) as well as for C.(1)(s), the situation is different, because these diagrams

merely involve the charge states $N = 0$ and $N = 1$. Therefore, their contribution is largest around the $N = 0 \leftrightarrow N = 1$ resonance at $V_{\mathsf{gate}} = 0$, and decaying on increasing distance from this degeneracy point. The finding that B.(1)(t) yields an increase, C.(1)(s) instead a decrease of the rate $\Gamma^{\sigma\to 0}$ can be understood as follows. Upon consulting Fig. 7(b) and (c), we realize for the B.(1)(t) diagrams that the charge fluctuation has a kind of 'forward' character, as it takes one of the initial states $|\sigma\rangle$ temporarily to the final state $|0\rangle$. It can be seen as an enhanced feeding of this state, which raises the rate $\Gamma^{\sigma\to 0}$. In contrast, C.(1)(s) describes a 'backward' fluctuation from the state $|0\rangle$ to the higher charge state. The rate $\Gamma^{\sigma\to 0}$ at which $|0\rangle$ is populated thereby diminishes.

2.4 Relation to a T-matrix based rate approach

A well-known tool for the derivation of cotunnelling rates is a T-matrix based rate approach utilising a generalised Fermi's golden rule [21]. In this section, we want to clarify the connection to our results and show that the grouping is of crucial importance. In particular, we can reveal the origin of the divergences occurring in the unregularised rates obtained in T-matrix based calculations.

The idea behind the approach is to apply scattering theory for the description of quantum transport. To calculate the time evolution $\dot{P}_{\tilde{n}}(t)$ of the occupation probability for a state $|\tilde{n}\rangle$ of the total system, all transition amplitudes

$$\langle \tilde{n} \,|\, \tilde{m}(t)\rangle = \left\langle \tilde{n} \right| e^{\frac{\mathrm{i}}{\hbar}\int_{t_0}^{t} \hat{H}_I^I(\tau)\,\mathrm{d}\tau} \left| \tilde{m} \right\rangle \tag{43}$$

are needed [21]. Let us underline at this point that one usually only takes into account the occupation probabilities of single states, i.e., the diagonal elements of the RDM. In general, this can be insufficient, as coherences play an important role for various models[10]; however, the shortcoming could rather easily be healed by a canonical generalisation of the method from $P_n(t) = \hat{\rho}_{nn}(t)$ to $\hat{\rho}_{nm}(t)$ (which we will not pursue here as it is unessential for what we like to demonstrate).

In Eq. (43) it is assumed that up to a time t_0, when the interaction was switched on, the total system was in its eigenstate $|\tilde{m}\rangle$, which could be written as a direct product of leads and quantum-dot state. From time t_0 on this state evolved as a consequence of the interaction to $|\tilde{m}(t)\rangle$, which is no longer separable. Expanding the exponential, one obtains

$$\begin{aligned}\langle \tilde{n} \,|\, \tilde{m}(t)\rangle = \Big\langle \tilde{n} \Big| \, 1 + \frac{\mathrm{i}}{\hbar}\int_{t_0}^{t} \hat{H}_I^I(\tau)\,\mathrm{d}\tau \\ + \left(\frac{\mathrm{i}}{\hbar}\right)^2 \int_{t_0}^{t} \hat{H}_I^I(\tau)\,\mathrm{d}\tau \int_{t_0}^{\tau} \hat{H}_I^I(\tau_1)\,\mathrm{d}\tau_1 + \cdots \Big| \tilde{m} \Big\rangle.\end{aligned} \tag{44}$$

[10] As pointed out before this is e.g. the case for orbital degeneracies [23, 24, 25, 26, 27] and/or non-collinear lead polarisations [28, 29, 30, 31, 32].

The corresponding transition rate is calculated from the amplitudes via

$$\Gamma_{\tilde{m}\to\tilde{n}}(t,t_0) = \frac{\mathrm{d}}{\mathrm{d}t}\left|\langle\tilde{n}\,|\,\tilde{m}(t)\rangle\right|^2 = \mathsf{Re}\left\{\left(\frac{\mathrm{d}}{\mathrm{d}t}\langle\tilde{n}\,|\,\tilde{m}(t)\rangle\right)\langle\tilde{m}(t)\,|\,\tilde{n}\rangle\right\}.$$

This gives us two ways to proceed. Either we perform the integrations first, and obtain from Eq. (44) the well-known result [21]

$$\left|\langle\tilde{n}\,|\,\tilde{m}(t)\rangle\right| = \left|\frac{e^{\eta t}}{E_{\tilde{n}}-E_{\tilde{m}}+\mathrm{i}\eta}\left\langle\tilde{n}\left|\hat{T}\right|\tilde{m}\right\rangle\right|, \quad \Gamma_{\tilde{m}\to\tilde{n}} = 2\pi\delta(E_{\tilde{n}}-E_{\tilde{m}})\left|\left\langle\tilde{n}\left|\hat{T}\right|\tilde{m}\right\rangle\right|^2,$$

where η is an infinitesimal quantity such that $\Gamma_{\tilde{m}\to\tilde{n}}$ is finally independent of t, as expected for the steady state ($t_0 \to -\infty$). Here, the *T-matrix* $\hat{T}$ is defined by a Dyson-like equation as

$$\hat{T} = \hat{H}_I + \hat{H}_I\frac{1}{E_{\tilde{m}}+\hat{H}_0+\mathrm{i}\eta}\hat{T},$$

which can be truncated at the desired order.

Alternatively, let us calculate $\Gamma_{\tilde{m}\to\tilde{n}}$ to fourth order without dissolving the integrations over time. Thereby we set $t_3 = t$ and, to keep formal correctness, use the time order operator $\hat{\mathcal{T}}$:

$$\begin{aligned}
&\mathsf{Re}\left\{\left(\frac{\mathrm{d}}{\mathrm{d}t}\langle\tilde{n}\,|\,\tilde{m}(t)\rangle\right)\langle\tilde{m}(t)\,|\,\tilde{n}\rangle\right\}\\
&\quad= \mathsf{Re}\left\{\left\langle\tilde{n}\left|\,\frac{\mathrm{i}}{\hbar}\hat{H}_I^I(t)\Big(1+\sum_{j=1}^{3}\left(\frac{\mathrm{i}}{\hbar}\right)^{4-j}\hat{\mathcal{T}}\prod_{k=j}^{3}\int_{t_0}^{t_k}\mathrm{d}t_{k-1}\hat{H}_I^I(t_{k-1})\Big)\right|\tilde{m}\right\rangle\right.\\
&\qquad\left.\times\left\langle\tilde{n}\left|\,1+\sum_{j=1}^{3}\left(\frac{\mathrm{i}}{\hbar}\right)^{4-j}\hat{\mathcal{T}}\prod_{k=j}^{3}\int_{t_0}^{t_k}\mathrm{d}t_{k-1}\hat{H}_I^I(t_{k-1})\right]\right|\tilde{m}\right\rangle^{\dagger}\right\}\\
&\qquad\qquad=: \Gamma^{(2)}_{\tilde{m}\to\tilde{n}}(t,t_0)+\Gamma^{(4)}_{\tilde{m}\to\tilde{n}}(t,t_0)\,. \quad (45)
\end{aligned}$$

With the hint that for the fourth order rate, the principle behind Eq. (38) must be applied backwards, it is easy to show the following equalities:

$$\Gamma^{(2)}_{\tilde{m}\to\tilde{n}}(t,t_0) = -\mathsf{Re}\left\langle\tilde{n}\right|\int_{t_0}^{t}\mathrm{d}\tau\;\hat{\mathcal{L}}_T^I(t)\hat{\mathcal{L}}_T^I(\tau)\big[|\tilde{m}\rangle\langle\tilde{m}|\big]\left|\tilde{n}\right\rangle, \quad (46a)$$

$$\Gamma^{(4)}_{\tilde{m}\to\tilde{n}}(t,t_0) = +\mathsf{Re}\left\langle\tilde{n}\right|\int_{t_0}^{t}\mathrm{d}\tau_2\int_{t_0}^{\tau_2}\mathrm{d}\tau_1\int_{t_0}^{\tau_1}\mathrm{d}\tau\;\hat{\mathcal{L}}_T^I(t)\hat{\mathcal{L}}_T^I(\tau_2)\hat{\mathcal{L}}_T^I(\tau_1)\hat{\mathcal{L}}_T^I(\tau)\big[|\tilde{m}\rangle\langle\tilde{m}|\big]\left|\tilde{n}\right\rangle. \quad (46b)$$

These relations establish a connection to the expressions appearing in the fourth order quantum master equation, which we discussed in Sect. 1.2. Taking the trace over the leads – which can safely be done because leads and quantum-dot states are by

definition not entangled in $|\tilde{n}\rangle$ and $|\tilde{m}\rangle$ – Eq. (46a) will reproduce the second order contribution in Eq. (21), while the fourth order rate obtained from the Fermi's golden rule corresponds to Eq. (21)(i).

What is obviously missing, however, is the subtraction of all the reducible parts among the fourth order contributions, as achieved by Eq. (21)(ii).

Nevertheless, the derivation from Eq. (43) is perfectly correct. The right question to ask is actually which amplitude we calculate with Eq. (43): It is the probability for a transition to the state $|\tilde{n}\rangle$ at time t, given that at time t_0 the system was prepared in state $|\tilde{m}\rangle$. This translates into the following rate equation:

$$\dot{P}_{\tilde{n}}(t) = \Gamma_{\tilde{m}\to\tilde{n}}(t,t_0)\, P_{\tilde{m}}(t_0) - \Gamma_{\tilde{n}\to\tilde{m}}(t,t_0)\, P_{\tilde{n}}(t_0).$$

As a matter of fact, this equation is not of the form we have investigated so far: Instead, in Eq. (21), the probabilities, or, more general, the density matrix elements on the right hand side of the equation are not to be taken at the initial time t_0, but at some time $\tau > t_0$ where the system has already approached the steady state. As it can be seen from Eq. (20), such discrepancy translates into corrections of order $(\hat{\mathcal{L}}_T^I)^2$, and thus is irrelevant in the terms of highest considered order. But from all lower orders, non-negligible corrections arise; explicitly, we had found in Sect. 1.2 that by replacing $\hat{\rho}(t_0)$ in the second order term of Eq. (19), exactly the contribution Eq. (21)(ii), which is missing in Eq. (46b), emerged.

Nevertheless, the typical –regularised– rates obtained from a T-matrix based approach [52] are rather similar to our expressions $A_{(2)}$ and $C_{(2)}$ as given in Tab. 2 (with the corresponding energy dependent functions $\tilde{A}_{(2)}$ and $\tilde{C}_{(2)}$ to be found at length in App. A.3.1). Before we compare in detail, let us uncover the deeper relation between the fourth order contributions in Eq. (45) and the diagram groups:
As explained in Sect. 1.3, in order to work with a secular density matrix it is actually necessary to re-include part of the reducible contributions in form of non-secular corrections $\hat{K}_C^{(4)}$, Eq. (29c), into an effective fourth order kernel $\hat{K}_{\text{eff}}^{(4)}$, Eq. (29b). This kernel is constructed from the nine diagram groups, as shown in Fig. 6, and to each a single analytical contribution is assigned, Tab. 2. The important fact that $\hat{K}_C^{(4)}$ contains not all, but exactly those reducible diagrams which exhibit *non-secular* intermediate free propagating states warrants finite contributions and is expressed in the fact that the energy dependent functions $\tilde{B}_{(0/1/2)}$ and $\tilde{C}_{(1/2)}$ of Tab. 2 have to distinguish a special secular case, compare App. A.3.
Contrary to this, the fourth order based T-matrix rates emerging from Eq. (45) a priori comprise, as immediately seen from Eq. (46b), *all* reducible contributions – and thus automatically the divergences occurring, see Sect. 1.3, for any combination of secular intermediate free propagating states. On the other hand, the analytical grouping according to Eq. (38) becomes applicable[11] without case distinction, which established

[11] Thereby, the secularity demand $E_a = E_{a'}$ for Eq. (38) does not pose any problems as merely populations are considered (i.e. $a = a'$).

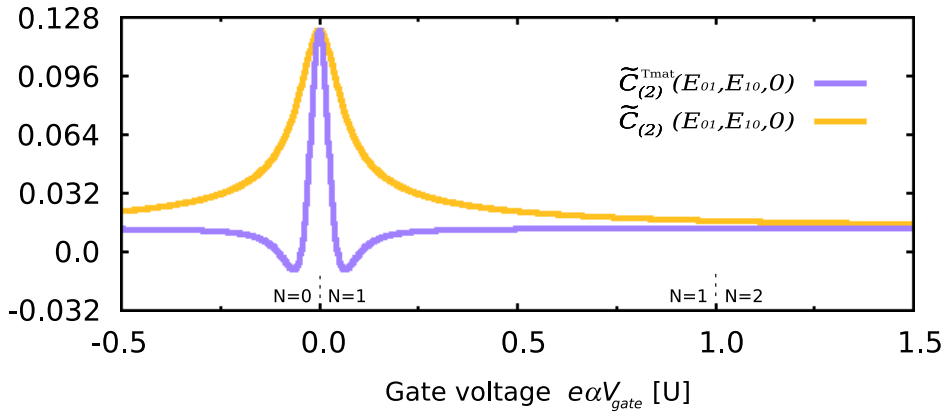

Figure 9: Comparison between $\tilde{C}_{(2)}$ and the corresponding T-matrix based expression $\tilde{C}^{\mathrm{Tmat}}_{(2)}$ for one of the contributions to the cotunnelling rate $\Gamma^{\sigma\to\sigma}$ in a SD model (parameters as for Fig. 8). In contributions related to supergroup A, both approaches are identical: $\tilde{A}_{(2)} = \tilde{A}^{\mathrm{Tmat}}_{(2)}$ (not shown).

the connection between Eq. (46b) and Eq. (45). From the latter, in principle the same nine contributions as listed in Tab. 2 emerge, with the subtle, but crucial, difference that the corresponding energy dependent functions $\tilde{B}^{\mathrm{Tmat}}_{(0/1/2)}$ and $\tilde{C}^{\mathrm{Tmat}}_{(1/2)}$ do not distinguish a special secular case and therefore require regularisation.
We illustrate this on our example from Sect. 2.3.1, namely the contribution $\tilde{C}_{(2)}$, Eq. (39), which obviously distinguishes the cases of secular ($E_m = E_{m'}$) and non-secular ($E_m \neq E_{m'}$) intermediate free propagating states, in order to avoid the inclusion of the divergent reducible term. For the corresponding expression emerging from Eq. (45), there is no such distinction and always the function for the non-secular case,

$$-\lim_{\eta\to 0}\mathrm{Re}\left[\frac{\beta}{\mathrm{i}\hbar}\int \mathrm{d}\omega \int \mathrm{d}\omega' \, \frac{1}{\omega-\beta\mu'+\mathrm{i}\eta}\,\frac{1}{\omega+\beta(\Delta-\mu)+\mathrm{i}\eta}\,\frac{f^-(\omega)\,f^-(\omega')}{\omega+\omega'-\beta\Delta+\mathrm{i}\eta}\right],$$

is to be considered. To ensures convergence for the secular case $\mu+\mu'=\Delta$, the expression is regularised in the following way [53, 54]:

$$\int \mathrm{d}\omega \frac{g(\omega)}{\omega^2+\eta^2} = \int \mathrm{d}\omega \frac{g(0)}{\omega^2+\eta^2} + \int \mathrm{d}\omega \frac{g(\omega)-g(0)}{\omega^2+\eta^2} = \underbrace{\frac{\pi}{\eta}g(0)}_{=\mathcal{O}(\eta^{-1})} + \int' \mathrm{d}\omega \frac{g(\omega)}{\omega^2+\eta^2},$$

where $\int'$ denotes a principal part integration. The contribution $\propto 1/\eta$ is assigned to sequential tunnelling processes and hence must be disregarded. One obtains

$$\tilde{C}^{\mathrm{Tmat}}_{(2)}(\Delta-\mu',\mu',\Delta)$$
$$= \frac{\beta}{\hbar}\mathrm{Re}\left(\mathrm{i}\int \mathrm{d}\omega \int \mathrm{d}\omega' \, \frac{1}{\omega-\beta\mu'+\mathrm{i}\eta}\,\frac{1}{\omega-\beta\mu'-\mathrm{i}\eta}\,\frac{f^-(\omega)\,f^-(\omega')}{\omega+\omega'-\beta\Delta+\mathrm{i}\eta}\right) - \mathcal{O}(\eta^{-1}) =$$

$$= \frac{\pi\beta}{\hbar}\int' \mathrm{d}\omega\, \frac{f^-(\omega)\, f^+(\omega-\beta\Delta)}{(\omega-\beta\mu')^2+\eta^2} = \frac{\pi\beta}{\hbar} b^-(\beta\Delta)\frac{\mathrm{d}}{\mathrm{d}(\beta\mu')}\int' \mathrm{d}\omega \frac{1-f^-(\omega)-f^+(\omega-\beta\Delta)}{\omega-\beta\mu'}$$
$$= -\frac{\beta}{2\hbar} b^-(\beta\Delta)\left(\mathsf{Im}\,\Psi^{(1)}\left(\frac{1}{2}+\frac{\mathrm{i}\beta\mu'}{2\pi}\right)+\mathsf{Im}\,\Psi^{(1)}\left(\frac{1}{2}+\frac{\mathrm{i}\beta(\Delta-\mu')}{2\pi}\right)\right). \quad (47a)$$

This result has to be compared with the correct expression for $\tilde{C}_{(2)}$ as given in Eq. (130). In the limit $\mu+\mu'=\Delta$:

$$\hbar\tilde{C}_{(2)}(\Delta-\mu',\mu',\Delta) = -\frac{\beta}{2}\left(b^-(\beta\Delta)+f^-(\beta\Delta-\beta\mu')\right)\mathsf{Im}\,\Psi^{(1)}\left(\frac{1}{2}+\frac{\mathrm{i}\beta\mu'}{2\pi}\right)$$
$$-\frac{\beta}{2}\left(b^-(\beta\Delta)+f^-(\beta\mu')\right)\mathsf{Im}\,\Psi^{(1)}\left(\frac{1}{2}+\frac{\mathrm{i}\beta(\Delta-\mu')}{2\pi}\right). \quad (47b)$$

The expressions Eq. (47a) and Eq. (47b) obvious match in the two terms involving the Bose function, while the two terms involving the Fermi function are absent in Eq. (47a). To visualise the discrepancy, we compare the two expressions in Fig. 9, for the elastic cotunnelling processes $|\sigma\rangle \to |\sigma\rangle$ in a SD model at zero bias [compare the sketch Fig. 7(c)]. Thereby, $\Delta = 0,\ \mu' = E_{10} := E_\sigma - E_0$. Though the deviations seem dramatic in Fig. 9, their impact on the current is in fact of minor nature. This for the following reasons: On the one hand, populations are untouched by a process $|\sigma\rangle \to |\sigma\rangle$ anyway. On the other hand, our two Fermi functions $f^+(\beta E_{10})$ and $f^-(\beta E_{10})$ are already present in second order inside the rates $\Gamma^{0\to\sigma}_{(2)}$ and $\Gamma^{\sigma\to 0}_{(2)}$, respectively. In the current, these sequential contributions effectively dominate over the contributions the Fermi function appear with in fourth order, such that whether or not putting them causes only a small relative difference.
Nevertheless, we have demonstrated that there exists a built-in fundamental discrepancy between T-matrix based rate equations and our generalised master equation Eq. (21). Importantly, the fourth order rates as emerging from Eq. (21) are *not* completely recovered from the T-matrix based expression by the usual regularisation procedure. Having demonstrated this explicitly for the function $\tilde{C}_{(2)}$ related to supergroup C, we want to amend that all expressions from supergroup A, as it contains no reducible diagrams, are identically reproduced by the T-matrix based approach. What concerns supergroup B, the related functions $\tilde{B}^{\mathrm{Tmat}}_{(0/1/2)}$ scale inversely with the energy difference of the free propagating intermediate states[12]. Thus, a regularisation dropping terms $\propto \eta^{-1}$ corresponds to a complete neglect in the special secular case, whereas the real $\tilde{B}_{(1/2)}$ do not vanish.

As a matter of fact, T-matrix based rate approaches further commonly invoke certain standard approximations, leading to additional deviations on top of the built-in difference:

- *Neglect of corrections to sequential tunnelling:* As addressed above, sequential contributions are of second order and thus usually dominate over any fourth order

[12] See in App. A.3, Eqs. (129), (130) the definition of $\tilde{B}_{(0/1/2)}$ for the non-secular case.

correction. Therefore the idea is to keep no fourth order contributions to rates $\Gamma^{N\to N\pm1}$. This translates into omitting supergroup B diagrams completely[13], and further dropping the groups A.(1) and C.(1). The latter approximation violates the fragile gain-loss chains shown in examples in Fig. 7 and would per se break the sum-rule Eq. (10). The reason why no problems arise from this fact is simply that in the T-matrix based rate approaches, no time evolution kernel, but just the pure rates are calculated. The desired ones emerge from diagram groups A.(2) and C.(2) and using them in a canonical rate equation, as e.g. in Eq. (35), one automatically complies with the sum-rule. Diagram groups A.(0) and C.(0) become redundant.

- *Neglect of pair-tunnelling:* Processes changing the charge state of the quantum-dot by two, $N \to N \pm 2$, are indeed strongly suppressed as any gate voltage favours at most two charge states N and $N+1$. Disregarding such events translates into omitting within the groups A.(2) and C.(2) those contributions where $p = p'$, which means in the language of the diagrams that both fermion lines point towards the same contour [for an example see the leftmost diagrams in Fig. 7(a)]. Only recently, the existence of a pair-tunnelling resonance line, which had so far been overlooked due to this approximation, has been pointed out [13].

In Sect. 3.2 we compare, for the rather complex model of a quantum double-dot, an exact calculation according to out theory and a T-matrix based calculation incorporating these additional approximations. Good agreement is found inside the Coulomb blockade regions and apart from resonance lines.
Major acceleration of calculations, but at the price of a shrunken validity range, is achieved upon invoking two more simplifications [21]:

- *Fixed charge limit:* By a Schrieffer-Wolff transformation [55], effectively all populations of states with charge other than N are set to zero inside the N electron Coulomb blockade diamond. Notice that this automatically excludes all sequential tunnelling events.

- *Low bias limit:* Under the assumption $eV_{\mathsf{bias}} \ll \mu'$ is is possible to neglect the ω dependence in denominators [21], with the effect that the sum over the two trigamma functions in Eq. (47a) turn into a constant with a simple energy dependence of $1/(\beta\mu')^2$.

A comparison in Sect. 3.2 shows still good agreement with the exact calculation for a limited gate and bias voltage region inside the Coulomb blockade diamond.

2.5 Conclusion

The first part of this thesis was dedicated to the theoretical description of transport across quantum-dots weakly connected to metallic contacts. Thereby, all the analysis

[13] We explained in Sect. 2.3.2 that supergroup B relates exclusively to fourth order amendments to sequential tunnelling.

carried out in Sect. 2 was built upon the compact introduction to the known theory given in Sect. 1, where we have followed a perturbative approach to account for electron transfer in second and fourth order of the tunnelling coupling, which includes all tunnelling processes involving one or two electrons.

In the course of the present section we have highlighted in particular the correspondence between the single terms emerging in the equation of motion and the diagrammatic representation [19], see Tab. 1. The equation of motion determines the time evolution of the quantum-dot density matrix. By inclusion of correction terms, which also can be represented diagrammatically, those elements of the matrix which are related to coherences between non-degenerate states can be set to zero. Amending the original terms by these corrections led to a central achievement: the grouping of diagrams, as depicted in Fig. 6. Such structuring has not been noticed so far and brings advantage from both the analytical and the numerical point of view, because within the 3×3 groups, contributions of diagrams combine and partially cancel. It should be mentioned that as a part of my work, the new possibility of diagram grouping was numerically implemented within the KinEq [20] project, speeding up calculations by factor of 10-20. Moreover, it opened a way for a physical interpretation of diagrams: we analysed and distinguished between the pure fourth order phenomena of cotunnelling and pair-tunnelling as well as fourth order amendments to sequential transport. Finally, the diagram grouping established a connection to the widely used T-matrix based rate equations. In particular, we revealed the origin of the divergences contained in those equations and that the typical regularisation does not completely reproduce our expressions.

A programming task for the near future is a numerically efficient implementation of those fourth order calculations which require coherences between secular states (as e.g. the case of non-collinearly magnetised electrodes). A long term challenge is clearly posed by a controlled inclusion of terms beyond fourth order. The most prominent motivation for this might be the Kondo effect. Frequently encountered in experimental reality, it can appear in the theory only from sixth order on. Level renormalisation effects (which can e.g. cause tunnelling magneto-resistance oscillations, a gate voltage dependence of the inelastic cotunnelling threshold or a splitting of the Kondo peak) demand even inclusion of certain contributions to all orders in the tunnelling coupling, in form of a Taylor series – an outlook to this is given in Sect. 5.3.3.
A problem which rapidly increases with the order of our perturbation theory is the number of terms (resp. diagrams) to be calculated. Already for the fourth order the numerical effort puts limits, at the moment to quantum-dot models with less than one hundred states (for a systematic analysis). Therefore, in particular for even higher orders, in addition to numerical optimisation most probably approximation methods will have to be invoked[14]. If thereby a selection among a full set of terms of a certain order shall take place, the knowledge on the underlying physical processes is a precondition

[14] In this context we compare in Sect. 3.2, on the example of a double quantum-dot model, between our theory and the two T-matrix based approximation methods introduced in Sect. 2.4.

for a consistent choice of diagrams. A tool for this working also beyond fourth order is certainly the grouping.

To conclude, the Liouville equation based perturbative approach to quantum transport, though known for years, still deserves to be topic of investigations. As we have seen here for the fourth order, the prize for a careful analysis can be rich insights into the physics of electron transfer across double-barrier structures.

Related publications:

S. Koller, M. Leijnse, M. R. Wegewijs, M. Grifoni. Prepared for Phys. Rev. B. (2010)
Density-operator approaches to transport through interacting quantum-dots: simplifications in fourth order perturbation theory.[15]

[15] The title of the final publication might differ.

APPLICATION:

TRANSPORT PHENOMENA IN INTERACTING QUANTUM-DOTS

This second part of the thesis, dedicated to results on transport across specific quantum-dot devices, is subdivided into three sections. First, the focus of Sect. 3 is on most easy, yet already quite instructive, minimal models for a one and two site system, which we refer to as quantum single-dot (SD) and quantum double-dot (DD), Sect. 3.1 and Sect. 3.2, respectively. Two examples of real carbon based systems are studied subsequently, namely graphene armchair nanoribbons (ACNRs), Sect. 4 and single wall carbon armchair nanotubes (SWCNTs), Sect. 5.
These latter systems require a more demanding theoretical modelling, which leaves already in second order transport a magnitude of signatures to be explained. Hence, to preserve the level of complexity, it is sensible to restrict for the analysis of fourth order transport to the minimal model systems, where the eigenstate problem does not pose a major problem by itself, and the Hilbert spaces are low-dimensional.

It should be mentioned that all transport data presented in the following was obtained with help of the KinEq [20] kinetic equation solver, which incorporates the transport theory presented in Sect. 1 in full generality. As model specific external input it requires the energy spectrum and the tunnelling matrix elements (TMEs) of that particular quantum-dot system which is to be subject of investigations, and an important part of my work was to provide for each of these systems a user-friendly program, allowing upon specification of the model specific parameters an automatic generation of the necessary input information for KinEq.

3 Minimal model systems

In a minimal model, a quantum-dot is accounted for with a single spin-degenerate level. This yields for the single/double quantum-dot (SD/DD) a four-/sixteen-dimensional Hilbert space, respectively. An eigenbasis of the former is formed trivially by the canonical set of states employed already in Sect. 2, in which the Coulomb interacting Hamiltonian is diagonal. For the DD, there exists on-site as well as inter-site Coulomb interaction and once hopping between the two sites is allowed, the canonical localised basis provides no longer the eigenstates. However, an analytical diagonalization is possible in case of an equal gate voltage dependence of both levels. The limited number of states makes the minimal models for SD and DD good candidates for in general costly numerical investigations of transport up to fourth order.

3.1 Quantum single-dots

Though –or maybe because– fourth order transport in the single-impurity Anderson model [56] (this is how the single-level description of a SD is called) is well-investigated [13, 30, 57, 58], it makes sense to shortly address it here. The stability diagrams we present in Fig. 10 in fact contain several universal features which are also encountered for more complex quantum-dots, but can be explained in clearer manner for this few-state system. In this way, we provide an easy start to fourth order and spin phenomena in transport. Besides, having made use of the single-impurity Anderson model in Sect. 2 for the analysis of fourth order rates, it is a matter of completeness to show the corresponding transport results.

The isolated level, as it is assumed, can be occupied at most with up to two electrons of opposite spin. The associated creation operators are $\hat{d}^\dagger_\uparrow$ and $\hat{d}^\dagger_\downarrow$, which we let act in the order $\hat{d}^\dagger_\uparrow \hat{d}^\dagger_\downarrow |0\rangle$ on the vacuum state $|0\rangle$. The Hamilton operator,

$$\hat{H}_\odot = \sum_\sigma \varepsilon_\sigma \hat{\mathcal{N}}_\sigma + U \hat{\mathcal{N}}_\uparrow \hat{\mathcal{N}}_\downarrow,$$

with $\hat{\mathcal{N}}_\sigma = \hat{d}^\dagger_\sigma \hat{d}_\sigma$ the number operator, lives in a four-dimensional Hilbert space, spanned by the eigenstates listed in Tab. 3. There are three charge states the system can take, $N_c \in \{0, 1, 2\}$, where for putting two electrons on the dot, $N_c = 2$, Coulomb repulsion demands a charging energy U to be paid. For a single occupation, $N_c = 1$, the states $|\uparrow\rangle$, $|\downarrow\rangle$ have to be distinguished due to the electron spin. The associated level positions are $\varepsilon_\uparrow = \varepsilon_\downarrow$, unless an external magnetic field lifts the degeneracy by a Zeeman splitting of $\varepsilon_\downarrow - \varepsilon_\uparrow = 2E_z$. Particle exchange with the source ($l = s$) and drain lead ($l = d$) is described by the tunnelling Hamiltonian Eq. (2) as presented in Sect. 1, where for the single level no orbital index is needed. Allowing for a parallel contact polarisation of magnitude P_l, $0 \leq P_l \leq 1$ in the respective lead l, all nonzero TMEs which are needed in the transport calculations are given by

$$T_{l\uparrow}(0,\uparrow) = T_{l\uparrow}(\downarrow,2) = \sqrt{\hbar\Gamma_l}\sqrt{\frac{1+P_l}{2}}\,, \quad T_{l\downarrow}(0,\downarrow) = -T_{l\downarrow}(\uparrow,2) = \sqrt{\hbar\Gamma_l}\sqrt{\frac{1-P_l}{2}}.$$

ENERGY	:	STATE	S_z $[\hbar]$	S $[\hbar]$
0	:	$\|0\rangle$	0	0
$\varepsilon_\downarrow + E_z$	:	$\|\downarrow\rangle$	$-1/2$	$1/2$
$\varepsilon_\uparrow - E_z$	:	$\|\uparrow\rangle$	$+1/2$	$1/2$
U	:	$\|2\rangle$	0	0

Table 3: The four states considered in the single impurity Anderson model, along with their eigenenergies and spin-projection S_z as well as total spin S.

Thermal energy	k_BT	0.01 meV
Tunnelling coupling	$\hbar\Gamma$	0.8 μeV
On-site Coulomb	U	1.0 meV
Level position	ε_σ	0.25 meV
Zeeman splitting	E_z	0.0 meV / 0.1 meV

Table 4: Parameters employed for the shown plots. Notice that the value of $\varepsilon_\sigma = \varepsilon_\uparrow = \varepsilon_\downarrow$ just causes a shift in the gate voltage.

Due to its simplicity, the single-impurity Anderson model is a preferred tool for many kinds of studies on interacting quantum-dot systems. Indeed, its small Hilbert space provides the possibility of deeper analytical investigation as well as of fast numerical implementation. Nevertheless, it should not be forgotten that it misses many features of real systems, like triplet formation or orbital degrees of freedom, which are rich sources of system specific effects and hence cannot be neglected in advanced analysis of realistic quantum-dots.
On the other hand, the absence of these complications makes the single-impurity Anderson model a good starting point for the study of *universal* effects in quantum transport physics, and as such we have already employed it in Sect. 2.

Fig. 10 shows the differential conductance across the single level for a full fourth order transport calculation in three distinct cases. Common to all three plots is the central Coulomb diamond belonging to a predominant single-electron occupation, $N_c = 1$, of the quantum-dot. In the leftmost plot of the figure, the unpolarised case without a Zeeman splitting is treated, i.e. the leads are non-magnetic and the two $N_c = 1$ states are degenerate. The basic structure of the figure is build on four transition lines, which cross to form the edges of the central diamond. They belong to two types of transitions: either $N_c = 0 \leftrightarrow N_c = 1$, $|0\rangle \leftrightarrow |\sigma\rangle$ or $N_c = 1 \leftrightarrow N_c = 2$, $|\sigma\rangle \leftrightarrow |2\rangle$. In the plot itself, we have directly indicated the underlying transition at each section of each line. Notice that the slope of a transition line determines whether it belongs to the opening of a forward ($N_c \to N_c + 1$) or a backward ($N_c + 1 \to N_c$) channel. Forward transition lines are slanted leftwards/rightwards for positive/negative bias voltage, and vice versa for the backwards case.
Fourth order contributions to transport comprise all correlated tunnelling events of two electrons at a time. They give rise to a small nonzero current even in the Coulomb blockade regime – manifesting in a lighter bluish interior of the diamond – as *elastic cotunnelling* allows to transfer an electron across the quantum-dot device preserving its charge and energy in the final state. During the process, virtual transitions to higher or lower charge states can take place, because any potential violation of energy conservation is temporary. Another effect is electron *pair-tunnelling* [13], i.e. charge

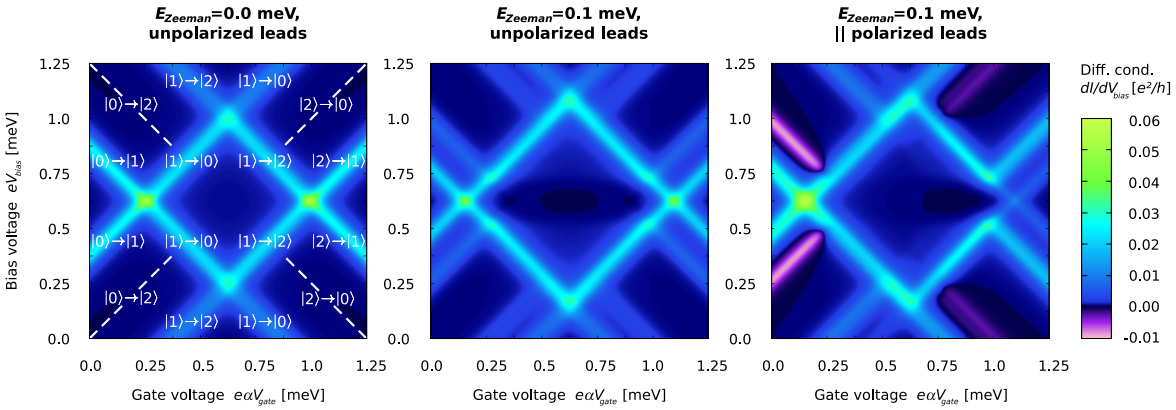

Figure 10: Differential conductance across a single level, in the spin degenerate case (left), with a Zeeman splitting $E_z = 0.1$ (middle) and for in parallel polarised leads, $P_s = P_d = 0.8$ (right). Due to elastic cotunnelling, there is always a small nonzero current flow inside the Coulomb diamond, which is hardly resolvable. In the presence of a magnetic field, the onset of inelastic cotunnelling for the Zeeman split levels is clearly visible. Upon assuming on top of the Zeeman splitting ferromagnetic contacts magnetised along the external field, the plot acquires a pronounced asymmetry, including negative differential conductance features. The origin is the preference of transport channels mediated by $\uparrow$ - electrons.

non-conserving processes $N_c \to N_c \pm 2$, setting in exactly in the middle between the parallel single electron transition lines, marked by white dashes in Fig. 10. A close look on the plot also exhibits a drop in the differential conductance just (in terms of $|eV_{\text{bias}}|$) below these resonances.
In fact, for a non-logarithmic scale these fourth order effects can only be resolved with a well-adapted colour gradient, because to justify the truncation of perturbation theory in fourth order, the tunnelling couplings have still to be taken rather small[16].

In the middle plot of Fig. 10, a Zeeman splitting is introduced such that $|\downarrow\rangle$ becomes an excited state: its energy is raised by E_z, while the energy of $|\uparrow\rangle$ is lowered by the same amount. Thus the Coulomb diamond widens by $2E_z$ and all single electron transition lines get split by this energy. Moreover, both elastic and *inelastic* cotunnelling is now observed inside the Coulomb blockade: below a bias threshold of $2E_z$, which coincides with the position where the excitation lines hit the edges of the Coulomb diamond, merely channels involving the $N_c = 1$ groundstate $|\uparrow\rangle$ are available for electron transfer. Consequently, compared to the case of $E_z = 0$ (which offers two groundstates), the differential conductance has visibly decreased. Only above the bias threshold, the energy gain for transferring one electron across the device allows to lift the quantum-dot into the excited $|\downarrow\rangle$ state, and the differential conductance regains a higher value.

Adding to this situation a parallel contact polarisation, of value $P_s = P_d = 0.8$, pointing along the external field, the plot changes according to the rightmost image of Fig. 10. The perfect mirror symmetry exhibited in the left and middle plot with respect

[16] In fact, numerical instabilities arise for too high values of the tunnelling coupling, as partly – and thus inconsistently – contained sixth order corrections gain weight.

to the central Coulomb diamond is completely broken. The reason is that due to the polarisation, the density of $\downarrow$ - electrons in the leads is diminished in favour of $\uparrow$ - electrons. Therefore transport via an $\uparrow$ - electron channel is strongly preferred. With $|\uparrow\rangle$ as $N_c = 1$ groundstate, this amplifies the $N_c = 0 \leftrightarrow N_c = 1$ conductance peak, while the groundstate transition $N_c = 1 \leftrightarrow N_c = 2$, which demands tunnelling of a $\downarrow$ - electron, gets suppressed. The resonance lines belonging to the transition $|0\rangle \rightarrow |\downarrow\rangle$ have transformed to strong negative differential conductance (NDC), as opening of this weak channel bears the possibility that from time to time the system gets trapped in the $|\downarrow\rangle$ state, from which it can return to $|0\rangle$ only by out-tunnelling of a minority charge carrier.
The two other, less pronounced, NDC lines on the right side of the diamond mark the back-transition $|\downarrow\rangle \rightarrow |0\rangle$, after which the $\uparrow$ - electron mediated forward transition $|0\rangle \rightarrow |\uparrow\rangle$ is likely to follow. For gate voltages favouring occupations $N_c = 1$ or $N_c = 2$, the state $|\uparrow\rangle$ is of blocking nature, because it is connected to the doubly occupied state $|2\rangle$ only by a disfavoured $\downarrow$ - electron transition.
What concerns the interior of the $N_c = 1$ Coulomb blockade diamond, there is the possibility of elastic cotunnelling $|\uparrow\rangle \rightarrow |\uparrow\rangle$ via C.(2) diagrams involving as an intermediate state merely $|0\rangle$, such that the process is completely mediated by $\uparrow$ - electrons, i.e. majority charge carriers. However, this polarisation favoured process, which dominates the left side of the Coulomb diamond, gets energetically suppressed with increasing distance from the $N_c = 0 \leftrightarrow N_c = 1$ resonance, being replaced by elastic cotunnelling $|\uparrow\rangle \rightarrow |\uparrow\rangle$ involving the $|2\rangle$ state. Purely carried by $\downarrow$ - electrons, that cotunnelling process is rare compared to the inelastic process $|\uparrow\rangle \rightarrow |\downarrow\rangle$, which demands in-tunnelling of a minority, but out-tunnelling of a majority electron. Hence, the inelastic cotunnelling threshold is pronounced in the right half of the diamond.

For further investigations we turn in the upcoming section to the more sophisticated model of a quantum double-dot, where excited states are already present without the need of an external magnetic field.

3.2 Quantum double-dots

Experimentally, two coupled quantum-dots in series, so-called double quantum-dots, have been realised in various kinds of systems, e.g. in semiconducting structures [59] or in carbon allotropes like nanotubes [60, 61] or graphene [62, 63], and are very attractive for studying fundamental spin correlations. Consisting of two sites modelled by a single spin-degenerate level each, the total number N_c of electrons that can reside on the DD ranges from zero to four. Taking into account all occupation possibilities we count sixteen states. A basis of this Hilbert space is given by localised states built up as a direct product of the SD states, $|i,j\rangle := |i\rangle_1 \cdot |j\rangle_2$, with $i,j \in \{0,\uparrow,\downarrow,2\}$ characterising the occupation of sites 1 and 2, respectively.

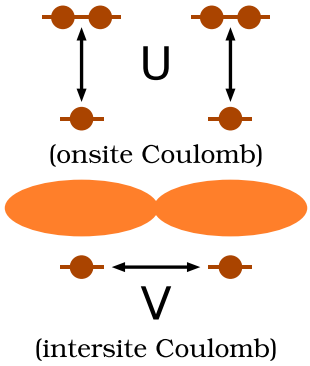

Figure 11: Relevant Coulomb interactions in a quantum double-dot

Importantly, the exchange Coulomb interaction between these two sites induces for the filling $N_c = 2$ a singlet-triplet splitting which can be used to perform logic gates [64]. Moreover, Coulomb interaction together with the Pauli principle can lead to a spin-blockade in case the two electrons have triplet correlations [65, 66, 67, 68]. This effect can be used to obtain a spin-polarised current even in the absence of spin-polarised leads, but it requires a strong asymmetry between the two on-site energies of the left and right dot.

This section, in contrast, will focus on a *symmetric* DD with equal on-site energies. Its theoretical description as well as the result on second order spin-polarised transport presented in the following have been published in collaboration with Ralph Peter Hornberger, Georg Begemann, Andrea Donarini and Milena Grifoni, Ref. [32]. The fourth order investigations have been carried out together with Georg Begemann, Jens Paaske and Milena Grifoni and are being prepared for publication.

3.2.1 Hamilton operator

The DD Hamiltonian emerging from a two-site Hubbard model with hopping and Coulomb interaction [69, 70] is the simplest variant of a Pariser-Parr-Popel Hamiltonian [71, 72] for a many site system, reading

$$\begin{aligned}\hat{H}_\odot \;=\; & \sum_{m=1}^{2}\sum_{\sigma} \varepsilon_m \hat{d}^\dagger_{m\sigma}\hat{d}_{m\sigma} + U\sum_{m=1}^{2} n_{m\uparrow}n_{m\downarrow} + V\big(n_{1\uparrow}+n_{1\downarrow}\big)\big(n_{2\uparrow}+n_{2\downarrow}\big) + \\ & + b\sum_{\sigma}\Big(\hat{d}^\dagger_{1\sigma}\hat{d}_{2\sigma} + \hat{d}^\dagger_{2\sigma}\hat{d}_{1\sigma}\Big) - \Big(\frac{U}{2}+V\Big)\sum_{m=1}^{2}\sum_{\sigma}\hat{d}^\dagger_{m\sigma}\hat{d}_{m\sigma}. \end{aligned} \tag{48}$$

Here, $\hat{d}^\dagger_{m\sigma}$ are the creation operators for an electron with spin $\sigma \in \{\uparrow,\downarrow\}$ on site $m \in \{1,2\}$, from which all states of the localised basis can be constructed when applied to

EIGENVALUE	:	EIGENSTATE	ABBR.	TOTAL SPIN S $[\hbar]$
0	:	$\|0,0\rangle$	$\|0\rangle$	0
b	:	$\frac{1}{\sqrt{2}}\left(\|\sigma,0\rangle + \|0,\sigma\rangle\right)$	$\|1e\sigma\rangle$	1/2
$-b$	:	$\frac{1}{\sqrt{2}}\left(\|\sigma,0\rangle - \|0,\sigma\rangle\right)$	$\|1o\sigma\rangle$	1/2
$\frac{1}{2}(U+V-\Delta)$	:	$\frac{\beta_0}{\sqrt{2}}\left(\|\uparrow,\downarrow\rangle + \|\downarrow,\uparrow\rangle\right)$ $+\frac{\alpha_0}{\sqrt{2}}\left(\|2,0\rangle + \|0,2\rangle\right)$	$\|2\rangle$	0
V	:	$\|\downarrow,\downarrow\rangle$	$\|2'(-1)\rangle$	1
V	:	$\frac{1}{\sqrt{2}}\left(\|\uparrow,\downarrow\rangle - \|\downarrow,\uparrow\rangle\right)$	$\|2'(0)\rangle$	1
V	:	$\|\uparrow,\uparrow\rangle$	$\|2'(+1)\rangle$	1
U	:	$\frac{1}{\sqrt{2}}\left(\|2,0\rangle - \|0,2\rangle\right)$	$\|2''\rangle$	0
$\frac{1}{2}(U+V+\Delta)$	:	$\frac{\beta_0}{\sqrt{2}}\left(\|\uparrow,\downarrow\rangle + \|\downarrow,\uparrow\rangle\right)$ $-\frac{\alpha_0}{\sqrt{2}}\left(\|2,0\rangle + \|0,2\rangle\right)$	$\|2'''\rangle$	0
$U+2V+b$	:	$\frac{1}{\sqrt{2}}\left(\|2,\sigma\rangle + \|\sigma,2\rangle\right)$	$\|3o\sigma\rangle$	1/2
$U+2V-b$	:	$\frac{1}{\sqrt{2}}\left(\|2,\sigma\rangle - \|\sigma,2\rangle\right)$	$\|3e\sigma\rangle$	1/2
$2U+4V$	:	$\|2,2\rangle$	$\|4\rangle$	0

in terms of $R = (U-V)/(4|b|)$:

$$\Delta = 4|b|\sqrt{1+R^2}, \quad \alpha_0 = \frac{1}{\sqrt{2}}\frac{1}{\sqrt{1+R^2-R\sqrt{1+R^2}}}, \quad \beta_0 = \sqrt{1-\alpha_0^2}$$

Table 5: Eigenstates of the double-dot system, corresponding eigenvalues and total spin. In the limit $|b| \to \infty$, where the inter-dot hopping is unhindered, $R \to 0$ and $\alpha_0 \to \beta_0$. For $|b| \to 0$, i.e. no inter-dot hopping takes place, we find, if $U > V$, that $R \to +\infty$ and $\alpha_0 \to 1$, $\beta_0 \to 0$; the state $|2\rangle$ then becomes degenerate with $|2'(0)\rangle$, forming a Heitler-London state. In turn, if $U < V$ then $R \to -\infty$ and $\alpha_0 \to 0$, $\beta_0 \to 1$.

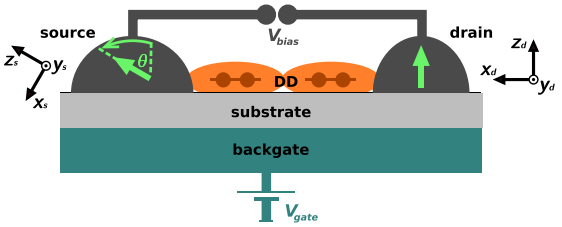

Figure 12: Transport setup with a quantum double-dot weakly coupled to source and drain contacts. The contact magnetisations, as indicated by the arrows, enclose an angle θ. The gate electrode, which acts on both sites, allows to shift the chemical potential.

Thermal energy	k_BT	0.04 meV
Tunnelling coupling	$\hbar\Gamma$	0.4 μeV
On-site Coulomb	U	6.0 meV
Inter-site Coulomb	V	1.6 meV
Hopping parameter	b	-1.0 meV

Table 6: Parameters employed for the shown plots unless specified differently. The hopping parameter has a negative value because delocalisation of electrons lowers the system energy. In case of polarised leads, contact polarisations $P_s = P_d = 0.8$ were chosen.

the vacuum state in the defined order $\hat{d}^\dagger_{1\uparrow}\hat{d}^\dagger_{2\uparrow}\hat{d}^\dagger_{1\downarrow}\hat{d}^\dagger_{2\downarrow}|0\rangle$. The tunnelling coupling between the two sites is b, which is of negative value because the delocalisation of electrons decreases the system energy. Further, U and V are the on-site and inter-site Coulomb interaction potentials. Notice that for the symmetric DD considered throughout this section, the action of the gate is uniform on both sites, and thus can be modelled by the standard term given in Sect. 1, Eq. (3). To understand transport properties of the two-site system in the weak tunnelling regime, we have to analyse the eigenstates of the isolated interacting system. These states, expressed in terms of the localised states, and the corresponding eigenvalues are listed in Tab. 5. The table also indicates the eigenvalues of the total spin operator. The groundstates of the DD with odd particle number are spin degenerate. In contrast, the groundstates with even particle number have total spin $S = 0$ and are non-degenerate. In the case of the two particles groundstate the parameters α_0 and β_0 determine whether the electrons prefer two pair in the same dot or are delocalised over the DD structure. Since the eigenstates are normalised to one, the condition $\alpha_0^2 + \beta_0^2 = 1$ holds. The energy difference between the $S = 0$ groundstate and the triplet is given by the exchange energy

$$J = \frac{1}{2}(\Delta - U + V) = 2|b|(R + \sqrt{1 + R^2})\,,$$

where $\Delta = 4|b|\sqrt{1 + R^2}$ and $R = (U - V)/(4|b|)$. Besides a triplet formation, one observes the presence of higher two-particles excited states with total spin $S = 0$.

3.2.2 Inclusion of spin-polarised leads

We have learned in Sects. 1-2 that a central system specific input to the equation of motion, besides the quantum-dot energy spectrum, are the tunnelling matrix elements $T_l(a, b)$, for all those states a, b from Tab. 5 which differ in charge by one, $|N_a - N_b| = 1$. For the description of tunnelling into or out of the DD, we can adopt the Hamiltonian Eq. (2), associating the orbital index m with our two sites, $m \in \{1, 2\}$. We must pay attention to the fact that in our DD model each site is coupled exclusively to

one of the leads[17]. A further slight complication arising in case of non-parallel spin-polarised leads, as depicted in Fig. 12, is posed by the necessity of an unique spin coordinate system on the dot. The choice is arbitrary, as long as the transformations of the electron operators into the new common coordinate system are set up properly. In what follows we employ the basis of one of the leads[18], e.g. the drain. Thus, the operator acting on site 2 is untouched, $\hat{d}_{2\sigma_{(d)}} = \hat{d}_{2\sigma}$, where the index (l) indicates the spin coordinate system of lead l and intuitively, $\sigma_{(l)} = \uparrow_{(l)} \Rightarrow \sigma = \uparrow$, $\mathrm{sgn}(\sigma) = +$; $\sigma_{(l)} = \downarrow_{(l)} \Rightarrow \sigma = \downarrow$, $\mathrm{sgn}(\sigma) = -$. From Fig. 12 it is evident that a rotation by the angle θ around the y_d-axis maps the drain onto the source coordinate system. With the help of the corresponding spin-1/2 rotation matrix one obtains for the electron operator of site 1, $\hat{d}_{1\sigma_{(s)}} = \cos(\theta/2)\hat{d}_{1\sigma} + \mathrm{sgn}(\sigma)\sin(\theta/2)\hat{d}_{1\bar{\sigma}}$. The TMEs are then given by

$$T^{-}_{s\sigma_{(s)}}(a,b) = \sqrt{\hbar\Gamma_s}\sqrt{\frac{1+\mathrm{sgn}(\sigma)P_s}{2}}\left\langle a\left|\cos(\theta/2)\hat{d}_{1\sigma} + \mathrm{sgn}(\sigma)\sin(\theta/2)\hat{d}_{1\bar{\sigma}}\right|b\right\rangle,$$

$$T^{-}_{d\sigma_{(d)}}(a,b) = \sqrt{\hbar\Gamma_d}\sqrt{\frac{1+\mathrm{sgn}(\sigma)P_d}{2}}\left\langle a\left|\hat{d}_{2\sigma}\right|b\right\rangle.$$

This choice has the advantage that for the anti-parallel configuration, $\theta = \pi$, it simply yields $\hat{d}_{1\uparrow_{(s)}} = \hat{d}_{1\downarrow}$, $\hat{d}_{1\downarrow_{(s)}} = -\hat{d}_{1\uparrow}$, i.e. there is no mixing between source spin-$\uparrow$ and -$\downarrow$ operators. Only then spin remains a good quantum number, because at least one of the TMEs $T_{l\uparrow_l}(a,b)$ or $T_{l\downarrow_l}(a,b)$ is zero for every combination of states $|a\rangle$, $|b\rangle$. As a consequence, the RDM cannot contain nonzero off-diagonal elements between states differing in S_z. For all non-collinear configurations, however, those coherences between states of different spin-projection S_z arise and must not be neglected. Replacing a, b by states from Tab. 5 written in terms of electron operators acting on the vacuum state, respecting the defined ordering of the electron operators (e.g. $\hat{d}_{2\uparrow}|\uparrow,2\rangle = \hat{d}_{2\uparrow}\hat{d}^{\dagger}_{1\uparrow}\hat{d}^{\dagger}_{2\uparrow}\hat{d}^{\dagger}_{2\downarrow}|0\rangle = -|\uparrow,\downarrow\rangle$) and exploiting the orthogonality of the localised basis, the value of any TME is obtained straightforwardly.

3.2.3 Linear conductance

For a quantum double-dot attached to leads whose magnetisation directions enclose an angle θ, a gate trace in the linear low bias regime yields a pattern of four peaks according to Fig. 13. While the right plot encodes in colour the magnitude of the conductance for arbitrary $\theta\,(\mathrm{mod}\ 2\pi)$, for the left plot three exemplary angles $\theta = 0$, $\theta = \frac{\pi}{2}$, $\theta = \pi$ were picked. Thereby, the temperature was increased to clearly resolve the differences between the three curves. Common to any θ is a mirror symmetry with respect to the half-filling ($N_c = 2$) gate voltage $e\alpha V_{\mathsf{gate}} = 7.0\,\mathrm{meV}$. Characteristically, the height of the two outer peaks exceeds the one of the inner peaks. For the

[17] The source can only exchange electrons with site 1, while the drain merely connects to site 2. For Eq. (2), this translates into $T_{s2q} = 0 = T_{d1q}\ \forall\, q$.

[18] For the numerics, this is quite a practical choice. For analytical purposes, it can be convenient to let one axis of the dot coordinate system bisect the angle θ, because of the symmetry $[d \leftrightarrow s] \mathrel{\hat{=}} [\theta/2 \leftrightarrow -\theta/2]$ in the resulting transformations [28, 29, 31, 32].

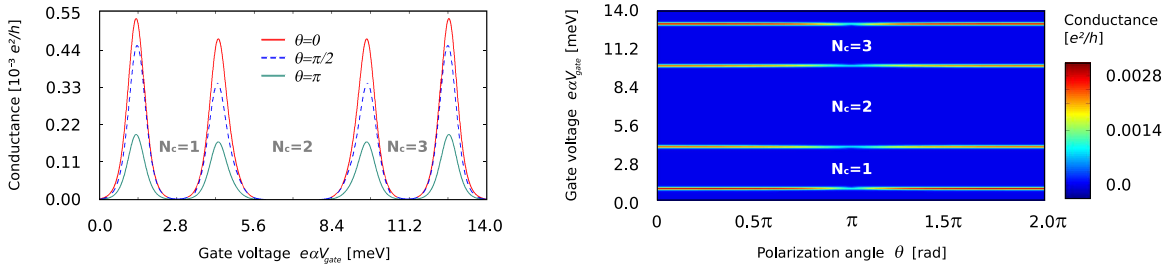

Figure 13: Conductance as a function of the polarisation angle and of the gate voltage. For the left plot, temperature was increased by a factor of five to reach a thermal energy of $k_B T = 0.2\,\mathrm{meV}$, where the peaks are nicely resolved. The minimum peak heights occur as expected at $\theta = \pi$.

collinear polarisations $\theta \in \{0, \pi\}$ the height ratio is solely determined by the ratio $|\langle 0|\hat{d}_{l\sigma}|1e\sigma\rangle|^2/|\langle 1e\bar{\sigma}|\hat{d}_{l\sigma}|2\rangle|^2 = |\langle 3o\bar{\sigma}|\hat{d}_{l\sigma}|4\rangle|^2/|\langle 2|\hat{d}_{l\sigma}|3o\sigma\rangle|^2$ of the squared absolute values of the corresponding groundstate transition matrix elements. Of particular interest is of course the angular dependence of the conductance. The colourmap plot Fig. 13, right, nicely captures an expected mirror symmetry with respect to the $\theta = \pi$, as well as the monotonous decrease of conductance towards this angle marking the anti-parallel configuration.

It has been shown [28, 29, 31, 32] that for non-collinear contact magnetisations, an effective exchange field builds up on the quantum-dot. Thereby, one must distinguish between two contributions to such a field. Intrinsic to our transport theory are *virtual tunnelling processes*, i.e. quantum fluctuations which are temporary in- or out-tunnelling events and hence not subjected to energy conservation. They are incorporated in the energy dependent function [Eq. (124a)] relating to the second order diagrams, via its imaginary part. The latter, however, is eliminated by the summation of hermitian conjugates for all except bubble diagrams off-diagonal in the initial or final states[19]. A contribution in similar form arises from interfacial exchange effects with the ferromagnetic contacts. During reflections at the interface between those and the quantum-dot, electrons pick up a phase depending on the orientation of their spin relative to the magnetisation of the ferromagnet. Concerning the order of magnitude of that effect, theoretically a contribution comparable to the aforementioned virtual processes has been claimed [29], demanding a perturbative treatment. Importantly, under the influence of any effective exchange field, an unpaired spin on the dot starts to precess, easing tunnelling from and to the polarised contacts. That is why for $\theta = \pi/2$ in Fig. 13, left, the peaks are noticeably shifted towards the $N_c = 1$ respectively $N_c = 3$ Coulomb blockade, as for these odd fillings an excess spin is present and the exchange field can act. A still more pronounced signature of the exchange field is expected in the nonlinear bias regime investigated in the next subsection.

[19] Connected to this is the absence of gain-loss partner diagrams, see Sect. 2.2.

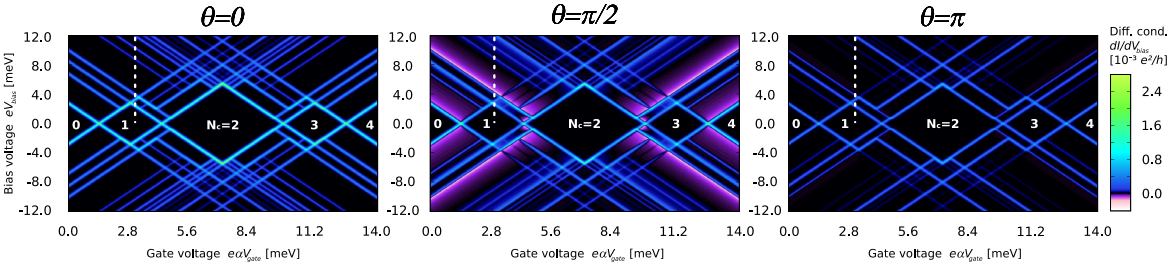

Figure 14: Differential conductance for the parallel ($\theta = 0$), perpendicular ($\theta = \pi/2$) and anti-parallel ($\theta = \pi$) contact magnetisations. Only second order contributions in the tunnelling are included. The two half diamonds and three complete diamonds correspond to regions of the bias and gate voltage where transport is Coulomb blocked. Bright excitation lines appear whenever transitions involving excited states become energetically available for transport. However, some of those excitation lines are hardly visible in the anti-parallel configuration and a negative differential conductance in form of pink shades is observed in the perpendicular case.

3.2.4 Differential conductance

The differential conductance of a quantum double-dot with specification as given in Tab. 6 is plotted in Fig. 14, for three distinct values $\theta = 0$, $\theta = \frac{\pi}{2}$ and $\theta = \pi$ for the angle enclosed by the contact magnetisation directions. The results confirm the electron-hole-symmetry and the symmetry upon bias voltage inversion. In all of the three cases we can nicely see the expected three closed and the two half-open diamonds, where the current is blocked and the occupation N_c of the double-dot system stays constant. At higher bias voltages the contribution of excited states is manifested in the appearance of several excitation lines. One clearly sees that several transition lines present in the parallel case are extremely suppressed in the anti-parallel case. Moreover, for a non-collinear polarisation, $\theta = \pi/2$, negative differential conductance is observed in form of light pink shades along certain transition lines.

In the following, we want not only to explain the origin of these two features, but alongside give another example for spin-blockade effects, which play a decisive role in the DD physics.

As a starting point, Fig. 15 (top) provides a bias trace of current through the system for the three different angles. The gate voltage is fixed at $e\alpha V_{\mathsf{gate}} = 3\,\mathrm{meV}$, and we restrict to the positive bias voltages (see dashed white lines in Fig. 14). We recognise, that for $eV_{\mathsf{bias}} < 2.4\,\mathrm{meV}$ the current is Coulomb-blocked in all of the three cases. In this configuration exactly one electron stays in the double-dot. From about $eV_{\mathsf{bias}} \geq 2.4\,\mathrm{meV}$ the channel $|1e\sigma\rangle \rightarrow |2\rangle$ opens and current begins to flow. With increasing bias more and more transport channels become energetically accessible. In particular, for all the polarisation angles θ we observe two consecutive steps corresponding to the backward transition $|1e\sigma\rangle \rightarrow |0\rangle$ and the forward transition $|1e\sigma\rangle \rightarrow |2'\rangle$, respectively. The latter, occurring at about $eV_{bias} = 4\,\mathrm{meV}$, involves the excited two-particle triplet states $|2'(S_z)\rangle$. The next excitation step, indicated with a circle in Fig. 15 (top), belongs to the transition $|1o\sigma\rangle \rightarrow |2''\rangle$. The associated line is hardly resolvable for the anti-parallel configuration, as well as the lines corresponding to $|1o\sigma\rangle \rightarrow |2'''\rangle$; $|1e\sigma\rangle \rightarrow |2''\rangle$; $|2\rangle \rightarrow |3o\sigma\rangle$; $|1e\sigma\rangle \leftrightarrow |2'''\rangle$. Crucially, in all of these transitions a two-particle state

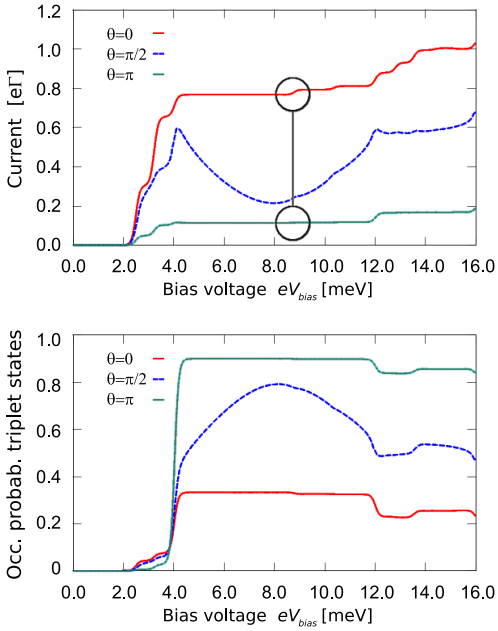

Figure 15: Current (top) and triplet occupation (bottom) along a positive bias trace for the two collinear ($\theta = 0$, $\theta = \pi$) cases and the perpendicular case ($\theta = \frac{\pi}{2}$) at a fixed gate voltage $e\alpha V_{\text{gate}} = 3\,\text{meV}$. Notice the occurrence of a pronounced negative differential conductance for the perpendicular polarisation $\theta = \pi/2$, while for $\theta = \pi$ the outstanding feature is a large enhancement of the triplet state population. A schematical explanation of the latter effect is provided in Fig. 16.

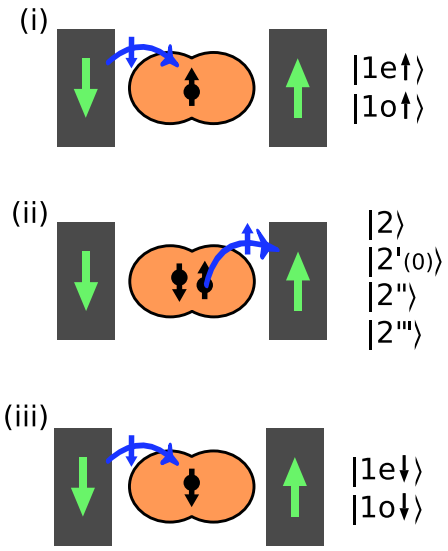

Figure 16: Schematic explaining the manifestation of a triplet blockade for anti-parallel lead magnetisations. Starting from a singly occupied DD in a spin-up state, preferably a $\downarrow$ - electron enters (i), while it is the $\uparrow$ - electron which is more likely to subsequently leave the DD (ii). The result is a spin flip. If now the triplet state $|2(-1)\rangle$ is accessible, transitions to any other $N_c = 2$ state become very unlikely, as in-tunnelling of $\uparrow$ - electrons is dispreferred (iii). Due to the spin-up polarisation of the drain, $|2(-1)\rangle$ forms then a trapping state.

with *total spin zero* is involved. In order to explain the weakness of these lines, let us e.g. focus on the first missing step in Fig. 15 (top), corresponding to the $|1o\sigma\rangle \rightarrow |2''\rangle$ resonance. In the parallel case (both contacts polarised spin-up) there is always an open channel corresponding to the situation in which the spin in the DD is anti-parallel to that in the leads (i.e. $|1o\downarrow\rangle$). In the anti-parallel case (source polarised spin-down, drain polarised spin-up) originally a $\uparrow$ - electron might be present in the dot. An electron which enters the DD from the source must then be spin-down, Fig. 16(i) (in order to form the state $|2''\rangle$), but as the drain is up-polarised, it will be the $\uparrow$ - electron which leaves the DD, which corresponds to a spin flip, Fig. 16(ii). For a transition to a two-particle state with total spin $S = 0$, in-tunnelling of an $\uparrow$ - electron is required, but as those are minority charge carriers in the source, such a transition is strongly suppressed. Instead, if $|2'(-1)\rangle$ is energetically reachable, a second effect comes into play as another $\downarrow$ - electron will enter the DD, Fig. 16(iii). Due to the fact that the spin-up polarisation of the drain hinders the out-tunnelling of $\downarrow$ - electrons, it remains there for a long time: $|2'(-1)\rangle$ acts as a blocking state in the anti-parallel configuration. This fact is nicely reflected in the occupation of the triplet state, Fig. 15

(bottom). Naturally, for all angles the probability to be in the triplet state increases above the resonance at $eV_{\mathsf{bias}} = 4\,\mathrm{meV}$, but for a parallel configuration a majority (i.e. $\uparrow$ -) electron can easily be transmitted through the DD via the triplet states $|2'(1)\rangle$ or $|2'(0)\rangle$. Notice that the here discussed spin-blockade effects are different from the Pauli spin-blockade [65, 67, 66, 68]: There, it is the asymmetry between the on-site energies which permanently traps an electron and thus localises a certain spin on one of the two dots; consequently, only electrons of the other spin species can be transmitted. Moreover, the formation of a $|2'(-1)\rangle$ trapping state, relying on the existence of the degenerate triplet, is also different from the spin-blockade found for a single-level quantum-dot [28], which requires non-collinear magnetisations. Rather the latter blockade effect, in interplay with the effective exchange field, is responsible for the negative differential conductance occurring for non-collinearly polarised leads as observed in Figs. 14, 15 for $\theta = \pi/2$. Without exchange field, we would just expect the magnitude of the current for the non-collinear polarisations to lie somewhere in between the values for the parallel and the anti-parallel current, because the source polarisation (Fig. 12) could in principle be rewritten in a terms of a component parallel and one anti-parallel with respect to the drain configuration. For a transition to a DD state with an *unpaired spin*, there is unhindered transmission via the parallel contribution, but the anti-parallel part leads to an accumulation of an average spin on the DD pointing in opposite direction to the drain polarisation, which causes a spin-blockade. The exchange field, inducing spin-precession, counteracts the blocking and enhances the current. The decisive point here is that the effective field is not only gate, but also bias voltage dependent, and reaches for our bias trace at $e\alpha V_{\mathsf{gate}} = 3\,\mathrm{meV}$ a minimum around $eV_{\mathsf{bias}} \approx 8\,\mathrm{meV}$. This explains the decreasing of the current – Fig. 15 (top), dashed blue line – up to this point. Afterwards the influence of the spin-precession regains weight. The blocking state in this case is $|2'(-1)\rangle$, affecting accordingly the triplet occupation, Fig. 15 (bottom), dashed blue line. Completely analogue considerations apply to the other NDC regions observed as glowing pink shades of certain resonance lines in Fig. 14 (middle), namely at a gate voltages $e\alpha V_{\mathsf{gate}} \lesssim 1.4\,\mathrm{meV}$ for the transition $|0\rangle \to |1e\downarrow\rangle$ (which is equivalent to the one described in Ref. [28]) and around $e\alpha V_{\mathsf{gate}} \approx 4.5\,\mathrm{meV}$ for the transition $|2\rangle \to |1e\downarrow\rangle$. Their electron-hole mirror images involve $|3o\downarrow\rangle$ instead of $|1e\downarrow\rangle$ as state with unpaired spin.

3.2.5 Fourth order transport

The differential conductance obtained from our transport theory by an effectively secular fourth order calculation is shown in Figs. 17(a)/(b) for an unpolarised setup. Unlike as for the SD, Fig. 10, we directly employ a logarithmic scale and have restricted the bias range to clearly resolve the fourth order features. The parameters used for Fig. 17(a) differ from Tab. 6 merely in an enhanced tunnelling coupling $\hbar\Gamma$, while for Fig. 17(b) we have additionally changed the hopping parameter to $b = -0.2\,\mathrm{meV}$. As a consequence, the $N_c = 1$ and $N_c = 3$ Coulomb blockade regions in plot (b) have, compared to plot (a), shrunken in width. Also, several excitation lines have moved closer together.

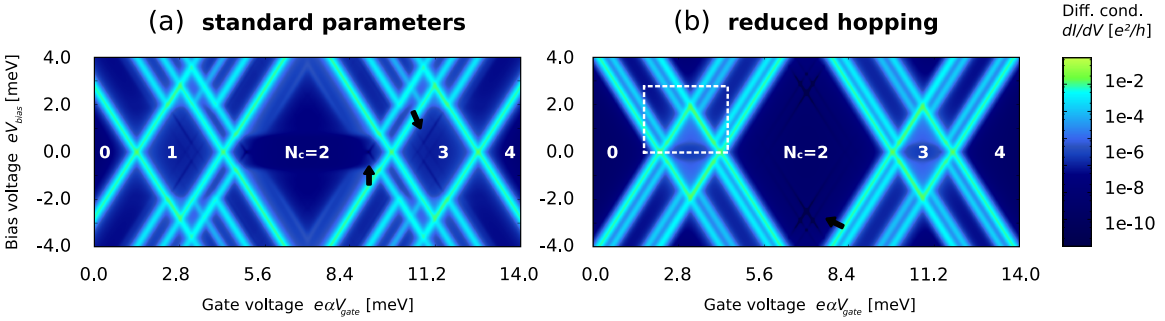

Figure 17: Differential conductance under inclusion of all fourth order contributions arising from our transport theory, Sect. 1. For plot (a) parameters were chosen according to Tab. 6, except for an enlarged tunnelling coupling $\hbar\Gamma = 2.5\,\mu$eV. Inelastic cotunnelling as well as cotunnelling assisted sequential tunnelling can nicely be observed in the central ($N_c = 2$) Coulomb diamond. Plot (b) differs from plot (a) by a change in the hopping parameter b from $-1.0\,$meV to $-0.2\,$meV. This in particular brings closer together the transition lines involving the singly occupied states $|1e\sigma\rangle$ and $1o\sigma\rangle$. The frame marks that region of gate and bias voltage for which we compare in Fig. 18 to non-exact calculations.

Due to the presence of excited states for the charge numbers $N_c \in \{1, 2, 3\}$, inelastic cotunnelling can in fact take place at – in contrast to the single-level quantum-dot – zero external magnetic field. We observe the corresponding thresholds for occupation of the triplet in the central ($N_c = 2$) and for the $|1o\sigma\rangle$ states at the tips of the adjacent ($N_c = 1/N_c = 3$) diamonds in Fig. 17(a), while in Fig. 17(b) inelastic cotunnelling, due to the shift in the resonance energies, is pronounced in the $N_c = 1/N_c = 3$ diamonds only.

What is moreover nicely visible in the central diamond of plot (a) is the onset of cotunnelling assisted sequential tunnelling [73]: From the higher lying triplet states, a transition to the $N_c = 1\,/\,N_c = 3$ groundstates requires less bias voltage as from the groundstate $|2\rangle$. In second order, the lines related to those transitions $|2'\rangle \to |1e\rangle\,/\,|2'\rangle \to |3o\rangle$ must nevertheless end at the edges of the $N_c = 2$ Coulomb blockade diamond, because only the groundstate $|2\rangle$ is available in there. But in fourth order the triplet gets significantly populated inside the diamond once inelastic cotunnelling sets in, which enables the sequential transitions. The corresponding resonance lines run in parallel to the Coulomb diamond edges, which is the reason for the typical feature as seen in Fig. 17(a): above the inelastic cotunnelling threshold, the region where the current is carried exclusively by cotunnelling processes is limited to a small inner triangle (dark). Outside of it, the cotunnelling assisted sequential tunnelling leads to a significant current increase (lighter surrounding of the dark inner region).

A weakly resolved feature is the direct continuation of certain resonance lines *below* the inelastic cotunnelling threshold (see e.g. black arrows), where the differential conductance along them is *reduced*. The origin is a tiny nonzero population of states with charge $N_c \pm 1$, which exists, as we pointed in Sect. 2.3.1, throughout the Coulomb diamond. But below the inelastic cotunnelling threshold, the current gain from sequential tunnelling involving these states is vanishing enough to be overlaid by another effect:

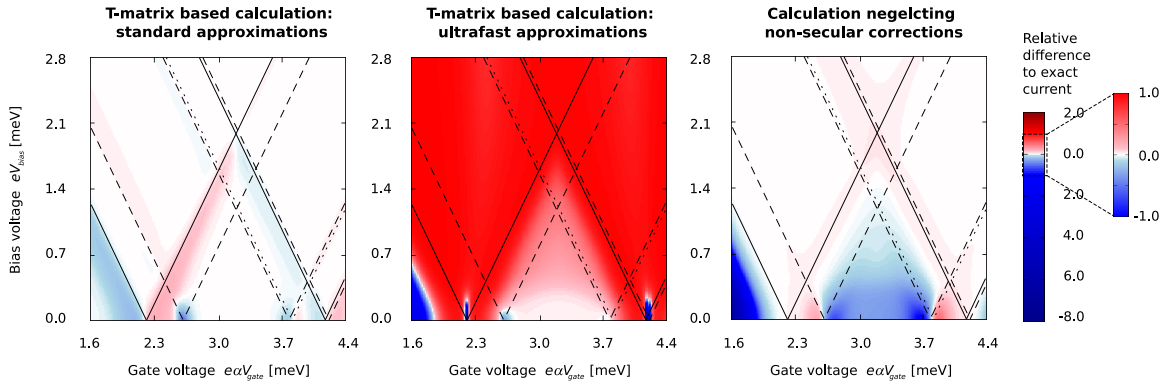

Figure 18: Relative differences $1-I_{app}/I$ between the exact current I as obtained from the transport theory presented in Sect. 1 and the currents I_{app} obtained upon invoking certain approximations. We focus on the $N_c = 1$ coulomb blockade diamond as indicated in Fig. 17(b). The black lines mark positions of resonance lines (solid: groundstate-to-groundstate transitions, dashed: groundstate and excited state involved, dotted: transition between excited states). Left: I_{app} as arising from a T-matrix based approach under neglect of both pair-tunnelling and corrections to sequential tunnelling. Middle: I_{app} as arising under the additional assumption of low bias as well as population of $N_c = 1$ charge states only. Right: I_{app} as arising from a secular calculation omitting non-secular corrections, which is in fact no approximation but a crucial mistake, as the rightmost plot proves.

around the resonances, within an energy window provided by temperature, transitions can be reversed, i.e electrons can not only tunnel out of but also back into the positively biased lead. This competes with the elastic cotunnelling processes and therefore reduces the differential conductance along the positions of the resonance lines a bit.

Comparison with T-matrix based approaches As plots of the quality of Fig. 17 already require quite some numerical effort[20], there is the desire to invoke faster methods. Zooming on the $N_c = 1$ Coulomb diamond[21] in Fig. 17(b), the left and middle plot of Fig. 18 give a comparison between the full fourth order calculation according to our theory and the T-matrix based approximation methods addressed in Sect. 2.4. In detail, for the leftmost plot, a T-matrix based rate equation neglecting corrections to sequential tunnelling as well as pair-tunnelling was invoked, as described in more detail on page 52. A non-negligible relative difference exists mainly in the vicinity of the resonance lines (their positions are indicated in the figure), which is exactly where the corrections to the sequential tunnelling are expected to act. To this approximation corresponds a reduction of computational time of about 80%. For the middle plot, two further approximations were applied, resulting in an even several hundred times faster computation. But, as predicted in the introduction of these further approximations on page 53, both come at some cost. The first one sets to zero the populations of states with charge other than $N_c = 1$, and this restricts the validity not only to inside of the Coulomb blockade diamond: in fact, every transition leading from an N electron

[20] I.e. in the order of few hours of computation on a standard year 2008 desktop machine.
[21] Here we can exclude coincidental cancellations by symmetry effects (as it could happen in the central diamond).

state to some state of charge $N_c \pm 1$ must be energetically out of reach. Only then the population of these other charge states by fourth order processes is vanishing enough to be neglected. This is the case in the middle plot of Fig. 18 within the innermost central triangular region enclosed by the transition lines $|0\rangle \rightarrow |1o\sigma\rangle$ and $|1o\sigma\rangle \rightarrow |2\rangle$ (dashed). Actually, for a hopping parameter $b = -1.0\,\mathrm{meV}$ these resonances overtake each other such that this region no longer exists, which is why we employ for the comparison Fig. 17(b) with the reduced value of $b = -0.2\,\mathrm{meV}$. The second approximation assumes a low bias limit, and indeed the raise of deviations with the bias voltage is clearly seen in the middle plot of Fig. 18. To summarise, a reduction of computational time is in any case connected with a loss of exactness. However, depending on what features in which gate and bias region one desires to analyse, it might be sensible to make use of the time saving T-matrix based calculations.

Importance of non-secular corrections The right plot in Fig. 18 finally shows the relevance of the non-secular corrections in an effectively secular fourth order calculation. We have worked out in Sect. 1.3 that a correction $\hat{K}_C$ must be added to the secular part of the fourth order kernel $\hat{K}_{ss}^{(4)}$ in order to exclude coherences between non-secular states. The huge relative difference inside the Coulomb blockade region emphasises that $\hat{K}_C$ has in fact a non-negligible influence and its inclusion is absolutely required for a qualitative as well as quantitative correct result.

3.3 Conclusion

We have shortly revised the well-known single-level description of a quantum-dot and shown results for fourth order transport. We thereby encountered several universal effects. For unpolarised contacts, elastic cotunnelling gives rise to a nonzero current inside the Coulomb blockade diamond for the single occupation ($N_c = 1$). Electron pair-tunnelling leaves a weak signature. With an external magnetic field applied, inelastic cotunnelling becomes observable due to the Zeeman splitting of the formerly spin-degenerate singly occupied states $|\uparrow\rangle$, $|\downarrow\rangle$. Assuming on top a contact polarisation along the magnetic field breaks the perfect mirror symmetry of the differential conductance with respect to the $N_c = 1$ filling gate voltage. The reason is the connection of the $|\uparrow\rangle$ groundstate to the empty state via the preferred $\uparrow$ - channel, but to the doubly occupied state via the dispreferred $\downarrow$ - electron channel. As a consequence, the differential conductance changes for certain transition lines from positive to negative values, marking an opening of a weak transport channel.

Due to its simplicity, the single-level model is always a good starting point for transport investigations on quantum-dots. In particular, it is a good reference point for the distinction between universal and system specific effects in more complex quantum-dot models.

For what concerns quantum double-dots, we have investigated linear and nonlinear spin-polarised transport through a double quantum-dot (DD) modelled by two spin-

degenerate levels.
The linear conductance characteristic of this system exhibits a typical pattern of four peaks with fixed peak height ratios and mirror-symmetric with respect to the half-filling gate voltage ($N_c = 2$), as a consequence of electron-hole-symmetry.
For non-collinear polarisations an interaction-induced exchange field causes a precession of the accumulated spin on the dot and therewith eases the tunnelling to and from the magnetised electrodes. This effect has various implications. It determines e.g. the gate voltage and angular dependence, the height of single conductance peaks and can yield negative differential conductance features in the nonlinear bias regime.
There, the presence of various excited states gives rise to interesting DD specific features. For example, a suppression of several excitation lines for an anti-parallel lead configuration originates from a spin-blockade effect. It occurs because a trapping state is formed whenever a transition involves a two-electron state with total spin zero. A second spin-blockade effect involves the two-electron triplet state. The common mechanism of these two spin-blockades is the following: in both cases, a tunnelling event can only occur if initially the dot is populated with an unpaired electron possessing the majority spin of the drain. The second step is that a majority electron of the source will enter, forming a spin-zero state. Then the first electron can leave the dot, causing a spin-flip. If the triplet state is involved, the dot will be left in a trapping state once a second majority electron from the source enters. Otherwise, we are directly in a blocking state.
Finally we compared the fourth order transport characteristics of double quantum-dots for two different values of the hopping parameter. As the splitting between various DD states depends upon this quantity, it influences the position (and therewith resolvability) of the inelastic cotunnelling threshold in the Coulomb diamonds for the fillings $N_c = 1, 2, 3$ and, consequently, of the cotunnelling assisted sequential tunnelling in the $N_c = 2$ diamond. The formation of a triplet as well as of even and odd states within a small Hilbert space makes the DD model a good candidate for comparison between an exact fourth order calculation and approximation approaches and to exemplify the importance of the non-secular corrections. We have considered two T-matrix based methods, which both provide a considerable speed-up of computations. The fastest method is valid only at a low bias voltage deep inside the Coulomb blockade, where it shows good agreement with the exact results. In contrast, upon a neglect of non-secular corrections, wrong values are obtained throughout the Coulomb diamond. The other T-matrix based approximation covers the whole gate and bias range, showing deviations in the vicinity of the resonance lines. Depending on which features are subject of interest, it can, at least for a pre-analysis, be useful to invoke one of these time saving approximations. This concerns in particular investigations on quantum-dot models with high-dimensional Hilbert spaces, where the multitude of states can gigantify the time scale for a full fourth order calculation.

In summary, double quantum-dot systems are particularly attractive for investigations, both on the theoretical and on the experimental side, because of a rather simple structure and universality, nevertheless combined with a multiplicity of properties. To

comply with experiments on double-dots with separately gated sites, a project has been started in collaboration with Sebastian Pfaller, Alexander Hupfer, Georg Begemann, Andrea Donarini and Milena Grifoni. A first success in the creation of an input generator for KinEq [20] is to be followed by systematic investigations.

Related publications:

R. P. Hornberger, S. Koller, G. Begemann, A. Donarini, M. Grifoni. Phys. Rev. B **77**, 245313 (2008)
Transport through a double-quantum-dot system with noncollinearly polarized leads. [32]

G. Begemann, S. Koller, J. Paaske, M. Grifoni. In preparation.
Inelastic cotunneling in complex quantum dots.[22]

[22] The title of the final publication might differ.

4 Carbon armchair nanoribbons

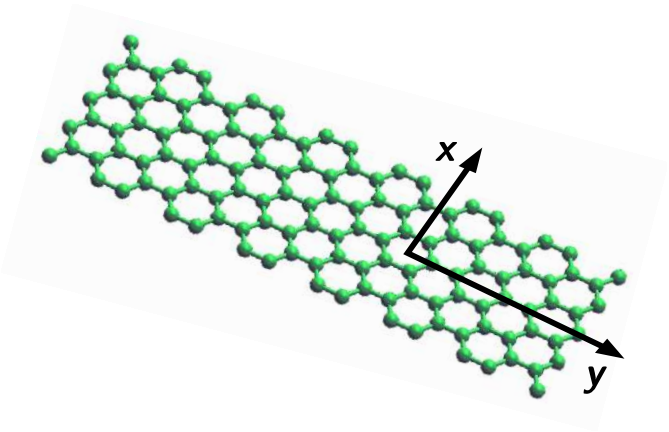

Figure 19: Graphene armchair nanoribbon.

The introduction to this thesis mentioned the "world smallest transistor", 1×10 atoms in dimension, which attracted some broader interest [3] in spring 2008. By end of 2008, IBM researchers had achieved to build the "world fastest transistor" [74]. Both devices were actually based on the same promising material: graphene. And actually, only four years had passed since the first successful separation of such a one atom thick sheet of graphite by Novoselov and Geim and coworkers [75].
Not only a great potential for applications [76, 77], but also fundamental physics issues [78] arise from the linear dispersion relation in the electronic band structure of graphene. Already decades ago, a Dirac-like behaviour was predicted for charge carriers in a honeycomb lattice theoretically [79] and indeed confirmed for graphene experimentally nearly sixty year later [75, 80, 81, 82].

Increasing effort is presently put in the understanding of the electronic properties of graphene nanodevices, which can be obtained by etching or lithographic techniques and may achieve lateral dimensions of a few tenth of nm [83, 84, 85]. Studies on the effects of electron-electron interactions and confinement in transport across graphene nanodevices have been carried out on single-dots [84, 86] and, only recently, on double-dot structures [62, 63]. Conductance quantisation has also been observed in 30nm wide ribbons [85], while an energy gap near the charge neutrality point scaling with the inverse ribbon width was reported in [83] and theoretically [87, 88] attributed to Coulomb interaction effects.
A desirable goal of course is the fabrication of clearly defined geometries, and of particular interest for applications [76] could be narrow stripes of graphene, so-called carbon nanoribbons. Crucial for the properties of such an object is the form of its ends. The two most regular possibilities are an armchair and a zig-zag end (see Fig. 19). At present, the shape of the ends cannot be controlled, but there is ongoing progress in developing methods to fabricate stripes with clear edges, by scanning tunnelling microscope lithography [89], chemical synthesis [90] or by unrolling carbon nanotubes [91]. Moreover, there exist theoretical studies [92, 93] claiming that any narrow stripe should

show either the behaviour of a zig-zag or of an armchair ribbon (ACNR), where the names specify the form of the long side edges.
A peculiar property of the zig-zag edge is the existence of localised states [94] which were indeed observed experimentally by means of scanning tunnelling microscopy [95, 96, 97]. Due to their high degeneracy, flat-band ferromagnetism is expected from the Hubbard model, leading to a spin-polarised many particle groundstate, and it was suggested [98, 99] to exploit this property for spintronic applications. Thereby, the focus was on zig-zag non-interacting ribbons, where transport is carried by the oppositely polarised channels along the two long edges.
In contrast, the following investigations concern interacting armchair ribbons. Interestingly, it turns out that the presence of localised states at the far apart zig-zag ends still is of crucial importance for the transport properties.

This section splits into three parts: First, we derive the Bloch waves for an unterminated layer of graphene, Eq. (50). These serve as basis for the analysis of special geometries, as the armchair nanoribbons which we study here in Sect. 4, or the armchair single wall nanotubes investigated Sect. 5, which both impose their characteristic boundary conditions onto the Bloch wave functions. Subsequently, we present in detail how a low energy theory for ACNRs is derived. It is based on the framework of a Tomonaga-Luttinger model for interacting fermions in one dimension, but importantly, our approaches go beyond the density-density interactions this model accounts for. Namely, the sublattice structure of graphene gives rise to a distinction between electron interactions on the same and on different sublattices and besides the long-ranged density-density processes, also short-ranged non-density-density interaction processes must be accounted for in narrow carbon nanoribbons as well as in small diameter carbon nanotubes [100, 101, 102, 103]. While a detailed low energy theory for the latter is provided in [104], an analogous description for ACNRs is found at length in this thesis. Remarkably, it turns out that for narrow ribbons short-ranged Coulomb interactions induce entanglement between the extended bulk states and the states localised at the ribbon ends. This has a decisive impact on eigenstates and transport properties.
The structure is held such that the technical sections can be skipped without loosing the track.

4.1 Charge carriers in the graphene honeycomb lattice

We shortly revise here the properties of carbon atoms arranged in a honeycomb lattice, because the resulting Bloch waves, Eq. (50), are the starting point for constructing the appropriate wave functions of specific graphene based systems.

As shown Fig. 20, the hexagonal lattice is not a Bravais lattice itself, but formed by a triangular lattice with two atoms per unit cell such that we can define two different sublattices $p = \pm$. In carbon, ${}_6C : 1s^2 2s^2 2p^2$, hybridization of the $2s$-orbital with the $2p_x$- and $2p_y$-orbitals leads to strong σ-bonds in the lattice plane. The electrons in the

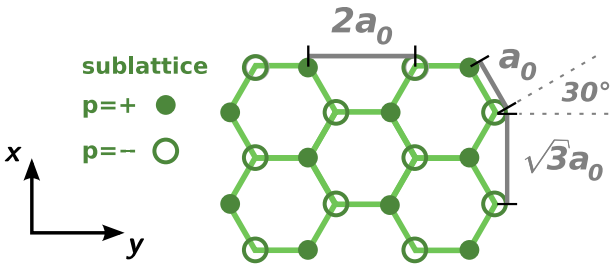

Figure 20: The sublattice structure of the graphene honeycomb lattice, where $a_0 \approx 0.14\,\text{nm}$. The underlying Bravais lattice is triangular, with a basis of two sites labelled $p = \pm$. We chose the orientation of the coordinate system such that the x-axis points along the zig-zag ends, the y-axis along the long armchair edges of the stripe.

remaining $2p_z$-orbitals form π-bands which determine the electronic properties at low energies. Characteristic for the structure of the π-band are the valence and conduction bands that touch at the corner points of the first Brillouin zone, also called Dirac points, Fig. 21. Since there is one p_z-electron per carbon atom, in isolated graphene the valence band is completely filled whereas the conduction band is empty. In the vicinity of the Dirac points the band structure exhibits a linear dispersion relation, Fig. 22a, resembling, up to a reduced propagation velocity of $v = 8.1 \cdot 10^5$ m/s, the one of massless relativistic particles. From now on we focus on the region of linear dispersion, which extends up to energies beyond 1 meV, i.e. far above room temperature. A description in terms of a Dirac equation for the p_z-electrons capturing the essential features of the π-band close to the Dirac points can be obtained by a nearest neighbour tight binding calculation [105].
The six corner points of the first Brillouin zone can be decomposed into two subsets of equivalent Dirac points. As particular representatives we choose (see also Fig. 21)

$$\vec{K}_F = F\frac{4\pi}{3\sqrt{3}a_0}\hat{k}_x =: F\vec{K}_0,\ F = \pm \tag{49}$$

where $a_0 \approx 0.14$ nm is the nearest neighbour distance. Restricting the discussion to the vicinity of $\pm\vec{K}_0$, the π-electrons are described by Bloch waves

$$\begin{aligned}\varphi_{F\alpha}(\vec{r},\vec{\kappa}) &= \frac{1}{\sqrt{2N_L}}\sum_{p=\pm}\eta_{F\alpha p}(\vec{\kappa})\sum_{\vec{R}} e^{\mathrm{i}\left(\vec{K}_F+\vec{\kappa}\right)\cdot\vec{R}}\chi_{\vec{R}p}(\vec{r}) \\ &=: \sum_{p=\pm}\eta_{F\alpha p}(\vec{\kappa})\varphi_{Fp}(\vec{r},\vec{\kappa}),\end{aligned} \tag{50}$$

where $\vec{r},\vec{R} \in \mathbb{R}^2$, N_L is the number of sites of the considered lattice, $\alpha = \pm$ denotes the conduction and valence band, respectively, and $\chi_{\vec{R}p}(\vec{r})$ is the p_z-orbital on sublattice p at lattice site $\vec{R}$. Finally, $\vec{\kappa}$ is the wave vector relative to the Dirac point $\vec{K}_F$. Defining the spinors

$$\eta_{F\alpha}(\vec{\kappa}) := \begin{pmatrix}\eta_{F\alpha-}(\kappa_x,\kappa_y)\\ \eta_{F\alpha+}(\kappa_x,\kappa_y)\end{pmatrix},\ \kappa_{x/y} \equiv \hat{k}_{x/y}\cdot\vec{\kappa}, \tag{51}$$

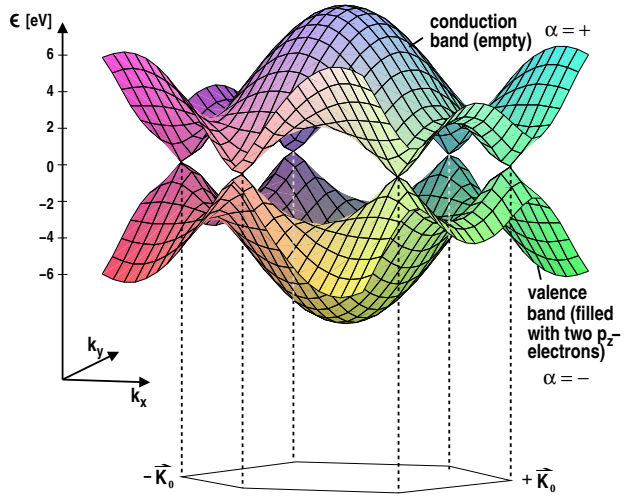

Figure 21: The band structure of graphene is characterised by two bands $\alpha = \pm$ touching at six Fermi points. The two inequivalent Fermi points are denoted by $\pm\vec{K}_0 (= \vec{K}_\pm)$.

it is found that they fulfil the Dirac equation

$$\hbar v \left(-F\sigma_x \kappa_x + \sigma_y \kappa_y\right) \eta_{F\alpha}(\kappa_x, \kappa_y) = \alpha\, \varepsilon(\kappa_x, \kappa_y)\, \eta_{F\alpha}(\kappa_x, \kappa_y), \tag{52}$$

where

$$\varepsilon(\kappa_x, \kappa_y) = \hbar v \sqrt{\kappa_x^2 + \kappa_y^2} \tag{53}$$

reflects the linear dispersion relation and σ_x, σ_y are the Pauli matrices. From (52) it follows that for $\kappa_y \neq \pm \mathrm{i}\kappa_x$ it holds the relation

$$\eta_{F\alpha +}(\kappa_x, \kappa_y) = -\alpha \frac{F\kappa_x - \mathrm{i}\kappa_y}{\sqrt{\kappa_x^2 + \kappa_y^2}}\, \eta_{F\alpha -}(\kappa_x, \kappa_y). \tag{54}$$

A specific solution of Eq. (54) we will use in the remaining thesis is given by

$$\eta_{F\alpha -}(\kappa_x, \kappa_y) = 1, \qquad \eta_{F\alpha +}(\kappa_x, \kappa_y) = -\alpha \frac{F\kappa_x - \mathrm{i}\kappa_y}{\sqrt{\kappa_x^2 + \kappa_y^2}}.$$

4.2 The low energy theory of ACNRs

Based on noninteracting bulk and end states emerging from proper boundary conditions in a finite graphene ribbon, we construct in Sect. 4.2.1 the electron operator, Eq. (60), of a metallic ACNR. The associated Hamiltonian $\hat{H}_0$ does not yet describe a realistic system, as Coulomb interaction between the electrons still have to be taken into account. For this reason, the Hamiltonians accounting for scattering processes between bulk electrons, as well as between end and bulk electrons, are set up and discussed in Sect. 4.2.2. It turns out that they can be divided into easily diagonalizable density-density interactions $\hat{V}_{\rho\rho}$ plus non-density-density corrections $\hat{V}_{n\rho\rho}$. Sect.

4.2.3 describes the diagonalization process for $\hat{H}_0 + \hat{V}_{\rho\rho}$, where the key results are the diagonal Hamiltonian Eq. (79) and its eigenstates, Eq. (81). It is important that those form not yet an eigenbasis of the real ACNR, but get mixed under the influence of $\hat{V}_{n\rho\rho}$. We calculate, partly in App. B, its matrix elements in terms of the truncated eigenbasis, arriving at Eq. (82) for the non-density-density bulk-bulk and Eq. (87) for the non-density-density end-bulk interaction.

4.2.1 Noninteracting metallic ACNRs

On the wave functions of graphene, Eq. (50), so far no boundary conditions have been imposed. However, we wish to discuss the electronic properties of finite size ACNRs, where the wave functions must vanish all along the borders of the sheet. Thereby we are interested in a geometry as depicted in Fig. 19: the long edges of the ribbon, along the y direction, are assumed in an armchair configuration, while the narrow terminations of the ribbon, along the x axis, have zig-zag character. Furthermore, we want to focus on quasi one-dimensional ribbons and thus restrict our discussion to ACNRs with a large aspect ratio $L_y \gg L_x$ where L_x and L_y are the extensions in x and y direction, respectively.

Boundary conditions From Fig. 20 we can easily see that the two zig-zag ends each consist of atoms either sitting on sublattice $p = +$ or $p = -$. We will use the convention that the "left" end at $y = 0$ is formed by atoms living on sublattice $p = -$ whereas on the other end (at $y = L_y$) we have atoms from sublattice $p = +$ only. The appropriate boundary condition for the zig-zag ends is to demand that the wave functions $\tilde{\varphi}_{F\alpha}(\vec{r}, \vec{\kappa})$ have to vanish on the "missing" atoms at the ends, namely on sublattice $p = +$ on the left end and $p = -$ on the other end. A lengthy but straightforward calculation leads to

$$\tilde{\varphi}_{F\alpha}\left(\vec{r}, \vec{\kappa} = (\kappa_x, \kappa_y)\right) = C_{zz}(F\kappa_x, \kappa_y)\left[\varphi_{F\alpha}\left(\vec{r}, (\kappa_x, \kappa_y)\right) - \varphi_{F\alpha}\left(\vec{r}, (\kappa_x, -\kappa_y)\right)\right], \tag{55a}$$

with a normalisation constant[23] $C_{zz}(F\kappa_x, \kappa_y) \in \mathbb{C}$ and the quantisation condition [106]

$$e^{\mathrm{i}2\kappa_y L_y} = \frac{F\kappa_x + \mathrm{i}\kappa_y}{F\kappa_x - \mathrm{i}\kappa_y}. \tag{55b}$$

Additionally, we ask the wave function to vanish at the armchair edges. In contrast to the zig-zag end, the terminating atoms where the wave function is required to vanish are from both sublattices. In order to build up suited linear combinations of the Bloch waves $\varphi_{F\alpha}(\vec{r}, \vec{\kappa})$, we have to mix states of Eq. (55a) which belong to different Dirac points. Then, the resulting wave function $\varphi_\alpha(\vec{r}, \vec{\kappa})$ vanishes on the lattice sites with $R_x = 0$ and $R_x = L_x$ for

$$\varphi_\alpha\left(\vec{r}, \vec{\kappa} = (\kappa_x, \kappa_y)\right) = C_{ac}(\kappa_x, \kappa_y)\left[\tilde{\varphi}_{K_+\alpha}\left(\vec{r}, (\kappa_x, \kappa_y)\right) - \tilde{\varphi}_{K_-\alpha}\left(\vec{r}, (-\kappa_x, \kappa_y)\right)\right], \tag{56a}$$

[23] The normalisation constant is non-trivial as the functions given in Eq. (50) are non-orthogonal. To verify that there is the dependence on $F\kappa_x$ and κ_y, but not on α, Eq. (50) must be consulted in combination with Eqs. (49), (54).

with $C_{ac}(\kappa_x, \kappa_y) \in \mathbb{C}$ another normalisation constant, and the quantisation [106]

$$K_\pm \pm \kappa_x = \frac{\pi}{L_x} n_x, \quad n_x \in \mathbb{Z}. \tag{56b}$$

Due to the relation $K_\pm = \pm K_0$, the two conditions in Eq. (56b) are in fact equivalent.

The eigenstates of metallic ACNRs In total we obtain with Eqs. (55a) and (56a) the following expression for the eigenstates of noninteracting electrons in finite size ACNRs,

$$\varphi_\alpha\left(\vec{r}, (\kappa_x, \kappa_y)\right) = C(\kappa_x, \kappa_y) \sum_{F,r=\pm} (Fr)\, \varphi_{F\alpha}\left(\vec{r}, (F\kappa_x, r\kappa_y)\right), \tag{57}$$

where the generally complex number $C(\kappa_x, \kappa_y) = C_{zz}(\kappa_x, \kappa_y) C_{ac}(\kappa_x, \kappa_y)$ guarantees that $\varphi_\alpha(\vec{r}, (\kappa_x, \kappa_y))$ is normalised to 1.

We want to investigate now the solutions of the Dirac equation fulfilling our quantisation conditions Eqs. (55b) and (56b). It has been shown [94, 92] that the presence of zig-zag ends leads to the formation of localised states characterised by a purely imaginary κ_y giving rise to an enhanced density of states around the Dirac energy. Though those states are localised at the zig-zag ends with an exponential decay in y direction, they will be of decisive relevance for the transport properties of ACNRs.

At first, however, let us focus on the ***bulk states***, where both κ_x and κ_y are real numbers. Since $L_y \gg L_x$, the quantisation condition Eq. (56b) leads to the formation of subbands assigned to different κ_x. For a metallic ACNR, the subband must cross the Dirac points $F = K_\pm$, which demands $\kappa_x = 0$, or equivalently $n_x = \frac{L_x}{\pi} K_0$, $n_x \in \mathbb{N}$, which follows from Eq. (56b). The width L_x depends on the number M of hexagons in a row parallel to $\hat{x}$ like $L_x = \sqrt{3} a_0 (M + 1/2)$ (compare Fig 19). Hence $n_x = [\text{Eq. (49)}] = \frac{1}{3}(4M + 2)$. Obviously, this means that the geometrical condition for having metallic ACNRs with gapless subbands reads $M \bmod 3 = 1$.
Focussing on such ribbons, $\vec{\kappa} \propto \hat{k}_y$ as $\kappa_x = 0$, which corresponds to a cut through the Dirac cone as shown in Fig. 22(a). The corresponding states are characterised by the band index α and κ_y, see Eq. (56a). With $\kappa_x = 0$, Eq. (55b) yields as allowed values of κ_y:

$$\kappa_y = (n + \frac{1}{2}) \frac{\pi}{L_y}, \; n \in \mathbb{Z}. \tag{58}$$

Since by definition, Eq. (57), $\varphi_\alpha\left(\vec{r}, (0, \kappa_y)\right) = -\varphi_\alpha\left(\vec{r}, (0, -\kappa_y)\right)$, we can further restrict for each α our analysis to either $\kappa_y > 0$ or $\kappa_y < 0$. Thus it is an allowed choice to just consider states with $\mathrm{sgn}(\kappa_y) = \mathrm{sgn}(\alpha)$, which we define as

$$\varphi^{\mathrm{b}}_{\kappa_y}(\vec{r}) := \varphi_{\alpha = \mathrm{sgn}(\kappa_y)}\left(\vec{r}, (0, \kappa_y)\right).$$

Doing so, we select the positive slope of the two branches of the dispersion relation Fig 22(a). Bearing in mind the form of the graphene Bloch waves, Eq. (50), we can of

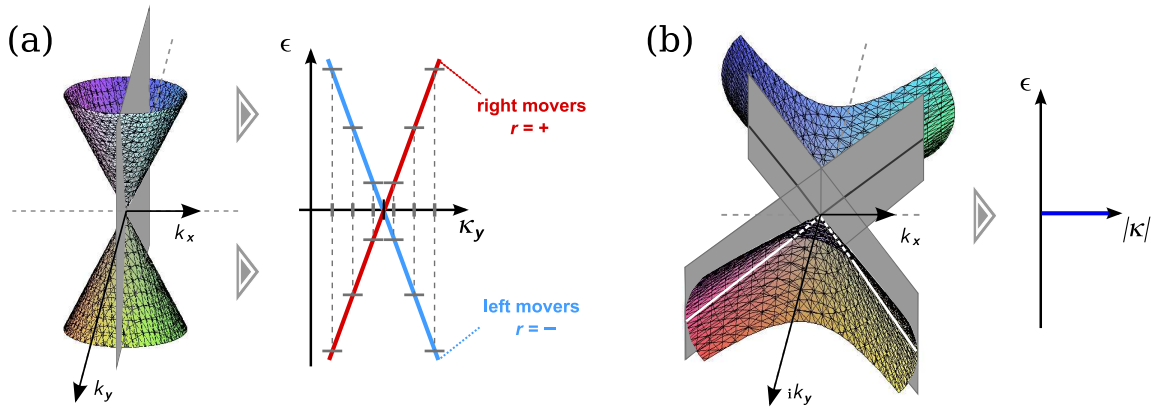

Figure 22: The dispersion relation of graphene, Eq. (53), for (a) real and (b) imaginary momenta κ_y. In both cases the boundary condition at the armchair edge mixes wave functions belonging to both Dirac points. (a) For solutions with real κ_y, in the low energy regime only subbands with $\kappa_x = 0$ play a role due to the condition $L_x \ll L_y$. The corresponding dispersion relation emerges thus from the intersection of the Dirac cone with the plane $k_x = 0$. (b) For solutions with imaginary κ_y the cone opens along $\mathrm{i}\hat{k}_y$ and is stretched perpendicular to the momentum plane by $\hbar v$. As for the eigenstates it must hold $\kappa_y = \pm\mathrm{i}\kappa_x$, the corresponding dispersion relation is obtained from the intersection of the cone with the two planes $k_x = \pm\mathrm{i}k_y$. There is only tangency along two straight lines within the k_x-ik_y-plane, resulting in a dispersion which is identically zero.

course express the states $\varphi^{\mathrm{b}}_{\kappa_y}$ in terms of the sublattice wave functions φ_{Fp},

$$\varphi^{\mathrm{b}}_{\kappa_y}(\vec{r}) = \frac{1}{2}\sum_{Fpr} f_{Fpr}\varphi_{Fp}\left(\vec{r}, (0, r\kappa_y)\right),$$

where up to a complex prefactor the coefficients f_{Fpr} are given by

$$f_{F+r} = rF\,, \quad f_{F-r} = \mathrm{i}F. \tag{59}$$

Note that the index r here denotes right ($r = +$) and left ($r = -$) moving waves [compare also to Fig. 22(a)].

Now we turn to the ***end states***, emerging for purely imaginary κ_y [105], which are allowed by both the Dirac equation Eq. (52) and the quantisation condition Eq. (55b). In more detail, there exist two imaginary solutions for each $\kappa_x > 1/L_y$, which holds in ACNRs for all $\kappa_x = n\pi/L_x$, $n \in \mathbb{N}$. Besides, the relation $L_x \ll L_y$ causes that to a very good approximation

$$\kappa_y = \pm\mathrm{i}\kappa_x,$$

satisfies Eq. (52) and Eq. (55b). The corresponding dispersion relation is given in Fig. 22(b). Notice that Eq. (54) is not applicable to $\kappa_y = \pm\mathrm{i}\kappa_x$ (as explicitly exempted before), and instead the spinors fulfilling the Dirac equation Eq. (52) are given by

$$\eta_{F\alpha p}(\kappa_x, \pm\mathrm{i}\kappa_x) = \delta_{p,\pm F}.$$

Using this in Eq. (50) and following the steps leading to Eq. (57), we obtain instead after straightforward insertions

$$\varphi_\alpha(\vec{r},(\kappa_x,\pm\mathrm{i}\kappa_x)) = \pm C(\kappa_x,\pm\mathrm{i}\kappa_x)\sum_{Fp} Fp\,\varphi_{Fp}\left(\vec{r},(F\kappa_x,\mathrm{i}p\kappa_x)\right).$$

The corresponding ACNR eigenstates can be chosen such that they live on one sublattice $p=\pm$ only:

$$\varphi^{\mathrm{e}}_{p\kappa_x}(\vec{r}) = \tilde{C}(\kappa_x)\sum_{F} F\varphi_{Fp}\left(\vec{r},(F\kappa_x,\mathrm{i}p\kappa_x)\right),$$

where $\tilde{C}(\kappa_x)$ is a normalisation constant. It is evident that the decay length of $\varphi^{\mathrm{e}}_{p\kappa_x}(\vec{r})$ from one of the ends to the interior of a specific ACNR is $L_x/(n_x\pi)$, which is always much shorter than the length of the ribbon. That is why one speaks of *localised end states*.

From the dispersion relation Eq. (53) it is easy to see that the energy of the end states is zero. Consequently, they will be unpopulated below half filling, but as soon as the Dirac point is reached, one electron will get trapped at each end (in an interacting system, Coulomb repulsion will hinder a second electron to enter). So we can conclude that at energies around the Dirac energy, not only the extended states with $\kappa_x = 0$, but also the localised end states can be of importance.

Electron and Hamilton operator of the metallic ACNR All in all, the appropriate operator describing an electron with spin σ at position $\vec{r}$ reads in the low energy regime

$$\hat{\Psi}_\sigma(\vec{r}) = \underbrace{\sum_{\kappa_y=(\mathbb{Z}+0.5)\pi/L_y} \varphi^{\mathrm{b}}_{\kappa_y}(\vec{r})\hat{c}_{\sigma\kappa_y}}_{=:\hat{\psi}_\sigma(\vec{r})} + \sum_p \underbrace{\sum_{\kappa_x=\mathbb{N}\pi/L_x} \varphi^{\mathrm{e}}_{p\kappa_x}(\vec{r})\hat{d}_{\sigma p\kappa_x}}_{=:\psi^{\mathrm{e}}_{p\sigma}(\vec{r})}, \tag{60}$$

where $\hat{c}_{\sigma k}$, $\hat{d}_{\sigma pk}$ are the annihilation operators for electrons of momentum k and spin σ in the bulk or end states, respectively. The one-dimensional (1D) character of ACNRs at low energies becomes evident by defining the slowly varying electron operators

$$\hat{\psi}_{r\sigma}(y) := \frac{1}{\sqrt{2L_y}} \sum_{\kappa_y=(\mathbb{Z}+0.5)\pi/L_y} e^{\mathrm{i}r\kappa_y}\hat{c}_{\sigma\kappa_y} \tag{61}$$

such that we obtain

$$\hat{\psi}_\sigma(\vec{r}) = \sqrt{L_y/2}\sum_{Fpr} f_{Fpr}\varphi_{Fp}(\vec{r})\hat{\psi}_{r\sigma}(y), \tag{62}$$

with $\varphi_{Fp}(\vec{r}) := \varphi_{Fp}(\vec{r},\vec{\kappa}=(0,0))$.

From the dispersion relations Fig. 22, it is easy to give the Hamilton operator of the noninteracting metallic ACNR,

$$\hat{H}_0 = \hbar v \sum_{\sigma\kappa_y} \kappa_y \hat{c}^\dagger_{\sigma\kappa_y} \hat{c}_{\sigma\kappa_y}, \tag{63}$$

with the Fermi velocity $v = 8.1 \times 10^5$ m/s corresponding to the absolute value of the slopes of the linear branches in Fig. 22(a). There is no contribution of the end states as those have zero energy, see Fig. 22(b). With the allowed values for κ_y, Eq. (58), there results obviously a level spacing

$$\varepsilon_0 := \frac{\hbar\pi v}{L_y}. \tag{64}$$

4.2.2 The interaction Hamiltonian

In the following we concentrate both on interaction effects regarding the extended bulk states in ACNRs as well as on correlations between end and bulk states. Ignoring exchange effects [98, 107], the many-body end states can be spin- or edge- degenerate. As claimed before, the charging energy of the end states exceeds, due to the strong localisation in position space, the charging energy of the extended states by far. A simple estimation modelling the Coulomb repulsion between two electrons localised at the same ribbon end via the Ohno potential given below, Eq. (67), yields energies of the order of 0.1 eV for ribbon width around 10 nm. In contrast, typical charging energies for the bulk states of such ACNRs range around $1 - 10$ meV. We can therefore assume that above half filling, within a reasonable energy range, both end states are populated with one single electron and the only relevant scattering processes between bulk and end states mediated by the Coulomb interaction are of the form

$$\hat{V}_{\mathrm{e-b}} = \sum_{\sigma\sigma'} \sum_{\tilde{p}} \iint \mathrm{d}^3r\, \mathrm{d}^3r' \left(\hat{\psi}^\dagger_\sigma(\vec{r}) \hat{\psi}^{\mathrm{e}\dagger}_{\sigma'\tilde{p}}(\vec{r}\,') U(\vec{r} - \vec{r}\,') \hat{\psi}^{\mathrm{e}}_{\sigma'\tilde{p}}(\vec{r}\,') \hat{\psi}_\sigma(\vec{r}) \right.$$
$$\left. + \hat{\psi}^\dagger_\sigma(\vec{r}) \hat{\psi}^{\mathrm{e}\dagger}_{\sigma'\tilde{p}}(\vec{r}\,')\, U(\vec{r} - \vec{r}\,') \hat{\psi}_{\sigma'}(\vec{r}\,') \hat{\psi}^{\mathrm{e}}_{\sigma\tilde{p}}(\vec{r}) \right). \tag{65}$$

All other processes should be strongly suppressed for energy reasons. For the bulk-bulk interaction, our scattering potential is described by the expression

$$\hat{V}_{\mathrm{b-b}} = \frac{1}{2} \sum_{\sigma\sigma'} \iint \mathrm{d}^3r\, \mathrm{d}^3r'\, \hat{\psi}^\dagger_\sigma(\vec{r}) \hat{\psi}^\dagger_{\sigma'}(\vec{r}\,') U(\vec{r} - \vec{r}\,') \hat{\psi}_\sigma(\vec{r}) \hat{\psi}_{\sigma'}(\vec{r}\,'). \tag{66}$$

In both Eqs. (65) and (66), the function $U(\vec{r} - \vec{r}\,')$ models the screened 3D Coulomb interaction potential. For our calculations we use the Ohno potential [108],

$$U(\vec{r} - \vec{r}\,') = U_0 \left(1 + \left(\frac{U_0 \epsilon |\vec{r} - \vec{r}\,'|}{14.397[\text{Å eV}]} \right)^2 \right)^{-\frac{1}{2}}, \tag{67}$$

with $U_0 = 15$ eV [109] and $\epsilon \simeq 1.4 - 2.4$ [100] the dielectric constant of graphene.
We proceed now with an analysis of the two different expressions. We start with the bulk-bulk processes, where the analysis follows largely the lines of an earlier work on interaction effects in metallic single wall carbon nanotubes (SWCNTs) [103].

Bulk-bulk interaction With the help of the reformulation of the 3D electron operator in terms of the 1D operators $\hat{\psi}_{r\sigma}(y)$, Eq. (62), we obtain after integrating over the coordinates perpendicular to the ribbon axis an effectively 1D expression for the interaction,

$$\hat{V}_{\mathrm{b-b}} = \sum_{\{[r]\}} \sum_{\sigma\sigma'} \underbrace{\iint \mathrm{d}y\, \mathrm{d}y'\, \hat{\psi}^{\dagger}_{r_1\sigma}(y) \hat{\psi}^{\dagger}_{r_2\sigma'}(y') \frac{1}{2} U_{[r]}(y,y') \hat{\psi}_{r_3\sigma'}(y') \hat{\psi}_{r_4\sigma}(y)}_{=:\hat{V}^{\mathrm{b-b}}_{[r][\sigma,\sigma',\sigma',\sigma]}}, \tag{68}$$

where $\sum_{\{[I]\}}$ denotes the sum over all possible quadruples $[I_1, I_2, I_3, I_4]$, in the former case for the band index $I = r$. The spin-independent 1D interaction potential $U_{[r]}(y,y')$ reads

$$U_{[r]}(y,y') = \frac{L_y^2}{4} \sum_{pp'} \sum_{\{[F]\}} f^*_{F_1 p r_1} f^*_{F_2 p' r_2} f_{F_3 p' r_3} f_{F_4 p r_4} \times \int_{\perp}\int_{\perp} \mathrm{d}^2 r\, \mathrm{d}^2 r'\, \varphi_{F_1 p}(\vec{r}) \varphi_{F_2 p'}(\vec{r}\,') U(\vec{r} - \vec{r}\,') \varphi_{F_3 p'}(\vec{r}\,') \varphi_{F_4 p}(\vec{r}), \tag{69}$$

with $\int_{\perp}$ indicating that the integration has to be performed over the coordinates perpendicular to y, y' (i.e. x, x', z, z'). Exploiting the explicit form, Eq. (59), of the coefficients f_{Fpr} we can easily identify those scattering processes which are indeed mediated by $U_{[r]}(y,y')$. In detail,

$$U_{[r]}(y,y') = \frac{1 + r_1 r_2 r_3 r_4}{2}\, U^{intra}(y,y') + \frac{r_1 r_4 + r_2 r_3}{2}\, U^{inter}(y,y'), \tag{70}$$

where we have defined the potentials

$$U^{intra/inter}(y,y') := \frac{L_y^2}{2} \sum_{p} \sum_{\{[F]\}} F_1 F_2 F_3 F_4 \times \int_{\perp}\int_{\perp} \mathrm{d}^2 r\, \mathrm{d}^2 r'\, \varphi^*_{F_1 p}(\vec{r}) \varphi^*_{F_2 \pm p}(\vec{r}\,') U(\vec{r} - \vec{r}\,') \varphi_{F_3 \pm p}(\vec{r}\,') \varphi_{F_4 p}(\vec{r}),$$

describing interactions between electrons residing on the same/different sublattices. From Eq. (70) it is clear that a non-vanishing interaction potential can only be assigned to processes characterised by $r_1 r_4 = r_2 r_3$, and those are the forward (f)-, back (b)-, and umklapp (u)- scattering. Denoting the scattering type by S_I, the corresponding quadruples are $[I]_{S_I = f^{\pm}} = [I, \pm I, \pm I, I]$, $[I]_b = [I, -I, I, -I]$ and $[I]_u = [I, I, -I, -I]$. In total this means that we can rewrite Eq. (68) as[24]

$$\hat{V}_{\mathrm{b-b}} = \sum_{S_r = u,b,f^{\pm}} \sum_{S_\sigma = f^{\pm}} \hat{V}^{\mathrm{b-b}}_{S_r S_\sigma}.$$

In the case of umklapp- and back-scattering with respect to r, the potential $U_{[r]}(y,y')$ is proportional to the difference of the inter- and intra-lattice interaction potential. Since

[24] The spin quadruple $[\sigma, \sigma', \sigma', \sigma]$ yields possible configurations $[\sigma]_{f^{\pm}} = [\sigma, \pm\sigma, \pm\sigma, \sigma]$.

the latter potentials differ only on the length scale of the lattice spacing $a_0 \approx 0.14\,\mathrm{nm}$, this means that in the case of $S_r = u, b$ the effective 1D potential $U_{[r]}(y, y')$ can be considered as point-like. Introducing the coupling constant

$$u := \frac{1}{4L_y^2} \iint \mathrm{d}y\, \mathrm{d}y' \, \left(U^{intra}(y, y') - U^{inter}(y, y') \right),$$

we can set in good approximation $U_{[r]}(y, y') = u\,\delta(y - y')$ and write the short-ranged interaction processes as

$$\hat{V}^{\mathrm{b-b}}_{bf^{\pm}} = \frac{u}{2} \sum_{r\sigma} \int \mathrm{d}y\, \hat{\psi}^{\dagger}_{r\sigma}(y) \hat{\psi}^{\dagger}_{-r\pm\sigma}(y) \hat{\psi}_{r\pm\sigma}(y) \hat{\psi}_{-r\sigma}(y), \tag{71a}$$

$$\hat{V}^{\mathrm{b-b}}_{uf^{-}} = \frac{u}{2} \sum_{r\sigma} \int \mathrm{d}y\, \hat{\psi}^{\dagger}_{r\sigma}(y) \hat{\psi}^{\dagger}_{r-\sigma}(y) \hat{\psi}_{-r-\sigma}(y) \hat{\psi}_{-r\sigma}(y). \tag{71b}$$

Since u is derived from a short-ranged interaction it scales inversely with the size of the underlying ribbon. We find typical values [110] of $uL_x/\varepsilon_0 = 0.1\,\mathrm{nm}$ for a level spacing ε_0, Eq. (64). The process $V^{\mathrm{b-b}}_{uf^{+}}$ vanishes identically, because it involves the operator product $\hat{\psi}_{-r\sigma}(y)\hat{\psi}_{-r\sigma}(y) = 0$. Only the forward scattering processes $V^{\mathrm{b-b}}_{f^{\pm}f^{\pm}}$ are long ranged.

Since easily diagonalizable by bosonisation, it is convenient to identify the density-density processes among the relevant bulk-bulk interaction processes, such that $\hat{V}_{\mathrm{b-b}}$ can be decomposed into

$$\hat{V}_{\mathrm{b-b}} = \hat{V}^{\mathrm{b-b}}_{\rho\rho} + \hat{V}^{\mathrm{b-b}}_{n\rho\rho},$$

with the density-density and non-density-density parts given by

$$\hat{V}^{\mathrm{b-b}}_{\rho\rho} = \hat{V}^{\mathrm{b-b}}_{f^{\pm}f^{\pm}} + \hat{V}^{\mathrm{b-b}}_{bf^{+}} \quad \text{and} \quad \hat{V}^{\mathrm{b-b}}_{n\rho\rho} = \hat{V}^{\mathrm{b-b}}_{bf^{-}} + \hat{V}^{\mathrm{b-b}}_{uf^{-}},$$

respectively.

End-bulk interaction In ACNRs, we additionally have to consider scattering between the electrons living in the bulk of the ribbon and the electrons trapped in the end state existing at both zig-zag terminations of the stripe. Below half-filling, the end states are unpopulated and thus all terms discussed in the following would be zero a priori. The range we want to concentrate on is the low energy regime above half-filling, where exactly one electron will permanently occupy each end state, so that we have in total two end electrons interacting with our bulk electrons.

If we insert into Eq. (65) the decomposition Eq. (62) for the bulk electron operator and $\psi^{\mathrm{e}}_{\tilde{p}\sigma}(\vec{r}) = \sum_{\kappa_x} \varphi^{\mathrm{e}}_{\tilde{p}\kappa_x}(\vec{r}) \hat{d}_{\sigma\tilde{p}\kappa_x}$ for the end electron operator, we obtain:

$$\begin{aligned} \hat{V}_{\mathrm{e-b}} = \frac{L_y}{2} \sum_{\kappa_x} \sum_{\sigma\sigma'} \sum_{rr'} \sum_{FF'} \sum_{p} f^{*}_{rFp} f_{r'F'p} \iint \mathrm{d}^3 r\, \mathrm{d}^3 r' \\ \times \Big(\hat{\psi}^{\dagger}_{r\sigma}(y) \hat{\psi}_{r'\sigma}(y) \varphi^{*}_{Fp}(\vec{r}) \varphi_{F'p}(\vec{r}) U(\vec{r} - \vec{r}\,') \sum_{\tilde{p}} \left| \varphi^{\mathrm{e}}_{\tilde{p}\kappa_x}(\vec{r}\,') \right|^2 \hat{d}^{\dagger}_{\sigma'\tilde{p}\kappa_x} \hat{d}_{\sigma'\tilde{p}\kappa_x} \\ - \hat{\psi}^{\dagger}_{r\sigma}(y) \hat{\psi}_{r'\sigma'}(y') \varphi^{*}_{Fp}(\vec{r}) \varphi_{F'p}(\vec{r}\,') U(\vec{r} - \vec{r}\,') \, \varphi^{\mathrm{e}*}_{p\kappa_x}(\vec{r}\,') \varphi^{\mathrm{e}*}_{p\kappa_x}(\vec{r}) \hat{d}^{\dagger}_{\sigma'p\kappa_x} \hat{d}_{\sigma p\kappa_x} \Big). \end{aligned} \tag{72}$$

Here we imposed that the wave functions of the localised p_z-orbitals have non-vanishing overlap for electrons on the same sublattice only. Moreover we demand that both end electron operators have to belong to the same end, and thus to the same sublattice, in order to give a nonzero contribution[25]. By setting in the coefficients from Eq. (59), Eq. (72) acquires the form:

$$\hat{V}_{\mathrm{e-b}} = \frac{L_y}{2} \sum_{\kappa_x} \sum_{\sigma\sigma'} \sum_{rr'} \sum_{\tilde{p}} \iint \mathrm{d}y\, \mathrm{d}y'\; \hat{d}^\dagger_{\sigma'\tilde{p}\kappa_x} \hat{\psi}^\dagger_{r\sigma}(y) \\ \times \left(\hat{\psi}_{r'\sigma}(y) \left[U^{\mathrm{e}}_{\rho}\right]^{\kappa_x\tilde{p}}_{rr'}(y,y') \hat{d}_{\sigma'\tilde{p}\kappa_x} - \hat{\psi}_{r'\sigma'}(y') \left[U^{\mathrm{e}}_{n\rho}\right]^{\kappa_x\tilde{p}}_{rr'}(y,y') \hat{d}_{\sigma\tilde{p}\kappa_x} \right).$$

We introduced an interaction potential related to densities,

$$\left[U^{\mathrm{e}}_{\rho}\right]^{\kappa_x\tilde{p}}_{rr'}(y,y') = \sum_{FF'} \int_{\perp}\int_{\perp} \mathrm{d}^2r\, \mathrm{d}^2r'\, FF'\, U(\vec{r}-\vec{r}\,') \\ \times \left(rr' \varphi^*_{F+}(\vec{r}) \varphi_{F'+}(\vec{r}) + \varphi^*_{F-}(\vec{r}) \varphi_{F'-}(\vec{r}) \right) \left| \varphi^{\mathrm{e}}_{\tilde{p}\kappa_x}(\vec{r}\,') \right|^2,$$

which for symmetry reasons fulfils both $\left[U^{\mathrm{e}}_{\rho}\right]^{\kappa_x\tilde{p}}_{rr'}(y,y') = \delta_{r,r'} \left[U^{\mathrm{e}}_{\rho}\right]^{\kappa_x\tilde{p}}_{++}(y,y')$ and further

$$\int \mathrm{d}y' \left[U^{\mathrm{e}}_{\rho}\right]^{\kappa_x+}_{++}(y,y') = \int \mathrm{d}y' \left[U^{\mathrm{e}}_{\rho}\right]^{\kappa_x-}_{++}(y,y') \equiv t^{\kappa_x}_{\rho}(y) \approx t_{\rho}(y)\ \forall \kappa_x.$$

We define a density-density part of the end-bulk interaction correspondingly as

$$\hat{V}^{\mathrm{e-b}}_{\rho\rho} = L_y \int \mathrm{d}y\; t_{\rho}(y) \left(\sum_{r\sigma} \hat{\psi}^\dagger_{r\sigma}(y) \hat{\psi}_{r\sigma}(y) \right), \tag{73}$$

where we exploited that each end state is populated with exactly one electron.

The second potential,

$$\left[U^{\mathrm{e}}_{n\rho}\right]^{\kappa_x\tilde{p}}_{rr'}(y,y') = \sum_{FF'} \int_{\perp}\int_{\perp} \mathrm{d}^2r\, \mathrm{d}^2r'\, FF'\, U(\vec{r}-\vec{r}\,') \left(\delta_{\tilde{p},+} rr' + \delta_{\tilde{p},-}\right) \\ \times \varphi^*_{F\tilde{p}}(\vec{r}) \varphi_{F'\tilde{p}}(\vec{r}\,') \varphi^{\mathrm{e}*}_{\tilde{p}\kappa_x}(\vec{r}\,') \varphi^{\mathrm{e}}_{\tilde{p}\kappa_x}(\vec{r}),$$

can be considered point-like due to the localisation of the end states at $y_{\tilde{p}=-} = 0$ or $y_{\tilde{p}=+} = L_y$, and hence simplifies to

$$\left[U^{\mathrm{e}}_{n\rho}\right]^{\kappa_x\tilde{p}}_{rr'}(y,y') = \left(\delta_{\tilde{p},-}\delta(y-0)\delta(y'-0) + \delta_{\tilde{p},+} rr' \delta(y-L_y)\delta(y'-L_y)\right) t^{\kappa_x}_{n\rho},$$

with a short-range coupling constant which is independent of $\tilde{p}$ for symmetry reasons,

$$t^{\kappa_x}_{n\rho} := \sum_{FF'} \iint \mathrm{d}^3r\, \mathrm{d}^3r'\, FF'\, U(\vec{r}-\vec{r}\,') \varphi^*_{F+}(\vec{r}) \varphi_{F'+}(\vec{r}\,') \varphi^{\mathrm{e}*}_{+\kappa_x}(\vec{r}\,') \varphi^{\mathrm{e}}_{+\kappa_x}(\vec{r}).$$

[25] Operators acting on different ends would change the population of each end state, which is not allowed.

For an ACNR of width L_x ranging from 5 to 25 nm, one finds [110] $t_{n\rho}^{\kappa_x} \approx t_{n\rho}$, with $t_{n\rho} L_x/\varepsilon_0 \approx 0.55\,\mathrm{nm}$, practically independent of κ_x. This means that the short-ranged end-bulk scattering is comparable in strength to the exchange interactions induced by the bipartite sublattice structure, and consequently we have to account for a non-negligible contribution

$$\hat{V}_{n\rho\rho}^{\mathrm{e-b}} = -\frac{L_y}{2} \sum_{\sigma\sigma'} \sum_{rr'} \sum_{p} \left(\delta_{p,+} rr' + \delta_{p,-}\right) \hat{\psi}_{r\sigma}^{\dagger}(y_p) \hat{\psi}_{r'\sigma'}(y_p)\, t_{n\rho} \sum_{\kappa_x} \hat{d}_{\sigma' p\kappa_x}^{\dagger} \hat{d}_{\sigma p\kappa_x} \tag{74}$$

in the total end-bulk interaction potential

$$\hat{V}_{\mathrm{e-b}} = \hat{V}_{\rho\rho}^{\mathrm{e-b}} + \hat{V}_{n\rho\rho}^{\mathrm{e-b}}.$$

4.2.3 Diagonalization of the ACNR Hamiltonian

In this section we calculate the spectrum and the eigenstates of the interacting p_z-electrons in metallic ACNRs. For this purpose we first diagonalize the Hamiltonian $\hat{H}_0 + \hat{V}_{\rho\rho}^{\mathrm{b-b}} + \hat{V}_{\rho\rho}^{\mathrm{e-b}}$ by bosonisation and subsequently express the total ACNR Hamiltonian,

$$\hat{H}_{\odot} := \hat{H}_0 + \underbrace{\hat{V}_{\rho\rho}^{\mathrm{b-b}} + \hat{V}_{\rho\rho}^{\mathrm{e-b}}}_{=:\hat{V}_{\rho\rho}} + \underbrace{\hat{V}_{n\rho\rho}^{\mathrm{b-b}} + \hat{V}_{n\rho\rho}^{\mathrm{e-b}}}_{=:\hat{V}_{n\rho\rho}}, \tag{75}$$

in the eigenbasis of $\hat{H}_0 + \hat{V}_{\rho\rho}$. Here, $\hat{H}_0$ describes the noninteracting extended ACNR eigenstates discussed in Sect. 4.2.1. A numerical diagonalization of the so constructed total Hamiltonian, however, yields reliable results only away from half-filling: as the eigenbasis needs to be truncated for the calculation, it is crucial that $\hat{V}_{n\rho\rho}$ is just a perturbation to $\hat{H}_0 + \hat{V}_{\rho\rho}$ in the sense that it only mixes states close in energy to each other. In the direct vicinity of the Dirac points, the process $\hat{V}_{uf-}^{\mathrm{b-b}}$ breaks this demand, while it vanishes away from half-filling, as it will become clear in the course of this section.

Diagonalization of the density-density part Diagonalization of $\hat{H}_0 + \hat{V}_{\rho\rho}$ can be achieved by bosonisation. We start by rewriting $\hat{H}_0 + \hat{V}_{\rho\rho}$ in terms of collective bosonic excitations. Concretely, we Fourier-expand the 1D electron densities $\hat{\rho}_{r\sigma}(y) = \hat{\psi}_{r\sigma}^{\dagger}(y)\hat{\psi}_{r\sigma}(y)$,

$$\hat{\rho}_{r\sigma}(y) = \frac{1}{2L_y} \sum_{q} e^{\mathrm{i}rqy} \hat{\rho}_{\sigma q}, \tag{76}$$

where the summation is over the wave numbers $q = \frac{\pi}{L} n_q$, $n_q \in \mathbb{Z}$. Then as shown e.g. in [111] the operators

$$\hat{b}_{\sigma q} := \frac{1}{\sqrt{n_q}} \hat{\rho}_{\sigma q}\,, \quad \hat{b}_{\sigma q}^{\dagger} := \frac{1}{\sqrt{n_q}} \hat{\rho}_{\sigma -q}, \quad q > 0, \tag{77}$$

fulfil the canonical bosonic commutation relations $[\hat{b}_{\sigma q}, \hat{b}^\dagger_{\sigma' q'}] = \delta_{\sigma\sigma'}\delta_{qq'}$.
As well known [111] the bosonisation of $\hat{H}_0$ yields

$$\hat{H}_0 = \varepsilon_0 \left(\sum_\sigma \sum_{q>0} n_q \hat{b}^\dagger_{\sigma q} \hat{b}_{\sigma q} + \frac{1}{2} \sum_\sigma \hat{\mathcal{N}}_\sigma^2 \right), \tag{78a}$$

where $\hat{\mathcal{N}}_\sigma = \sum_{\kappa_y} \hat{c}^\dagger_{\sigma\kappa_y} \hat{c}_{\sigma\kappa_y}$ counts the number of electrons with spin σ. The first term in Eq. (78a) accounts for collective particle-hole excitations, whereas the second term is due to Pauli's principle and describes the energy cost for filling up the spin degenerate single-electron states. Terms proportional to the total number of electrons have been omitted since they merely lead to a shift of the chemical potential in transport experiments.
Bosonisation of $\hat{V}^{\mathrm{b-b}}_{\rho\rho}$ can be achieved by rewriting the involved potentials in terms of electron densities and inserting the Fourier expansion Eq. (76), thereby making use of the definition Eq. (77). We obtain

$$\begin{aligned} \hat{V}^{\mathrm{b-b}}_{\rho\rho} &= \hat{V}^{\mathrm{b-b}}_{f^+f^+} + \hat{V}^{\mathrm{b-b}}_{f^+f^-} + \hat{V}^{\mathrm{b-b}}_{f^-f^+} + \hat{V}^{\mathrm{b-b}}_{f^-f^-} + \hat{V}^{\mathrm{b-b}}_{bf^+} \\ &= \frac{1}{4} \sum_{\sigma\sigma'} \sum_q n_q W_q \left(\hat{b}_{\sigma q} + \hat{b}^\dagger_{\sigma q} \right) \left(\hat{b}_{\sigma' q'} + \hat{b}^\dagger_{\sigma' q'} \right) \\ &\quad - \frac{u}{4} \sum_\sigma \sum_{q>0} n_q \left(\hat{b}_{\sigma q} \hat{b}_{\sigma q} + \hat{b}^\dagger_{\sigma q} \hat{b}^\dagger_{\sigma q} \right) + \frac{1}{2} W_0 \hat{\mathcal{N}}_c^2 - \frac{u}{4} \sum_\sigma \hat{\mathcal{N}}_\sigma^2, \end{aligned} \tag{78b}$$

where the coefficients W_q determine the strength of the long-ranged interactions $\hat{V}_{f^\pm f^\pm} + \hat{V}_{bf^+}$ via

$$W_q = \frac{1}{L_y^2} \int_0^{L_y} \mathrm{d}y \int_0^{L_y} \mathrm{d}y' \left(U^{intra}(y, y') + U^{inter}(y, y') \right) \cos(qy) \cos(qy').$$

The last line of Eq. (78b) describes the contribution of $\hat{V}^{\mathrm{b-b}}_{\rho\rho}$ to the system energy depending on the number of electrons in the two spin-bands. Here, $E_c = W_0$ is the ACNR charging energy; $\hat{\mathcal{N}}_c = \hat{\mathcal{N}}_\uparrow + \hat{\mathcal{N}}_\downarrow$ counts the total number of electrons. Spin alignment of electrons is favoured by the term proportional to u, because it counteracts the energy cost for the shell filling in Eq. (78a).
Finally, the bosonised form of the end-bulk contribution Eq. (73) to $\hat{V}_{\rho\rho}$ is

$$\hat{V}^{\mathrm{e-b}}_{\rho\rho} = \frac{1}{4} \int \mathrm{d}y \; t_\rho(y) \sum_\sigma \sum_{q>0} \sqrt{n_q} \left(\hat{b}_{\sigma q} + \hat{b}^\dagger_{\sigma q} \right) \cos(qy), \tag{78c}$$

which is linear in the bosonic operators, while those appear quadratically in Eqs. (78a), (78b).
In fact, terms of in the form of Eq. (78c) are absorbed in the quadratic part of the Hamiltonian without any relevant impact on the spectrum [112], and we remain with

$\hat{H}_0+\hat{V}^{\mathrm{b-b}}_{\rho\rho}$, which can be diagonalized in a standard way [111]: Introducing new bosonic operators $\hat{a}_{jq}$ and $\hat{a}^\dagger_{jq}$ via the Bogoliubov transformation [113] given below by Eq. (80a), we obtain

$$\hat{H}_0+\hat{V}_{\rho\rho}=\frac{1}{2}W_0\hat{\mathcal{N}}_c^2+\frac{1}{2}\varepsilon_0\hat{\mathcal{N}}_c+\frac{1}{2}\left(\varepsilon_0-\frac{u}{2}\right)\sum_\sigma\hat{\mathcal{N}}_\sigma^2+\sum_{j=c,s}\sum_{q>0}\varepsilon_{jq}\,\hat{a}^\dagger_{jq}\hat{a}_{jq}. \tag{79}$$

The first three purely fermionic contributions in Eq. (79) account for charging and shell filling and have already been explained above. The newly arising last term counts the bosonic excitations of the system, created/annihilated by the operators $\hat{a}^\dagger_{jq}$ / $\hat{a}_{jq}$. The two channels $j=c,s$ are associated to charge (c) and spin (s) excitations. The decoupling of these two modes, the so called spin-charge separation, will, in contrast to what is found for SWCNTs [103], hardly be affected by the non-diagonal bulk-bulk interaction $\hat{V}^{\mathrm{b-b}}_{n\rho\rho}$. The excitation energies ε_{jq} and the relation between the new bosonic operators $\hat{a}_{jq}$ and the old operators $\hat{b}_{\sigma q}$ are determined by the Bogoliubov transformation. In detail, we find

$$\varepsilon_{jq}=\sqrt{X_{jq}^2-A_{jq}^2}\,,\ \text{with}\ \ X_{jq}=n_q\left[\delta_{j,c}W_q+\varepsilon_0\right]\,,\ A_{jq}=n_q\left[\delta_{j,c}W_q-\frac{u}{2}\right].$$

The energies of the charge channel are dominated by the long-ranged interactions via W_q. For the transformation from the old bosonic operators, $\hat{b}_{\sigma q}$, to the new ones, $\hat{a}_{jq}$, we have

$$\hat{b}_{\sigma q}=\sum_j\Lambda^j_\sigma\left(B_{jq}\hat{a}_{jq}+D_{jq}\hat{a}^\dagger_{jq}\right)\quad q>0, \tag{80a}$$

where

$$\Lambda^c_\sigma=\frac{1}{\sqrt{2}}\,,\quad \Lambda^s_\sigma=\frac{\mathrm{sgn}(\sigma)}{\sqrt{2}}. \tag{80b}$$

The transformation coefficients B_{jq} and D_{jq} can be expressed in terms of X_{jq} and A_{jq}:

$$B_{jq}=\frac{\varepsilon_{jq}+X_{jq}}{\sqrt{(\varepsilon_{jq}+X_{jq})^2-A_q^2}},\quad D_{jq}=-\frac{A_{jq}}{\sqrt{(\varepsilon_{jq}+X_{jq})^2-A_q^2}}.$$

With our values for X_{jq} and A_{jq} we find approximately

$$\varepsilon_{cq}=\varepsilon_0 n_q\sqrt{1+\frac{W_q}{\varepsilon_0}},\quad \varepsilon_{sq}=\varepsilon_0 n_q\sqrt{1-\left(\frac{u}{2\varepsilon_0}\right)^2}\approx\varepsilon_0 n_q,$$

and for the transformation coefficients to the spin mode

$$B_{sq}=1,\qquad D_{sq}=0. \tag{80c}$$

The transformation coefficients for the charge modes depend, as for SWCNTs [103, 114], on the ratio $g_q=\varepsilon_{0q}/\varepsilon_{cq}$:

$$B_{cq}=\frac{1}{2}\left(\sqrt{g_q}+\frac{1}{\sqrt{g_q}}\right),\qquad D_{cq}=\frac{1}{2}\left(\sqrt{g_q}-\frac{1}{\sqrt{g_q}}\right). \tag{80d}$$

Finally, we can give the eigenbasis of $H_0 + V_{\rho\rho}^{\mathrm{b-b}}$ in terms of states

$$\left|\vec{N}, \vec{\sigma}^{\mathrm{e}}, \vec{m}\right\rangle = \prod_{j=c,s} \prod_{q>0} \frac{\left(a_{jq}^{\dagger}\right)^{m_{jq}}}{\sqrt{m_{jq}!}} \left|\vec{N}, \vec{\sigma}^{\mathrm{e}}, 0\right\rangle, \tag{81}$$

where $|\vec{N}, \vec{\sigma}^{\mathrm{e}}, 0\rangle$ has no bosonic excitation. The fermionic configuration $\vec{N} = (N_\uparrow, N_\downarrow)$ defines the number of electrons in each spin band. The occupation of the end states is determined by $\vec{\sigma}^{\mathrm{e}} = (\sigma_+^{\mathrm{e}}, \sigma_-^{\mathrm{e}})$, where '$-$' relates to $y_- = 0$ and '$+$' to $y_+ = L_y$ as before. Below half filling the end states are empty, such that there is only one possible configuration: $\sigma_+^{\mathrm{e}} = 0 = \sigma_-^{\mathrm{e}}$. Above half filling, exactly one electron occupies each end state and thus $\sigma_+^{\mathrm{e}}, \sigma_-^{\mathrm{e}} \in \{\uparrow, \downarrow\}$. Finally, $\vec{m} = (\vec{m}_s, \vec{m}_c)$, with $m_{jq} = (\vec{m}_j)_q$ containing the information how many bosonic excitations are present in level q for mode $j = c, s$.

Non-density-density interaction In the following we use the states from Eq. (81) as basis to examine the effect of $\hat{V}_{n\rho\rho}$. For this purpose we evaluate the matrix elements of the potentials $\hat{V}_{n\rho\rho}^{\mathrm{b-b}}$ and $\hat{V}_{n\rho\rho}^{\mathrm{e-b}}$, using the bosonisation identity for the 1D electron operators.

The matrix elements $\left\langle \vec{N}\vec{\sigma}^{\mathrm{e}}\vec{m} \left| \hat{V}_{n\rho\rho}^{\mathrm{b-b}} \right| \vec{N}'\vec{\sigma}^{\mathrm{e}\prime}\vec{m}' \right\rangle$ Generally, $\hat{V}_{n\rho\rho}^{\mathrm{b-b}}$ does not conserve the quantity $\vec{m}$, while it must neither mix states with different electron configurations $\vec{N}$, nor with different end spin configurations $\vec{\sigma}^{\mathrm{e}}$: the Coulomb interaction between bulk electrons cannot change the quantity $S_z = \frac{1}{2}(N_\uparrow - N_\downarrow)$, and it cannot touch the end states. Further, we already know that both processes $\hat{V}_{uf^-}^{\mathrm{b-b}}$ and $\hat{V}_{bf^-}^{\mathrm{b-b}}$ contained in $\hat{V}_{n\rho\rho}^{\mathrm{b-b}}$ are effectively local interactions, see Eqs. (71a), (71b), such that the matrix elements of the non-diagonal bulk-bulk interaction scale with the exchange-coupling parameter u,

$$\begin{aligned}\left\langle \vec{N}\vec{\sigma}^{\mathrm{e}}\vec{m} \left| \hat{V}_{n\rho\rho}^{\mathrm{b-b}} \right| \vec{N}'\vec{\sigma}^{\mathrm{e}\prime}\vec{m}' \right\rangle &= \frac{u}{2L_y} \delta_{\vec{N},\vec{N}'} \delta_{\vec{m}_c,\vec{m}_c'} \delta_{\vec{\sigma}^{\mathrm{e}},\vec{\sigma}^{\mathrm{e}\prime}} \\ &\times \sum_{r\sigma} \int \mathrm{d}y \frac{e^{-\mathrm{i}\frac{2\pi}{L_y}\mathrm{sgn}(r)(N_\sigma - N_{-\sigma})y}}{4\sin^2(\pi y/L_y)} \prod_q F(\tilde{\lambda}^{sq}_{[r]_b[\sigma]_{f^-}}(y), m_{sq}, m'_{sq}).\end{aligned} \tag{82}$$

The derivation of this expression is given in App. B.1, as well as the definitions of $F(\lambda, m, m')$ and $\tilde{\lambda}^{jq}_{[r][\sigma]}(y)$, Eq. (145) and Eq. (143), respectively. In fact it turns out that in comparison to the end-bulk non-diagonal interaction, the bulk-bulk non-diagonal interaction has only minor impact on spectrum and transport properties of narrow ACNRs.

The matrix elements $\left\langle \vec{N}\vec{\sigma}^{\mathrm{e}}\vec{m}\left|\hat{V}^{\mathrm{e-b}}_{n\rho\rho}\right|\vec{N}'\vec{\sigma}^{\mathrm{e}\prime}\vec{m}'\right\rangle$ For the non-diagonal end-bulk interaction, we have to evaluate matrix elements of Eq. (74), of the form

$$M^{p}_{r\sigma r'\sigma'}(\vec{N},\vec{\sigma}^{\mathrm{e}},\vec{m},\vec{N}',\vec{\sigma}^{\mathrm{e}\prime},\vec{m}') := \left\langle \vec{N}\vec{\sigma}^{\mathrm{e}}\vec{m}\left|\hat{\psi}^{\dagger}_{r\sigma}(y_p)\hat{\psi}_{r'\sigma'}(y_p)\sum\nolimits_{\kappa_x}\hat{d}^{\dagger}_{\sigma' p\kappa_x}\hat{d}_{\sigma p\kappa_x}\right|\vec{N}'\vec{\sigma}^{\mathrm{e}\prime}\vec{m}'\right\rangle, \quad (83)$$

with $y_-{=}0$, $y_+{=}L_y$ as employed previously. We can factorise the matrix elements into a fermionic, a bosonic, and an end part

$$M^{p}_{r\sigma r'\sigma'}(\vec{N},\vec{\sigma}^{\mathrm{e}},\vec{m},\vec{N}',\vec{\sigma}^{\mathrm{e}\prime},\vec{m}') = M^{p}_{r\sigma r'\sigma'}(\vec{N},\vec{N}')M^{p}_{r\sigma r'\sigma'}(\vec{m},\vec{m}')M^{p}_{\sigma\sigma'}(\vec{\sigma}^{\mathrm{e}},\vec{\sigma}^{\mathrm{e}\prime}).$$

The easiest to give is the end contribution:

$$M^{p}_{\sigma\sigma'}(\vec{\sigma}^{\mathrm{e}},\vec{\sigma}^{\mathrm{e}\prime}) = \sum_{\kappa_x}\left\langle\vec{\sigma}^{\mathrm{e}}\left|d^{\dagger}_{\sigma' p\kappa_x}d_{\sigma p\kappa_x}\right|\vec{\sigma}^{\mathrm{e}\prime}\right\rangle = \delta_{\sigma^{\mathrm{e}}_{\bar{p}},\sigma^{\mathrm{e}\prime}_{\bar{p}}}\,\delta_{\sigma^{\mathrm{e}}_{p},\sigma'}\,\delta_{\sigma^{\mathrm{e}\prime}_{p},\sigma}. \quad (84a)$$

The end electron operators act on the configuration at the p-end only, trying to transform the spin from σ to σ', while the spin at $\bar{p}=-p$ must be untouched.

What remains is $\langle\vec{N}\vec{m}|\hat{\psi}^{\dagger}_{r\sigma}(y_p)\hat{\psi}_{r'\sigma'}(y_p)|\vec{N}'\vec{m}'\rangle$. Upon applying the bosonisation identity Eq. (135) to rewrite $\hat{\psi}_{r\sigma}(y_p)$, it becomes a product of the bosonic part $M^{p}_{r\sigma r'\sigma'}(\vec{m},\vec{m}')$, which is calculated in App. B.2, and the fermionic part

$$M^{p}_{r\sigma r'\sigma'}(\vec{N},\vec{N}') = \left\langle\vec{N}\left|\hat{K}^{\dagger}_{r\sigma}(y_p)\hat{\eta}^{\dagger}_{\sigma}\hat{\eta}_{\sigma'}\hat{K}_{r'\sigma'}(y_p)\right|\vec{N}'\right\rangle = \frac{1}{2L_y}\delta_{\vec{N},\vec{N}'+\vec{e}_{\sigma}-\vec{e}_{\sigma'}}(-1)^{(1-\delta_{\sigma,\sigma'})(N'_{\uparrow}-\delta_{\sigma,\downarrow})}e^{\mathrm{i}\frac{\pi}{L_y}\left[r'\left(N'_{\sigma'}+\frac{1}{2}\right)-r\left(N'_{\sigma}+\frac{3}{2}\right)\right]y_p}, \quad (84b)$$

where the Klein factors $\hat{\eta}_{\sigma}$, Eq. (136a), and the phase factors $\hat{K}_{r\sigma}(y)$, Eq. (136b), were straightforward to evaluate. We split now the sum $\sum_{\sigma\sigma'}$ contained in $\hat{V}^{\mathrm{e-b}}_{n\rho\rho}$, Eq. (74), and therewith the further analysis, into two cases.

First, let $\sigma'=\sigma$ hold. Then,

$$M^{p}_{r\sigma r'\sigma}(\vec{N},\vec{N}') = \frac{\delta_{\vec{N},\vec{N}'}}{2L_y}\left\{\begin{array}{ll} e^{-\mathrm{isgn}(r)\frac{\pi}{L_y}y_p} & r=r' \\ e^{\mathrm{isgn}(r')\frac{2\pi}{L_y}(N'_{\sigma}+1)y_p} & r=-r' \end{array}\right\} = \left\{\begin{array}{ll} \delta_{\vec{N},\vec{N}'}/\left(2L_y\right) & y_p=y_-=0\,, \\ -\mathrm{sgn}(rr')\,\delta_{\vec{N},\vec{N}'}/\left(2L_y\right) & y_p=y_+=L_y\,. \end{array}\right.$$

The total contribution related to this case is

$$\frac{t_{n\rho}}{4}\delta_{\vec{N},\vec{N}'}\sum_{\sigma}\sum_{rr'}\sum_{p}\left(\delta_{p,+}-\delta_{p,-}\right)M^{p}_{r\sigma r'\sigma}(\vec{m},\vec{m}')\delta_{\sigma^{\mathrm{e}}_{\bar{p}},\sigma^{\mathrm{e}\prime}_{\bar{p}}}\,\delta_{\sigma,\sigma^{\mathrm{e}}_{p}}\,\delta_{\sigma,\sigma^{\mathrm{e}\prime}_{p}}.$$

As it is derived in App. B.2, Eq. (150), in fact $M^{+}_{r\sigma r'\sigma}(\vec{m},\vec{m}') = M^{-}_{r\sigma r'\sigma}(\vec{m},\vec{m}') \equiv const.$ and so this contribution identically vanishes.

We are left with the part of the sum where $\sigma' \neq \sigma$, for which we can read off the following fermionic contributions from Eq. (84b):

$$\begin{aligned} M^{p=-}_{r\sigma r'-\sigma}(\vec{N},\vec{N}') &= \frac{1}{2L_y}\delta_{\vec{N},\vec{N}'+\vec{e}_\sigma-\vec{e}_{-\sigma}}\mathrm{sgn}(\sigma)(-1)^{N'_\uparrow}, \\ M^{p=+}_{r\sigma r'-\sigma}(\vec{N},\vec{N}') &= -\frac{1}{2L_y}\delta_{\vec{N},\vec{N}'+\vec{e}_\sigma-\vec{e}_{-\sigma}}\mathrm{sgn}(\sigma r r')(-1)^{N'_\downarrow}. \end{aligned} \tag{85}$$

To obtain the first equality we used $(-1)^{N'_\uparrow-\delta_{\sigma,\downarrow}} = -(-1)^{N'_\uparrow}\mathrm{sgn}(\sigma)$, while for the second one we needed $\exp\{\mathrm{i}\pi[r'(N'_{-\sigma}+0.5) - r(N'_\sigma+1.5)]\} = -\mathrm{sgn}(rr')(-1)^{N'_\sigma}(-1)^{N'_{-\sigma}}$. The bosonic part is given in Eq. (150), App. B.2, as

$$\begin{aligned} M^{p}_{r\sigma r'-\sigma}(\vec{m},\vec{m}') &= \langle\vec{m}|\, e^{-\mathrm{i}\hat{\phi}^\dagger_{r\sigma}(y_p)}e^{-\mathrm{i}\hat{\phi}_{r\sigma}(y_p)}e^{\mathrm{i}\hat{\phi}^\dagger_{r'-\sigma}(y_p)}e^{\mathrm{i}\hat{\phi}_{r'-\sigma}(y_p)}\,|\vec{m}'\rangle = \\ &= \delta_{\vec{m}_c,\vec{m}'_c}\prod_{q>0}F(\mathrm{sgn}(p\sigma)\sqrt{2/n_q}, m_{sq}, m'_{sq}). \end{aligned} \tag{86}$$

Putting Eqs. (84a), (85) and (86) together, the final result for the non-diagonal end-bulk-scattering is ($t := t_{n\rho}$):

$$\begin{aligned} &\left\langle \vec{N}\ \vec{\sigma}^{\mathrm{e}} = (\sigma_+,\sigma_-)\ \vec{m}\left|\hat{V}^{\mathrm{e-b}}_{n\rho\rho}\right|\vec{N}'\ \vec{\sigma}^{\mathrm{e}\prime} = (\sigma'_+,\sigma'_-)\ \vec{m}'\right\rangle \\ &\quad = t\sum_p \delta_{\vec{N},\vec{N}'+\vec{e}_{\sigma'_p}-\vec{e}_{\sigma_p}}\delta_{\vec{m}_c,\vec{m}'_c}\delta_{\sigma_p,-\sigma'_p}\delta_{\sigma_{\bar{p}},\sigma'_{\bar{p}}}\left[\delta_{p,-}(-1)^{N'_\uparrow} - \delta_{p,+}(-1)^{N'_\downarrow}\right] \\ &\qquad\qquad \times \mathrm{sgn}(\sigma_p)\prod_q F\left(p\,\mathrm{sgn}(\sigma'_p)\sqrt{2/n_q}, m_{sq}, m'_{sq}\right). \end{aligned} \tag{87}$$

The action of this scattering process is to flip the localised spin at the p end, $\sigma'_p \to \sigma_p \overset{!}{=} -\sigma'_p$, while at the same time a bulk spin must be inverted to preserve the spin-projection S_z: $N'_{\sigma'_p} \to N_{\sigma'_p} \overset{!}{=} N'_{\sigma'_p}+1$, $N'_{-\sigma'_p} \to N_{-\sigma'_p} \overset{!}{=} N'_{-\sigma'_p}-1$. The localised spin at the $\bar{p}$ end must be conserved: $\sigma_{\bar{p}} = \sigma'_{\bar{p}}$.

4.3 The spectrum of ACNRs

In Sect. 4.2.3 we have shown how to exactly diagonalize the Hamiltonian $\hat{H}_0 + \hat{V}_{\rho\rho}$ describing a graphene armchair nanoribbon with long-ranged Coulomb interaction plus *diagonal* – density-density, i.e. $\vec{N}, \vec{m}$ and $\vec{\sigma}^{\mathrm{e}}$ (fermionic, bosonic and end spin configuration) conserving – short-range contributions. We have further determined the matrix elements of the short-ranged non-density-density interaction, giving rise to corrections *non-diagonal* in the eigenbasis Eq. (81) of $\hat{H}_0 + \hat{V}_{\rho\rho}$. Fortunately, away from half filling, all those off-diagonal matrix elements of the full Hamiltonian $\hat{H}_\odot = \hat{H}_0 + \hat{V}_{\rho\rho} + \hat{V}_{n\rho\rho}$ are small and in particular introduce no significant mixing between states far apart in energy. So we can still use our basis vectors from Eq. (81) as a

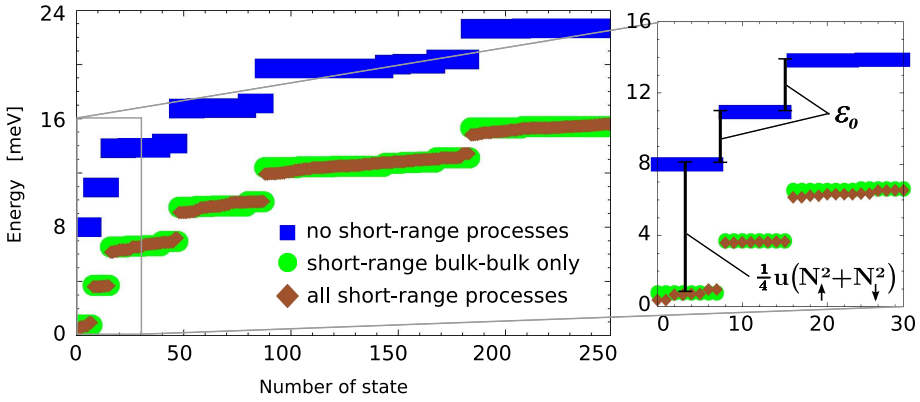

Figure 23: The energy spectrum of a graphene armchair nanoribbon of 572 nm length and 7.8 nm width, filled with an odd number of electrons. We show the different numerical results if all scattering processes (brown diamonds), just bulk-bulk scattering (green disks) or only long-ranged bulk-bulk interactions (blue boxes) are included. The inset zooms on the lowest lying 50 states, where both the influence of the short-ranged bulk-bulk scattering as well as the separation due to end-bulk interaction becomes evident.

truncated eigenbasis to represent the ACNR system. With help of Eqs. (82), (87) for the non-diagonal bulk-bulk respectively end-bulk scattering terms, it is straightforward to numerically calculate and diagonalize the full ACNR Hamiltonian $\hat{H}_{\odot}$.
In Sect. 4.3.1, we shortly discuss the resulting eigenspectrum of an ACNR. Afterwards, Sect. 4.3.2, we analyse a minimal set of states relevant for the explanation of features in transport across ACNRs. Specifically, we find that scattering between end and bulk electrons causes an entanglement of states with the same total spin-projection S_z, but different configurations of end and bulk spins, which could be a handicap for proposed quantum information applications [76].

4.3.1 Full spectrum

The energies of the 250 lowest lying states of a 572 nm × 7.8 nm ribbon of odd filling can be found in Fig. 23. We plot not only the result including all types of scattering (brown diamonds), but for a comparison we also give the energies without the end-bulk interaction (green disks) and for only long-ranged interactions (blue boxes). Remarkably, in contrast to what was found for SWCNTs [103], the short-ranged bulk-bulk interactions do not spoil the spin-charge separation of the spectrum. This is due to the fact that, unlike as for nanotubes, only the spin-modes are affected by short-ranged processes, which can be seen from Eq. (82): while there is a mixing between all states of the same fermionic $\vec{N} = \vec{N}'$, but different bosonic s-configuration ($\vec{m}_s \neq \vec{m}'_s$), states with different c-excitations cannot be combined ($\vec{m}_c \stackrel{!}{=} \vec{m}'_c$).
We will, however, discover in Sect. 4.3.2 that the presence of the end states leads to formations of peculiar linear combinations between states of different bulk and end spin configurations, preserving total charge and spin-projection S_z. This induces a mixing between the various kinds of excited states and the groundstates, which smears out

the spectrum as observed in Fig. 23.

4.3.2 Minimal model

In the following, we examine how the lowest-lying states in the truncated eigenbasis Eq. (81) transform under the influence of $\hat{V}_{n\rho\rho}$. To explain the most outstanding effects, it is sufficient to restrict to a minimal set of states: For the even fillings, $N_c = 2n$, $n \in \mathbb{N}$, we have to take into account twelve states, allowing up to one fermionic excitation. The reason is that without an unpaired bulk spin no mixing can take place[26]. For the odd fillings, $N_c = 2n+1$, it is enough to include the eightfold degenerate groundstate of $\hat{H}_0 + \hat{V}_{\rho\rho}$. To preserve lucidity, bosonically excited states are left out from our analysis, as they do not change qualitatively the mechanisms behind the observed effects. The $\vec{N}$ and $\vec{m}_c$ conserving bulk-bulk scattering $\hat{V}^{\mathrm{b-b}}_{n\rho\rho}$ can also be disregarded: besides for slight shifts in energy, forming linear combinations of states differing just in $\vec{m}_s$ but identical in $\vec{N}$, $\vec{m}_c$ has not much impact. The restriction to the minimal model applies only for the subsequent analytics. Concerning the numerical calculations, an energy cutoff of $7.9\epsilon_0$ above the groundstates was used for the spectrum, respectively $1.9\epsilon_0$ for the transport, including every energetically allowed bosonic or fermionic excitation.

Even electron fillings For even electron fillings, $N_c = 2n$, we want to restrict to the following subset of the states described by Eq. (81):

$$\begin{aligned} \vec{N} = (N_\uparrow, N_\downarrow) &\in \{(n,n), (n \pm 1, n \mp 1)\} \quad n \in \mathbb{N}, \\ \vec{\sigma}^{\mathrm{e}} = (\sigma^{\mathrm{e}}_+, \sigma^{\mathrm{e}}_-) &\in \{(\uparrow,\uparrow), (\uparrow,\downarrow), (\downarrow,\uparrow), (\downarrow,\downarrow)\}, \\ \vec{m} = (\vec{m}_c, \vec{m}_s) &= (\vec{0}, \vec{0}). \end{aligned}$$

To abbreviate our notation we introduce

$$\left|\vec{N}, \vec{\sigma}^{\mathrm{e}}, \vec{0}\right\rangle := \begin{cases} \left|\sigma^{\mathrm{e}}_-, \uparrow\downarrow, \sigma^{\mathrm{e}}_+\right\rangle & N_\uparrow = N_\downarrow = n, \\ \left|\sigma^{\mathrm{e}}_-, \uparrow\uparrow, \sigma^{\mathrm{e}}_+\right\rangle & N_\uparrow = n+1,\ N_\downarrow = n-1, \\ \left|\sigma^{\mathrm{e}}_-, \downarrow\downarrow, \sigma^{\mathrm{e}}_+\right\rangle & N_\uparrow = n-1,\ N_\downarrow = n+1. \end{cases}$$

Notice that the second and the third case describes fermionically excited states. Building now all possible combinations for our minimal set of states for even fillings, we get the following set of possibilities:

- $S_z = 0$: ***four states*** $|a\rangle$, $|b\rangle$, $|c_\pm\rangle$

$$\begin{aligned} |\uparrow,\uparrow\downarrow,\downarrow\rangle =: |a\rangle, \qquad & |\downarrow,\uparrow\downarrow,\uparrow\rangle =: |b\rangle, \\ |\uparrow,\downarrow\downarrow,\uparrow\rangle =: |c_+\rangle, \qquad & |\downarrow,\uparrow\uparrow,\downarrow\rangle =: |c_-\rangle, \end{aligned}$$

[26] For transport, this is fatal, as introducing the end spins degree of freedom a priori yields four identical, completely decoupled channels. This makes the kinetic equations ill-defined [115, 116]. Only the end-bulk interaction induced mixing guarantees a unique solution for the transport problem.

- $S_z = \pm\hbar$: ***six states*** $|d_{\sigma\sigma}\rangle$, $|f_{\sigma\sigma}\rangle$, $|g_{\sigma\sigma}\rangle$ $(\sigma \in \{\uparrow,\downarrow\})$

$$\begin{aligned} |\uparrow,\uparrow\downarrow,\uparrow\rangle &=: |d_{\uparrow\uparrow}\rangle, \qquad |\downarrow,\uparrow\downarrow,\downarrow\rangle =: |d_{\downarrow\downarrow}\rangle, \\ |\uparrow,\uparrow\uparrow,\downarrow\rangle &=: |f_{\uparrow\uparrow}\rangle, \qquad |\uparrow,\downarrow\downarrow,\downarrow\rangle =: |f_{\downarrow\downarrow}\rangle, \\ |\downarrow,\uparrow\uparrow,\uparrow\rangle &=: |g_{\uparrow\uparrow}\rangle, \qquad |\downarrow,\downarrow\downarrow,\uparrow\rangle =: |g_{\downarrow\downarrow}\rangle, \end{aligned}$$

- $S_z = \pm 2\hbar$: ***two states*** $|\sigma,\sigma\sigma,\sigma\rangle$ $(\sigma \in \{\uparrow,\downarrow\})$

$$|\uparrow,\uparrow\uparrow,\uparrow\rangle\,, \quad |\downarrow,\downarrow\downarrow,\downarrow\rangle\,.$$

There are four degenerate groundstates $|a\rangle$, $|b\rangle$, $|d_{\sigma\sigma}\rangle$ with energy $E_{N_c}^{(0)} = E_{2n}^{(0)}$, while the remaining singly fermionic excited states $|f_{\sigma\sigma}\rangle$, $|g_{\sigma\sigma}\rangle$, $|\sigma,\sigma\sigma,\sigma\rangle$ have an energy $E_{2n}^{(f)}$.

The end-bulk interaction can only mix states with same spin-projection S_z. To the highest values, $S_z = \pm 2\hbar$, it belongs only one state and thus no mixing occurs. In contrast, the three states $|d_{\sigma\sigma}\rangle$, $|f_{\sigma\sigma}\rangle$, $|g_{\sigma\sigma}\rangle$ with $S_z = \mathrm{sgn}(\sigma)\hbar$ get coupled to each other. Also the four states $|a\rangle$, $|b\rangle$, $|c_\pm\rangle$ with $S_z = 0$ can in principle transform into one another under the influence of end-bulk scattering. With help of Eq. (87) we can set up the corresponding blocks of the full Hamiltonian $\hat{H}_\odot$ in the truncated eigenbasis (assuming n even[27]):

$$\left(\hat{H}_\odot\right)_{N_c=2n,S_z=0} = \begin{array}{c} \begin{array}{cccc} |a\rangle & |b\rangle & |c_+\rangle & |c_-\rangle \end{array} \\ \begin{pmatrix} E_{2n}^{(0)} & 0 & -t & -t \\ 0 & E_{2n}^{(0)} & +t & +t \\ -t & +t & E_{2n}^{(f)} & 0 \\ -t & +t & 0 & E_{2n}^{(f)} \end{pmatrix} \end{array} \begin{array}{l} |a\rangle \\ |b\rangle \\ |c_+\rangle \\ |c_-\rangle \end{array},$$

$$\left(\hat{H}_\odot\right)_{N_c=2n,S_z=\pm\hbar} = \begin{array}{c} \begin{array}{ccc} |d_{\sigma\sigma}\rangle & |f_{\sigma\sigma}\rangle & |g_{\sigma\sigma}\rangle \end{array} \\ \begin{pmatrix} E_{2n}^{(0)} & +t & -t \\ +t & E_{2n}^{(f)} & 0 \\ -t & 0 & E_{2n}^{(f)} \end{pmatrix} \end{array} \begin{array}{l} |d_{\sigma\sigma}\rangle \\ |f_{\sigma\sigma}\rangle \\ |g_{\sigma\sigma}\rangle \end{array}.$$

Diagonalization leads to the eigenstates and eigenenergies listed in Tab. 7. We employ there the abbreviation

$$\xi_{\alpha\alpha'}(\gamma) = \frac{1}{2}\left(E_{2n}^{(f)} + \alpha E_{2n}^{(0)} + \alpha'\sqrt{\left(E_{2n}^{(f)} - E_{2n}^{(0)}\right)^2 + \gamma^2}\right), \tag{88a}$$

with $\alpha,\alpha' \in \{\pm 1\}$. Obviously, $\xi_{++}(\gamma) > \xi_{+-}(\gamma)\,, \quad \xi_{-+}(\gamma) > \xi_{--}(\gamma)$, and as in our context $\gamma \simeq t$, and hence $\gamma \ll E_{2n}^{(f)} - E_{2n}^{(0)}$ holds, we can rely on the relations

$$\xi_{++}(\gamma) \approx E_{2n}^{(f)}\,, \quad \xi_{+-}(\gamma) \approx E_{2n}^{(0)}\,, \quad \xi_{-+}(\gamma) \gg t\,, \quad \xi_{--}(\gamma) \ll t. \tag{88b}$$

[27] For odd n the sign of the off-diagonal entries must be inverted.

$$N_c = 2n$$

ENERGY	:	EIGENSTATE (NOT NORMALISED)	ABBR.		SPIN S_z $[\hbar]$
$\xi_{+-}(4t) \approx 0$	:	$\frac{2\sqrt{2}t}{\xi_{--}(4t)}(\lvert a\rangle - \lvert b\rangle) - (\lvert c_+\rangle + \lvert c_-\rangle)$	(g_1)		0
$\xi_{+-}(2\sqrt{2}t) \approx 0$	:	$\frac{2\sqrt{2}t}{\xi_{--}(2\sqrt{2}t)}\lvert d_{\sigma\sigma}\rangle + (\lvert f_{\sigma\sigma}\rangle - \lvert g_{\sigma\sigma}\rangle)$	$(\mathrm{g}_2)_{\sigma\sigma}$		$\mathrm{sgn}(\sigma)$
0	:	$\sqrt{\frac{1}{2}}(\lvert a\rangle + \lvert b\rangle)$	(g_3)		0
$\xi_{++}(4t) \approx \varepsilon_0$	:	$\frac{2\sqrt{2}t}{\xi_{-+}(4t)}(\lvert a\rangle - \lvert b\rangle) - (\lvert c_+\rangle + \lvert c_-\rangle)$	(e_1)		0
$E^{(f)}_{2n} \approx \varepsilon_0$	:	$\frac{1}{\sqrt{2}}(\lvert f_{\sigma\sigma}\rangle + \lvert g_{\sigma\sigma}\rangle)$			$\mathrm{sgn}(\sigma)$
$E^{(f)}_{2n} \approx \varepsilon_0$	:	$\sqrt{\frac{1}{2}}(\lvert c_+\rangle + \lvert c_-\rangle)$			0
$E^{(f)}_{2n} \approx \varepsilon_0$	:	$\lvert \sigma, \sigma\sigma, \sigma\rangle$			$2\mathrm{sgn}(\sigma)$
$\xi_{++}(2\sqrt{2}t) \approx \varepsilon_0$	:	$\frac{2\sqrt{2}t}{\xi_{-+}(2\sqrt{2}t)}\lvert d_{\sigma\sigma}\rangle + (\lvert f_{\sigma\sigma}\rangle - \lvert g_{\sigma\sigma}\rangle)$	$(\mathrm{e}_2)_{\sigma\sigma}$		$\mathrm{sgn}(\sigma)$

Table 7: The minimal model consists of twelve different states for even electron fillings of the ACNR ($\sigma \in \{\uparrow, \downarrow\}$). We have set $E^{(0)}_{2n} = 0$. Importantly, fermionically excited states mix with non excited ones. States relevant for explanations in the main text are marked with text labels. The colour and shape of the symbols encodes the nature of the state, classified by spin-projection and behaviour under exchange of the end spins. The boxes indicate $S_z = 0$, related colours are red (symmetric component $|a\rangle + |b\rangle$) and blue (antisymmetric combination $|a\rangle - |b\rangle$). For the disks $|S_z| = \hbar$, colours olive (symmetric components) and green (antisymmetric: $|f_{\sigma\sigma}\rangle - |g_{\sigma\sigma}\rangle$). Grey diamonds: $|S_z| = 2\hbar$.

The resulting energy landscape is sketched on the left side of Fig. 24, where we used differently coloured and shaped symbols to indicate the composition of states. In our simple model, we find then from Tab. 7 that the interaction has hardly lifted the degeneracies between the various states. It can be verified with Eq. (88a) that there is a slight splitting in the groundstates, such that their energy grows from (g_1) to (g_3). Also the excited states, of which only the two labelled ones turn out to be important for later explanations, are listed increasing in energy. Crucial is the mixing of states with different bulk and end configurations. We can single out linear combinations which are either symmetric or antisymmetric under exchange of the end spins. For the features we will observe in transport, the decisive entanglement is the one between the four $S_z = 0$ states $|a\rangle$, $|b\rangle$, $|c_+\rangle$, $|c_-\rangle$, leading to two states containing the antisymmetric combination $|a\rangle - |b\rangle$: A groundstate (g_1) with small contribution of the fermionically

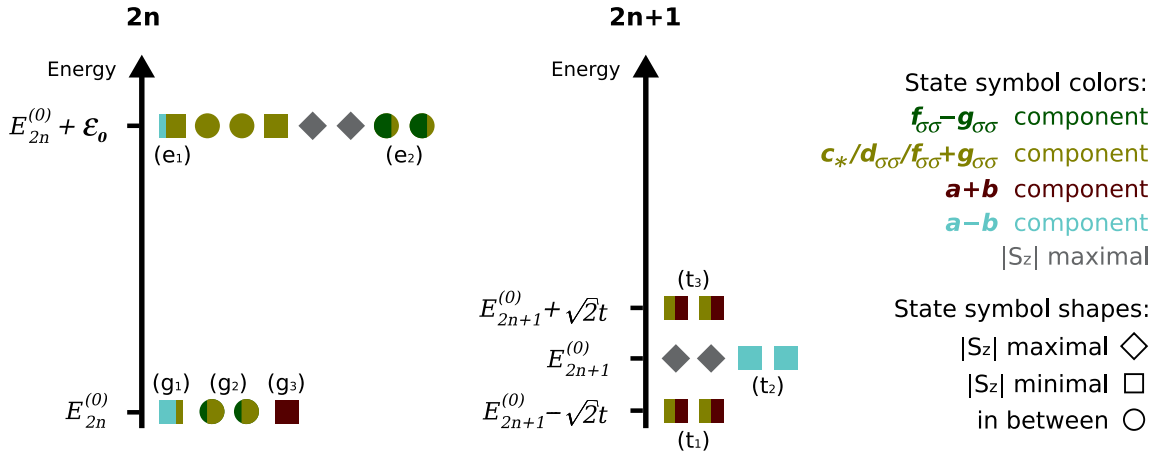

Figure 24: Energy landscape for a minimal set of lowest ACNR eigenstates for even ($N_c = 2n$) and odd ($N_c = 2n+1$) electron fillings, in accordance with Tabs. 7, 8. To visualise the relevant contributions in the composition of the eigenstates, different coloured and shaped symbols were used. The states relevant for later considerations are labelled.

excited states $|c_+\rangle + |c_-\rangle$, and an excited state ($e_1$) where those dominate [as found with Eq. (88b)].

Odd electron fillings Here, due to the fact that with $N_c = 2n+1$ we necessarily always have an unpaired spin, it is sufficient to consider merely the groundstates with energy $E^{(0)}_{N_c} = E^{(0)}_{2n+1}$ emerging from Eq. (81):

$$\begin{aligned} \vec{N} = (N_\uparrow, N_\downarrow) &\in \{(n+1,n),(n,n+1)\} \quad n \in \mathbb{N}, \\ \vec{\sigma}^{\mathrm{e}} = (\sigma^{\mathrm{e}}_+, \sigma^{\mathrm{e}}_-) &\in \{(\uparrow,\uparrow),(\uparrow,\downarrow),(\downarrow,\uparrow),(\downarrow,\downarrow)\}, \\ \vec{m} = (\vec{m}_c, \vec{m}_s) &= (\vec{0},\vec{0}). \end{aligned}$$

Again we abbreviate our notation and introduce

$$\left|\vec{N}, \vec{\sigma}^{\mathrm{e}}, \vec{0}\right\rangle := \begin{cases} \left|\sigma^{\mathrm{e}}_-, \uparrow, \sigma^{\mathrm{e}}_+\right\rangle & N_\uparrow = n+1,\ N_\downarrow = n, \\ \left|\sigma^{\mathrm{e}}_-, \downarrow, \sigma^{\mathrm{e}}_+\right\rangle & N_\uparrow = n,\ N_\downarrow = n+1. \end{cases}$$

We get the following set of possibilities:

- $S_z = \pm\hbar/2$: ***six states*** $|a_\sigma\rangle$, $|b_\sigma\rangle$, $|c_\sigma\rangle$ $(\sigma \in \{\uparrow,\downarrow\})$

$$|\uparrow,\sigma,\downarrow\rangle =: |a_\sigma\rangle, \quad |\downarrow,\sigma,\uparrow\rangle =: |b_\sigma\rangle, \quad |\sigma,\bar{\sigma},\sigma\rangle =: |c_\sigma\rangle,$$

- $S_z = \pm 3\hbar/2$: ***two states*** $|\sigma,\sigma,\sigma\rangle$ $(\sigma \in \{\uparrow,\downarrow\})$

$$|\uparrow,\uparrow,\uparrow\rangle, \quad |\downarrow,\downarrow,\downarrow\rangle.$$

$$N_c = 2n + 1$$

ENERGY	:	EIGENSTATE (NORMALISED)	ABBR.		SPIN S_z $[\hbar]$
$-\sqrt{2}t$	:	$\frac{1}{2}(\lvert a_\sigma\rangle + \lvert b_\sigma\rangle) + \sqrt{\frac{1}{2}}\lvert c_\sigma\rangle$	$(\mathrm{t}_1)_\sigma$		$\mathrm{sgn}(\sigma)/2$
0	:	$\sqrt{\frac{1}{2}}(\lvert a_\sigma\rangle - \lvert b_\sigma\rangle)$	$(\mathrm{t}_2)_\sigma$		$\mathrm{sgn}(\sigma)/2$
0	:	$\lvert\,\sigma,\sigma,\sigma\rangle$			$3\mathrm{sgn}(\sigma)/2$
$+\sqrt{2}t$	:	$\frac{1}{2}(\lvert a_\sigma\rangle + \lvert b_\sigma\rangle) - \sqrt{\frac{1}{2}}\lvert c_\sigma\rangle$	$(\mathrm{t}_3)_\sigma$		$\mathrm{sgn}(\sigma)/2$

Table 8: Lowest lying eigenstates of an ACNR filled with an odd number of electrons ($\sigma \in \{\uparrow, \downarrow\}$). Due to spin-degeneracy, the total number of possible states is eight. The two states with $|S_z| = 3\hbar/2$ are marked by grey diamonds. Red and olive boxes stand for the symmetric components $|a_\sigma\rangle + |b_\sigma\rangle$ and $|c_\sigma\rangle$, respectively. Blue boxes label the antisymmetric combinations $|a_\sigma\rangle - |b_\sigma\rangle$. Notice that all states behave purely symmetric or antisymmetric with respect to end spin exchange.

In the case of $S_z = \pm 3\hbar/2$ there is only one state each.
For the three states with $S_z = \pm\hbar/2$, from Eqs. (79) and (87) the following mixing matrix is found (still n is assumed even):

$$\left(\hat{H}_\odot\right)_{N_c=2n+1,S_z=\pm\hbar/2} = \begin{array}{c} \begin{matrix} \lvert a_\sigma\rangle & \lvert b_\sigma\rangle & \lvert c_\sigma\rangle \end{matrix} \\ \begin{pmatrix} E^{(0)}_{2n+1} & 0 & -t \\ 0 & E^{(0)}_{2n+1} & -t \\ -t & -t & E^{(0)}_{2n+1} \end{pmatrix} \end{array} \begin{matrix} \lvert a_\sigma\rangle \\ \lvert b_\sigma\rangle \\ \lvert c_\sigma\rangle \end{matrix} .$$

The matrix is easily diagonalizable and yields eigenstates according to Tab. 8 at three distinct eigenenergies (compare also to Fig. 24, right). Notice that for the odd filling all emerging states are purely symmetric or antisymmetric under exchange of the two end spins. Thereby, the symmetric states $(\mathrm{t}_1)_\sigma$ and $(\mathrm{t}_3)_\sigma$ essentially have the same tunnelling properties, because they only differ by the sign in front of $|c_\sigma\rangle$. It is of crucial importance that the state $(\mathrm{t}_2)_\sigma$ is formed by the *antisymmetric* combination $|a_\sigma\rangle - |b_\sigma\rangle$. Comparing the definition of the $2n$ states $|a\rangle$, $|b\rangle$ and $|a_\sigma\rangle$, $|b_\sigma\rangle$, we see that from the $2n$ groundstate (g_3), a tunnelling event can *exclusively* lead to one of the $2n+1$ states $(\mathrm{t}_1)_\sigma$ or $(\mathrm{t}_3)_\sigma$. Via their $|c_\sigma\rangle$ components, these connect to $|c_+\rangle + |c_-\rangle$ as well as to $|d_{\sigma\sigma}\rangle$, and thus to all the other labelled $2n$ states from Tab. 7, but the link to (g_1), $(\mathrm{e}_2)_{\sigma\sigma}$ is weak due to Eq. (88b). This will be the key ingredient for the explanation of the stability diagrams in Sect. 4.4.

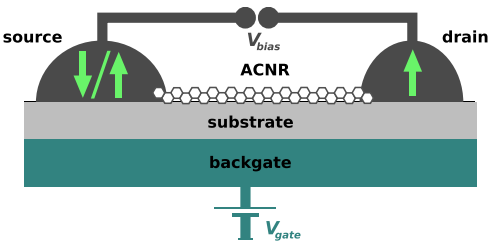

Figure 25: For our results on spin-polarised transport, we assume the ACNR to be attached to magnetised leads. Relative to the ↑ - polarised drain, the spin of the source is either aligned in parallel (PA) or in anti-parallel (AP) configuration. The number of electrons on the device can be controlled via a gate electrode.

Energy cutoff	E_{max}	$1.9\varepsilon_0$
Thermal energy	k_BT	0.01 meV
Charging energy [110]	W_0	2.31 meV
Ribbon length	L_y	572 nm
Level spacing	ϵ_0	2.93 meV
Ribbon width	L_x	7.8 nm
Bulk-bulk exchange	u	0.036 meV
End-bulk exchange	t	0.21 meV

Table 9: Parameters employed for all viewed plots unless specified differently. The values of charging energy, bulk-bulk and end-bulk exchange-coupling were numerically verified for ribbon lengths ranging from $5 - 20$ nm. For the spectrum calculation, Fig. 23, bosonic and fermionic excitations up to an energy of $7.9\,\varepsilon_0$ above the groundstate for a certain filling were taken into account.

4.4 Transport across quantum-dot ACNRs

While without a special signature in the spectrum, the formation of states symmetric or antisymmetric under the exchange of end spins leaves strong fingerprints in transport. The most prominent features are pronounced negative differential conductance (NDC) lines occurring for a completely symmetric and unpolarised setup, which is discussed in Sect. 4.4.1. We furthermore investigate spin-dependent transport for collinear lead magnetisations, predicting negative tunnelling magneto-resistance (TMR) within a narrow region along the edges of the Coulomb diamonds for even fillings, Sect. 4.4.2. Finally we explain how the transport characteristic is expected to change under application of an external magnetic field, both for non-magnetic and collinearly polarised contacts, Sect. 4.4.3.

Besides the energy spectrum, the other system specific input required for transport calculations are the tunnelling matrix elements of the ACNR bulk electron operator,

$$\left\langle \vec{N}\vec{\sigma}^{\mathrm{e}}\vec{m}\left|\hat{\Psi}_\sigma(\vec{r})\right|\vec{N}'\vec{\sigma}^{\mathrm{e}\prime}\vec{m}'\right\rangle = \frac{1}{2}\delta_{\vec{N},\vec{N}'+\vec{e}_\sigma}\delta_{\vec{\sigma}^{\mathrm{e}},\vec{\sigma}^{\mathrm{e}\prime}}\,(-1)^{\delta_{\sigma,\downarrow}N_\uparrow} \times\sum_{Fpr} f_{Fpr}\varphi_{Fp}(\vec{r})e^{\mathrm{i}\frac{\pi}{L_y}(N_\sigma+\frac{1}{2})ry}\prod_{q>0}\prod_{j=s,c}F(\lambda^{jq}_{r\sigma}(y),m_{jq},m'_{jq}), \quad (89)$$

with the function $F(\lambda,m,m')$ and the parameter $\lambda^{jq}_{r\sigma}(y)$ as given in App. B.1 in Eq. (145) respectively Eq. (142). We omit here the calculation of this identity, because the fermionic contribution follows straightforward from Eqs. (135)-(136b), while the bosonic contribution emerges in the same manner as for the more complicated matrix elements involving more than one electron operator evaluated in App. B.1. Moreover, the detailed derivation of the corresponding expression for SWCNTs can be found in Ref. [114].

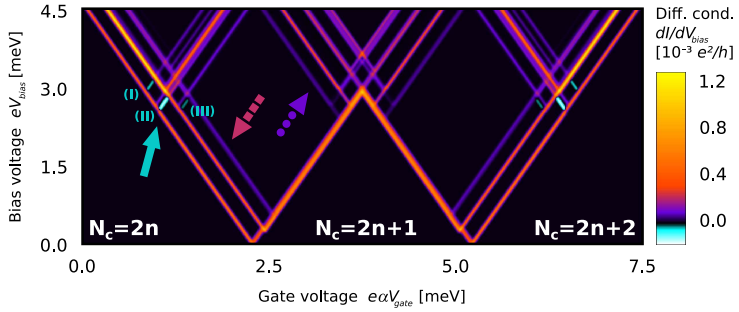

Figure 26: Differential conductance for a completely symmetric ACNR transport setup. Strong negative differential conductance (NDC) arises if the external voltages are adjusted such that a transition from $(t_1)_\sigma$ to (e_1) is allowed, while a transition from (g_1) to $(t_2)_\sigma$ is forbidden.

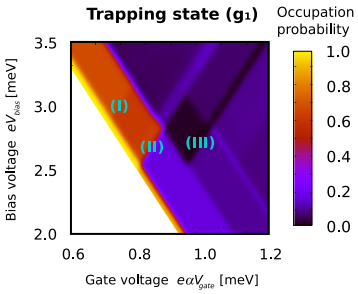

Figure 27: Occupation probability of the trapping state (g_1) around the region exhibiting various NDC features. Notice that no numerically stable data can be obtained inside the Coulomb diamond.

4.4.1 Unpolarised transport for a symmetrical setup

Fig. 26 shows the stability diagram obtained for an ACNR completely symmetrically coupled to unpolarised leads. Due to electron-hole symmetry around the $2n$ filling, the diagram is mirror-symmetric with respect to the central diamond. Already for such a standard measurement, end states leave various signatures, which result from the mixing of states with same spin-projection S_z, but distinct end spin configurations. The mechanisms behind the main features of the plot can be explained in terms of the minimal set of states discussed in Sect. 4.3.2, Tabs. 7, 8. Let us shortly recall their properties and alongside explain in which points we have to expect discrepancy with respect to the full set of real eigenstates which was employed for all calculations:

First, the eight states from Tab. 8, $(t_1)_\sigma$, $(t_2)_\sigma$, $(t_3)_\sigma$ and $|\sigma,\sigma,\sigma\rangle$, will in the following frequently be called the *lowest lying* $2n+1$ *states*. They occur at only three distinct energies $\pm\sqrt{2}t$, 0.0. Inclusion of excitations within an energy cutoff of $1.9\,\varepsilon_0$ slightly lifts the degeneracy of $(t_2)_\sigma$ and $|\sigma,\sigma,\sigma\rangle$, and introduces eight high lying excited states which are almost degenerate. Second, for what concerns the even fillings, we refer to (g_1), $(g_2)_{\sigma\sigma}$, (g_3) as *2n groundstates*. The fact that they are almost, but not perfectly degenerate, and that their energy grows from (g_1) to (g_3), is not changed upon the inclusion of further excitations and plays some role in the following. Moreover, mixing between the states from Tab. 7 and bosonically excited $2n$ states takes place in general, but actually preserves the types of linear combinations occurring in Tab. 7, which is the relevant point for our explanations. In summary, the main effect of inclusion of excitations within an energy cutoff of $1.9\,\varepsilon_0$ is the lifting of the degeneracies among the *excited* $2n$ states. In fact, the lowest lying excited state will be of the same nature as (e_1), and the separation to the state corresponding to $(e_2)_{\sigma\sigma}$ exceeds $\sqrt{2}t$, thus it is well resolvable. With this additional information to Tabs. 7, 8 we can now start to explain the features marked by the different arrows in Fig. 26.

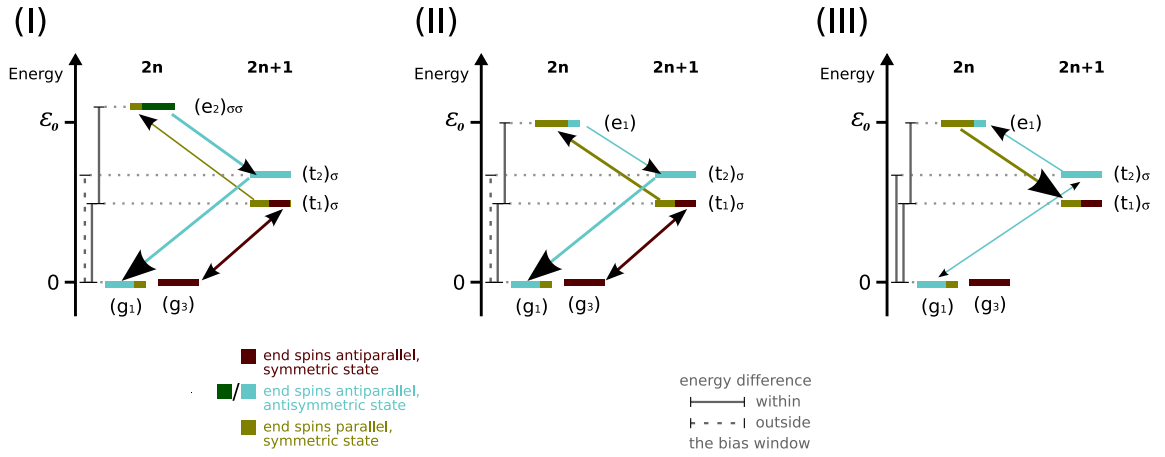

Figure 28: Schematic explaining the mechanisms causing the NDC features (I), (II) and (III) in Fig. 26. Only states and transitions relevant for the NDCs are drawn. The crucial transition is marked by a big arrow head. (I)/(II) Opening of the channel $(t_1)_\sigma \rightarrow (e_2)_{\sigma\sigma}$, respectively $(t_1)_\sigma \rightarrow (e_1)$, leads to a decay into the trapping state (g_1), depleting the transport channel $(g_3) \leftrightarrow (t_1)_\sigma$. (III) Opening of the channel $(t_2)_\sigma \rightarrow (e_1)$ depletes the transport channel $(g_1) \leftrightarrow (t_2)_\sigma$.

▪▪▪▶ The dashed red arrow points towards a triple of three parallel lines which are split by $\sqrt{2}t$. Those mark transitions from the $2n$ groundstates to the $2n+1$ lowest lying states. Hereby, the antisymmetric state $(t_2)_\sigma$, associated to the second line of the triple, is special, because it is the only one strongly connected to the $2n$ state (g_1). The first line of the triple is the $(g_3) \rightarrow (t_1)_\sigma$ groundstate transition line.

•••▶ The blue dotted arrow marks the lines around the tip of the Coulomb diamond. Those appear in four clearly distinct positions, separated by about $\sqrt{2}t$. The lower lying triple of lines arises from transitions of the lowest lying $2n+1$ states to the $2n+2$ groundstates. By coincidence of parameters, the highest line, which is split, follows also in a distance of about $\sqrt{2}t$ and marks transitions from $2n$ groundstates to the aforementioned higher lying excited $2n+1$ states arising upon inclusion of bosonic excitations.

▶ The solid green arrow highlights the negative differential conductance features (I), (II) and (III). The former two originate from trapping in the state (g_1), while the latter occurs due to depletion of the transport channel $(t_2)_\sigma \leftrightarrow (g_1)$.
The mechanisms work as follows:
The NDCs (I) and (II) mark the opening of the $2n+1 \rightarrow 2n$ back-transition channels $(t_1)_\sigma \rightarrow (e_2)_{\sigma\sigma}$ and $(t_1)_\sigma \rightarrow (e_1)$, respectively. The situation is sketched in Fig. 28. Once they get populated, from both of these excited $2n$ states the system can decay into any of the lowest lying $2n+1$ states, and in particular there is a chance to populate the antisymmetric state $(t_2)_\sigma$. This state is strongly connected to the $2n$ groundstate (g_1), which contains a large contribution of the antisymmetric combination $|a\rangle - |b\rangle$. But in the region where the NDCs occurs, the forward channel $(g_1) \rightarrow (t_2)_\sigma$ is not yet

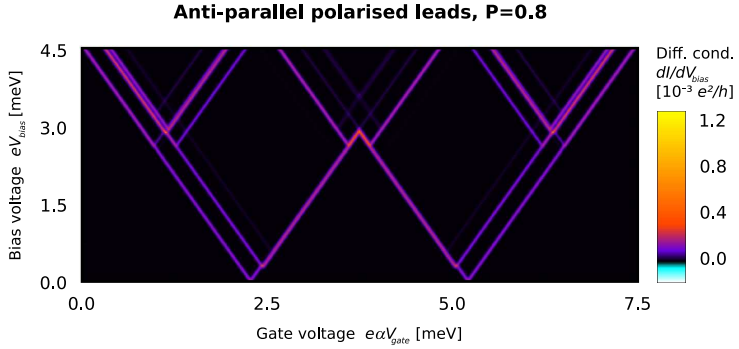

Figure 29: Differential conductance for an ACNR quantum-dot connected to anti-parallel polarised leads, with a polarisation strength $P := P_s = P_d = 0.8$. The number of visible transition lines is strongly decreased as compared to the unpolarised case Fig. 26. Further, all NDC features have vanished.

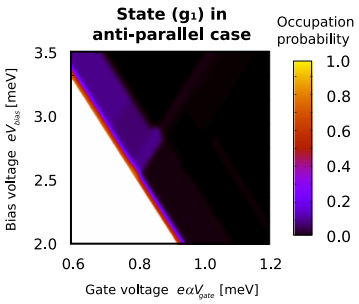

Figure 30: Occupation probability of the state (g_1) for the same bias and gate range as in Fig. 27. For an anti-parallel contact configuration, the population of the state is strongly decreased.

within the bias window such that (g_1) serves as a trapping state. Fig. 27 confirms this explanation: the population of the state (g_1) is strongly enhanced in the concerned region where the back-transitions $(t_1)_\sigma \rightarrow (e_2)_{\sigma\sigma}$ and $(t_1)_\sigma \rightarrow (e_1)$ can take place, while the forward transition $(g_1) \rightarrow (t_2)_\sigma$ is still forbidden.
NDC (III) belongs to the back-transition $(t_2)_\sigma \rightarrow (e_1)$, which is a weak channel because $(t_2)_\sigma$ is a purely antisymmetric state, while the antisymmetric contribution in (e_1) is rather small. From time to time, nevertheless the transition will take place, and once it happens the system is unlikely to fall back to $(t_2)_\sigma$, but will rather change to a symmetric $2n+1$ state. Thus the state $(t_2)_\sigma$ is depleted, and with it the transport channel $(t_2)_\sigma \leftrightarrow (g_1)$, which leads to NDC. The statement can also be verified from the plot of the occupation probability for (g_1), Fig. 27: a pronounced dark region of decreased population follows upon the NDC transition.

4.4.2 Spin-polarised transport for collinear lead magnetisations

We investigate now the transport behaviour for an ACNR quantum-dot with collinearly polarised leads, as shown in Fig. 25. Major changes in the stability diagram of the ACNR are observed for anti-parallel contact configuration, Fig. 29: Compared to Fig. 26, various transitions lines are suppressed and the NDC features have vanished. The reason is that an anti-parallel contact configuration as drawn in Fig. 25 favours $(g_2)_{\downarrow\downarrow}$ as $2n$ groundstate, because in-tunnelling of $\downarrow$ - electrons and subsequent out-tunnelling of $\uparrow$ - electrons is preferred. As a consequence, all transport channels related to (g_1) and (g_3) are of minor relevance, which weakens various transition lines and in particular destroys the NDCs effects: in the anti-parallel configuration, the occupation of the trapping state (g_1) is significantly lowered, as seen in Fig. 30.
In detail, starting from the $2n$ groundstate $(g_3) = \frac{1}{\sqrt{2}}(|a\rangle + |b\rangle)$, in-tunnelling of a majority $(\downarrow$ -) electron from the source takes the system to $(t_1)_\downarrow = \frac{1}{\sqrt{2}}(|a_\downarrow\rangle + |b_\downarrow\rangle) + |c_\downarrow\rangle$. Via the $|c_\downarrow\rangle$ $(= |\downarrow,\uparrow,\downarrow\rangle)$ - component of this state, it is possible to tunnel out with

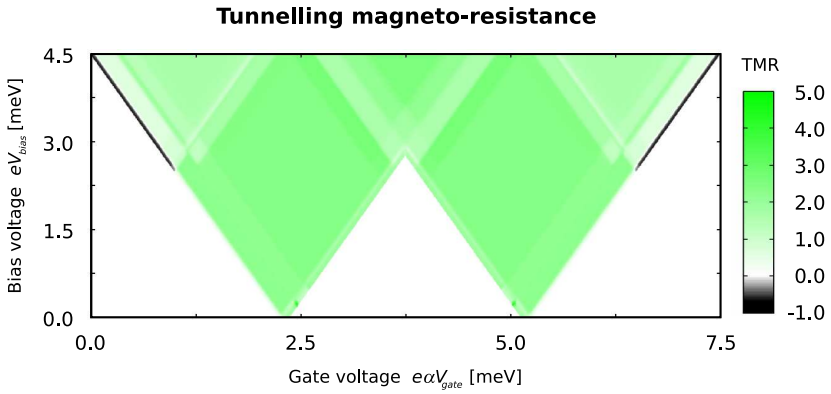

Figure 31: Tunnelling magneto-resistance $I_{PA}/I_{AP} - 1$, where $I_{PA/AP}$ denotes the current for parallel/anti-parallel polarised leads. We observe a negative value, i.e. $I_{PA} < I_{AP}$, along the edges of the $2n/2n+2$ Coulomb diamonds as soon as the channel $(\mathrm{t}_1)_\sigma \rightarrow (\mathrm{e}_1)$ has opened. The reason is the decreased population of the (g_1) state in the anti-parallel case (Fig. 30) as compared to the unpolarised or parallel case (Fig. 27).

a majority ($\uparrow$ -) electron of the drain, yielding a transition to $(\mathrm{g}_2)_{\downarrow\downarrow}$. Similarly, also starting from (g_1) in-tunnelling of a $\downarrow$ - and subsequent out-tunnelling of an $\uparrow$ - electron changes the $2n$ groundstate to $(\mathrm{g}_2)_{\downarrow\downarrow}$. Depending on the bias voltage, transport is either carried by $\uparrow$ - electron via the groundstate channel $(\mathrm{g}_2)_{\downarrow\downarrow} \leftrightarrow (\mathrm{t}_1)_\downarrow$, or by $\downarrow$ - electrons via $(\mathrm{g}_2)_{\downarrow\downarrow} \leftrightarrow |\downarrow,\downarrow,\downarrow\rangle$, where $|\downarrow,\downarrow,\downarrow\rangle$ forms a blocking state unless a back-transition to the $2n$ excited state $|\downarrow,\downarrow\downarrow,\downarrow\rangle$ is energetically allowed.

In Fig. 31 we have plotted the tunnelling magneto-resistance (TMR),

$$\mathrm{TMR} := \frac{I_{PA} - I_{AP}}{I_{AP}},$$

which is a measure for the ratio of the current in the parallel configuration, I_{PA} to the current in the anti-parallel configuration, I_{PA}. Along the edge of the $2n$ Coulomb diamond, the TMR acquires a negative value, i.e. I_{AP} exceeds I_{PA}. This is unusual: for lowest order calculations without Zeeman splitting between the spin species typically strictly positive TMR is observed [31, 32]. For the ACNR, however, the effect originates from a reduced feeding of the (g_1) trapping state. This statement can be confirmed by comparing its occupation probability for the unpolarised, Fig. 27, and anti-parallel polarised case, Fig. 30, in the concerned region.
Namely, lying slightly lower in energy than (g_3), (g_1) can serve as a *perfect* trapping state within a narrow region along the edge of the $2n$ Coulomb diamond: here, the bias is high enough to allow the groundstate transition $(\mathrm{g}_3) \rightarrow (\mathrm{t}_1)_\sigma$, but not $(\mathrm{g}_1) \rightarrow (\mathrm{t}_1)_\sigma$. Though the latter channel is weak in any case, it nevertheless provides a nonzero escape rate from (g_1). That is why in Fig. 27, in the region where the NDC mechanism Fig. 28 (II) can populate (g_1), the occupation probability approaches 1 only straight along the edge of the Coulomb diamond, and a value of $0.6 - 0.8$ further apart from it. In contrast, we observe no comparable increase of the (g_1) population in Fig. 30, because

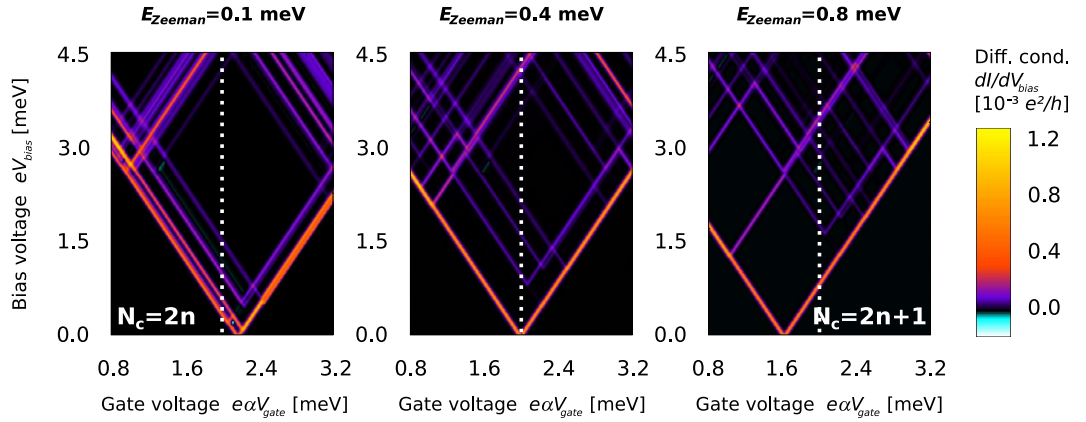

Figure 32: Differential conductance in the region between the $2n$ and $2n+1$ Coulomb blockade diamonds for an ACNR quantum-dot at three different values of an external magnetic field. The contacts are assumed non-magnetic, i.e. unpolarised. The dashed white lines mark the gate voltage at which the plots Fig. 33 are taken.

for the anti-parallel configuration, as explained above, the transition channels involved in the NDC mechanisms are strongly disfavoured compared to $(g_2)_{\downarrow\downarrow} \leftrightarrow (t_1)_{\downarrow}$. For this reason, no trapping occurs and I_{AP} can exceed I_{PA}, leading to the negative TMR.

4.4.3 Magnetic field sweep

Finally we study the transport behaviour under the influence of an external magnetic field. In its presence, formerly degenerate states with different spin projections S_z components become Zeeman split. This means, at a fixed gate voltage one half of the transitions occur at a higher, one half at a lower bias compared to the situation without magnetic field. In detail, simple thoughts can confirm that the forward transitions involving $\uparrow$ - electrons, i.e. $2n \xrightarrow{\uparrow} 2n+1$, as well as all backward transitions mediated by $\downarrow$ - electrons, i.e. $2n+1 \xrightarrow{\downarrow} 2n$, are *lowered* in bias, while processes $2n \xrightarrow{\downarrow} 2n+1$ and $2n+1 \xrightarrow{\uparrow} 2n$ are *raised*.

For three distinct values of the Zeeman splitting, Fig. 32 shows stability diagram zooming on the region between the $2n$ and $2n+1$ Coulomb blockade diamonds. Those plots complement Fig. 33, where we show the differential conductance versus bias and Zeeman splitting, at a fixed gate voltage $e\alpha V_{\text{gate}} \approx 2.0\,\text{meV}$ (marked in Fig. 32 with the dashed line). In turn, the three values of the Zeeman splitting considered in Fig. 32 are marked in Fig. 33 by dashed white lines.
At first we focus on Fig. 33(a), describing the case of unpolarised leads.
A small Zeeman splitting will actually select $(g_2)_{\uparrow\uparrow}$ as $2n$ groundstate. The $2n \to 2n+1$ groundstate-to-groundstate transition is then $(g_2)_{\uparrow\uparrow} \to (t_1)_{\uparrow}$, as indicated left of the figure. It is the first line of a triple marking transitions to the lowest lying $2n+1$ states. Upon introducing a Zeeman energy, the spin-degeneracies of those are lifted, but only the two excited lines split in "V"-like manner, while the groundstate-to-groundstate

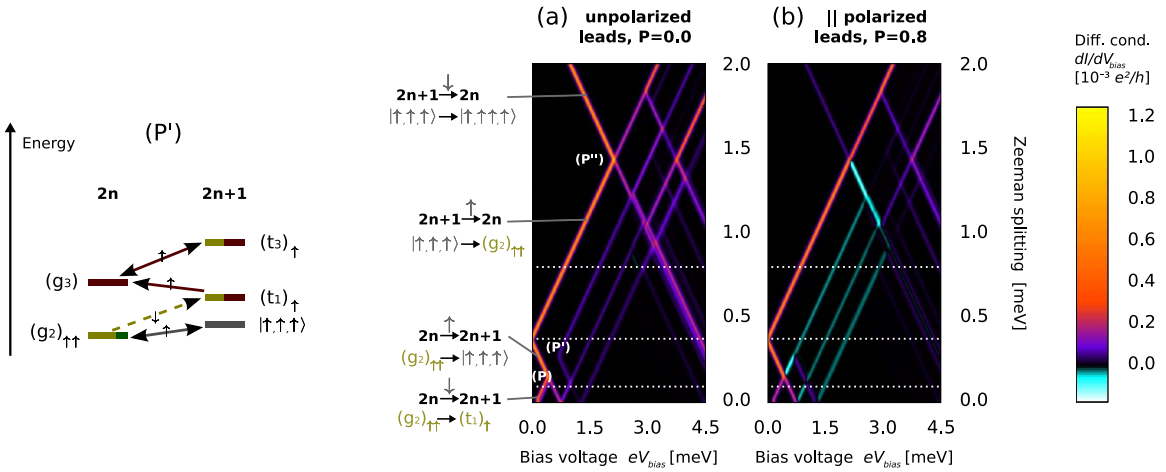

Figure 33: Differential conductance vs. bias voltage and Zeeman splitting at a fixed gate voltage of approx. 2.0 meV, for an ACNR transport setup with (a) unpolarised and (b) parallel polarised contacts. The sketch (P') on the left explains why the channel $(g_2)_{\uparrow\uparrow} \rightarrow (t_1)_\uparrow$ (dashed arrow) must be open in order to see transitions $(g_3) \leftrightarrow (t_3)_\uparrow$.

transition $(g_2)_{\uparrow\uparrow} \rightarrow (t_1)_\uparrow$ has only one rightwards slanted branch (i.e. raises in energy with increasing field). The reason is that $(g_2)_{\uparrow\uparrow}$ is connected to the $|c_\uparrow\rangle$ $(= |\uparrow,\downarrow,\uparrow\rangle)$ - component of the energetically favoured state $(t_1)_\uparrow = \frac{1}{\sqrt{2}}(|a_\uparrow\rangle + |b_\uparrow\rangle) + |c_\uparrow\rangle$ by in-tunnelling of $\downarrow$ - electrons. There is no possibility for a transition with $\uparrow$ - electrons, hence a left branch does not exist.

At a Zeeman splitting of $\sqrt{2}t/2$, the process $(g_2)_{\uparrow\uparrow} \xrightarrow{\uparrow} |\uparrow,\uparrow,\uparrow\rangle$ becomes the groundstate-to-groundstate transition. The crossover is marked with (P) in Fig. 33(a). Due to the *in-tunnelling* of $\uparrow$ - electrons, this resonance is continuously lowered in bias upon increasing the Zeeman energy further.

At a Zeeman splitting of about 0.4 meV, we are exactly at resonance. As seen in the middle plot of Fig. 32, a line triple has clearly separated from the groundstate transition line. Upon comparison with Fig. 33(a) it is immediately understood that it belongs to $\downarrow$ - electron transitions to the lowest lying $2n+1$ states. Concerning the corresponding $\uparrow$ - electron transitions, something interesting happens: In the point (P'), the left branch of the second "V"-shaped pattern, which belongs to the $2n+1$ state $(t_3)_\uparrow$, ends. The reason is that $(t_3)_\uparrow$ consists of the same components as $(t_1)_\uparrow$. By in-tunnelling of $\uparrow$ - electrons, it can thus not be connected to $(g_2)_{\uparrow\uparrow}$, but rather to (g_3) $[= \frac{1}{\sqrt{2}}(|a\rangle + |b\rangle)]$, see Fig. 33, sketch (P'). This $2n$ state is, compared to $(g_2)_{\uparrow\uparrow}$, lifted by the Zeeman energy and can only be populated by back-transitions from $(t_1)_\uparrow$. The state $(t_1)_\uparrow$, however, is not available below the transition $(g_2)_{\uparrow\uparrow} \rightarrow (t_1)_\uparrow$ [Fig. 33, sketch (P'), dashed arrow]. This explains why the point (P') is positioned at the crossing with the resonance line marking this transition.

Going on to a value of 0.8 meV of the Zeeman splitting, where the rightmost plot in Fig. 32 is taken, we reside at low bias voltages within the $2n+1$ Coulomb blockade diamond; the groundstate transition is now the *out-tunnelling* process $|\uparrow,\uparrow,\uparrow\rangle \xrightarrow{\uparrow} (g_2)_{\uparrow\uparrow}$, thus raising in bias for an increasing magnetic field. The behaviour reverts again in

the point (P"), where the Zeeman splitting has lowered the excited $2n$ state $|\uparrow,\uparrow\uparrow,\uparrow\rangle$ enough to change the groundstate transition to $|\uparrow,\uparrow,\uparrow\rangle \rightarrow |\uparrow,\uparrow\uparrow,\uparrow\rangle$, which involves out-tunnelling of $\downarrow$ - electrons.

Finally, the Fig. 33(b) shows the data obtained if the calculation yielding Fig. 33(a) is performed for ferromagnetic leads, polarised in parallel to the applied field. The only thing changing is the intensity of the lines. In particular, several of them are transformed into negative differential conductance lines. This is a standard effect for a single electron transistor with parallel polarised contacts in magnetic field: upon opening a channel to a state from which the system can only escape via a weak (in our case $\downarrow$ - mediated) transition, NDC occurs as such slow processes hinder the current flow. The only exception are the groundstate-to-groundstate transitions, i.e. the edges of the Coulomb diamonds, where current starts to flow: to those, of course always positive differential conductance (PDC) lines belong. An obvious example is the $|\uparrow,\uparrow,\uparrow\rangle \stackrel{-\downarrow}{\rightarrow} |\uparrow,\uparrow\uparrow,\uparrow\rangle$ transition, which turns from NDC to PDC beyond the point (P").

4.5 Conclusion

We have studied the spectrum and transport characteristics of fully interacting graphene armchair nanoribbons (ACNRs).
We have taken advantage of the known theory [104] for quasi-onedimensional interacting electrons in small diameter single wall carbon nanotubes to develop an analogous theory for narrow metallic ACNRs. We discovered an essential impact of short-ranged Coulomb interactions. Those lead to an entanglement between bulk states and the ones localised at the zig-zag ends of the ribbon. As a consequence, degeneracies between various states get lifted, and we have in particular predicted a smearing of any spin-charge separation.
Importantly, the entanglement makes the bulk spin-S_z component no longer a conserved quantity, which leaves strong fingerprints in transport. There is a two-electron periodicity distinguishing between even and odd electron fillings. For the latter, eight formerly degenerate groundstates get split under the influence of the end-bulk interaction, where the lifting is determined by the end-bulk exchange coupling t. This shows up in form of a characteristic transition line triple. Further, pronounced negative differential conductance (NDC) occurs for a symmetric, unpolarised setup in zero magnetic field. Its origin lies in the interaction-induced formation of states symmetric or anti-symmetric under exchange of the ribbon ends. It is mainly the population of an anti-symmetric trapping state which decreases the current in certain regions of the gate and bias voltage.
For an anti-parallel contact polarisation, absence of various transition lines is observed due to spin-blockade effects and also the NDC features have vanished. The reason is that transition channels feeding the trapping state are disfavoured, which leads even to a negative tunnelling magneto-resistance.
Finally we have investigated the transport behaviour in magnetic field, for unpolarised

as well as for in parallel polarised contacts. A change of the odd filling groundstate with $S_z = \hbar/2$ to one with $S_z = 3\hbar/2$ is observed at a Zeeman splitting of $\sqrt{2}t/2$, such that the value of the end-bulk exchange coupling t can directly be read off. Upon imposing a parallel contact magnetisation, standard effects change for several transition lines the differential conductance from the positive to the negative regime, because all $\downarrow$ - mediated transport channels become weak.

All in all, we found that short-ranged Coulomb interactions yield a strong influence of localised end states on the properties of ACNRs. Due to this fact, ACNRs might not be as ideal candidates for certain spintronic devices as previously regarded. Instead, the entanglement between bulk and end states is a rich source of ACNR specific features in transport. Recent achievements in fabrication of carbon nanostripes with defined geometries [90, 91] raise the hope of an experimental confirmation of our predictions within the near future.
On the theoretical side, non-collinear contact magnetisations as well as higher order effects in ACNRs wait to be explored.

Related publications:

S. Koller, L. Mayrhofer, M. Grifoni. EPL **88**, 57001 (2009)
Graphene armchair nanoribbon single-electron transistors: the peculiar influence of end states. [117]

S. Koller, L. Mayrhofer, M. Grifoni. Accepted for publication in New J. Phys. (2010)
Spin-dependent transport through interacting graphene armchair nanoribbons. [118]

5 Single wall carbon armchair nanotubes

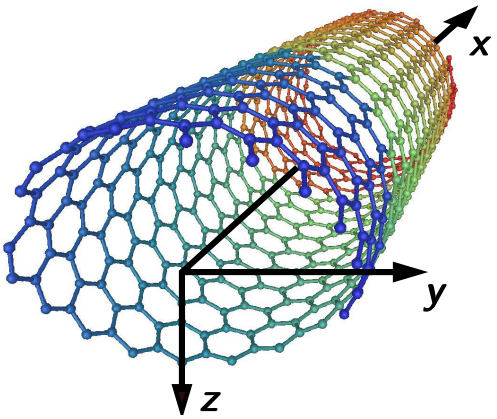

Figure 34: Single wall armchair carbon nanotube [119].

Graphene was known in rolled up form as single wall carbon nanotubes (SWCNTs) already since 1993, when Iijima and Ichihashi [120] achieved synthesis of such abundant single-shell tubular fullerenes. Outstanding qualities both from the mechanical and the electrical point of view [121] have made them subject of ongoing intense investigation. They had soon been recognised as extraordinary strong and stiff molecules, as well as excellent heat [122] and electricity conductors [123]. At low energies, they represent an almost perfect realization of a one-dimensional (1D) system of interacting electrons with an additional orbital degree of freedom due to the sublattice structure of graphene. Nowadays experiments on carbon nanotubes touch quite a variety of fundamental physical topics, ranging from Luttinger liquid behaviour [124, 125] over the Kondo effect [126, 127] to electron-vibron coupling in suspended tubes [128, 129, 130]. Around the half-filling regime, where there is exactly one electron per carbon atom inside the tube, spin-orbit coupling [131, 132] and signatures of a Mott-insulating transition [133] have been observed. Also proximity-induced superconductivity [134, 135] has been demonstrated and exploited for fabrication of gate-controllable carbon nanotube Josephson junctions [136, 137, 138].
Further, carbon nanotubes have also attracted much attention for their potential applications in spintronic devices [139]. They are particularly interesting because they have a long spin lifetime and can be contacted with ferromagnetic materials. Indeed, spin-dependent transport in carbon nanotube spin valves has been demonstrated by various experimental groups [14, 140, 15], ranging from the Fabry-Perot [140, 14] to the Kondo regime [15].

Accounting for spin and orbital degrees of freedom implies that for carbon nanotubes an electronic shell structure is expected, where each shell can accommodate up to four electrons. In the absence of Coulomb interaction the energy levels are spin degenerate, while the orbital degeneracy is usually lifted due to the nanotube finite length. Coulomb interactions, however, modify this picture. Similar as for the armchair carbon

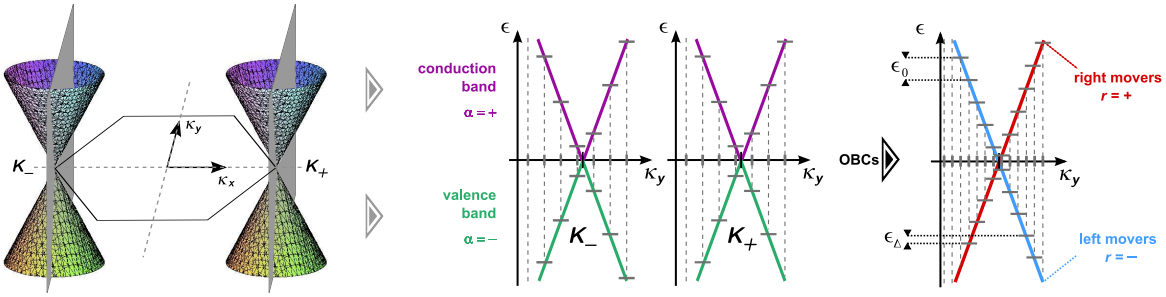

Figure 35: Open boundary conditions (OBCs) in x direction map the low energy dispersions around the two Fermi-points onto two linear branches, $r = \pm$, of slopes $\pm\hbar v$ determined by the Fermi velocity v. The quantities ϵ_0 and ϵ_Δ are the intra-band level spacing and the orbital mismatch energy, respectively.

nanoribbons (ACNRs), their short-ranged parts play a crucial role, causing in finite size nanotubes exchange effects leading for a tube filling of $4n+2$ to a non-degenerate groundstate with either total spin $S = 0$ or a triplet with $S = \hbar$ [103]. Signatures of the exchange interactions have indeed been inferred from stability diagrams of carbon-nanotube-based quantum-dots [141, 142, 143]. In particular it was shown by Moriyama *et al.* [141] that an applied magnetic field can be used to reversible change the ground-state from the singlet to one of the triplet states.

This section is split into two parts: The first one contains some basic information on a low energy description of SWCNTs. Like the spectrum and the results on lowest order transport, discussed in the second part, it has been excerpted from a publication in collaboration with Christoph Schenke, Leonhard Mayrhofer and Milena Grifoni, Ref. [144]. The second part concludes with an outlook on the impact of higher order effects, treated in collaboration with Jens Paaske and Milena Grifoni.

5.1 The low energy theory of SWCNTs

A theoretical description of SWCNTs valid in the linear dispersion regime above half-filling is constructed widely in analogy to the one for ACNRs, Sect. 4, and has been presented in great detail in Ref. [104]. Thus at this place we only sketch how to obtain the electron operator, Eq. (94), and the density-density part of the interacting Hamilton operator, Eq. (97), to which we need to refer in the subsequent second part.

5.1.1 Noninteracting electrons in finite size SWCNTs

As a starting point for the determination of the wave functions in armchair SWCNTs serve the Bloch waves of the carbon honeycomb lattice, Eq. (50). Wrapping a sheet of graphene up to form a tube, periodic boundary conditions around the circumference must be imposed. This leads to the formation of transverse subbands. For the low energy electronic structure of metallic SWCNTs, only the subbands touching at the Fermi-points are of relevance. In the following we consider an armchair SWCNT, which

is automatically metallic [121], of finite length L. In accordance with the previously introduced coordinate system Fig. 20, the elongation of an armchair tube is along the x-axis. At the two ends of the tube, $x = 0$ and $x = L$, open boundary conditions are appropriate: the wave function must vanish at the armchair terminations. To fulfil all boundary conditions, functions belonging to the two inequivalent Fermi points $K_\pm = \pm K_0$, Eq. (49), of the first Brillouin zone of graphene have to be mixed. The appropriate linear combinations read [114, 103]

$$\varphi_{r\kappa_x}(\vec{r}) = \frac{1}{\sqrt{2}} \sum_{Fp} F f_{pr} \varphi_{Fp}(\vec{r}, (F\kappa_x, 0)), \tag{90}$$

with prefactors f_{pr} given by

$$f_{+r} = 1\,, \quad f_{-r} = -r. \tag{91}$$

The allowed values for the quasi-momentum are

$$\kappa_x = \frac{\pi}{L}(n + \Delta), \quad n \in \mathbb{Z}, \tag{92}$$

where L is the tube length and Δ accounts for the fact that K_0 might not be an integer multiple of π/L. The corresponding linear dispersion relation is depicted in Fig. 35. As for ACNRs, it is characterised by two linear branches $r = \pm$, corresponding to right and left moving wave packets, with slopes $\pm\hbar v$, $v \approx 8.1 \cdot 10^5 \frac{m}{s}$ as before denoting the Fermi velocity. The field operator for an electron with spin σ at position $\vec{r}$ inside a SWCNT is

$$\hat{\Psi}_\sigma(\vec{r}) = \sum_{\kappa \in (\mathbb{Z}+\Delta)\pi/L} \varphi_{r\kappa}(\vec{r}) \hat{c}_{r\sigma\kappa} = \sqrt{L} \sum_{Fpr} F f_{pr} \varphi_{Fp}(\vec{r}) \hat{\psi}_{rF\sigma}(x), \tag{93}$$

where $\varphi_{Fp}(\vec{r}) \equiv \varphi_{Fp}(\vec{r}, \vec{\kappa} = (0,0)^T)$. Further, $\hat{c}_{r\sigma\kappa}$ annihilates an electron in the SWCNT with momentum κ and spin σ in branch r, and a slowly varying 1D electron operator was defined as

$$\hat{\psi}_{rF\sigma}(x) = \frac{1}{\sqrt{2L}} \sum_{\kappa \in (\mathbb{Z}+\Delta)\pi/L} e^{\mathrm{i}F\kappa x} \hat{c}_{r\sigma\kappa}. \tag{94}$$

The related noninteracting Hamilton operator of the SWCNT is

$$\hat{H}_0 = \hbar v \sum_{r\sigma\kappa} \kappa \hat{c}^\dagger_{r\sigma\kappa} \hat{c}_{r\sigma\kappa} + \epsilon_\Delta \sum_{r\sigma} r \hat{\mathcal{N}}_{r\sigma}, \tag{95}$$

accounting for a level spacing $\epsilon_0 = \hbar v \pi / L$ as well as an offset energy $\epsilon_\Delta \equiv \epsilon_0 \Delta$ between the two branches. Here, the operator $\hat{\mathcal{N}}_{r\sigma}$ counts the total electron number in branch r and of spin σ.

5.1.2 The interacting Hamiltonian

For a realistic system, scattering between the electrons must be included by adding to $\hat{H}_0$ the interaction part

$$\hat{V} = \frac{1}{2}\sum_{\sigma\sigma'}\iint \mathrm{d}^3r\,\mathrm{d}^3r'\,\hat{\Psi}^\dagger_\sigma(\vec{r})\hat{\Psi}^\dagger_{\sigma'}(\vec{r}\,')U(\vec{r}-\vec{r}\,')\hat{\Psi}_{\sigma'}(\vec{r}\,')\hat{\Psi}_\sigma(\vec{r}), \tag{96}$$

with the fermion field operators from Eq. (93) and the Ohno potential $U(\vec{r}-\vec{r}\,')$ modelling the screened 3D Coulomb interaction as before, Eq. (67). Similar as for ACNRs, one can split the interaction into density-density and non density-density contributions [103], so that the total Hamiltonian reads

$$\hat{H}_\odot = \hat{H}_0 + \hat{V}_{\rho\rho} + \hat{V}_{n\rho\rho}.$$

With the help of bosonisation [111] it is possible to diagonalize the density-density part $\hat{H}_0 + \hat{V}_{\rho\rho}$, and to eventually arrive at a Hamiltonian taking the form [103]:

$$\begin{aligned}\hat{H}_0 + \hat{V}_{\rho\rho} =& \frac{1}{2}E_c\hat{\mathcal{N}}_c^2 + \frac{1}{2}\sum_{r\sigma}\hat{\mathcal{N}}_{r\sigma}\left[-\frac{J}{2}\hat{\mathcal{N}}_{-r\sigma} + \left(\epsilon_0 - u^+\right)\hat{\mathcal{N}}_{r\sigma} + r\epsilon_\Delta\right] \\ &+ \sum_{j\delta q>0}\epsilon_{j\delta q}\hat{a}^\dagger_{j\delta q}\hat{a}_{j\delta q}.\end{aligned} \tag{97}$$

The last term counts the bosonic excitations, which are now fourfold distinguished by total/relative ($\delta = +/-$) charge ($j = c$) and spin ($j = s$) modes. Their energies $\epsilon_{j\delta q}$ are given by

$$\epsilon_{j\delta q} \cong \epsilon_0 n_q\sqrt{1 + \delta_{j,c}\delta_{\delta,+}8W_q/\epsilon_0}$$

Hereby, $q = n_q\pi/L$ for $n_q \in \mathbb{Z}$ and

$$W_q = \frac{1}{N_L^2}\sum_{\vec{R},\vec{R}'}\cos(qR_x)\cos(qR'_x)\left[U(\vec{R}-\vec{R}\,') + U(\vec{R}-\vec{R}\,'+\vec{\tau}_+-\vec{\tau}_-)\right].$$

Involving the sum of Coulomb interaction potentials for electrons living in the same and different sublattices, W_q emerges from long-ranged density-density processes.

The first line of Eq. (97) starts with a charging term, stemming also from the long-ranged part of the Coulomb interaction, and involving the charging energy $E_c = W_{q=0}$. It determines the energy one has to spend to put $N_c = \sum_{r\sigma} N_{r\sigma}$ electrons on the dot, no matter what spin $\sigma \in \{\uparrow,\downarrow\}$ or pseudo-spin $r \in \{+,-\}$ they have. In square brackets, three contributions follow. The first one is an exchange term favouring spin alignment. The exchange splitting,

$$J = \frac{1}{2N_L^2}\sum_{\vec{R},\vec{R}'}(1 + e^{-\mathrm{i}2K_+(R_x-R'_x)})\left[U(\vec{R}-\vec{R}\,') - U(\vec{R}-\vec{R}\,'+\vec{\tau}_+-\vec{\tau}_-)\right], \tag{98}$$

being proportional to the difference of the Coulomb interaction for electrons on the same and on different sublattices, results from short-ranged processes. The next term reflects the Pauli principle, demanding an extra energy cost for adding more and more electrons of same spin into the same branch. The correction u^+ is

$$u^+ = \frac{1}{4N_L^2} \sum_{\vec{R},\vec{R}'} e^{-\mathrm{i}2K_+(R_x - R'_x)} \left[U(\vec{R} - \vec{R}') + U(\vec{R} - \vec{R}' + \vec{\tau}_+ - \vec{\tau}_-) \right] . \tag{99}$$

Finally, the last term in the square brackets accounts for a possible band-mismatch, see Fig. 35.
The eigenstates of $\hat{H}_0 + \hat{V}_{\rho\rho}$ are spanned by

$$\left| \vec{N}, \vec{m} \right\rangle = \prod_{j\delta q} \frac{\left(\hat{a}^\dagger_{j\delta q} \right)^{m_{j\delta q}}}{\sqrt{m_{j\delta q}!}} \left| \vec{N}, 0 \right\rangle \ . \tag{100}$$

Here $\vec{N}$ and $\vec{m}$ denote the fermionic and the bosonic configuration, respectively, such that the state $|\vec{N}, 0\rangle$ has no bosonic excitation. The fermionic configuration is given by the number of electrons in each branch with a certain spin, $\vec{N} = (N_{-\uparrow}, N_{-\downarrow}, N_{+\uparrow}, N_{+\downarrow})$. These eigenstates can be used to calculate the contribution of the non-density-density part of the interaction, i.e., $\langle \vec{N}, \vec{m} | V_{n\rho\rho} | \vec{N}', \vec{m}' \rangle$. Away from half-filling, they only couple states close in energy and one is allowed to work with a truncated eigenbasis, while at half-filling a Mott-insulating transition is expected for long SWCNTs due to umklapp scattering [145]. Indeed, the here presented theory of finite size tubes breaks down around half-filling, because umklapp processes acquire increasing weight [103], which is a possible signature of the Mott instability. In recent experiments [133], actually the observation of the Mott transition in SWCNT quantum-dots was claimed.

5.2 Low energy spectrum

A prerequisite for investigations on transport is the knowledge of how the low energy spectrum of SWCNTs is changed by the non-density-density interactions. As demonstrated in the following, they crucially affect the groundstate for tube fillings $N_c = 2n + 2, \ n \in \mathbb{N}$.
For our purposes, it is sufficient to restrict to the low energy regime, where the energies that can be transferred to the system by the bias voltage and the temperature stay below ϵ_0. This means no bosonic excitations are present, i.e., $\vec{m} = (0, 0, 0, 0)$, and also no fermionic excitations are allowed, i.e., the four bands will be filled as equal as possible: $|N_{r\sigma} - N_{r'\sigma'}| \leq 1 \, \forall \, r\sigma, r'\sigma'$. Our starting point are the eigenstates, Eq. (100), of the Hamiltonian Eq. (97) which accounts for the kinetic and the density part of the full Hamiltonian. Now we have to split the examination into two cases.
At first we consider states with total charge N_c equal to $4n$, $4n + 1$ and $4n + 3$. Those are unambiguously described by the fermionic configuration $\vec{N}$ because they are not mixed by non-density-density effects. If fact, the only impact of $\hat{V}_{n\rho\rho}$ terms on these

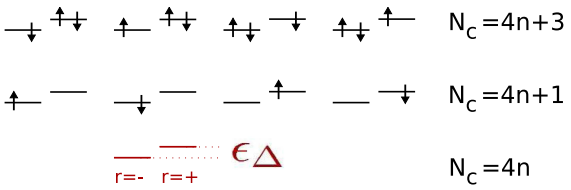

Figure 36: Lowest lying states for fillings $N_c = 4n+1$ and $N_c = 4n+3$. For simplicity only the configuration of the last partially filled shell is shown.

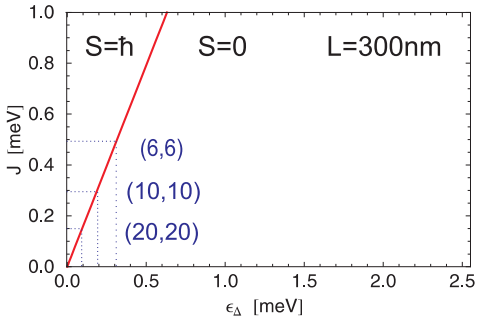

Figure 37: Phase diagram to determine the groundstate of different tubes of length 300nm. The chance to find a triplet groundstate increases with increasing exchange parameter J, i.e., with decreasing tube diameters.

states is given by an energy penalty for double occupation of one branch r, a common shift for all eigenstates with fixed $N_c \neq 4n+2$. Therefore we are left with [103]

$$E_{\vec{N}} = \frac{1}{2}E_c N_c^2 + u^+ \sum_r \min\left(N_{r\uparrow}, N_{r\downarrow}\right) + \frac{1}{2}\sum_{r\sigma} N_{r\sigma}\left[-\frac{J}{2}N_{-r\sigma} + \left(\epsilon_0 - u^+\right)N_{r\sigma} + r\epsilon_\Delta\right] \tag{101}$$

for their energy. If $\epsilon_\Delta \neq 0$, states with the maximum allowed number of electrons in the $r=-$ branch will be the groundstates. For $N_c = 4n$ the pseudo-spin branches $r = \pm$ are equally occupied, yielding an unique $N_c = 4n$ groundstate. The corresponding configuration is taken as reference configuration for the $N_c = 4n+1,\ 4n+2$ and $4n+3$ cases. The lowest lying states for $N_c \in \{4n+1,\ 4n+3\}$ are presented in Fig. 36. E.g., for the case $N_c = 4n+1$ we obtain four possible states corresponding to $\vec{N} \in \{(n+1,n,n,n),\ (n,n+1,n,n),\ (n,n,n+1,n),\ (n,n,n,n+1)\}$. For simplicity we introduce for the states with an unpaired electron in the $r=-$ branch the notation $|\uparrow,\cdot\rangle,\ |\downarrow,\cdot\rangle$. For electrons in the $r=+$ branch we set $|\cdot,\uparrow\rangle,\ |\cdot,\downarrow\rangle$.
Analogously, neglecting exchange effects and setting $\epsilon_\Delta = 0$ for the moment, the groundstates for the $N_c = 4n+2$ filling are represented by the six states $|\uparrow,\uparrow\rangle$, $|\downarrow,\downarrow\rangle$, $|\uparrow,\downarrow\rangle$, $|\downarrow,\uparrow\rangle$, $|\uparrow\downarrow,\cdot\rangle$ and $|\cdot,\uparrow\downarrow\rangle$[28]. Here the different fermionic configurations mix under the influence of the $V_{n\rho\rho}$ processes and the groundstate structure will change dramatically due to the off-diagonal contributions

$$\langle\uparrow,\downarrow|V_{n\rho\rho}|\downarrow,\uparrow\rangle = -J/2\,, \quad \langle\uparrow\downarrow,\cdot|V_{n\rho\rho}|\cdot,\uparrow\downarrow\rangle = J/2. \tag{102}$$

The diagonal entries of the 6×6 mixing matrix are the energies of the considered $2n+2$ states according to Eq. (101). Diagonalization yields the groundstate spectrum as it is shown in Tab. 10. It is clear that the states $|s\rangle$ and $|b\rangle$ will always be excited states,

[28] E.g., $|\uparrow,\uparrow\rangle$ means each branch $r=\pm$ is occupied with one electron of spin $\uparrow$.

RELATIVE ENERGY	:	EIGENSTATE (NORMALISED)	ABBR.	TOTAL SPIN S $[\hbar]$
$-J/2$	:	$\lvert\uparrow,\uparrow\rangle$	$\lvert t_1\rangle$	1
$-J/2$	:	$\lvert\downarrow,\downarrow\rangle$	$\lvert t_{-1}\rangle$	1
$-J/2$	:	$\frac{1}{\sqrt{2}}\left(\lvert\uparrow,\downarrow\rangle + \lvert\downarrow,\uparrow\rangle\right)$	$\lvert t_0\rangle$	1
$u^+ - \sqrt{\left(\frac{J}{2}\right)^2 + \epsilon_\Delta^2}$	:	$\frac{1}{\sqrt{c_1^2+1}}\left(-c_1\lvert\uparrow\downarrow,\cdot\rangle + \lvert\cdot,\uparrow\downarrow\rangle\right)$	$\lvert a\rangle$	0
$+J/2$	:	$\frac{1}{\sqrt{2}}\left(\lvert\uparrow,\downarrow\rangle - \lvert\downarrow,\uparrow\rangle\right)$	$\lvert s\rangle$	0
$u^+ + \sqrt{\left(\frac{J}{2}\right)^2 + \epsilon_\Delta^2}$	:	$\frac{1}{\sqrt{c_2^2+1}}\left(-c_2\lvert\uparrow\downarrow,\cdot\rangle + \lvert\cdot,\uparrow\downarrow\rangle\right)$	$\lvert b\rangle$	0

$$c_1 = \frac{2\epsilon_\Delta + \sqrt{J^2+(2\epsilon_\Delta)^2}}{J}, \quad c_2 = \frac{2\epsilon_\Delta - \sqrt{J^2+(2\epsilon_\Delta)^2}}{J}$$

Table 10: The six lowest lying eigenstates for the filling $N_c = 4n+2$ of an interacting SWNT. The energies are given relative to $E_{0,4n+2} = \frac{1}{2}E_c N_c^2 + (2n^2+2n+1)(\epsilon_0 - u^+) - \frac{J}{2}(2n^2+2n) + 2u^+ n$. Due to short-ranged interactions, the former degeneracy of the states is lifted and a triplet, i.e. three degenerate states of total spin $S = \hbar$, as well as three non-degenerate states of total spin $S = 0$ emerge.

while the spin triplet, $S = \hbar$, is energy degenerate. Now the question arises which states, the triplet or the $|a\rangle$ state, are the groundstate of the system. In accordance with Tab. 10, the condition for a triplet groundstate is given by:

$$\epsilon_\Delta^2 < (u^+)^2 + Ju^+.$$

For a dielectric constant $\epsilon = 1.4$ it holds $J = 0.72$ Å $\frac{\epsilon_0}{d}$ and $u^+ = 0.22$ Å $\frac{\epsilon_0}{d}$. Hence we find in terms of the level spacing ϵ_0 and the tube diameter d:

$$|\epsilon_\Delta| < 0.4548 \text{ Å } \frac{\epsilon_0}{d}.$$

Obviously this makes the triplet groundstate more unlikely compared to the $S = 0$ groundstate as it can be seen in Fig. 37. For a (6,6) nanotube of 300 nm length, the band-mismatch must be $\epsilon_\Delta < 0.3\,\text{meV} \cong 0.06\epsilon_0$ to be in a triplet groundstate. In the experiments [142, 143] band-mismatches are of the order of $0.3\epsilon_0$ and, as expected from our theory, $|a\rangle$ groundstates are observed. Due to the inverse proportionality to the diameter, exchange effects are less pronounced for large diameter tubes. E.g., preserving the tube length but scaling up the diameter to $d = 2.7\,\text{nm}$ – a (20,20) tube – the short-range parameters amount only to tiny fractions of ϵ_0, namely $J/2 \approx 0.013\epsilon_0$ and $u^+ \approx 0.008\epsilon_0$, such that for $\epsilon_\Delta = 0$ practically no splitting and no mixing between the six $4n+2$ groundstates is expected.

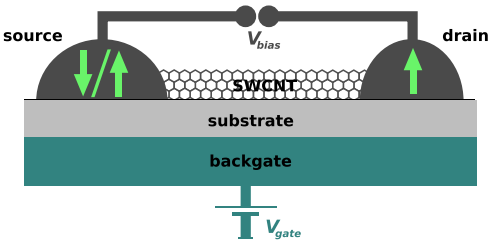

Table 11: Transport setup with a single-walled carbon nanotube (SWCNT) which is weakly attached to source and drain contacts. The contact magnetisation may either be parallel or anti-parallel. The gate electrode allows to shift the chemical potential inside the SWCNT.

Thermal energy	k_BT	4.0 μeV
Charging energy [110]	W_0	6.7 meV
SWCNT length	L	300 nm
Level spacing	ϵ_0	5.6 meV
SWCNT diameter	d	0.81 nm
Coulomb excess energy	u^+	0.15 meV
Exchange energy	J	0.49 meV
Band-mismatch	ϵ_Δ	0.0 meV / 1.68 meV

Table 12: Parameter set for the (6,6) SWCNT employed for all viewed plots unless specified differently. A triplet groundstate is obtained for $\epsilon_\Delta = 0.0$ meV, the other value yields the $|a\rangle$ groundstate. For the investigated tube, the length variation deciding upon these band-mismatches is about 0.02 % and thus not relevant.

5.3 Transport across quantum-dot SWCNTs

In this section, the impact of the short-ranged interactions on the transport characteristics of a SWCNT is studied, for the unpolarised current as well as in the differential conductance for collinearly polarised contacts, Sect. 5.3.1, as well as in small and high magnetic fields, Sect. 5.3.2. Thereby, we observe characteristics and effects distinguishing between the two types of potentially allowed groundstates of a small diameter SWCNT filled with $N_c = 2n + 2$, $n \in \mathbb{N}$ electrons. These investigations are amended by an outlook on higher order effects in transport across large diameter tubes, Sect. 5.3.3.

Fig. 38 compares the sequential current as a function of the gate and the bias voltage for a (6,6) and a (20,20) SWCNT, both for a band-mismatch $\epsilon_\Delta = 1.68$ meV [Fig. 38 (a)] and $\epsilon_\Delta = 0.0$ meV [Fig. 38 (b)]. All remaining parameters were taken from Tab. 12, and states with up to one bosonic excitation have been included in the calculation. For all cases the four-electron periodicity of the Coulomb diamonds is clearly seen and a mirror-symmetry with respect to the $N_c = 4n+2$ Coulomb blockade diamond exists because of electron-hole symmetry. At high bias voltages a smearing of the transitions due to the multitude of bosonic excitations is observed, in agreement with typical experimental data [142, 143, 146, 147, 148].
The differences between the four plots are, as it is expected, most pronounced for fillings $N_c = 4n + 2$, which we found to be strongly affected by the short-ranged interactions, see Tab. 10. An interesting region is thus the intermediate bias regime, $eV_{\text{bias}} \leq \epsilon_0$, in between $4n+1$ and $4n+2$ diamonds, which should still be well resolvable in experiment. Thereby, investigation of the small diameter tubes offers richer physics because of the degeneracy lifting and mixing of the six $N_c = 4n+2$ lowest lying states,

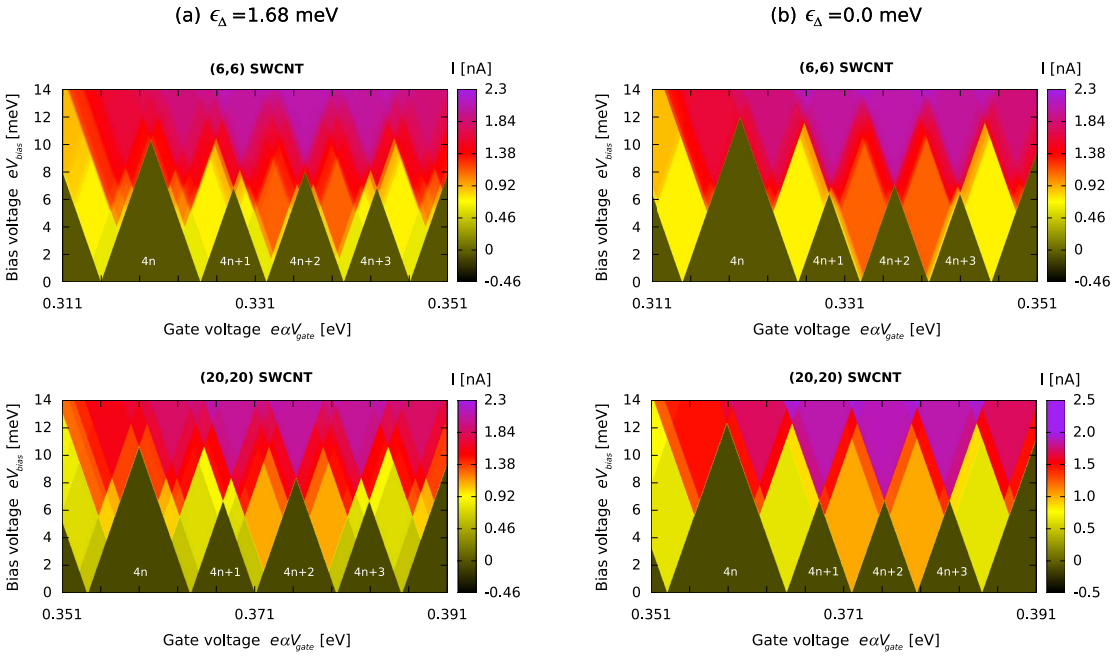

Figure 38: Unpolarised current versus gate and bias voltages across a (6,6) SWCNT (diameter 0.8 nm) as well as across a (20,20) SWCNT (diameter 2.7 nm), for which exchange effects do not play a role. In total 176 states have been included, which corresponds to all states with at most one bosonic excitation. For $4n+2$-filling this amounts to 32 different states. In all cases the four-electron periodicity of the Coulomb diamonds, stemming from the orbital and spin degree of freedom, is nicely observed. (a) Band-mismatch $\epsilon_\Delta = 0.3\epsilon_0$ corresponding to a $|a\rangle$, i.e. $S = 0$, groundstate for the $4n+2$ filling. (b) Band-mismatch $\epsilon_\Delta = 0$ corresponding to a triplet, i.e. $S = \hbar$, groundstate at filling $4n+2$.

which manifests in the more diversified colour landscape for the (6,6) SWCNTs in the plots Fig. 38.

In the upcoming three subsubsections on sequential, collinearly spin-polarised transport in small diameter SWCNTs, the focus is on the gate voltage region around the $4n+1 \leftrightarrow 4n+2$, which deserves particular interest because of the short-ranged interaction caused band-entanglement and energy lifting among the lowest lying states for the $N_c = 4n+2$ filling.
Unless stated else, equal contact polarisations $P_s = P_d = P = 0.9$ are chosen.
For all following plots, bosonic excitations were omitted to avoid a multitude of transitions not relevant for the coming discussion.
The final ingredient necessary for transport calculations are the tunnelling matrix elements of the electron operator Eq. (93), under exclusion of bosonic excitations simply reading [114]

$$\left\langle \vec{N}\vec{0}\left|\hat{\Psi}_\sigma(\vec{r})\right|\vec{N}'\vec{0}\right\rangle = \frac{1}{\sqrt{2}}\,(-1)^{\delta_{r,-}\delta_{\sigma,\uparrow}N_{-\downarrow}+\delta_{r,+}(N_{-\downarrow}+N_{-\uparrow}+\delta_{\sigma,\uparrow}N_{+\downarrow})} \times \sum_{Fpr} F\, f_{pr}\varphi_{Fp}(\vec{r})\,\delta_{\vec{N},\vec{N}'+\vec{e}_{r\sigma}}\, e^{\mathrm{i}\frac{\pi}{L}(rN_{r\sigma}+\Delta)Fx}.$$

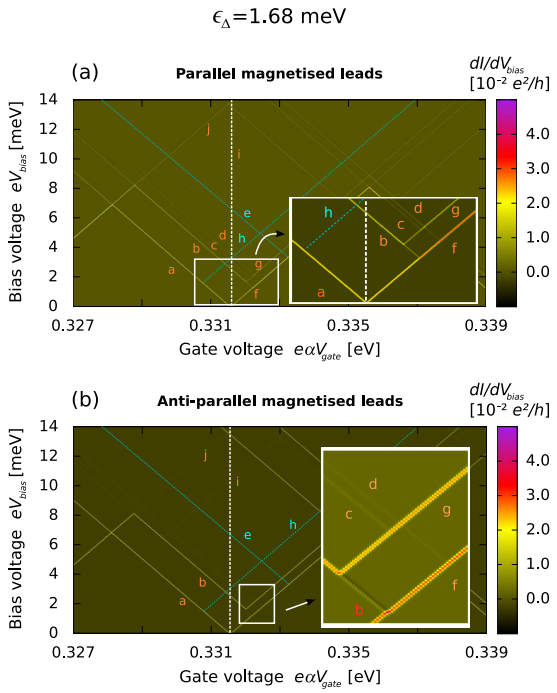

Figure 39: Differential conductance for transitions between $4n+1 \leftrightarrow 4n+2$ fillings in the $|a\rangle$ - groundstate. The polarisation has been chosen to be $P = 0.9$. The four lowest lying states for $N_c = 4n+1$ and the six ones for $N_c = 4n+2$ were included. The vertical white line is the bias trace we follow to explain the distinct transition lines in Fig. 41. (a) The leads are magnetised in parallel. (b) Anti-parallel magnetised leads. The intensity of various excitation lines has decreased compared to the parallel case. In particular a pronounced negative differential conductance (NDC) occurs in correspondence of the transition between $|\sigma, \cdot\rangle$ and the triplet (line b).

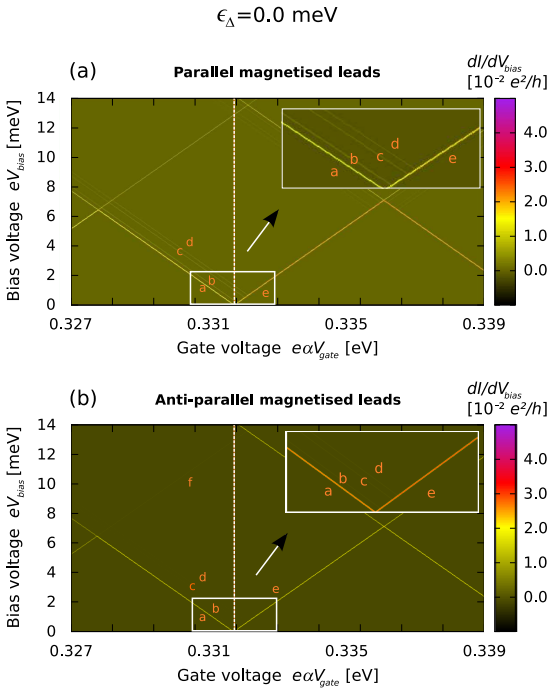

Figure 40: Differential conductance for transitions between $4n+1 \leftrightarrow 4n+2$ filling in the triplet groundstate. The polarisation has again been set to $P = 0.9$, and the four lowest lying states were included for $N_c = 4n+1$, the six lowest ones for $N_c = 4n+2$. The leads are magnetised (a) in parallel, (b) in anti-parallel. From the stability diagrams it is possible to directly extract the exchange parameters u^+ and J since the bias voltage $V_b/2 = u^+$ is needed to open transition line b and $V_b/2 = J$ for line c.

5.3.1 Differential conductance for collinear contact magnetisations

Figs. 39(a) and 39(b) show the stability diagrams for parallel and anti-parallel lead magnetisations, respectively, for the case of the $|a\rangle$ groundstate. The two transition lines h and e were emphasised by a dashed line because their intensity is too low to resolve them together with the other, stronger, transitions. The most obvious difference between the parallel and the anti-parallel setup is the weakness of all transition lines beyond the triplet occupation (line b) for an anti-parallel configuration. Moreover in line b an NDC feature not present in the parallel magnetisation case, is observed.

In order to explain the line positions in Fig. 39(a) and (b) we provide the schematic Fig. 41 which is based on a bias trace at the particular gate voltage which aligns the groundstates (white vertical lines in Fig. 39). The different arrows stand for new

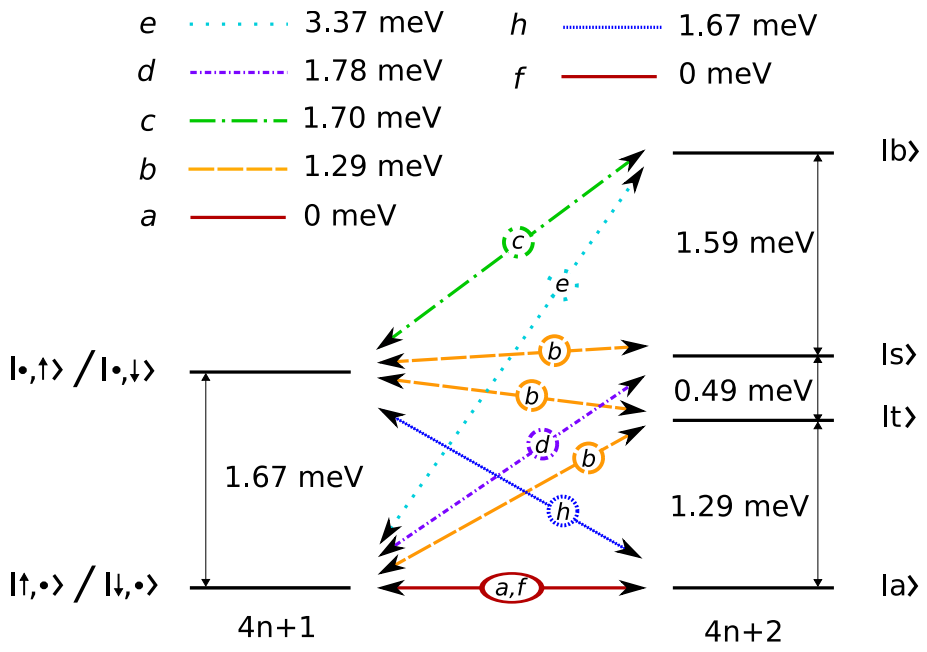

Figure 41: Schematic for the possible transitions occurring by sweeping the bias voltage at the $4n+1 \leftrightarrow 4n+2$ resonance, i.e. the fixed gate voltage which aligns the $|\sigma, \cdot\rangle$ and the $|a\rangle$ state (white dashed line in Fig. 39).

transport channels that open at certain bias voltages. The channels open in the order of a to e for the forward transitions $4n+1 \rightarrow 4n+2$ and f to h for the backward transitions $4n+2 \rightarrow 4n+1$. Sometimes opening of a new channel also opens other channels that have been blocked before and one does not see distinct lines for these transitions. Fig. 41 relates the concerned transitions to the required bias voltages. Line g, which does not appear in Fig. 41, marks backward transitions from the triplet to the $|\cdot, \sigma\rangle$ states, i.e., tunnelling between excited states. To explain the NDC feature in Fig. 39(b) which follows upon line b in the range between lines f and line g, we observe that – in correspondence of the b line – below that resonance only the transitions from $|\sigma, \cdot\rangle$ to the $|a\rangle$ state is possible. Above, also the triplet is accessible. For the case of anti-parallel polarisation, both provide only weak transport channels: Below the resonance transport is mostly mediated by $\uparrow$ - electrons, $|\downarrow, \cdot\rangle \overset{\uparrow}{\leftrightarrow} |a\rangle$, which are minority electrons for the source contact. Above resonance, after some tunnelling processes the system will always end up in $|t_{-1}\rangle$ which is a trapping state. Just at the exact resonance, the thermal energy allows electrons to tunnel forth and back, i.e., a $\downarrow$ - electron has the possibility to tunnel back into the source contact and transport is slightly enhanced. Once the bias voltage exceeds the exact resonance the trapping state $|t_{-1}\rangle$ gets occupied for long times and the current diminishes again. The fact that the $|\downarrow, \cdot\rangle \overset{\downarrow}{\leftrightarrow} |t_{-1}\rangle$ transition serves as the major transport channel once it has been opened is also the reason why all transition lines above line b are so weak.
In Figs. 40(a) and 40(b) the stability diagrams for the triplet groundstate are shown. They look a lot simpler than the ones in Fig. 39 due to the absence of a band-mismatch,

causing a degeneracy of the four lowest lying state for the $N_c = 4n + 1$ filling. Line a is the groundstate-to-groundstate transition. Lines b to d indicate transitions from the $4n+1$ groundstates to the $2n+2$ excited states $|a\rangle$, $|s\rangle$ and $|b\rangle$, respectively. They appear in the expected order, at an applied bias voltage $eV_{\mathsf{bias}}/2$ equal to u^+, J and $J + u^+$, as listed in Tab. 10. Line e stands for the back-transition from the triplet to one of the $4n + 1$ groundstates. For the anti-parallel setup, Fig. 40(b), we observe the same effect as in Fig. 39(b), i.e., all lines beyond the transition to the triplet decrease in intensity. Since the triplet is the groundstate, this means all excitation lines are weak and can practically not be resolved in the figure.

5.3.2 Transport in magnetic field

We now additionally allow for an externally applied magnetic field, which lifts all spin degeneracies by a Zeeman splitting and supports the parallel contact configuration.

Linear conductance in small magnetic field Investigating the impact of contact polarisation on the $2n + 1 \leftrightarrow 2n + 2$ resonance peak in the low bias regime, a striking effect, uniquely distinguishing the $|a\rangle$ and triplet groundstates, is found in small external magnetic fields. The corresponding plots can be seen in Figs. 42(a) and 43(a), for $|a\rangle$ and triplet groundstate respectively, where we considered exposure to a field of 0.07 T in strength, causing a Zeeman splitting which equals in magnitude[29] the thermal energy of $k_BT = 4\,\mu$eV. Both contacts are magnetised in parallel to the external field, while for the SWCNT a situation with a finite occupation probability for all included states is provided. Specifically, this means that also the energetically disfavoured states with spin-projection $S_z < 0$ will be populated, but of course states with spin along the field, $S_z > 0$, will be preferred. The first thing we observe in both Fig. 42(a) and 43(a) is that the conductance depends on the polarisation, which is not the case without Zeeman splitting [144]. Thereby, the peaks of the curves belonging to less polarised leads continuously move to higher gate voltages and in particular the conductance *decreases/increases* with increasing polarisation for the a/t cases, respectively.
Let us examine these results starting with the $|a\rangle$ groundstate, Fig. 42(a). We must divide the analysis in two cases, slightly polarised leads and strongly polarised leads. For only slightly polarised or non-polarised leads the situation is intricate as we have to deal with *competing processes*. On the one hand the $|\uparrow, \cdot\rangle$ state will be highly, the $|\downarrow, \cdot\rangle$ state slightly populated. From this point of view, the system favours the transition channel $|\uparrow, \cdot\rangle \overset{\downarrow}{\leftrightarrow} |a\rangle$ involving the preferred $|\uparrow, \cdot\rangle$ state [Fig. 42, sketch (b), lower left panel]. Only rarely, the $\uparrow$ - electron tunnels out, as this would result in a spin-flip to the disfavoured $|\downarrow, \cdot\rangle$ state [Fig. 42, sketch (b), upper left panel]. On the other hand, entering of $\downarrow$ - electrons is suppressed compared to transport of $\uparrow$ - electrons, not so much by the small polarisation, but primarily due to the Zeeman splitting E_z: in-tunnelling of $\downarrow$ - electrons is energetically more costly than in-tunnelling of $\uparrow$ - electrons. Due to $E_z \simeq k_BT$, the $\downarrow$ - channel is not completely forbidden but just disfavoured, and in

[29] A gyro-magnetic value of $g = 2$ and hence $E_z = \mu_B B$ was found experimentally in transport spectroscopy experiments with SWCNTs [141].

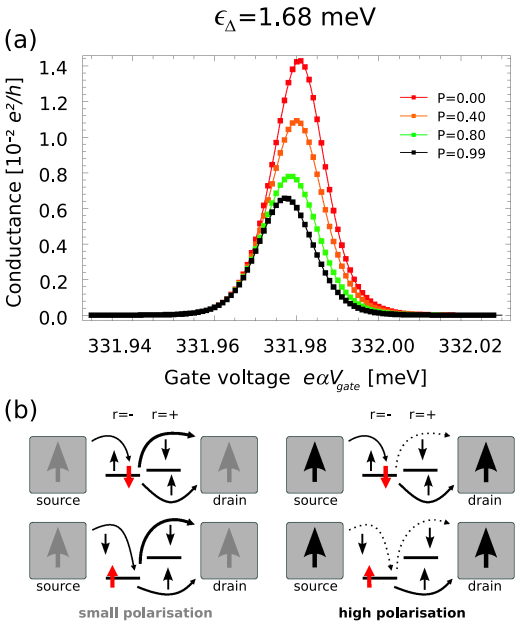

Figure 42: (a) Conductance near the $|\sigma, \cdot\rangle \leftrightarrow |a\rangle$ transition for parallel magnetised leads and applied magnetic field. The peaks corresponding to higher polarisations are shifted to lower gate voltages. (b) Schematical explanation for the amplitude and gate-voltage dependence of the conductance curve for small (left sketch) and large (right sketch) polarisation. The red spin indicates the spin of the excess electron initially present on the dot. The thick and thin lines are frequent and less frequent transitions, while dashed lines indicate rare transitions (for a detailed explanation see the main text).

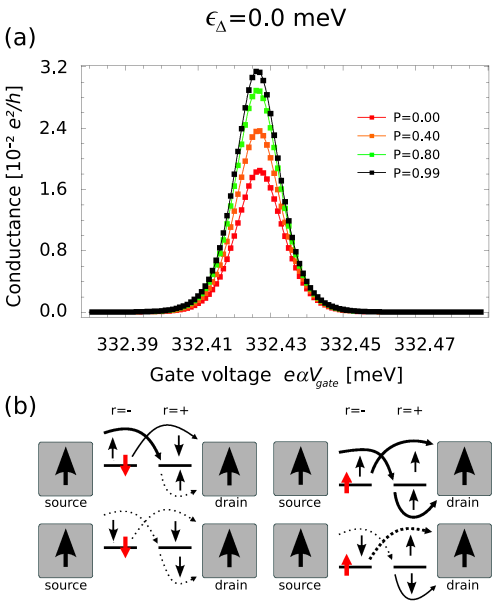

Figure 43: (a) Conductance near the triplet resonance for parallel magnetised leads and applied magnetic field. In contrast to the case of a singlet resonance, Fig. 42, transport increases as the polarisation is enhanced. (b) Schematical explanation with colour and line coding as in Fig. 42(b). All four possible tunnelling processes are depicted.

the end it will be a mixture of mainly $\downarrow$ - electrons and some $\uparrow$ - electrons responsible for transport. This can be seen by the fact that the curves for small polarisations are shifted to higher gate voltages which accounts for the higher chemical potential of the $\downarrow$ - electrons. In addition, the total amplitude of the conductance is decreased compared to a case without magnetic field [144], as either the small population of the $|\downarrow, \cdot\rangle$ or the energy penalty for in-tunnelling $\downarrow$ - electrons hinders transport. In the case of highly polarised leads only very few $\downarrow$ - electrons are available in the leads. As temperature provides a small, but nonzero population of the slightly excited state $|\downarrow, \cdot\rangle$, current basically flows via the polarisation-favoured $\uparrow$ - electron channel. Since those are energetically favoured for in-tunnelling, the transition takes place at slightly lower gate voltages as compared to the cases of small lead polarisation. The situation again is visualised in the sketch (b) of Fig. 42, in the upper and lower right panel. At the triplet resonance we observe not only quantitative, but also qualitative changes. The plot can be seen in Fig. 43(a) and all relevant tunnelling processes are sketched in Fig. 43(b). First we focus again on unpolarised or just slightly polarised leads. For

the filling $N_c = 4n + 1$, there is a large population of the degenerate[30] states $|\uparrow, \cdot\rangle$ and $|\cdot, \uparrow\rangle$. For $N_c = 4n + 2$, it is the $|t_1\rangle$ triplet state which will be preferably occupied, such that transport is mainly mediated via $\uparrow$ - electrons, i.e. majority charge carriers [Fig. 43(b), upper right panel]. However, the resulting current is smaller than in the case without magnetic field since it is harder to make use of the $\downarrow$ - electrons that are still largely at disposal in the leads [Fig. 43(b), all left and lower right panels]. A high polarisation decreases the number of these obstructive $\downarrow$ - electrons in the leads in favour of the $\uparrow$ - electron number, resulting in a strong enhancement of transport via the already preferred $|t_1\rangle$ channel. As a consequence, the conductance by far *exceeds* the conductance without magnetic field and polarisation.
Employing contact materials with a good gyro-magnetic ratio[31], the effect should be nicely detectable in an experimental setup and would clearly distinguish between the triplet or the $|a\rangle$ state as groundstate.

Magnetic field sweep In a seminal experiment Moriyama *et al.* [141] demonstrated a transition from a $S = 0$ groundstate to a $S_z = \hbar$ groundstate upon magnetic field sweep in a SWCNT quantum-dot. We have computationally reproduced the experimentally obtained data in Fig. 44(a), and moreover predict the measurement results expected in case of ferromagnetic leads, Fig. 44(b) (a symmetric contact polarisation of value $P = 0.9$ was assumed). With a band-mismatch of $0.24\epsilon_0$ (smaller than previously used) we start at $B = 0$ from the $|a\rangle$ groundstate. A change in groundstate from $|a\rangle$ to the triplet state $|t_1\rangle$ is observed at a magnetic field $\simeq 6\,\mathrm{T}$, as it has been measured [141]. To observe well visible patterns, we increased the temperature by a factor of ten compared to Tab. 12.
At gate voltages of approximately 0.322 and 0.323 meV, two "V"-shaped transition patterns (a and b) show up, each of width $2E_z = 2\mu_B B$. The separation between a and b at zero field is the band-mismatch ϵ_Δ. Interestingly, for polarised leads, Fig. 44(b), the rightwards slanted branches of the "V"-patterns, which belong to transitions involving $|\downarrow, \cdot\rangle$ or $|\cdot, \downarrow\rangle$, are NDC lines. The reason is the same as addressed already in Sect. 4: once the $\downarrow$ - channel becomes available, there is some chance that from time to time a minority charge carrier ($\downarrow$ - electron) enters from the source. As the drain is polarised in parallel to the source, it will take quite a while until this electron can leave the SWCNT again, such that transport gets hindered. At the gate voltage of approximately 0.328 meV, one enters the $N_c = 4n + 1$ Coulomb diamond (line c) and transport gets completely suppressed. For $B \neq 0$, $|\uparrow, \cdot\rangle$ gets selected as groundstate. At $V_g \simeq 0.329\,\mathrm{meV}$, we leave the $4n + 1$ Coulomb blockade and transport to the $|a\rangle$ state is enabled (line d). Notice that this is a groundstate-to-groundstate transition involving $\downarrow$ - electrons, and thus the corresponding line is slanted rightwards, while a leftwards slanted branch does not exist. The next three patterns e, f and g involve excited $4n + 2$ states and are split by $2E_z$ each. In all cases, the positively sloped branches are now again of NDC nature for a parallel lead polarisation. The first "V",

[30] $\epsilon_\Delta = 0$ in case of a triplet groundstate.
[31] In order to be able to tune the polarisation without dramatically affecting the Zeeman splitting for the SWCNT.

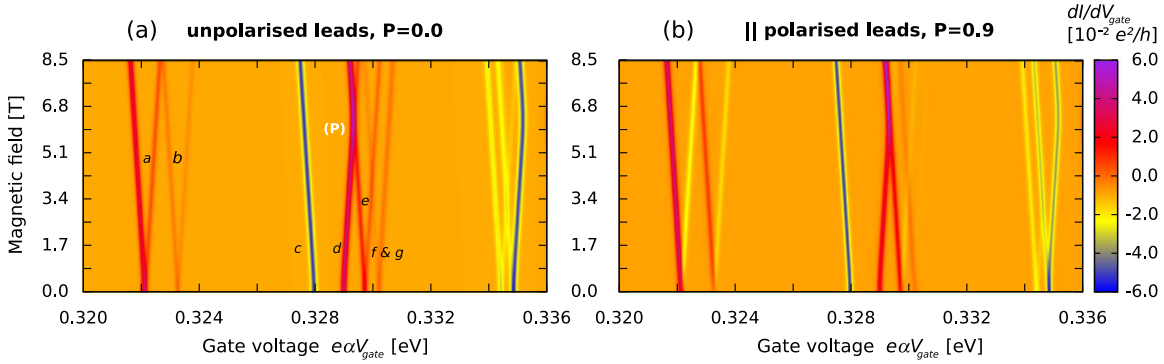

Figure 44: (a) Differential conductance $\mathrm{d}I/\mathrm{d}V_{\mathrm{gate}}$ for a B-field sweep in the case of an $|a\rangle$ ground-state and non-magnetic contacts. The applied bias voltage was fixed at 5.8 meV. Red lines indicate transitions that become possible at a certain gate voltage and blue lines show a transition that drops out of the transport window. Under the influence of the magnetic field, most lines are split in "V"-like manner by $2E_z$. (b) Ferromagnetic leads, polarised in parallel with $P = 0.9$, are assumed. This changes the intensity of the transitions, while their positions are preserved. Moreover, transitions to excited states involving spin-down electrons are disfavoured channels and hence converted from positive to negative differential conductance lines.

pattern e, belongs to the triplet and is of stronger intensity than the following two. The transitions $|\uparrow,\cdot\rangle \leftrightarrow |t_1\rangle$ and $|\downarrow,\cdot\rangle \leftrightarrow |t_0\rangle$ contribute to the negatively sloped part, while $|\uparrow,\cdot\rangle \leftrightarrow |t_0\rangle$ and $|\downarrow,\cdot\rangle \leftrightarrow |t_{-1}\rangle$ are responsible for the rightwards slanted branch. The crossing of the e and d lines occurring at $B \cong 6\,\mathrm{T}$, point (P), indicates *the change of the groundstate from* $|a\rangle$ *to the state* $|t_1\rangle$.
From the triplet pattern e an additional gate voltage equal to the exchange energy J is needed to arrive at the last two "V" - shaped patterns f and g. Compared to the lines for the triplet transition they are quite close to each other and of less intensity. These lines belong to a transition from both the $|\downarrow,\cdot\rangle$ and the $|\uparrow,\cdot\rangle$ states to the $|s\rangle$ (pattern f) and the $|b\rangle$ state (pattern g). Finally, the lines on the right edges of the plots are mirror images and belong to backward transitions from $4n+2 \rightarrow 4n+1$. For this reason they mark a decrease of current for both polarised and unpolarised leads.

5.3.3 Higher order level renormalisation

An important quantity in spin-polarised transport is the tunnelling magneto-resistance,

$$\mathrm{TMR} := \frac{I_{PA} - I_{AP}}{I_{AP}},$$

giving a measure for the ratio between the current in a parallel, I_{PA}, and an anti-parallel, I_{AP}, lead configuration.

Interestingly, in many experiments on spin-polarised transport in SWCNTs, a gate voltage dependent TMR which periodically becomes negative has been observed [14, 140], whereas second order transport theory predicts for equal lead polarisations $P_s = P_d = P$ and a coupling asymmetry $\gamma = \Gamma_s/\Gamma_d$ in the linear bias regime a constant

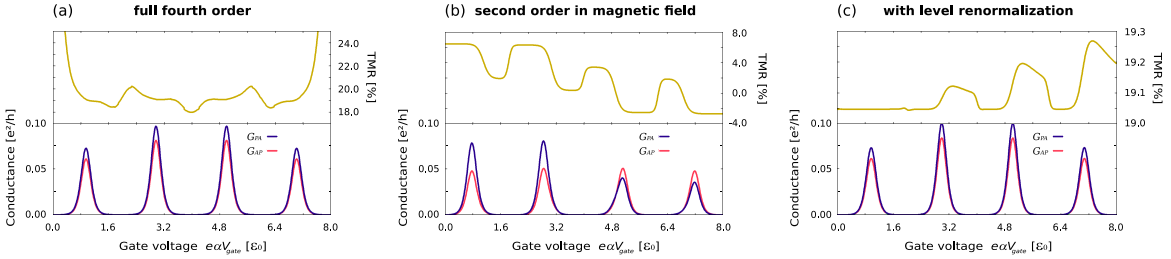

Figure 45: Parallel (I_{PA}) and anti-parallel (I_{AP}) current along with the resulting tunnelling magneto-resistance (TMR) for a large diameter SWCNT of 500 nm length and without band-mismatch. The thermal energy was set to $k_BT = 0.3\,\text{meV}$, the contact polarisation to $P = 0.4$, and a symmetric tunnelling coupling $\hbar\Gamma_s = \hbar\Gamma_d = 3\,\mu\text{eV}$ was chosen. (a) For a full fourth order calculation a mirror-symmetric TMR slightly oscillating around a value of 20% is obtained. (b) In magnetic field, a Zeeman splitting can cause negative values of the TMR (without inclusion of any fourth order contributions). (c) Taking into account level renormalisation terms to all orders, huge qualitative changes in the gate voltage dependence of the TMR arise.

value of [31]

$$\text{TMR} = \frac{4\gamma P^2}{(1-P^2)\,(1+\gamma)^2}.$$

It is thus reasonable to investigate the TMR under inclusion of higher orders in transport. We concentrate on a large diameter SWCNT without band-mismatch and further specifications as listed in the caption of Fig. 45. The outcome of a full consistent fourth order calculation according to the theory presented in Sect. 1 is shown in Fig. 45(a). A polarisation of $P = 0.4$ and a symmetric coupling to the leads, i.e. $\gamma = 1$, was assumed. The TMR has acquired an oscillatory gate voltage dependence, but the variation is rather small. Notice that the increase at the edges of the plot is non-physical, stemming from a limitation of the numerical calculation to six charge states. Thus, the average value of the TMR is about 0.19, i.e. slightly higher than the prediction of 0.16 from the formula for the sequential regime and far away from becoming negative, indicating that perturbation to fourth order in the tunnelling is clearly missing a crucial ingredient.

An assured source of negative TMR is a Zeeman splitting in the SWCNT [32, 149]. The origin of the splitting can be stray fields as well as phase shifts picked up by the electrons on reflection at the interface to the ferromagnetic contacts [149]. The mechanism causing negative TMR, as seen in Fig. 45(b), is that among the formerly degenerate lowest lying states, the ones with maximum spin-projection S_z are selected as ground-states. Specifically, those are $|\cdot,\cdot\rangle$ for $N_c = 4n$, $|\uparrow,\cdot\rangle$ and $|\uparrow,\cdot\rangle$ for $N_c = 4n+1$, $|\uparrow,\uparrow\rangle$ for $N_c = 4n+2$, $|\uparrow,\uparrow\downarrow\rangle$ and $|\uparrow\downarrow,\uparrow\rangle$ for $N_c = 4n+3$ and $|\uparrow\downarrow,\uparrow\downarrow\rangle$ for $N_c = 4(n+1)$. Hence transport is mediated by $\uparrow$ - electrons at the first two, by $\downarrow$ - electrons at the last two resonances. For an anti-parallel magnetisation of the contacts, both spin species are minority charge carriers in one of the two leads and thus provide equally weak transport channels. The mirror-symmetry of the conductance with respect to

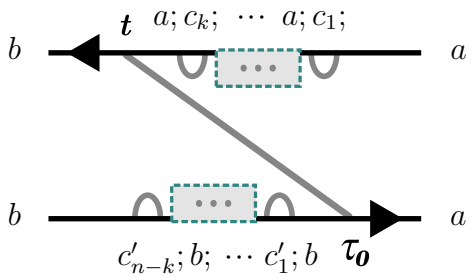

Figure 46: Level renormalisation diagram with k charge fluctuations in the initial and $n-k$ charge fluctuations in the final state.

the $N_c = 4n+2$ filling is thus preserved, see Fig. 45(b), red curve. For a parallel configuration, however, transport via the $\uparrow$ - electron channel is strongly preferred, while the rare density of $\downarrow$ - electrons in both contacts limits that channel. This breaks the symmetry in the conductance curve, by enhancing the first two peaks while suppressing the last two. Further, the heights of the first and second, as well as of third and fourth resonance peak, equalise. Typically, for a large diameter SWCNT without band-mismatch, a sequence of peak heights as in Fig. 45(a) and (c) is expected, due to the sixfold degeneracy of the $4n+2$ groundstate, compared to the unique groundstate for $N_c = 4n$ [25]. In magnetic field, the degeneracy is lifted and mainly the single state $|\uparrow,\uparrow\rangle$ contributes to transport, resulting in an assimilation of peak heights. All in all, a change of TMR from positive to negative values is expected and indeed observed around the half-filled shell $N_c = 4n+2$ in Fig. 45(b). The results exhibit similarity to the respective findings in Ref. [149], where, however, a non-equilibrium Green's function approach non-perturbative in the tunnelling coupling was used. What concerns experimental data, see Fig. 47(b), still the shape of the magnetic field induced TMR poorly matches the measurements.

At this point, an observation made before in Sect. 2 comes into play: we noticed that certain diagrams, namely the ones describing charge fluctuations during a tunnelling process, contain the first term of a Taylor expansion in a spin-dependent level renormalisation, i.e. an effective Zeeman splitting. This nourishes the presumption that there should exist a class of diagrams, which, summed up in all orders, yields the whole Taylor series and therewith an actual level shift. A promising choice is a diagram associated to multiple charge fluctuations during a tunnelling event, as shown e.g. in Fig. 46.

That sketch stands for a diagram of order $2n+2$ which corrects the tunnel event $|a\rangle \to |b\rangle$ by k charge fluctuations in the initial state, i.e. k "bubbles" on the upper contour, and $n-k$ charge fluctuations in the final state, translating in $n-k$ "bubbles" on the lower contour. We thereby look at fluctuations isolated, in the sense of separated in time, from each other: each bubble must start and end at consecutive times τ_i, τ_{i+1} $(1 \le i,j \le 2n-1)$. The electron transfer event is initialised at the earliest time $\tau = \tau_0$, and ending at the latest time $\tau_{2n+1} = t$. This gives $\binom{n}{k}$ possibilities for the time ordering of the bubbles among the contours, and summing all those plus their

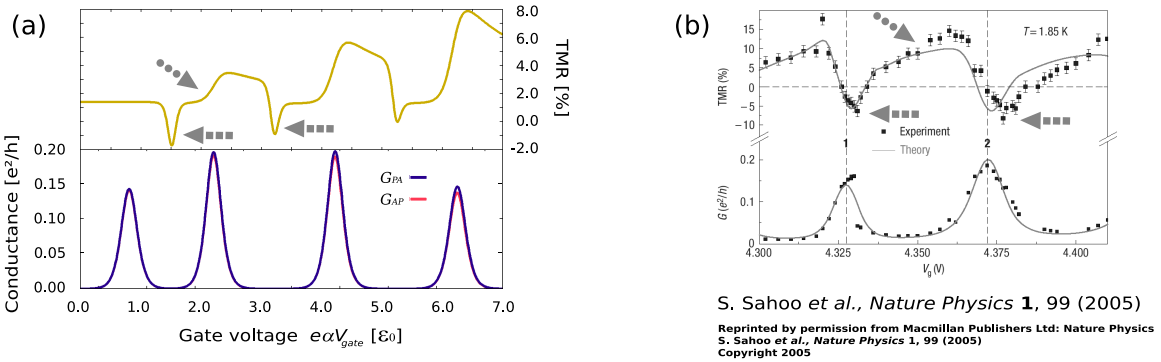

Figure 47: (a) On inclusion of level renormalisation terms in all orders, negative TMR occurs for a SWCNT asymmetrically coupled to the contacts. Except for $\Gamma_s = 0.02\Gamma_d$, all specification are the same as in Fig. 45. The asymmetric coupling has amended dips negative to the characteristic shape of the level renormalised TMR curve Fig. 45(c). (b) Though we selected only a tiny subset of terms relevant for all order transport calculations, experimental data [14] exhibits dips and shoulders of striking similarity to our results. Notice that our curves can just give an outlook to all order effects. For quantitative agreement, concerning both TMR magnitude and dip positions, a more systematic inclusion of higher order contributions to transport is required.

hermitian conjugates, the total contribution is:

$$\begin{aligned}
&\binom{n}{k}\mathsf{Re}\,\frac{2\mathrm{i}}{\hbar}\int \mathrm{d}\omega f_l^p(\omega)\left(\frac{1}{-p\omega - E_{ab} + \mathrm{i}\eta}\right)^{n+1} |T_{l\sigma}^p(a,b)|^2 \\
&\qquad\times\left[\prod_{j=1}^{k}\int \mathrm{d}\omega_j \frac{f_{l_j}^{p_j}(\omega_j)\left|T_{l_j\sigma_j}^{p_j}(c_j,a)\right|^2}{p_j\omega_j - E_{c_jb} - p\omega + \mathrm{i}\eta}\prod_{i=1}^{n-k}\int \mathrm{d}\omega_i \frac{f_{l_i}^{p_i}(\omega_i)\left|T_{l_i\sigma_i}^{p_i}(c_i',b)\right|^2}{-p_i\omega_i - E_{ac_i'} - p\omega + \mathrm{i}\eta}\right] \\
&= \binom{n}{k}\mathsf{Re}\,\frac{2\mathrm{i}}{\hbar}\int \mathrm{d}\omega f_l^p(\omega)\frac{1}{n!}\left(\frac{\mathrm{d}}{\mathrm{d}^n E_{ab}}\frac{1}{-p\omega - E_{ab} + \mathrm{i}\eta}\right)|T_{l\sigma}^p(a,b)|^2 \\
&\qquad\times\left[\prod_{j=1}^{k}\int \mathrm{d}\omega_j \frac{f_{l_j}^{p_j}(\omega_j)\left|T_{l_j\sigma_j}^{p_j}(c_j,a)\right|^2}{p_j\omega_j - E_{c_jb} - p\omega + \mathrm{i}\eta}\prod_{i=1}^{n-k}\int \mathrm{d}\omega_i \frac{f_{l_i}^{p_i}(\omega_i)\left|T_{l_i\sigma_i}^{p_i}(c_i',b)\right|^2}{-p_i\omega_i - E_{ac_i'} - p\omega + \mathrm{i}\eta}\right].
\end{aligned}$$

Here c_j, c_i' serve as placeholders for the possible intermediate states; the lead indices $l, l_i, l_j \in \{s, d\}$ as well as the spin indices $\sigma, \sigma_i, \sigma_j$ are summed over in general.
A whole bunch of terms emerges from this expression when applying the decomposition Eq. (126), page 168, for all fractions and expanding the product. We want to zoom on a certain one, namely the combination where the first fraction, involving merely ω, has been replaced by the delta function, and all others by their principal parts.
In terms of $f^+(\omega) = f(\omega) = (1+e^{\omega})^{-1}$, $f^-(\omega) = 1 - f(\omega)$, $f^{(n)}(\omega) = \frac{\mathrm{d}}{\mathrm{d}^n\omega} f(\omega)$, consult Eq. (122) for the necessary transformations, it reads:

$$\frac{2\pi}{\hbar}\frac{1}{n!}f^{(n)}(\beta E_{ba}+\beta peV_l)\left|T^p_{l\sigma}(a,b)\right|^2$$
$$\times\beta^n\binom{n}{k}\mathsf{Re}\left[\prod_{j=1}^{k}\int'\mathrm{d}\omega_j\frac{f^+(\omega_j)\left|T^{p_j}_{l_j\sigma_j}(c_j,a)\right|^2}{\omega_j-\beta E_{c_ja}-p_j\beta eV_{l_j}}\prod_{i=1}^{n-k}\int'\mathrm{d}\omega_i\frac{f^-(\omega_i)\left|T^{p_i}_{l_i\sigma_i}(c'_i,b)\right|^2}{\omega_i-\beta E_{bc'_i}+p_i\beta eV_{l_i}}\right]$$
$$=\frac{2\pi}{\hbar}\frac{1}{n!}f^{(n)}(\beta E_{ba}+\beta peV_l)\left|T^p_{l\sigma}(a,b)\right|^2\prod_{j=1}^{k}\left[\left|T^{p_j}_{l_j\sigma_j}(a,c_j)\right|^2\Psi^{(0)}\left(\frac{1}{2}+\frac{\mathrm{i}\beta(E_{c_ja}+p_jeV_{l_j})}{2\pi}\right)\right]$$
$$\times\beta^n\binom{n}{k}\prod_{i=1}^{n-k}\left[-\left|T^{p_i}_{l_i\sigma_i}(c'_i,b)\right|^2\Psi^{(0)}\left(\frac{1}{2}-\frac{\mathrm{i}\beta(E_{c'_ib}+p_ieV_{l_i})}{2\pi}\right)\right].$$

Exhausting all possibilities of choosing the states c_j, c'_i as well as setting $k=1\cdots n$, it is clear that one generates all kinds of terms appearing in an expansion of the power n of a quantity Δ_{ba} defined as

$$\Delta_{ba}=\sum_{p\in\{+,-\}}\sum_{l\in\{s,d\}}\sum_{\sigma}\left(\sum_{c}\left|T^p_{l\sigma}(c,a)\right|^2\Psi^{(0)}\left(\frac{1}{2}+\frac{\mathrm{i}\beta(E_{ca}+peV_l)}{2\pi}\right)\right.$$
$$\left.-\sum_{c'}\left|T^p_{l\sigma}(c',b)\right|^2\Psi^{(0)}\left(\frac{1}{2}-\frac{\mathrm{i}\beta(E_{c'b}+peV_l)}{2\pi}\right)\right),\quad(103)$$

where c and c' run over all states connected to $|a\rangle$ respectively $|b\rangle$ via a charge fluctuation. In total, we obtain the nth term $\frac{2\pi}{\hbar}\frac{1}{n!}f^{(n)}(\beta(E_{ba}+peV_l))\left|T^p_{l\sigma}(a,b)\right|^2(\beta\Delta_{ba})^n$ in the Taylor expansion of a Fermi function $\frac{2\pi}{\hbar}f(\beta(E_{ba}+eV_l+\Delta_{ba}))\left|T^p_{l\sigma}(a,b)\right|^2$. So effectively, the considered contribution of the initial and final state charge fluctuations renormalises any energy difference E_{ba} to $E_{ba}+\Delta_{ba}$.

An implementation of this selected effect in second order transport calculations leads to results as shown in Fig. 45(c) and Fig. 47(a). While the zero field conductances Fig. 45(a) and Fig. 45(c) can hardly be distinguished by eye, the impact on the TMR is tremendous: although its value still ranges around 0.19, the line shape has changed completely, exhibiting now pronounced periodic humps as in the magnetic field case, but of distinct appearance. In an effort to compare to experimental data, we produced as an outlook Fig. 47(a), putting an asymmetry of $\gamma=0.02$ in the tunnelling coupling. This is an absolutely realistic value for the ratio between the contact transparencies [14], as experiments on spin polarised transport across quantum-dots exploit asymmetric contact geometries to allow a switching of the leads to an anti-parallel magnetisation[32]. Amazingly, we succeeded not only to obtain negative TMR, but also characteristic features clearly resolved in the experimental data Fig. 47(b): the negative TMR occurs at narrow dips (dashed arrows) and shoulders in the TMR emerge

[32] Typically, the contacts considerably differ in width. Performing a magnetic field sweep, due to hysteresis effects, the contact magnetisation flips at a finite opposite field, and in particular the field strength required for the switching depends on the contact width. Hence, for some range of the magnetic field an anti-parallel configuration is obtained.

(dotted arrow). Discrepancy between our curves and the measured data is clearly observed in the relative positions of conductance peaks and TMR dips, but at this level, missing in any case a consistent inclusion of higher order effects, quantitative agreement should neither be expected nor enforced by a multi-parameter fit.
Instead, the message is that an effective, gate voltage dependent Zeeman splitting induced by initial and final state charge fluctuation certainly plays a role for the occurrence of negative TMR in transport across SWCNTs. In the same way as for the sequential tunnelling, charge fluctuations during inelastic cotunnelling (appearing first in sixth order) give a renormalisation of the inelastic cotunnelling threshold. In the Kondo regime, measurements [15] have already quantitatively determined the effectively acting Zeeman splitting. Besides a constant background, a gate voltage dependent level renormalisation in the same form as contained in Eq. (103) has been found.

5.4 Conclusion

We have shown results on spin dependent transport through fully interacting single wall carbon armchair nanotubes (SWCNTs) in both the linear and the nonlinear regime, with and without an applied magnetic field.
Peculiar of metallic small diameter SWCNTs is the possibility, due to exchange interactions, to find the system at a filling with $4n+2$ electrons either in a groundstate of total spin $S = 0$ or $S = \hbar$. Which of the two groundstates occurs in a real nanotube depends on the relation between the exchange energy and the orbital band-mismatch. Thus, with focus on transitions involving $4n+1 \leftrightarrow 4n+2$ fillings, we investigated both situations and demonstrated pronounced differences in the current-voltage characteristics depending on the considered groundstate.
For example in the linear regime the conductance for parallel lead magnetisation and finite magnetic field increases by raising the polarisation for the case of a triplet groundstate but it decreases for the $S = 0$ groundstate. This is due to the fact that for the triplet groundstate transport is dominated by a majority electron channel involving the triplet state with both spins aligned along the external field ($S_z = +\hbar$). For the $S = 0$ case transport via this preferred channel requires to make use of a $N_c = 4n+1$ states with $S_z = -\hbar/2$, which is Zeeman split from the groundstate and hence less favourable.
In the nonlinear regime we presented stability diagrams with parallel and anti-parallel lead magnetisation for both groundstates. In the anti-parallel case it was possible to observe a negative differential conductance (NDC) effect for the $S = 0$ groundstate, following immediately after a conductance enhancement at the opening of a trapping channel to the excited triplet state with $S_z = -\hbar$. Right at that resonance, electrons can, just by thermal activation, tunnel back *and* fourth, such that trapping can not yet act, leading to an intermediate conductance increase. Away from resonance, the blocking effect fully occurs, resulting in the NDC.
We also showed results for the differential conductance versus gate voltage and magnetic field at a finite fixed value of the bias. These magnetic field sweeps allow to

instantaneously recognise the nature of the $4n+2$ filling groundstate at zero field, as well as to tune the nature of the groundstate from $S=0$ to $S_z=\hbar$ upon variation of the field amplitude. Our results for unpolarised leads *quantitatively* reproduce experimental data of Moriyama *et al.* [141] on a small-diameter SWCNT. Importantly, the sweep at zero field also permits to directly read off the values of the short-range quantities J and u^+. Specifically, J is the singlet-triplet exchange splitting and u^+ characterises at zero orbital mismatch the energy difference between two of the low energy states of total spin $S=0$. In the presence of polarised leads the magnetic field sweep also reveals lines of NDC due to the trapping nature of all $\downarrow$ - channels.

The outcomes of our theory are in quantitative agreement with experimental results obtained so far for unpolarised leads [141, 142, 143]. Due to recent achievements on spin-polarised transport in SWCNTs [14, 140, 15], our predictions on spin-dependent transport are within the reach of present experiments.
Those suggest also several extension of the applied theory, towards the regime of half-filling, the inclusion of spin-orbit coupling as well as of vibrational degrees of freedom. The latter two issues are subject of current investigations carried out by my colleagues Magdalena Margańska-Łyżniak (spin-orbit coupling) and Abdullah Yar (vibrations).

Concerning higher order effects in SWCNTs, which have been subject of various recent research activities, we sketched how an inclusion of terms in all orders of the tunnelling coupling can lead to a spin-dependent level renormalisation, giving rise to oscillations and sign inversion in the tunnelling magneto-resistance similar to experimental observations. The logical continuation of the presented outlook is a systematic and consistent investigation of such effects.

Related publications:

C. Schenke, S. Koller, L. Mayrhofer, M. Grifoni. Phys. Rev. B **80**, 035412 (2009)
Exchange effects in spin polarized transport through carbon nanotube quantum-dots. [144]

S. Koller, J. Paaske, M. Grifoni. In preparation.
Tunneling induced level shifts in diagrammatic language.[33]

[33] The title of the final publication might differ.

ACKNOWLEDGEMENT:

Ein Dankeschön

In the course of the approx. 3.6 years for which I have by now been part of Milena Grifoni's 'Quantum Transport and Spintronics' group, there have been many occasions which I remember with pleasure and gratitude. I want to give my thanks to all of you people who shared one or more of those moments with me, and I hope you have the same happy memory of them as I.

In direct connection with the scientific content of my work I want to thank first of all my doctoral mother Milena Grifoni, my office mate Andrea Donarini and my carbon nanotube and -ribbon advisor Leo Mayrhofer, as well as my transport fellow Georg Begemann, the nanotube lady Magdalena Marganska-Łyżniak, my collaborator and host in Copenhagen Jens Paaske and my collaborators from Aachen Maarten Wegewijs and Martin Leijnse. All of them have, more than once, sacrificed their time for enlightening discussions which really brought forward my understanding of physics. Further I enjoyed a fruitful and nice collaboration with the former diploma students Peter Hornberger and Christoph Schenke.

Moral support was provided by numerous members of the group, of my family and my circle of friends. Be assured that I have not forgotten your kind words, though space is too limited to mention all of you at this place; let me representatively as well as in particular name Dana Darau, my parents Renate and Helmut Koller, and Johannes Kolb. Lizy Lazar deserves to be called the group's fairy godmother, not only because she assists in all kinds of bureaucratic affairs. Of those, my colleague Sergey Smirnov and me overcame quite some during the last pre-doctorate weeks.

Common trips are always good opportunities to get better known to each other, and I gladly recall the 21st IWEPNM in Kirchberg (Tirol), the DPG meetings in Berlin 2008 and in Dresden 2009, two beautiful group excursions to the alps and several day-trips around Regensburg, the spanish-italian wedding in El Bierzo and a day-trip to the Asturias coast, the 4th Capri Spring School and my time in Copenhagen. Another possibility is to sit in the same office; Dear Andrea, it was always an honour for me! All the best to you and your girls Miriam DelValle and Sara Donarini DelValle.

Many of my collegues gave me an insight to culture, religion, ways of life and conditions in their home countries, among those Italy, Spain, Danmark, Poland, Pakistan, Romania, Russia, Brazil and China. In this spirit:

MILLE GRAZIE  MUCHAS GRACIAS  MANGE TAK

DZIĘKUJĘ BARDZO  مننه  MULŢUMESC MULT

БОЛЬШОЕ СПАСИБО  MUITO OBRIGADO  謝謝

My work was supported by the DFG under the program SFB 689.

Last but not least, I want to thank
Andreas Schäfer, Klaus Rith and Klaus Mecke
for their dedication to the accelerated course ‘Physik mit integriertem Doktorandenkolleg’ in the framework of the ‘Elitenetzwerk Bayern’.

APPENDIX A:

TRANSPORT THEORY

This first appendix relates completely to the transport theoretical sections Sect. 1 and Sect. 2. It provides several amendments to the main text. Thereby, Sect. A.1, holds, for the interested reader, information ancillary to Sect. 1.2. In contrast, Sect. A.2 works out details on the explicit evaluation of kernel elements from Sect. 2.1. In particular, Sect. A.2.4 provides a full list of irreducible contributions in second and fourth order, both as analytical expressions and in terms of diagrams. Finally, App. A.3 is dedicated to details on the diagram grouping, Sect. 2.3.

A.1 Derivation of the quantum master equation

In the first subsections, Sect. A.1.1, the question about a time-local fourth order quantum master equation is addressed, in the second subsection Sect. A.1.2 we shortly revise two derivations of the time-nonlocal fourth order quantum master equation which a completely equivalent to the approach presented in the main text.

A.1.1 A time-local 4QME

Assume we could find a generalised *time-local* quantum master equation, i.e.,

$$\dot{\hat{\rho}}_{\odot}(t) = -\frac{\mathrm{i}}{\hbar}\left[\hat{H}_0, \hat{\rho}_{\odot}(t)\right] + \int_{t_0}^{t} \mathrm{d}t'\; \hat{\mathcal{F}}(t-t')\hat{\rho}_{\odot}(\boldsymbol{t}). \tag{104}$$

The steady state limit of this equation obviously yields the form of Eq. (7), *without* performing the Laplace transform:

$$\lim_{t\to\infty}\lim_{t_0\to-\infty} \dot{\hat{\rho}}_{\odot}(t) = 0 = -\frac{\mathrm{i}}{\hbar}\left[\hat{H}_0, \hat{\rho}_{\odot}^{\infty}\right] + \int_{0}^{\infty} \mathrm{d}\tau'\, \hat{\mathcal{F}}(\tau')\, \hat{\rho}_{\odot}^{\infty}. \tag{105}$$

In fact we have mentioned in Sect. 1.2 during the derivation of the time-nonlocal kinetic equation how to equivalently obtain the time-local form. Namely, instead of Eq. (20) we must set into Eq. (19) the relation

$$\hat{\rho}_{\odot}^{I}(t_0) = \hat{\rho}_{\odot}^{I}(t) + \int_{t_0}^{t} \mathrm{d}\tau_1 \int_{t_0}^{\tau_1} \mathrm{d}\tau\; \mathsf{Tr}_R\left\{\hat{\mathcal{L}}_T^I(\tau_1)\hat{\mathcal{L}}_T^I(\tau)\hat{\rho}_{\odot}^I(\tau)\hat{\rho}_R\right\} + \mathcal{O}\left((\hat{\mathcal{L}}_T^I)^4\right), \tag{106}$$

which directly emerges from Eq. (17) upon tracing out the leads. One obtains

$$
\begin{aligned}
\dot{\hat{\rho}}^I_\odot(t) = \quad & - \int_{t_0}^{t} \mathrm{d}\tau \; \mathsf{Tr}_R \left\{ \hat{\mathcal{L}}^I_T(t) \hat{\mathcal{L}}^I_T(\tau) \hat{\rho}_\odot(t) \hat{\rho}_R \right\} \\
\text{(i)} \quad & + \int_{t_0}^{t} \mathrm{d}\tau_2 \int_{t_0}^{\tau_2} \mathrm{d}\tau_1 \int_{t_0}^{\tau_1} \mathrm{d}\tau \; \mathsf{Tr}_R \left\{ \hat{\mathcal{L}}^I_T(t) \hat{\mathcal{L}}^I_T(\tau_2) \hat{\mathcal{L}}^I_T(\tau_1) \hat{\mathcal{L}}^I_T(\tau) \hat{\rho}^I_\odot(t) \hat{\rho}_R \right\} \\
\text{(ii)} \quad & - \int_{t_0}^{t} \mathrm{d}\tau_2 \int_{t_0}^{\tau_2} \mathrm{d}\tau_1 \int_{t_0}^{\tau_1} \mathrm{d}\tau \; \mathsf{Tr}_R \left\{ \hat{\mathcal{L}}^I_T(t) \hat{\mathcal{L}}^I_T(\tau_2) \mathsf{Tr}_R \left\{ \hat{\mathcal{L}}^I_T(\tau_1) \hat{\mathcal{L}}^I_T(\tau) \hat{\rho}^I_\odot(t) \hat{\rho}_R \right\} \hat{\rho}_R \right\} \\
\text{(iii)} \quad & - \int_{t_0}^{t} \mathrm{d}\tau_2 \int_{t_0}^{\tau_2} \mathrm{d}\tau_1 \int_{t_0}^{\tau_1} \mathrm{d}\tau \; \mathsf{Tr}_R \left\{ \hat{\mathcal{L}}^I_T(t) \hat{\mathcal{L}}^I_T(\tau_1) \mathsf{Tr}_R \left\{ \hat{\mathcal{L}}^I_T(\tau_2) \hat{\mathcal{L}}^I_T(\tau) \hat{\rho}^I_\odot(t) \hat{\rho}_R \right\} \hat{\rho}_R \right\} \\
\text{(iv)} \quad & - \int_{t_0}^{t} \mathrm{d}\tau_2 \int_{t_0}^{\tau_2} \mathrm{d}\tau_1 \int_{t_0}^{\tau_1} \mathrm{d}\tau \; \mathsf{Tr}_R \left\{ \hat{\mathcal{L}}^I_T(t) \hat{\mathcal{L}}^I_T(\tau) \mathsf{Tr}_R \left\{ \hat{\mathcal{L}}^I_T(\tau_2) \hat{\mathcal{L}}^I_T(\tau_1) \hat{\rho}^I_\odot(t) \hat{\rho}_R \right\} \hat{\rho}_R \right\},
\end{aligned}
\tag{107}
$$

where we have exploited the following integral transformations to come to the time-convolutionless quantum-master equation in a common form [37]:

$$
\int_{t_0}^{t} \mathrm{d}\tau_2 \int_{t_0}^{t} \mathrm{d}\tau_1 \int_{t_0}^{\tau_1} \mathrm{d}\tau \rightarrow \boxed{\int_{t_0}^{t} \mathrm{d}\tau_2 \int_{t_0}^{\tau_2} \mathrm{d}\tau_1 \int_{t_0}^{\tau_1} \mathrm{d}\tau} + \int_{t_0}^{t} \mathrm{d}\tau_2 \int_{\tau_2}^{t} \mathrm{d}\tau_1 \int_{t_0}^{\tau_1} \mathrm{d}\tau
$$

$$
\int_{t_0}^{t} \mathrm{d}\tau_2 \int_{\tau_2}^{t} \mathrm{d}\tau_1 \int_{t_0}^{\tau_1} \mathrm{d}\tau \rightarrow \int_{t_0}^{t} \mathrm{d}\tau_1 \int_{t_0}^{\tau_1} \mathrm{d}\tau_2 \int_{t_0}^{\tau_1} \mathrm{d}\tau \rightarrow \boxed{\int_{t_0}^{t} \mathrm{d}\tau_1 \int_{t_0}^{\tau_1} \mathrm{d}\tau_2 \int_{t_0}^{\tau_2} \mathrm{d}\tau} + \int_{t_0}^{t} \mathrm{d}\tau_1 \int_{t_0}^{\tau_1} \mathrm{d}\tau_2 \int_{\tau_2}^{\tau_1} \mathrm{d}\tau
$$

$$
\int_{t_0}^{t} \mathrm{d}\tau_1 \int_{t_0}^{\tau_1} \mathrm{d}\tau_2 \int_{\tau_2}^{\tau_1} \mathrm{d}\tau \rightarrow \boxed{\int_{t_0}^{t} \mathrm{d}\tau_1 \int_{t_0}^{\tau_1} \mathrm{d}\tau \int_{t_0}^{\tau} \mathrm{d}\tau_2}
$$

Further, we were free to replace in the fourth order terms τ by t as this yields only corrections of the order $(\hat{\mathcal{L}}^I_T)^6$. For details on relation and equivalence with respect to out time-nonlocal variant Eq. (21), we recommend the work of C. Timm, Ref. [33], containing a broad discussion of the time-local fourth order quantum master equation.

A.1.2 Alternative derivations of the time-nonlocal 4QME

The main text referred to two alternative approaches to obtain Eq. (21) respectively Eqs. (22a), (22b). As both methods are well-know, the aim of this section is a brief review of the notation and the steps involved in the derivation of the time evolution kernel in the time-domain, which is performed concisely in the interaction picture. This enables a straightforward comparison to Sect. 1.2. Hereby, the current kernels are not explicitly addressed as they relate in a similar fashion.

A.1.3 Nakajima-Zwanzig projection operator technique

The standard Nakajima-Zwanzig projection operator technique [35, 36] allows for a compact and concise derivation of an exact expression for the kernel, see e.g. [37, 38] and the references therein. One decomposes the total density matrix according to $\hat{\rho}^I_{\mathsf{tot}} = \hat{\mathcal{P}} \hat{\rho}^I_{\mathsf{tot}} + \hat{\mathcal{Q}} \hat{\rho}^I_{\mathsf{tot}}$, thereby using operators $\hat{\mathcal{P}} = \hat{\rho}_R \mathsf{Tr}_R$ and $\hat{\mathcal{Q}} = 1 - \hat{\mathcal{P}}$. These allow to project the interaction-picture Liouville equation Eq. (14) for the full system

$$
\hat{\mathcal{P}} \dot{\hat{\rho}}^I_{\mathsf{tot}}(t) = -\mathrm{i}\, \hat{\mathcal{P}} \hat{\mathcal{L}}^I_T(t) \hat{\mathcal{Q}}\, \hat{\rho}^I_{\mathsf{tot}}(t) \tag{108a}
$$

$$
\hat{\mathcal{Q}} \dot{\rho}^I_{\mathsf{tot}}(t) = -\mathrm{i}\, \hat{\mathcal{Q}} \hat{\mathcal{L}}^I_T(t) \hat{\mathcal{Q}} \hat{\rho}^I_{\mathsf{tot}}(t) - \mathrm{i}\, \hat{\mathcal{Q}} \hat{\mathcal{L}}^I_T(t) \hat{\mathcal{P}} \rho^I_{\mathsf{tot}}(t) \tag{108b}
$$

Here, the crucial property $\hat{\mathcal{P}}\hat{\mathcal{L}}_T^I(t)\hat{\mathcal{P}} = 0$ was used, which is due to the fact that the tunnelling Hamiltonian, Eq. (2), and thus also $\hat{\mathcal{L}}_T^I$, Eq. (15), contains exactly one lead operator: the trace must yield zero. Next, the second equation is formally integrated using $\hat{\mathcal{Q}}\hat{\rho}_{\text{tot}}^I(t_0) = 0$ and treating the term with $\hat{\mathcal{P}}\rho_{\text{tot}}^I$ as a given inhomogeneous term:

$$\hat{\mathcal{Q}}\hat{\rho}_{\text{tot}}^I(t) = -\mathrm{i}\int_{t_0}^{t} \mathrm{d}\tau\ \hat{\mathcal{T}} e^{-\mathrm{i}\int_\tau^t \mathrm{d}\tau \hat{\mathcal{Q}}\hat{\mathcal{L}}_T^I(\tau)\hat{\mathcal{Q}}} \underbrace{\hat{\mathcal{Q}}\hat{\mathcal{L}}_T^I(\tau)\hat{\mathcal{P}}}_{=\hat{\mathcal{L}}_T^I(\tau)\hat{\mathcal{P}}} \hat{\rho}_{\text{tot}}^I(\tau). \tag{109}$$

Here $\hat{\mathcal{T}}$ is the time-ordering superoperator as introduced before in Sect. 1.1. Substitution into Eq. (108a) and exploiting $\hat{\mathcal{P}}\hat{\rho}_{\text{tot}}^I(\tau) = \hat{\rho}_R\hat{\rho}_\odot^I(\tau)$ gives the kinetic equation Eq. (23) with the formally exact kernel:

$$\hat{\mathcal{K}}^I(t,\tau)[\hat{\rho}_\odot^I(\tau)] = -\mathsf{Tr}_R\left\{\hat{\mathcal{T}}\hat{\mathcal{L}}_T^I(t)e^{-\mathrm{i}\hat{\mathcal{Q}}\int_\tau^t \mathrm{d}\tau\hat{\mathcal{L}}_T^I(\tau)\hat{\mathcal{Q}}}\hat{\mathcal{L}}_T^I(\tau)\hat{\rho}_\odot^I(\tau)\hat{\rho}_R\right\}, \tag{110}$$

which contains a non-trivial evolution operator that can be expanded in the perturbation $\hat{\mathcal{Q}}\hat{\mathcal{L}}_T^I(\tau)\hat{\mathcal{Q}}$,

$$e^{-\mathrm{i}\hat{\mathcal{Q}}\int_\tau^t \mathrm{d}\tau\hat{\mathcal{L}}_T^I(\tau)\hat{\mathcal{Q}}} = 1 - \mathrm{i}\int_\tau^t \mathrm{d}\tau_1\ \hat{\mathcal{Q}}\hat{\mathcal{L}}_T^I(\tau_1)\hat{\mathcal{Q}} - \int_\tau^t \mathrm{d}\tau_1\int_{\tau_1}^t \mathrm{d}\tau_2\ \hat{\mathcal{Q}}\hat{\mathcal{L}}_T^I(\tau_2)\hat{\mathcal{Q}}\hat{\mathcal{L}}_T^I(\tau_1)\hat{\mathcal{Q}} + \dots\ .$$

Inserting $\hat{\mathcal{Q}} = 1 - \hat{\mathcal{P}}$ everywhere and use that $\hat{\mathcal{P}}$ gives nonzero only when acting on an even number of $\hat{\mathcal{L}}_T^I$ by Wick's theorem, we obtain to fourth order the kernel

$$\begin{aligned}\hat{\mathcal{K}}^I(t,\tau)[\hat{\rho}_\odot^I(\tau)] = &-\mathsf{Tr}_R\left\{\hat{\mathcal{L}}_T^I(t)\hat{\mathcal{L}}_T^I(\tau)\hat{\rho}_\odot^I(\tau)\hat{\rho}_R\right\} \\ &+\int_\tau^t \mathrm{d}\tau_1\int_{\tau_1}^t \mathrm{d}\tau_2 \mathsf{Tr}_R\left\{\hat{\mathcal{L}}_T^I(t)\hat{\mathcal{L}}_T^I(\tau_2)(1-\hat{\mathcal{P}})\hat{\mathcal{L}}_T^I(\tau_1)\hat{\mathcal{L}}_T^I(\tau)\hat{\rho}_\odot^I(\tau)\hat{\rho}_R\right\}.\end{aligned} \tag{111}$$

Alternatively, on may also first integrate Eq. (108a) for $\hat{\mathcal{P}}\hat{\rho}_{\text{tot}}^I$ with initial condition $\hat{\mathcal{P}}\hat{\rho}_{\text{tot}}^I(t_0) = \hat{\rho}_{\text{tot}}^I(t_0)$:

$$\hat{\mathcal{P}}\hat{\rho}_{\text{tot}}^I(t) = \hat{\rho}_{\text{tot}}^I(t_0) - \mathrm{i}\int_{t_0}^t \mathrm{d}\tau_2\ \hat{\mathcal{P}}\hat{\mathcal{L}}_T^I(\tau_2)\hat{\mathcal{Q}}\hat{\rho}_{\text{tot}}^I(\tau_2) \tag{112}$$

Substitution of Eq. (109) into the right hand side of Eq. (112) and taking the trace gives an Dyson-type integro-differential equation for the reduced density operator $\hat{\rho}_\odot^I(t) = \mathsf{Tr}_R\hat{\mathcal{P}}\hat{\rho}_{\text{tot}}^I(t)$:

$$\hat{\rho}_\odot^I(t) = \hat{\rho}_\odot^I(t_0) - \mathsf{Tr}_R\int_{t_0}^t \mathrm{d}\tau_2\int_{t_0}^{\tau_2}\mathrm{d}\tau_1\ \hat{\mathcal{T}}\hat{\mathcal{L}}_T^I(\tau_2)e^{-\mathrm{i}\int_{\tau_1}^{\tau_2}\mathrm{d}\tau\hat{\mathcal{Q}}\hat{\mathcal{L}}_T^I(\tau_1)\hat{\mathcal{Q}}}\hat{\mathcal{L}}_T^I(\tau_1)\hat{\mathcal{P}}\hat{\rho}_{\text{tot}}^I(\tau_1).$$

This form allows to read off an equivalent equation for the *propagator* $\hat{\Pi}^I(t,t_0)$ defined via $\hat{\rho}_\odot^I(t) = \hat{\Pi}^I(t,t_0)\hat{\rho}_\odot^I(t_0)$, namely

$$\hat{\Pi}^I(t,t_0) = 1 + \int_{t_0}^t \mathrm{d}\tau_2\int_{t_0}^{\tau_2}\mathrm{d}\tau_1\ \hat{\mathcal{K}}^I(\tau_2,\tau_1)\,\hat{\Pi}^I(\tau_1,t_0), \tag{113}$$

which is helpful for the comparison to the real-time approach Sect. A.1.4.

A.1.4 Real-time diagrammatic technique

The real-time approach has been discussed on a general level in many works [39, 40, 19]. We shall just recall here how one efficiently arrives at the kinetic equation and its kernel by exploiting Wick's theorem. Starting from the Liouville equation Eq. (14) for the full system in the interaction picture and formally integrating it yields

$$\hat{\rho}^I_{\mathsf{tot}}(t) = \hat{\mathcal{T}} e^{-\mathrm{i}\int_{t_0}^{t} \mathrm{d}\tau \hat{\mathcal{L}}^I_T(\tau)} \hat{\rho}^I_{\mathsf{tot}}(t_0), \tag{114}$$

where $\hat{\mathcal{T}}$ is the time-ordering superoperator. Using $\hat{\rho}^I_{\mathsf{tot}}(t_0) = \hat{\rho}_{\mathsf{tot}}(t_0) = \hat{\rho}^I_R(t_0)\hat{\rho}^I_\odot(t_0)$, and defining the superoperator

$$\hat{\Pi}^I(t,t_0)\mathrm{X}^I = \mathsf{Tr}_R\left\{\hat{\mathcal{T}} e^{-\mathrm{i}\int_{t_0}^{t} \mathrm{d}\tau \hat{\mathcal{L}}^I_T(\tau)} \mathrm{X}^I \hat{\rho}_R(t_0)\right\}, \tag{115}$$

the time-evolution of the reduced density matrix can formally be written as:

$$\hat{\rho}^I_\odot(t) = \hat{\Pi}^I(t,t_0)\hat{\rho}^I_\odot(t_0). \tag{116}$$

Expanding the time-ordered exponential inside the superoperator, the trace over the leads can be explicitly evaluated term by term by Wick's theorem: Knowing that each Liouvillian contains exactly one reservoir operator, one formally builds all possible combinations for pair contractions between them, indicated by contraction lines. The propagator to fourth order then reads:

$$\begin{aligned}
\hat{\Pi}^I(t,t_0) =& 1 - \int_{t_0}^{t}\mathrm{d}\tau_3 \int_{t_0}^{\tau_3}\mathrm{d}\tau\ \hat{\mathcal{L}}^I_T(\tau_3)\hat{\mathcal{L}}^I_T(\tau) \\
&+ \int_{t_0}^{t}\mathrm{d}\tau_3 \int_{t_0}^{\tau_3}\mathrm{d}\tau_2 \int_{t_0}^{\tau_2}\mathrm{d}\tau_1 \int_{t_0}^{\tau_1}\mathrm{d}\tau \Bigg[\hat{\mathcal{L}}^I_T(\tau_3)\hat{\mathcal{L}}^I_T(\tau_2)\hat{\mathcal{L}}^I_T(\tau_1)\hat{\mathcal{L}}^I_T(\tau) \\
&+ \hat{\mathcal{L}}^I_T(\tau_3)\hat{\mathcal{L}}^I_T(\tau_2)\hat{\mathcal{L}}^I_T(\tau_1)\hat{\mathcal{L}}^I_T(\tau) + \hat{\mathcal{L}}^I_T(\tau_3)\hat{\mathcal{L}}^I_T(\tau_2)\hat{\mathcal{L}}^I_T(\tau_1)\hat{\mathcal{L}}^I_T(\tau) \Bigg] + \mathcal{O}\left((\hat{\mathcal{L}}^I_T)^6\right),
\end{aligned} \tag{117}$$

where $\hat{\mathcal{L}}^I_T(t)\hat{\mathcal{L}}^I_T(\tau) := \mathsf{Tr}_R\{\hat{\mathcal{L}}^I_T(t)\hat{\mathcal{L}}^I_T(\tau)\hat{\rho}_R\}$. Importantly, when pairing reservoir operators, the dot operators are left in their order. The crucial step is now to decompose $\hat{\Pi}^I(t,t_0)$ into a reducible and an irreducible part, depending on whether or not the contractions of the vertices separate into disconnected blocks. Collecting all irreducible parts into the kernel

$$\begin{aligned}
\hat{\mathcal{K}}^I(\tau_3,\tau) :=& -\hat{\mathcal{L}}^I_T(\tau_3)\hat{\mathcal{L}}^I_T(\tau) \\
&+ \int_{\tau}^{\tau_3}\mathrm{d}\tau_2 \int_{\tau}^{\tau_2}\mathrm{d}\tau_1 \left[\hat{\mathcal{L}}^I_T(\tau_3)\hat{\mathcal{L}}^I_T(\tau_2)\hat{\mathcal{L}}^I_T(\tau_1)\hat{\mathcal{L}}^I_T(\tau) + \hat{\mathcal{L}}^I_T(\tau_3)\hat{\mathcal{L}}^I_T(\tau_2)\hat{\mathcal{L}}^I_T(\tau_1)\hat{\mathcal{L}}^I_T(\tau) \right],
\end{aligned} \tag{118}$$

a Dyson equation in the same form as Eq. (113) is obtained:

$$\hat{\Pi}^I(t,t_0) = \mathbf{1} + \int_{t_0}^{t} \mathrm{d}\tau_3 \int_{t_0}^{\tau_3} \mathrm{d}\tau \; \hat{\mathcal{K}}^I(\tau_3,\tau)\hat{\Pi}^I(\tau,t_0). \tag{119}$$

The unity in Eq. (119) corresponds, in the interaction picture, to free propagation. Applying this Dyson equation to $\hat{\rho}_\odot(t_0)$ and taking the time derivative, one arrives at the kinetic equation in the interaction picture, Eq. (23). Transformed back to the Schrödinger picture we obtain Eq. (6).

A.2 Contributions to the kernel

In the following subsections contain details which appeared too lengthy for the main text. First, in Sect. A.2.1 the contributions to the time evolution kernel in the interaction picture, listed Tab. 1 as $\hat{\mathcal{K}}^{I(2)}(t,\tau)\hat{\rho}^I_\odot(\tau)$ and $\hat{\mathcal{K}}^{I(4)}(t,\tau_2,\tau_1,\tau)\hat{\rho}^I_\odot(\tau)$, are derived. Importantly, those still need to undergo some analytical transformation and evaluation before yielding what we are looking for, i.e. the elements of $\hat{K}(\lambda = 0)$. This procedure is shown in Sect. A.2.2 in an exemplary calculation of specific kernel elements in second and fourth order. A shortcut avoiding such calculations is offered by the diagrammatic rules, as explained in Sect. A.2.3, which allow to directly extract the analytical expressions for any element of $\hat{K}(\lambda = 0)$ from irreducible diagrams. Finally, a complete list of the 8 second and 128 fourth order irreducible diagrams, alongside with their analytical contributions to all elements of a submatrix $(\hat{K})_{nn'}$ of the time evolution kernel, is provided in Sect. A.2.4. The thereby appearing energy dependent functions are analysed in more detail in Sect. A.2.5.

A.2.1 Contributions in time domain as given in Tab. 1

We show how to come from Eqs. (31a), (31b) to the terms in given in Tab. 1. For the second order part of the kernel, we have to dissolve a double-commmutator. This procedure is easy, and one finds for Eq. (31a)

$$\begin{aligned}\hat{\mathcal{K}}^{I(2)}(t,\tau)\hat{\rho}^I_\odot(\tau) &= -\sum_{\substack{p_0,p_3\\ \in\{+,-\}}} \mathsf{Tr}_R\Big[\hat{A}_3^{p_3}, \big[\hat{A}_0^{p_0}, \hat{\rho}^I_\odot(\tau)\hat{\rho}_R\big]\Big] \\ &= \sum_{p\in\{+,-\}} \Big(\Big\langle \hat{C}_0^p \hat{C}_3^{\bar{p}}\Big\rangle \Big(\hat{D}_3^p\, \hat{\rho}^I_\odot(\tau)\hat{D}_0^{\bar{p}}\Big) - \Big\langle \hat{C}_3^{\bar{p}}\hat{C}_0^p\Big\rangle \Big(\hat{D}_3^p\hat{D}_0^{\bar{p}}\,\hat{\rho}^I_\odot(\tau)\Big)\Big) + \text{h.c.}\,. \end{aligned} \tag{120a}$$

Here, we have invoked the cyclic property of the trace and set in the correlator $\langle\cdots\rangle \equiv \mathsf{Tr}_R\{\cdots\hat{\rho}_R\}$. Notice that it yields non-vanishing contributions only if exactly one creation and one annihilation operator is involved, this means we have to combine an in-tunnelling part with an out-tunnelling part, $p := p_3 = -p_0$.
The second order diagrams Eq. (120a) is mapped on are given in Tab. 1. Explicitly specifying p and hermitian conjugates, four distinct diagrams arise; those are given in App. A.2.4.

The fourth order is more elaborate to treat as four nested commutators need to be dissolved. The two contributions to Eq. (31b) are first

$$
\begin{aligned}
&\mathsf{Tr}_R\big[\hat{A}_3^{p_3},\big[\hat{A}_2^{p_2},\big[\hat{A}_1^{p_1},\big[\hat{A}_0^{p_0},\hat{\rho}_\odot^I(\tau)\hat{\rho}_R\big]\big]\big]\big] \\
&= \Big[+ \Big\langle \hat{C}_3^{\bar{p}_3}\hat{C}_2^{\bar{p}_2}\hat{C}_1^{\bar{p}_1}\hat{C}_0^{\bar{p}_0}\Big\rangle \hat{D}_3^{p_3}\hat{D}_2^{p_2}\hat{D}_1^{p_1}\hat{D}_0^{p_0}\hat{\rho}_\odot^I(\tau) - \Big\langle \hat{C}_2^{\bar{p}_2}\hat{C}_3^{\bar{p}_3}\hat{C}_1^{\bar{p}_1}\hat{C}_0^{\bar{p}_0}\Big\rangle \hat{D}_3^{p_3}\hat{D}_1^{p_1}\hat{D}_0^{p_0}\hat{\rho}_\odot^I(\tau)\hat{D}_2^{p_2} \\
&\quad + \Big\langle \hat{C}_0^{\bar{p}_0}\hat{C}_1^{\bar{p}_1}\hat{C}_3^{\bar{p}_3}\hat{C}_2^{\bar{p}_2}\Big\rangle \hat{D}_3^{p_3}\hat{D}_2^{p_2}\hat{\rho}_\odot^I(\tau)\hat{D}_0^{p_0}\hat{D}_1^{p_1} - \Big\langle \hat{C}_0^{\bar{p}_0}\hat{C}_1^{\bar{p}_1}\hat{C}_2^{\bar{p}_2}\hat{C}_3^{\bar{p}_3}\Big\rangle \hat{D}_3^{p_3}\hat{\rho}_\odot^I(\tau)\hat{D}_0^{p_0}\hat{D}_1^{p_1}\hat{D}_2^{p_2} \\
&\quad - \Big\langle \hat{C}_0^{\bar{p}_0}\hat{C}_3^{\bar{p}_3}\hat{C}_2^{\bar{p}_2}\hat{C}_1^{\bar{p}_1}\Big\rangle \hat{D}_3^{p_3}\hat{D}_2^{p_2}\hat{D}_1^{p_1}\hat{\rho}_\odot^I(\tau)\hat{D}_0^{p_0} + \Big\langle \hat{C}_0^{\bar{p}_0}\hat{C}_2^{\bar{p}_2}\hat{C}_3^{\bar{p}_3}\hat{C}_1^{\bar{p}_1}\Big\rangle \hat{D}_3^{p_3}\hat{D}_1^{p_1}\hat{\rho}_\odot^I(\tau)\hat{D}_0^{p_0}\hat{D}_2^{p_2} \\
&\quad - \Big\langle \hat{C}_1^{\bar{p}_1}\hat{C}_3^{\bar{p}_3}\hat{C}_2^{\bar{p}_2}\hat{C}_0^{\bar{p}_0}\Big\rangle \hat{D}_3^{p_3}\hat{D}_2^{p_2}\hat{D}_0^{p_0}\hat{\rho}_\odot^I(\tau)\hat{D}_1^{p_1} + \Big\langle \hat{C}_1^{\bar{p}_1}\hat{C}_2^{\bar{p}_2}\hat{C}_3^{\bar{p}_3}\hat{C}_0^{\bar{p}_0}\Big\rangle \hat{D}_3^{p_3}\hat{D}_0^{p_0}\hat{\rho}_\odot^I(\tau)\hat{D}_1^{p_1}\hat{D}_2^{p_2}\Big] \\
&\quad + \text{h.c.}\,,
\end{aligned}
$$

stemming from Eq. (21), line (i) and building all possible contractions upon applying Wick's rule for fermionic operators of noninteracting particles,

$$
\Big\langle \hat{C}_a^{p_a}\hat{C}_b^{p_b}\hat{C}_c^{p_c}\hat{C}_d^{p_d}\Big\rangle = \underbrace{\Big\langle \hat{C}_a^{p_a}\hat{C}_b^{p_b}\Big\rangle\Big\langle \hat{C}_c^{p_c}\hat{C}_d^{p_d}\Big\rangle}_{\propto\delta_{p_a,-p_b}\delta_{p_c,-p_d}} - \underbrace{\Big\langle \hat{C}_a^{p_a}\hat{C}_c^{p_c}\Big\rangle\Big\langle \hat{C}_b^{p_b}\hat{C}_d^{p_d}\Big\rangle}_{\propto\delta_{p_a,-p_c}\delta_{p_b,-p_d}} + \underbrace{\Big\langle \hat{C}_a^{p_a}\hat{C}_d^{p_d}\Big\rangle\Big\langle \hat{C}_b^{p_b}\hat{C}_c^{p_c}\Big\rangle}_{\propto\delta_{p_a,-p_d}\delta_{p_b,-p_c}}.
$$

and second the part cancelling out all reducible terms,

$$
\begin{aligned}
&\mathsf{Tr}_R\big[\hat{A}^{p},\big[\hat{A}_2^{\bar{p}},\mathsf{Tr}_R\big\{\big[\hat{A}_1^{\bar{p}'},\big[\hat{A}_0^{p'},\hat{\rho}_\odot^I(\tau)\hat{\rho}_R\big]\big]\big\}\hat{\rho}_R\big]\big] \\
&\quad = + \Big\langle \hat{C}_1^{p'}\hat{C}_0^{\bar{p}'}\Big\rangle\Big\langle \hat{C}_3^{\bar{p}}\hat{C}_2^{p}\Big\rangle \hat{D}^{p}\hat{D}_2^{\bar{p}}\hat{D}_1^{\bar{p}'}\hat{D}_0^{p'}\hat{\rho}_\odot^I(\tau) - \Big\langle \hat{C}_1^{p'}\hat{C}_0^{\bar{p}'}\Big\rangle\Big\langle \hat{C}_2^{p}\hat{C}_3^{\bar{p}}\Big\rangle \hat{D}^{p}\hat{D}_1^{\bar{p}'}\hat{D}_0^{p'}\hat{\rho}_\odot^I(\tau)\hat{D}_2^{\bar{p}} \\
&\qquad + \Big\langle \hat{C}_0^{\bar{p}'}\hat{C}_1^{p'}\Big\rangle\Big\langle \hat{C}_3^{\bar{p}}\hat{C}_2^{p}\Big\rangle \hat{D}^{p}\hat{D}_2^{\bar{p}}\hat{\rho}_\odot^I(\tau)\hat{D}_0^{p'}\hat{D}_1^{\bar{p}'} - \Big\langle \hat{C}_0^{\bar{p}'}\hat{C}_1^{p'}\Big\rangle\Big\langle \hat{C}_2^{p}\hat{C}_3^{\bar{p}}\Big\rangle \hat{D}^{p}\hat{\rho}_\odot^I(\tau)\hat{D}_0^{p'}\hat{D}_1^{\bar{p}'}\hat{D}_2^{\bar{p}} \\
&\qquad - \Big\langle \hat{C}_0^{\bar{p}'}\hat{C}_1^{p'}\Big\rangle\Big\langle \hat{C}_3^{\bar{p}}\hat{C}_2^{p}\Big\rangle \hat{D}^{p}\hat{D}_2^{\bar{p}}\hat{D}_1^{\bar{p}'}\hat{\rho}_\odot^I(\tau)\hat{D}_0^{p'} + \Big\langle \hat{C}_0^{\bar{p}'}\hat{C}_1^{p'}\Big\rangle\Big\langle \hat{C}_2^{p}\hat{C}_3^{\bar{p}}\Big\rangle \hat{D}^{p}\hat{D}_1^{\bar{p}'}\hat{\rho}_\odot^I(\tau)\hat{D}_0^{p'}\hat{D}_2^{\bar{p}} \\
&\qquad - \Big\langle \hat{C}_1^{p'}\hat{C}_0^{\bar{p}'}\Big\rangle\Big\langle \hat{C}_3^{\bar{p}}\hat{C}_2^{p}\Big\rangle \hat{D}^{p}\hat{D}_2^{\bar{p}}\hat{D}_0^{p'}\hat{\rho}_\odot^I(\tau)\hat{D}_1^{\bar{p}'} + \Big\langle \hat{C}_1^{p'}\hat{C}_0^{\bar{p}'}\Big\rangle\Big\langle \hat{C}_2^{p}\hat{C}_3^{\bar{p}}\Big\rangle \hat{D}^{p}\hat{D}_0^{p'}\hat{\rho}_\odot^I(\tau)\hat{D}_1^{\bar{p}'}\hat{D}_2^{\bar{p}} \\
&\qquad + \text{h.c.}\,,
\end{aligned}
$$

where we already set in $p = p_3 = -p_2,\ p' = p_0 = -p_1$, such restricting to the nonzero

contributions. Summing over, the following sixteen fourth order contributions are left:

$$\begin{aligned}
\hat{\mathcal{K}}^{I(4)}(t,\tau_2,\tau_1,\tau)\hat{\rho}^I_\odot(\tau)_\odot = \sum_{p,p'\in\{+,-\}} \\
\Big[&+ \left\langle \hat{C}_2^{\bar{p}'}\hat{C}_1^{p'}\right\rangle \left\langle \hat{C}_3^{\bar{p}}\hat{C}_0^{p}\right\rangle \left(\hat{D}_3^p\hat{D}_2^{p'}\hat{D}_1^{\bar{p}'}\hat{D}_0^{\bar{p}}\,\hat{\rho}^I_\odot(\tau) + \hat{D}_3^p\hat{D}_1^{\bar{p}'}\hat{D}_0^{\bar{p}}\,\hat{\rho}^I_\odot(\tau)\,\hat{D}_2^{p'}\right) \\
&- \left\langle \hat{C}_3^{\bar{p}}\hat{C}_1^{p}\right\rangle \left\langle \hat{C}_2^{\bar{p}'}\hat{C}_0^{p'}\right\rangle \left(\hat{D}_3^p\hat{D}_2^{p'}\hat{D}_1^{\bar{p}}\hat{D}_0^{\bar{p}'}\,\hat{\rho}^I_\odot(\tau) + \hat{D}_3^p\hat{D}_1^{\bar{p}}\hat{D}_0^{\bar{p}'}\,\hat{\rho}^I_\odot(\tau)\,\hat{D}_2^{p'}\right) \\
&+ \left\langle \hat{C}_1^{p}\hat{C}_3^{\bar{p}}\right\rangle \left\langle \hat{C}_0^{p'}\hat{C}_2^{\bar{p}'}\right\rangle \left(\hat{D}_3^p\hat{D}_2^{p'}\,\hat{\rho}^I_\odot(\tau)\,\hat{D}_0^{\bar{p}'}\hat{D}_1^{\bar{p}} + \hat{D}_3^p\,\hat{\rho}^I_\odot(\tau)\,\hat{D}_0^{\bar{p}'}\hat{D}_1^{\bar{p}}\hat{D}_2^{p'}\right) \\
&- \left\langle \hat{C}_0^{p}\hat{C}_3^{\bar{p}}\right\rangle \left\langle \hat{C}_1^{p'}\hat{C}_2^{\bar{p}'}\right\rangle \left(\hat{D}_3^p\hat{D}_2^{p'}\,\hat{\rho}^I_\odot(\tau)\,\hat{D}_0^{\bar{p}}\hat{D}_1^{\bar{p}'} + \hat{D}_3^p\,\hat{\rho}^I_\odot(\tau)\,\hat{D}_0^{\bar{p}}\hat{D}_1^{\bar{p}'}\hat{D}_2^{p'}\right) \\
&- \left\langle \hat{C}_0^{p}\hat{C}_3^{\bar{p}}\right\rangle \left\langle \hat{C}_2^{\bar{p}'}\hat{C}_1^{p'}\right\rangle \left(\hat{D}_3^p\hat{D}_2^{p'}\hat{D}_1^{\bar{p}'}\,\hat{\rho}^I_\odot(\tau)\,\hat{D}_0^{\bar{p}} + \hat{D}_3^p\hat{D}_1^{\bar{p}'}\,\hat{\rho}^I_\odot(\tau)\,\hat{D}_0^{\bar{p}}\hat{D}_2^{p'}\right) \\
&+ \left\langle \hat{C}_0^{p'}\hat{C}_2^{\bar{p}'}\right\rangle \left\langle \hat{C}_3^{\bar{p}}\hat{C}_1^{p}\right\rangle \left(\hat{D}_3^p\hat{D}_2^{p'}\hat{D}_1^{\bar{p}}\,\hat{\rho}^I_\odot(\tau)\,\hat{D}_0^{\bar{p}'} + \hat{D}_3^p\hat{D}_1^{\bar{p}}\,\hat{\rho}^I_\odot(\tau)\,\hat{D}_0^{\bar{p}'}\hat{D}_2^{p'}\right) \\
&- \left\langle \hat{C}_1^{p}\hat{C}_3^{\bar{p}}\right\rangle \left\langle \hat{C}_2^{\bar{p}'}\hat{C}_0^{p'}\right\rangle \left(\hat{D}_3^p\hat{D}_2^{p'}\hat{D}_0^{\bar{p}'}\,\hat{\rho}^I_\odot(\tau)\,\hat{D}_1^{\bar{p}} + \hat{D}_3^p\hat{D}_0^{\bar{p}'}\,\hat{\rho}^I_\odot(\tau)\,\hat{D}_1^{\bar{p}}\hat{D}_2^{p'}\right) \\
&+ \left\langle \hat{C}_1^{p'}\hat{C}_2^{\bar{p}'}\right\rangle \left\langle \hat{C}_3^{\bar{p}}\hat{C}_0^{p}\right\rangle \left(\hat{D}_3^p\hat{D}_2^{p'}\hat{D}_0^{\bar{p}}\,\hat{\rho}^I_\odot(\tau)\,\hat{D}_1^{\bar{p}'} + \hat{D}_3^p\hat{D}_0^{\bar{p}}\,\hat{\rho}^I_\odot(\tau)\,\hat{D}_1^{\bar{p}'}\hat{D}_2^{p'}\right) \Big] \\
&+ h.c. \qquad \text{(120b)}
\end{aligned}$$

Still the placeholders $\hat{C}_i^{p_i}$ and $\hat{D}_i^{p_i}$ need to be expanded by Eq. (30). By the sum over $p, p' \in \{+,-\}$, each correlator generates two combinations of lead operators, producing four non-vanishing possibilities per term. Together with all the hermitian conjugates, this makes up for 128 terms in total. All of them are listed in App. A.2.4 along with their diagrammatic representation and analytical contribution.
Eqs. (120a), (120b) are mapped on the real-time diagrams as shown in Tab. 1.

A.2.2 Exemplary calculation of specific kernel elements

As a basis for App. A.2.3, we explicitly show here how to calculate, starting from Eq. (32), one contribution for the second and fourth order of the time evolution kernel element $(\hat{K})^{22}_{22}$ of the single-level model for a quantum-dot, which was addressed in the main text both in Sect. 2.2 and in Sect. 3.1. It works with the four states $|0\rangle$, $|\uparrow\rangle$, $|\downarrow\rangle$, $|2\rangle$, denoting occupation of the single level with zero, an $\uparrow$ - or a $\downarrow$ - electron or both of them, with associated eigenenergies E_0, $E_\uparrow$, $E_\downarrow$ and E_2, respectively. We will employ the abbreviation $\sigma \in \{\uparrow,\downarrow\}$ for the two possible spin projections.

2nd order The quantity to be evaluated in second order is

$$\left(\hat{K}^{(2)}\right)^{22}_{22} = \lim_{\lambda\to 0}\int_0^\infty \mathrm{d}\tau'\, e^{-\lambda\tau'} \left\langle 2\left|\hat{\mathcal{K}}^{I(2)}(t,t-\tau')[|2\rangle\langle 2|]\right|2\right\rangle .$$

Here, the exponentials from Eq. (32) have already been evaluated by exploiting $\hat{H}_0|2\rangle = E_2|2\rangle$ and cancelled against each other.

From Tab. 1, we can immediately the nonzero contributions to the kernel diagrammatically,

$$\left(\hat{K}^{(2)}\right)^{22}_{22} = \sum_\sigma \Bigg(\begin{array}{c} 2 \xleftarrow{\quad\sigma\quad} 2 \\ 2 \xrightarrow{\qquad} 2 \end{array} + \begin{array}{c} 2 \xleftarrow{\qquad} 2 \\ 2 \xrightarrow{\quad\sigma\quad} 2 \end{array} \Bigg)$$

$$= -\sum_\sigma \lim_{\lambda\to 0} \int_0^\infty \mathrm{d}\tau'\; e^{-\lambda\tau'} \left\langle \hat{C}_3^- \hat{C}_0^+ \right\rangle \langle 2|\, \hat{D}_3^+ \,|\sigma\rangle \langle\sigma|\, \hat{D}_0^- \,|2\rangle + \text{h.c.}\,. \tag{121}$$

We have now to re-substitute the placeholders C_0^+, C_3^- and D_0^-, D_3^+ by the contact and dot operators, according to Eq. (30). In general the thermal correlators of two contact operators, $\langle \hat{C}_a^{p_a} \hat{C}_b^{p_b} \rangle$, is only nonzero if exactly one creation and one annihilation operator is involved and all quantum numbers are identical. Setting in the decomposition Eq. (33), the definition Eq. (34) as well as $\eta := \hbar\lambda$, Eq. (121) becomes (remember that $\tau_3 = t$, $\tau_0 = \tau$, $\tau' = t - \tau$)

$$\left(\hat{K}^{(2)}\right)^{22}_{22} = -\hbar^{-2} \lim_{\eta\to 0} \sum_{l\sigma} \int \mathrm{d}\omega\; f_l^-(\omega) \int_0^\infty \mathrm{d}\tau'\; e^{\frac{\mathrm{i}}{\hbar}(E_2 - E_\sigma - \omega + \mathrm{i}\eta)\tau'} T_{l\sigma}^+(2,\sigma) T_{l\sigma}^-(\sigma,2) + \text{h.c.}$$

$$= -\frac{\mathrm{i}}{\hbar} \lim_{\eta\to 0} \sum_{l\sigma} \int \mathrm{d}\omega\; \frac{f_l^-(\omega)}{-\omega + E_2 - E_\sigma + \mathrm{i}\eta} \left|T_{l\sigma}^+(2,\sigma)\right|^2 + \text{h.c.}\,.$$

As stated in the main part of the text in Sect. 1.1, no dependence on t is left. Notice that in terms of $f^+(\omega) = f(\omega) = (1 + e^\omega)^{-1}$, $f^-(\omega) = 1 - f(\omega)$,

$$\int \mathrm{d}\omega \frac{f_l^p(\omega)}{d\omega - \mu} = \int \mathrm{d}\omega \frac{f^p(\beta\omega + \beta e V_l)}{d\omega - \mu} = \int \frac{\mathrm{d}\tilde{\omega}}{\beta} \frac{f^p(\tilde{\omega})}{d(\tilde{\omega}\beta^{-1} - eV_l) - \mu} =$$

$$\int \mathrm{d}\tilde{\tilde{\omega}} \frac{f^p(d\tilde{\tilde{\omega}})}{\tilde{\tilde{\omega}} - d\beta e V_l - \beta\mu} = \int \mathrm{d}\omega \frac{f^{pd}(\omega)}{\omega - d\beta e V_l - \beta\mu}. \tag{122}$$

Using this transformation it becomes clear that the energy dependent part of this contribution corresponds to the analytical function $Y_+^+(E_{\sigma 2} - eV_l)$ as defined in Eq. (124a) and calculated in App. A.2.5. It splits into an energy conserving real part, corresponding to the out-tunnelling process $2 \to \sigma$, and an imaginary part allowing for an energy non-conserving process, a so-called virtual transition, where the electron tunnels out only temporarily.

Overall, it is clear that the energy dependence of any 2nd order contribution will be of the form

$$-\frac{\mathrm{i}}{\hbar} \int \mathrm{d}\omega\; \frac{f_l^p(\omega)}{\Delta_0}\,.$$

The denominator Δ_0 emerges from the exponential $e^{\frac{\mathrm{i}}{\hbar}\Delta_0\tau'}$, the sign $p \in \{+,-\}$ depends on the order of the contact operators, compare Eq. (33).

4th order For the fourth order we have to deal with

$$\left(\hat{K}^{(4)}\right)_{22}^{22} = \lim_{\lambda\to 0}\int_0^\infty \mathrm{d}\tau'\, e^{-\lambda\tau'}\int_0^{\tau'}\mathrm{d}\tau_1'\int_0^{\tau_1'}\mathrm{d}\tau_2'\left\langle 2\left|\hat{\mathcal{K}}^{I(4)}(t,t-\tau_2',t-\tau_1',t-\tau')[|2\rangle\langle 2|]\right|2\right\rangle$$

$$= \sum_\sigma \Bigg(\quad + \quad + \sum_{\sigma'} \Bigg\{ \quad + \quad \Bigg\}$$

$$+ \quad + \quad + \text{h.c.} \Bigg).$$

Here, we want to focus exemplarily on the contribution related to the last shown diagram. Employing Eqs. (33), (34) and further definitions as used in the previous paragraph we obtain

$$\begin{aligned}
&\lim_{\lambda\to 0}\sum_\sigma\int_0^\infty \mathrm{d}\tau'\; e^{-\lambda\tau'}\int_0^{\tau'}\mathrm{d}\tau_1'\int_0^{\tau_1'}\mathrm{d}\tau_2'\left\langle \hat{C}_1^+\hat{C}_3^-\right\rangle\left\langle \hat{C}_0^-\hat{C}_2^+\right\rangle \\
&\qquad\qquad \times\left\langle 2\left|\hat{D}_3^+\right|\sigma\right\rangle\left\langle\sigma\left|\hat{D}_2^-\right|2\right\rangle\left\langle 2\left|\hat{D}_0^+\right|\sigma\right\rangle\left\langle\sigma\left|\hat{D}_1^-\right|2\right\rangle \\
&= \hbar^{-4}\lim_{\eta\to\infty}\sum_{ll'\sigma}\int_0^\infty \mathrm{d}\tau_2'\int_{\tau_2'}^\infty \mathrm{d}\tau_1'\int_{\tau_1'}^\infty \mathrm{d}\tau'\int\mathrm{d}\omega\int\mathrm{d}\omega'\, f_l^+(\omega)\, f_{l'}^-(\omega') \\
&\qquad\qquad \times e^{\frac{\mathrm{i}}{\hbar}(-\omega+E_2-E_\sigma)\tau_1'}\, e^{\frac{\mathrm{i}}{\hbar}(-\omega'+E_2-E_\sigma)\tau_2'} e^{\frac{\mathrm{i}}{\hbar}(\omega'-E_2+E_\sigma+\mathrm{i}\eta)\tau'} \\
&\qquad\qquad\qquad \times T_{l\sigma}^+(2,\sigma)T_{l'\sigma}^-(\sigma,2)T_{l'\sigma}^+(2,\sigma)T_{l\sigma}^-(\sigma,2) \\
&= -\frac{\mathrm{i}}{\hbar}\lim_{\eta\to 0}\sum_{ll'\sigma}\int\mathrm{d}\omega\int\mathrm{d}\omega'\, f_l^+(\omega)f_{l'}^-(\omega')\,\left|T_{l\sigma}^+(2,\sigma)\right|^2\left|T_{l'\sigma}^+(2,\sigma)\right|^2 \\
&\qquad\qquad \times\frac{1}{-\omega+\omega'+\mathrm{i}\eta}\,\frac{1}{-\omega+E_2-E_\sigma+\mathrm{i}\eta}\,\frac{1}{\omega'-E_2+E_\sigma+\mathrm{i}\eta}.
\end{aligned}$$

For the evaluation of the time ordered integrations in the last step, the variable transformations $\tilde{\tau}_1 = \tau_1' - \tau_2'$, $\tilde{\tau} = \tau' - \tau_1'$, which decouple the three time integrations, were applied. In terms of the helper function defined in Eq. (124b), the energy dependent part of this contribution corresponds to ${}^+X_{-+}^{+-}(E_{2\sigma}+eV_l, E_{2\sigma}+eV_{l'}, -eV_l+eV_{l'}) = {}^+X_{++}^{--}(E_{\sigma 2}-eV_l, E_{2\sigma}+eV_{l'}, -eV_l+eV_{l'})$.

The common structure of the integrals appearing in the fourth order contributions is:

$$-\frac{\mathrm{i}}{\hbar}\int\mathrm{d}\omega\int\mathrm{d}\omega'\; f_l^p(\omega)\, f_{l'}^{p'}(\omega')\;\frac{1}{\Delta_0}\,\frac{1}{\Delta_0+\Delta_1}\,\frac{1}{\Delta_0+\Delta_1+\Delta_2}\,.$$

Here, $\frac{\mathrm{i}}{\hbar}\Delta_{0/1/2}$ were the arguments of the exponentials containing τ', τ_1', τ_2' respectively. Again, $p/p' \in \{+,-\}$, depending on the order of the associated contact operators.

A.2.3 Diagrammatic rules

As announced in Sect. 2.1, we shortly review the diagrammatic rules [19], by which one can directly extract from any diagram the corresponding analytical contribution. In general, as we have seen previously, e.g. in Sect. A.2.2, any nth order contribution splits into a product of n tunnelling matrix elements and an energy dependent function. By construction, as explained in Sect. 2.1, there is the one-to-one correspondence between the structure of the diagrams and the kernel components in the time domain – see also Tab. 1. Therefore, from any diagram the tunnelling matrix elements are straightforward to obtain: each vertex yields $T^{p}_{l\sigma}(b,a)$, where – with respect to the contour – state a is the one before, state b the one after the vertex. Further, $p = +/-$ for the fermion line pointing towards/away from the concerned vertex and l/σ is the lead respectively the spin assigned to the connected fermion line.

For the energy dependent function, it is less obvious how one manages to directly extract the Laplace transformed expression from the diagram. We list the single steps and afterwards explain how they work. Alongside, our previous 2nd and 4th order examples are employed to demonstrate the procedure. In general we start from a diagram of order $2n$ (recall that any odd order vanishes when tracing over the lead operators).

1a. To each of the n fermion lines, assign an energy ω_i, as well as the lead and spin indices indices l_i, σ_i, respectively. $(1 \leq i \leq n)$

1b. To each section on the contours, assign the energy of the corresponding state.

2a. Between two consecutive times τ_j and τ_{j+1}, perform a vertical cut.
$(0 \leq j \leq 2n-2,\ \tau_0 = \tau,\ \tau_{2n-1} = t)$

$\boxed{2nd}$

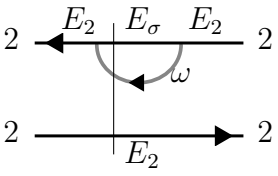

$\boxed{4th}$

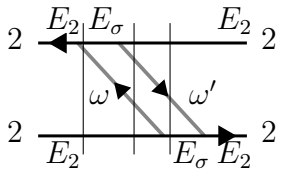

2b. From each cut obtain a denominator A_j: for each intersection of the cut with a fermion line or a contour, one adds up with a specific sign the energy assigned to the fermion line, respectively to the contour at the intersection. Thereby, the sign is determined by the directions of the fermion line, respectively the contour: If they hit the cut from the right, their energy has to be counted negative, if they come from the left, the sign is positive.

$\boxed{2nd}$ $\Rightarrow A_0 = E_2 - \omega - E_\sigma,$

$\boxed{4th}$ $\Rightarrow A_0 = E_\sigma + \omega' - E_2,\ A_1 = E_2 - \omega + \omega' - E_2,\ A_2 = E_2 - \omega + E_\sigma.$

3. For each fermion line, determine a sign p_i, which tells whether it belongs to an in-tunnelling ($p_i = +$) or an out-tunnelling process ($p_i = -$): if the connected vertices lie on the same contour, for a forward[33] pointing line it is $p_i = -$, for a backward[33] pointing line $p_i = +$. If the vertices lie on different contours, it is the other way round.

$\boxed{2nd} \quad \Rightarrow p = -, \qquad \boxed{4th} \quad \Rightarrow p = +,\ p' = -.$

4. Determine q, which is the number of vertices on the lower contour plus the number of crossings of fermion lines.

$\boxed{2nd} \quad \Rightarrow q = 0, \qquad \boxed{4th} \quad \Rightarrow q = 0 + 2 = 2.$

5. Write down your final integral:

$$-(-1)^q \frac{\mathrm{i}}{\hbar} \lim_{\eta\to 0} \prod_{i=1}^{2n} \int \mathrm{d}\omega_i \; f_{l_i}^{p_i}(\omega_i) \prod_{j=0}^{2n-2} \frac{1}{A_j + \mathrm{i}\eta}\,. \tag{123}$$

$\boxed{2nd} \quad \Rightarrow -\frac{\mathrm{i}}{\hbar} \lim_{\eta\to 0} \int \mathrm{d}\omega \; \frac{f_l^-(\omega)}{-\omega+E_2-E_\sigma+\mathrm{i}\eta},$

$\boxed{4th} \quad \Rightarrow -\frac{\mathrm{i}}{\hbar} \lim_{\eta\to 0} \int \mathrm{d}\omega \int \mathrm{d}\omega' \; \frac{1}{-\omega+\omega'+\mathrm{i}\eta} \frac{f_l^+(\omega)}{-\omega+E_2-E_\sigma+\mathrm{i}\eta} \frac{f_{l'}^-(\omega')}{\omega'-E_2+E_\sigma+\mathrm{i}\eta}.$

Now we investigate how by applying these rules the calculation of contributions, as shown in App. A.2.2, is performed automatically.

In reverse order, we start with the prefactor $-\mathrm{i}\hbar^{-1}$ occurring in step **5**;
From the iteration procedure in the derivation of the quantum master equation, each step gives a factor $\frac{\mathrm{i}}{\hbar}$. Further, dissolving the nested integrations, from each of the $2n-1$ time dependent exponentials $\mathrm{i}\hbar$ comes; together:

$$\left(\frac{\mathrm{i}}{\hbar}\right)^{2n} (\mathrm{i}\hbar)^{2n-1} = \underbrace{\mathrm{i}^{4n}}_{=+1} \frac{1}{\hbar} \underbrace{\frac{1}{\mathrm{i}}}_{=-\mathrm{i}} = -\frac{\mathrm{i}}{\hbar}\,.$$

Rule **4** fixes the number q and hence the overall sign of a contribution;
Thereby, the number of interchanges due to the commutators contained in the Liouville superoperators is relevant. For an odd number of interchanges, i.e. an odd number of electron operators to each side of the RDM, a relative negative sign has to be put, while for an even number of interchanges (even number of operators to each side of the RDM), the relative sign is positive. So one could just take for q the number on either, e.g. the lower, contour. From the fourth order on, however, dissolving the lead correlators by Wick's theorem also yields relative signs. Thus, the correct rule is to

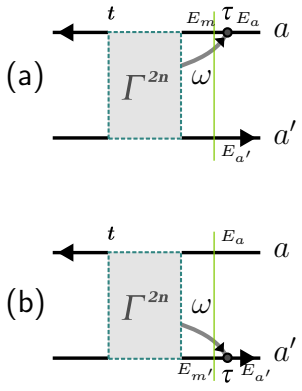

Figure 48: Obtaining A_0 via the diagrammatic rules, for the vertex at τ lying on the upper (a) or lower (b) contour.

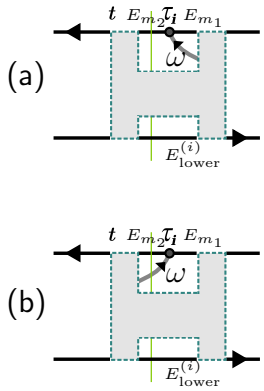

Figure 49: Obtaining A_i via the diagrammatic rules, for the fermion line connecting to the vertex at τ_i from the right (a) or the left (b).

take for q the number of vertices on the lower contour *plus* the number of crossings of fermion lines. A quick look on Tab. 1 confirms the validity of this statement.

Rule **3** determines the sign p_i;
Its value can be extracted from the direction of the corresponding fermion line in the diagram: If the connected vertices lie on the same contour, this means that the ordering of the associated lead operators has not to be changed when tracing over the leads, compare Sect. A.2.1. Then a forward[34] pointing line belongs to negative p_i ($\hat{D}_a^+ \cdots \hat{D}_b^- \;\to\; \langle \hat{C}_a^- \hat{C}_b^+ \rangle \;\to\; f^-$), a backward[34] pointing line to positive p_i ($\hat{D}_a^- \cdots \hat{D}_b^+ \;\to\; \langle \hat{C}_a^+ \hat{C}_b^- \rangle \;\to\; f^+$). If the vertices lie on different contour, a cyclic permutation of operators in needed before tracing and the assignment is the other way round.

Rule **2b** yields the denominators $A_0, \ldots, A_{2n-2}$. We need to understand why they match exactly the values of Δ_0, $\Delta_0 + \Delta_1$, ... , $\Delta_0 + \cdots + \Delta_{2n-2}$, as defined in Sect. A.2.2.
For A_0, obtained from the earliest cut, i.e. the one between τ and τ_1, we can easily understand why it yields the argument of the exponential $e^{\frac{\mathrm{i}}{\hbar}\Delta_0 \tau'}$. The two possible situations are sketched in Fig. 48, where we decided for the fermion line to point towards the vertex, i.e. $p_0 = +$. The vertex at time τ can either lie on the upper [Fig. 48(a)] or the lower contour [Fig. 48(b)], and the state of the quantum-dot is assumed to changes at the vertex from a to m or from m' to a', respectively. Rule **2b** gives then

$$A_0 = \omega + E^{(0)}_{\text{lower}} - E^{(0)}_{\text{upper}} = \begin{cases} \omega + E_{a'} - E_m, & \text{(vertex on upper contour)} \\ \omega + E_{m'} - E_a. & \text{(vertex on lower contour)} \end{cases}$$

In general, $E^{(i)}_{\text{upper/lower}}$ denotes the energy assigned to the upper/lower contour at the intersection with the cut between times τ_i and τ_{i+1}.

[34] Forward/backward with respect to the direction of the contours.

What concerns Δ_0, three contributions emerge in a calculation: first, from the transformation to the Schrödinger picture there is the exponential

$$e^{\frac{\mathrm{i}}{\hbar}(E_a - E_{a'})\tau},$$

compare Eq. (24). Second, there is the time dependence of the dot operator $D_0^{p_0}$. Depending on whether the vertex at time τ is located on the upper or on the lower contour, it appears in $\langle m| \hat{D}_0^{p_0} |a\rangle$ respectively $\langle a'| \hat{D}_0^{p_0} |m'\rangle$, resulting, independent of p_0, in an exponential

$$e^{\frac{\mathrm{i}}{\hbar}(E_m - E_a)\tau} \quad \text{respectively} \quad e^{\frac{\mathrm{i}}{\hbar}(E_{a'} - E_{m'})\tau}.$$

Finally, there is the associated contact operator $C_0^{\bar{p}_0}$ yielding, compare Eq. (33),

$$e^{-p_0 \frac{\mathrm{i}}{\hbar}\omega\tau}.$$

In total, respecting $\tau = t - \tau'$, this leads for our example ($p_0 = +$) to

$$\Delta_0 = \omega - E_m + E_{a'} \quad \text{respectively} \quad \Delta_0 = \omega - E_a + E_{m'},$$

in perfect agreement with the result for A_0 obtained from the diagrammatic rules. Upon inversion of the fermion line direction, the sign of ω changes in A_0 as well as in Δ_0. So we have shown in general that $A_0 = \Delta_0$, which we use as basic step for a mathematical induction.
With the assumption $A_{i-1} =: E_{\text{lower}}^{(i-1)} - E_{\text{upper}}^{(i-1)} + E_\omega^{(i-1)} = \Delta_0 + \cdots + \Delta_{i-1}$, where $E_\omega^{(i-1)}$ cumulates the energy contributions from all fermion lines crossing a cut between times τ_{i-1} and τ_i, we can start the inductive step:
A_i is obtained from a vertical cut between times τ_i and τ_{i+1}. Let us for simplicity assume that the vertex τ_i, where the quantum-dot state changes from m_1 to m_2, is placed on the upper contour, and that the fermion line points towards this vertex[35]. The situation is illustrated in Fig. 49 and we immediately obtain therewith $E_{\text{lower}}^{(i)} = E_{\text{lower}}^{(i-1)}$. Further, $E_{\text{upper}}^{(i)} = E_{\text{upper}}^{(i-1)} + (E_{\text{upper}}^{(i)} - E_{\text{upper}}^{(i-1)}) = E_{\text{upper}}^{(i-1)} + E_{m_2} - E_{m_1}$. The energies summed in $E_\omega^{(i)}$ can differ from $E_\omega^{(i-1)}$ only by the contribution of the fermion line ending in the vertex at τ_i, actually independent on whether it connects to a vertex at a time τ_h larger or smaller then τ_i: If $\tau_h < \tau_i$, Fig. 49(a), the contribution of that fermion line is $-\omega$ and contained in $E_\omega^{(i-1)}$ but must not appear in $E_\omega^{(i)}$: $E_\omega^{(i)} = E_\omega^{(i-1)} - (-\omega) = E_\omega^{(i-1)} + \omega$. If $\tau_h > \tau_i$, Fig. 49(b), the contribution is $+\omega$ and not contained in $E_\omega^{(i-1)}$. Thus we also get $E_\omega^{(i)} = E_\omega^{(i-1)} + \omega$. In total, $A_i - A_{i-1} = E_{m_1} - E_{m_2} + \omega$.

On the other hand, from the time dependences of C_i^- and $\langle m_2| \hat{D}_i^+ |m_1\rangle$ we would obtain an exponential $e^{\frac{\mathrm{i}}{\hbar}(E_{m_1} - E_{m_2} + \omega)\tau_i'} \equiv e^{\frac{\mathrm{i}}{\hbar}\Delta_i \tau_i'}$.
Obviously, this confirms $A_i = A_{i-1} + \Delta_i$, which completes our proof. □

[35] For the vertex lying on the lower contour and/or for a fermion line pointing away from the vertex, all arguments can be used in the analogous manner.

A.2.4 All irreducible second and fourth order diagrams

In order to list along with the second and fourth order irreducible diagrams their analytical contribution to $(\hat{K}^{(2)})_{nn'}$ respectively $(\hat{K}^{(4)})_{nn'}$, some abbreviations for lengthy analytical expressions are necessary (and have already been mentioned in Sect. A.2.2).

First, we define a function

$$Y_d^p(\mu) := (\mathrm{i}\hbar)^{-1} \lim_{\eta\to 0} \int \mathrm{d}\omega f^p(\omega) \, \frac{1}{d(\omega-\beta\mu)+\mathrm{i}\eta}, \tag{124a}$$

which is found in the second order irreducible diagrams as well as for the non-secular corrections addressed in App. A.3. An integral transformation $\omega \to k_B T\omega = \beta^{-1}\omega$ has allowed to use for the Fermi functions simply temperature independent expressions, $f^+(\omega) = f(\omega) = (1+e^{\omega})^{-1}$ and $f^-(\omega) = 1 - f(\omega)$.
For the fourth order we have to introduce two types ${}^{\pm}X_{dd'}^{pp'}$ and ${}^{\pm}D_{dd'}^{pp'}$ of double integrals, where $p, p' \in \{\pm\}$, $d, d' \in \{\pm 1\}$ and t:

$$\begin{aligned} {}^{\pm}X_{dd'}^{pp'}(\mu,\mu',\Delta) = \frac{\beta}{\mathrm{i}\hbar} \lim_{\eta\to 0} \int \mathrm{d}\omega \int \mathrm{d}\omega' \, f^p(\omega) f^{p'}(\omega') \\ \times \frac{1}{d(\omega-\tilde{\mu})+\mathrm{i}\eta} \, \frac{1}{d\omega + d'\omega' - \tilde{\Delta} + \mathrm{i}\eta} \, \frac{1}{d'(\pm\omega'-\tilde{\mu}')+\mathrm{i}\eta}, \end{aligned} \tag{124b}$$

$$\begin{aligned} {}^{\pm}D_{dd'}^{pp'}(\mu,\mu',\Delta) = \frac{\beta}{\mathrm{i}\hbar} \lim_{\eta\to 0} \int \mathrm{d}\omega \int \mathrm{d}\omega' \, f^p(\omega) f^{p'}(\omega') \\ \times \frac{1}{d(\omega-\tilde{\mu})+\mathrm{i}\eta} \, \frac{1}{d\omega + d'\omega' - \tilde{\Delta} + \mathrm{i}\eta} \, \frac{1}{d(\pm\omega-\tilde{\mu}')+\mathrm{i}\eta}, \end{aligned} \tag{124c}$$

with $\tilde{\mu} = \beta\mu$, $\tilde{\mu}' = \beta\mu'$, $\tilde{\Delta} = \beta\Delta$ and the prefactor β stemming from the integral transformation. It is straightforward to show the following identities:

$$\begin{aligned} Y_d^p(\mu) &= Y_+^{pd}(d\mu), \\ {}^{\pm}X_{dd'}^{pp'}(\mu,\mu',\Delta) &= {}^{\pm}X_{++}^{(dp)(d'p')}(d\mu, d'\mu', \Delta), \\ {}^{\pm}D_{dd'}^{pp'}(\mu,\mu',\Delta) &= {}^{\pm}D_{++}^{(dp)(d'p')}(d\mu, d\mu', \Delta). \end{aligned}$$

These definitions allow an elegant formulation of all the energy-dependent expressions involved in. For the function Eq. (124a), which contains only the single integration, it is possible to give both its real and its imaginary part in one line:

$$\hbar Y_+^p(\mu) = -\pi f^p(\tilde{\mu}) - \mathrm{i}p\Big(\mathsf{Re}\,\Psi^{(0)}\left(\frac{1}{2} + \frac{\mathrm{i}\tilde{\mu}}{2\pi}\right) - C\Big).$$

The explicit calculation is carried out in Sect. A.2.5. The digamma function $\Psi^{(0)}$ was already introduced in the main text, Sect. 2.3.1. The constant $C = \Psi^{(0)}(0.5 + 0.5W/\pi)$ is finite if a finite bandwidth W is assumed. Typically, the constant drops from the

final results due to a summation over in-, as well as out-tunnelling processes ($p = \pm$). The analytical expression for the functions Eqs. (124b), (124c), which involve two integrations, are to lengthy to be written down in full generality at this place. An evaluation of their real parts is sufficient for certain kinds of calculations and also given in Sect. A.2.5.

The last ingredient for the listing of all irreducible second and fourth order contributions are the following correspondences for colours/symbols used in the upcoming diagrammatic representations:

FERMION LINES			CONTOURS		
symbol	$\leftrightarrow$	**Fermi function**	**symbol**	$\leftrightarrow$	**number of electrons**
	$\leftrightarrow$	f^+		$\leftrightarrow$	N
	$\leftrightarrow$	f^-		$\leftrightarrow$	$N-1$
				$\leftrightarrow$	$N-2$
				$\leftrightarrow$	$N+1$
				$\leftrightarrow$	$N+2$

Notice that those are merely introduced for clarity in the visual appearance.
Further, the electron operators of the quantum-dot will be called $\hat{\Psi}_\sigma$, and $\hat{\rho}_\odot^N$ denotes that block of the reduced density matrix which belongs to charge N.

The structure of the next one+sixteen pages is as follows:
We explicitly show all 8+128 irreducible second+fourth order diagrams constructing the full[36] kernels $\hat{K}^{(2)} + \hat{K}^{(4)}$ as emerge from Eq. (22b). Alongside, the corresponding analytical expression like in Tab. 1, but also the resulting term as appearing in the final form of the generalised master equation, are given:

expression like in Tab. 1,		diagram.
term in final form,		

[36] There is no restriction to secular states, thus no non-secular corrections are to be included and consequently just the irreducible diagrams contribute.

$$-\left\langle \hat{c}^\dagger_\sigma(t)\,\hat{c}_\sigma(\tau)\right\rangle \left\langle n\left|\hat{\Psi}_\sigma(t)\hat{\Psi}^\dagger_\sigma(\tau)\hat{\rho}^I_\odot(\tau)\right|n'\right\rangle$$
$$-T^-_{l\sigma}(n,\tilde{k})T^+_{l\sigma}(\tilde{k},j)\left(\hat{\rho}^N_\odot\right)_{jn'}\,Y^+_+(E_{\tilde{k}n'}+eV_l)$$

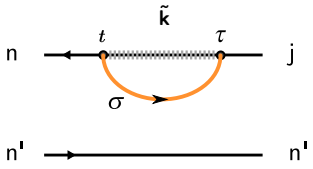

$$-\left\langle \hat{c}^\dagger_\sigma(\tau)\,\hat{c}_\sigma(t)\right\rangle \left\langle n\left|\hat{\rho}^I_\odot(\tau)\hat{\Psi}_\sigma(\tau)\hat{\Psi}^\dagger_\sigma(t)\right|n'\right\rangle$$
$$-\left(\hat{\rho}^N_\odot\right)_{nj'}T^-_{l\sigma}(j',\tilde{k}')T^+_{l\sigma}(\tilde{k}',n')\,Y^-_+(E_{n\tilde{k}'}-eV_l)$$

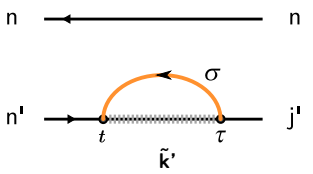

$$-\left\langle \hat{c}_\sigma(t)\,\hat{c}^\dagger_\sigma(\tau)\right\rangle \left\langle n\left|\hat{\Psi}^\dagger_\sigma(t)\hat{\Psi}_\sigma(\tau)\hat{\rho}^I_\odot(\tau)\right|n'\right\rangle$$
$$-T^+_{l\sigma}(n,\tilde{i})T^-_{l\sigma}(\tilde{i},j)\left(\hat{\rho}^N_\odot\right)_{jn'}\,Y^+_+(E_{\tilde{i}n'}-eV_l)$$

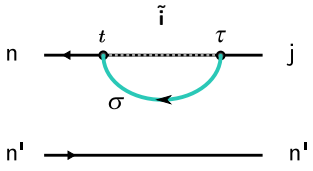

$$-\left\langle \hat{c}_\sigma(\tau)\,\hat{c}^\dagger_\sigma(t)\right\rangle \left\langle n\left|\hat{\rho}^I_\odot(\tau)\hat{\Psi}^\dagger_\sigma(\tau)\hat{\Psi}_\sigma(t)\right|n'\right\rangle$$
$$-\left(\hat{\rho}^N_\odot\right)_{nj'}T^+_{l\sigma}(j',\tilde{i}')T^-_{l\sigma}(\tilde{i}',n')\,Y^-_+(E_{n\tilde{i}'}+eV_l)$$

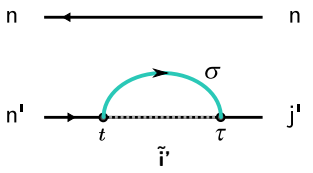

$$+\left\langle \hat{c}_\sigma(t)\,\hat{c}^\dagger_\sigma(\tau)\right\rangle \left\langle n\left|\hat{\Psi}_\sigma(t)\hat{\rho}^I_\odot(\tau)\hat{\Psi}^\dagger_\sigma(\tau)\right|n'\right\rangle$$
$$+T^-_{l\sigma}(n,k)(\hat{\rho}^{N+1}_\odot)_{kk'}T^+_{l\sigma}(k',n')\,Y^-_+(E_{kn'}+eV_l)$$

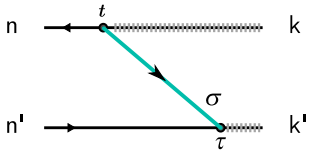

$$+\left\langle \hat{c}_\sigma(\tau)\,\hat{c}^\dagger_\sigma(t)\right\rangle \left\langle n\left|\hat{\Psi}_\sigma(\tau)\hat{\rho}^I_\odot(\tau)\hat{\Psi}^\dagger_\sigma(t)\right|n'\right\rangle$$
$$+T^-_{l\sigma}(n,k)(\hat{\rho}^{N+1}_\odot)_{kk'}T^+_{l\sigma}(k',n')\,Y^+_+(E_{nk'}-eV_l)$$

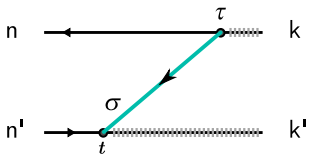

$$+\left\langle \hat{c}^\dagger_\sigma(t)\,\hat{c}_\sigma(\tau)\right\rangle \left\langle n\left|\hat{\Psi}^\dagger_\sigma(t)\hat{\rho}^I_\odot(\tau)\hat{\Psi}_\sigma(\tau)\right|n'\right\rangle$$
$$+T^+_{l\sigma}(n,i)(\hat{\rho}^{N-1}_\odot)_{ii'}T^-_{l\sigma}(i',n')\,Y^-_+(E_{in'}-eV_l)$$

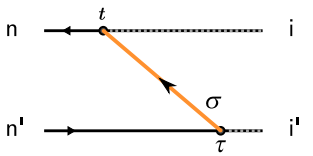

$$+\left\langle \hat{c}^\dagger_\sigma(\tau)\,\hat{c}_\sigma(t)\right\rangle \left\langle n\left|\hat{\Psi}^\dagger_\sigma(\tau)\hat{\rho}^I_\odot(\tau)\hat{\Psi}_\sigma(t)\right|n'\right\rangle$$
$$+T^+_{l\sigma}(n,i)(\hat{\rho}^{N-1}_\odot)_{ii'}T^-_{l\sigma}(i',n')\,Y^+_+(E_{ni'}+eV_l)$$

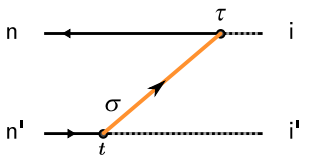

$$+\left\langle \hat{C}_3^p \hat{C}_0^{\bar{p}} \right\rangle \left\langle \hat{C}_2^{p'} \hat{C}_1^{\bar{p}'} \right\rangle \hat{D}_3^{\bar{p}} \hat{D}_2^{\bar{p}'} \hat{D}_1^{p'} \hat{D}_0^{p} \hat{\rho}_\odot$$

$$+\left\langle \hat{c}_\sigma^\dagger(t)\hat{c}_\sigma(\tau)\right\rangle \left\langle \hat{c}_{\sigma'}(\tau_2)\hat{c}_{\sigma'}^\dagger(\tau_1)\right\rangle \left\langle n\left|\hat{\Psi}_\sigma(t)\hat{\Psi}_{\sigma'}^\dagger(\tau_2)\hat{\Psi}_{\sigma'}(\tau_1)\hat{\Psi}_\sigma^\dagger(\tau)\hat{\rho}_\odot^I(\tau)\right|n'\right\rangle$$
$$+{}^{+}\mathcal{D}_{++}^{++}(E_{\tilde{k}_2 n'}+eV_l, E_{\tilde{k}_1 n'}+eV_l, E_{\tilde{n}n'}+eV_l-eV_{l'})$$
$$\times T_{l\sigma}^{-}(n,\tilde{k}_2)T_{l'\sigma'}^{+}(\tilde{k}_2,\tilde{n})T_{l'\sigma'}^{-}(\tilde{n},\tilde{k}_1)T_{l\sigma}^{+}(\tilde{k}_1,j)\left(\hat{\rho}_\odot^N\right)_{jn'}$$

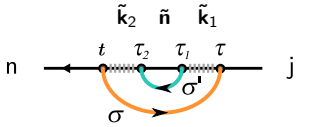

$$+\left\langle \hat{c}_\sigma^\dagger(\tau)\hat{c}_\sigma(t)\right\rangle \left\langle \hat{c}_{\sigma'}(\tau_1)\hat{c}_{\sigma'}^\dagger(\tau_2)\right\rangle \left\langle n\left|\hat{\rho}_\odot^I(\tau)\hat{\Psi}_\sigma(\tau)\hat{\Psi}_{\sigma'}^\dagger(\tau_1)\hat{\Psi}_{\sigma'}(\tau_2)\hat{\Psi}_\sigma^\dagger(t)\right|n'\right\rangle$$
$$+{}^{+}\mathcal{D}_{++}^{--}(E_{n\tilde{k}_2'}-eV_l, E_{n\tilde{k}_1'}-eV_l, E_{n\tilde{n}'}-eV_l+eV_{l'})$$
$$\times \left(\hat{\rho}_\odot^N\right)_{nj'} T_{l\sigma}^{-}(j',\tilde{k}_1')T_{l'\sigma'}^{+}(\tilde{k}_1',\tilde{n}')T_{l'\sigma'}^{-}(\tilde{k}',\tilde{k}_2')T_{l\sigma}^{+}(\tilde{k}_2',n')$$

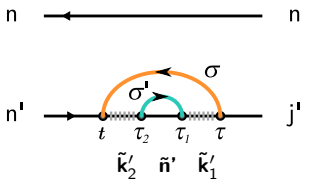

$$+\left\langle \hat{c}_\sigma(t)\hat{c}_\sigma^\dagger(\tau)\right\rangle \left\langle \hat{c}_{\sigma'}^\dagger(\tau_2)\hat{c}_{\sigma'}(\tau_1)\right\rangle \left\langle n\left|\hat{\Psi}_\sigma^\dagger(t)\hat{\Psi}_{\sigma'}(\tau_2)\hat{\Psi}_{\sigma'}^\dagger(\tau_1)\hat{\Psi}_\sigma(\tau)\hat{\rho}_\odot^I(\tau)\right|n'\right\rangle$$
$$+{}^{+}\mathcal{D}_{++}^{++}(E_{\tilde{i}_2 n'}-eV_l, E_{\tilde{i}_1 n'}-eV_l, E_{\tilde{n}n'}-eV_l+eV_{l'})$$
$$\times T_{l\sigma}^{+}(n,\tilde{i}_2)T_{l'\sigma'}^{-}(\tilde{i}_2,\tilde{n})T_{l'\sigma'}^{+}(\tilde{n},\tilde{i}_1)T_{l\sigma}^{-}(\tilde{i}_1,j)\left(\hat{\rho}_\odot^N\right)_{jn'}$$

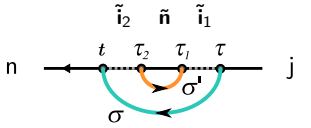

$$+\left\langle \hat{c}_\sigma(\tau)\hat{c}_\sigma^\dagger(t)\right\rangle \left\langle \hat{c}_{\sigma'}^\dagger(\tau_1)\hat{c}_{\sigma'}(\tau_2)\right\rangle \left\langle n\left|\hat{\rho}_\odot^I(\tau)\hat{\Psi}_\sigma^\dagger(\tau)\hat{\Psi}_{\sigma'}(\tau_1)\hat{\Psi}_{\sigma'}^\dagger(\tau_2)\hat{\Psi}_\sigma(t)\right|n'\right\rangle$$
$$+{}^{+}\mathcal{D}_{++}^{--}(E_{n\tilde{i}_2'}+eV_l, E_{n\tilde{i}_1'}+eV_l, E_{n\tilde{i}'}+eV_l-eV_{l'})$$
$$\times \left(\hat{\rho}_\odot^N\right)_{nj'} T_{l\sigma}^{+}(j',\tilde{i}_1')T_{l'\sigma'}^{-}(\tilde{i}_1',\tilde{n}')T_{l'\sigma'}^{+}(\tilde{n}',\tilde{i}_2')T_{l\sigma}^{-}(\tilde{i}_2',n')$$

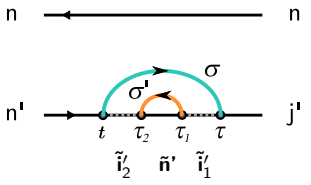

$$+\left\langle \hat{c}_\sigma(t)\hat{c}_\sigma^\dagger(\tau)\right\rangle \left\langle \hat{c}_{\sigma'}(\tau_2)\hat{c}_{\sigma'}^\dagger(\tau_1)\right\rangle \left\langle n\left|\hat{\Psi}_\sigma^\dagger(t)\hat{\Psi}_{\sigma'}(\tau_2)\hat{\Psi}_{\sigma'}^\dagger(\tau_1)\hat{\Psi}_\sigma(\tau)\hat{\rho}_\odot^I(\tau)\right|n'\right\rangle$$
$$+{}^{+}\mathcal{D}_{++}^{++}(E_{\tilde{i}_2 n'}-eV_l, E_{\tilde{i}_1 n'}-eV_l, E_{\tilde{i}n'}-eV_l-eV_{l'})$$
$$\times T_{l\sigma}^{+}(\tilde{i}_2,n)T_{l'\sigma'}^{+}(\tilde{i}_2,\tilde{i})T_{l'\sigma'}^{-}(\tilde{i},\tilde{i}_1)T_{l\sigma}^{-}(\tilde{i}_1,j)\left(\hat{\rho}_\odot^N\right)_{jn'}$$

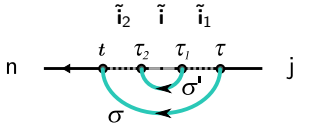

$$+\left\langle \hat{c}_\sigma(\tau)\hat{c}_\sigma^\dagger(t)\right\rangle \left\langle \hat{c}_{\sigma'}^\dagger(\tau_1)\hat{c}_{\sigma'}(\tau_2)\right\rangle \left\langle n\left|\hat{\rho}_\odot^I(\tau)\hat{\Psi}_\sigma^\dagger(\tau)\hat{\Psi}_{\sigma'}(\tau_1)\hat{\Psi}_{\sigma'}^\dagger(\tau_2)\hat{\Psi}_\sigma(t)\right|n'\right\rangle$$
$$+{}^{+}\mathcal{D}_{++}^{--}(E_{n\tilde{i}_2'}+eV_l, E_{n\tilde{i}_1'}+eV_l, E_{n\tilde{i}'}+eV_l+eV_{l'})$$
$$\times \left(\hat{\rho}_\odot^N\right)_{nj'} T_{l\sigma}^{+}(j',\tilde{i}_1')T_{l'\sigma'}^{-}(\tilde{i}_1',\tilde{i}')T_{l'\sigma'}^{+}(\tilde{i}',\tilde{i}_2')T_{l\sigma}^{-}(\tilde{i}_2',n')$$

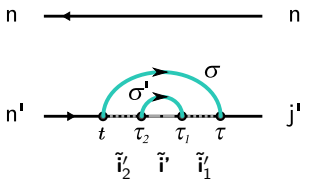

$$+\left\langle \hat{c}_\sigma^\dagger(t)\hat{c}_\sigma(\tau)\right\rangle \left\langle \hat{c}_{\sigma'}^\dagger(\tau_2)\hat{c}_{\sigma'}(\tau_1)\right\rangle \left\langle n\left|\hat{\Psi}_\sigma(t)\hat{\Psi}_{\sigma'}^\dagger(\tau_2)\hat{\Psi}_{\sigma'}(\tau_1)\hat{\Psi}_\sigma^\dagger(\tau)\hat{\rho}_\odot^I(\tau)\right|n'\right\rangle$$
$$+{}^{+}\mathcal{D}_{++}^{++}(E_{\tilde{k}_2 n'}+eV_l, E_{\tilde{k}_1 n'}+eV_l, E_{\tilde{k}n'}+eV_l+eV_{l'})$$
$$\times T_{l\sigma}^{-}(\tilde{k}_2,n)T_{l'\sigma'}^{-}(\tilde{k}_2,\tilde{k})T_{l'\sigma'}^{+}(\tilde{k},\tilde{k}_1)T_{l\sigma}^{+}(\tilde{k}_1,j)\left(\hat{\rho}_\odot^N\right)_{jn'}$$

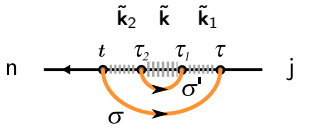

$$+\left\langle \hat{c}_\sigma^\dagger(\tau)\hat{c}_\sigma(t)\right\rangle \left\langle \hat{c}_{\sigma'}^\dagger(\tau_1)\hat{c}_{\sigma'}(\tau_2)\right\rangle \left\langle n\left|\hat{\rho}_\odot^I(\tau)\hat{\Psi}_\sigma(\tau)\hat{\Psi}_{\sigma'}(\tau_1)\hat{\Psi}_{\sigma'}^\dagger(\tau_2)\hat{\Psi}_\sigma^\dagger(t)\right|n'\right\rangle$$
$$+{}^{+}\mathcal{D}_{++}^{--}(E_{n\tilde{k}_2'}-eV_l, E_{n\tilde{k}_1'}-eV_l, E_{n\tilde{k}'}-eV_l-eV_{l'})$$
$$\times \left(\hat{\rho}_\odot^N\right)_{nj'} T_{l\sigma}^{-}(j',\tilde{k}_1')T_{l'\sigma'}^{-}(\tilde{k}_1',\tilde{k}')T_{l'\sigma'}^{+}(\tilde{k}',\tilde{k}_2')T_{l\sigma}^{+}(\tilde{k}_2',n')$$

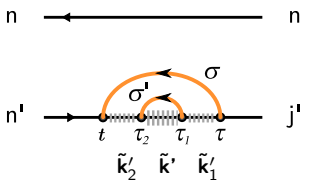

$$-\left\langle \hat{C}_3^p \hat{C}_1^{\bar{p}} \right\rangle \left\langle \hat{C}_2^{p'} \hat{C}_0^{\bar{p}'} \right\rangle \hat{D}_3^{\bar{p}} \hat{D}_2^{\bar{p}'} \hat{D}_1^{p} \hat{D}_0^{p'} \; \hat{\rho}_{\odot}$$

$$-\left\langle \hat{c}_\sigma^\dagger(t)\,\hat{c}_\sigma(\tau_1)\right\rangle \left\langle \hat{c}_{\sigma'}(\tau_2)\,\hat{c}_{\sigma'}^\dagger(\tau)\right\rangle \left\langle n\left|\hat{\Psi}_\sigma(t)\hat{\Psi}_{\sigma'}^\dagger(\tau_2)\hat{\Psi}_\sigma^\dagger(\tau_1)\hat{\Psi}_{\sigma'}(\tau)\hat{\rho}_\odot^I(\tau)\right|n'\right\rangle$$
$$-{}^{+}X_{++}^{++}(E_{\tilde{k}n'}+eV_l, E_{\tilde{i}n'}-eV_{l'}, E_{\tilde{n}n'}+eV_l-eV_{l'})$$
$$\times T_{l\sigma}^{-}(n,\tilde{k})T_{l'\sigma'}^{+}(\tilde{k},\tilde{n})T_{l\sigma}^{+}(\tilde{n},\tilde{i})T_{l'\sigma'}^{-}(\tilde{i},j)\left(\hat{\rho}_\odot^N\right)_{jn'}$$

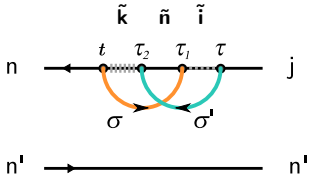

$$-\left\langle \hat{c}_\sigma^\dagger(\tau_1)\,\hat{c}_\sigma(t)\right\rangle \left\langle \hat{c}_{\sigma'}(\tau)\,\hat{c}_{\sigma'}^\dagger(\tau_2)\right\rangle \left\langle n\left|\hat{\rho}_\odot^I(\tau)\hat{\Psi}_{\sigma'}^\dagger(\tau)\hat{\Psi}_\sigma(\tau_1)\hat{\Psi}_{\sigma'}(\tau_2)\hat{\Psi}_\sigma^\dagger(t)\right|n'\right\rangle$$
$$-{}^{+}X_{++}^{--}(E_{n\tilde{k}'}-eV_l, E_{n\tilde{i}'}+eV_{l'}, E_{n\tilde{n}'}-eV_l+eV_{l'})$$
$$\times \left(\hat{\rho}_\odot^N\right)_{nj'} T_{l'\sigma'}^{+}(j',\tilde{i}')T_{l\sigma}^{-}(\tilde{i}',\tilde{n}')T_{l'\sigma'}^{-}(\tilde{n}',\tilde{k}')T_{l\sigma}^{+}(\tilde{k}',n')$$

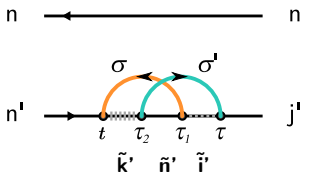

$$-\left\langle \hat{c}_\sigma(t)\,\hat{c}_\sigma^\dagger(\tau_1)\right\rangle \left\langle \hat{c}_{\sigma'}^\dagger(\tau_2)\,\hat{c}_{\sigma'}(\tau)\right\rangle \left\langle n\left|\hat{\Psi}_\sigma^\dagger(t)\hat{\Psi}_{\sigma'}(\tau_2)\hat{\Psi}_\sigma(\tau_1)\hat{\Psi}_{\sigma'}^\dagger(\tau)\hat{\rho}_\odot^I(\tau)\right|n'\right\rangle$$
$$-{}^{+}X_{++}^{++}(E_{\tilde{i}n'}-eV_l, E_{\tilde{k}n'}+eV_{l'}, E_{\tilde{n}n'}-eV_l+eV_{l'})$$
$$\times T_{l\sigma}^{+}(n,\tilde{i})T_{l'\sigma'}^{-}(\tilde{i},\tilde{n})T_{l\sigma}^{-}(\tilde{n},\tilde{k})T_{l'\sigma'}^{+}(\tilde{k},j)\left(\hat{\rho}_\odot^N\right)_{jn'}$$

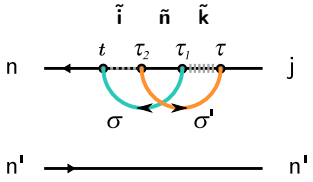

$$-\left\langle \hat{c}_\sigma(\tau_1)\,\hat{c}_\sigma^\dagger(t)\right\rangle \left\langle \hat{c}_{\sigma'}^\dagger(\tau)\,\hat{c}_{\sigma'}(\tau_2)\right\rangle \left\langle n\left|\hat{\rho}_\odot^I(\tau)\hat{\Psi}_{\sigma'}(\tau)\hat{\Psi}_\sigma^\dagger(\tau_1)\hat{\Psi}_{\sigma'}^\dagger(\tau_2)\hat{\Psi}_\sigma(t)\right|n'\right\rangle$$
$$-{}^{+}X_{++}^{--}(E_{n\tilde{i}'}+eV_l, E_{n\tilde{k}'}-eV_{l'}, E_{n\tilde{n}'}+eV_l-eV_{l'})$$
$$\times \left(\hat{\rho}_\odot^N\right)_{nj'} T_{l'\sigma'}^{-}(j',\tilde{k}')T_{l\sigma}^{+}(\tilde{k}',\tilde{n}')T_{l'\sigma'}^{+}(\tilde{n}',\tilde{i}')T_{l\sigma}^{-}(\tilde{i}',n')$$

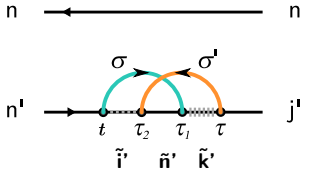

$$-\left\langle \hat{c}_\sigma(t)\,\hat{c}_\sigma^\dagger(\tau_1)\right\rangle \left\langle \hat{c}_{\sigma'}(\tau_2)\,\hat{c}_{\sigma'}^\dagger(\tau)\right\rangle \left\langle n\left|\hat{\Psi}_\sigma^\dagger(t)\hat{\Psi}_{\sigma'}(\tau_2)\hat{\Psi}_\sigma(\tau_1)\hat{\Psi}_{\sigma'}^\dagger(\tau)\hat{\rho}_\odot^I(\tau)\right|n'\right\rangle$$
$$-{}^{+}X_{++}^{++}(E_{\tilde{i}_2n'}-eV_l, E_{\tilde{i}_1n'}-eV_{l'}, E_{\tilde{i}n'}-eV_l-eV_{l'})$$
$$\times T_{l\sigma}^{+}(n,\tilde{i}_2)T_{l'\sigma'}^{+}(\tilde{i}_2,\tilde{i})T_{l\sigma}^{-}(\tilde{i},\tilde{i}_1)T_{l'\sigma'}^{-}(\tilde{i}_1,j)\left(\hat{\rho}_\odot^N\right)_{jn'}$$

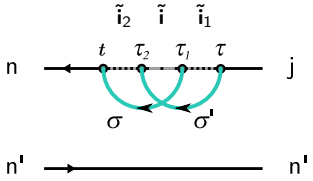

$$-\left\langle \hat{c}_\sigma(\tau_1)\,\hat{c}_\sigma^\dagger(t)\right\rangle \left\langle \hat{c}_{\sigma'}(\tau)\,\hat{c}_{\sigma'}^\dagger(\tau_2)\right\rangle \left\langle n\left|\hat{\rho}_\odot^I(\tau)\hat{\Psi}_{\sigma'}^\dagger(\tau)\hat{\Psi}_\sigma^\dagger(\tau_1)\hat{\Psi}_{\sigma'}(\tau_2)\hat{\Psi}_\sigma(t)\right|n'\right\rangle$$
$$-{}^{+}X_{++}^{--}(E_{n\tilde{i}_2'}+eV_l, E_{n\tilde{i}_1'}+eV_{l'}, E_{n\tilde{i}'}+eV_l+eV_{l'})$$
$$\times \left(\hat{\rho}_\odot^N\right)_{nj'} T_{l'\sigma'}^{+}(j',\tilde{i}_1')T_{l\sigma}^{+}(\tilde{i}_1',\tilde{i}')T_{l'\sigma'}^{-}(\tilde{i}',\tilde{i}_2')T_{l\sigma}^{-}(\tilde{i}_2',n')$$

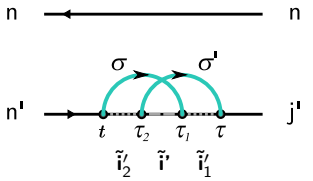

$$-\left\langle \hat{c}_\sigma^\dagger(t)\,\hat{c}_\sigma(\tau_1)\right\rangle \left\langle \hat{c}_{\sigma'}^\dagger(\tau_2)\,\hat{c}_{\sigma'}(\tau)\right\rangle \left\langle n\left|\hat{\Psi}_\sigma(t)\hat{\Psi}_{\sigma'}^\dagger(\tau_2)\hat{\Psi}_\sigma^\dagger(\tau_1)\hat{\Psi}_{\sigma'}(\tau)\hat{\rho}_\odot^I(\tau)\right|n'\right\rangle$$
$$-{}^{+}X_{++}^{++}(E_{\tilde{k}_2n'}+eV_l, E_{\tilde{k}_1n'}+eV_{l'}, E_{\tilde{k}n'}+eV_l+eV_{l'})$$
$$\times T_{l\sigma}^{-}(n,\tilde{k}_2)T_{l'\sigma'}^{-}(\tilde{k}_2,\tilde{k})T_{l\sigma}^{+}(\tilde{k},\tilde{k}_1)T_{l'\sigma'}^{+}(\tilde{k}_1,j)\left(\hat{\rho}_\odot^N\right)_{jn'}$$

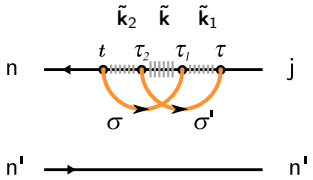

$$-\left\langle \hat{c}_\sigma^\dagger(\tau_1)\,\hat{c}_\sigma(t)\right\rangle \left\langle \hat{c}_{\sigma'}^\dagger(\tau)\,\hat{c}_{\sigma'}(\tau_2)\right\rangle \left\langle n\left|\hat{\rho}_\odot^I(\tau)\hat{\Psi}_{\sigma'}(\tau)\hat{\Psi}_\sigma(\tau_1)\hat{\Psi}_{\sigma'}^\dagger(\tau_2)\hat{\Psi}_\sigma^\dagger(t)\right|n'\right\rangle$$
$$-{}^{+}X_{++}^{--}(E_{n\tilde{k}_2'}-eV_l, E_{n\tilde{k}_1'}-eV_{l'}, E_{n\tilde{k}'}-eV_l-eV_{l'})$$
$$\times \left(\hat{\rho}_\odot^N\right)_{nj'} T_{l'\sigma'}^{-}(j',\tilde{k}_1')T_{l\sigma}^{-}(\tilde{k}_1',\tilde{k}')T_{l'\sigma'}^{+}(\tilde{k}',\tilde{k}_2')T_{l\sigma}^{+}(\tilde{k}_2',n')$$

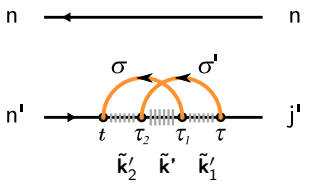

$$+\left\langle \hat{C}_1^p \hat{C}_3^{\bar{p}} \right\rangle \left\langle \hat{C}_0^{p'} \hat{C}_2^{\bar{p}'} \right\rangle \hat{D}_3^p \hat{D}_2^{p'} \ \hat{\rho}_\odot \ \hat{D}_0^{\bar{p}'} \hat{D}_1^{\bar{p}}$$

$$+\left\langle \hat{c}_\sigma^\dagger(\tau_1)\hat{c}_\sigma(t)\right\rangle \left\langle \hat{c}_{\sigma'}(\tau)\hat{c}_{\sigma'}^\dagger(\tau_2)\right\rangle \left\langle n\left|\hat{\Psi}_\sigma^\dagger(t)\hat{\Psi}_{\sigma'}(\tau_2)\hat{\rho}_\odot^I(\tau)\hat{\Psi}_{\sigma'}^\dagger(\tau)\hat{\Psi}_\sigma(\tau_1)\right|n'\right\rangle$$
$$+{}^{+}X_{++}^{--}(E_{\tilde{i}n'}-eV_l, E_{j\tilde{i}'}+eV_{l'}, E_{jn'}-eV_l+eV_{l'})$$
$$\times T_{l\sigma}^{+}(n,\tilde{i})T_{l'\sigma'}^{-}(\tilde{i},j)\left(\hat{\rho}_\odot^N\right)_{jj'}T_{l'\sigma'}^{+}(j',\tilde{i}')T_{l\sigma}^{-}(\tilde{i}',n')$$

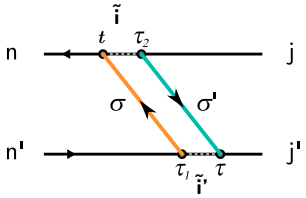

$$+\left\langle \hat{c}_\sigma^\dagger(t)\hat{c}_\sigma(\tau_1)\right\rangle \left\langle \hat{c}_{\sigma'}(\tau_2)\hat{c}_{\sigma'}^\dagger(\tau)\right\rangle \left\langle n\left|\hat{\Psi}_\sigma^\dagger(\tau_1)\hat{\Psi}_{\sigma'}(\tau)\hat{\rho}_\odot^I(\tau)\hat{\Psi}_{\sigma'}^\dagger(\tau_2)\hat{\Psi}_\sigma(t)\right|n'\right\rangle$$
$$+{}^{+}X_{++}^{++}(E_{n\tilde{i}'}+eV_l, E_{\tilde{i}j'}-eV_{l'}, E_{nj'}+eV_l-eV_{l'})$$
$$\times T_{l\sigma}^{+}(n,\tilde{i})T_{l'\sigma'}^{-}(\tilde{i},j)\left(\hat{\rho}_\odot^N\right)_{jj'}T_{l'\sigma'}^{+}(j',\tilde{i}')T_{l\sigma}^{-}(\tilde{i}',n')$$

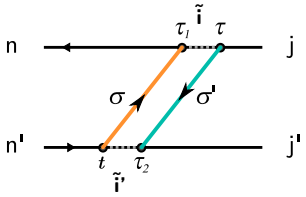

$$+\left\langle \hat{c}_\sigma(\tau_1)\hat{c}_\sigma^\dagger(t)\right\rangle \left\langle \hat{c}_{\sigma'}^\dagger(\tau)\hat{c}_{\sigma'}(\tau_2)\right\rangle \left\langle n\left|\hat{\Psi}_\sigma(t)\hat{\Psi}_{\sigma'}^\dagger(\tau_2)\hat{\rho}_\odot^I(\tau)\hat{\Psi}_{\sigma'}(\tau)\hat{\Psi}_\sigma^\dagger(\tau_1)\right|n'\right\rangle$$
$$+{}^{+}X_{++}^{--}(E_{\tilde{k}n'}+eV_l, E_{j\tilde{k}'}-eV_{l'}, E_{jn'}+eV_l-eV_{l'})$$
$$\times T_{l\sigma}^{-}(n,\tilde{k})T_{l'\sigma'}^{+}(\tilde{k},j)\left(\hat{\rho}_\odot^N\right)_{jj'}T_{l'\sigma'}^{-}(j',\tilde{k}')T_{l\sigma}^{+}(\tilde{k}',n')$$

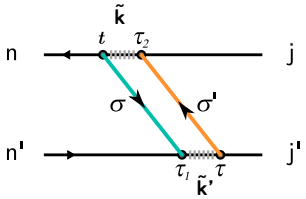

$$+\left\langle \hat{c}_\sigma(t)\hat{c}_\sigma^\dagger(\tau_1)\right\rangle \left\langle \hat{c}_{\sigma'}^\dagger(\tau_2)\hat{c}_{\sigma'}(\tau)\right\rangle \left\langle n\left|\hat{\Psi}_\sigma(\tau_1)\hat{\Psi}_{\sigma'}^\dagger(\tau)\hat{\rho}_\odot^I(\tau)\hat{\Psi}_{\sigma'}(\tau_2)\hat{\Psi}_\sigma^\dagger(t)\right|n'\right\rangle$$
$$+{}^{+}X_{++}^{++}(E_{n\tilde{k}'}-eV_l, E_{\tilde{k}j'}+eV_{l'}, E_{nj'}-eV_l+eV_{l'})$$
$$\times T_{l\sigma}^{-}(n,\tilde{k})T_{l'\sigma'}^{+}(\tilde{k},j)\left(\hat{\rho}_\odot^N\right)_{jj'}T_{l'\sigma'}^{-}(j',\tilde{k}')T_{l\sigma}^{+}(\tilde{k}',n')$$

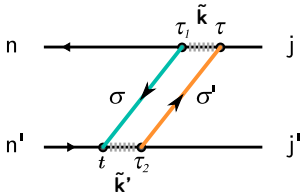

$$+\left\langle \hat{c}_\sigma(\tau_1)\hat{c}_\sigma^\dagger(t)\right\rangle \left\langle \hat{c}_{\sigma'}(\tau)\hat{c}_{\sigma'}^\dagger(\tau_2)\right\rangle \left\langle n\left|\hat{\Psi}_\sigma(t)\hat{\Psi}_{\sigma'}(\tau_2)\hat{\rho}_\odot^I(\tau)\hat{\Psi}_{\sigma'}^\dagger(\tau)\hat{\Psi}_\sigma^\dagger(\tau_1)\right|n'\right\rangle$$
$$+{}^{+}X_{++}^{--}(E_{\tilde{k}n'}+eV_l, E_{k\tilde{k}'}+eV_{l'}, E_{kn'}+eV_l+eV_{l'})$$
$$\times T_{l\sigma}^{-}(n,\tilde{k})T_{l'\sigma'}^{-}(\tilde{k},k)(\hat{\rho}_\odot^{N+2})_{kk'}T_{l'\sigma'}^{+}(k',\tilde{k}')T_{l\sigma}^{+}(\tilde{k}',n')$$

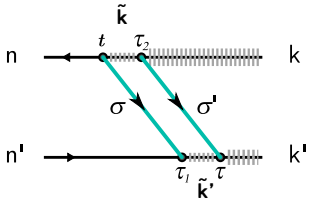

$$+\left\langle \hat{c}_\sigma(t)\hat{c}_\sigma^\dagger(\tau_1)\right\rangle \left\langle \hat{c}_{\sigma'}(\tau_2)\hat{c}_{\sigma'}^\dagger(\tau)\right\rangle \left\langle n\left|\hat{\Psi}_\sigma(\tau_1)\hat{\Psi}_{\sigma'}^\dagger(\tau)\hat{\rho}_\odot^I(\tau)\hat{\Psi}_{\sigma'}^\dagger(\tau_2)\hat{\Psi}_\sigma^\dagger(t)\right|n'\right\rangle$$
$$+{}^{+}X_{++}^{++}(E_{n\tilde{k}'}-eV_l, E_{\tilde{k}k'}-eV_{l'}, E_{nk'}-eV_l-eV_{l'})$$
$$\times T_{l\sigma}^{-}(n,\tilde{k})T_{l'\sigma'}^{-}(\tilde{k},k)(\hat{\rho}_\odot^{N+2})_{kk'}T_{l'\sigma'}^{+}(k',\tilde{k}')T_{l\sigma}^{+}(\tilde{k}',n')$$

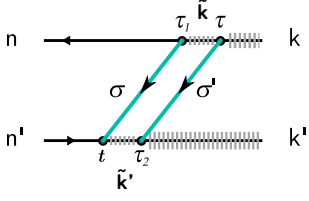

$$+\left\langle \hat{c}_\sigma^\dagger(\tau_1)\hat{c}_\sigma(t)\right\rangle \left\langle \hat{c}_{\sigma'}^\dagger(\tau)\hat{c}_{\sigma'}(\tau_2)\right\rangle \left\langle n\left|\hat{\Psi}_\sigma^\dagger(t)\hat{\Psi}_{\sigma'}^\dagger(\tau_2)\hat{\rho}_\odot^I(\tau)\hat{\Psi}_{\sigma'}(\tau)\hat{\Psi}_\sigma(\tau_1)\right|n'\right\rangle$$
$$+{}^{+}X_{++}^{--}(E_{\tilde{i}n'}-eV_l, E_{i\tilde{i}'}-eV_{l'}, E_{in'}-eV_l-eV_{l'})$$
$$\times T_{l\sigma}^{+}(n,\tilde{i})T_{l'\sigma'}^{+}(\tilde{i},i)(\hat{\rho}_\odot^{N-2})_{ii'}T_{l'\sigma'}^{-}(i',\tilde{i}')T_{l\sigma}^{-}(\tilde{i}',n')$$

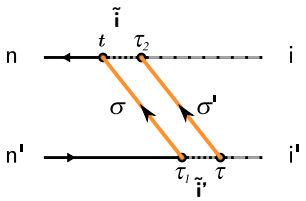

$$+\left\langle \hat{c}_\sigma^\dagger(t)\hat{c}_\sigma(\tau_1)\right\rangle \left\langle \hat{c}_{\sigma'}^\dagger(\tau_2)\hat{c}_{\sigma'}(\tau)\right\rangle \left\langle n\left|\hat{\Psi}_\sigma^\dagger(\tau_1)\hat{\Psi}_{\sigma'}^\dagger(\tau)\hat{\rho}_\odot^I(\tau)\hat{\Psi}_{\sigma'}(\tau_2)\hat{\Psi}_\sigma(t)\right|n'\right\rangle$$
$$+{}^{+}X_{++}^{++}(E_{n\tilde{i}'}+eV_l, E_{\tilde{i}i'}+eV_{l'}, E_{ni'}+eV_l+eV_{l'})$$
$$\times T_{l\sigma}^{+}(n,\tilde{i})T_{l'\sigma'}^{+}(\tilde{i},i)(\hat{\rho}_\odot^{N-2})_{ii'}T_{l'\sigma'}^{-}(i',\tilde{i}')T_{l\sigma}^{-}(\tilde{i}',n')$$

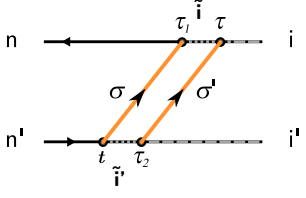

$$-\left\langle \hat{C}_0^p \hat{C}_3^{\bar{p}} \right\rangle \left\langle \hat{C}_1^{p'} \hat{C}_2^{\bar{p}'} \right\rangle \hat{D}_3^p \hat{D}_2^{p'} \; \hat{\rho}_\odot \; \hat{D}_0^{\bar{p}} \hat{D}_1^{\bar{p}'}$$

$$-\left\langle \hat{c}_\sigma^\dagger(\tau)\hat{c}_\sigma(t)\right\rangle \left\langle \hat{c}_{\sigma'}(\tau_1)\hat{c}_{\sigma'}^\dagger(\tau_2)\right\rangle \left\langle n\left|\hat{\Psi}_\sigma^\dagger(t)\hat{\Psi}_{\sigma'}(\tau_2)\hat{\rho}_\odot^I(\tau)\hat{\Psi}_\sigma(\tau)\hat{\Psi}_{\sigma'}^\dagger(\tau_1)\right|n'\right\rangle$$
$$-{}^{+}\mathcal{D}_{++}^{--}(E_{\tilde{i}n'}-eV_l, E_{j\tilde{k}'}-eV_l, E_{jn'}-eV_l+eV_{l'})$$
$$\times T_{l\sigma}^{+}(n,\tilde{i})T_{l'\sigma'}^{-}(\tilde{i},j)\left(\hat{\rho}_\odot^N\right)_{jj'}T_{l\sigma}^{-}(j',\tilde{k}')T_{l'\sigma'}^{+}(\tilde{k}',n')$$

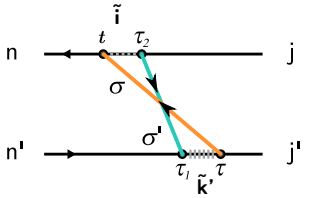

$$-\left\langle \hat{c}_\sigma^\dagger(t)\hat{c}_\sigma(\tau)\right\rangle \left\langle \hat{c}_{\sigma'}(\tau_2)\hat{c}_{\sigma'}^\dagger(\tau_1)\right\rangle \left\langle n\left|\hat{\Psi}_{\sigma'}(\tau_1)\hat{\Psi}_\sigma^\dagger(\tau)\hat{\rho}_\odot^I(\tau)\hat{\Psi}_{\sigma'}^\dagger(\tau_2)\hat{\Psi}_\sigma(t)\right|n'\right\rangle$$
$$-{}^{+}\mathcal{D}_{++}^{++}(E_{n\tilde{i}'}+eV_l, E_{\tilde{k}j'}+eV_l, E_{nj'}+eV_l-eV_{l'})$$
$$\times T_{l'\sigma'}^{-}(n,\tilde{k})T_{l\sigma}^{+}(\tilde{k},j)\left(\hat{\rho}_\odot^N\right)_{jj'}T_{l'\sigma'}^{+}(j',\tilde{i}')T_{l\sigma}^{-}(\tilde{i}',n')$$

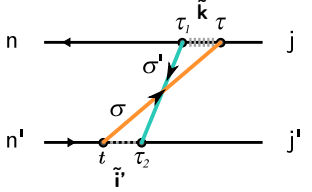

$$-\left\langle \hat{c}_\sigma(\tau)\hat{c}_\sigma^\dagger(t)\right\rangle \left\langle \hat{c}_{\sigma'}^\dagger(\tau_1)\hat{c}_{\sigma'}(\tau_2)\right\rangle \left\langle n\left|\hat{\Psi}_\sigma(t)\hat{\Psi}_{\sigma'}^\dagger(\tau_2)\hat{\rho}_\odot^I(\tau)\hat{\Psi}_\sigma^\dagger(\tau)\hat{\Psi}_{\sigma'}(\tau_1)\right|n'\right\rangle$$
$$-{}^{+}\mathcal{D}_{++}^{--}(E_{\tilde{k}n'}+eV_l, E_{j\tilde{i}'}+eV_l, E_{jn'}+eV_l-eV_{l'})$$
$$\times T_{l\sigma}^{-}(n,\tilde{k})T_{l'\sigma'}^{+}(\tilde{k},j)\left(\hat{\rho}_\odot^N\right)_{jj'}T_{l\sigma}^{+}(j',\tilde{i}')T_{l'\sigma'}^{-}(\tilde{i}',n')$$

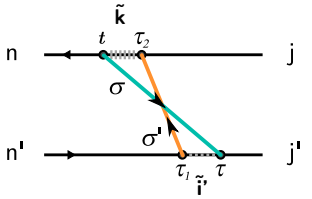

$$-\left\langle \hat{c}_\sigma(\tau)\hat{c}_\sigma^\dagger(t)\right\rangle \left\langle \hat{c}_{\sigma'}^\dagger(\tau_2)\hat{c}_{\sigma'}(\tau_1)\right\rangle \left\langle n\left|\hat{\Psi}_{\sigma'}^\dagger(\tau_1)\hat{\Psi}_\sigma(\tau)\hat{\rho}_\odot^I(\tau)\hat{\Psi}_{\sigma'}(\tau_2)\hat{\Psi}_\sigma^\dagger(t)\right|n'\right\rangle$$
$$-{}^{+}\mathcal{D}_{++}^{++}(E_{n\tilde{k}'}+eV_l, E_{\tilde{i}j'}+eV_l, E_{nj'}+eV_l-eV_{l'})$$
$$\times T_{l'\sigma'}^{+}(n,\tilde{i})T_{l\sigma}^{-}(\tilde{i},j)\left(\hat{\rho}_\odot^N\right)_{jj'}T_{l'\sigma'}^{-}(j',\tilde{k}')T_{l\sigma}^{+}(\tilde{k}',n')$$

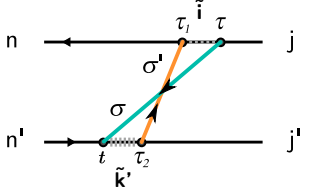

$$-\left\langle \hat{c}_\sigma(\tau)\hat{c}_\sigma^\dagger(t)\right\rangle \left\langle \hat{c}_{\sigma'}(\tau_1)\hat{c}_{\sigma'}^\dagger(\tau_2)\right\rangle \left\langle n\left|\hat{\Psi}_\sigma(t)\hat{\Psi}_{\sigma'}(\tau_2)\hat{\rho}_\odot^I(\tau)\hat{\Psi}_\sigma^\dagger(\tau)\hat{\Psi}_{\sigma'}^\dagger(\tau_1)\right|n'\right\rangle$$
$$-{}^{+}\mathcal{D}_{++}^{--}(E_{\tilde{k}n'}+eV_l, E_{k\tilde{k}'}+eV_l, E_{kn'}+eV_l+eV_{l'})$$
$$\times T_{l\sigma}^{-}(n,\tilde{k})T_{l'\sigma'}^{-}(\tilde{k},k)(\hat{\rho}_\odot^{N+2})_{kk'}T_{l\sigma}^{+}(j',\tilde{k}')T_{l'\sigma'}^{+}(\tilde{k}',n')$$

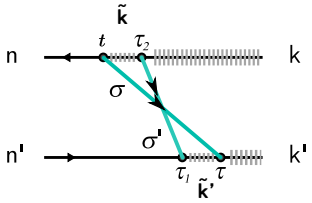

$$-\left\langle \hat{c}_\sigma(t)\hat{c}_\sigma^\dagger(\tau)\right\rangle \left\langle \hat{c}_{\sigma'}(\tau_2)\hat{c}_{\sigma'}^\dagger(\tau_1)\right\rangle \left\langle n\left|\hat{\Psi}_{\sigma'}(\tau_1)\hat{\Psi}_\sigma(\tau)\hat{\rho}_\odot^I(\tau)\hat{\Psi}_{\sigma'}^\dagger(\tau_2)\hat{\Psi}_\sigma^\dagger(t)\right|n'\right\rangle$$
$$-{}^{+}\mathcal{D}_{++}^{++}(E_{n\tilde{k}'}+eV_l, E_{\tilde{k}k'}+eV_l, E_{nk'}+eV_l+eV_{l'})$$
$$\times T_{l'\sigma'}^{+}(n,\tilde{k})T_{l\sigma}^{-}(\tilde{k},k)(\hat{\rho}_\odot^{N+2})_{kk'}T_{l'\sigma'}^{+}(k',\tilde{k}')T_{l\sigma}^{+}(\tilde{k}',n')$$

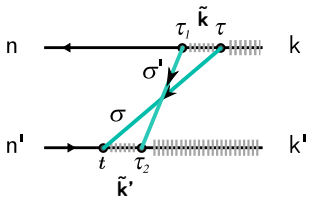

$$-\left\langle \hat{c}_\sigma^\dagger(\tau)\hat{c}_\sigma(t)\right\rangle \left\langle \hat{c}_{\sigma'}^\dagger(\tau_1)\hat{c}_{\sigma'}(\tau_2)\right\rangle \left\langle n\left|\hat{\Psi}_\sigma^\dagger(t)\hat{\Psi}_{\sigma'}^\dagger(\tau_2)\hat{\rho}_\odot^I(\tau)\hat{\Psi}_\sigma(\tau)\hat{\Psi}_{\sigma'}(\tau_1)\right|n'\right\rangle$$
$$-{}^{+}\mathcal{D}_{++}^{--}(E_{\tilde{i}n'}-eV_l, E_{i\tilde{i}'}-eV_l, E_{in'}-eV_l-eV_{l'})$$
$$\times T_{l\sigma}^{+}(n,\tilde{i})T_{l'\sigma'}^{+}(\tilde{i},i)(\hat{\rho}_\odot^{N-2})_{ii'}T_{l\sigma}^{-}(i',\tilde{i}')T_{l'\sigma'}^{-}(\tilde{i}',n')$$

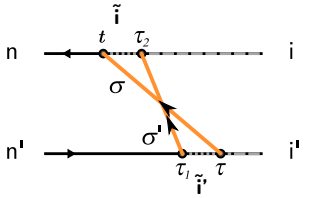

$$-\left\langle \hat{c}_\sigma^\dagger(t)\hat{c}_\sigma(\tau)\right\rangle \left\langle \hat{c}_{\sigma'}^\dagger(\tau_2)\hat{c}_{\sigma'}(\tau_1)\right\rangle \left\langle n\left|\hat{\Psi}_{\sigma'}^\dagger(\tau_1)\hat{\Psi}_\sigma^\dagger(\tau)\hat{\rho}_\odot^I(\tau)\hat{\Psi}_{\sigma'}(\tau_2)\hat{\Psi}_\sigma(t)\right|n'\right\rangle$$
$$-{}^{+}\mathcal{D}_{++}^{++}(E_{n\tilde{i}'}+eV_l, E_{\tilde{i}i'}+eV_l, E_{ni'}+eV_l+eV_{l'})$$
$$\times T_{l'\sigma'}^{+}(n,\tilde{i})T_{l\sigma}^{+}(\tilde{i},i)(\hat{\rho}_\odot^{N-2})_{ii'}T_{l'\sigma'}^{-}(i',\tilde{i}')T_{l\sigma}^{-}(\tilde{i}',n')$$

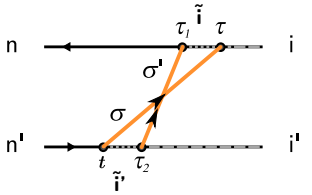

$$+\left\langle \hat{C}_3^p \hat{C}_1^{\bar{p}} \right\rangle \left\langle \hat{C}_0^{p'} \hat{C}_2^{\bar{p}'} \right\rangle \hat{D}_3^{\bar{p}} \hat{D}_1^{p} \; \hat{\rho}_\odot \; \hat{D}_0^{\bar{p}'} \hat{D}_2^{p'}$$

$$+\left\langle \hat{c}^\dagger_\sigma(t)\,\hat{c}_\sigma(\tau_1)\right\rangle \left\langle \hat{c}_{\sigma'}(\tau)\,\hat{c}^\dagger_{\sigma'}(\tau_2)\right\rangle \left\langle n\left|\hat{\Psi}_\sigma(t)\hat{\Psi}^\dagger_\sigma(\tau_1)\hat{\rho}^I_\odot(\tau)\hat{\Psi}^\dagger_{\sigma'}(\tau)\hat{\Psi}_{\sigma'}(\tau_2)\right|n'\right\rangle$$
$$+{}^{+}X^{+-}_{++}(E_{\tilde{k}n'}+eV_l, E_{j\tilde{i}'}+eV_{l'}, E_{\tilde{k}\tilde{i}'}+eV_l+eV_{l'})$$
$$\times T^-_{l\sigma}(n,\tilde{k})T^+_{l\sigma}(\tilde{k},j)\left(\hat{\rho}^N_\odot\right)_{jj'} T^+_{l'\sigma'}(j',\tilde{i}')T^-_{l'\sigma'}(\tilde{i}',n')$$

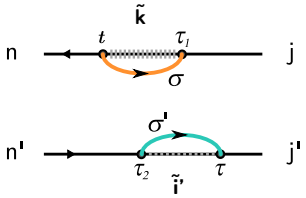

$$+\left\langle \hat{c}^\dagger_\sigma(\tau_1)\,\hat{c}_\sigma(t)\right\rangle \left\langle \hat{c}_{\sigma'}(\tau_2)\,\hat{c}^\dagger_{\sigma'}(\tau)\right\rangle \left\langle n\left|\hat{\Psi}^\dagger_{\sigma'}(\tau_2)\hat{\Psi}_{\sigma'}(\tau)\hat{\rho}^I_\odot(\tau)\hat{\Psi}_\sigma(\tau_1)\hat{\Psi}^\dagger_\sigma(t)\right|n'\right\rangle$$
$$+{}^{+}X^{-+}_{++}(E_{n\tilde{k}'}-eV_l, E_{\tilde{i}j'}-eV_{l'}, E_{\tilde{i}\tilde{k}'}-eV_l-eV_{l'})$$
$$\times T^+_{l'\sigma'}(n,\tilde{i})T^-_{l'\sigma'}(\tilde{i},j)\left(\hat{\rho}^N_\odot\right)_{jj'} T^-_{l\sigma}(j',\tilde{k}')T^+_{l\sigma}(\tilde{k}',n')$$

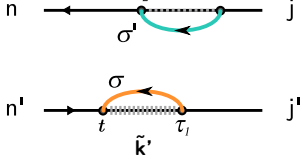

$$+\left\langle \hat{c}_\sigma(t)\,\hat{c}^\dagger_\sigma(\tau_1)\right\rangle \left\langle \hat{c}^\dagger_{\sigma'}(\tau)\,\hat{c}_{\sigma'}(\tau_2)\right\rangle \left\langle n\left|\hat{\Psi}^\dagger_\sigma(t)\hat{\Psi}_\sigma(\tau_1)\hat{\rho}^I_\odot(\tau)\hat{\Psi}_{\sigma'}(\tau)\hat{\Psi}^\dagger_{\sigma'}(\tau_2)\right|n'\right\rangle$$
$$+{}^{+}X^{+-}_{++}(E_{\tilde{i}n'}-eV_l, E_{j\tilde{k}'}-eV_{l'}, E_{\tilde{i}\tilde{k}'}-eV_l-eV_{l'})$$
$$\times T^+_{l\sigma}(n,\tilde{i})T^-_{l\sigma}(\tilde{i},j)\left(\hat{\rho}^N_\odot\right)_{jj'} T^-_{l'\sigma'}(j',\tilde{k}')T^+_{l'\sigma'}(\tilde{k}',n')$$

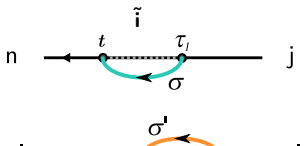

$$+\left\langle \hat{c}_\sigma(\tau_1)\,\hat{c}^\dagger_\sigma(t)\right\rangle \left\langle \hat{c}^\dagger_{\sigma'}(\tau_2)\,\hat{c}_{\sigma'}(\tau)\right\rangle \left\langle n\left|\hat{\Psi}_{\sigma'}(\tau_2)\hat{\Psi}^\dagger_{\sigma'}(\tau)\hat{\rho}^I_\odot(\tau)\hat{\Psi}^\dagger_\sigma(\tau_1)\hat{\Psi}_\sigma(t)\right|n'\right\rangle$$
$$+{}^{+}X^{-+}_{++}(E_{n\tilde{i}'}+eV_l, E_{\tilde{k}j'}+eV_{l'}, E_{\tilde{k}\tilde{i}'}+eV_l+eV_{l'})$$
$$\times T^-_{l'\sigma'}(n,\tilde{k})T^+_{l'\sigma'}(\tilde{k},j)\left(\hat{\rho}^N_\odot\right)_{jj'} T^+_{l\sigma}(j',\tilde{i}')T^-_{l\sigma}(\tilde{i}',n')$$

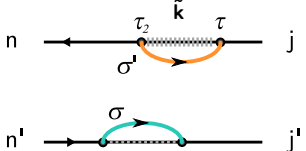

$$+\left\langle \hat{c}_\sigma(t)\,\hat{c}^\dagger_\sigma(\tau_1)\right\rangle \left\langle \hat{c}_{\sigma'}(\tau)\,\hat{c}^\dagger_{\sigma'}(\tau_2)\right\rangle \left\langle n\left|\hat{\Psi}^\dagger_\sigma(t)\hat{\Psi}_\sigma(\tau_1)\hat{\rho}^I_\odot(\tau)\hat{\Psi}^\dagger_{\sigma'}(\tau)\hat{\Psi}_{\sigma'}(\tau_2)\right|n'\right\rangle$$
$$+{}^{+}X^{+-}_{++}(E_{\tilde{i}n'}-eV_l, E_{j\tilde{i}'}+eV_{l'}, E_{\tilde{i}\tilde{i}'}-eV_l+eV_{l'})$$
$$\times T^+_{l\sigma}(n,\tilde{i})T^-_{l\sigma}(\tilde{i},j)\left(\hat{\rho}^N_\odot\right)_{jj'} T^+_{l'\sigma'}(j',\tilde{i}')T^-_{l'\sigma'}(\tilde{i}',n')$$

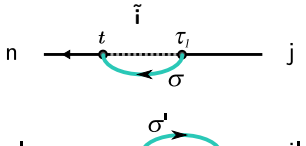

$$+\left\langle \hat{c}_\sigma(\tau_1)\,\hat{c}^\dagger_\sigma(t)\right\rangle \left\langle \hat{c}^\dagger_{\sigma'}(\tau_2)\,\hat{c}_{\sigma'}(\tau)\right\rangle \left\langle n\left|\hat{\Psi}^\dagger_{\sigma'}(\tau_2)\hat{\Psi}_{\sigma'}(\tau)\hat{\rho}^I_\odot(\tau)\hat{\Psi}^\dagger_\sigma(\tau_1)\hat{\Psi}_\sigma(t)\right|n'\right\rangle$$
$$+{}^{+}X^{-+}_{++}(E_{n\tilde{i}'}+eV_l, E_{\tilde{i}j'}-eV_{l'}, E_{\tilde{i}\tilde{i}'}+eV_l-eV_{l'})$$
$$\times T^+_{l'\sigma'}(n,\tilde{i})T^-_{l'\sigma'}(\tilde{i},j)\left(\hat{\rho}^N_\odot\right)_{jj'} T^+_{l\sigma}(j',\tilde{i}')T^-_{l\sigma}(\tilde{i}',n')$$

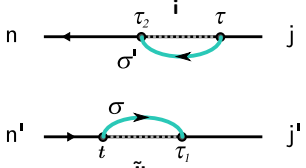

$$+\left\langle \hat{c}^\dagger_\sigma(t)\,\hat{c}_\sigma(\tau_1)\right\rangle \left\langle \hat{c}^\dagger_{\sigma'}(\tau)\,\hat{c}_{\sigma'}(\tau_2)\right\rangle \left\langle n\left|\hat{\Psi}_\sigma(t)\hat{\Psi}^\dagger_\sigma(\tau_1)\hat{\rho}^I_\odot(\tau)\hat{\Psi}_{\sigma'}(\tau)\hat{\Psi}^\dagger_{\sigma'}(\tau_2)\right|n'\right\rangle$$
$$+{}^{+}X^{+-}_{++}(E_{\tilde{k}n'}+eV_l, E_{j\tilde{k}'}-eV_{l'}, E_{\tilde{k}\tilde{k}'}+eV_l-eV_{l'})$$
$$\times T^-_{l\sigma}(n,\tilde{k})T^+_{l\sigma}(\tilde{k},j)\left(\hat{\rho}^N_\odot\right)_{jj'} T^-_{l'\sigma'}(j',\tilde{k}')T^+_{l'\sigma'}(\tilde{k}',n')$$

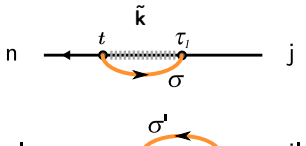

$$+\left\langle \hat{c}^\dagger_\sigma(\tau_1)\,\hat{c}_\sigma(t)\right\rangle \left\langle \hat{c}^\dagger_{\sigma'}(\tau_2)\,\hat{c}_{\sigma'}(\tau)\right\rangle \left\langle n\left|\hat{\Psi}_{\sigma'}(\tau_2)\hat{\Psi}^\dagger_{\sigma'}(\tau)\hat{\rho}^I_\odot(\tau)\hat{\Psi}_\sigma(\tau_1)\hat{\Psi}^\dagger_\sigma(t)\right|n'\right\rangle$$
$$+{}^{+}X^{-+}_{++}(E_{n\tilde{k}'}-eV_l, E_{\tilde{k}j'}+eV_{l'}, E_{\tilde{k}\tilde{k}'}-eV_l+eV_{l'})$$
$$\times T^-_{l'\sigma'}(n,\tilde{k})T^+_{l'\sigma'}(\tilde{k},j)\left(\hat{\rho}^N_\odot\right)_{jj'} T^-_{l\sigma}(j',\tilde{k}')T^+_{l\sigma}(\tilde{k}',n')$$

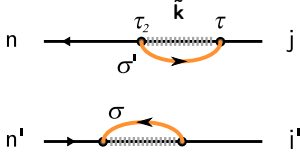

$$-\left\langle \hat{C}_0^p \hat{C}_3^{\bar{p}} \right\rangle \left\langle \hat{C}_2^{p'} \hat{C}_1^{\bar{p}'} \right\rangle \hat{D}_3^p \hat{D}_1^{p'} \; \hat{\rho}_\odot \; \hat{D}_0^{\bar{p}} \hat{D}_2^{\bar{p}'}$$

$$-\left\langle \hat{c}_\sigma^\dagger(\tau)\hat{c}_\sigma(t)\right\rangle \left\langle \hat{c}_{\sigma'}(\tau_2)\hat{c}_{\sigma'}^\dagger(\tau_1)\right\rangle \left\langle n\left|\hat{\Psi}_\sigma^\dagger(t)\hat{\Psi}_{\sigma'}(\tau_1)\hat{\rho}_\odot^I(\tau)\hat{\Psi}_\sigma(\tau)\hat{\Psi}_{\sigma'}^\dagger(\tau_2)\right|n'\right\rangle$$
$$-{}^{+}\mathcal{D}_{++}^{-+}(E_{\tilde{i}n'}-eV_l, E_{j\tilde{k}'}-eV_l, E_{\tilde{i}\tilde{k}'}-eV_l-eV_{l'})$$
$$\times T_{l\sigma}^{+}(n,\tilde{i})T_{l'\sigma'}^{-}(\tilde{i},j)\left(\hat{\rho}_\odot^N\right)_{jj'}T_{l\sigma}^{-}(j',\tilde{k}')T_{l'\sigma'}^{+}(\tilde{k}',n')$$

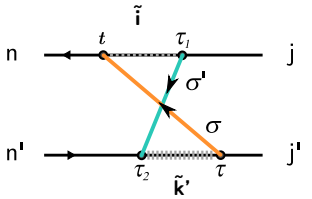

$$-\left\langle \hat{c}_\sigma^\dagger(t)\hat{c}_\sigma(\tau)\right\rangle \left\langle \hat{c}_{\sigma'}(\tau_1)\hat{c}_{\sigma'}^\dagger(\tau_2)\right\rangle \left\langle n\left|\hat{\Psi}_{\sigma'}(\tau_2)\hat{\Psi}_\sigma^\dagger(\tau)\hat{\rho}_\odot^I(\tau)\hat{\Psi}_{\sigma'}^\dagger(\tau_1)\hat{\Psi}_\sigma(t)\right|n'\right\rangle$$
$$-{}^{+}\mathcal{D}_{++}^{+-}(E_{n\tilde{i}'}+eV_l, E_{\tilde{k}j'}+eV_l, E_{\tilde{k}\tilde{i}'}+eV_l+eV_{l'})$$
$$\times T_{l'\sigma'}^{-}(n,\tilde{k})T_{l\sigma}^{+}(\tilde{k},j)\left(\hat{\rho}_\odot^N\right)_{jj'}T_{l'\sigma'}^{+}(j',\tilde{i}')T_{l\sigma}^{-}(\tilde{i}',n')$$

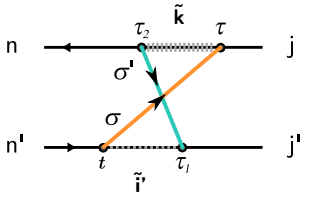

$$-\left\langle \hat{c}_\sigma(\tau)\hat{c}_\sigma^\dagger(t)\right\rangle \left\langle \hat{c}_{\sigma'}^\dagger(\tau_2)\hat{c}_{\sigma'}(\tau_1)\right\rangle \left\langle n\left|\hat{\Psi}_\sigma(t)\hat{\Psi}_{\sigma'}^\dagger(\tau_1)\hat{\rho}_\odot^I(\tau)\hat{\Psi}_\sigma^\dagger(\tau)\hat{\Psi}_{\sigma'}(\tau_2)\right|n'\right\rangle$$
$$-{}^{+}\mathcal{D}_{++}^{-+}(E_{\tilde{k}n'}+eV_l, E_{j\tilde{i}'}+eV_l, E_{\tilde{k}\tilde{i}'}+eV_l+eV_{l'})$$
$$\times T_{l\sigma}^{-}(n,\tilde{k})T_{l'\sigma'}^{+}(\tilde{k},j)\left(\hat{\rho}_\odot^N\right)_{jj'}T_{l\sigma}^{+}(j',\tilde{i}')T_{l'\sigma'}^{-}(\tilde{i}',n')$$

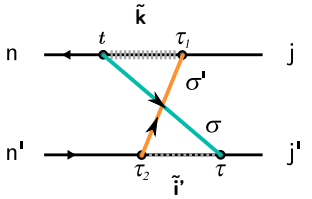

$$-\left\langle \hat{c}_\sigma(t)\hat{c}_\sigma^\dagger(\tau)\right\rangle \left\langle \hat{c}_{\sigma'}^\dagger(\tau_1)\hat{c}_{\sigma'}(\tau_2)\right\rangle \left\langle n\left|\hat{\Psi}_{\sigma'}^\dagger(\tau_2)\hat{\Psi}_\sigma(\tau)\hat{\rho}_\odot^I(\tau)\hat{\Psi}_{\sigma'}(\tau_1)\hat{\Psi}_\sigma^\dagger(t)\right|n'\right\rangle$$
$$-{}^{+}\mathcal{D}_{++}^{+-}(E_{n\tilde{k}'}-eV_l, E_{\tilde{i}j'}-eV_l, E_{\tilde{i}\tilde{k}'}-eV_l-eV_{l'})$$
$$\times T_{l'\sigma'}^{+}(n,\tilde{i})T_{l\sigma}^{-}(\tilde{i},j)\left(\hat{\rho}_\odot^N\right)_{jj'}T_{l'\sigma'}^{-}(j',\tilde{k}')T_{l\sigma}^{+}(\tilde{k}',n')$$

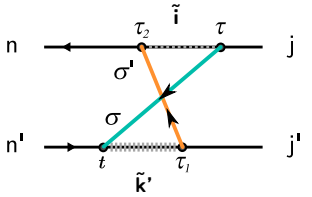

$$-\left\langle \hat{c}_\sigma(\tau)\hat{c}_\sigma^\dagger(t)\right\rangle \left\langle \hat{c}_{\sigma'}(\tau_2)\hat{c}_{\sigma'}^\dagger(\tau_1)\right\rangle \left\langle n\left|\hat{\Psi}_\sigma(t)\hat{\Psi}_{\sigma'}(\tau_1)\hat{\rho}_\odot^I(\tau)\hat{\Psi}_\sigma^\dagger(\tau)\hat{\Psi}_{\sigma'}^\dagger(\tau_2)\right|n'\right\rangle$$
$$-{}^{+}\mathcal{D}_{++}^{-+}(E_{\tilde{k}n'}+eV_l, E_{k\tilde{k}'}+eV_l, E_{\tilde{k}\tilde{k}'}+eV_l-eV_{l'})$$
$$\times T_{l\sigma}^{-}(n,\tilde{k})T_{l'\sigma'}^{-}(\tilde{k},k)(\hat{\rho}_\odot^{N+2})_{kk'}T_{l\sigma}^{+}(j',\tilde{k}')T_{l'\sigma'}^{+}(\tilde{k}',n')$$

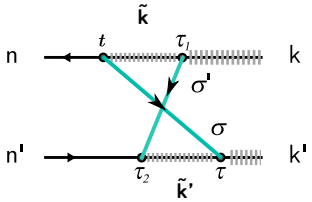

$$-\left\langle \hat{c}_\sigma(t)\hat{c}_\sigma^\dagger(\tau)\right\rangle \left\langle \hat{c}_{\sigma'}(\tau_1)\hat{c}_{\sigma'}^\dagger(\tau_2)\right\rangle \left\langle n\left|\hat{\Psi}_{\sigma'}(\tau_2)\hat{\Psi}_\sigma(\tau)\hat{\rho}_\odot^I(\tau)\hat{\Psi}_{\sigma'}^\dagger(\tau_1)\hat{\Psi}_\sigma^\dagger(t)\right|n'\right\rangle$$
$$-{}^{+}\mathcal{D}_{++}^{+-}(E_{n\tilde{k}'}-eV_l, E_{\tilde{k}k'}-eV_l, E_{\tilde{k}\tilde{k}'}-eV_l+eV_{l'})$$
$$\times T_{l'\sigma'}^{+}(n,\tilde{k})T_{l\sigma}^{-}(\tilde{k},k)(\hat{\rho}_\odot^{N+2})_{kk'}T_{l'\sigma'}^{+}(k',\tilde{k}')T_{l\sigma}^{+}(\tilde{k}',n')$$

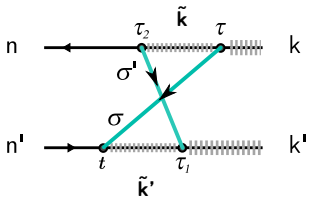

$$-\left\langle \hat{c}_\sigma^\dagger(\tau)\hat{c}_\sigma(t)\right\rangle \left\langle \hat{c}_{\sigma'}^\dagger(\tau_2)\hat{c}_{\sigma'}(\tau_1)\right\rangle \left\langle n\left|\hat{\Psi}_\sigma^\dagger(t)\hat{\Psi}_{\sigma'}^\dagger(\tau_1)\hat{\rho}_\odot^I(\tau)\hat{\Psi}_\sigma(\tau)\hat{\Psi}_{\sigma'}(\tau_2)\right|n'\right\rangle$$
$$-{}^{+}\mathcal{D}_{++}^{-+}(E_{\tilde{i}n'}-eV_l, E_{i\tilde{i}'}-eV_l, E_{\tilde{i}\tilde{i}'}-eV_l+eV_{l'})$$
$$\times T_{l\sigma}^{+}(n,\tilde{i})T_{l'\sigma'}^{+}(\tilde{i},i)(\hat{\rho}_\odot^{N-2})_{ii'}T_{l\sigma}^{-}(i',\tilde{i}')T_{l'\sigma'}^{-}(\tilde{i}',n')$$

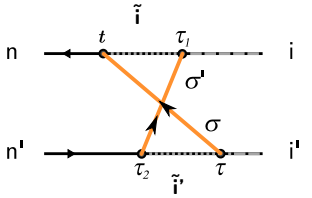

$$-\left\langle \hat{c}_\sigma^\dagger(t)\hat{c}_\sigma(\tau)\right\rangle \left\langle \hat{c}_{\sigma'}^\dagger(\tau_1)\hat{c}_{\sigma'}(\tau_2)\right\rangle \left\langle n\left|\hat{\Psi}_{\sigma'}^\dagger(\tau_2)\hat{\Psi}_\sigma^\dagger(\tau)\hat{\rho}_\odot^I(\tau)\hat{\Psi}_{\sigma'}(\tau_1)\hat{\Psi}_\sigma(t)\right|n'\right\rangle$$
$$-{}^{+}\mathcal{D}_{++}^{+-}(E_{n\tilde{i}'}+eV_l, E_{\tilde{i}i'}+eV_l, E_{\tilde{i}\tilde{i}'}+eV_l-eV_{l'})$$
$$\times T_{l'\sigma'}^{+}(n,\tilde{i})T_{l\sigma}^{+}(\tilde{i},i)(\hat{\rho}_\odot^{N-2})_{ii'}T_{l'\sigma'}^{-}(i',\tilde{i}')T_{l\sigma}^{-}(\tilde{i}',n')$$

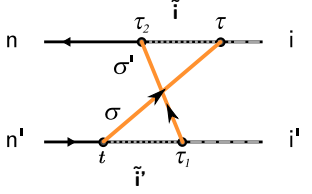

$$+\left\langle \hat{C}_3^p \hat{C}_0^{\bar{p}} \right\rangle \left\langle \hat{C}_1^{p'} \hat{C}_2^{\bar{p}'} \right\rangle \hat{D}_3^{\bar{p}} \hat{D}_0^{p} \; \hat{\rho}_{\odot} \; \hat{D}_1^{\bar{p}'} \hat{D}_2^{p'}$$

$$+\left\langle \hat{c}_\sigma^\dagger(t)\,\hat{c}_\sigma(\tau)\right\rangle \left\langle \hat{c}_{\sigma'}(\tau_1)\,\hat{c}_{\sigma'}^\dagger(\tau_2)\right\rangle \left\langle n\left|\hat{\Psi}_\sigma(t)\hat{\Psi}_\sigma^\dagger(\tau)\hat{\rho}_\odot^I(\tau)\hat{\Psi}_{\sigma'}^\dagger(\tau_1)\hat{\Psi}_{\sigma'}(\tau_2)\right|n'\right\rangle$$
$$+{}^{+}\mathcal{D}_{++}^{+-}(E_{\tilde{k}n'}+eV_l, E_{\tilde{k}j'}+eV_l, E_{\tilde{k}\tilde{i}'}+eV_l+eV_{l'})$$
$$\times T_{l\sigma}^{-}(n,\tilde{k})T_{l\sigma}^{+}(\tilde{k},j)\left(\hat{\rho}_\odot^N\right)_{jj'} T_{l'\sigma'}^{+}(j',\tilde{i}')T_{l'\sigma'}^{-}(\tilde{i}',n')$$

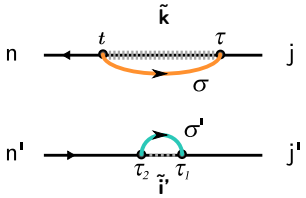

$$+\left\langle \hat{c}_\sigma^\dagger(\tau)\,\hat{c}_\sigma(t)\right\rangle \left\langle \hat{c}_{\sigma'}(\tau_2)\,\hat{c}_{\sigma'}^\dagger(\tau_1)\right\rangle \left\langle n\left|\hat{\Psi}_{\sigma'}^\dagger(\tau_2)\hat{\Psi}_{\sigma'}(\tau_1)\hat{\rho}_\odot^I(\tau)\hat{\Psi}_\sigma(\tau)\hat{\Psi}_\sigma^\dagger(t)\right|n'\right\rangle$$
$$+{}^{+}\mathcal{D}_{++}^{-+}(E_{n\tilde{k}'}-eV_l, E_{j\tilde{k}'}-eV_l, E_{\tilde{i}\tilde{k}'}-eV_l-eV_{l'})$$
$$\times T_{l'\sigma'}^{+}(n,\tilde{i})T_{l'\sigma'}^{-}(\tilde{i},j)\left(\hat{\rho}_\odot^N\right)_{jj'} T_{l\sigma}^{-}(j',\tilde{k}')T_{l\sigma}^{+}(\tilde{k}',n')$$

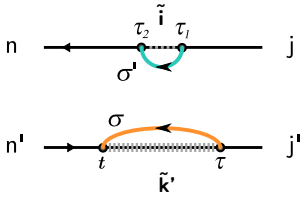

$$+\left\langle \hat{c}_\sigma(t)\,\hat{c}_\sigma^\dagger(\tau)\right\rangle \left\langle \hat{c}_{\sigma'}^\dagger(\tau_1)\,\hat{c}_{\sigma'}(\tau_2)\right\rangle \left\langle n\left|\hat{\Psi}_\sigma^\dagger(t)\hat{\Psi}_\sigma(\tau)\hat{\rho}_\odot^I(\tau)\hat{\Psi}_{\sigma'}(\tau_1)\hat{\Psi}_{\sigma'}^\dagger(\tau_2)\right|n'\right\rangle$$
$$+{}^{+}\mathcal{D}_{++}^{+-}(E_{\tilde{i}n'}-eV_l, E_{\tilde{i}j'}-eV_l, E_{\tilde{i}\tilde{k}'}-eV_l-eV_{l'})$$
$$\times T_{l\sigma}^{+}(n,\tilde{i})T_{l\sigma}^{-}(\tilde{i},j)\left(\hat{\rho}_\odot^N\right)_{jj'} T_{l'\sigma'}^{-}(j',\tilde{k}')T_{l'\sigma'}^{+}(\tilde{k}',n')$$

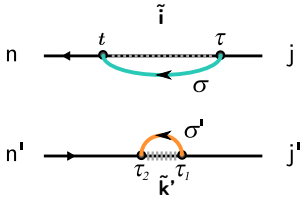

$$+\left\langle \hat{c}_\sigma(\tau)\,\hat{c}_\sigma^\dagger(t)\right\rangle \left\langle \hat{c}_{\sigma'}^\dagger(\tau_2)\,\hat{c}_{\sigma'}(\tau_1)\right\rangle \left\langle n\left|\hat{\Psi}_{\sigma'}(\tau_2)\hat{\Psi}_{\sigma'}^\dagger(\tau_1)\hat{\rho}_\odot^I(\tau)\hat{\Psi}_\sigma^\dagger(\tau)\hat{\Psi}_\sigma(t)\right|n'\right\rangle$$
$$+{}^{+}\mathcal{D}_{++}^{-+}(E_{n\tilde{i}'}+eV_l, E_{j\tilde{i}'}+eV_l, E_{\tilde{k}\tilde{i}'}+eV_l+eV_{l'})$$
$$\times T_{l'\sigma'}^{-}(n,\tilde{k})T_{l'\sigma'}^{+}(\tilde{k},j)\left(\hat{\rho}_\odot^N\right)_{jj'} T_{l\sigma}^{+}(j',\tilde{i}')T_{l\sigma}^{-}(\tilde{i}',n')$$

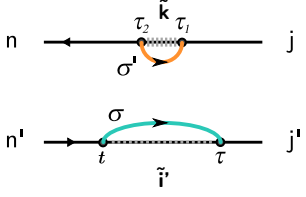

$$+\left\langle \hat{c}_\sigma(t)\,\hat{c}_\sigma^\dagger(\tau)\right\rangle \left\langle \hat{c}_{\sigma'}(\tau_1)\,\hat{c}_{\sigma'}^\dagger(\tau_2)\right\rangle \left\langle n\left|\hat{\Psi}_\sigma(t)\hat{\Psi}_\sigma^\dagger(\tau)\hat{\rho}_\odot^I(\tau)\hat{\Psi}_{\sigma'}^\dagger(\tau_1)\hat{\Psi}_{\sigma'}(\tau_2)\right|n'\right\rangle$$
$$+{}^{+}\mathcal{D}_{++}^{+-}(E_{\tilde{i}n'}-eV_l, E_{\tilde{i}j'}-eV_l, E_{\tilde{i}\tilde{i}'}-eV_l+eV_{l'})$$
$$\times T_{l\sigma}^{+}(n,\tilde{i})T_{l\sigma}^{-}(\tilde{i},j)\left(\hat{\rho}_\odot^N\right)_{jj'} T_{l'\sigma'}^{+}(j',\tilde{i}')T_{l'\sigma'}^{-}(\tilde{i}',n')$$

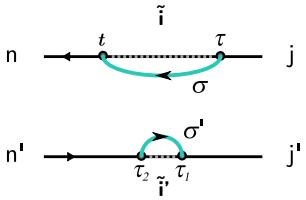

$$+\left\langle \hat{c}_\sigma(\tau)\,\hat{c}_\sigma^\dagger(t)\right\rangle \left\langle \hat{c}_{\sigma'}^\dagger(\tau_2)\,\hat{c}_{\sigma'}(\tau_1)\right\rangle \left\langle n\left|\hat{\Psi}_{\sigma'}^\dagger(\tau_2)\hat{\Psi}_{\sigma'}(\tau_1)\hat{\rho}_\odot^I(\tau)\hat{\Psi}_\sigma^\dagger(\tau)\hat{\Psi}_\sigma(t)\right|n'\right\rangle$$
$$+{}^{+}\mathcal{D}_{++}^{-+}(E_{n\tilde{i}'}+eV_l, E_{j\tilde{i}'}+eV_l, E_{\tilde{i}\tilde{i}'}+eV_l-eV_{l'})$$
$$\times T_{l'\sigma'}^{+}(n,\tilde{i})T_{l'\sigma'}^{-}(\tilde{i},j)\left(\hat{\rho}_\odot^N\right)_{jj'} T_{l\sigma}^{+}(j',\tilde{i}')T_{l\sigma}^{-}(\tilde{i}',n')$$

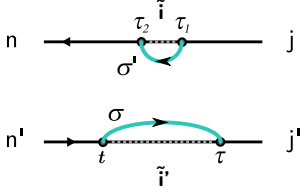

$$+\left\langle \hat{c}_\sigma^\dagger(t)\,\hat{c}_\sigma(\tau)\right\rangle \left\langle \hat{c}_{\sigma'}^\dagger(\tau_1)\,\hat{c}_{\sigma'}(\tau_2)\right\rangle \left\langle n\left|\hat{\Psi}_\sigma(t)\hat{\Psi}_\sigma^\dagger(\tau)\hat{\rho}_\odot^I(\tau)\hat{\Psi}_{\sigma'}(\tau_1)\hat{\Psi}_{\sigma'}^\dagger(\tau_2)\right|n'\right\rangle$$
$$+{}^{+}\mathcal{D}_{++}^{+-}(E_{\tilde{k}n'}+eV_l, E_{\tilde{k}j'}+eV_l, E_{\tilde{k}\tilde{k}'}+eV_l-eV_{l'})$$
$$\times T_{l\sigma}^{-}(n,\tilde{k})T_{l\sigma}^{+}(\tilde{k},j)\left(\hat{\rho}_\odot^N\right)_{jj'} T_{l'\sigma'}^{-}(j',\tilde{k}')T_{l'\sigma'}^{+}(\tilde{k}',n')$$

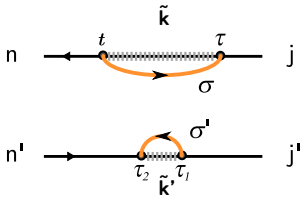

$$+\left\langle \hat{c}_\sigma^\dagger(\tau)\,\hat{c}_\sigma(t)\right\rangle \left\langle \hat{c}_{\sigma'}^\dagger(\tau_2)\,\hat{c}_{\sigma'}(\tau_1)\right\rangle \left\langle n\left|\hat{\Psi}_{\sigma'}(\tau_2)\hat{\Psi}_{\sigma'}^\dagger(\tau_1)\hat{\rho}_\odot^I(\tau)\hat{\Psi}_\sigma(\tau)\hat{\Psi}_\sigma^\dagger(t)\right|n'\right\rangle$$
$$+{}^{+}\mathcal{D}_{++}^{-+}(E_{n\tilde{k}'}-eV_l, E_{j\tilde{k}'}-eV_l, E_{\tilde{k}\tilde{k}'}-eV_l+eV_{l'})$$
$$\times T_{l'\sigma'}^{-}(n,\tilde{k})T_{l'\sigma'}^{+}(\tilde{k},j)\left(\hat{\rho}_\odot^N\right)_{jj'} T_{l\sigma}^{-}(j',\tilde{k}')T_{l\sigma}^{+}(\tilde{k}',n')$$

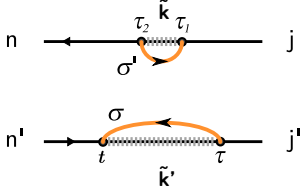

$$-\left\langle \hat{c}^\dagger_\sigma(\tau_1)\,\hat{c}_\sigma(t)\right\rangle \left\langle \hat{c}_{\sigma'}(\tau_2)\,\hat{c}^\dagger_{\sigma'}(\tau)\right\rangle \left\langle n\left|\hat{\Psi}^\dagger_\sigma(t)\hat{\Psi}_{\sigma'}(\tau)\hat{\rho}^I_\odot(\tau)\hat{\Psi}_\sigma(\tau_1)\hat{\Psi}^\dagger_{\sigma'}(\tau_2)\right|n'\right\rangle$$
$$-{}^{+}X^{-+}_{++}(E_{\tilde{i}n'}-eV_l, E_{\tilde{i}j'}-eV_{l'}, E_{\tilde{i}\tilde{k}'}-eV_l-eV_{l'})$$
$$\times T^{+}_{l\sigma}(n,\tilde{i})T^{-}_{l'\sigma'}(\tilde{i},j)\left(\hat{\rho}^N_\odot\right)_{jj'}T^{-}_{l\sigma}(j',\tilde{k}')T^{+}_{l'\sigma'}(\tilde{k}',n')$$

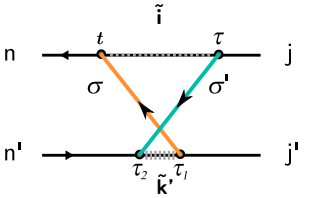

$$-\left\langle \hat{c}^\dagger_\sigma(t)\,\hat{c}_\sigma(\tau_1)\right\rangle \left\langle \hat{c}_{\sigma'}(\tau)\,\hat{c}^\dagger_{\sigma'}(\tau_2)\right\rangle \left\langle n\left|\hat{\Psi}_{\sigma'}(\tau_2)\hat{\Psi}^\dagger_\sigma(\tau_1)\hat{\rho}^I_\odot(\tau)\hat{\Psi}^\dagger_{\sigma'}(\tau)\hat{\Psi}_\sigma(t)\right|n'\right\rangle$$
$$-{}^{+}X^{+-}_{++}(E_{n\tilde{i}'}+eV_l, E_{j\tilde{i}'}+eV_{l'}, E_{\tilde{k}\tilde{i}'}+eV_l+eV_{l'})$$
$$\times T^{-}_{l'\sigma'}(n,\tilde{k})T^{+}_{l\sigma}(\tilde{k},j)\left(\hat{\rho}^N_\odot\right)_{jj'}T^{+}_{l'\sigma'}(j',\tilde{i}')T^{-}_{l\sigma}(\tilde{i}',n')$$

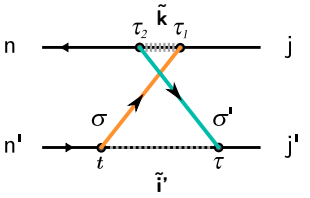

$$-\left\langle \hat{c}_\sigma(\tau_1)\,\hat{c}^\dagger_\sigma(t)\right\rangle \left\langle \hat{c}^\dagger_{\sigma'}(\tau_2)\,\hat{c}_{\sigma'}(\tau)\right\rangle \left\langle n\left|\hat{\Psi}_\sigma(t)\hat{\Psi}^\dagger_{\sigma'}(\tau)\hat{\rho}^I_\odot(\tau)\hat{\Psi}^\dagger_\sigma(\tau_1)\hat{\Psi}_{\sigma'}(\tau_2)\right|n'\right\rangle$$
$$-{}^{+}X^{-+}_{++}(E_{\tilde{k}n'}+eV_l, E_{\tilde{k}j'}+eV_{l'}, E_{\tilde{k}\tilde{i}'}+eV_l+eV_{l'})$$
$$\times T^{-}_{l\sigma}(n,\tilde{k})T^{+}_{l'\sigma'}(\tilde{k},j)\left(\hat{\rho}^N_\odot\right)_{jj'}T^{+}_{l\sigma}(j',\tilde{i}')T^{-}_{l'\sigma'}(\tilde{i}',n')$$

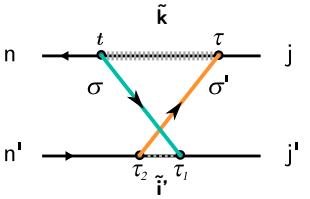

$$-\left\langle \hat{c}_\sigma(t)\,\hat{c}^\dagger_\sigma(\tau_1)\right\rangle \left\langle \hat{c}^\dagger_{\sigma'}(\tau)\,\hat{c}_{\sigma'}(\tau_2)\right\rangle \left\langle n\left|\hat{\Psi}^\dagger_{\sigma'}(\tau_2)\hat{\Psi}_\sigma(\tau_1)\hat{\rho}^I_\odot(\tau)\hat{\Psi}_{\sigma'}(\tau)\hat{\Psi}^\dagger_\sigma(t)\right|n'\right\rangle$$
$$-{}^{+}X^{+-}_{++}(E_{n\tilde{k}'}-eV_l, E_{j\tilde{k}'}-eV_{l'}, E_{\tilde{i}\tilde{k}'}-eV_l-eV_{l'})$$
$$\times T^{+}_{l'\sigma'}(n,\tilde{i})T^{-}_{l\sigma}(\tilde{i},j)\left(\hat{\rho}^N_\odot\right)_{jj'}T^{-}_{l'\sigma'}(j',\tilde{k}')T^{+}_{l\sigma}(\tilde{k}',n')$$

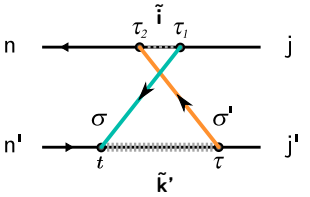

$$-\left\langle \hat{c}_\sigma(\tau_1)\,\hat{c}^\dagger_\sigma(t)\right\rangle \left\langle \hat{c}_{\sigma'}(\tau_2)\,\hat{c}^\dagger_{\sigma'}(\tau)\right\rangle \left\langle n\left|\hat{\Psi}_\sigma(t)\hat{\Psi}_{\sigma'}(\tau)\hat{\rho}^I_\odot(\tau)\hat{\Psi}^\dagger_\sigma(\tau_1)\hat{\Psi}^\dagger_{\sigma'}(\tau_2)\right|n'\right\rangle$$
$$+{}^{+}X^{-+}_{++}(E_{\tilde{k}n'}+eV_l, E_{\tilde{k}k'}-eV_{l'}, E_{\tilde{k}\tilde{k}'}+eV_l-eV_{l'})$$
$$\times T^{-}_{l\sigma}(n,\tilde{k})T^{-}_{l'\sigma'}(\tilde{k},k)(\hat{\rho}^{N+2}_\odot)_{kk'}T^{+}_{l\sigma}(j',\tilde{k}')T^{+}_{l'\sigma'}(\tilde{k}',n')$$

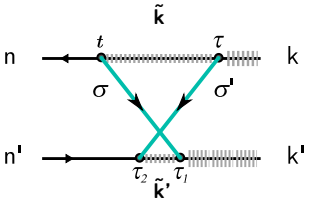

$$-\left\langle \hat{c}_\sigma(t)\,\hat{c}^\dagger_\sigma(\tau_1)\right\rangle \left\langle \hat{c}_{\sigma'}(\tau)\,\hat{c}^\dagger_{\sigma'}(\tau_2)\right\rangle \left\langle n\left|\hat{\Psi}_{\sigma'}(\tau_2)\hat{\Psi}_\sigma(\tau_1)\hat{\rho}^I_\odot(\tau)\hat{\Psi}^\dagger_{\sigma'}(\tau)\hat{\Psi}^\dagger_\sigma(t)\right|n'\right\rangle$$
$$+{}^{+}X^{+-}_{++}(E_{n\tilde{k}'}-eV_l, E_{k\tilde{k}'}+eV_{l'}, E_{\tilde{k}\tilde{k}'}-eV_l+eV_{l'})$$
$$\times T^{+}_{l'\sigma'}(n,\tilde{k})T^{-}_{l\sigma}(\tilde{k},k)(\hat{\rho}^{N+2}_\odot)_{kk'}T^{+}_{l'\sigma'}(k',\tilde{k}')T^{+}_{l\sigma}(\tilde{k}',n')$$

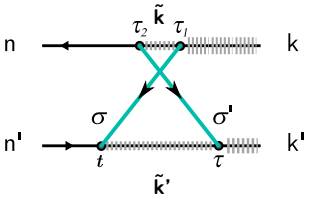

$$-\left\langle \hat{c}^\dagger_\sigma(\tau_1)\,\hat{c}_\sigma(t)\right\rangle \left\langle \hat{c}^\dagger_{\sigma'}(\tau_2)\,\hat{c}_{\sigma'}(\tau)\right\rangle \left\langle n\left|\hat{\Psi}^\dagger_\sigma(t)\hat{\Psi}^\dagger_{\sigma'}(\tau)\hat{\rho}^I_\odot(\tau)\hat{\Psi}_\sigma(\tau_1)\hat{\Psi}_{\sigma'}(\tau_2)\right|n'\right\rangle$$
$$+{}^{+}X^{-+}_{++}(E_{\tilde{i}n'}-eV_l, E_{\tilde{i}i'}+eV_{l'}, E_{\tilde{i}\tilde{i}'}-eV_l+eV_{l'})$$
$$\times T^{+}_{l\sigma}(n,\tilde{i})T^{+}_{l'\sigma'}(\tilde{i},i)(\hat{\rho}^{N-2}_\odot)_{ii'}T^{-}_{l\sigma}(i',\tilde{i}')T^{-}_{l'\sigma'}(\tilde{i}',n')$$

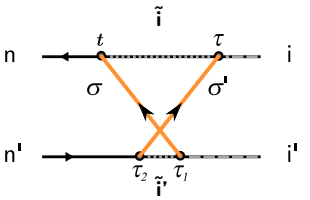

$$-\left\langle \hat{c}^\dagger_\sigma(t)\,\hat{c}_\sigma(\tau_1)\right\rangle \left\langle \hat{c}^\dagger_{\sigma'}(\tau)\,\hat{c}_{\sigma'}(\tau_2)\right\rangle \left\langle n\left|\hat{\Psi}^\dagger_{\sigma'}(\tau_2)\hat{\Psi}^\dagger_\sigma(\tau_1)\hat{\rho}^I_\odot(\tau)\hat{\Psi}_{\sigma'}(\tau)\hat{\Psi}_\sigma(t)\right|n'\right\rangle$$
$$+{}^{+}X^{+-}_{++}(E_{n\tilde{i}'}+eV_l, E_{i\tilde{i}'}-eV_{l'}, E_{\tilde{i}\tilde{i}'}+eV_l-eV_{l'})$$
$$\times T^{+}_{l'\sigma'}(n,\tilde{i})T^{+}_{l\sigma}(\tilde{i},i)(\hat{\rho}^{N-2}_\odot)_{ii'}T^{-}_{l'\sigma'}(i',\tilde{i}')T^{-}_{l\sigma}(\tilde{i}',n')$$

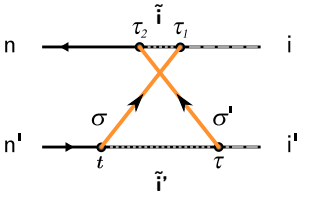

$$+\left\langle \hat{c}_\sigma^\dagger(t)\hat{c}_\sigma(\tau)\right\rangle \left\langle \hat{c}_{\sigma'}^\dagger(\tau_2)\hat{c}_{\sigma'}(\tau_1)\right\rangle \left\langle n\left|\hat{\Psi}_\sigma(t)\hat{\Psi}_{\sigma'}^\dagger(\tau_1)\hat{\Psi}_\sigma^\dagger(\tau)\hat{\rho}_\odot^I(\tau)\hat{\Psi}_{\sigma'}(\tau_2)\right|n'\right\rangle$$
$$+{}^{+}D_{++}^{++}(E_{\tilde{k}n'}+eV_l, E_{\tilde{n}i'}+eV_l, E_{\tilde{k}i'}+eV_l+eV_{l'})$$
$$\times T_{l\sigma}^-(n,\tilde{k})T_{l'\sigma'}^+(\tilde{k},\tilde{n})T_{l\sigma}^+(\tilde{n},i)(\hat{\rho}_\odot^{N-1})_{ii'}T_{l'\sigma'}^-(i',n')$$

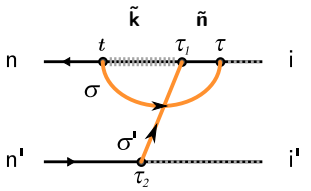

$$+\left\langle \hat{c}_\sigma^\dagger(\tau)\hat{c}_\sigma(t)\right\rangle \left\langle \hat{c}_{\sigma'}^\dagger(\tau_1)\hat{c}_{\sigma'}(\tau_2)\right\rangle \left\langle n\left|\hat{\Psi}_{\sigma'}^\dagger(\tau_2)\hat{\rho}_\odot^I(\tau)\hat{\Psi}_\sigma(\tau)\hat{\Psi}_{\sigma'}(\tau_1)\hat{\Psi}_\sigma^\dagger(t)\right|n'\right\rangle$$
$$+{}^{+}D_{++}^{--}(E_{n\tilde{k}'}-eV_l, E_{i\tilde{n}'}-eV_l, E_{i\tilde{k}'}-eV_l-eV_{l'})$$
$$\times T_{l'\sigma'}^+(n,i)(\hat{\rho}_\odot^{N-1})_{ii'}T_{l\sigma}^-(i',\tilde{n}')T_{l'\sigma'}^-(\tilde{n}',\tilde{k}')T_{l\sigma}^+(\tilde{k}',n')$$

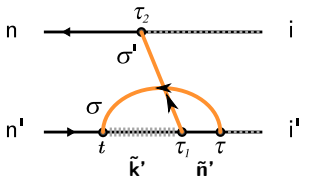

$$+\left\langle \hat{c}_\sigma(t)\hat{c}_\sigma^\dagger(\tau)\right\rangle \left\langle \hat{c}_{\sigma'}(\tau_2)\hat{c}_{\sigma'}^\dagger(\tau_1)\right\rangle \left\langle n\left|\hat{\Psi}_\sigma^\dagger(t)\hat{\Psi}_{\sigma'}(\tau_1)\hat{\Psi}_\sigma(\tau)\hat{\rho}_\odot^I(\tau)\hat{\Psi}_{\sigma'}^\dagger(\tau_2)\right|n'\right\rangle$$
$$+{}^{+}D_{++}^{++}(E_{\tilde{i}n'}-eV_l, E_{\tilde{n}k'}-eV_l, E_{\tilde{i}k'}-eV_l-eV_{l'})$$
$$\times T_{l\sigma}^+(n,\tilde{i})T_{l'\sigma'}^-(\tilde{i},\tilde{n})T_{l\sigma}^-(\tilde{n},k)(\hat{\rho}_\odot^{N+1})_{kk'}T_{l'\sigma'}^+(k',n')$$

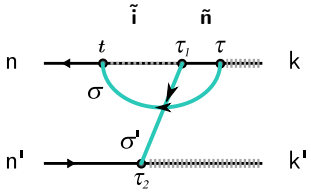

$$+\left\langle \hat{c}_\sigma(\tau)\hat{c}_\sigma^\dagger(t)\right\rangle \left\langle \hat{c}_{\sigma'}(\tau_1)\hat{c}_{\sigma'}^\dagger(\tau_2)\right\rangle \left\langle n\left|\hat{\Psi}_{\sigma'}(\tau_2)\hat{\rho}_\odot^I(\tau)\hat{\Psi}_\sigma^\dagger(\tau)\hat{\Psi}_{\sigma'}^\dagger(\tau_1)\hat{\Psi}_\sigma(t)\right|n'\right\rangle$$
$$+{}^{+}D_{++}^{--}(E_{n\tilde{i}'}+eV_l, E_{k\tilde{n}'}+eV_l, E_{k\tilde{i}'}+eV_l+eV_{l'})$$
$$\times T_{l'\sigma'}^-(n,k)(\hat{\rho}_\odot^{N+1})_{kk'}T_{l\sigma}^+(k',\tilde{n}')T_{l'\sigma'}^+(\tilde{n}',\tilde{i}')T_{l\sigma}^-(\tilde{i}',n')$$

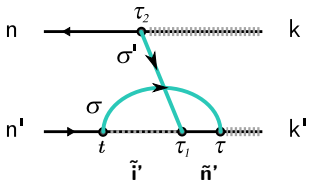

$$+\left\langle \hat{c}_\sigma(t)\hat{c}_\sigma^\dagger(\tau)\right\rangle \left\langle \hat{c}_{\sigma'}^\dagger(\tau_2)\hat{c}_{\sigma'}(\tau_1)\right\rangle \left\langle n\left|\hat{\Psi}_\sigma^\dagger(t)\hat{\Psi}_{\sigma'}^\dagger(\tau_1)\hat{\Psi}_\sigma(\tau)\hat{\rho}_\odot^I(\tau)\hat{\Psi}_{\sigma'}(\tau_2)\right|n'\right\rangle$$
$$+{}^{+}D_{++}^{++}(E_{\tilde{i}_2n'}-eV_l, E_{\tilde{i}_1i'}-eV_l, E_{\tilde{i}_2i'}-eV_l+eV_{l'})$$
$$\times T_{l\sigma}^+(n,\tilde{i}_2)T_{l'\sigma'}^+(\tilde{i}_2,\tilde{i}_1)T_{l\sigma}^-(\tilde{i}_1,i)(\hat{\rho}_\odot^{N-1})_{ii'}T_{l'\sigma'}^-(i',n')$$

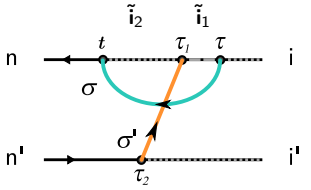

$$+\left\langle \hat{c}_\sigma(\tau)\hat{c}_\sigma^\dagger(t)\right\rangle \left\langle \hat{c}_{\sigma'}^\dagger(\tau_1)\hat{c}_{\sigma'}(\tau_2)\right\rangle \left\langle n\left|\hat{\Psi}_{\sigma'}^\dagger(\tau_2)\hat{\rho}_\odot^I(\tau)\hat{\Psi}_\sigma^\dagger(\tau)\hat{\Psi}_{\sigma'}(\tau_1)\hat{\Psi}_\sigma(t)\right|n'\right\rangle$$
$$+{}^{+}D_{++}^{--}(E_{n\tilde{i}_2'}+eV_l, E_{i\tilde{i}_1'}+eV_l, E_{i\tilde{i}_2'}+eV_l-eV_{l'})$$
$$\times T_{l'\sigma'}^+(n,i)(\hat{\rho}_\odot^{N-1})_{ii'}T_{l\sigma}^+(i',\tilde{i}_1')T_{l'\sigma'}^-(\tilde{i}_1',\tilde{i}_2')T_{l\sigma}^-(\tilde{i}_2',n')$$

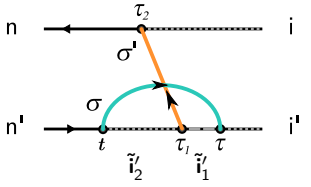

$$+\left\langle \hat{c}_\sigma^\dagger(t)\hat{c}_\sigma(\tau)\right\rangle \left\langle \hat{c}_{\sigma'}(\tau_2)\hat{c}_{\sigma'}^\dagger(\tau_1)\right\rangle \left\langle n\left|\hat{\Psi}_\sigma(t)\hat{\Psi}_{\sigma'}(\tau_1)\hat{\Psi}_\sigma^\dagger(\tau)\hat{\rho}_\odot^I(\tau)\hat{\Psi}_{\sigma'}^\dagger(\tau_2)\right|n'\right\rangle$$
$$+{}^{+}D_{++}^{++}(E_{\tilde{k}_2n'}+eV_l, E_{\tilde{k}_1k'}+eV_l, E_{\tilde{k}_2k'}+eV_l-eV_{l'})$$
$$\times T_{l\sigma}^-(n,\tilde{k}_2)T_{l'\sigma'}^-(\tilde{k}_2,\tilde{k}_1)T_{l\sigma}^+(\tilde{k}_1,k)(\hat{\rho}_\odot^{N+1})_{kk'}T_{l'\sigma'}^+(k',n')$$

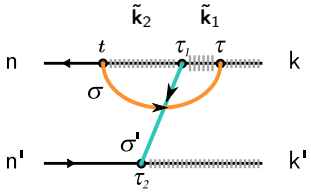

$$+\left\langle \hat{c}_\sigma^\dagger(\tau)\hat{c}_\sigma(t)\right\rangle \left\langle \hat{c}_{\sigma'}(\tau_1)\hat{c}_{\sigma'}^\dagger(\tau_2)\right\rangle \left\langle n\left|\hat{\Psi}_{\sigma'}(\tau_2)\hat{\rho}_\odot^I(\tau)\hat{\Psi}_\sigma(\tau)\hat{\Psi}_{\sigma'}^\dagger(\tau_1)\hat{\Psi}_\sigma^\dagger(t)\right|n'\right\rangle$$
$$+{}^{+}D_{++}^{--}(E_{n\tilde{k}_2'}-eV_l, E_{k\tilde{k}_1'}-eV_l, E_{k\tilde{k}_2'}-eV_l+eV_{l'})$$
$$\times T_{l'\sigma'}^-(n,k)(\hat{\rho}_\odot^{N+1})_{kk'}T_{l\sigma}^-(k',\tilde{k}_1')T_{l'\sigma'}^+(\tilde{k}_1',\tilde{k}_2')T_{l\sigma}^+(\tilde{k}_2',n')$$

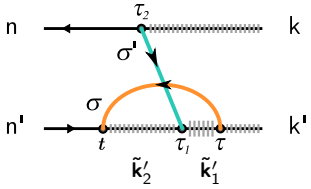

$$-\left\langle \hat{c}_\sigma^\dagger(t)\,\hat{c}_\sigma(\tau_1)\right\rangle \left\langle \hat{c}_{\sigma'}^\dagger(\tau_2)\,\hat{c}_{\sigma'}(\tau)\right\rangle \left\langle n\left|\hat{\Psi}_\sigma(t)\hat{\Psi}_\sigma^\dagger(\tau_1)\hat{\Psi}_{\sigma'}^\dagger(\tau)\hat{\rho}_\odot^I(\tau)\hat{\Psi}_{\sigma'}(\tau_2)\right|n'\right\rangle$$
$$-{}^{+}X_{++}^{++}(E_{\tilde{k}n'}+eV_l, E_{\tilde{n}i'}+eV_{l'}, E_{\tilde{k}i'}+eV_l+eV_{l'})$$
$$\times T_{l\sigma}^{-}(n,\tilde{k})T_{l\sigma}^{+}(\tilde{k},\tilde{n})T_{l'\sigma'}^{+}(\tilde{n},i)(\hat{\rho}_\odot^{N-1})_{ii'}T_{l'\sigma'}^{-}(i',n')$$

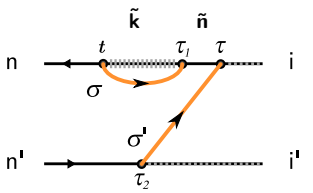

$$-\left\langle \hat{c}_\sigma^\dagger(\tau_1)\,\hat{c}_\sigma(t)\right\rangle \left\langle \hat{c}_{\sigma'}^\dagger(\tau)\,\hat{c}_{\sigma'}(\tau_2)\right\rangle \left\langle n\left|\hat{\Psi}_{\sigma'}^\dagger(\tau_2)\hat{\rho}_\odot^I(\tau)\hat{\Psi}_{\sigma'}(\tau)\hat{\Psi}_\sigma(\tau_1)\hat{\Psi}_\sigma^\dagger(t)\right|n'\right\rangle$$
$$-{}^{+}X_{++}^{--}(E_{n\tilde{k}'}-eV_l, E_{i\tilde{n}'}-eV_{l'}, E_{i\tilde{k}'}-eV_l-eV_{l'})$$
$$\times T_{l'\sigma'}^{+}(n,i)(\hat{\rho}_\odot^{N-1})_{ii'}T_{l'\sigma'}^{-}(i',\tilde{n}')T_{l\sigma}^{-}(\tilde{n}',\tilde{k}')T_{l\sigma}^{+}(\tilde{k}',n')$$

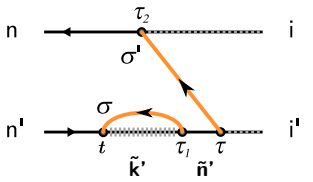

$$-\left\langle \hat{c}_\sigma(t)\,\hat{c}_\sigma^\dagger(\tau_1)\right\rangle \left\langle \hat{c}_{\sigma'}(\tau_2)\,\hat{c}_{\sigma'}^\dagger(\tau)\right\rangle \left\langle n\left|\hat{\Psi}_\sigma^\dagger(t)\hat{\Psi}_\sigma(\tau_1)\hat{\Psi}_{\sigma'}(\tau)\hat{\rho}_\odot^I(\tau)\hat{\Psi}_{\sigma'}^\dagger(\tau_2)\right|n'\right\rangle$$
$$-{}^{+}X_{++}^{++}(E_{\tilde{i}n'}-eV_l, E_{\tilde{n}k'}-eV_{l'}, E_{\tilde{i}k'}-eV_l-eV_{l'})$$
$$\times T_{l\sigma}^{+}(n,\tilde{i})T_{l\sigma}^{-}(\tilde{i},\tilde{n})T_{l'\sigma'}^{-}(\tilde{n},k)(\hat{\rho}_\odot^{N+1})_{kk'}T_{l'\sigma'}^{+}(k',n')$$

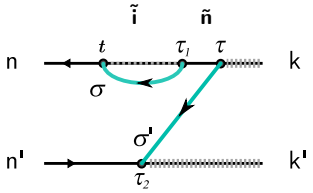

$$-\left\langle \hat{c}_\sigma(\tau_1)\,\hat{c}_\sigma^\dagger(t)\right\rangle \left\langle \hat{c}_{\sigma'}(\tau)\,\hat{c}_{\sigma'}^\dagger(\tau_2)\right\rangle \left\langle n\left|\hat{\Psi}_{\sigma'}(\tau_2)\hat{\rho}_\odot^I(\tau)\hat{\Psi}_{\sigma'}^\dagger(\tau)\hat{\Psi}_\sigma^\dagger(\tau_1)\hat{\Psi}_\sigma(t)\right|n'\right\rangle$$
$$-{}^{+}X_{++}^{--}(E_{n\tilde{i}'}+eV_l, E_{k\tilde{n}'}+eV_{l'}, E_{k\tilde{i}'}+eV_l+eV_{l'})$$
$$\times T_{l'\sigma'}^{-}(n,k)(\hat{\rho}_\odot^{N+1})_{kk'}T_{l'\sigma'}^{+}(k',\tilde{n}')T_{l\sigma}^{+}(\tilde{n}',\tilde{i}')T_{l\sigma}^{-}(\tilde{i}',n')$$

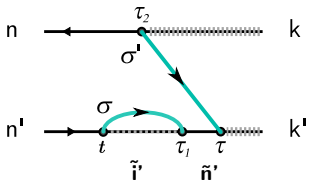

$$-\left\langle \hat{c}_\sigma(t)\,\hat{c}_\sigma^\dagger(\tau_1)\right\rangle \left\langle \hat{c}_{\sigma'}(\tau_2)\,\hat{c}_{\sigma'}(\tau)\right\rangle \left\langle n\left|\hat{\Psi}_\sigma^\dagger(t)\hat{\Psi}_\sigma(\tau_1)\hat{\Psi}_{\sigma'}^\dagger(\tau)\hat{\rho}_\odot^I(\tau)\hat{\Psi}_{\sigma'}(\tau_2)\right|n'\right\rangle$$
$$-{}^{+}X_{++}^{++}(E_{\tilde{i}n'}-eV_l, E_{\tilde{n}i'}+eV_{l'}, E_{\tilde{i}i'}-eV_l+eV_{l'})$$
$$\times T_{l\sigma}^{+}(n,\tilde{i})T_{l\sigma}^{-}(\tilde{i},\tilde{n})T_{l'\sigma'}^{+}(\tilde{n},i)(\hat{\rho}_\odot^{N-1})_{ii'}T_{l'\sigma'}^{-}(i',n')$$

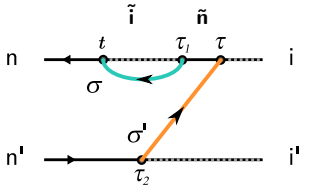

$$-\left\langle \hat{c}_\sigma(\tau_1)\,\hat{c}_\sigma^\dagger(t)\right\rangle \left\langle \hat{c}_{\sigma'}(\tau)\,\hat{c}_{\sigma'}(\tau_2)\right\rangle \left\langle n\left|\hat{\Psi}_{\sigma'}^\dagger(\tau_2)\hat{\rho}_\odot^I(\tau)\hat{\Psi}_{\sigma'}(\tau)\hat{\Psi}_\sigma^\dagger(\tau_1)\hat{\Psi}_\sigma(t)\right|n'\right\rangle$$
$$-{}^{+}X_{++}^{--}(E_{n\tilde{i}'}+eV_l, E_{i\tilde{n}'}-eV_{l'}, E_{i\tilde{i}'}+eV_l-eV_{l'})$$
$$\times T_{l'\sigma'}^{+}(n,i)(\hat{\rho}_\odot^{N-1})_{ii'}T_{l'\sigma'}^{-}(i',\tilde{n}')T_{l\sigma}^{+}(\tilde{n}',\tilde{i}')T_{l\sigma}^{-}(\tilde{i}',n')$$

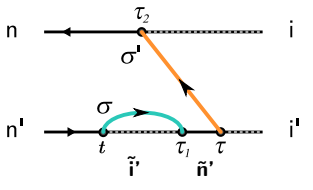

$$-\left\langle \hat{c}_\sigma^\dagger(t)\,\hat{c}_\sigma(\tau_1)\right\rangle \left\langle \hat{c}_{\sigma'}(\tau_2)\,\hat{c}_{\sigma'}^\dagger(\tau)\right\rangle \left\langle n\left|\hat{\Psi}_\sigma(t)\hat{\Psi}_\sigma^\dagger(\tau_1)\hat{\Psi}_{\sigma'}(\tau)\hat{\rho}_\odot^I(\tau)\hat{\Psi}_{\sigma'}^\dagger(\tau_2)\right|n'\right\rangle$$
$$-{}^{+}X_{++}^{++}(E_{\tilde{k}n'}+eV_l, E_{\tilde{n}k'}-eV_{l'}, E_{\tilde{k}k'}+eV_l-eV_{l'})$$
$$\times T_{l\sigma}^{-}(n,\tilde{k})T_{l\sigma}^{+}(\tilde{k},\tilde{n})T_{l'\sigma'}^{-}(\tilde{n},k)(\hat{\rho}_\odot^{N+1})_{kk'}T_{l'\sigma'}^{+}(k',n')$$

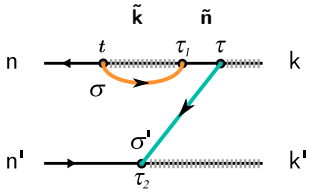

$$-\left\langle \hat{c}_\sigma^\dagger(\tau_1)\,\hat{c}_\sigma(t)\right\rangle \left\langle \hat{c}_{\sigma'}(\tau)\,\hat{c}_{\sigma'}^\dagger(\tau_2)\right\rangle \left\langle n\left|\hat{\Psi}_{\sigma'}(\tau_2)\hat{\rho}_\odot^I(\tau)\hat{\Psi}_{\sigma'}^\dagger(\tau)\hat{\Psi}_\sigma(\tau_1)\hat{\Psi}_\sigma^\dagger(t)\right|n'\right\rangle$$
$$-{}^{+}X_{++}^{--}(E_{n\tilde{k}'}-eV_l, E_{k\tilde{n}'}+eV_{l'}, E_{k\tilde{k}'}-eV_l+eV_{l'})$$
$$\times T_{l'\sigma'}^{-}(n,k)(\hat{\rho}_\odot^{N+1})_{kk'}T_{l'\sigma'}^{+}(k',\tilde{n}')T_{l\sigma}^{-}(\tilde{n}',\tilde{k}')T_{l\sigma}^{+}(\tilde{k}',n')$$

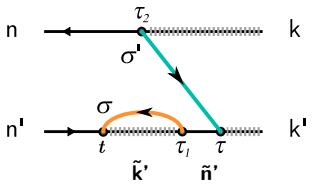

$$+\left\langle \hat{c}^\dagger_\sigma(\tau_1)\,\hat{c}_\sigma(t)\right\rangle \left\langle \hat{c}^\dagger_{\sigma'}(\tau)\,\hat{c}_{\sigma'}(\tau_2)\right\rangle \left\langle n\left|\hat{\Psi}^\dagger_\sigma(t)\hat{\rho}^I_\odot(\tau)\hat{\Psi}_{\sigma'}(\tau)\hat{\Psi}_\sigma(\tau_1)\hat{\Psi}^\dagger_{\sigma'}(\tau_2)\right|n'\right\rangle$$
$$+{}^{+}X^{--}_{++}(E_{in'}-eV_l, E_{i\tilde{n}'}-eV_{l'}, E_{i\tilde{k}'}-eV_l-eV_{l'})$$
$$\times T^+_{l\sigma}(n,i)(\hat{\rho}^{N-1}_\odot)_{ii'}T^-_{l'\sigma'}(i',\tilde{n}')T^-_{l\sigma}(\tilde{n}',\tilde{k}')T^+_{l'\sigma'}(\tilde{k}',n')$$

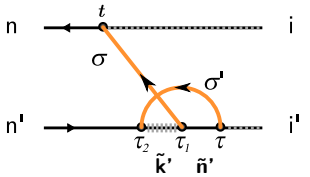

$$+\left\langle \hat{c}^\dagger_\sigma(t)\,\hat{c}_\sigma(\tau_1)\right\rangle \left\langle \hat{c}^\dagger_{\sigma'}(\tau_2)\,\hat{c}_{\sigma'}(\tau)\right\rangle \left\langle n\left|\hat{\Psi}_{\sigma'}(\tau_2)\hat{\Psi}^\dagger_\sigma(\tau_1)\hat{\Psi}^\dagger_{\sigma'}(\tau)\hat{\rho}^I_\odot(\tau)\hat{\Psi}_\sigma(t)\right|n'\right\rangle$$
$$+{}^{+}X^{++}_{++}(E_{ni'}+eV_l, E_{\tilde{n}i'}+eV_{l'}, E_{\tilde{k}i'}+eV_l+eV_{l'})$$
$$\times T^-_{l'\sigma'}(n,\tilde{k})T^+_{l\sigma}(\tilde{k},\tilde{n})T^+_{l'\sigma'}(\tilde{n},i)(\hat{\rho}^{N-1}_\odot)_{ii'}T^-_{l\sigma}(i',n')$$

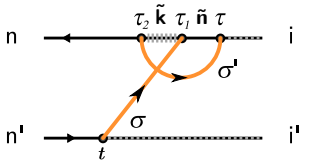

$$+\left\langle \hat{c}_\sigma(\tau_1)\,\hat{c}^\dagger_\sigma(t)\right\rangle \left\langle \hat{c}_{\sigma'}(\tau)\,\hat{c}^\dagger_{\sigma'}(\tau_2)\right\rangle \left\langle n\left|\hat{\Psi}_\sigma(t)\hat{\rho}^I_\odot(\tau)\hat{\Psi}^\dagger_{\sigma'}(\tau)\hat{\Psi}^\dagger_\sigma(\tau_1)\hat{\Psi}_{\sigma'}(\tau_2)\right|n'\right\rangle$$
$$+{}^{+}X^{--}_{++}(E_{kn'}+eV_l, E_{k\tilde{n}'}+eV_{l'}, E_{k\tilde{i}'}+eV_l+eV_{l'})$$
$$\times T^-_{l\sigma}(n,k)(\hat{\rho}^{N+1}_\odot)_{kk'}T^+_{l'\sigma'}(k',\tilde{n}')T^+_{l\sigma}(\tilde{n}',\tilde{i}')T^-_{l'\sigma'}(\tilde{i}',n')$$

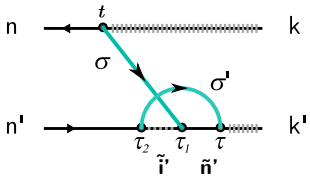

$$+\left\langle \hat{c}_\sigma(t)\,\hat{c}^\dagger_\sigma(\tau_1)\right\rangle \left\langle \hat{c}_{\sigma'}(\tau_2)\,\hat{c}^\dagger_{\sigma'}(\tau)\right\rangle \left\langle n\left|\hat{\Psi}^\dagger_{\sigma'}(\tau_2)\hat{\Psi}_\sigma(\tau_1)\hat{\Psi}_{\sigma'}(\tau)\hat{\rho}^I_\odot(\tau)\hat{\Psi}^\dagger_\sigma(t)\right|n'\right\rangle$$
$$+{}^{+}X^{++}_{++}(E_{nk'}-eV_l, E_{\tilde{n}k'}-eV_{l'}, E_{\tilde{i}k'}-eV_l-eV_{l'})$$
$$\times T^+_{l'\sigma'}(n,\tilde{i})T^-_{l\sigma}(\tilde{i},\tilde{n})T^-_{l'\sigma'}(\tilde{n},k)(\hat{\rho}^{N+1}_\odot)_{kk'}T^+_{l\sigma}(k',n')$$

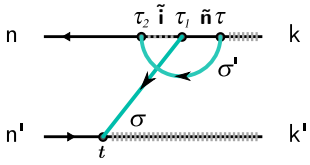

$$+\left\langle \hat{c}_\sigma(\tau_1)\,\hat{c}^\dagger_\sigma(t)\right\rangle \left\langle \hat{c}^\dagger_{\sigma'}(\tau)\,\hat{c}_{\sigma'}(\tau_2)\right\rangle \left\langle n\left|\hat{\Psi}_\sigma(t)\hat{\rho}^I_\odot(\tau)\hat{\Psi}_{\sigma'}(\tau)\hat{\Psi}^\dagger_\sigma(\tau_1)\hat{\Psi}^\dagger_{\sigma'}(\tau_2)\right|n'\right\rangle$$
$$+{}^{+}X^{--}_{++}(E_{kn'}+eV_l, E_{k\tilde{k}'_2}-eV_{l'}, E_{k\tilde{k}'_1}+eV_l-eV_{l'})$$
$$\times T^-_{l\sigma}(n,k)(\hat{\rho}^{N+1}_\odot)_{kk'}T^-_{l'\sigma'}(k',\tilde{k}'_2)T^+_{l\sigma}(\tilde{k}'_2,\tilde{k}'_1)T^+_{l'\sigma'}(\tilde{k}'_1,n')$$

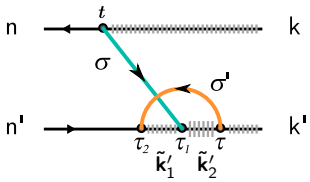

$$+\left\langle \hat{c}_\sigma(t)\,\hat{c}^\dagger_\sigma(\tau_1)\right\rangle \left\langle \hat{c}^\dagger_{\sigma'}(\tau_2)\,\hat{c}_{\sigma'}(\tau)\right\rangle \left\langle n\left|\hat{\Psi}_{\sigma'}(\tau_2)\hat{\Psi}_\sigma(\tau_1)\hat{\Psi}^\dagger_{\sigma'}(\tau)\hat{\rho}^I_\odot(\tau)\hat{\Psi}^\dagger_\sigma(t)\right|n'\right\rangle$$
$$+{}^{+}X^{++}_{++}(E_{nk'}-eV_l, E_{\tilde{k}_2k'}+eV_{l'}, E_{\tilde{k}_1k'}-eV_l+eV_{l'})$$
$$\times T^-_{l'\sigma'}(n,\tilde{k}_1)T^-_{l\sigma}(\tilde{k}_1,\tilde{k}_2)T^+_{l'\sigma'}(\tilde{k}_2,k)(\hat{\rho}^{N+1}_\odot)_{kk'}T^+_{l\sigma}(k',n')$$

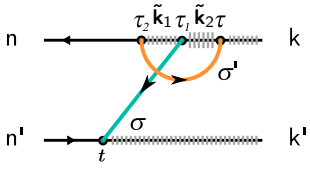

$$+\left\langle \hat{c}^\dagger_\sigma(\tau_1)\,\hat{c}_\sigma(t)\right\rangle \left\langle \hat{c}_{\sigma'}(\tau)\,\hat{c}^\dagger_{\sigma'}(\tau_2)\right\rangle \left\langle n\left|\hat{\Psi}^\dagger_\sigma(t)\hat{\rho}^I_\odot(\tau)\hat{\Psi}^\dagger_{\sigma'}(\tau)\hat{\Psi}_\sigma(\tau_1)\hat{\Psi}_{\sigma'}(\tau_2)\right|n'\right\rangle$$
$$+{}^{+}X^{--}_{++}(E_{in'}-eV_l, E_{i\tilde{i}'_2}+eV_{l'}, E_{i\tilde{i}'_1}-eV_l+eV_{l'})$$
$$\times T^+_{l\sigma}(n,i)(\hat{\rho}^{N-1}_\odot)_{ii'}T^+_{l'\sigma'}(i',\tilde{i}'_2)T^-_{l\sigma}(\tilde{i}'_2,\tilde{i}'_1)T^-_{l'\sigma'}(\tilde{i}'_1,n')$$

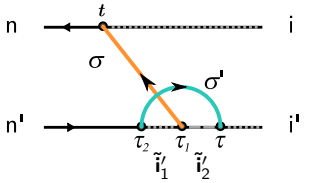

$$+\left\langle \hat{c}^\dagger_\sigma(t)\,\hat{c}_\sigma(\tau_1)\right\rangle \left\langle \hat{c}_{\sigma'}(\tau_2)\,\hat{c}^\dagger_{\sigma'}(\tau)\right\rangle \left\langle n\left|\hat{\Psi}^\dagger_{\sigma'}(\tau_2)\hat{\Psi}^\dagger_\sigma(\tau_1)\hat{\Psi}_{\sigma'}(\tau)\hat{\rho}^I_\odot(\tau)\hat{\Psi}_\sigma(t)\right|n'\right\rangle$$
$$+{}^{+}X^{++}_{++}(E_{ni'}+eV_l, E_{\tilde{i}_2i'}-eV_{l'}, E_{\tilde{i}_1i'}+eV_l-eV_{l'})$$
$$\times T^+_{l'\sigma'}(n,\tilde{i}_1)T^+_{l\sigma}(\tilde{i}_1,\tilde{i}_2)T^-_{l'\sigma'}(\tilde{i}_2,i)(\hat{\rho}^{N-1}_\odot)_{ii'}T^-_{l\sigma}(i',n')$$

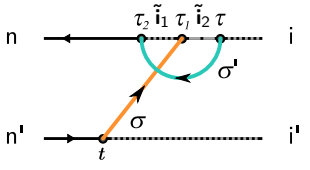

$$-\left\langle \hat{c}_\sigma^\dagger(\tau)\hat{c}_\sigma(t)\right\rangle \left\langle \hat{c}_{\sigma'}^\dagger(\tau_1)\hat{c}_{\sigma'}(\tau_2)\right\rangle \left\langle n\left|\hat{\Psi}_\sigma^\dagger(t)\hat{\rho}_\odot^I(\tau)\hat{\Psi}_\sigma(\tau)\hat{\Psi}_{\sigma'}(\tau_1)\hat{\Psi}_{\sigma'}^\dagger(\tau_2)\right|n'\right\rangle$$
$$-{}^{+}D_{++}^{--}(E_{in'}-eV_l, E_{i\tilde{n}'}-eV_l, E_{i\tilde{k}'}-eV_l-eV_{l'})$$
$$\times T_{l\sigma}^{+}(n,i)(\hat{\rho}_\odot^{N-1})_{ii'}T_{l'\sigma'}^{-}(i',\tilde{n}')T_{l'\sigma'}^{-}(\tilde{n}',\tilde{k}')T_{l\sigma}^{+}(\tilde{k}',n')$$

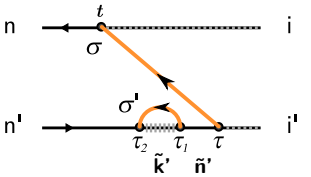

$$-\left\langle \hat{c}_\sigma^\dagger(t)\hat{c}_\sigma(\tau)\right\rangle \left\langle \hat{c}_{\sigma'}^\dagger(\tau_2)\hat{c}_{\sigma'}(\tau_1)\right\rangle \left\langle n\left|\hat{\Psi}_{\sigma'}(\tau_2)\hat{\Psi}_{\sigma'}^\dagger(\tau_1)\hat{\Psi}_\sigma^\dagger(\tau)\hat{\rho}_\odot^I(\tau)\hat{\Psi}_\sigma(t)\right|n'\right\rangle$$
$$-{}^{+}D_{++}^{++}(E_{ni'}+eV_l, E_{\tilde{n}i'}+eV_l, E_{\tilde{k}i'}+eV_l+eV_{l'})$$
$$\times T_{l'\sigma'}^{-}(n,\tilde{k})T_{l'\sigma'}^{+}(\tilde{k},\tilde{n})T_{l\sigma}^{+}(\tilde{n},i)(\hat{\rho}_\odot^{N-1})_{ii'}T_{l\sigma}^{-}(i',n')$$

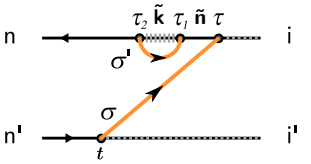

$$-\left\langle \hat{c}_\sigma(\tau)\hat{c}_\sigma^\dagger(t)\right\rangle \left\langle \hat{c}_{\sigma'}(\tau_1)\hat{c}_{\sigma'}^\dagger(\tau_2)\right\rangle \left\langle n\left|\hat{\Psi}_\sigma(t)\hat{\rho}_\odot^I(\tau)\hat{\Psi}_\sigma^\dagger(\tau)\hat{\Psi}_{\sigma'}^\dagger(\tau_1)\hat{\Psi}_{\sigma'}(\tau_2)\right|n'\right\rangle$$
$$-{}^{+}D_{++}^{--}(E_{kn'}+eV_l, E_{k\tilde{n}'}+eV_l, E_{k\tilde{i}'}+eV_l+eV_{l'})$$
$$\times T_{l\sigma}^{-}(n,k)(\hat{\rho}_\odot^{N+1})_{kk'}T_{l\sigma}^{+}(k',\tilde{n}')T_{l'\sigma'}^{+}(\tilde{n}',\tilde{i}')T_{l'\sigma'}^{-}(\tilde{i}',n')$$

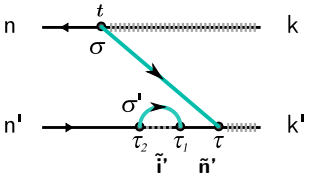

$$-\left\langle \hat{c}_\sigma(t)\hat{c}_\sigma^\dagger(\tau)\right\rangle \left\langle \hat{c}_{\sigma'}(\tau_2)\hat{c}_{\sigma'}^\dagger(\tau_1)\right\rangle \left\langle n\left|\hat{\Psi}_{\sigma'}^\dagger(\tau_2)\hat{\Psi}_{\sigma'}(\tau_1)\hat{\Psi}_\sigma(\tau)\hat{\rho}_\odot^I(\tau)\hat{\Psi}_\sigma^\dagger(t)\right|n'\right\rangle$$
$$-{}^{+}D_{++}^{++}(E_{nk'}-eV_l, E_{\tilde{n}k'}-eV_l, E_{\tilde{i}k'}-eV_l-eV_{l'})$$
$$\times T_{l'\sigma'}^{+}(n,\tilde{i})T_{l'\sigma'}^{-}(\tilde{i},\tilde{n})T_{l\sigma}^{-}(\tilde{n},k)(\hat{\rho}_\odot^{N+1})_{kk'}T_{l\sigma}^{+}(k',n')$$

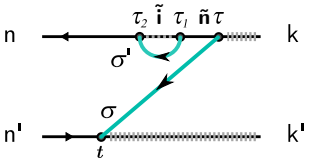

$$-\left\langle \hat{c}_\sigma(\tau)\hat{c}_\sigma^\dagger(t)\right\rangle \left\langle \hat{c}_{\sigma'}^\dagger(\tau_1)\hat{c}_{\sigma'}(\tau_2)\right\rangle \left\langle n\left|\hat{\Psi}_\sigma(t)\hat{\rho}_\odot^I(\tau)\hat{\Psi}_\sigma^\dagger(\tau)\hat{\Psi}_{\sigma'}(\tau_1)\hat{\Psi}_{\sigma'}^\dagger(\tau_2)\right|n'\right\rangle$$
$$-{}^{+}D_{++}^{--}(E_{kn'}+eV_l, E_{k\tilde{n}'}+eV_l, E_{k\tilde{k}'}+eV_l-eV_{l'})$$
$$\times T_{l\sigma}^{-}(n,k)(\hat{\rho}_\odot^{N+1})_{kk'}T_{l\sigma}^{+}(k',\tilde{n}')T_{l'\sigma'}^{-}(\tilde{n}',\tilde{k}')T_{l'\sigma'}^{+}(\tilde{k}',n')$$

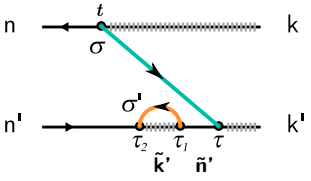

$$-\left\langle \hat{c}_\sigma(t)\hat{c}_\sigma^\dagger(\tau)\right\rangle \left\langle \hat{c}_{\sigma'}^\dagger(\tau_2)\hat{c}_{\sigma'}(\tau_1)\right\rangle \left\langle n\left|\hat{\Psi}_{\sigma'}(\tau_2)\hat{\Psi}_{\sigma'}^\dagger(\tau_1)\hat{\Psi}_\sigma(\tau)\hat{\rho}_\odot^I(\tau)\hat{\Psi}_\sigma^\dagger(t)\right|n'\right\rangle$$
$$-{}^{+}D_{++}^{++}(E_{nk'}-eV_l, E_{\tilde{n}k'}-eV_l, E_{\tilde{k}k'}-eV_l+eV_{l'})$$
$$\times T_{l\sigma}^{-}(n,\tilde{k})T_{l'\sigma'}^{+}(\tilde{k},\tilde{n})T_{l\sigma}^{-}(\tilde{n},k)(\hat{\rho}_\odot^{N+1})_{kk'}T_{l\sigma}^{+}(k',n')$$

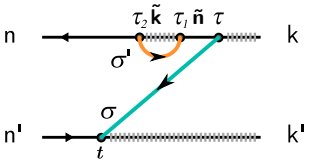

$$-\left\langle \hat{c}_\sigma^\dagger(\tau)\hat{c}_\sigma(t)\right\rangle \left\langle \hat{c}_{\sigma'}(\tau_1)\hat{c}_{\sigma'}^\dagger(\tau_2)\right\rangle \left\langle n\left|\hat{\Psi}_\sigma^\dagger(t)\hat{\rho}_\odot^I(\tau)\hat{\Psi}_\sigma(\tau)\hat{\Psi}_{\sigma'}^\dagger(\tau_1)\hat{\Psi}_{\sigma'}(\tau_2)\right|n'\right\rangle$$
$$-{}^{+}D_{++}^{--}(E_{in'}-eV_l, E_{i\tilde{n}'}-eV_l, E_{i\tilde{i}'}-eV_l+eV_{l'})$$
$$\times T_{l\sigma}^{+}(n,i)(\hat{\rho}_\odot^{N-1})_{ii'}T_{l\sigma}^{-}(i',\tilde{n}')T_{l'\sigma'}^{+}(\tilde{n}',\tilde{i}')T_{l'\sigma'}^{-}(\tilde{i}',n')$$

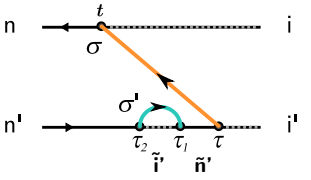

$$-\left\langle \hat{c}_\sigma^\dagger(t)\hat{c}_\sigma(\tau)\right\rangle \left\langle \hat{c}_{\sigma'}(\tau_2)\hat{c}_{\sigma'}^\dagger(\tau_1)\right\rangle \left\langle n\left|\hat{\Psi}_{\sigma'}^\dagger(\tau_2)\hat{\Psi}_{\sigma'}(\tau_1)\hat{\Psi}_\sigma^\dagger(\tau)\hat{\rho}_\odot^I(\tau)\hat{\Psi}_\sigma(t)\right|n'\right\rangle$$
$$-{}^{+}D_{++}^{++}(E_{ni'}+eV_l, E_{\tilde{n}i'}+eV_l, E_{\tilde{i}i'}+eV_l-eV_{l'})$$
$$\times T_{l'\sigma'}^{+}(n,\tilde{i})T_{l'\sigma'}^{-}(\tilde{i},\tilde{n})T_{l\sigma}^{+}(\tilde{n},i)(\hat{\rho}_\odot^{N-1})_{ii'}T_{l\sigma}^{-}(i',n')$$

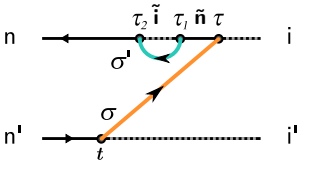

$$+\left\langle \hat{C}_3^p \hat{C}_1^{\bar{p}} \right\rangle \left\langle \hat{C}_0^{p'} \hat{C}_2^{\bar{p}'} \right\rangle \hat{D}_3^{\bar{p}} \hat{D}_2^{p'} \hat{D}_1^{p} \hat{\rho}_{\odot} \hat{D}_0^{\bar{p}'}$$

$$+\left\langle \hat{c}_\sigma^\dagger(t)\,\hat{c}_\sigma(\tau_1)\right\rangle \left\langle \hat{c}_{\sigma'}^\dagger(\tau)\,\hat{c}_{\sigma'}(\tau_2)\right\rangle \left\langle n\left|\hat{\Psi}_\sigma(t)\hat{\Psi}_{\sigma'}^\dagger(\tau_2)\hat{\Psi}_\sigma^\dagger(\tau_1)\hat{\rho}_\odot^I(\tau)\hat{\Psi}_{\sigma'}(\tau)\right|n'\right\rangle$$
$$+{}^{+}X_{++}^{+-}(E_{\tilde{k}n'}+eV_l, E_{in'}-eV_{l'}, E_{\tilde{n}n'}+eV_l-eV_{l'})$$
$$\times T_{l\sigma}^-(n,\tilde{k})T_{l'\sigma'}^+(\tilde{k},\tilde{n})T_{l\sigma}^+(\tilde{n},i)(\hat{\rho}_\odot^{N-1})_{ii'}T_{l'\sigma'}^-(i',n')$$

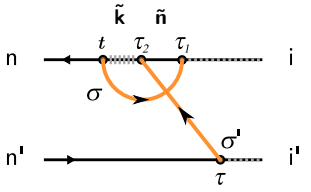

$$+\left\langle \hat{c}_\sigma^\dagger(\tau_1)\,\hat{c}_\sigma(t)\right\rangle \left\langle \hat{c}_{\sigma'}^\dagger(\tau_2)\,\hat{c}_{\sigma'}(\tau)\right\rangle \left\langle n\left|\hat{\Psi}_{\sigma'}^\dagger(\tau)\hat{\rho}_\odot^I(\tau)\hat{\Psi}_\sigma(\tau_1)\hat{\Psi}_{\sigma'}(\tau_2)\hat{\Psi}_\sigma^\dagger(t)\right|n'\right\rangle$$
$$+{}^{+}X_{++}^{-+}(E_{n\tilde{k}'}-eV_l, E_{ni'}+eV_{l'}, E_{n\tilde{n}'}-eV_l+eV_{l'})$$
$$\times T_{l'\sigma'}^+(n,i)(\hat{\rho}_\odot^{N-1})_{ii'}T_{l\sigma}^-(i',\tilde{n}')T_{l'\sigma'}^-(\tilde{n}',\tilde{k}')T_{l\sigma}^+(\tilde{k}',n')$$

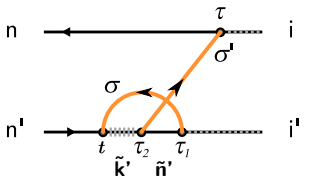

$$+\left\langle \hat{c}_\sigma(t)\,\hat{c}_\sigma^\dagger(\tau_1)\right\rangle \left\langle \hat{c}_{\sigma'}(\tau)\,\hat{c}_{\sigma'}^\dagger(\tau_2)\right\rangle \left\langle n\left|\hat{\Psi}_\sigma^\dagger(t)\hat{\Psi}_{\sigma'}(\tau_2)\hat{\Psi}_\sigma(\tau_1)\hat{\rho}_\odot^I(\tau)\hat{\Psi}_{\sigma'}^\dagger(\tau)\right|n'\right\rangle$$
$$+{}^{+}X_{++}^{+-}(E_{\tilde{i}n'}-eV_l, E_{kn'}+eV_{l'}, E_{\tilde{n}n'}-eV_l+eV_{l'})$$
$$\times T_{l\sigma}^+(n,\tilde{i})T_{l'\sigma'}^-(\tilde{i},\tilde{n})T_{l\sigma}^-(\tilde{n},k)(\hat{\rho}_\odot^{N+1})_{kk'}T_{l'\sigma'}^+(k',n')$$

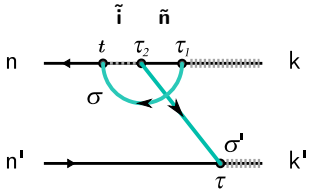

$$+\left\langle \hat{c}_\sigma(\tau_1)\,\hat{c}_\sigma^\dagger(t)\right\rangle \left\langle \hat{c}_{\sigma'}(\tau_2)\,\hat{c}_{\sigma'}^\dagger(\tau)\right\rangle \left\langle n\left|\hat{\Psi}_{\sigma'}(\tau)\hat{\rho}_\odot^I(\tau)\hat{\Psi}_\sigma^\dagger(\tau_1)\hat{\Psi}_{\sigma'}^\dagger(\tau_2)\hat{\Psi}_\sigma(t)\right|n'\right\rangle$$
$$+{}^{+}X_{++}^{-+}(E_{n\tilde{i}'}+eV_l, E_{nk'}-eV_{l'}, E_{n\tilde{n}'}+eV_l-eV_{l'})$$
$$\times T_{l'\sigma'}^-(n,k)(\hat{\rho}_\odot^{N+1})_{kk'}T_{l\sigma}^+(k',\tilde{n}')T_{l'\sigma'}^+(\tilde{n}',\tilde{i}')T_{l\sigma}^-(\tilde{i}',n')$$

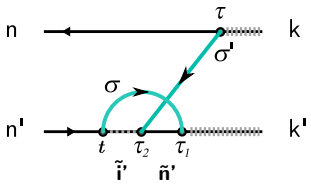

$$+\left\langle \hat{c}_\sigma(t)\,\hat{c}_\sigma^\dagger(\tau_1)\right\rangle \left\langle \hat{c}_{\sigma'}(\tau)\,\hat{c}_{\sigma'}^\dagger(\tau_2)\right\rangle \left\langle n\left|\hat{\Psi}_\sigma^\dagger(t)\hat{\Psi}_{\sigma'}^\dagger(\tau_2)\hat{\Psi}_\sigma(\tau_1)\hat{\rho}_\odot^I(\tau)\hat{\Psi}_{\sigma'}(\tau)\right|n'\right\rangle$$
$$+{}^{+}X_{++}^{+-}(E_{\tilde{i}_2n'}-eV_l, E_{in'}-eV_{l'}, E_{\tilde{i}_1n'}-eV_l-eV_{l'})$$
$$\times T_{l\sigma}^+(n,\tilde{i}_2)T_{l'\sigma'}^+(\tilde{i}_2,\tilde{i}_1)T_{l\sigma}^-(\tilde{i}_1,i)(\hat{\rho}_\odot^{N-1})_{ii'}T_{l'\sigma'}^-(i',n')$$

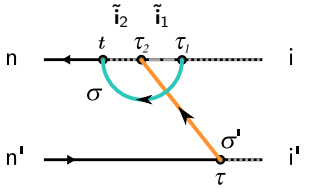

$$+\left\langle \hat{c}_\sigma(\tau_1)\,\hat{c}_\sigma^\dagger(t)\right\rangle \left\langle \hat{c}_{\sigma'}(\tau_2)\,\hat{c}_{\sigma'}^\dagger(\tau)\right\rangle \left\langle n\left|\hat{\Psi}_{\sigma'}^\dagger(\tau)\hat{\rho}_\odot^I(\tau)\hat{\Psi}_\sigma^\dagger(\tau_1)\hat{\Psi}_{\sigma'}(\tau_2)\hat{\Psi}_\sigma(t)\right|n'\right\rangle$$
$$+{}^{+}X_{++}^{-+}(E_{n\tilde{i}_2'}+eV_l, E_{ni'}+eV_{l'}, E_{n\tilde{i}_1'}+eV_l+eV_{l'})$$
$$\times T_{l'\sigma'}^+(n,i)(\hat{\rho}_\odot^{N-1})_{ii'}T_{l\sigma}^+(i',\tilde{i}_1')T_{l'\sigma'}^-(\tilde{i}_1',\tilde{i}_2')T_{l\sigma}^-(\tilde{i}_2',n')$$

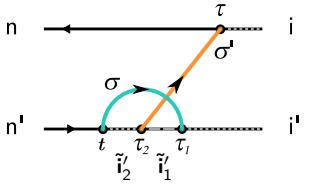

$$+\left\langle \hat{c}_\sigma^\dagger(t)\,\hat{c}_\sigma(\tau_1)\right\rangle \left\langle \hat{c}_{\sigma'}(\tau)\,\hat{c}_{\sigma'}^\dagger(\tau_2)\right\rangle \left\langle n\left|\hat{\Psi}_\sigma(t)\hat{\Psi}_{\sigma'}(\tau_2)\hat{\Psi}_\sigma^\dagger(\tau_1)\hat{\rho}_\odot^I(\tau)\hat{\Psi}_{\sigma'}^\dagger(\tau)\right|n'\right\rangle$$
$$+{}^{+}X_{++}^{+-}(E_{\tilde{k}_2n'}+eV_l, E_{kn'}+eV_{l'}, E_{\tilde{k}_1n'}+eV_l+eV_{l'})$$
$$\times T_{l\sigma}^-(n,\tilde{k}_2)T_{l'\sigma'}^-(\tilde{k}_2,\tilde{k}_1)T_{l\sigma}^+(\tilde{k}_1,k)(\hat{\rho}_\odot^{N+1})_{kk'}T_{l'\sigma'}^+(k',n')$$

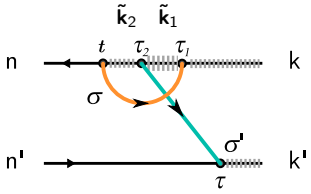

$$+\left\langle \hat{c}_\sigma^\dagger(\tau_1)\,\hat{c}_\sigma(t)\right\rangle \left\langle \hat{c}_{\sigma'}(\tau_2)\,\hat{c}_{\sigma'}^\dagger(\tau)\right\rangle \left\langle n\left|\hat{\Psi}_{\sigma'}(\tau)\hat{\rho}_\odot^I(\tau)\hat{\Psi}_\sigma(\tau_1)\hat{\Psi}_{\sigma'}^\dagger(\tau_2)\hat{\Psi}_\sigma^\dagger(t)\right|n'\right\rangle$$
$$+{}^{+}X_{++}^{-+}(E_{n\tilde{k}_2'}-eV_l, E_{nk'}-eV_{l'}, E_{n\tilde{k}_1'}-eV_l-eV_{l'})$$
$$\times T_{l'\sigma'}^-(n,k)(\hat{\rho}_\odot^{N+1})_{kk'}T_{l\sigma}^-(k',\tilde{k}_1')T_{l'\sigma'}^+(\tilde{k}_1',\tilde{k}_2')T_{l\sigma}^+(\tilde{k}_2',n')$$

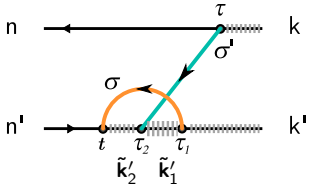

$$-\left\langle \hat{C}_0^p \hat{C}_3^{\bar{p}} \right\rangle \left\langle \hat{C}_2^{p'} \hat{C}_1^{\bar{p}'} \right\rangle \hat{D}_3^p \hat{D}_2^{\bar{p}'} \hat{D}_1^{p'} \hat{\rho}_\odot \hat{D}_0^{\bar{p}}$$

$$-\left\langle \hat{c}_\sigma^\dagger(\tau)\hat{c}_\sigma(t)\right\rangle \left\langle \hat{c}_{\sigma'}^\dagger(\tau_2)\hat{c}_{\sigma'}(\tau_1)\right\rangle \left\langle n\left|\hat{\Psi}_\sigma^\dagger(t)\hat{\Psi}_{\sigma'}(\tau_2)\hat{\Psi}_{\sigma'}^\dagger(\tau_1)\hat{\rho}_\odot^I(\tau)\hat{\Psi}_\sigma(\tau)\right|n'\right\rangle$$
$$-{}^+D_{++}^{-+}(E_{\tilde{i}n'}-eV_l, E_{in'}-eV_l, E_{\tilde{n}n'}-eV_l+eV_{l'})$$
$$\times T_{l\sigma}^+(n,\tilde{i})T_{l'\sigma'}^-(\tilde{i},\tilde{n})T_{l'\sigma'}^+(\tilde{n},i)(\hat{\rho}_\odot^{N-1})_{ii'}T_{l\sigma}^-(i',n')$$

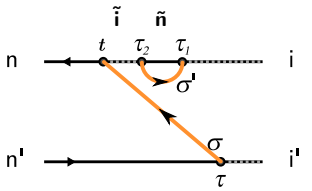

$$-\left\langle \hat{c}_\sigma^\dagger(t)\hat{c}_\sigma(\tau)\right\rangle \left\langle \hat{c}_{\sigma'}^\dagger(\tau_1)\hat{c}_{\sigma'}(\tau_2)\right\rangle \left\langle n\left|\hat{\Psi}_\sigma^\dagger(\tau)\hat{\rho}_\odot^I(\tau)\hat{\Psi}_{\sigma'}(\tau_1)\hat{\Psi}_{\sigma'}^\dagger(\tau_2)\hat{\Psi}_\sigma(t)\right|n'\right\rangle$$
$$-{}^+D_{++}^{+-}(E_{n\tilde{i}'}+eV_l, E_{ni'}+eV_l, E_{n\tilde{n}'}+eV_l-eV_{l'})$$
$$\times T_{l\sigma}^+(n,i)(\hat{\rho}_\odot^{N-1})_{ii'}T_{l'\sigma'}^-(i',\tilde{n}')T_{l'\sigma'}^+(\tilde{n}',\tilde{i}')T_{l\sigma}^-(\tilde{i}',n')$$

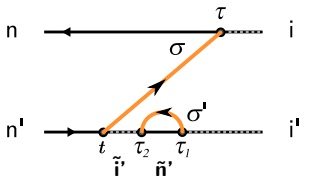

$$-\left\langle \hat{c}_\sigma(\tau)\hat{c}_\sigma^\dagger(t)\right\rangle \left\langle \hat{c}_{\sigma'}(\tau_2)\hat{c}_{\sigma'}^\dagger(\tau_1)\right\rangle \left\langle n\left|\hat{\Psi}_\sigma(t)\hat{\Psi}_{\sigma'}^\dagger(\tau_2)\hat{\Psi}_{\sigma'}(\tau_1)\hat{\rho}_\odot^I(\tau)\hat{\Psi}_\sigma^\dagger(\tau)\right|n'\right\rangle$$
$$-{}^+D_{++}^{-+}(E_{\tilde{k}n'}+eV_l, E_{kn'}+eV_l, E_{\tilde{n}n'}+eV_l-eV_{l'})$$
$$\times T_{l\sigma}^-(n,\tilde{k})T_{l\sigma}^+(\tilde{k},\tilde{n})T_{l'\sigma'}^-(\tilde{n},k)(\hat{\rho}_\odot^{N+1})_{kk'}T_{l\sigma}^+(k',n')$$

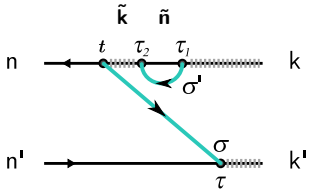

$$-\left\langle \hat{c}_\sigma(t)\hat{c}_\sigma^\dagger(\tau)\right\rangle \left\langle \hat{c}_{\sigma'}(\tau_1)\hat{c}_{\sigma'}^\dagger(\tau_2)\right\rangle \left\langle n\left|\hat{\Psi}_\sigma(\tau)\hat{\rho}_\odot^I(\tau)\hat{\Psi}_{\sigma'}^\dagger(\tau_1)\hat{\Psi}_{\sigma'}(\tau_2)\hat{\Psi}_\sigma^\dagger(t)\right|n'\right\rangle$$
$$-{}^+D_{++}^{+-}(E_{n\tilde{k}'}-eV_l, E_{nk'}-eV_l, E_{n\tilde{n}'}-eV_l+eV_{l'})$$
$$\times T_{l\sigma}^-(n,k)(\hat{\rho}_\odot^{N+1})_{kk'}T_{l'\sigma'}^+(k',\tilde{n}')T_{l'\sigma'}^-(\tilde{n}',\tilde{k}')T_{l\sigma}^+(\tilde{k}',n')$$

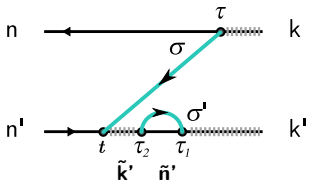

$$-\left\langle \hat{c}_\sigma(\tau)\hat{c}_\sigma^\dagger(t)\right\rangle \left\langle \hat{c}_{\sigma'}^\dagger(\tau_2)\hat{c}_{\sigma'}(\tau_1)\right\rangle \left\langle n\left|\hat{\Psi}_\sigma(t)\hat{\Psi}_{\sigma'}(\tau_2)\hat{\Psi}_{\sigma'}^\dagger(\tau_1)\hat{\rho}_\odot^I(\tau)\hat{\Psi}_\sigma^\dagger(\tau)\right|n'\right\rangle$$
$$-{}^+D_{++}^{-+}(E_{\tilde{k}_2n'}+eV_l, E_{kn'}+eV_l, E_{\tilde{k}_1n'}+eV_l+eV_{l'})$$
$$\times T_{l\sigma}^-(n,\tilde{k}_2)T_{l'\sigma'}^-(\tilde{k}_2,\tilde{k}_1)T_{l'\sigma'}^+(\tilde{k}_1,k)(\hat{\rho}_\odot^{N+1})_{kk'}T_{l\sigma}^+(k',n')$$

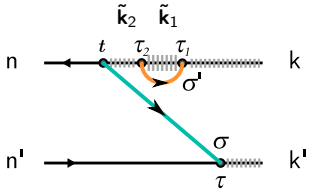

$$-\left\langle \hat{c}_\sigma(\tau)\hat{c}_\sigma^\dagger(t)\right\rangle \left\langle \hat{c}_{\sigma'}^\dagger(\tau_1)\hat{c}_{\sigma'}(\tau_2)\right\rangle \left\langle n\left|\hat{\Psi}_\sigma(\tau)\hat{\rho}_\odot^I(\tau)\hat{\Psi}_{\sigma'}^\dagger(\tau_1)\hat{\Psi}_{\sigma'}(\tau_2)\hat{\Psi}_\sigma^\dagger(t)\right|n'\right\rangle$$
$$-{}^+D_{++}^{+-}(E_{n\tilde{k}_2'}-eV_l, E_{nk'}-eV_l, E_{n\tilde{k}_1'}-eV_l-eV_{l'})$$
$$\times T_{l\sigma}^-(n,k)(\hat{\rho}_\odot^{N+1})_{kk'}T_{l'\sigma'}^-(k',\tilde{k}_1')T_{l'\sigma'}^+(\tilde{k}_1',\tilde{k}_2')T_{l\sigma}^+(\tilde{k}_2',n')$$

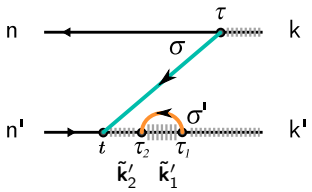

$$-\left\langle \hat{c}_\sigma^\dagger(\tau)\hat{c}_\sigma(t)\right\rangle \left\langle \hat{c}_{\sigma'}(\tau_2)\hat{c}_{\sigma'}^\dagger(\tau_1)\right\rangle \left\langle n\left|\hat{\Psi}_\sigma^\dagger(t)\hat{\Psi}_{\sigma'}^\dagger(\tau_2)\hat{\Psi}_{\sigma'}(\tau_1)\hat{\rho}_\odot^I(\tau)\hat{\Psi}_\sigma(\tau)\right|n'\right\rangle$$
$$-{}^+D_{++}^{-+}(E_{\tilde{i}_2n'}-eV_l, E_{in'}-eV_l, E_{\tilde{i}_1n'}-eV_l-eV_{l'})$$
$$\times T_{l\sigma}^+(n,\tilde{i}_2)T_{l'\sigma'}^+(\tilde{i}_2,\tilde{i}_1)T_{l'\sigma'}^-(\tilde{i}_1,i)(\hat{\rho}_\odot^{N-1})_{ii'}T_{l\sigma}^-(i',n')$$

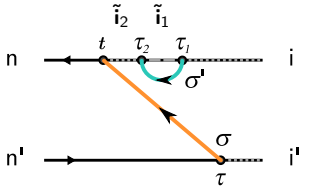

$$-\left\langle \hat{c}_\sigma^\dagger(t)\hat{c}_\sigma(\tau)\right\rangle \left\langle \hat{c}_{\sigma'}(\tau_1)\hat{c}_{\sigma'}^\dagger(\tau_2)\right\rangle \left\langle n\left|\hat{\Psi}_\sigma^\dagger(\tau)\hat{\rho}_\odot^I(\tau)\hat{\Psi}_{\sigma'}^\dagger(\tau_1)\hat{\Psi}_{\sigma'}(\tau_2)\hat{\Psi}_\sigma(t)\right|n'\right\rangle$$
$$-{}^+D_{++}^{+-}(E_{n\tilde{i}_2'}+eV_l, E_{ni'}+eV_l, E_{n\tilde{i}_1'}+eV_l+eV_{l'})$$
$$\times T_{l\sigma}^+(n,i)(\hat{\rho}_\odot^{N-1})_{ii'}T_{l'\sigma'}^+(i',\tilde{i}_1')T_{l'\sigma'}^-(\tilde{i}_1',\tilde{i}_2')T_{l\sigma}^-(\tilde{i}_2',n')$$

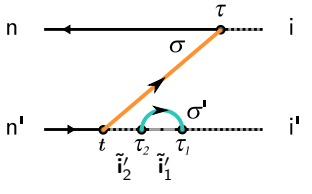

$$+\left\langle \hat{c}_\sigma^\dagger(t)\,\hat{c}_\sigma(\tau)\right\rangle \left\langle \hat{c}_{\sigma'}^\dagger(\tau_1)\,\hat{c}_{\sigma'}(\tau_2)\right\rangle \left\langle n\left|\hat{\Psi}_\sigma(t)\hat{\Psi}_{\sigma'}^\dagger(\tau_2)\hat{\Psi}_\sigma^\dagger(\tau)\hat{\rho}_\odot^I(\tau)\hat{\Psi}_{\sigma'}(\tau_1)\right|n'\right\rangle$$
$$+{}^{+}D_{++}^{+-}(E_{\tilde{k}n'}+eV_l, E_{\tilde{n}i'}+eV_l, E_{\tilde{n}n'}+eV_l-eV_{l'})$$
$$\times T_{l\sigma}^-(n,\tilde{k})T_{l'\sigma'}^+(\tilde{k},\tilde{n})T_{l\sigma}^+(\tilde{n},i)(\hat{\rho}_\odot^{N-1})_{ii'}T_{l'\sigma'}^-(i',n')$$

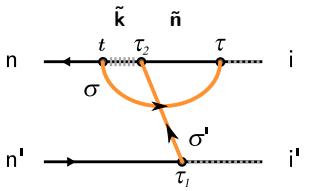

$$+\left\langle \hat{c}_\sigma^\dagger(\tau)\,\hat{c}_\sigma(t)\right\rangle \left\langle \hat{c}_{\sigma'}^\dagger(\tau_2)\,\hat{c}_{\sigma'}(\tau_1)\right\rangle \left\langle n\left|\hat{\Psi}_{\sigma'}^\dagger(\tau_1)\hat{\rho}_\odot^I(\tau)\hat{\Psi}_\sigma(\tau)\hat{\Psi}_{\sigma'}(\tau_2)\hat{\Psi}_\sigma^\dagger(t)\right|n'\right\rangle$$
$$+{}^{+}D_{++}^{-+}(E_{n\tilde{k}'}-eV_l, E_{i\tilde{n}'}-eV_l, E_{n\tilde{n}'}-eV_l+eV_{l'})$$
$$\times T_{l'\sigma'}^+(n,i)(\hat{\rho}_\odot^{N-1})_{ii'}T_{l\sigma}^-(i',\tilde{n}')T_{l'\sigma'}^-(\tilde{n}',\tilde{k}')T_{l\sigma}^+(\tilde{k}',n')$$

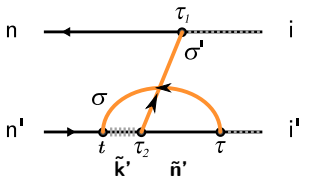

$$+\left\langle \hat{c}_\sigma(t)\,\hat{c}_\sigma^\dagger(\tau)\right\rangle \left\langle \hat{c}_{\sigma'}(\tau_1)\,\hat{c}_{\sigma'}^\dagger(\tau_2)\right\rangle \left\langle n\left|\hat{\Psi}_\sigma^\dagger(t)\hat{\Psi}_{\sigma'}(\tau_2)\hat{\Psi}_\sigma(\tau)\hat{\rho}_\odot^I(\tau)\hat{\Psi}_{\sigma'}^\dagger(\tau_1)\right|n'\right\rangle$$
$$+{}^{+}D_{++}^{+-}(E_{\tilde{i}n'}-eV_l, E_{\tilde{n}k'}-eV_l, E_{\tilde{n}n'}-eV_l+eV_{l'})$$
$$\times T_{l\sigma}^+(n,\tilde{i})T_{l'\sigma'}^-(\tilde{i},\tilde{n})T_{l\sigma}^-(\tilde{n},k)(\hat{\rho}_\odot^{N+1})_{kk'}T_{l'\sigma'}^+(k',n')$$

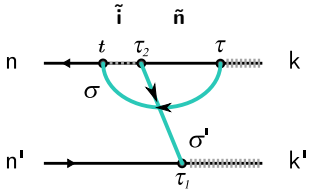

$$+\left\langle \hat{c}_\sigma(\tau)\,\hat{c}_\sigma^\dagger(t)\right\rangle \left\langle \hat{c}_{\sigma'}(\tau_2)\,\hat{c}_{\sigma'}^\dagger(\tau_1)\right\rangle \left\langle n\left|\hat{\Psi}_{\sigma'}(\tau_1)\hat{\rho}_\odot^I(\tau)\hat{\Psi}_\sigma^\dagger(\tau)\hat{\Psi}_{\sigma'}^\dagger(\tau_2)\hat{\Psi}_\sigma(t)\right|n'\right\rangle$$
$$+{}^{+}D_{++}^{-+}(E_{n\tilde{i}'}+eV_l, E_{k\tilde{n}'}+eV_l, E_{n\tilde{n}'}+eV_l-eV_{l'})$$
$$\times T_{l'\sigma'}^-(n,k)(\hat{\rho}_\odot^{N+1})_{kk'}T_{l\sigma}^+(k',\tilde{n}')T_{l'\sigma'}^+(\tilde{n}',\tilde{i}')T_{l\sigma}^-(\tilde{i}',n')$$

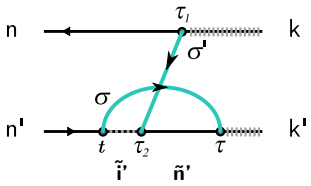

$$+\left\langle \hat{c}_\sigma(t)\,\hat{c}_\sigma^\dagger(\tau)\right\rangle \left\langle \hat{c}_{\sigma'}^\dagger(\tau_1)\,\hat{c}_{\sigma'}(\tau_2)\right\rangle \left\langle n\left|\hat{\Psi}_\sigma^\dagger(t)\hat{\Psi}_{\sigma'}^\dagger(\tau_2)\hat{\Psi}_\sigma(\tau)\hat{\rho}_\odot^I(\tau)\hat{\Psi}_{\sigma'}(\tau_1)\right|n'\right\rangle$$
$$+{}^{+}D_{++}^{+-}(E_{\tilde{i}_2n'}-eV_l, E_{\tilde{i}_1i'}-eV_l, E_{\tilde{i}_1n'}-eV_l-eV_{l'})$$
$$\times T_{l\sigma}^+(n,\tilde{i}_2)T_{l'\sigma'}^+(\tilde{i}_2,\tilde{i}_1)T_{l\sigma}^-(\tilde{i}_1,i)(\hat{\rho}_\odot^{N-1})_{ii'}T_{l'\sigma'}^-(i',n')$$

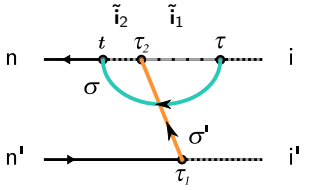

$$+\left\langle \hat{c}_\sigma(\tau)\,\hat{c}_\sigma^\dagger(t)\right\rangle \left\langle \hat{c}_{\sigma'}^\dagger(\tau_2)\,\hat{c}_{\sigma'}(\tau_1)\right\rangle \left\langle n\left|\hat{\Psi}_{\sigma'}^\dagger(\tau_1)\hat{\rho}_\odot^I(\tau)\hat{\Psi}_\sigma^\dagger(\tau)\hat{\Psi}_{\sigma'}(\tau_2)\hat{\Psi}_\sigma(t)\right|n'\right\rangle$$
$$+{}^{+}D_{++}^{-+}(E_{n\tilde{i}_2'}+eV_l, E_{i\tilde{i}_1'}+eV_l, E_{n\tilde{i}_1'}+eV_l+eV_{l'})$$
$$\times T_{l'\sigma'}^+(n,i)(\hat{\rho}_\odot^{N-1})_{ii'}T_{l\sigma}^+(i',\tilde{i}_1')T_{l'\sigma'}^-(\tilde{i}_1',\tilde{i}_2')T_{l\sigma}^-(\tilde{i}_2',n')$$

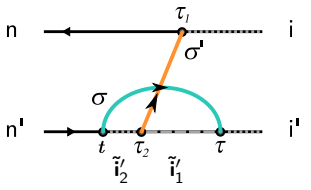

$$+\left\langle \hat{c}_\sigma^\dagger(t)\,\hat{c}_\sigma(\tau)\right\rangle \left\langle \hat{c}_{\sigma'}(\tau_1)\,\hat{c}_{\sigma'}^\dagger(\tau_2)\right\rangle \left\langle n\left|\hat{\Psi}_\sigma(t)\hat{\Psi}_{\sigma'}(\tau_2)\hat{\Psi}_\sigma^\dagger(\tau)\hat{\rho}_\odot^I(\tau)\hat{\Psi}_{\sigma'}^\dagger(\tau_1)\right|n'\right\rangle$$
$$+{}^{+}D_{++}^{+-}(E_{\tilde{k}_2n'}+eV_l, E_{\tilde{k}_1k'}+eV_l, E_{\tilde{k}_1n'}+eV_l+eV_{l'})$$
$$\times T_{l\sigma}^-(n,\tilde{k}_2)T_{l'\sigma'}^-(\tilde{k}_2,\tilde{k}_1)T_{l\sigma}^+(\tilde{k}_1,k)(\hat{\rho}_\odot^{N+1})_{kk'}T_{l'\sigma'}^+(k',n')$$

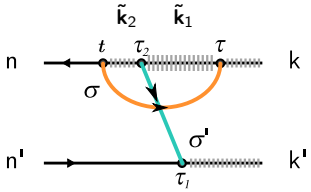

$$+\left\langle \hat{c}_\sigma^\dagger(\tau)\,\hat{c}_\sigma(t)\right\rangle \left\langle \hat{c}_{\sigma'}(\tau_2)\,\hat{c}_{\sigma'}^\dagger(\tau_1)\right\rangle \left\langle n\left|\hat{\Psi}_{\sigma'}(\tau_1)\hat{\rho}_\odot^I(\tau)\hat{\Psi}_\sigma(\tau)\hat{\Psi}_{\sigma'}^\dagger(\tau_2)\hat{\Psi}_\sigma^\dagger(t)\right|n'\right\rangle$$
$$+{}^{+}D_{++}^{-+}(E_{n\tilde{k}_2'}-eV_l, E_{k\tilde{k}_1'}-eV_l, E_{n\tilde{k}_1'}-eV_l-eV_{l'})$$
$$\times T_{l'\sigma'}^-(n,k)(\hat{\rho}_\odot^{N+1})_{kk'}T_{l\sigma}^-(k',\tilde{k}_1')T_{l'\sigma'}^+(\tilde{k}_1',\tilde{k}_2')T_{l\sigma}^+(\tilde{k}_2',n')$$

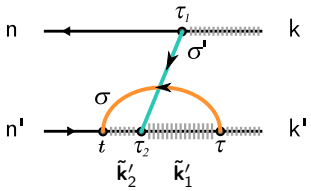

$$-\left\langle \hat{c}^\dagger_\sigma(\tau_1)\hat{c}_\sigma(t)\right\rangle\left\langle \hat{c}^\dagger_{\sigma'}(\tau_2)\hat{c}_{\sigma'}(\tau)\right\rangle\left\langle n\left|\hat{\Psi}^\dagger_\sigma(t)\hat{\Psi}_{\sigma'}(\tau_2)\hat{\Psi}^\dagger_{\sigma'}(\tau)\hat{\rho}^I_\odot(\tau)\hat{\Psi}_\sigma(\tau_1)\right|n'\right\rangle$$
$$-{}^{+}X^{-+}_{++}(E_{\tilde{i}n'}-eV_l, E_{\tilde{n}i'}+eV_{l'}, E_{\tilde{n}n'}-eV_l+eV_{l'})$$
$$\times T^+_{l\sigma}(n,\tilde{i})T^-_{l'\sigma'}(\tilde{i},\tilde{n})T^+_{l'\sigma'}(\tilde{n},i)(\hat{\rho}^{N-1}_\odot)_{ii'}T^-_{l\sigma}(i',n')$$

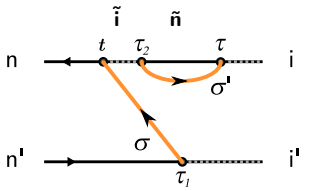

$$-\left\langle \hat{c}^\dagger_\sigma(t)\hat{c}_\sigma(\tau_1)\right\rangle\left\langle \hat{c}^\dagger_{\sigma'}(\tau)\hat{c}_{\sigma'}(\tau_2)\right\rangle\left\langle n\left|\hat{\Psi}^\dagger_\sigma(\tau_1)\hat{\rho}^I_\odot(\tau)\hat{\Psi}_{\sigma'}(\tau)\hat{\Psi}^\dagger_{\sigma'}(\tau_2)\hat{\Psi}_\sigma(t)\right|n'\right\rangle$$
$$-{}^{+}X^{+-}_{++}(E_{n\tilde{i}'}+eV_l, E_{i\tilde{n}'}-eV_{l'}, E_{n\tilde{n}'}+eV_l-eV_{l'})$$
$$\times T^+_{l\sigma}(n,i)(\hat{\rho}^{N-1}_\odot)_{ii'}T^-_{l'\sigma'}(i',\tilde{n}')T^+_{l'\sigma'}(\tilde{n}',\tilde{i}')T^-_{l\sigma}(\tilde{i}',n')$$

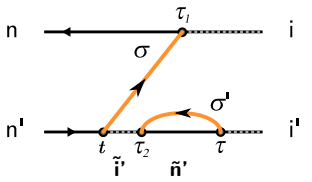

$$-\left\langle \hat{c}_\sigma(\tau_1)\hat{c}^\dagger_\sigma(t)\right\rangle\left\langle \hat{c}_{\sigma'}(\tau_2)\hat{c}^\dagger_{\sigma'}(\tau)\right\rangle\left\langle n\left|\hat{\Psi}_\sigma(t)\hat{\Psi}^\dagger_{\sigma'}(\tau_2)\hat{\Psi}_{\sigma'}(\tau)\hat{\rho}^I_\odot(\tau)\hat{\Psi}^\dagger_\sigma(\tau_1)\right|n'\right\rangle$$
$$-{}^{+}X^{-+}_{++}(E_{\tilde{k}n'}+eV_l, E_{\tilde{n}k'}-eV_{l'}, E_{\tilde{n}n'}+eV_l-eV_{l'})$$
$$\times T^-_{l\sigma}(n,\tilde{k})T^+_{l\sigma}(\tilde{k},\tilde{n})T^-_{l'\sigma'}(\tilde{n},k)(\hat{\rho}^{N+1}_\odot)_{kk'}T^+_{l\sigma}(k',n')$$

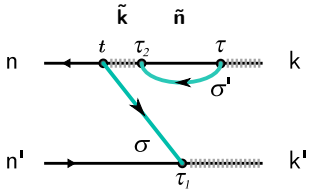

$$-\left\langle \hat{c}_\sigma(t)\hat{c}^\dagger_\sigma(\tau_1)\right\rangle\left\langle \hat{c}_{\sigma'}(\tau)\hat{c}^\dagger_{\sigma'}(\tau_2)\right\rangle\left\langle n\left|\hat{\Psi}_\sigma(\tau_1)\hat{\rho}^I_\odot(\tau)\hat{\Psi}^\dagger_{\sigma'}(\tau)\hat{\Psi}_{\sigma'}(\tau_2)\hat{\Psi}^\dagger_\sigma(t)\right|n'\right\rangle$$
$$-{}^{+}X^{+-}_{++}(E_{n\tilde{k}'}-eV_l, E_{k\tilde{n}'}+eV_{l'}, E_{n\tilde{n}'}-eV_l+eV_{l'})$$
$$\times T^-_{l\sigma}(n,k)(\hat{\rho}^{N+1}_\odot)_{kk'}T^+_{l'\sigma'}(k',\tilde{n}')T^-_{l'\sigma'}(\tilde{n}',\tilde{k}')T^+_{l\sigma}(\tilde{k}',n')$$

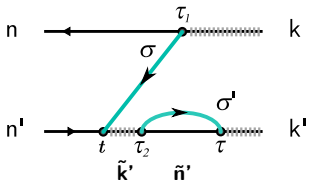

$$-\left\langle \hat{c}_\sigma(\tau_1)\hat{c}^\dagger_\sigma(t)\right\rangle\left\langle \hat{c}^\dagger_{\sigma'}(\tau_2)\hat{c}_{\sigma'}(\tau)\right\rangle\left\langle n\left|\hat{\Psi}_\sigma(t)\hat{\Psi}_{\sigma'}(\tau_2)\hat{\Psi}^\dagger_{\sigma'}(\tau)\hat{\rho}^I_\odot(\tau)\hat{\Psi}^\dagger_\sigma(\tau_1)\right|n'\right\rangle$$
$$-{}^{+}X^{-+}_{++}(E_{\tilde{k}_2n'}+eV_l, E_{\tilde{k}_1k'}+eV_{l'}, E_{\tilde{k}_1n'}+eV_l+eV_{l'})$$
$$\times T^-_{l\sigma}(n,\tilde{k}_2)T^-_{l'\sigma'}(\tilde{k}_2,\tilde{k}_1)T^+_{l'\sigma'}(\tilde{k}_1,k)(\hat{\rho}^{N+1}_\odot)_{kk'}T^+_{l\sigma}(k',n')$$

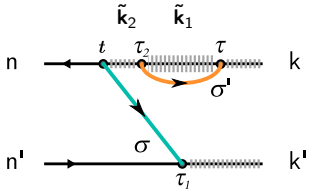

$$-\left\langle \hat{c}_\sigma(t)\hat{c}^\dagger_\sigma(\tau_1)\right\rangle\left\langle \hat{c}^\dagger_{\sigma'}(\tau)\hat{c}_{\sigma'}(\tau_2)\right\rangle\left\langle n\left|\hat{\Psi}_\sigma(\tau_1)\hat{\rho}^I_\odot(\tau)\hat{\Psi}^\dagger_{\sigma'}(\tau)\hat{\Psi}^\dagger_{\sigma'}(\tau_2)\hat{\Psi}^\dagger_\sigma(t)\right|n'\right\rangle$$
$$-{}^{+}X^{+-}_{++}(E_{n\tilde{k}'_2}-eV_l, E_{k\tilde{k}'_1}-eV_{l'}, E_{n\tilde{k}'_1}-eV_l-eV_{l'})$$
$$\times T^-_{l\sigma}(n,k)(\hat{\rho}^{N+1}_\odot)_{kk'}T^-_{l'\sigma'}(k',\tilde{k}'_1)T^+_{l'\sigma'}(\tilde{k}'_1,\tilde{k}'_2)T^+_{l\sigma}(\tilde{k}'_2,n')$$

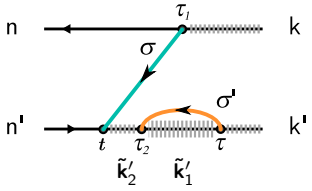

$$-\left\langle \hat{c}^\dagger_\sigma(\tau_1)\hat{c}_\sigma(t)\right\rangle\left\langle \hat{c}_{\sigma'}(\tau_2)\hat{c}^\dagger_{\sigma'}(\tau)\right\rangle\left\langle n\left|\hat{\Psi}^\dagger_\sigma(t)\hat{\Psi}^\dagger_{\sigma'}(\tau_2)\hat{\Psi}_{\sigma'}(\tau)\hat{\rho}^I_\odot(\tau)\hat{\Psi}_\sigma(\tau_1)\right|n'\right\rangle$$
$$-{}^{+}X^{-+}_{++}(E_{\tilde{i}_2n'}-eV_l, E_{\tilde{i}_1i'}-eV_{l'}, E_{\tilde{i}_1n'}-eV_l-eV_{l'})$$
$$\times T^+_{l\sigma}(n,\tilde{i}_2)T^+_{l'\sigma'}(\tilde{i}_2,\tilde{i}_1)T^-_{l'\sigma'}(\tilde{i}_1,i)(\hat{\rho}^{N-1}_\odot)_{ii'}T^-_{l\sigma}(i',n')$$

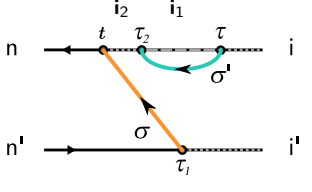

$$-\left\langle \hat{c}^\dagger_\sigma(t)\hat{c}_\sigma(\tau_1)\right\rangle\left\langle \hat{c}_{\sigma'}(\tau)\hat{c}^\dagger_{\sigma'}(\tau_2)\right\rangle\left\langle n\left|\hat{\Psi}^\dagger_\sigma(\tau_1)\hat{\rho}^I_\odot(\tau)\hat{\Psi}^\dagger_{\sigma'}(\tau)\hat{\Psi}_{\sigma'}(\tau_2)\hat{\Psi}_\sigma(t)\right|n'\right\rangle$$
$$-{}^{+}X^{+-}_{++}(E_{n\tilde{i}'_2}+eV_l, E_{i\tilde{i}'_1}+eV_{l'}, E_{n\tilde{i}'_1}+eV_l+eV_{l'})$$
$$\times T^+_{l\sigma}(n,i)(\hat{\rho}^{N-1}_\odot)_{ii'}T^+_{l'\sigma'}(i',\tilde{i}'_1)T^-_{l'\sigma'}(\tilde{i}'_1,\tilde{i}'_2)T^-_{l\sigma}(\tilde{i}'_2,n')$$

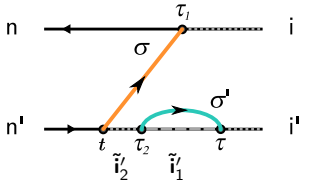

A.2.5 Calculation of Y, X and D

Finally we show how to evaluate the functions Y, X and D as defined in Eq. (124a), Eq. (124b) and Eq. (124c), respectively. In those equations we employed $\tilde{\mu} = \beta\mu, \tilde{\mu}' = \beta\mu', \tilde{\Delta} = \beta\Delta$ on the right hand side of the equations. For reasons of clarity, we want to avoid the tildes in this whole section. Such we assume that these quantities μ, μ, Δ are always given in units of temperature. Consequently, to stay compliant with the definitions of the functions Eq. (124a), Eq. (124b) and Eq. (124c), we have to set in $\mu/\beta, \mu'/\beta, \Delta/\beta$ on the left hand side.

The functions Eqs. (124b), (124c) describing the energy dependence of most fourth order processes, relate to two different types of integrations. To solve those, it is necessary to apply partial fraction decompositions [150]. For the 'X'-type integrals, belonging to Eq. (124b) we need

$$\begin{aligned}\frac{1}{\omega-\mu+\mathrm{i}\eta}\,\frac{1}{\omega+\omega'-\Delta+\mathrm{i}\eta}\,\frac{1}{\pm\omega'-\mu'+\mathrm{i}\eta} &= \left(\pm\frac{1}{\omega-\mu+\mathrm{i}\eta}+\frac{1}{\pm\omega'-\mu'+\mathrm{i}\eta}\right)\\ &\times\begin{cases}\frac{\mathrm{d}}{\mathrm{d}\Delta}\,\frac{1}{\omega+\omega'-\Delta+\mathrm{i}\eta} & \text{if}\quad \mu\pm\mu'=\Delta\,,\\ \frac{1}{\mu\pm\mu'-\Delta}\left(\frac{1}{\omega+\omega'-\mu\mp\mu'+\mathrm{i}\eta}-\frac{1}{\omega+\omega'-\Delta+\mathrm{i}\eta}\right) & \text{if}\quad \mu\pm\mu'\neq\Delta\,,\end{cases}\end{aligned} \tag{125a}$$

and for Eq. (124c), the 'D'-type integrals,

$$\begin{aligned}&\frac{1}{\omega-\mu+\mathrm{i}\eta}\,\frac{1}{\omega+\omega'-\Delta+\mathrm{i}\eta}\,\frac{1}{\omega-\mu'+\mathrm{i}\eta}\\ &\qquad=\begin{cases}\frac{\mathrm{d}}{\mathrm{d}\mu}\,\frac{1}{\omega-\mu+\mathrm{i}\eta}\,\frac{1}{\omega+\omega'-\Delta+\mathrm{i}\eta} & \text{if}\quad \mu=\mu'\,,\\ \frac{1}{\mu-\mu'}\,\frac{1}{\omega+\omega'-\Delta+\mathrm{i}\eta}\left(\frac{1}{\omega-\mu+\mathrm{i}\eta}-\frac{1}{\omega-\mu'+\mathrm{i}\eta}\right) & \text{if}\quad \mu\neq\mu'\,,\end{cases}\\ &\frac{1}{\omega-\mu+\mathrm{i}\eta}\,\frac{1}{\omega+\omega'-\Delta+\mathrm{i}\eta}\,\frac{1}{-\omega-\mu'+\mathrm{i}\eta}\\ &\quad=\frac{1}{\mu+\mu'}\,\frac{1}{\omega+\omega'-\Delta+\mathrm{i}\eta}\left(-\frac{1}{\omega-\mu+\mathrm{i}\eta}+\frac{1}{-\omega-\mu'+\mathrm{i}\eta}\right)\quad\text{if}\quad\mu\neq-\mu'\,.\end{aligned} \tag{125b}$$

In any of the end results of Eqs. (125a), (125b), we have achieved that either ω or ω' appears only in one of the fractions. The trick is now to perform first the integration over this singled out variable, which means nothing else than to solve the integration of the form contained in Eq. (124a),

$$\int \mathrm{d}\omega\, f^{p}(\omega)\,\frac{1}{\pm\omega-\mu+\mathrm{i}\eta}=\int \mathrm{d}\omega\, f^{\pm p}(\omega)\,\frac{1}{\omega-\mu+\mathrm{i}\eta}.$$

Given that there exists ε such that $f(\omega)$ is has no poles within the proximity $B_\varepsilon(\mu)$

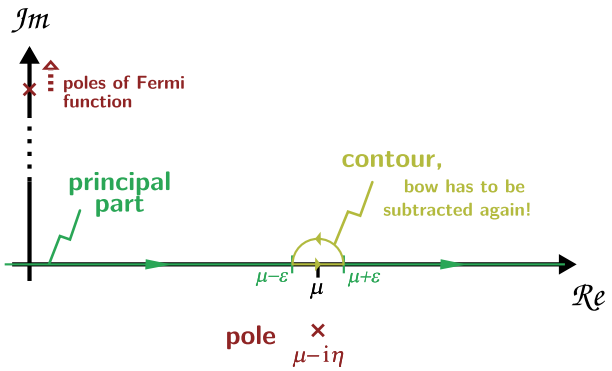

Figure 50: Integration paths and the positions of the poles in the complex plane as needed for the evaluation of Eq. (124a).

– which is true for the Fermi function – Cauchy's formula can help us to for the task, see Fig. 50. The analytical solution reads:

$$\begin{aligned}
&\lim_{\eta\to 0}\int_{-\infty}^{\infty} \mathrm{d}\omega\, \frac{f^p(\omega)}{\omega-\mu+\mathrm{i}\eta} \\
&\quad= \lim_{\eta\to 0}\lim_{\varepsilon\to 0}\left(\int_{-\infty}^{\mu-\varepsilon} \mathrm{d}\omega\, \frac{f^p(\omega)}{\omega-\mu+\mathrm{i}\eta} + \int_{\mu+\varepsilon}^{+\infty} \mathrm{d}\omega\, \frac{f^p(\omega)}{\omega-\mu+\mathrm{i}\eta} + \int_{\mu-\varepsilon}^{\mu+\varepsilon} \mathrm{d}\omega\, \frac{f^p(\omega)}{\omega-\mu+\mathrm{i}\eta}\right) \\
&\quad= \lim_{\eta\to 0}\int' \mathrm{d}\omega\, \frac{f^p(\omega)}{\omega-\mu+\mathrm{i}\eta} + \lim_{\eta\to 0}\lim_{\epsilon\to 0} f^p(\mu)\left(\underbrace{\oint_{\cup_\epsilon} \mathrm{d}\omega\, \frac{1}{\omega+\mathrm{i}\eta}}_{=0} - \underbrace{\oint_{\cap_\epsilon} \mathrm{d}\omega\, \frac{1}{\omega+\mathrm{i}\eta}}_{=\mathrm{i}\pi}\right) \\
&\quad= \int' \mathrm{d}\omega\, \frac{f^p(\omega)}{\omega-\mu} - \mathrm{i}\pi\, f^p(\mu)\,. \qquad (126)
\end{aligned}$$

Here, $f^{\pm}(\omega) = (1+\mathrm{e}^{\pm\omega})^{-1}$ and $\int'$ marks a principal part integration.
From this we can extract:

$$\mathsf{Re}\left(\lim_{\eta\to 0}\int_{-\infty}^{+\infty} \frac{\mathrm{d}\omega\, f^p(\omega)}{\omega-\mu+\mathrm{i}\eta}\right) = \int' \mathrm{d}\omega\, \frac{f^p(\omega)}{\omega-\mu}\,, \quad \mathsf{Im}\left(\lim_{\eta\to 0}\int_{-\infty}^{+\infty} \frac{\mathrm{d}\omega\, f^p(\omega)}{\omega-\mu+\mathrm{i}\eta}\right) = -\pi\, f^p(\mu)\,.$$

To obtain the solution for the principal part integration, we at first apply a trick by introducing the Lorentzian $L(\omega, W)$:

$$\mathsf{Re}\int_{-\infty}^{\infty} \mathrm{d}\omega\, \frac{f^p(\omega)}{\omega-\mu+\mathrm{i}\eta} = \lim_{W\to\infty} \mathsf{Re}\int_{-\infty}^{\infty} \mathrm{d}\omega\, \frac{f^p(\omega)}{\omega-\mu+\mathrm{i}\eta}\underbrace{\frac{W^2}{W^2+\omega^2}}_{=:L(\omega,W)}\,.$$

The Lorentzian ensures that the integrand vanishes along the bow by which we close the contour. For the evaluation, the following table helps:

function	pole	residuum
$f^p(\omega)$	$\mathrm{i}\omega_k = 2\pi\mathrm{i}\left(k+\frac{1}{2}\right)\,,\ k\in\mathbb{Z}$	$-p$
$L(\omega,W)$	$\omega = \pm\mathrm{i}W$	$\frac{1}{2}\left(\mp\mathrm{i}W\right)$
$(\omega-\mu+\mathrm{i}\eta)^{-1}$	$\omega = \mu-\mathrm{i}\eta$	$+1$

Closing the contour in the upper half of the complex plane, we obtain in the limit $\eta\to 0$, as appearing in all Eqs. (124a)-(124c):

$$\lim_{\eta\to 0}\mathsf{Re}\int_{-\infty}^{\infty}\mathrm{d}\omega\,\frac{f^p(\omega)L(\omega,W)}{\pm\omega-\mu+\mathrm{i}\eta} = \lim_{\eta\to 0}\mathsf{Re}\int_{-\infty}^{\infty}\mathrm{d}\omega\,\frac{f^{\pm p}(\omega)L(\omega,W)}{\omega-\mu+\mathrm{i}\eta}$$
$$= \mathsf{Re}\,2\pi\left(\mathrm{i}\sum_{k=0}^{\infty}\underbrace{\frac{L(\mathrm{i}\omega_k)}{\mathrm{i}\omega_k-\mu}}_{(a)}\left(\mp p\right)+\underbrace{f^{(\pm p)}(+\mathrm{i}W)}_{(b)}\frac{\mathrm{i}}{\mathrm{i}W-\mu}\left(-\frac{1}{2}\mathrm{i}W\right)\right).$$

Some lines of reformulation show that

$$(a)\quad \tfrac{L(i\omega_k)}{\mathrm{i}\omega_k-\mu} = \tfrac{W^2}{W^2-\omega_k^2}\tfrac{1}{\mathrm{i}\omega_k-\mu} = \mathrm{i}\,L(\mu,W)\left[\tfrac{1}{2}\left(\tfrac{1-\mathrm{i}\mu/W}{\omega_k-W}+\tfrac{1+\mathrm{i}\mu/W}{\omega_k+W}\right)-\tfrac{1}{\omega_k+\mathrm{i}\mu}\right],$$
$$(b)\quad f^{(\pm p)}(\mathrm{i}W) = \tfrac{1}{2}\Big(1\mp p\tanh\left(\mathrm{i}W/2\right)\Big) = \tfrac{1}{2}\Big(1\mp \mathrm{i}p\tan\left(W/2\right)\Big).$$

Thus:

$$\lim_{\eta\to 0}\mathsf{Re}\int_{-\infty}^{\infty}\mathrm{d}\omega\,\frac{f^p(\omega)L(\omega,W)}{\pm\omega-\mu+\mathrm{i}\eta}$$
$$= L(\mu,W)\left(\pm\sum_{k=0}^{\infty}\left[\frac{\pi p}{\omega_k-W}+\frac{\pi p}{\omega_k+W}-\mathsf{Re}\,\frac{2\pi p}{\omega_k+\mathrm{i}\mu}\right]-\frac{\pi}{2W}\,\mathsf{Re}\left[(\mu+\mathrm{i}W)\left(1\mp\mathrm{i}p\tan\left(W/2\right)\right)\right]\right)$$
$$= L(\mu,W)\left(-\frac{\mu\pi}{2W}\mp p\left[\frac{\pi}{2}\tan\frac{W}{2}-\frac{1}{2}\sum_{k=0}^{\infty}\left(\frac{1}{k+\frac{1}{2}-\frac{W}{2\pi}}+\frac{1}{k+\frac{1}{2}+\frac{W}{2\pi}}-2\mathsf{Re}\frac{1}{k+\frac{1}{2}+\frac{\mathrm{i}\mu}{2\pi}}\right)\right]\right)$$
$$\overset{(\star)}{=} L(\mu,W)\left(-\frac{\mu\pi}{2W}\mp p\left[\frac{\pi}{2}\tan\frac{W}{2}+\frac{1}{2}\left\{\Psi^{(0)}\left(\frac{\pi-W}{2\pi}\right)+\Psi^{(0)}\left(\frac{\pi+W}{2\pi}\right)\right\}-\mathsf{Re}\,\Psi^{(0)}\left(\frac{\pi+\mathrm{i}\mu}{2\pi}\right)\right]\right)$$
$$\overset{(\bullet)}{=} L(\mu,W)\Big(-\frac{\mu\pi}{2W}\mp p\left[\Psi^{(0)}\left(\frac{1}{2}+\frac{W}{2\pi}\right)-\mathsf{Re}\,\Psi^{(0)}\left(\frac{1}{2}+\frac{\mathrm{i}\mu}{2\pi}\right)\right]\Big)\overset{W\to\infty}{\longrightarrow}\pm p\Big(\mathsf{Re}\,\Psi^{(0)}\left(\frac{1}{2}+\frac{\mathrm{i}\mu}{2\pi}\right)-C\Big),$$

where we introduced the *digamma function* (see e.g. [51]),

$$(\star):\ \Psi^{(0)}(z) = -\sum_{n=0}^{\infty}\frac{1}{n+z}+\sum_{n=1}^{\infty}\log(1+1/n)\,,$$

and exploited the relation

$$(\bullet):\ \Psi^{(0)}(0.5+x)+\Psi^{(0)}(0.5-x) = \pi\tan(x\pi)\,.$$

For numerical calculations, a large, but still finite bandwidth W is assumed, such that $C = \Psi^{(0)}(0.5 + 0.5W/\pi)$ is well behaved. Typically, the constant drops from the final results due to a summation over in-, as well as out-tunnelling processes ($p = \pm$).

A second integral that will appear in the calculations is

$$\begin{aligned}\lim_{\eta\to 0}\int_{-\infty}^{\infty} \mathrm{d}\omega\, \frac{f^p(\omega)}{(\pm\omega - \mu + \mathrm{i}\eta)^2} &= 2\pi\mathrm{i}\left(\sum_{k=0}^{\infty}\frac{1}{(\mathrm{i}\omega_k - \mu)^2}\,(\mp p) - f^+(\mu)f^-(\mu)\right)\\ &= \mp\frac{p}{2\pi}\mathsf{Im}\,\Psi^{(1)}\left(\frac{1}{2} + \frac{\mathrm{i}\mu}{2\pi}\right) \pm \mathrm{i}\left(\frac{p}{2\pi}\mathsf{Re}\,\Psi^{(1)}\left(\frac{1}{2} + \frac{\mathrm{i}\mu}{2\pi}\right) \mp 2\pi f^+(\mu)f^-(\mu)\right),\end{aligned}$$

which is solvable by a usual contour integral. The definition of the involved *trigamma function* [51] is:

$$\Psi^{(1)}(z) = \sum_{n=0}^{\infty}\frac{1}{(n+z)^2}\,.$$

The last important ingredient is the expansion of the Fermi function product according to $f^p(\omega)f^p(\omega') = b^p(\omega+\omega')(1 - f^p(\omega) - f^p(\omega'))$, leading to the more general equality

$$f^p(\omega)f^{p'}(\omega') = b^p(\omega+\omega')\left(\delta_{p,p'} - f^{p'}(\omega')\right) - b^{p'}(\omega+\omega')f^p(\omega)\,. \tag{127}$$

Knowing that $b^{\pm}(\epsilon) = (1 - \mathrm{e}^{p\epsilon})^{-1}$ is the Bose function, this equivalence is trivial to prove.

On the following pages, we evaluate the real parts of the functions ${}^{\pm}X^{pp'}_{++}(\mu,\mu',\Delta)$ and ${}^{\pm}D^{pp'}_{++}(\mu,\mu',\Delta)$, Eq. (124b) and Eq. (124c), respectively, as well as of the helper function

$$DX^{pp'}_{++}(\mu,\mu',\Delta) := {}^{+}X^{pp'}_{++}(\mu,\mu',\Delta) + {}^{+}D^{pp'}_{++}(\mu,\Delta-\mu',\Delta). \tag{128}$$

The obtained expressions are the ones relevant for a diagonal calculation involving real tunnelling matrix elements. Actually, various models comply with these restrictions in the case of no or collinear spin-polarisation, see e.g. the cases investigated in Sect. 3 of this thesis.

X.i Given $\mu \pm \mu' = \Delta$.

$\hbar/\beta\, \mathsf{Re}\, {}^{\pm}X^{pp'}_{++}(\mu/\beta, \mu'/\beta, \Delta/\beta) =$

$$= \mathsf{Im} \int \mathrm{d}\omega \int \mathrm{d}\omega' \, \frac{f^{p}(\omega)}{\omega - \mu + \mathrm{i}\eta} \, \frac{1}{\omega + \omega' - \Delta + \mathrm{i}\eta} \, \frac{f^{p'}(\omega')}{\pm\omega' - \mu' + \mathrm{i}\eta}$$

$$= [\text{Eq. } 125a] = \mathsf{Im} \int \mathrm{d}\omega \int \mathrm{d}\omega' \, \frac{\mathrm{d}}{\mathrm{d}\Delta} \, \frac{f^{p}(\omega) f^{p'}(\omega')}{\omega + \omega' - \Delta + \mathrm{i}\eta} \left(\pm \frac{1}{\omega - \mu + \mathrm{i}\eta} + \frac{1}{\pm\omega' - \mu' + \mathrm{i}\eta} \right)$$

$$\begin{aligned} = [\text{Eq. } (127)] = {} & \mp\pi \int' \mathrm{d}\omega \, \frac{\mathrm{d}}{\mathrm{d}\Delta} \, \frac{\delta_{p,p'}\, b^{p}(\Delta) - f^{p}(\omega)\, b^{p'}(\Delta) - f^{p'}(\Delta - \omega)\, b^{p}(\Delta)}{\omega - \mu + \mathrm{i}\eta} \\ & - \pi \int' \mathrm{d}\omega' \, \frac{\mathrm{d}}{\mathrm{d}\Delta} \, \frac{\delta_{p,p'}\, b^{p}(\Delta) - f^{p}(\Delta - \omega')\, b^{p'}(\Delta) - f^{p'}(\omega')\, b^{p}(\Delta)}{\pm\omega' - \mu' + \mathrm{i}\eta} \\ & \mp \pi \int' \mathrm{d}\omega' \, \frac{\mathrm{d}}{\mathrm{d}\Delta} \, \frac{f^{p}(\mu) f^{p'}(\omega')}{\mu + \omega' - \Delta + \mathrm{i}\eta} - \pi \int' \mathrm{d}\omega \, \frac{\mathrm{d}}{\mathrm{d}\Delta} \, \frac{f^{p}(\omega) f^{p'}(\pm\mu')}{\omega \pm \mu' - \Delta + \mathrm{i}\eta} \end{aligned}$$

$$\begin{aligned} = \pi \Bigg(& \pm\delta_{p,p'}\, p\beta\; b^{p}(\Delta)\, b^{\bar{p}}(\Delta) \int' \frac{\mathrm{d}\omega}{\omega - \mu + \mathrm{i}\eta} \mp p'\beta\; b^{p'}(\Delta)\, b^{\bar{p}'}(\Delta) \int' \mathrm{d}\omega \, \frac{f^{p}(\omega)}{\omega - \mu + \mathrm{i}\eta} \\ & \mp p\beta\; b^{p}(\Delta)\, b^{\bar{p}}(\Delta) \int' \mathrm{d}\tilde{\omega} \, \frac{f^{p'}(\tilde{\omega})}{\Delta - \tilde{\omega} - \mu + \mathrm{i}\eta} \mp b^{p}(\Delta) \int' \mathrm{d}\tilde{\omega} \, \frac{f^{p'}(\tilde{\omega})}{(\Delta - \tilde{\omega} - \mu + \mathrm{i}\eta)^2} \\ & + \delta_{p,p'}\, p\, \beta\; b^{p}(\Delta)\, b^{\bar{p}}(\Delta) \int' \frac{\mathrm{d}\omega'}{\pm\omega' - \mu' + \mathrm{i}\eta} - p'\beta\; b^{p'}(\Delta)\, b^{\bar{p}'}(\Delta) \int' \mathrm{d}\tilde{\omega} \, \frac{f^{p}(\tilde{\omega})}{\pm\Delta \mp \tilde{\omega} - \mu' + \mathrm{i}\eta} \\ & \mp b^{p'}(\Delta) \int' \mathrm{d}\tilde{\omega} \, \frac{f^{p}(\tilde{\omega})}{(\pm\Delta \mp \tilde{\omega} - \mu' + \mathrm{i}\eta)^2} - p\beta\; b^{p}(\Delta)\, b^{\bar{p}}(\Delta) \int' \mathrm{d}\omega' \, \frac{f^{p'}(\omega')}{\pm\omega' - \mu' + \mathrm{i}\eta} \\ & \mp f^{p}(\mu) \int' \mathrm{d}\omega' \, \frac{f^{p'}(\omega')}{(\mu + \omega' - \Delta + \mathrm{i}\eta)^2} - f^{p'}(\pm\mu') \int' \mathrm{d}\omega \, \frac{f^{p}(\omega)}{(\omega \pm \mu' - \Delta + \mathrm{i}\eta)^2} \Bigg) \end{aligned}$$

$$\begin{aligned} = {} & \pm\, \pi\beta p p'\, b^{p}(\Delta)\, b^{\bar{p}}(\Delta) \left\{ \mathsf{Re}\, \Psi^{(0)} \left(\frac{1}{2} - \frac{\mathrm{i}(\Delta - \mu)}{2\pi} \right) - \mathsf{Re}\, \Psi^{(0)} \left(\frac{1}{2} + \frac{\mathrm{i}\mu'}{2\pi} \right) \right\} \\ & \pm\, \pi\beta p p'\, b^{p'}(\Delta)\, b^{\bar{p}'}(\Delta) \left\{ \mathsf{Re}\, \Psi^{(0)} \left(\frac{1}{2} - \frac{\mathrm{i}(\Delta - \mu')}{2\pi} \right) - \mathsf{Re}\, \Psi^{(0)} \left(\frac{1}{2} + \frac{\mathrm{i}\mu}{2\pi} \right) \right\} \\ & \pm \frac{p'}{2}\, b^{p}(\Delta)\, \mathsf{Im}\, \Psi^{(1)} \left(\frac{1}{2} + \frac{\mathrm{i}(\Delta - \mu)}{2\pi} \right) \pm \frac{p}{2}\, b^{p'}(\Delta)\, \mathsf{Im}\, \Psi^{(1)} \left(\frac{1}{2} + \frac{\mathrm{i}(\Delta \mp \mu')}{2\pi} \right) \\ & \pm \frac{p'}{2}\, f^{p}(\mu)\, \mathsf{Im}\, \Psi^{(1)} \left(\frac{1}{2} + \frac{\mathrm{i}(\Delta - \mu)}{2\pi} \right) + \frac{p}{2}\, f^{p'}(\pm\mu')\, \mathsf{Im}\, \Psi^{(1)} \left(\frac{1}{2} + \frac{\mathrm{i}(\Delta \mp \mu')}{2\pi} \right) \end{aligned}$$

$$= \Big[\Delta - \mu = \pm\mu', \Delta \mp \mu' = \mu \Big] =$$

$$= \begin{cases} \dfrac{p'}{2} \left(b^{p}(\Delta) + f^{p}(\mu) \right) \mathsf{Im}\, \Psi^{(1)} \left(\dfrac{1}{2} + \dfrac{\mathrm{i}\mu'}{2\pi} \right) + \dfrac{p}{2} \left(\pm b^{p'}(\Delta) + f^{p'}(\pm\mu') \right) \mathsf{Im}\, \Psi^{(1)} \left(\dfrac{1}{2} + \dfrac{\mathrm{i}\mu}{2\pi} \right) & \Delta \neq 0, \\ \dfrac{1}{2} \left(p f^{p'}(-\mu) \mp p' f^{p}(\mu) \right) \mathsf{Im}\, \Psi^{(1)} \left(\dfrac{1}{2} + \dfrac{\mathrm{i}\mu}{2\pi} \right) \pm \dfrac{pp'}{4\pi}\, \mathsf{Re}\, \Psi^{(2)} \left(\dfrac{1}{2} + \dfrac{\mathrm{i}\mu}{2\pi} \right) & \Delta = 0. \end{cases}$$

X.ii Given $\mu \pm \mu' = \Sigma \neq \Delta$.

$$\hbar/\beta\, \mathsf{Re}\, {}^{\pm}X^{pp'}_{++}(\mu/\beta, \mu'/\beta, \Delta/\beta) =$$

$$= \mathsf{Im} \int \mathrm{d}\omega \int \mathrm{d}\omega' \, \frac{f^p(\omega)}{\omega - \mu + \mathrm{i}\eta} \, \frac{1}{\omega + \omega' - \Delta + \mathrm{i}\eta} \, \frac{f^{p'}(\omega')}{\pm\omega' - \mu' + \mathrm{i}\eta}$$

$$= [\text{Eq. } (125a)] = \frac{1}{\mu \pm \mu' - \Delta} \, \mathsf{Im} \int \mathrm{d}\omega \int \mathrm{d}\omega' \left(\pm \frac{1}{\omega - \mu + \mathrm{i}\eta} + \frac{1}{\pm\omega' - \mu' + \mathrm{i}\eta} \right) \times \left(\frac{f^p(\omega) f^{p'}(\omega')}{\omega + \omega' - \mu \mp \mu' + \mathrm{i}\eta} - \frac{f^p(\omega) f^{p'}(\omega')}{\omega + \omega' - \Delta + \mathrm{i}\eta} \right)$$

$$\begin{aligned} = [\text{Eq. } (127)] = {} & \mp \frac{\pi}{\mu \pm \mu' - \Delta} \int' \mathrm{d}\omega' \left(\frac{f^p(\mu) f^{p'}(\omega')}{\omega' \mp \mu' + \mathrm{i}\eta} - \frac{f^p(\mu) f^{p'}(\omega')}{\mu + \omega' - \Delta + \mathrm{i}\eta} \right) \\ & + \frac{-\pi}{\mu \pm \mu' - \Delta} \int' \mathrm{d}\omega \left(\frac{f^p(\omega) f^{p'}(\pm\mu')}{\omega - \mu + \mathrm{i}\eta} - \frac{f^p(\omega) f^{p'}(\pm\mu')}{\omega \pm \mu' - \Delta + \mathrm{i}\eta} \right) \\ & \pm \frac{-\pi}{\mu \pm \mu' - \Delta} \int' \mathrm{d}\omega \, \frac{\delta_{p,p'}\, b^p(\Sigma) - f^p(\omega)\, b^{p'}(\Sigma) - f^{p'}(\Sigma - \omega)\, b^p(\Sigma)}{\omega - \mu + \mathrm{i}\eta} \\ & + \frac{-\pi}{\mu \pm \mu' - \Delta} \int' \mathrm{d}\omega' \, \frac{\delta_{p,p'}\, b^p(\Sigma) - f^p(\Sigma - \omega')\, b^{p'}(\Sigma) - f^{p'}(\omega')\, b^p(\Sigma)}{\pm\omega' - \mu' + \mathrm{i}\eta} \\ & \mp \frac{-\pi}{\mu \pm \mu' - \Delta} \int' \mathrm{d}\omega \, \frac{\delta_{p,p'}\, b^p(\Delta) - f^p(\omega)\, b^{p'}(\Delta) - f^{p'}(\Delta - \omega)\, b^p(\Delta)}{\omega - \mu + \mathrm{i}\eta} \\ & - \frac{-\pi}{\mu \pm \mu' - \Delta} \int' \mathrm{d}\omega' \, \frac{\delta_{p,p'}\, b^p(\Delta) - f^p(\Delta - \omega')\, b^{p'}(\Delta) - f^{p'}(\omega')\, b^p(\Delta)}{\pm\omega' - \mu' + \mathrm{i}\eta} \end{aligned}$$

$$\begin{aligned} = \frac{\pi}{\mu \pm \mu' - \Delta} \Bigg(& \mp p' \, f^p(\mu) \left\{ \mathsf{Re}\, \Psi^{(0)} \left(\frac{1}{2} \pm \frac{\mathrm{i}\mu'}{2\pi} \right) - \mathsf{Re}\, \Psi^{(0)} \left(\frac{1}{2} + \frac{\mathrm{i}(\Delta - \mu)}{2\pi} \right) \right\} \\ & - p \, f^{p'}(\pm\mu') \left\{ \mathsf{Re}\, \Psi^{(0)} \left(\frac{1}{2} + \frac{\mathrm{i}\mu}{2\pi} \right) - \mathsf{Re}\, \Psi^{(0)} \left(\frac{1}{2} + \frac{\mathrm{i}(\Delta \mp \mu')}{2\pi} \right) \right\} \\ & \pm p' \, b^p(\Sigma) \left\{ \mathsf{Re}\, \Psi^{(0)} \left(\frac{1}{2} + \frac{\mathrm{i}\mu'}{2\pi} \right) - \mathsf{Re}\, \Psi^{(0)} \left(\frac{1}{2} - \frac{\mathrm{i}(\Sigma - \mu)}{2\pi} \right) \right\} \\ & \pm p \, b^{p'}(\Sigma) \left\{ \mathsf{Re}\, \Psi^{(0)} \left(\frac{1}{2} + \frac{\mathrm{i}\mu}{2\pi} \right) - \mathsf{Re}\, \Psi^{(0)} \left(\frac{1}{2} \mp \frac{\mathrm{i}(\Sigma \mp \mu')}{2\pi} \right) \right\} \\ & \mp p' \, b^p(\Delta) \left\{ \mathsf{Re}\, \Psi^{(0)} \left(\frac{1}{2} + \frac{\mathrm{i}\mu'}{2\pi} \right) - \mathsf{Re}\, \Psi^{(0)} \left(\frac{1}{2} - \frac{\mathrm{i}(\Delta - \mu)}{2\pi} \right) \right\} \\ & \mp p \, b^{p'}(\Delta) \left\{ \mathsf{Re}\, \Psi^{(0)} \left(\frac{1}{2} + \frac{\mathrm{i}\mu}{2\pi} \right) - \mathsf{Re}\, \Psi^{(0)} \left(\frac{1}{2} \mp \frac{\mathrm{i}(\Delta \mp \mu')}{2\pi} \right) \right\} \Bigg) \end{aligned}$$

$$= \Big[\Sigma - \mu = \pm\mu', \Sigma \mp \mu' = \mu \Big] =$$

$$= \begin{cases} \dfrac{\pi}{\mu \pm \mu' - \Delta} \Bigg(\pm p' \left(f^p(\mu) + b^p(\Delta) \right) \left\{ \mathsf{Re}\, \Psi^{(0)} \left(\dfrac{1}{2} + \dfrac{\mathrm{i}(\Delta - \mu)}{2\pi} \right) - \mathsf{Re}\, \Psi^{(0)} \left(\dfrac{1}{2} + \dfrac{\mathrm{i}\mu'}{2\pi} \right) \right\} \\ \qquad + p \left(f^{p'}(\pm\mu') \pm b^{p'}(\Delta) \right) \left\{ \mathsf{Re}\, \Psi^{(0)} \left(\dfrac{1}{2} + \dfrac{\mathrm{i}(\Delta \mp \mu')}{2\pi} \right) - \mathsf{Re}\, \Psi^{(0)} \left(\dfrac{1}{2} + \dfrac{\mathrm{i}\mu}{2\pi} \right) \right\} \Bigg) & \Delta \neq 0, \\ \dfrac{\pi}{\mu \pm \mu'} \left(\pm p' f^p(\mu) - p f^{p'}(\pm\mu') \right) \left(\mathsf{Re}\, \Psi^{(0)} \left(\dfrac{1}{2} + \dfrac{\mathrm{i}\mu}{2\pi} \right) - \mathsf{Re}\, \Psi^{(0)} \left(\dfrac{1}{2} + \dfrac{\mathrm{i}\mu'}{2\pi} \right) \right) \\ \qquad \pm \dfrac{pp'}{2} \dfrac{1}{\mu \pm \mu'} \left(\mathsf{Im}\, \Psi^{(1)} \left(\dfrac{1}{2} + \dfrac{\mathrm{i}\mu}{2\pi} \right) \pm \mathsf{Im}\, \Psi^{(1)} \left(\dfrac{1}{2} + \dfrac{\mathrm{i}\mu'}{2\pi} \right) \right) & \Delta = 0. \end{cases}$$

D.i Given $\mu = \mu'$.

$$\hbar/\beta\,\mathsf{Re}\,{}^{+}D^{pp'}_{++}(\mu/\beta,\mu/\beta,\Delta/\beta) =$$

$$= \mathsf{Im}\int \mathrm{d}\omega \int \mathrm{d}\omega'\, \frac{f^{p}(\omega)}{\omega-\mu+\mathrm{i}\eta}\,\frac{1}{\omega+\omega'-\Delta+\mathrm{i}\eta}\,\frac{f^{p'}(\omega')}{\omega-\mu+\mathrm{i}\eta}$$

$$= \text{Eq. } (125b) = \mathsf{Im}\int \mathrm{d}\omega \int \mathrm{d}\omega'\, \frac{\mathrm{d}}{\mathrm{d}\mu}\,\frac{1}{\omega-\mu+\mathrm{i}\eta}\,\frac{f^{p}(\omega)f^{p'}(\omega')}{\omega+\omega'-\Delta+\mathrm{i}\eta}$$

$$= \text{Eq. } (127) = -\pi\int' \mathrm{d}\omega'\,\frac{\mathrm{d}}{\mathrm{d}\mu}\,\frac{f^{p}(\mu)f^{p'}(\omega')}{\mu+\omega'-\Delta+\mathrm{i}\eta} - \pi\int' \mathrm{d}\omega'\,\frac{\mathrm{d}}{\mathrm{d}\mu}\,\frac{\delta_{p,p'}\,b^{p}(\Delta) - f^{p}(\Delta-\omega')\,b^{p'}(\Delta) - f^{p'}(\omega')\,b^{p}(\Delta)}{\Delta-\omega'-\mu+\mathrm{i}\eta}$$

$$= -\pi\left(\delta_{p,p'}b^{p}(\Delta)\int' \frac{\mathrm{d}\omega'}{(\Delta-\omega'-\mu+\mathrm{i}\eta)^2} - b^{p'}(\Delta)\int' \mathrm{d}\tilde{\omega}\,\frac{f^{p}(\tilde{\omega})}{(\tilde{\omega}-\mu+\mathrm{i}\eta)^2} - b^{p}(\Delta)\int' \mathrm{d}\omega'\,\frac{f^{p'}(\omega')}{(\Delta-\omega'-\mu+\mathrm{i}\eta)^2}\right.$$
$$\left. -f^{p}(\mu)\int' \mathrm{d}\omega'\,\frac{f^{p'}(\omega')}{(\omega'+\mu-\Delta+\mathrm{i}\eta)^2} - p\beta\; f^{p}(\mu)f^{\bar{p}}(\mu)\int' \mathrm{d}\omega'\,\frac{f^{p'}(\omega')}{\omega'+\mu-\Delta+\mathrm{i}\eta}\right)$$

$$= \begin{cases} -\dfrac{p}{2}\,b^{p'}(\Delta)\,\mathsf{Im}\,\Psi^{(1)}\left(\dfrac{1}{2}+\dfrac{\mathrm{i}\mu}{2\pi}\right) - \dfrac{p'}{2}\left(b^{p}(\Delta)+f^{p}(\mu)\right)\,\mathsf{Im}\,\Psi^{(1)}\left(\dfrac{1}{2}+\dfrac{\mathrm{i}(\Delta-\mu)}{2\pi}\right) \\ \qquad\qquad +\pi\beta pp'\,f^{+}(\mu)f^{-}(\mu)\left\{\mathsf{Re}\,\Psi^{(0)}\left(\dfrac{1}{2}+\dfrac{\mathrm{i}(\Delta-\mu)}{2\pi}\right) - C\right\} & \Delta\neq 0, \\ -\dfrac{pp'}{4\pi}\,\mathsf{Re}\,\Psi^{(2)}\left(\dfrac{1}{2}+\dfrac{\mathrm{i}\mu}{2\pi}\right) + \dfrac{p'}{2}f^{p}(\mu)\,\mathsf{Im}\,\Psi^{(1)}\left(\dfrac{1}{2}+\dfrac{\mathrm{i}\mu}{2\pi}\right) \\ \qquad\qquad +\pi\beta pp'\,f^{+}(\mu)f^{-}(\mu)\left\{\mathsf{Re}\,\Psi^{(0)}\left(\dfrac{1}{2}+\dfrac{\mathrm{i}\mu}{2\pi}\right) - C\right\} & \Delta = 0. \end{cases}$$

DX.i Given $\mu+\mu' = \Delta$.

$$DX^{pp'}_{++}(\mu,\mu',\Delta) = {}^{+}D^{pp'}_{++}(\mu,\Delta-\mu',\Delta) + {}^{+}X^{pp'}_{++}(\mu,\mu',\Delta),$$
$$\hbar/\beta\,\mathsf{Re}\,DX^{pp'}_{++}(\mu/\beta,\mu'/\beta,\Delta/\beta) = \frac{p}{2}f^{p'}(\mu')\,\mathsf{Im}\,\Psi^{(1)}\left(\frac{1}{2}+\frac{\mathrm{i}\mu}{2\pi}\right) + \pi\beta pp'\,f^{+}(\mu)f^{-}(\mu)\left\{\mathsf{Re}\,\Psi^{(0)}\left(\frac{1}{2}+\frac{\mathrm{i}\mu'}{2\pi}\right) - C\right\}.$$

D.ii Given $\mu \neq \pm\mu'$.

$$\hbar/\beta\,\mathsf{Re}\,{}^{\pm}D^{pp'}_{++}(\mu/\beta,\mu'/\beta,\Delta/\beta) =$$

$$= \mathsf{Im}\int \mathrm{d}\omega \int \mathrm{d}\omega' \, \frac{f^{p}(\omega)}{\omega-\mu+\mathrm{i}\eta}\,\frac{1}{\omega+\omega'-\Delta+\mathrm{i}\eta}\,\frac{f^{p'}(\omega')}{\pm\omega-\mu'+\mathrm{i}\eta}$$

$$= \text{Eq. (125}b\text{)} = \frac{1}{\mu\mp\mu'}\,\mathsf{Im}\int \mathrm{d}\omega \int \mathrm{d}\omega' \, \frac{f^{p}(\omega) f^{p'}(\omega')}{\omega+\omega'-\Delta+\mathrm{i}\eta}\left(\pm\frac{1}{\omega-\mu+\mathrm{i}\eta} - \frac{1}{\pm\omega-\mu'+\mathrm{i}\eta}\right)$$

$$= \text{Eq. (127)} = -\frac{\pi}{\mu\mp\mu'}\int{}' \mathrm{d}\omega' \left(\pm\frac{f^{p}(\mu) f^{p'}(\omega')}{\mu+\omega'-\Delta+\mathrm{i}\eta} - \frac{f^{p}(\pm\mu') f^{p'}(\omega')}{\pm\mu'+\omega'-\Delta+\mathrm{i}\eta}\right)$$
$$-\frac{\pi}{\mu\mp\mu'}\int{}' \mathrm{d}\omega \left(\pm\frac{\delta_{p,p'}\, b^{p}(\Delta) - f^{p}(\omega)\, b^{p'}(\Delta) - f^{p'}(\Delta-\omega)\, b^{p}(\Delta)}{\omega-\mu+\mathrm{i}\eta}\right.$$
$$\left. -\frac{\delta_{p,p'}\, b^{p}(\Delta) - f^{p}(\omega)\, b^{p'}(\Delta) - f^{p'}(\Delta-\omega)\, b^{p}(\Delta)}{\omega-\mu'+\mathrm{i}\eta}\right)$$

$$= \begin{cases} \dfrac{\pi}{\mu\mp\mu'}\left(\pm p\, b^{p'}(\Delta)\left\{\mathsf{Re}\,\Psi^{(0)}\left(\frac{1}{2}+\frac{\mathrm{i}\mu}{2\pi}\right) - \mathsf{Re}\,\Psi^{(0)}\left(\frac{1}{2}\pm\frac{\mathrm{i}\mu'}{2\pi}\right)\right\}\right. & \\ \qquad +p'\left(f^{p}(\pm\mu')\pm b^{p}(\Delta)\right)\left\{\mathsf{Re}\,\Psi^{(0)}\left(\frac{1}{2}+\frac{\mathrm{i}(\Delta\mp\mu')}{2\pi}\right) - C\right\} & \\ \left. \qquad \mp p'\left(f^{p}(\mu)+b^{p}(\Delta)\right)\left\{\mathsf{Re}\,\Psi^{(0)}\left(\frac{1}{2}+\frac{\mathrm{i}(\Delta-\mu)}{2\pi}\right) - C\right\}\right) & \Delta\neq 0, \\ \dfrac{\pi}{\mu\mp\mu'}\left(p'\, f^{p}(\pm\mu')\left\{\mathsf{Re}\,\Psi^{(0)}\left(\frac{1}{2}+\frac{\mathrm{i}\mu'}{2\pi}\right) - C\right\} \mp p'\, f^{p}(\mu)\left\{\mathsf{Re}\,\Psi^{(0)}\left(\frac{1}{2}+\frac{\mathrm{i}\mu}{2\pi}\right) - C\right\}\right) & \\ \qquad +\dfrac{pp'}{2}\dfrac{1}{\mu\mp\mu'}\left(\mathsf{Im}\,\Psi^{(1)}\left(\frac{1}{2}+\frac{\mathrm{i}\mu'}{2\pi}\right) \mp \mathsf{Im}\,\Psi^{(1)}\left(\frac{1}{2}+\frac{\mathrm{i}\mu}{2\pi}\right)\right) & \Delta = 0. \end{cases}$$

D$\boldsymbol{X}$**.ii** Given $\mu+\mu' \neq \Delta$.

$$D\!X^{pp'}_{++}(\mu,\mu',\Delta) = {}^{+}D^{pp'}_{++}(\mu,\Delta-\mu',\Delta) + {}^{+}X^{pp'}_{++}(\mu,\mu',\Delta),$$
$$\hbar/\beta\,\mathsf{Re}\,D\!X^{pp'}_{++}(\mu/\beta,\mu'/\beta,\Delta/\beta) = \frac{\pi}{\mu+\mu'-\Delta}\left(p'\left(f^{p}(\Delta-\mu')-f^{p}(\mu)\right)\left\{\mathsf{Re}\,\Psi^{(0)}\left(\frac{1}{2}+\frac{\mathrm{i}\mu'}{2\pi}\right) - C\right\}\right.$$
$$\left. +p f^{p'}(\mu')\left\{\mathsf{Re}\,\Psi^{(0)}\left(\frac{1}{2}+\frac{\mathrm{i}(\Delta-\mu')}{2\pi}\right) - \mathsf{Re}\,\Psi^{(0)}\left(\frac{1}{2}+\frac{\mathrm{i}\mu}{2\pi}\right)\right\}\right).$$

A.3 Diagram grouping

In Sect. 1.3 of the main part of this thesis we showed that an effectively secular fourth order kernel, Eq. (29b),

$$\hat{K}^{(4)}_{\mathsf{eff}} \equiv \hat{K}^{(4)}_{ss} + \hat{K}_C,$$

which already incorporates the influence of any coherence between non-secular states in the RDM, is constructed of 128 irreducible diagram plus 64 reducible non-secular correcting diagrams. Working with this kernel holds the advantage that the generalised master equation must merely be solved for the secular part of the reduced density matrix, see Eq. (29a). The analysis in Sect. 2.3.1 has shown that the in total 192 fourth order diagrams, or equivalently their 24 representatives, can be sorted into three supergroups A, B and C which further subdivide into three groups (0), (1) and (2). The grouping structure is shown in Fig. 6. Conveniently, exactly one analytical expression relates to each of the nine subgroups G.(x), G$\in$ {A,B,C}, x$\in$ $\{0,1,2\}$, and in general, any element of the effective secular fourth order kernel can indeed be calculated as

$$\left(\hat{K}^{(4)}_{\mathsf{eff}}\right)^{aa'}_{bb'} = \sum_{\mathrm{x}\in\{0,1,2\}} \left(\left(\mathrm{A}_{(\mathrm{x})}\right)^{aa'}_{bb'} + \left(\mathrm{B}_{(\mathrm{x})}\right)^{aa'}_{bb'} + \left(\mathrm{C}_{(\mathrm{x})}\right)^{aa'}_{bb'} \right)$$

according to Tab. 2, where energy dependent functions $\tilde{G}_{\mathrm{x}}$ are employed. Their definition is as follows:

$$\begin{aligned}
&\tilde{A}_{(0)}(\mu,\mu',\Delta) := {}^{+}X^{--}_{++}(\mu,\mu',\Delta),\\
&\tilde{A}_{(1)}(\mu,\mu',\Delta;\nu,\nu') := \tilde{A}_{(0)}(\nu'-\mu',\mu,\Delta) + \tilde{A}_{(2)}(\mu,\mu',\Delta),\\
&\tilde{A}_{(2)}(\mu,\mu',\Delta;\nu) := {}^{+}D^{--}_{++}(\mu'+\Delta,\mu,\Delta) + {}^{+}D^{-+}_{++}(\mu'+\Delta,\mu,\mu+\mu')\\
&\qquad\qquad + {}^{+}X^{-+}_{++}(\mu'+\Delta,\mu'+\nu,\mu+\mu'),
\end{aligned}$$

$$\begin{aligned}
&\tilde{B}_{(0)}(\mu,\mu',\Delta) := (\delta_{\Delta,0}-1)\, Y^{-}_{+}(\mu)\frac{\mathrm{i}\hbar}{\Delta}Y^{-}_{+}(\mu'),\\
&\tilde{B}_{(1)}(\mu,\mu',\Delta;\nu,\nu') := \tilde{B}_{(0)}(\nu'-\mu',\mu,\Delta) + \tilde{B}_{(2)}(\mu,\mu',\Delta),\\
&\tilde{B}_{(2)}(\mu,\mu',\Delta;\nu) := {}^{+}X^{+-}_{++}(\mu'+\Delta,\mu,\mu+\mu') + {}^{+}D^{+-}_{++}(\mu'+\Delta,\mu'+\nu,\mu+\mu')\\
&\qquad\qquad + (\delta_{\Delta,0}-1)\, Y^{-}_{+}(\mu)\,\{\mathrm{i}\hbar/\Delta\}\, Y^{+}_{+}(\mu'+\Delta),
\end{aligned}$$

$$\begin{aligned}
&\tilde{C}_{(0)}(\mu,\mu',\Delta) := {}^{+}D^{--}_{++}(\mu,\mu',\Delta),\\
&\tilde{C}_{(1)}(\mu,\mu',\Delta;\nu,\nu') := \tilde{C}_{(0)}(\nu'-\mu',\mu,\Delta) + \tilde{C}_{(2)}(\mu,\mu',\Delta),\\
&\tilde{C}_{(2)}(\mu,\mu',\Delta;\nu) := {}^{+}X^{--}_{++}(\mu'+\Delta,\mu,\Delta) + (\delta_{\mu,-\mu'}-1)\, Y^{-}_{+}(\mu'+\Delta)\\
&\qquad\qquad \times \{\mathrm{i}\hbar/(\mu+\mu')\}\left(Y^{-}_{+}(\mu) + Y^{+}_{+}(\mu'+\nu)\right).
\end{aligned} \tag{129}$$

These are generally valid expressions. Notice that as a consequence of gain-loss relations (remember Sect. 2.2 and compare to Fig. 6) the $\tilde{G}_{(1)}$ contributions are simply the

sum of a $\tilde{G}_{(0)}$ and a $\tilde{G}_{(2)}$ function. The employed helper functions Y^{p}_{+}, ${}^{\pm}X^{pp'}_{++}$, ${}^{\pm}D^{pp'}_{++}$ and $DX^{pp'}_{++}$ have been defined in Sect. A.2.4, Eq. (124a)-Eq. (124c) and Eq. (128), respectively. For the first one, Y^{p}_{+}, an analytical solution is given on page 148 while the real parts of the latter three functions have been evaluated on page 171-174. Cancellation among the summed expressions occur, but major simplification is possible in the special case of $\nu = 0$, corresponding to secular initial states of the diagrams. This case is addressed in the following subsection.

A.3.1 The special case of secular initial states

In the case of diagonal or non-diagonal secular initial states, $\nu = 0$, the expressions $\tilde{G}_{(2)}$, G$\in \{A, B, C\}$, in Eq. (129) combine further, namely to

$$\begin{aligned}
\tilde{A}_{(2)}(\mu,\mu',\Delta) &= {}^{-}X^{--}_{++}(\mu,\mu',\Delta),\\
\tilde{B}_{(2)}(\mu,\mu',\Delta) &= \begin{cases} -Y^{-}_{+}(\mu)\frac{\mathrm{i}\hbar}{\Delta}Y^{+}_{+}(\mu') & \Delta \neq 0,\\ DX^{+-}_{++}(\mu',\mu,\mu+\mu') & \Delta = 0,\end{cases}\\
\tilde{C}_{(2)}(\mu,\mu',\Delta) &= \begin{cases} {}^{-}D^{--}_{++}(\mu,\mu',\Delta) & \mu+\mu' \neq \Delta,\\ {}^{+}X^{--}_{++}(\mu'+\Delta,\mu,\Delta) & \mu+\mu' = \Delta.\end{cases}
\end{aligned} \tag{130}$$

On the following pages we show how to obtain for each diagram group G.(2), G$\in$ {A,B,C}, its function as given Eq. (130). Before, we spend, as promised in Sect. 2.3.1, some words on the validity of the relation

$$\begin{aligned}
&\lim_{\lambda\to 0}\int_{\infty\geq\tau'\geq\tau_1'\geq\tau_2'\geq 0} \mathrm{d}\tau'\,\mathrm{d}\tau_1'\,\mathrm{d}\tau_2'\; e^{-\lambda(\tau'+\tau_2')}\mathcal{G}^{I}_{(x)}(t,t-\tau_2',t-\tau_1',t-\tau')\\
&\qquad = \lim_{\lambda\to 0}\int_{\infty\geq\tau'\geq\tau_1'\geq\tau_2'\geq 0} \mathrm{d}\tau'\,\mathrm{d}\tau_1'\,\mathrm{d}\tau_2'\; e^{-\lambda\tau'}\mathcal{G}^{I}_{(x)}(t,t-\tau_2',t-\tau_1',t-\tau'),
\end{aligned} \tag{131}$$

on which Eq. (38) relies on. We know e.g. from App. A.2.2 and A.2.4 which kind of functions emerge after dissolving the time integrations, and it is straightforward to show that the right-hand-side of Eq. (131) always acquires a form equivalent[37] to

$$\lim_{\eta\to 0}\int \mathrm{d}\omega\;\frac{1}{\omega+\mathrm{i}\eta}\;g_{\eta}(\omega), \tag{132a}$$

while the left-hand-side would indeed yield

$$\lim_{\eta\to 0}\int \mathrm{d}\omega\;\frac{1}{\omega+2\mathrm{i}\eta}\;g_{\eta}(\omega). \tag{132b}$$

[37] Transformation or renaming of the integration variables might be necessary.

The function $g_\eta(\omega)$ comprises the Fermi functions, two more denominators involving both ω and ω' and finally an integration over ω' [compare to Eqs. (124b), (124c)]. Though the limit $\eta \to 0$ must not be interchanged with the integration over ω, it is nevertheless comprehensible that Eq. (132a) and Eq. (132b) are equivalent. The crucial point is that the function $g_\eta(\omega)$ is well-behaved in the sense that it possess a countable number of poles and decays decently such that the residue theorem can be applied for evaluation of the integration. Closing thereby the bow in the upper half of the complex plane as demonstrated in App. A.2.5, we do not even need to demand a particularly small value of η to find for both cases Eqs. (132a), (132b) the very same poles within the chosen contour. Automatically, this makes the results of the integrations identical.

Now we can turn to the derivation of the functions Eq. (130). The structure of the following is intended to be compact and self-explaining. For each G$\in$ {A,B,C}, we start from the three G.(2) diagrams as listed in Tab. 1, whereas we assign the associated contribution in Eq. (37). We specify all states along the contours of the diagram which demands no change in its integration variables. From writing out the time evolution of its operators we obtain a time and energy dependent integrand. Upon performing the Laplace transform, see Eq. (32), whereas the integration over $\tau_2' = t - \tau_2$ is no longer subject to time order according to Eq. (38), we obtain the desired energy dependent part of the group's contribution to the time evolution kernel.

A.(2)

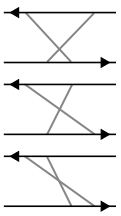

$$-\left\langle \hat{C}_1^p \hat{C}_3^{\bar{p}} \right\rangle \left\langle \hat{C}_2^{p'} \hat{C}_0^{\bar{p}'} \right\rangle \hat{D}_3^p \hat{D}_0^{p'} \hat{\rho}_\odot^I(\tau) \hat{D}_1^{\bar{p}} \hat{D}_2^{\bar{p}'} = \hat{\mathcal{A}}(t, \tau, \tau_2, \tau_1)[\hat{\rho}_\odot^I(\tau)]$$

$$-\left\langle \hat{C}_0^p \hat{C}_3^{\bar{p}} \right\rangle \left\langle \hat{C}_2^{p'} \hat{C}_1^{\bar{p}'} \right\rangle \hat{D}_3^p \hat{D}_1^{p'} \hat{\rho}_\odot^I(\tau) \hat{D}_0^{\bar{p}} \hat{D}_2^{\bar{p}'} = \hat{\mathcal{A}}(t, \tau_1, \tau_2, \tau)[\hat{\rho}_\odot^I(\tau)]$$

$$-\left\langle \hat{C}_0^p \hat{C}_3^{\bar{p}} \right\rangle \left\langle \hat{C}_1^{p'} \hat{C}_2^{\bar{p}'} \right\rangle \hat{D}_3^p \hat{D}_2^{p'} \hat{\rho}_\odot^I(\tau) \hat{D}_0^{\bar{p}} \hat{D}_1^{\bar{p}'} = \hat{\mathcal{A}}(t, \tau_2, \tau_1, \tau)[\hat{\rho}_\odot^I(\tau)]$$

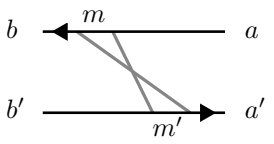

$$-\left\langle \hat{C}_0^p \hat{C}_3^{\bar{p}} \right\rangle \left\langle \hat{C}_1^{\bar{p}'} \hat{C}_2^{p'} \right\rangle \times$$
$$\times \langle b| \hat{D}_3^p |m\rangle \langle m| \hat{D}_2^{p'} |a\rangle \left\langle a \left| \hat{\rho}_\odot^I(\tau) \right| a' \right\rangle \langle a'| \hat{D}_0^{\bar{p}} |m'\rangle \langle m'| \hat{D}_1^{\bar{p}'} |b'\rangle$$

All three diagrams are irreducible and contribute for arbitrary intermediate states m, m'. For $E_a = E_{a'}$, the energy dependent integral parts can be put together to:

$$\tilde{A}_{(2)}(E_{am'} - peV_l, E_{ma} + p'eV_{l'}, E_{ab'} - peV_l - p'eV_{l'}, 0) =$$

$$= \hbar^{-4} \lim_{\eta\to 0} \int_0^\infty \mathrm{d}\tau' \int_0^{\tau'} \mathrm{d}\tau_1' \int_0^\infty \mathrm{d}\tau_2' \int \mathrm{d}\omega \int \mathrm{d}\omega' \; f^p(\omega + eV_l) f^{p'}(\omega' + eV_{l'}) \times$$
$$\times\, e^{\frac{\mathrm{i}}{\hbar}\tau'(-p\omega - E_a + E_{m'} + \mathrm{i}\eta)} e^{\frac{\mathrm{i}}{\hbar}\tau_1'(-p'\omega' - E_{m'} + E_{b'})} e^{\frac{\mathrm{i}}{\hbar}\tau_2'(p'\omega' - E_m + E_a + \mathrm{i}\eta)} =$$

$$= \int \mathrm{d}\omega \int \mathrm{d}\omega' \; \mathrm{i}\hbar \frac{f^{p'}(\omega' + eV_{l'})}{p'\omega' - E_m + E_a + \mathrm{i}\eta} (\mathrm{i}\hbar)^2 \frac{\hbar^{-4}}{-p\omega - p'\omega' - E_a + E_{b'} + \mathrm{i}\eta} \frac{f^p(\omega + eV_l)}{-p\omega - E_a + E_{m'} + \mathrm{i}\eta} =$$

$$= {}^{-}X^{pp'}_{(-p)(-p')}(pE_{m'a} + eV_l, p'E_{am} - eV_{l'}, E_{ab'} - peV_l - p'eV_{l'}) =$$

$$\boxed{= {}^{-}X^{--}_{++}(E_{am'} - peV_l, E_{ma} + p'eV_{l'}, E_{ab'} - peV_l - p'eV_{l'})}$$

B.(2)

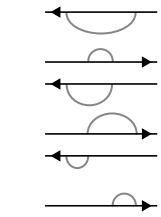

$$+ \left\langle \hat{C}_3^p \hat{C}_0^{\bar{p}} \right\rangle \left\langle \hat{C}_1^{p'} \hat{C}_2^{\bar{p}'} \right\rangle \hat{D}_3^{\bar{p}} \hat{D}_0^p \hat{\rho}^I_\odot(\tau) \hat{D}_1^{\bar{p}'} \hat{D}_2^{p'} = \hat{\mathcal{B}}(t, \tau, \tau_2, \tau_1)[\hat{\rho}^I_\odot(\tau)]$$
$$+ \left\langle \hat{C}_3^p \hat{C}_1^{\bar{p}} \right\rangle \left\langle \hat{C}_0^{p'} \hat{C}_2^{\bar{p}'} \right\rangle \hat{D}_3^{\bar{p}} \hat{D}_1^p \hat{\rho}^I_\odot(\tau) \hat{D}_0^{\bar{p}'} \hat{D}_2^{p'} = \hat{\mathcal{B}}(t, \tau_1, \tau_2, \tau)[\hat{\rho}^I_\odot(\tau)]$$
$$+ \left\langle \hat{C}_3^p \hat{C}_2^{\bar{p}} \right\rangle \left\langle \hat{C}_0^{p'} \hat{C}_1^{\bar{p}'} \right\rangle \hat{D}_3^{\bar{p}} \hat{D}_2^p \hat{\rho}^I_\odot(\tau) \hat{D}_0^{\bar{p}'} \hat{D}_1^{p'} = \hat{\mathcal{B}}(t, \tau_2, \tau_1, \tau)[\hat{\rho}^I_\odot(\tau)]$$

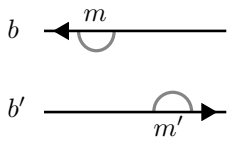

$$+ \left\langle \hat{C}_3^p \hat{C}_2^{\bar{p}} \right\rangle \left\langle \hat{C}_0^{p'} \hat{C}_1^{\bar{p}'} \right\rangle \times$$
$$\times \langle b| \hat{D}_3^{\bar{p}} |m\rangle \langle m| \hat{D}_2^p |a\rangle \langle a'| \hat{D}_0^{\bar{p}'} |m'\rangle \langle m'| \hat{D}_1^{p'} |b'\rangle$$

Only the first two of the three diagrams are irreducible. Thus the function resulting for $E_a = E_{a'}$ must distinguish between secular or non-secular involved states a, b',

$$\boxed{\tilde{B}_{(2)}(E_{am'} - p'eV_{l'}, E_{ma} + peV_l, E_{ab'}, 0) =}$$

- $E_a = E_{b'}$: the third diagram must be omitted. The energy dependent integral parts of the first two diagrams (pages 157 and 155) add up[38].

$$= {}^{+}D^{+-}_{++}(E_{mb'} + peV_l, E_{ma'} + peV_l, E_{mm'} + peV_l - p'eV_{l'}) +$$
$$+ {}^{+}X^{+-}_{++}(E_{mb'} + peV_l, E_{am'} - p'eV_{l'}, E_{mm'} + peV_l - p'eV_{l'}) =$$

$$\boxed{= DX^{+-}_{++}(E_{mb'} + peV_l, E_{am'} - p'eV_{l'}, E_{mm'} + peV_l - p'eV_{l'})}$$

[38] See definitions of $DX^{pp'}_{dd'}$, Eq. (128) and notice that $(E_{mm'} + peV_l + p'eV_{l'}) - (E_{am'} + p'eV_{l'}) =$ [$E_a = E_{a'}$ secular states] $= E_{ma'} + peV_l$.

- $E_a \neq E_{b'}$: the third diagram has to be added to account for non-secular corrections and the energy dependent integral parts can be put together.

$$= \hbar^{-4} \lim_{\eta\to 0} \int_0^\infty \mathrm{d}\tau' \int_0^{\tau'} \mathrm{d}\tau_1' \int_0^\infty \mathrm{d}\tau_2' \int \mathrm{d}\omega \int \mathrm{d}\omega' f^p(\omega + eV_l) f^{p'}(\omega' + eV_{l'}) \times$$
$$\times e^{\frac{\mathrm{i}}{\hbar}\tau'(-p'\omega' - E_a + E_{m'} + \mathrm{i}\eta)} e^{\frac{\mathrm{i}}{\hbar}\tau_1'(p'\omega' - E_{m'} + E_{b'})} e^{\frac{\mathrm{i}}{\hbar}\tau_2'(p\omega - E_m + E_a + \mathrm{i}\eta)} =$$
$$= \int \mathrm{d}\omega \int \mathrm{d}\omega' \; \mathrm{i}\hbar \frac{f^p(\omega + eV_l)}{p\omega - E_m + E_a + \mathrm{i}\eta} (\mathrm{i}\hbar)^2 \frac{\hbar^{-4}}{E_{b'} - E_a} \frac{f^{p'}(\omega' + eV_{l'})}{-p'\omega' - E_a + E_{m'} + \mathrm{i}\eta} =$$

$$= Y_p^p(pE_{ma} + eV_l) \frac{\mathrm{i}\hbar}{E_{b'a}} Y_{-p'}^{p'}(p'E_{m'a} + eV_{l'}) =$$

$$\boxed{= Y_+^+(E_{ma} + peV_l) \frac{\mathrm{i}\hbar}{E_{b'a}} Y_+^-(E_{am'} - p'eV_{l'})}$$

C.(2)

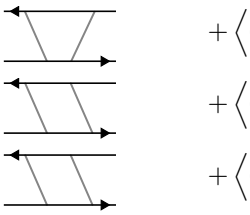

$$+ \left\langle \hat{C}_1^{p'} \hat{C}_0^{\bar{p}'} \right\rangle \left\langle \hat{C}_2^p \hat{C}_3^{\bar{p}} \right\rangle \hat{D}_3^p \hat{D}_0^{p'} \hat{\rho}_\odot^I(\tau) \hat{D}_1^{\bar{p}'} \hat{D}_2^{\bar{p}} = \hat{\mathcal{C}}(t, \tau, \tau_2, \tau_1)[\hat{\rho}_\odot^I(\tau)]$$
$$+ \left\langle \hat{C}_0^{p'} \hat{C}_1^{\bar{p}'} \right\rangle \left\langle \hat{C}_2^p \hat{C}_3^{\bar{p}} \right\rangle \hat{D}_3^p \hat{D}_1^{p'} \hat{\rho}_\odot^I(\tau) \hat{D}_0^{\bar{p}'} \hat{D}_2^{\bar{p}} = \hat{\mathcal{C}}(t, \tau_1, \tau_2, \tau)[\hat{\rho}_\odot^I(\tau)]$$
$$+ \left\langle \hat{C}_0^{p'} \hat{C}_2^{\bar{p}'} \right\rangle \left\langle \hat{C}_1^p \hat{C}_3^{\bar{p}} \right\rangle \hat{D}_3^p \hat{D}_2^{p'} \hat{\rho}_\odot^I(\tau) \hat{D}_0^{\bar{p}'} \hat{D}_1^{\bar{p}} = \hat{\mathcal{C}}(t, \tau_2, \tau_1, \tau)[\hat{\rho}_\odot^I(\tau)]$$

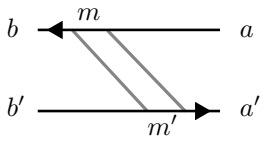

$$+ \left\langle \hat{C}_1^p \hat{C}_3^{\bar{p}} \right\rangle \left\langle \hat{C}_0^{p'} \hat{C}_2^{\bar{p}'} \right\rangle \times$$
$$\times \langle b| \hat{D}_3^p |m\rangle \langle m| \hat{D}_2^{p'} |a\rangle \langle a'| \hat{D}_0^{\bar{p}'} |m'\rangle \langle m'| \hat{D}_1^{\bar{p}} |b'\rangle$$

Only the last diagram is irreducible. Thus for the function resulting for $E_a = E_{a'}$ must distinguish between secular or non-secular involved states m, m',

$$\boxed{\tilde{C}_{(2)}(E_{am'} - p'eV_{l'}, E_{ma} + p'eV_{l'}, E_{ab'} - peV_l - p'eV_{l'}, 0) =}$$

- $E_m = E_{m'}$: the first two diagrams must be omitted and only the energy dependent integral part of the last diagram remains (cf. page 153).

$$\boxed{= {}^{+}X_{++}^{--}(E_{mb'} - peV_l, E_{am'} - p'eV_{l'}, E_{ab'} - peV_l - p'eV_{l'})}$$

- $E_m \neq E_{m'}$: the first two diagrams have to be added to account for non-secular corrections. The energy dependent integral parts can be put together.

$$= \hbar^{-4} \lim_{\eta\to 0} \int_0^\infty \mathrm{d}\tau' \int_0^{\tau'} \mathrm{d}\tau_1' \int_0^\infty \mathrm{d}\tau_2' \int \mathrm{d}\omega \int \mathrm{d}\omega' f^p(\omega + eV_l) f^{p'}(\omega' + eV_{l'}) \times$$
$$\times e^{\frac{\mathrm{i}}{\hbar}\tau'(-p'\omega' - E_a + E_{m'} + \mathrm{i}\eta)} e^{\frac{\mathrm{i}}{\hbar}\tau_1'(-p\omega - E_{m'} + E_{b'})} e^{\frac{\mathrm{i}}{\hbar}\tau_2'(p'\omega' - E_m + E_a + \mathrm{i}\eta)} =$$
$$= \int \mathrm{d}\omega \int \mathrm{d}\omega' \, \mathrm{i}\hbar \frac{\hbar^{-2}}{p'\omega' - E_m + E_a + \mathrm{i}\eta} (\mathrm{i}\hbar)^2 \frac{f^p(\omega + eV_l) f^{p'}(\omega' + eV_{l'})}{-p\omega - p'\omega' - E_a + E_{b'} + \mathrm{i}\eta} \frac{\hbar^{-2}}{-p'\omega' - E_a + E_{m'} + \mathrm{i}\eta} =$$
$$= {}^{-}\!D^{p'p}_{-p'-p}(p'E_{m'a} + eV_{l'}, p'E_{am} - eV_{l'}, E_{ab'} - peV_l - p'eV_{l'}) =$$
$$\boxed{= {}^{-}\!D^{--}_{++}(E_{am'} - p'eV_{l'}, E_{ma} + p'eV_{l'}, E_{ab'} - peV_l - p'eV_{l'})}$$

Secular final states If in addition to $\nu = 0$ also $\nu' = 0$, i.e. the final states of the diagram are secular as well, the functions $\tilde{G}_{(1)}$ from Eq. (129) simplify to

$$\tilde{A}_{(1)}(\mu, \mu', \Delta, 0, 0) = {}^{\Sigma}\!X^{--}_{++}(\mu, \mu', \Delta),$$
$$\tilde{B}_{(1)}(\mu, \mu', \Delta, 0, 0) = \begin{cases} -Y^-_+(\mu) \frac{\mathrm{i}\hbar}{\Delta} {}^{\Sigma}\!Y^+_+(\mu') & \Delta \neq 0, \\ D\!X^{+-}_{++}(\mu', \mu, \mu + \mu') & \Delta = 0, \end{cases}$$
$$\tilde{C}_{(1)}(\mu, \mu', \Delta, 0, 0) = \begin{cases} {}^{\Sigma}\!D^{--}_{++}(\mu, \mu', \Delta) & \mu + \mu' \neq 0, \\ D\!X^{--}_{++}(\mu, \Delta - \mu, \Delta) & \mu + \mu' = 0. \end{cases} \tag{133}$$

Thereby it was sensible to define the abbreviations

$$\begin{aligned} {}^{\Sigma}\!X^{pp'}_{++}(\mu, \mu', \Delta) &:= {}^{+}\!X^{pp'}_{++}(-\mu', \mu, \Delta) + {}^{-}\!X^{pp'}_{++}(\mu, \mu', \Delta), \\ {}^{\Sigma}\!D^{pp'}_{++}(\mu, \mu', \Delta) &:= {}^{+}\!D^{pp'}_{++}(-\mu', \mu, \Delta) + {}^{-}\!D^{pp'}_{++}(\mu, \mu', \Delta), \\ {}^{\Sigma}\!Y^p_+(\mu) &:= Y^p_+(\mu) - Y^{-p}_+(-\mu), \end{aligned}$$

as major cancellations occur. For the real parts of these functions, e.g.,

$$2\,\hbar\,\mathsf{Re}\left({}^{\Sigma}\!X^{--}_{++}(\mu, \mu', \Delta)\right) = -\frac{2\pi\beta}{\tilde{\mu} - \tilde{\mu}' - \tilde{\Delta}} f^-(\tilde{\mu}') \left\{ \mathsf{Re}\,\tilde{\Psi}\left(\frac{1}{2} + \frac{\mathrm{i}(\tilde{\Delta} + \tilde{\mu}')}{2\pi}\right) - \mathsf{Re}\,\tilde{\Psi}\left(\frac{1}{2} + \frac{\mathrm{i}\tilde{\mu}}{2\pi}\right) \right\},$$

$$2\,\hbar\,\mathsf{Re}\left({}^{\Sigma}\!D^{--}_{++}(\mu, \mu', \Delta)\right) = -\frac{2\pi\beta}{\tilde{\mu} + \tilde{\mu}'} f^-(\tilde{\mu}') \left\{ \mathsf{Re}\,\tilde{\Psi}\left(\frac{1}{2} + \frac{\mathrm{i}(\tilde{\Delta} + \tilde{\mu}')}{2\pi}\right) - C \right\},$$

$$2\,\hbar\,\mathsf{Re}\left({}^{\Sigma}\!Y^+_+(\mu) \frac{\mathrm{i}}{\Delta} Y^-_+(\mu')\right) = \frac{2\pi\beta}{\tilde{\Delta}} f^-(\tilde{\mu}') \left\{ \mathsf{Re}\,\tilde{\Psi}\left(\frac{1}{2} + \frac{\mathrm{i}\tilde{\mu}}{2\pi}\right) - C \right\}.$$

APPENDIX B:

CARBON ARMCHAIR NANORIBBONS

This second appendix contains calculations related to non-diagonal part of interactions relevant in the low energy theory of ACNRs, Sect. 4, which were too lengthy to be carried out in detail in the main text.

B.1 The matrix elements $\left\langle \vec{N}\vec{\sigma}^{\mathrm{e}}\vec{m}\left|\hat{V}^{\mathrm{b-b}}_{n\rho\rho}\right|\vec{N}'\vec{\sigma}^{\mathrm{e}\prime}\vec{m}'\right\rangle$

The evaluation of the non-diagonal bulk-bulk terms follows closely the procedure applied for SWCNTs [103]. In order to calculate the matrix elements of the non-diagonal bulk-bulk interaction we have to derive an expression for

$$M_{[r][\sigma]_{f^-}}(\vec{N},\vec{\sigma}^{\mathrm{e}},\vec{m},\vec{N}',\vec{\sigma}^{\mathrm{e}\prime},\vec{m}',y) := \delta_{\vec{N},\vec{N}'}\delta_{\vec{\sigma}^{\mathrm{e}},\vec{\sigma}^{\mathrm{e}\prime}} \times \left\langle \vec{N}\vec{\sigma}^{\mathrm{e}}\vec{m}\left|\hat{\psi}^{\dagger}_{r_1\sigma}(y)\hat{\psi}^{\dagger}_{r_2-\sigma}(y)\hat{\psi}_{r_3-\sigma}(y)\hat{\psi}_{r_4\sigma}(y)\right|\vec{N}\vec{\sigma}^{\mathrm{e}}\vec{m}'\right\rangle . \quad (134)$$

For this purpose we express the operators $\hat{\psi}_{r\sigma}(y)$ in terms of the bosonic operators $\hat{b}_{\sigma q}$ and $\hat{b}^{\dagger}_{\sigma q}$, $q>0$, using the bosonisation identity [111],

$$\hat{\psi}_{r\sigma F}(y) = \hat{\eta}_{\sigma}\hat{K}_{r\sigma}(y)e^{\mathrm{i}\hat{\phi}^{\dagger}_{r\sigma}(y)}e^{\mathrm{i}\hat{\phi}_{r\sigma}(y)}. \quad (135)$$

The operator $\hat{\eta}_{\sigma}$ is the so called Klein factor, which annihilates an electron in the σ-branch and thereby takes care of the right sign as required from the fermionic anti-commutation relations; in detail,

$$\hat{\eta}_{\sigma}\left|\vec{N},\vec{m}\right\rangle = (-1)^{\delta_{\sigma,\downarrow}N_{\uparrow}}\left|\vec{N}-\vec{e}_{\sigma},\vec{m}\right\rangle . \quad (136a)$$

$\hat{K}_{r\sigma}(y)$ yields a phase factor depending on the number of electrons of spin σ,

$$\hat{K}_{r\sigma}(y) = \frac{1}{\sqrt{2L_y}}e^{\mathrm{i}\frac{\pi}{L_y}\mathrm{sgn}(r)(\hat{\mathcal{N}}_{\sigma}+\frac{1}{2})y}. \quad (136b)$$

Finally, we have the boson fields $\mathrm{i}\hat{\phi}_{r\sigma}(y)$,

$$\mathrm{i}\hat{\phi}_{r\sigma}(y) = \sum_{q>0}\frac{1}{\sqrt{n_q}}e^{\mathrm{isgn}(r)qy}\hat{b}_{\sigma q}. \quad (136c)$$

The matrix elements from Eq. (134) factorise into a fermionic and a bosonic part,

$$M_{[r][\sigma]_{f^-}}(\vec{N},\vec{\sigma}^{\mathrm{e}},\vec{m},\vec{N}',\vec{\sigma}^{\mathrm{e}\prime},\vec{m}',y) = \delta_{\vec{N},\vec{N}'}\,\delta_{\vec{\sigma}^{\mathrm{e}},\vec{\sigma}^{\mathrm{e}\prime}}\,M_{[r][\sigma]_{f^-}}(\vec{N},y)M_{[r][\sigma]_{f^-}}(\vec{m},\vec{m}',y).$$

The fermionic part is given by

$$M_{[l]}(\vec{N},y)=\left\langle \vec{N}\right|\hat{K}^{\dagger}_{l_1}(y)\hat{\eta}^{\dagger}_{l_1}\hat{K}^{\dagger}_{l_2}(y)\hat{\eta}^{\dagger}_{l_2}\hat{K}_{l_3}(y)\hat{\eta}_{l_3}\hat{K}_{l_4}(y)\hat{\eta}_{l_4}\left|\vec{N}'\right\rangle \tag{137a}$$

and the bosonic part reads

$$M_{[l]}(\vec{m},\vec{m}',y)=\langle\vec{m}|\,e^{-\mathrm{i}\hat{\phi}^{\dagger}_{l_1}(y)}e^{-\mathrm{i}\hat{\phi}_{l_1}(y)}e^{-\mathrm{i}\hat{\phi}^{\dagger}_{l_2}(y)}e^{-\mathrm{i}\hat{\phi}_{l_2}(y)}e^{\mathrm{i}\hat{\phi}^{\dagger}_{l_3}(y)}e^{\mathrm{i}\hat{\phi}_{l_3}(y)}e^{\mathrm{i}\hat{\phi}^{\dagger}_{l_4}(y)}e^{\mathrm{i}\hat{\phi}_{l_4}(y)}\,|\vec{m}'\rangle\,. \tag{137b}$$

In order to improve readability we have replaced the indices $r\sigma$ by a single index l. Using the relation (136a) for the Klein factors $\hat{\eta}_\sigma$, together with the fact that $S_\sigma = f^-$, $[\sigma]_{f^-}=[\sigma,-\sigma,-\sigma,\sigma]$, and the definition Eq. (136b) of the phase factor $\hat{K}_{r\sigma}(y)$, it is straightforward to show that

$$M_{[r][\sigma]_{f^-}}(\vec{N},y)=\frac{1}{(2L_y)^2}Q_{\vec{N}[r]\sigma}(y), \tag{138}$$

where

$$Q_{\vec{N}[r]\sigma}(y)=\exp\left[\mathrm{i}\frac{\pi}{L_y}\Big(N_\sigma\,\mathrm{sgn}(r_4-r_1)-N_{-\sigma}\,\mathrm{sgn}(r_3-r_2)+\frac{\mathrm{sgn}(r_4+r_3-r_2-r_1)}{2}\Big)y\right].$$

Hence, for $S_r=u$, $[r]_u=[r,r,-r,-r]$, we obtain

$$Q_{\vec{N}[r]_u\sigma}(y)=\ =\exp\left[-\mathrm{i}\frac{2\pi}{L_y}\mathrm{sgn}(r)\,(N_\sigma+N_{-\sigma}+1)\,y\right],$$

which is oscillating fast with $N_c=N_\uparrow+N_\downarrow$ and thus completely suppresses the $S_r=u$ contribution away from half-filling. The only remaining term in $V^{\mathrm{b-b}}_{n\rho\rho}$ is consequently $S_rS_\sigma=bf^-$, for which we get with $[r]_b=[r,-r,r,-r]$

$$Q_{\vec{N}[r]_b\sigma}(y)=\exp\left[-\mathrm{i}\frac{2\pi}{L_y}\mathrm{sgn}(r)\,(N_\sigma-N_{-\sigma})\,y\right].$$

We can now restrict our further analysis to the bosonic part $M_{[r]_b[\sigma]_{f^-}}(\vec{m},\vec{m}',y)$. We are going to express the fields $\mathrm{i}\hat{\phi}_{r\sigma}(y)$ in Eq. (137b) in terms of the bosonic operators $\hat{a}_{jq}$, $\hat{a}^{\dagger}_{jq}$ and subsequent normal ordering, i.e., commuting all annihilation operators $\hat{a}_{jq}$ to the right side and all creation operators $\hat{a}^{\dagger}_{jq}$ to the left side. In a first step we use the relation

$$e^{\mathrm{i}\phi_l(y)}e^{\mathrm{i}\hat{\phi}^{\dagger}_l(y)}=e^{\mathrm{i}\hat{\phi}^{\dagger}_l(y)}e^{\mathrm{i}\hat{\phi}_l(y)}e^{[\mathrm{i}\hat{\phi}_l(y),\mathrm{i}\hat{\phi}^{\dagger}_l(y)]},$$

following from the Baker-Hausdorff formula,

$$e^{\hat{A}}e^{\hat{B}}=e^{\hat{A}+\hat{B}}e^{\frac{1}{2}[\hat{A},\hat{B}]}\ \text{ if }\ [\hat{A},\hat{B}]\in\mathbb{C},$$

to obtain from Eq. (137b)

$$M_{[l]}(\vec{m},\vec{m}',y)=C_{[l]}(y)\left\langle\vec{m}\left|e^{-\mathrm{i}\tilde{\sum}_{n=1}^{4}\hat{\phi}^{\dagger}_{l_n}(y)}e^{-\mathrm{i}\tilde{\sum}_{n=1}^{4}\hat{\phi}_{l_n}(y)}\right|\vec{m}'\right\rangle, \tag{139}$$

where $\tilde{\sum}_{l=1}^{4}\hat{\phi}_{l_n}$ denotes the sum $\hat{\phi}_{l_1}+\hat{\phi}_{l_2}-\hat{\phi}_{l_3}-\hat{\phi}_{l_4}$ and

$$C_{[l]}(y)=e^{[\mathrm{i}\hat{\phi}_{l_3}(y),\mathrm{i}\hat{\phi}^\dagger_{l_4}(y)]}e^{[-\mathrm{i}\hat{\phi}_{l_2}(y),\mathrm{i}\hat{\phi}^\dagger_{l_3}(y)+\mathrm{i}\hat{\phi}^\dagger_{l_4}(y)]}e^{[-\mathrm{i}\hat{\phi}_{l_1}(y),-\mathrm{i}\hat{\phi}^\dagger_{l_2}(y)+\mathrm{i}\hat{\phi}^\dagger_{l_3}(y)+\mathrm{i}\hat{\phi}^\dagger_{l_4}(y)]}.$$

With the definition Eq. (136c) of the boson fields, we can easily derive the anti-commutator relation

$$\left[\mathrm{i}\hat{\phi}_{r\sigma}(y),\mathrm{i}\hat{\phi}^\dagger_{r'\sigma'}(y')\right]=-\delta_{\sigma,\sigma'}\sum_{q>0}\frac{e^{\mathrm{i}q(ry-r'y')}}{n_q}, \tag{140}$$

which allows us to simplify for $S_r=b$, $S_\sigma=f^-$:

$$\begin{aligned}C_{[r]_b[\sigma]_{f^-}}(y)&=e^{[-\mathrm{i}\hat{\phi}_{-r\sigma}(y),\mathrm{i}\hat{\phi}^\dagger_{r\sigma}(y)]}e^{[-\mathrm{i}\hat{\phi}_{r\sigma}(y),\mathrm{i}\hat{\phi}^\dagger_{-r\sigma}(y)]}\\&=\frac{1}{1-e^{-2\mathrm{i}r\frac{\pi}{L_y}y}}\frac{1}{1-e^{2\mathrm{i}r\frac{\pi}{L_y}y}}=\frac{1}{4\sin^2(\pi y/L_y)}.\end{aligned}$$

Applying the Baker-Hausdorff formula once more, we obtain further for the second contribution to Eq. (139)

$$e^{-\mathrm{i}\tilde{\sum}_{n=1}^{4}\hat{\phi}^\dagger_{l_n}(y)}e^{-\mathrm{i}\tilde{\sum}_{n=1}^{4}\hat{\phi}_{l_n}(y)}=e^{-\mathrm{i}\tilde{\sum}_{n=1}^{4}\left(\hat{\phi}_{l_n}(y)+\hat{\phi}^\dagger_{l_n}(y)\right)}e^{\frac{1}{2}\left[\mathrm{i}\tilde{\sum}_{n=1}^{4}\hat{\phi}^\dagger_{l_n}(y),\mathrm{i}\tilde{\sum}_{n'=1}^{4}\hat{\phi}_{l_{n'}}(y)\right]}.$$

Using the definition Eq. (136c) together with the transformation between the operators $\hat{b}_{\sigma q}$ and $\hat{a}_{jq}$, Eq. (80a), we get

$$\mathrm{i}\hat{\phi}_{r\sigma}(y)+\mathrm{i}\hat{\phi}^\dagger_{r\sigma}(y)=\sum_{jq>0}\left(\lambda^{jq}_{r\sigma}(y)\hat{a}_{jq}-\lambda^{*jq}_{r\sigma}(y)\hat{a}^\dagger_{jq}\right). \tag{141}$$

In terms of Λ^j_σ, B_{jq} and D_{jq}, which were introduced in Sect. 4.2.3, the coefficients $\lambda^{jq}_{r\sigma}(x)$ read

$$\lambda^{jq}_{r\sigma}(y)=\frac{\Lambda^j_\sigma}{\sqrt{n_q}}\left(e^{\mathrm{i}\mathrm{sgn}(r)qy}B_{jq}-e^{-\mathrm{i}\mathrm{sgn}(r)qy}D_{jq}\right), \tag{142}$$

and plugging in the corresponding values, cf. Eqs. (80b), (80c) and (80d), it is easy to calculate

$$\tilde{\lambda}^{jq}_{[l]}(y):=-\tilde{\sum}_{n=1}^{4}\lambda^{jq}_{l_n}(y) \tag{143}$$

for $[l]=[r]_b[\sigma]_{f^-}$. We find that

$$\tilde{\lambda}^{cq}_{[r]_b[\sigma]_{f^-}}(y)=0\,,\quad \tilde{\lambda}^{sq}_{[r]_b[\sigma]_{f^-}}(y)=-2\mathrm{i}\sqrt{\frac{2}{n_q}}\mathrm{sgn}(r\sigma)\Big(\underbrace{B_{sq}}_{\approx 1}+\underbrace{D_{sq}}_{\approx 0}\Big)\sin(qy).$$

Again using the Baker-Hausdorff formula, we arrive at

$$e^{-\mathrm{i}\tilde{\sum}_{n=1}^{4}\left(\hat{\phi}_{l_n}(y)+\hat{\phi}^\dagger_{l_n}(y)\right)}=e^{-\frac{1}{2}\sum_{q>0}\left|\tilde{\lambda}^{sq}_{[r]_b[\sigma]_{f^-}}(y)\right|^2}e^{-\sum_{q>0}\tilde{\lambda}^{*sq}_{[r]_b[\sigma]_{f^-}}(y)\hat{a}^\dagger_{sq}}e^{\sum_{q>0}\tilde{\lambda}^{sq}_{[r]_b[\sigma]_{f^-}}(y)\hat{a}_{sq}},$$

such that in total

$$\left\langle \vec{m} \left| e^{-\mathrm{i}\tilde{\sum}_{n=1}^{4}\hat{\phi}^{\dagger}_{r_n\sigma_n}(y)} e^{-\mathrm{i}\tilde{\sum}_{n=1}^{4}\hat{\phi}_{r_n\sigma_n}(y)} \right| \vec{m}' \right\rangle = \delta_{\vec{m}_c,\vec{m}'_c} A_{[r]_b[\sigma]_{f^-}}(y) \prod_q F(\tilde{\lambda}^{sq}_{[r]_b[\sigma]_{f^-}}(y), m_{sq}, m'_{sq}), \quad (144)$$

where we have introduced

$$A_{[r]_b[\sigma]_{f^-}}(y) := e^{\frac{1}{2}\left[\mathrm{i}\tilde{\sum}_{n=1}^{4}\hat{\phi}^{\dagger}_{r_n\sigma_n}(y), \mathrm{i}\tilde{\sum}_{n'=1}^{4}\hat{\phi}_{r_{n'}\sigma_{n'}}(y)\right]} e^{-\frac{1}{2}\sum_{q>0}\left|\tilde{\lambda}^{sq}_{[r]_b[\sigma]_{f^-}}(y)\right|^2}.$$

An explicit evaluation shows

$$A_{[r]_b[\sigma]_{f^-}}(y) = e^{\sum_{q>0}\frac{1}{nq}\left(2-e^{-2\mathrm{i}rqy}-e^{2\mathrm{i}rqy}\right)} e^{-4\sum_{q>0}\frac{1}{nq}\sin^2(qy)} = 1.$$

The function $F(\lambda, m_{sq}, m'_{sq}) = \left\langle \vec{m}_s \left| e^{-\lambda^*\hat{a}^{\dagger}_{sq}} e^{\lambda\hat{a}_{sq}} \right| \vec{m}'_s \right\rangle$ is given by [114, 103]

$$F(\lambda, m, m') = \left(\Theta(m'-m)\lambda^{m'-m} + \Theta(m-m')\left(-\lambda^*\right)^{m-m'}\right) \times \sqrt{\frac{m_{min}!}{m_{max}!}} \sum_{l=0}^{m_{min}} \frac{\left(-|\lambda|^2\right)^l}{l!(l+m_{max}-m_{min})!} \frac{m_{max}!}{(m_{min}-l)!}, \quad (145)$$

where $m_{min/max} = \min / \max(m, m')$. Combining Eq. (139) and Eq. (144) we finally obtain

$$M_{[r]_b[\sigma]_{f^-}}(\vec{m}, \vec{m}', y) = \delta_{\vec{m}_c,\vec{m}'_c} \frac{1}{4\sin^2(\pi y/L_y)} \prod_q F(\tilde{\lambda}^{sq}_{[r]_b[\sigma]_{f^-}}(y), m_{sq}, m'_{sq}). \quad (146)$$

Altogether, we get with Eqs. (138), (146) to an expression for the matrix elements of $\hat{V}^{\mathrm{b-b}}_{n\rho\rho}$ away from half-filling,

$$\left\langle \vec{N}\vec{\sigma}^{\mathrm{e}}\vec{m} \left| \hat{V}^{\mathrm{b-b}}_{n\rho\rho} \right| \vec{N}'\vec{\sigma}^{\mathrm{e}\prime}\vec{m}' \right\rangle = \left\langle \vec{N}\vec{\sigma}^{\mathrm{e}}\vec{m} \left| \hat{V}^{\mathrm{b-b}}_{bf^-} \right| \vec{N}'\vec{\sigma}^{\mathrm{e}\prime}\vec{m}' \right\rangle = \frac{u}{2L_y}\delta_{\vec{N},\vec{N}'}\delta_{\vec{m}_c,\vec{m}'_c}\delta_{\vec{\sigma}^{\mathrm{e}},\vec{\sigma}^{\mathrm{e}\prime}} \sum_{r\sigma}\int \mathrm{d}y \frac{Q_{\vec{N}[r]_b\sigma}(y)}{4\sin^2(\pi y/L_y)} \prod_q F(\tilde{\lambda}^{sq}_{[r]_b[\sigma]_{f^-}}(y), m_{sq}, m'_{sq}). \quad (147)$$

For $\sum_q \left|m_{sq} - m'_{sq}\right| \leq 1$, the evaluation of Eq. (147) is problematic as the divergence arising from $1/[4\sin^2(\pi y/L_y)]$ remains uncompensated. Hence, the evaluation of the corresponding matrix elements needs special care. The origin of this divergence lies in the fact that, if no bosonic excitations are present, the $\vec{N}$ conserving processes depend on the total number of electrons in the single branches [compare to the fermionic contributions to $\hat{H}_0 + \hat{V}_{\rho\rho}$ in Eq. (79)]. Since the bosonisation approach requires the assumption of an infinitely deep Fermi sea [111], this leads, without the correct regularisation, necessarily to divergences. These findings are in complete analogy to the theory for SWCNTs [103]. In the following we exemplify the proper calculation for $\left\langle \vec{N}\vec{m} \left| \hat{V}^{\mathrm{b-b}}_{bf^-} \right| \vec{N}\vec{m} \right\rangle$, resulting in Eq. (148).

Regularisation of $M_{[r]_b[\sigma]_{f^-}}(\vec{N},\vec{\sigma}^{\mathrm{e}},\vec{m},\vec{N}',\vec{\sigma}^{\mathrm{e}\prime},\vec{m}',y)$ ***for*** $\vec{m}=\vec{m}'$ Regularisation for the matrix elements of the non-density-density bulk-bulk interaction is needed in case of $\sum_{jq}|m_{jq}-m'_{jq}|<2$, since in that situation $M_{[r]_b[\sigma]_{f^-}}(\vec{N},\vec{\sigma}^{\mathrm{e}},\vec{m},\vec{N}',\vec{\sigma}^{\mathrm{e}\prime},\vec{m}',y)$ diverges due to the factor $1/4\sin^2(\frac{\pi}{L_y}y)$ in Eq. (146).
Here we show the details of the proper regularisation for $\vec{m}=\vec{m}'$. In this case we make the expansion

$$\prod_q F(\tilde{\lambda}^{sq}_{[r]_b[\sigma]_{f^-}}(y),\vec{m},\vec{m})=1+\mathcal{O}(\sin^2),$$

where $\mathcal{O}(\sin^2)$ contains only terms $\prod_q(\sin(qy))^{t_q}$ with $\sum_q t_q\geq 2$ and which 'cure' the $1/\sin^2(\pi y/L_y)$ divergence appearing in $M_{[r]_b[\sigma]_{f^-}}(\vec{N},\vec{m},\vec{m},y)$. Therefore we are, compare to Eq. (147), left with the regularisation of

$$\frac{Q_{\vec{N}[r]_b\sigma}(y)}{4\sin^2(\pi y/L_y)}=\frac{e^{-\mathrm{i}\frac{2\pi}{L_y}r(N_\sigma-N_{-\sigma})y}}{4\sin^2(\pi y/L_y)}=\frac{e^{-2\mathrm{i}\frac{\pi}{L_y}rN_\sigma y}}{1-e^{\mathrm{i}r\frac{2\pi}{L_y}y}}\frac{e^{2\mathrm{i}\frac{\pi}{L_y}rN_{-\sigma}y}}{1-e^{-\mathrm{i}r\frac{2\pi}{L_y}y}},$$

with the second equality obtained following [103]. Using further

$$\sum_{n=-\infty}^{N}e^{-\mathrm{i}nx}=\frac{e^{-\mathrm{i}Nx}}{1-e^{\mathrm{i}x}},$$

this leads to

$$\frac{Q_{\vec{N}[r]_b\sigma}(y)}{4\sin^2(\pi y/L_y)}=\sum_{n=-\infty}^{N_\sigma}e^{-\mathrm{i}nr\frac{2\pi}{L_y}y}\sum_{n'=-\infty}^{N_{-\sigma}}e^{\mathrm{i}n'r\frac{2\pi}{L_y}y}.$$

Integration over y brings us to

$$\int\mathrm{d}y\,\frac{Q_{\vec{N}[r]_b\sigma}(y)}{4\sin^2(\pi y/L_y)}=\sum_{n=-\infty}^{N_\sigma}\sum_{n'=-\infty}^{N_{-\sigma}}L_y\,\delta_{n,n'}=L_y\min(N_\sigma,N_{-\sigma}).$$

Summarising, the regularised form of Eq. (147) is:

$$\left\langle\vec{N}\vec{\sigma}^{\mathrm{e}}\vec{m}\left|\hat{V}^{\mathrm{b-b}}_{bf^-}\right|\vec{N}'\vec{\sigma}^{\mathrm{e}}\vec{m}\right\rangle=u\,\delta_{\vec{N},\vec{N}'}\delta_{\vec{\sigma}^{\mathrm{e}},\vec{\sigma}^{\mathrm{e}\prime}}\left[\sum_\sigma\min(N_\sigma,N_{-\sigma})\right.$$
$$\left.+\frac{1}{2L_y}\sum_{r\sigma}\int\mathrm{d}y\,\frac{Q_{\vec{N}[r]_b\sigma}(y)}{4\sin^2(\pi y/L_y)}\prod_q\left(F(\tilde{\lambda}^{sq}_{[r]_b[\sigma]_{f^-}}(y),m_{sq},m_{sq})-1\right)\right]. \quad (148)$$

B.2 The matrix element $M^p_{r\sigma r'\sigma'}(\vec{N},\vec{\sigma}^{\mathrm{e}},\vec{m},\vec{N}',\vec{\sigma}^{\mathrm{e}\prime},\vec{m}')$

Also for the non-density-density end-bulk-scattering, we omitted some longer calculations in the main part of the text and give the detailed evaluations here. Again, the contribution was split, this time into a bosonic, an end and a fermionic part,

$$M^p_{r\sigma r'\sigma'}(\vec{N},\vec{\sigma}^{\mathrm{e}},\vec{m},\vec{N}',\vec{\sigma}^{\mathrm{e}\prime},\vec{m}')=M^p_{r\sigma r'\sigma'}(\vec{m},\vec{m}')M^p_{\sigma\sigma'}(\vec{\sigma}^{\mathrm{e}},\vec{\sigma}^{\mathrm{e}\prime})M^p_{r\sigma r'\sigma'}(\vec{N},\vec{N}'),$$

where two latter were already figured out in Sect. 4.2.3, Eqs. (84a), (84b), respectively. The calculation of the bosonic part, which was skipped in the main text, is given in the following. Explicitly, abbreviating $r\sigma$ by l and $r'\sigma'$ by l',

$$M^p_{ll'}(\vec{m},\vec{m}') = \left\langle \vec{m} \left| e^{-\mathrm{i}\hat{\phi}^\dagger_l(y_p)} e^{-\mathrm{i}\hat{\phi}_l(y_p)} e^{\mathrm{i}\hat{\phi}^\dagger_{l'}(y_p)} e^{\mathrm{i}\hat{\phi}_{l'}(y_p)} \right| \vec{m}' \right\rangle$$
$$= C_{ll'}(y_p) \left\langle \vec{m} \left| e^{-\mathrm{i}\left(\hat{\phi}^\dagger_l(y_p) - \hat{\phi}^\dagger_{l'}(y_p)\right)} e^{-\mathrm{i}\left(\hat{\phi}_l(y_p) - \hat{\phi}_{l'}(y_p)\right)} \right| \vec{m}' \right\rangle,$$

where we exploit Eq. (140) to obtain

$$C_{ll'}(y) = e^{\left[-\mathrm{i}\hat{\phi}_l(y), \mathrm{i}\hat{\phi}^\dagger_{l'}(y)\right]} = e^{\delta_{\sigma,\sigma'} \sum_{q>0} \frac{1}{n_q} e^{\mathrm{i}(r-r')qy}}$$
$$= e^{\delta_{\sigma,\sigma'} \sum_{q>0} \frac{1}{n_q} \left\{ \cos(2\delta_{r,-r'} qy) + \mathrm{isgn}(r) \sin(2\delta_{r,-r'} qy) \right\}}.$$

We can continue with the remaining exponentials as we did for the bulk-bulk scattering in App. B.1:

$$\left\langle \vec{m} \left| e^{-\mathrm{i}\left(\hat{\phi}^\dagger_l(y) - \hat{\phi}^\dagger_{l'}(y)\right)} e^{-\mathrm{i}\left(\hat{\phi}_l(y) - \hat{\phi}_{l'}(y)\right)} \right| \vec{m}' \right\rangle$$
$$= e^{\frac{1}{2}\left[\mathrm{i}\{\hat{\phi}^\dagger_l(y) - \hat{\phi}^\dagger_{l'}(y)\}, \mathrm{i}\{\hat{\phi}_l(y) - \hat{\phi}_{l'}(y)\}\right]} \left\langle \vec{m} \left| e^{-\mathrm{i}\left(\{\hat{\phi}^\dagger_l(y) + \hat{\phi}_l(y)\} - \{\hat{\phi}^\dagger_{l'}(y) + \hat{\phi}_{l'}(y)\}\right)} \right| \vec{m}' \right\rangle$$
$$= A_{ll'}(y) \left\langle \vec{m} \left| e^{-\sum_{j,q>0} \tilde{\lambda}^{*jq}_{ll'}(y) \hat{a}^\dagger_{jq}} e^{\sum_{j,q>0} \tilde{\lambda}^{jq}_{ll'}(y) \hat{a}_{jq}} \right| \vec{m}' \right\rangle = A_{ll'}(y) \prod_{j,q>0} F(\tilde{\lambda}^{jq}_{ll'}(y), m_{jq}, m'_{jq}).$$

Here, we employed the function $F(\lambda, m, m')$ as defined in App. B.1, Eq. (145), and

$$A_{ll'}(y) = e^{\frac{1}{2}\left[\mathrm{i}\left(\hat{\phi}^\dagger_l(x) - \hat{\phi}^\dagger_{l'}(x)\right), \mathrm{i}\left(\hat{\phi}_l(x) - \hat{\phi}_{l'}(x)\right)\right]} e^{-\frac{1}{2}\sum_{jq} \left|\tilde{\lambda}^{jq}_{ll'}\right|^2}$$
$$= e^{\sum_{q>0} \frac{1}{n_q}(1 - \delta_{\sigma,\sigma'} \cos(2\delta_{r,r'} qy))} e^{-\frac{1}{2}\sum_{jq} \left|\tilde{\lambda}^{jq}_{ll'}(y)\right|^2},$$

such that

$$A_{ll'}(y) C_{ll'}(y) = e^{\sum_{q>0} \frac{1}{n_q}\left(1 + \mathrm{i}\delta_{r,-r'} \mathrm{sgn}(r) \sin(2qy)\right)} e^{-\frac{1}{2}\sum_{jq} \left|\tilde{\lambda}^{jq}_{ll'}\right|^2}. \tag{149}$$

Further, we set in Eq. (142) to expand

$$\tilde{\lambda}^{jq}_{ll'}(y) := -\lambda^{jq}_l(y) + \lambda^{jq}_{l'}(y)$$
$$= \frac{1}{\sqrt{n_q}} \left[B_{jq} \left(\Lambda^j_{\sigma'} e^{\mathrm{isgn}(r')qy} - \Lambda^j_\sigma e^{\mathrm{isgn}(r)qy} \right) - D_{jq} \left(\Lambda^j_{\sigma'} e^{-\mathrm{isgn}(r')qy} - \Lambda^j_\sigma e^{-\mathrm{isgn}(r)qy} \right) \right].$$

For our matrix element $M^p_{ll'}(\vec{m},\vec{m}')$ we have only to consider the two cases $y = y_- = 0$ and $y = y_+ = L_y$, where the expression simplifies under application of Eqs. (80b), (80c) along with $\sin(0) = \sin(\pm qL_y) = 0,\ \cos(0) = 1,\ \cos(\pm qL_y) = -1$ to

$$\tilde{\lambda}^{jq}_{ll'}(y_p) = \delta_{j,s} \delta_{\sigma,-\sigma'} \mathrm{sgn}(p\sigma) \sqrt{2/n_q}.$$

Using this result in Eq. (149) yields

$$A_{ll'}(y_p) C_{ll'}(y_p) = \begin{cases} const. & \sigma' = \sigma, \\ 1 & \sigma' = -\sigma. \end{cases}$$

With this ingredients we arrive eventually at the result crucial for the main part of the text,

$$M^p_{ll'}(\vec{m},\vec{m}') = \begin{cases} const. & \sigma' = \sigma, \\ \delta_{\vec{m}_c,\vec{m}'_c} \prod_{q>0} F(\mathrm{sgn}(p\sigma)\sqrt{2/n_q}, m_{sq}, m'_{sq}) & \sigma' = -\sigma. \end{cases} \tag{150}$$

References

[1] M. Riordan, L. Hoddeson, and C. Herring, *The invention of the transistor*, Rev. Mod. Phys. **71**, S336 (1999).

[2] W. F. Brinkman and D. V. Lang, *Physics and the communications industry*, Rev. Mod. Phys. **71**, S480 (1999).

[3] L. A. Ponomarenko, F. Schedin, M. I. Katsnelson, R. Yang, E. W. Hill, K. S. Novoselov, and A. K. Geim, *Chaotic Dirac billiard in graphene quantum dots*, Science **320**, 356 (2008).

[4] G. Ingold and Y. V. Nazarov, *Charge tunneling rates in ultrasmall junctions*, in *Single charge tunneling*, edited by H. Grabert and M. H. Devoret, Plenum Press, New York, 1992.

[5] Y. Alhassid, *The statistical theory of quantum dots*, Rev. Mod. Phys. **72**, 895 (2000).

[6] J. M. Thijssen and H. S. J. v. d. Zant, *Charge transport and single-electron effects in nanoscale systems*, Phys. Stat. Sol. (b) **245**, 1455 (2008).

[7] R. Hanson, L. P. Kouwenhoven, J. R. Petta, S. Tarucha, and L. M. Vandersypen, *Spins in few electron quantum dots*, Rev. Mod. Phys. **79**, 1217 (2007).

[8] M. Biercuk, S. Ilani, C. Marcus, and P. McEuen, *Electrical Transport in Single-Wall Carbon Nanotubes*, in *Carbon Nanotubes*, edited by A. Jorio, G. Dresselhaus, and M. S. Dresselhaus, Springer, 2008.

[9] E. Osorio, T. Bjornholm, J.-M. Lehn, M. Ruben, and H. v. d. Zant, *Single-molecule transport in three-terminal devices*, Jour. Phys. Cond. Mat. **20**, 374121 (2008).

[10] L. P. Kouwenhoven, C. M. Marcus, P. L. McEuen, S. Tarucha, R. M. Westervelt, and N. S. Wingreen, *Electron Transport in Quantum Dots*, in *Mesoscopic electron transport*, edited by L. L. Sohn, L. P. Kouwenhoven, and G. Schön, Kluwer, 1997.

[11] M. N. Baibich, J. M. Broto, A. Fert, F. N. v. Dau, F. Petroff, P. Etienne, G. Creuzet, A. Friederich, and J. Chazelas, *Giant Magnetoresistance of (001)Fe/(001)Cr Magnetic Superlattices*, Phys. Rev. Lett. **61**, 2472 (1988).

[12] G. Binasch, P. Grünberg, F. Saurenbach, and W. Zinn, *Enhanced magnetoresistance in layered magnetic structures with antiferromagnetic interlayer exchange*, Phys. Rev. B **39**, 4828 (1989).

[13] M. Leijnse, M. R. Wegewijs, and M. H. Hettler, *Pair-tunneling resonance in the single-electron transport regime*, Submitted to PRL, 2009.

[14] S. Sahoo, T. Kontos, J. Furer, C. Hoffmann, M. Gräber, A. Cottet, and C. Schönenberger, *Electric field control of spin transport*, Nat. Phys. **1**, 99 (2005).

[15] J. R. Hauptmann, J. Paaske, and P. E. Lindelof, *Electric-field-controlled spin reversal in a quantum dot with ferromagnetic contacts*, Nat. Phys **4**, 373 (2008).

[16] J. V. Holm, H. I. Jørgensen, K. Grove-Rasmussen, J. Paaske, K. Flensberg, and P. E. Lindelof, *Gate-dependent tunneling-induced level shifts observed in carbon nanotube quantum dots*, Phys. Rev. B **77**, 161406(R) (2008).

[17] J. Kondo, *Resistance Minimum in Dilute Magnetic Alloys*, Prog. Theor. Phys. **32**, 37 (1964).

[18] M. Pustilnik and L. Glazman, *Kondo effect in quantum dots*, J. Phys. Condens. Matter **16**, R513 (2004).

[19] H. Schoeller, *Transport theory of interacting quantum dots*, in *Mesoscopic Electron Transport*, edited by L. L. Sohn, L. P. Kouwenhoven, and G. Schön, Kluwer, 1997.

[20] KinEq is a C++ application initiated by and developed in collaboration with Martin Leijnse and Maarten Wegewijs. It implements the transport theory presented in Sect. 1 of this thesis, thereby keeping as much generality as possible. To be independent of the particular type of quantum-dot system studied, external supply of precalculated model specific spectrum data and tunnelling matrix elements is required.

[21] H. Bruus and K. Flensberg, *Many-Body Quantum Theory in Condensed Matter Physics* (Oxford University Press, Oxford, 2004).

[22] H. Kreuzer, *Nonequilibrium Thermodynamics and its Statistical Foundations* (Oxford University Press, Oxford, 1981).

[23] B. Wunsch, M. Braun, J. König, and D. Pfannkuche, *Probing level renormalization by sequential transport through double quantum dots*, Phys. Rev. B **72**, 205319 (2005).

[24] U. Harbola, M. Esposito, and S. Mukamel, *Quantum master equation for electron transport through quantum dots and single molecules*, Phys. Rev. B **74**, 235309 (2006).

[25] L. Mayrhofer and M. Grifoni, *Non-Fermi liquid behaviour in transport across carbon nanotube quantum dots*, Phys. Rev. B **74**, 121403(R) (2006).

[26] A. Donarini, M. Grifoni, and K. Richter, *Dynamical Symmetry Breaking in Transport through Molecules*, Phys. Rev. Lett. **97**, 166801 (2006).

[27] G. Begemann, D. Darau, A. Donarini, and M. Grifoni, *Symmetry fingerprints of a benzene single-electron transistor*, Phys. Rev. B **77**, 201406(R) (2008).

[28] M. Braun, J. König, and J. Martinek, *Theory of Transport through Quantum-Dot Spin Valves in the Weak-Coupling Regime*, Phys. Rev. B **70**, 195345 (2004).

[29] W. Wetzels, G. E. W. Bauer, and M. Grifoni, *Exchange effects on electron transport through single-electron spin-valve transistors*, Phys. Rev. B **74**, 224406 (2006).

[30] I. Weymann and J. Barnas, *Cotunneling through quantum dots coupled to magnetic leads: Zero-bias anomaly for noncollinear magnetic configurations*, Phys. Rev. B **75**, 155308 (2007).

[31] S. Koller, L. Mayrhofer, and M. Grifoni, *Spin transport across carbon nanotube quantum dots*, New J. Phys. **9**, 348 (2007).

[32] R. P. Hornberger, S. Koller, G. Begemann, A. Donarini, and M. Grifoni, *Transport through a double-quantum-dot system with noncollinearly polarized leads*, Phys. Rev. B **77**, 245313 (2008).

[33] C. Timm, *Tunneling through molecules and quantum dots: Master-equation approaches*, Phys. Rev. B **77**, 195416 (2008).

[34] K. Blum, *Density Matrix Theory and Applications* (Plenum Press, New York, 1996).

[35] S. Nakajima, *On Quantum Theory of Transport Phenomena*, Prog. Theor. Phys. **20**, 948 (1958).

[36] R. Zwanzig, *Ensemble method in the theory of irreversibility*, J. Chem. Phys. **33**, 1338 (1960).

[37] P. Breuer and F. Petruccione, *The Theory of Open Quantum Systems* (Oxford University Press, Oxford, 2002).

[38] E. Fick and G. Sauermann, *The Quantum Statistics of Dynamical Processes* (Springer, Berlin, 1990).

[39] H. Schoeller and G. Schön, *Mesoscopic quantum transport: Resonant tunneling in the presence of a strong Coulomb interaction*, Phys. Rev. B **50**, 18436 (1994).

[40] J. König, H. Schoeller, and G. Schön, *Cotunneling at Resonance for the Single-Electron Transistor*, Phys. Rev. Lett. **78**, 4482 (1997).

[41] C. Timm, *Tunneling through magnetic molecules with arbitrary angle between easy axis and magnetic field*, Phys. Rev. B **76**, 014421 (2007).

[42] R. K. Wangsness and F. Bloch, *The Dynamical Theory of Nuclear Induction*, Phys. Rev. **89**, 728 (1953).

[43] F. Bloch, *Generalized Theory of Relaxation*, Phys. Rev. **105**, 1206 (1957).

[44] A. G. Redfield, *The theory of relaxation processes*, Adv. Magn. Reson. **1**, 1 (1965).

[45] B. B. Laird, J. Budimir, and J. L. Skinner, *Quantum-mechanical derivation of the bloch equations: Beyond the weak-coupling limit*, J. Chem. Phys. B **9**, 4391 (1990).

[46] M. Governale, M. G. Pala, and J. König, *Real-time diagrammatic approach to transport across interacting quantum dots with normal and superconducting leads*, Phys. Rev. B **77**, 134513 (2008).

[47] M. Leijnse and M. R. Wegewijs, *Kinetic equations for transport through single-molecule transistors*, Phys. Rev. B **78**, 235424 (2008).

[48] J. König, H. Schoeller, and G. Schön, *Resonant tunneling and Coulomb Oscillations*, EPL **31**, 31 (1995).

[49] J. König, J. Schmid, H. Schoeller, and G. Schön, *Resonant tunneling through ultrasmall quantum dots: Zero-bias anomalies, magnetic-field dependence, and boson-assisted transport*, Phys. Rev. B **54**, 16820 (1996).

[50] J. König, H. Schoeller, and G. Schön, *Zero-Bias Anomalies and Boson-Assisted Tunneling Through Quantum Dots*, Phys. Rev. Lett. **76**, 1715 (1996).

[51] M. Abramowitz and I. A. Stegun, *Handbook of mathematical functions* (Dover publications, Inc., New York, 1965).

[52] J. Koch, F. v. Oppen, and A. V. Andreev, *Theory of the Franck-Condon blockade regime*, Phys. Rev. B **74**, 205438 (2006).

[53] M. Turek and K. A. Matveev, *Cotunneling thermopower of single electron transistors*, Phys. Rev. B **65**, 115332 (2002).

[54] J. Koch, F. v. Oppen, Y. Oreg, and E. Sela, *Thermopower of single-molecule devices*, Phys. Rev. B **70**, 19510 (2004).

[55] J. R. Schrieffer and P. A. Wolff, *Relation between the Anderson and Kondo Hamiltonians*, Phys. Rev. **149**, 491 (1966).

[56] P. W. Anderson, *Localized Magnetic States in Metals*, Phys. Rev. **124**, 41 (1961).

[57] I. Weymann, J. König, J. Martinek, J. Barnas, and G. Schön, *Tunnel magnetoresistance of quantum dots coupled to ferromagnetic leads in the sequential and cotunneling regimes*, Phys. Rev. B **72**, 115334 (2005).

[58] D. Becker and D. Pfannkuche, *Coulomb-blocked transport through a quantum dot with spin-split level: Increase of differential conductance peaks by spin relaxation*, Phys. Rev. B **77**, 205307 (2008).

[59] W. G. v. d. Wiel, S. D. Franceschi, J. M. Elzerman, T. Fujisawa, S. Tarucha, and L. P. Kouwenhoven, *Electron transport through double quantum dots*, Rev. Mod. Phys. **75**, 1 (2002).

[60] M. R. Gräber, W. A. Coish, C. Hoffmann, M. Weiss, J. Furer, S. Oberholzer, D. Loss, and C. Schönenberger, *Molecular states in carbon nanotube double quantum dots*, Phys. Rev. B **74**, 075427 (2006).

[61] S. Sapmaz, C. Meyer, P. Beliczynski, P. Jarillo-Herrero, and L. P. Kouwenhoven, *Excited state spectroscopy in carbon nanotube double quantum dots*, Nano Lett. **6**, 1350 (2006).

[62] F. Molitor, S. Dröscher, J. Güttinger, A. Jacobsen, C. Stampfer, T. Ihn, and K. Ensslin, *Transport through graphene double dots*, Appl. Phys. Lett. **94**, 222107 (2009).

[63] S. Moriyama, D. Tsuya, E. Watanabe, S. Uji, M. Shimizu, T. Mori, T. Yamaguchi, and K. Ishibashi, *Coupled Quantum Dots in a Graphene-Based Two-Dimensional Semimetal*, Nano Lett. **9**, 2891 (2009).

[64] D. Loss and D. D. Vincenzo, *Quantum computation with quantum dots*, Phys. Rev. A **57**, 120 (1998).

[65] K. Ono, D. G. Austing, Y. Tokura, and S. Tarucha, *Current rectification by Pauli exclusion in a weakly coupled double quantum dot system*, Science **297**, 1313 (2002).

[66] A. C. Johnson, J. R. Petta, C. M. Marcus, M. P. Hanson, and A. C. Gossard, *Singlet-triplet spin blockade and charge sensing in a few-electron double quantum dot*, Phys. Rev. B **72**, 165308 (2005).

[67] H. W. Liu, T. Fujisawa, T. Hayashi, and Y. Hirayama, *Pauli spin blockade in cotunneling transport through a double quantum dot*, Phys. Rev. B **72**, 161305(R) (2005).

[68] J. Fransson and M. Råsander, *Pauli spin blockade in weakly coupled double quantum dots*, Phys. Rev. B **73**, 205333 (2006).

[69] S. Lamba and S. K. Joshi, *Transport through a coupled quantum dot system: Role of interdot interactions*, Phys. Rev. B **62**, 1580 (2000).

[70] B. R. Bułka and T. Kostyrko, *Electronic correlations in coherent transport through a two quantum dot system*, Phys. Rev. B **70**, 205333 (2004).

[71] R. Pariser and R. G. Parr, *A Semi-Empirical Theory of the Electronic Spectra and electronic Structure of complex Unsaturated Molecules II*, J. Chem. Phys. **21**, 767 (1953).

[72] J. A. Popel, *Electron interactions in unsaturated hydrocarbons*, Trans. Faraday Soc. **49**, 1375 (1953).

[73] J. Aghassi, M. Hettler, and G. Schön, *Cotunneling assisted sequential tunneling in multilevel quantum dots*, APL **92**, 202101 (2008).

[74] Y.-M. Lin, K. A. Jenkins, A. Valdes-Garcia, J. P. Small, D. B. Farmer, and P. Avouris, *Operation of Graphene Transistors at Gigahertz Frequencies*, Nano Lett. **9**, 422 (2009).

[75] K. S. Novoselov, A. K. Geim, S. V. Morozov, D. Jiang, Y. Zhang, S. V. Dubonos, I. V. Grigorieva, and A. A. Firsov, *Electric field effect in atomically thin carbon films*, Science **306**, 666 (2004).

[76] V. Fal'ko1, *Graphene: Quantum information on chicken wire*, Nature Physics **3**, 151 (2007).

[77] J.-H. Chen, C. Jang, S. Xiao, M. Ishigami, and M. S. Fuhrer, *Intrinsic and extrinsic performance limits of graphene devices on SiO2*, Nature Nanotechnology **3**, 206 (2008).

[78] C. W. J. Beenakker, *Colloquium: Andreev reflection and Klein tunneling in graphene*, Rev. Mod. Phys. **80**, 1337 (2008).

[79] P. R. Wallace, *The Band Theory of Graphite*, Phys. Rev. **71**, 622 (1947).

[80] Y. Zhang, Y.-W. Tan, H. L. Stormer, and P. Kim, *Experimental observation of the quantum Hall effect and Berry's phase in graphene*, Nature **438**, 201 (2005).

[81] S. Y. Zhou, G.-H. Gweon, J. Graf, A. V. Federov, C. D. Spatura, R. D. Diehl, Y. Kopelevich, D.-H. Lee, S. G. Louie, and A. Lanzara, *First direct observation of Dirac fermions in graphite*, Nat. Phys. **2**, 595 (2006).

[82] A. Bostwick, T. Ohta, T. Seyller, H. K. Horn, and E. Rotenberg, *Quasiparticle dynamics in graphene*, Nat. Phys. **3**, 36 (2007).

[83] J. E. Han and R. J. Heary, *Imaginary-Time Formulation of Steady-State Nonequilibrium: Application to Strongly Correlated Transport*, Physical Review Letters **99**, 236808 (2007).

[84] C. Stampfer, J. Güttinger, S. Hellmüller, F. Molitor, K. Ensslin, and T. Ihn, *Energy gaps in etched graphene nanoribbons*, Nano Lett. **8**, 2378 (2008).

[85] Y.-M. Lin, V. Perebeinos, Z. Chen, and P. Avouris, *Electrical observation of subband formation in graphene nanoribbons*, Phys. Rev. B **78**, 161409(R) (2008).

[86] S. Schnez, F. Molitor, C. Stampfer, J. Güttinger, I. Shorubalko, T. Ihn, and K. Ensslin, *Observation of excited states in a graphene quantum dot*, Appl. Phys. Lett. **94**, 012107 (2009).

[87] F. G. F. Sols and A. H. Castro-Neto, *Coulomb Blockade in Graphene Nanoribbons*, Phys. Rev. Lett. **99**, 166803 (2007).

[88] M. Zarea and N. Sandler, *Electron-Electron and Spin-Orbit Interactions in Armchair Graphene Ribbons*, Phys. Rev. Lett. **99**, 256804 (2007).

[89] L. Tapaszto, G. Dobrik, P. Lambin, and L. Biro, *Tailoring the atomic structure of graphene nanoribbons by scanning tunneling microscope lithography*, Nature Nanotechnology **3**, 397 (2008).

[90] X. Yang, X. Dou, A. Rouhanipour, L. Zhi, H. J. Räder, and K. Müllen, *Two-dimensional graphene nanoribbons*, JACS **130**, 4216 (2008).

[91] L. Jiao, L. Zhang, X. Wang, G. Diankov, and H. Dai, *Narrow graphene nanoribbons from carbon nanotubes*, Nature **458**, 877 (2009).

[92] K. Nakada, M. Fujita, G. Dresselhaus, and M. S. Dresselhaus, *Edge state in graphene ribbons: Nanometer size effect and edge shape dependence*, Phys. Rev. B **54**, 17954 (1996).

[93] A. R. Akhmerov and C. W. J. Beenakker, *Boundary conditions for Dirac fermions on a terminated honeycomb lattice*, Phys. Rev. B **77**, 085423 (2008).

[94] M. Fujita, K. Wakabayashi, K. Nakada, and K. Kusakabe, *Peculiar Localized State at Zigzag Graphite Edge*, J. Phys. Soc. Jpn. **65**, 1920 (1996).

[95] Z. Klusek, W. Kozlowski, Z. Waqar, S. Datta, J. S. Burnell-Gray, I. V. Makarenko, N. R. Gall, E. V. Rutkov, A. Y. Tontegode, and A. Titko, *Local electronic edge states of graphene layer deposited on Ir(1 1 1) surface studied by STM/CITS*, Applied Surface Science **252**, 1221 (2005).

[96] Y. Kobayashi, K. Fukui, T. Enoki, and K. Kusakabe, *Edge state on hydrogen-terminated graphite edges investigated by scanning tunneling microscopy*, Phys. Rev. B **73**, 125415 (2006).

[97] Y. Niimi, T. Matsui, H. Kambara, K. Tagami, M. Tsukada, and H. Fukuyama, *Scanning tunneling microscopy and spectroscopy of the electronic local density of states of graphite surfaces near monoatomic step edges*, Phys. Rev. B **73**, 085421 (2006).

[98] Y.-W. Son, M. L. Cohen, and S. G. Louie, *Half-metallic graphene nanoribbons*, Nature **444**, 347 (2006).

[99] M. Wimmer, I. Adaglideli, S. Berber, D. Tománek, and K. Richter, *Spin currents in rough graphene nanoribbons: Universal fluctuations and spin injection*, Appl. Phys. Lett. **94**, 222107 (2009).

[100] R. Egger and A. O. Gogolin, *Effective low-energy theory for correlated carbon nanotubes*, Phys. Rev. Lett. **79**, 5082 (1997).

[101] A. A. Odintsov and H. Yoshioka, *Universality of electron correlations in conducting carbon nanotubes*, Phys. Rev. B **59**, R10457 (1999).

[102] Y. Oreg, K. Byczuk, and B. I. Halperin, *Spin Configurations of a Carbon Nanotube in a Nonuniform External Potential*, Phys. Rev. Lett. **85**, 365 (2000).

[103] L. Mayrhofer and M. Grifoni, *The spectrum of interacting metallic carbon nanotubes: exchange effects and universality*, Eur. Phys. J. B **63**, 43 (2008).

[104] L. Mayrhofer, *Spectrum and transport properties of interacting carbon nanotubes*, Doctoral thesis, Universität Regensburg, 2008.

[105] A. H. Castro-Neto, F. Guinea, N. M. R. Peres, K. S. Novoselov, and A. K. Geim, *The electronic properties of graphene*, Rev. Mod. Phys. **81**, 109 (2009).

[106] L. Brey and H. A. Fertig, *Electronic states of graphene nanoribbons studied with the Dirac equation*, Phys. Rev. B **73**, 235411 (2006).

[107] H. Lee, Y.-W. Son, N. Park, S. Han, and J. Yu, *Magnetic ordering at the edges of graphitic fragments: Magnetic tail interactions between the edge-localized states*, Phys. Rev. B **72**, 174431 (2005).

[108] W. Barford, *Electronic and Optical Properties of Conjugated Polymers* (Clarendon Press, Oxford, 2005).

[109] P. Fulde, *Electron Correlations in Molecules and Solids* (Springer, Berlin, 1995).

[110] Calculation performed by Leonhard Mayrhofer. A dielectric constant $\epsilon = 1.4$ was assumed.

[111] J. v. Delft and H. Schoeller, *Bosonization for beginners - refermionization for experts*, Annalen Phys. **7**, 225 (1998).

[112] L. Mayrhofer, private discussion.

[113] J. Avery, *Creation and Annihilation Operators* (McGraw-Hill, New York, 1976).

[114] L. Mayrhofer and M. Grifoni, *Linear and non-linear transport across carbon nanotube quantum dots*, Europ. Phys. J. B **56**, 107 (2007).

[115] A. Donarini, private discussion.

[116] M. Leijnse and M. Wegewijs, private discussion.

[117] S. Koller, L. Mayrhofer, and M. Grifoni, *Graphene armchair nanoribbon single-electron transistors: the peculiar influence of end states*, EPL **88**, 57001 (2009).

[118] S. Koller, L. Mayrhofer, and M. Grifoni, *Spin-dependent transport through interacting graphene armchair nanoribbons*, New J. Phys. (2010), in press. [arXiv:0910.5265].

[119] The picture was extracted from a larger image provided by Michael Ströck under GDFL (2006).
`http://en.wikipedia.org/wiki/Image:Types_of_Carbon_Nanotubes.png`.

[120] S. Iijima and T. Ichihashi, *Single-shell carbon nanotubes of 1-nm diameter*, Nature **363**, 603 (1993).

[121] R. Saito, G. Dresselhaus, and M. Dresselhaus, *Physical Properties of Carbon Nanotubes* (Imperial College Press, London, 1998).

[122] S. Berber, Y.-K. Kwon, and D. Tománek, *Unusually High Thermal Conductivity of Carbon Nanotubes*, Phys. Rev. Lett. **84**, 4613 (2000).

[123] M. Mintmire, B. I. Dunlap, and C. T. White, *Are Fullerene Tubules Metallic?*, Phys. Rev. Lett. **68**, 631 (1992).

[124] M. Bockrath, D. H. Cobden, J. Lu, A. G. Rinzler, R. E. Smalley, L. Balents, and P. L. McEuen, *Luttinger-liquid behaviour in carbon nanotubes*, Nature **397**, 598 (1999).

[125] H. Ishii, H. Kataura, H. Shiozawa, H. Yoshioka, H. Otsubo, Y. Takayama, T. Miyahara, S. Suzuki, Y. Achiba, M. Nakatake, T. Narimura, M. Higashiguchi, K. Shimada, H. Namatame, and M. Taniguchi, *Direct observation of Tomonaga-Luttinger-liquid state in carbon nanotubes at low temperatures*, Nature **462**, 540 (2003).

[126] J. Nygård, D. H. Cobden, and P. E. Lindelof, *Kondo physics in carbon nanotubes*, Nature **408**, 342 (2000).

[127] P. Jarillo-Herrero, J. Kong, H. S. J. v. d. Zant, C. Dekker, L. P. Kouwenhoven, and S. D. Franceschi, *Orbital Kondo effect in carbon nanotubes*, Nature **434**, 484 (2005).

[128] S. Sapmaz, P. Jarillo-Herrero, Y. Blanter, C. Dekker, and H. S. J. v. d. Zant, *Tunneling in Suspended Carbon Nanotubes Assisted by Longitudinal Phonons*, Phys. Rev. Lett. **96**, 026801 (2006).

[129] A. K. Huettel, B. Witkamp, M. Leijnse, M. R. Wegewijs, and H. S. J. v. d. Zant, *Pumping of vibrational excitations in a Coulomb blockaded suspended carbon nanotube*, Phys. Rev. Lett. **102**, 225501 (2009).

[130] R. Leturcq, C. Stampfer, K. Inderbitzin, L. Durrer, C. Hierold, E. Mariani, M. G. Schultz, F. v. Oppen, and K. Ensslin, *Franck-Condon blockade in suspended carbon nanotube quantum dots*, Nature Physics **5**, 327 (2009).

[131] F. Kuemmeth, S. Ilani, D. Ralph, and P. L. McEuen, *Coupling of spin and orbital motion of electrons in carbon nanotubes*, Nature **452**, 448 (2008).

[132] S. H. Jhang, M. Marganska, Y. Skourski, D. Preusche, B. Witkamp, M. Grifoni, H. S. J. v. d. Zant, J. Wosnitza, and C. Strunk, *Spin polarization by spin-orbit interaction in chiral carbon nanotubes*, Submitted to Nature Physics, 2009.

[133] V. V. Deshpande, B. Chandra, R. Caldwell, D. S. Novikov, J. Hone, and M. Bockrath, *Mott insulating state in ultraclean carbon nanotubes*, Science **323**, 106 (2009).

[134] A. Y. Kasumov, R. Deblock, M. Kociak, B. Reulet, H. Bouchiat, I. I. Khodos, Y. B. Gorbatov, V. T. Volkov, C. Journet, and M. Burghard, *Supercurrents Through Single-Walled Carbon Nanotubes*, Science **284**, 1508 (1999).

[135] A. F. Morpurgo, J. Kong, C. M. Marcus, and H. Dai, *Gate-Controlled Superconducting Proximity Effect in Carbon Nanotubes*, Science **286**, 263 (1999).

[136] J.-P. Cleuziou, W. Wernsdorfer, V. Bouchiat, T. Ondarçuhu, and M. Monthioux, *Carbon nanotube superconducting quantum interference device*, Nature Nanotechnology **1**, 53 (2006).

[137] P. Jarillo-Herrereo, J. A. v. Dam, and L. P. Kouwenhoven, *Quantum supercurrent transistors in carbon nanotubes*, Nature **439**, 953 (2006).

[138] E. Pallecchi, M. Gaass, D. Ryndyk, and C. Strunk, *Carbon Nanotube Quantum Dots with Nb Contacts*, Appl. Phys. Lett. **93**, 072501 (2008).

[139] A. Cottet, T. Kontos, S. Sahoo, H. T. Man, M.-S. Choi, W. Belzig, C. Bruder, A. F. Morpurgo, and C. Schönenberger, *Nanospintronics with carbon nanotubes*, Semicond. Sci. Technol. **21**, S78 (2006).

[140] H. T. Man, I. J. W. Wever, and A. F. Morpurgo, *Spin-dependent quantum interference in single-wall carbon nanotubes with ferromagnetic contacts*, Phys. Rev. B **73**, 241401(R) (2006).

[141] S. Moriyama, T. Fuse, M. Suzuki, Y. Aoyagi, and K. Ishibashi, *Four-Electron Shell Structures and an Interacting Two-Electron System in Carbon-Nanotube Quantum Dots*, Phys. Rev. Lett. **94**, 186806 (2005).

[142] S. Sapmaz, P. Jarillo-Herrero, J. Kong, C. Dekker, L. P. Kouwenhoven, and H. S. J. v. d. Zant, *Electronic excitation spectrum of metallic carbon nanotubes*, Phys. Rev. B **71**, 153402 (2005).

[143] W. Liang, M. Bockrath, and H. Park, *Shell filling and exchange coupling in metallic single-walled carbon nanotubes*, Phys. Rev. Lett. **88**, 126801 (2002).

[144] C. Schenke, S. Koller, L. Mayrhofer, and M. Grifoni, *Exchange effects in spin polarized transport through carbon nanotube quantum dots*, Phys. Rev. B **80**, 035412 (2009).

[145] H. Yoshioka and A. Odintsov, *Electronic Properties of Armchair Carbon Nanotubes: Bosonization Approach*, Phys. Rev. Lett. **82**, 374 (1999).

[146] D. H. Cobden and J. Nygård, *Shell Filling in Closed Single-Wall Carbon Nanotube Quantum Dots*, Phys. Rev. Lett. **89**, 046803 (2002).

[147] S. Moriyama, T. Fuse, Y. Aoyagi, and K. Ishibashi, *Excitation spectroscopy of two-electron shell structures in carbon nanotube quantum dots in magnetic field*, Appl. Phys. Lett. **87**, 073103 (2005).

[148] A. Makarovski, L. An, J. Liu, and G. Finkelstein, *Persistent orbital degeneracy in carbon nanotubes*, Phys. Rev. B **74**, 155431 (2006).

[149] A. Cottet and M.-S. Choi, *Magnetoresistance of a quantum dot with spin-active interfaces*, Phys. Rev. B **74**, 235316 (2006).

[150] B. Kubala and J. König, *Quantum-fluctuation effects on the thermopower of a single-electron transistor*, Phys. Rev. B **73**, 195316 (2006).